Transactions of the ASME®

Transactions of the ASME, Journal of Turbomachinery (ISSN 0889-504X) is published quarterly (Jan., Apr., July, Oct.) for $125.00 per year by The American Society of Mechanical Engineers, 345 East 47th Street, New York, NY 10017. Second class postage paid at New York, NY and additional mailing offices. POSTMASTER: Send address change to Transactions of the ASME, Journal of Turbomachinery, c/o THE AMERICAN SOCIETY OF MECHANICAL ENGINEERS, 22 Law Drive, Box 2300, Fairfield, NJ 07007-2300.

CHANGES OF ADDRESS must be received at Society headquarters seven weeks before they are to be effective. Please send old label and new address.

PRICES: To members, $36.00, annually; to nonmembers, $125.00. Add $15.00 for postage to countries outside the United States and Canada.

INDEXED by Applied Mechanics Reviews and Engineering Information, Inc.

Journal of Turbomachinery

Published Quarterly by The American Society of Mechanical Engineers

VOLUME 112 • NUMBER 4 • OCTOBER 1990

TECHNICAL PAPERS

(Contents continued on p. 578)

Highly Loaded Axial Flow Compressors: History and Current Developments

A. J. Wennerstrom
Aero Propulsion and Power Laboratory,
Wright Research and Development Center
(AFSC),
Wright-Patterson Air Force Base, OH
45433-6563

This paper discusses approaches taken over many years to achieve very high loading levels in axial-flow compressors. These efforts have been associated predominantly with aircraft turbine engines. The objective has been to reduce the size and weight of the powerplant, to increase its simplicity and ruggedness, and, whenever possible, to reduce cost. In the introduction, some fundamentals are reviewed that indicate that increased work per stage can only be obtained at a cost of increased Mach number, increased diffusion, or both. The earliest examples cited are some ambitious development programs of the 1950s and 1960s. Some innovative schemes to increase diffusion limits are described that took place in the 1960s and 1970s. Major advancements in dealing with higher Mach number were made in the 1980s. Finally, a few thoughts directed toward potential future developments are presented.

Introduction

One of the most obvious ways to reduce the weight of the axial-flow compressor in an aircraft turbine engine is to reduce the number of stages it requires. Inasmuch as the engine cycle will dictate the overall pressure ratio required, a reduction in the number of stages inevitably means that each stage must do more work. Maximizing the work per stage while retaining acceptable overall performance has been a goal of the aircraft engine designer ever since an axial-flow compressor was first incorporated into an aircraft engine. In this section, I want to illustrate what more work per stage means to the compressor. Then in subsequent sections I will illustrate several research and development efforts to which this has led and then will conclude with a few comments concerning future prospects.

The most fundamental expression for work per stage is the Euler Equation of Turbomachinery, which, neglecting radius change, can be written for compressors

$$\Delta h_t = U(V_{\theta 2} - V_{\theta 1}) \tag{1}$$

This tells us that the work per stage is directly proportional to the wheel speed and the change in absolute swirl velocity across the rotor. The upper limit for wheel sped is most often defined by some structural limitation. However, since as wheel speed increases, relative flow velocities and hence Mach numbers increase, in some instances such as high bypass turbofans, wheel speed may be Mach number limited for reasons of thermodynamic efficiency . The permissible change in swirl velocity across a rotor is, on the other hand, almost always limited by some aerodynamic constraint. This constraint may be Mach number or some loading parameter related to boundary layer separation.

Contributed by the International Gas Turbine Institute and presented as an invited lecture at the Ninth International Symposium on Air Breathing Engines, Athens, Greece, September 3-8, 1989. Manuscript received at ASME Headquarters February 5, 1990.

Losses, and hence efficiency, and also stall margin are also related to work per stage. Although losses result from many different phenomena, the majority of losses can be divided into those related to Mach number (shock waves) and viscous losses related to diffusion acting on boundary layers. Some of the earliest indices of loading considered only inlet to exit conditions across a blade row. These guidelines were arrived at by examination of a very limited range of low-speed data. They included the static pressure rise coefficient

$$\frac{p_2 - p_1}{\frac{1}{2}\rho W_1^2} < 0.6 \tag{2}$$

and the de Haller number

$$\frac{W_2}{W_1} > 0.72 \tag{3}$$

The former defined the maximum practical static pressure rise as a function of inlet dynamic head. The latter defined a minimum exit-to-inlet relative velocity ratio to achieve acceptable performance. Neither of these indices were correlated against losses. The most useful diffusion parameter to be introduced was the diffusion factor presented by Lieblein et al. (1953). This not only provided some guidance relative to practical upper limits for conventional blade rows, but it also proved a useful correlation parameter for relative total pressure viscous losses.

The diffusion factor, again neglecting radius change, can be written

$$D = 1 - \frac{W_2}{W_1} + \frac{V_{\theta 2} - V_{\theta 1}}{2\sigma W_1} \tag{4}$$

Through a series of simplifying assumptions in its derivation,

the above factor is intended to be an approximate representation of the local suction surface diffusion factor defined by

$$D_{\text{local}} = \frac{W_{\max} - W_2}{W_{\text{avg}}}$$

It is interesting to compare these three parameters for the extreme case of an impulse blade row. For the sake of simplicity, let us further consider the flow to be incompressible and to have no inlet absolute velocity swirl, i.e., $V_{\theta 1} = 0$. Since impulse blading has no static pressure change, the pressure rise coefficient

$$\frac{p_2 - p_1}{\frac{1}{2}\rho W_1^2} = 0$$

An impulse blade row in incompressible flow will have symmetric inlet and exit velocity diagrams in the relative frame. Hence $W_2 = W_1$ and the de Haller number

$$\frac{W_2}{W_1} = 1.0$$

Therefore, according to these criteria, the blade row has no loading whatsoever. However, the diffusion factor can have a substantial value and will be

$$D = \frac{V_{\theta 2}}{2\sigma W_1} = \frac{U}{\sigma W_1}$$

or, in terms of angles,

$$D = \frac{\sin \beta_1}{\sigma}$$

Although the magnitude of this diffusion factor may be meaningless because the existing correlations were derived for such different blading, the diffusion factor does correctly indicate that there can be a large amount of diffusion even in an impulse blade row. The fluid will accelerate to a peak velocity somewhere on the suction surface while turning and then must inevitably diffuse to a much lower value to achieve equilibrium exit conditions.

In order to see the combined effect of wheel speed and diffusion on stage work capacity, we can combine the Euler equation, equation (1), with the equation for diffusion factor, equation (4). This leads to

$$\Delta h_t = 2\sigma U W_1 \left(D - 1 + \frac{W_2}{W_1}\right)$$

We see from this that work capacity is directly proportional to wheel speed, is nearly proportional to inlet relative velocity, and varies in some proportion with diffusion factor; if $W_2/W_1 = 1.0$ it would be directly proportional. One also observes that stage work capacity is directly proportional to solidity. However, this is subject to several practical constraints in that skin friction losses will increase with wetted surface, increased blade blockage will reduce choking mass flow, and finally the weight will increase in more than direct proportion to the blade count. Hence, it is readily apparent why all efforts to increase stage work capacity have concentrated on increasing wheel speed, Mach number (relative velocity), and diffusion.

Supersonic Compressors

Early History. As was pointed out in the previous section, the most obvious way to increase work per stage was to increase wheel speeds, whirl velocities, and hence Mach numbers. This was pointed out many years ago and the idea of operating a compressor at supersonic relative velocities with normal shock waves in the blading is generally first credited to Weise (1937) in Germany. Two excellent summaries of early work with supersonic compressors are presented by Klapproth (1961) and Erwin (1964).

Klapproth made the astute observation that the early design approach for supersonic compressors was developed more from supersonic diffuser design criteria than from conventional compressor design criteria. As a consequence, early work with supersonic compressors was not a logical evolution of work with lower speed machines but rather attempted to make a quantum leap forward with little regard for past turbomachinery experience. Hindsight has shown that many of the loading criteria developed for lower-speed machinery have retained a remarkable validity for high-speed machinery, as illogical as it might seem. The more successful machines built over the years have combined concepts of dealing with higher Mach numbers with older, more conventional concepts of blade aerodynamic loading limits.

Most work concerning supersonic compressors has already been published in the open literature. What I would like to present here, in approximately chronological order, are four early, very serious development efforts that have not previously been published because they were originally classified. Each of these incorporated a supersonic compressor, which went through extensive engineering development. All four represented extremely ambitious exploratory or advanced development programs, had varying degrees of success because of that, and hence never found their way into any production engine.

The J-55 Turbojet. This is probably the first gas turbine to run as an engine incorporating a supersonic compressor. Its development was initiated in 1947 with the objective of powering a target drone. Its compression system was unique in incorporating a single-stage supersonic axial compressor of the shock-in-rotor type, designed to provide a 2.75 total pressure ratio at a corrected tip speed of about 488 m/s (1600 ft/s). It included inlet guide vanes, which provided some counterswirl at the hub and incorporated a tandem-bladed stator. The overall engine never achieved enough of its design goals to be put into production. However, by the conclusion of the contract, the compressor had achieved a total pressure ratio of approximately 2.9 at an isentropic efficiency of about 0.76 at design speed. Lower in its speed range its efficiency peaked at about 0.82. One of the major development problems was achieving adequate performance from the supersonic compressor. In 1947, the contractor, Fredrick Flader, Inc., was optimistic enough to state, "we are convinced that this development has progressed to a point where its incorporation

Nomenclature

D = diffusion factor
D_{local} = local diffusion factor
h = enthalpy
p = static pressure
U = wheel speed
V_θ = absolute swirl velocity
W = relative velocity
$W_{\max}$ = peak suction surface relative velocity
W_{avg} = average suction surface relative velocity
β = relative flow angle measured from axial
ρ = static density
σ = solidity (chord/spacing)

Subscripts

1 = blade-row inlet
2 = blade-row exit
t = stagnation quantity

Table 1 Counterrotating compressor design characteristics at sea-level takeoff conditions

Low-pressure rotor	Impulse type
Design tip speed	442 m/s (1450 ft/s)
Total pressure ratio (design)	3.69/1
Adiabatic efficiency	0.847
Inlet diameter ratio	0.65
Exit diameter ratio	0.772
High-pressure rotor	Shock-in-rotor type
Design tip speed	266 m/s (874 ft/s)
Total pressure ratio (design)	1.829/1
Adiabatic efficiency	0.623
Inlet diameter ratio	0.772
Exit diameter ratio	0.827
Overall compressor	Statorless
Overall pressure ratio (excluding inlet losses)	6.75
Overall adiabatic efficiency	0.775
Compressor o.d.	406 mm (16 in.)
Compressor weight flow (design)	17.7 kg/s (39.0 lb/s)
Weight flow/frontal area	135.7 kg/s/m^2 (27.8 lb/s/ft^2)

in this design proposal is warranted." History showed this conclusion to be somewhat premature. These bits of information were derived from Downs (1953) and Blanton (1989).

Curtiss-Wright Counterrotating Compressor. This was probably one of the most ambitious of all supersonic compressor designs ever attempted. The effort took place in the mid-1950s and the design was reported by Sabel and Sabatiuk (1957a). It was designed for a flight Mach number of 3.0, to accept an axially supersonic inlet Mach number at this condition utilizing an integral fixed-geometry free-stream inlet, and to be able to take off from a sea-level static condition with a choked inlet. One of its major goals was to eliminate the necessity for a heavy, complex, variable-geometry inlet and its controls and actuating mechanisims. Its objective was to employ counterrotating rotors to avoid the necessity for any inlet guide vanes or stators and to achieve an adequate pressure ratio over its flight regime through this means.

Its projected design features are summarized in Table 1 for the sea-level takeoff condition. Most notable is the fact that it was proposed to do this with an impulse first rotor and a shock-in-rotor second rotor. As with several of its predecessors, supersonic diffuser design practice guided design of the second rotor. Conventional compressor loading criteria were completely ignored. Because of the sea-level static takeoff requirement, the leading edges of the first rotor were staggered at an angle of two or three degrees at this condition. However, at the flight cruise condition, the first rotor was anticipated to operate at negative incidence and with a swallowed shock pattern.

The first rotor incorporated all of the technology conceivable at the time. This included leading edge sweep designed to keep the sonic line coincident with the surface of revolution defined by the leading edge. An axisymmetric stream filament design technique was used employing simple radial equilibrium theory. As understood today, this would exclude internal computing stations and streamline curvature effects. The choice of solidity and aspect ratio was based on previous recent NACA experience. The mean solidity of the first rotor was approximately 2.8. Maximum thickness varied from 3.3 percent chord at the tip to 7.9 percent chord at the hub. A method-of-characteristics computation was made to insure a reasonable probability of passing design flow.

The second rotor was designed for an average relative inlet Mach number of 2.34. The internal one-dimensional area contraction of the blading was designed to permit starting a relative approach flow of Mach 2.0. Twenty-five degrees of leading-edge sweep was incorporated to enhance starting of the supersonic flow. Today we would say that this rotor was designed with significant precompression, and from the throat to the trailing edge plane an equivalent cone angle of approximately eight degrees was employed. The mean solidity was approximately 2.05. The same aerodynamic design technique was employed as for the first stage. An approximately midradius cross section of both rotors is shown in Fig. 1. The second rotor is shown assembled in Fig. 2.

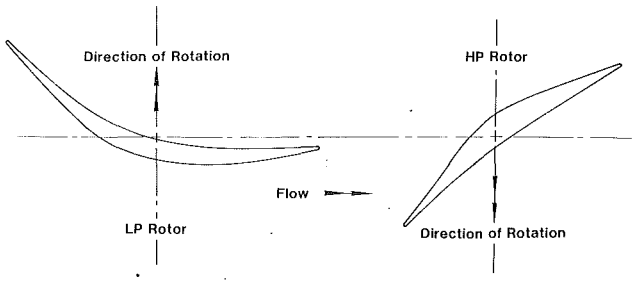

Fig. 1 Near-midspan cross section of rotor blading

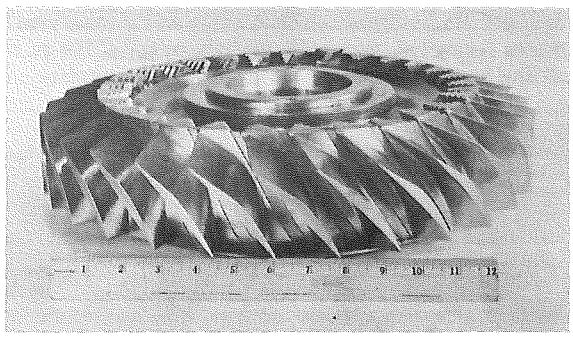

Fig. 2 Photograph of high-pressure rotor

Interestingly enough, diffusion factors were calculated. At sea-level take-off conditions, they were 0.258 for the low-pressure rotor and 1.00 for the high-pressure rotor. For the first rotor of impulse design, the diffusion factor is not terribly meaningful. However, the diffusion factor of 1.00 for the second rotor is typical of so many unsuccessful designs of that era. When one looks back on the overall experience, it is remarkable to what degree performance does correlate with diffusion factor under circumstances far removed from those under which it was derived.

The experimental results of sea-level static testing were reported by Sabel and Sabatiuk (1957b). Choking in the first rotor limited weight flow to approximately 79 percent of the design value. Measured performance recorded with both spools at design speed was an overall total pressure ratio of 3.24 and an isentropic efficiency based on temperature rise of 73.3 percent. This efficiency seems surprisingly high when it is noted that the total pressure ratio is only 48 percent of the design value. Observation of casing static pressures presented in Fig. 3 shows that most of the static pressure diffusion actually occurred downstream of the second rotor rather than within it. Inasmuch as the exit plane instrumentation was within this region, it is likely than when exit mixing losses are taken into account, the true efficiency would be much lower.

The casing static pressures tell another interesting story. The static pressure ratio across the first impulse rotor was intended to be about unity and this was the result achieved. However, the static pressure ratio intended to exist across the second rotor was about 11.7 according to the design. In fact, the experimental results show a negligible static pressure rise also

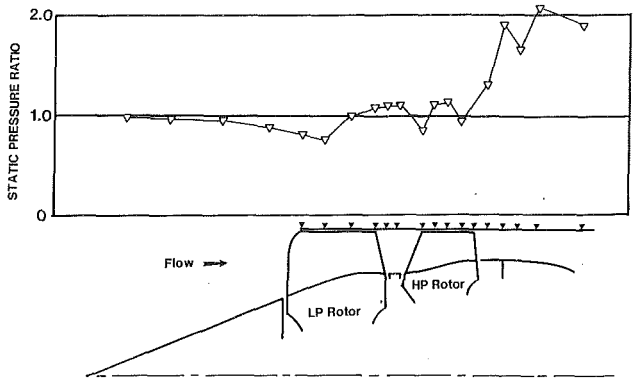

Fig. 3 Casing static pressure distribution

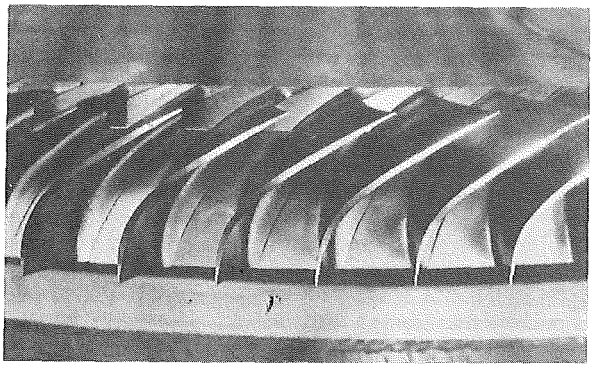

Fig. 5 Close-up of assembled high-pressure rotor viewed along span

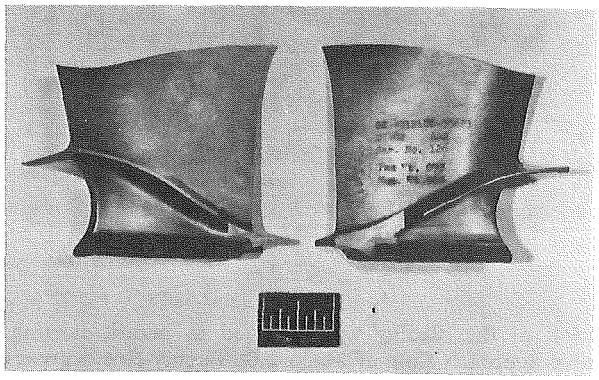

Fig. 4 DLD gas generator supersonic compressor blade

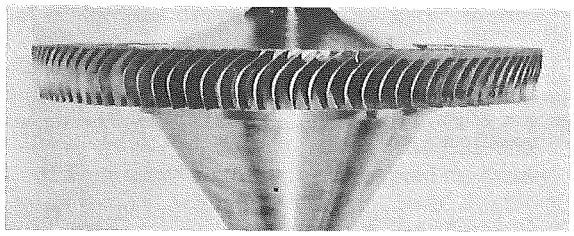

Fig. 6 TS-10 supersonic rotor

across the second rotor. From inlet to exit, an overall static pressure ratio of only about 2.0 was achieved and all of this occurred over a distance of several annulus widths downstream of the second rotor.

Several additional tests were made with this rig. However, a major facility-related mechanical failure destroyed the compressor and this program was terminated without further significant accomplishment.

Direct Lift Demonstrator. This was a program accomplished by the General Electric Company in the mid-1960s. Its objective was to develop the major components of a turbofan engine to a level of technology consistent with direct lift (VTOL) requirements and then to assemble them as an engine and test it in a typical environment. It was a two-spool turbofan. The low-pressure spool had a single transonic fan stage. The high-pressure spool had a single supersonic compressor stage. My remarks will be limited to aerodynamic aspects of the supersonic core stage. The data used were presented by Conliffe (1971).

The supersonic stage was a shock-in-rotor/shock-in-stator configuration. Its design characteristics included a design total pressure ratio of 3.15 at a corrected tip speed of 420 m/s (1378 ft/s) and with a projected isentropic efficiency of 75 percent. The inlet hub/tip radius ratio was approximately 0.82. Relative Mach numbers ranged from about 1.2 to 1.4 across the leading edge of the rotor and from about 1.4 to 1.5 across the leading edge of the stator. Design static pressure ratios at the outer casing for both rotor and stator were approximately 1.9. Rotor solidity was approximately 2.2; stator solidity was about 4.8. Mean aspect ratios were approximately 0.88 and 0.27 respectively. An example of the rotor blading is shown in Fig. 4. A close-up of the assembled rotor is shown in Fig. 5.

The performance achieved for the best configuration subsequently used in the gas generator was a total pressure ratio of about 3.5 at 71.4 percent isentropic efficiency. A large number of configurations were examined during the development program. The majority were aimed at improving the stator performance. Although the indicated performance of the rotor had been quite good throughout the program, the stator total pressure recovery and discharge flow distribution remained quite poor. In this instance, the designers observed generally accepted limits for loading parameters such as diffusion factor. However, once again, the inability of a stator to accept Mach numbers and static pressure ratios as high as those of rotors had been demonstrated and nothing the designers attempted altered this situation substantially.

Turboaccelerator (TS-10). This was a program accomplished by Pratt & Whitney Aircraft also in the mid-1960s. One portion of this program involved a three-stage axial compressor, the second stage of which was a supersonic compressor. This was the most critical stage in the entire compressor. It employed a relatively low corrected mean wheel speed, 295 m/s (968 ft/s), but had rotor relative inlet Mach numbers ranging from 1.14 to 1.22 as a result of counterswirl in the approaching air. Average rotor turning was very high, about 75 degrees, but loading limits were held at conventional levels and the peak static pressure ratio was about 1.53. Its design total pressure ratio was 2.75. Mean solidity was about 3.8. The rotor is pictured in Fig. 6.

Pratt & Whitney had access to substantially the same information in the same time frame as the General Electric Company and unfortunately reached about the same conclusions concerning their stator design. Inlet Mach numbers were about 1.3 and the stator static pressure ratio was about 1.61. The turning angle was about 40 degrees. The estimated peak static pressure ratio required for adequate surge margin was about 1.9, the same as the General Electric stator. Solidity was also about the same at 5.1, and the design contemplated a pseudoshock diffusion pattern in the stator. The stator was once again the nemesis of this design. Measured stage isentropic efficiency did not exceed 70 percent at design speed.

Increased Diffusion Limits

Background. Practically all efforts to increase diffusion limits have been associated with some form of boundary-layer

control. In general, passive approaches have been favored such as vortex generators and slots. Tandem blading has been examined, which is essentially another version of a slot. Active schemes have also been considered such as suction and blowing. Several of these program are reviewed in the following sections. The programs selected are not meant to be a comprehensive survey of everything done along these lines, but they are felt to be representative of the type of results achieved. All of these concepts have been derived from methods successfully applied to aircraft wings and control surfaces.

Slots. Slots are one of the older forms of boundary layer control and have been widely and successfully applied to aircraft. Their application to turbomachinery has been much less successful. Some of the most extensive investigations of slots applied to compressor blading have been sponsored by the National Aeronautics and Space Administration (NASA). One of these was accomplished under a series of two contracts by Pratt & Whitney Aircraft beginning in about 1965.

The first of these contracts was summarized by Rockenbach (1968). In this effort, three slotted rotor and three slotted stator configurations were designed and tested in various combinations. The rotors were designed for levels of tip diffusion factor increasing from 0.53 to 0.70 and the stators with hub diffusion factor increasing from 0.60 to 0.76. Rotor tip relative Mach number was approximately 0.8 and stator hub Mach number was about 0.64. All blading was NACA 65-series. Based on some boundary layer analyses and annular cascade tests, rotor slots were located at 50 percent chord and stator slots at 55 percent chord. A typical rotor blade cross section is shown in Fig. 7. The stators were slotted similarly. The hub/tip radius ratio was approximately 0.8 and rotor and stator aspect ratios were approximately 1.7.

Results obtained indicated good performance from the midspan regions of both slotted rotors and stators, but poor performance near both end walls. The relative effectiveness of the slots at midspan and their ineffectiveness near the walls was attributed to chordal placement of the slots and their inability to reduce the large secondary flows in the wall regions. As a result, the design radial work gradients for the slotted rotor blading did not compensate for the high loss gradients measured near the wall, which resulted in low total pressure ratio and low efficiency in those regions. The conclusion was that advanced design concepts to increase stage loading should be addressed to the problem of secondary flow and associated high losses near the wall.

This led to the second NASA-sponsored investigation by Pratt & Whitney described by Rockenbach et al. (1970) and concluded by Brent (1971) and Rockenbach and Brent (1971). In this follow-on effort, three things were attempted. Additional blade end slots upstream of the original slots and secondary flow fences were added to the most highly loaded configuration from the first investigation. Two new stages were designed with more work input near the end walls to compensate for the higher end-wall losses. Additional blade slots and secondary flow fences or end-wall vortex generators were planned for incorporation into these two new stages.

In the first case, the additional slots were positioned at 25 percent chord in both rotor and stator, just near the end walls. A typical cross section is shown in Fig. 8 corresponding to a hub section. The fences were mounted on the end walls within the blade row to reduce the migration of boundary layer fluid on the end wall toward the suction surface. These devices were found to be ineffective and the poor performance was traceable to problems in the end-wall region. Loss coefficients were not reduced by these modifications; some actually increased. It was concluded that the wall boundary layer and its interaction with the blade adverse pressure gradient controls the performance. Blade element performance must be the limiting factor before slots could be expected to help. It was recommended that future efforts concentrate on the end-wall problem and the use of vortex generators was one solution recommended.

There were a few more NASA-sponsored efforts involving slots as well as other devices. However, inasmuch as some of these included end-wall vortex generators, these will be addressed under that topic. To conclude this discussion, it might be noted that Griepentrog (1970) suggested a tentative loss correlation for slots. It appeared to be based on very fragmentary evidence. However, two trends that he predicted appear substantially correct. Specifically, he indicated that slots might be expected to have some positive benefit at lower aspect ratios and lower Mach numbers; otherwise their influence might be negative. One experiment reported by Wennerstrom (1987) was consistent with this hypothesis in which a stator of very low aspect ratio showed a substantial improvement with the addition of slots.

Tandem Airfoils. Tandem airfoils are only slightly removed from slots. For all practical purposes, they amount to a full-span slot. In most cases the airfoils have been connected with a series of webs across the gap in order to retain structural stiffness. Much of the work with tandem airfoils was also sponsored by NASA and parallels, both in time and in results achieved, the work with slots.

One of the larger of these efforts was also conducted by Pratt & Whitney under contract and was summarized by Brent and Clemmons (1974). A compressor was employed very similar to the one in which most of the slotted airfoil investigations were pursued. It was a single stage of 0.8 hub/tip radius ratio and about 0.8 tip relative inlet Mach number. The first phase compared a baseline conventional rotor airfoil with two tandem versions, which differed in the loading split between the paired airfoils. In a second phase, a similar comparison was made but an attempt was also made to account for the actual inlet velocity profile and to correct for effects of axial velocity ratio and secondary flow.

From the first phase it was concluded that a 50/50 percent loading split between paired airfoils far exceeded the performance of the alternative 20/80 percent loading split examined. It also did better than the conventionally bladed baseline, which did not meet its expectations. In the second phase, the baseline stage did achieve design performance. The corresponding stage with a tandem rotor having a 50/50 percent loading split slightly exceeded design pressure ratio but was 1.5 points low in efficiency.

No improvement in the operating range between peak efficiency and incipient surge was noted for the tandem-bladed stages. Thus, the original hypotheses that tandem blades should have a larger operating range than conventional blades and that tandem configurations designed with the majority of loading on the rear airfoil should have a larger operating range were not substantiated. Even though the tandem rotors

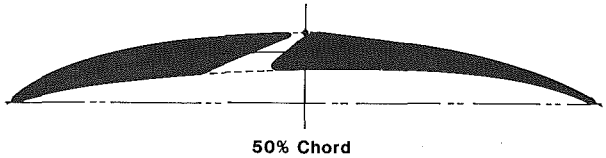

Fig. 7 Typical slotted blade or vane

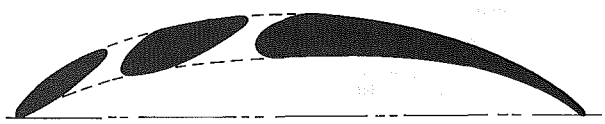

Fig. 8 Second slot added to end-wall regions

demonstrated a higher pressure rise capability, it was not apparent that simply adding more camber to the conventional blade could not have achieved the same result with much less cost and complexity.

Another similar effort was focused on a high-speed inlet or fan stage configuration. This stage had an inlet hub/tip radius ratio of 0.5 and an inlet relative Mach number at the rotor tip of about 1.6. A conventional version with multiple circular arc airfoils achieved an isentropic stage efficiency of 84.5 percent at approximately design pressure ratio (1.94) and was about 3.5 percent below design flow. A tandem-bladed version, otherwise identical, achieved an isentropic stage efficiency of 83.1 percent at about the same pressure ratio and was about 5.0 percent below design flow. Both stages stalled at the same flow but the conventional stage had both a higher choking flow and a higher maximum stage pressure ratio and thus had considerably more useful range. This work was reported by Sulam et al. (1970) and Burger and Keenan (1971).

Vortex Generators. One of the recommendations of Rockenbach and Brent (1970) who found flow fences unsuccessful in treating the endwall problem in combination with slotted blades and vanes was that vortex generators on the end walls be explored as an alternative. This was subsequently accomplished and was reported by Brent (1970). Vortex generators were installed on both the inner and outer casing and were located upstream of the rotor as well as between the rotor and stator. All vortex generators were designed as symmetric pairs to produce counterrotating vortices. They were tested in several combinations, and the results are summarized in Table 2.

As is evident from the table, the vortex generators accomplished relatively little. In no case did any of the configurations achieve the predicted performance. This even included the unslotted design with no vortex generators. The best configuration including vortex generators was slightly worse than the plain version at design speed and flow. Its peak efficiency and peak pressure ratio at design speed slightly exceeded it. However, its stall margin was about 10 percent greater because it could be throttled to a lower flow. This was a small but positive result, which gave some encouragement to further work.

Some other ideas concerning vortex generator applications were reported by Holtman et al. (1972). In this instance, a configuration structurally suitable for mounting on a rotor blade was tested on a cascade simulating a near-midspan section of a supersonic rotor. The results were somewhat favorable although they did not influence the cascade spill point and thus, presumably, stall margin. The results, as far as relative total pressure loss coefficient, are shown in Fig. 9. The effect on other parameters was minimal.

The virtues of vortex generators on the outer casing as well as on rotor blades were explored further on a supersonic compressor as described by Wennerstrom (1987). When installed on the outer casing upstream of the rotor, flow and efficiency increased 1 to 2 percent, and stall margin increased somewhat. When added to the rotor in the near-tip region where diffusion was highest, efficiency was maintained and stall margin was slightly further increased at design speed and above. Below design speed, the effect was negligible.

The above results, while disappointing relative to their expectations, encouraged one more effort reported by Wennerstrom (1984). In this last instance, the effect of vortex generators installed upstream of a transonic rotor on the outer casing and also mounted on the rotor near the tip was examined. Unlike most of the previous stages with which vortex generators were explored, this stage was exceptionally efficient in its original form, unaided by any means of boundary-layer control. Several configurations of vortex generators installed on the outer casing upstream of the rotor were investigated. The effect of vortex generators installed on the suction surface of the rotor near the tip was also evaluated.

The results achieved were interesting and are summarized in Fig. 10. The configurations with vortex generators produced higher peak efficiency, higher pressure ratio, and more range in the upper speed range, i.e., 90 to 100 percent design speed. The improvements were small but they were at least favorable rather than negative. As identified in Fig. 10, Configuration 3 was plain; Configuration 3.1 included a group of three vortex generators located on the rotor suction surface near the tip; Configuration 3.1B added to the above a row of vortex generators on the outer casing upstream of the rotor tip.

Considering the variety of boundary-layer control measures explored with compressors, this application of vortex generators has to be considered one of the more successful attempts. Even though the benefits were small, they were at least favorable, whereas most other attempts produced negative results. It is both curious and interesting to note that the best

Table 2 Summary of NASA-sponsored experiments with vortex generators reported by Brent (1970)

Configuration	Predicted performance for design equivalent rotor speed and corrected flow[1]				Measured performance at design equivalent rotor speed and corrected flow[2]				Measured peak efficiency and corresponding pressure ratio at design equivalent rotor speed			
	Rotor		Stage		Rotor		Stage		Rotor		Stage	
	η	PR	η	PR	η	PR	η	PR	η	PR	η	PR
Unslotted rotor 4–unslotted stator 4	0.868	1.335	0.781	1.305	0.858	1.298	0.730	1.254	0.874	1.324	0.748	1.274
Slotted rotor 4–slotted stator 4	0.895	1.349	0.838	1.324	0.800	1.258	0.665	1.210	0.857	1.318	0.740	1.271
Slotted rotor 4–slotted stator 4 with vortex generators ahead of the rotor	0.895	1.349	0.838	1.324	0.795	1.254	0.650	1.203	0.862	1.317	0.747	1.279
Unslotted rotor 4–slotted stator 4 with vortex generators ahead of the rotor and between the rotor and stator	0.895	1.349	0.838	1.324	0.865	1.300	0.723	1.247	0.882	1.326	0.769	1.281

[1]The predicted performance for the rotor 4–stator 4 configuration is based on rotor and stator blade element loss data. The predicted performance for the remaining configurations is based on the assumption that slots and vortex generators would reduce the blade element losses below the level of the blade element loss data.

[2]Design equivalent rotor tip speed and corrected flow are 231 m/s (757 ft/s) and 49.8 kg/s (110 lb/s), respectively.

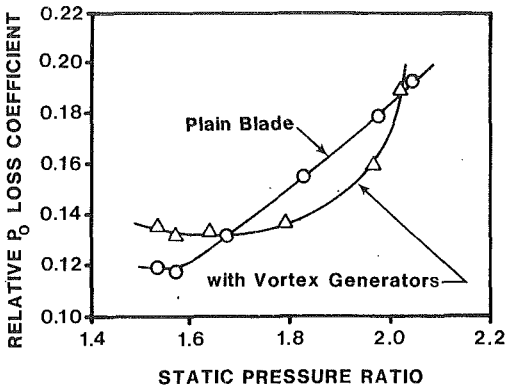

Fig. 9 Supersonic cascade performance with and without vortex generators

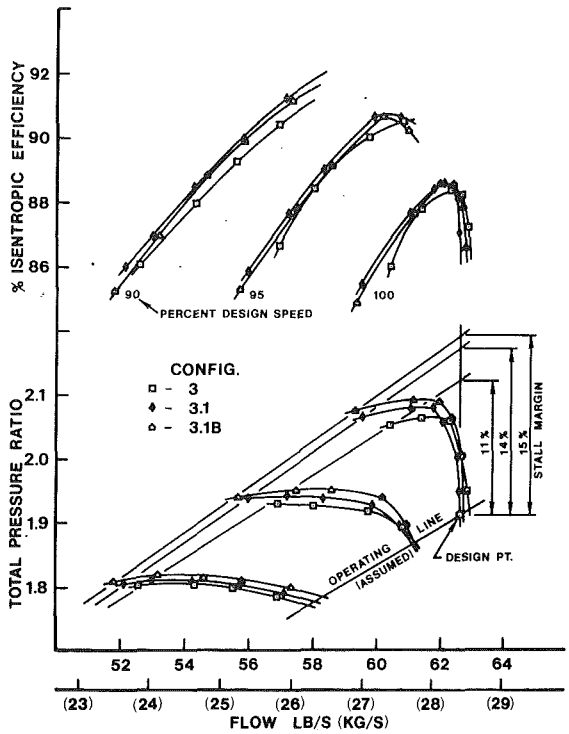

Fig. 10 Influence of vortex generators on a transonic axial flow compressor

results were achieved with a compressor that was already performing very well in its basic original configuration. Although vortex generators as well as other means of boundary-layer control were originally viewed as a possible means of significantly improving design-point limits, little of this has materialized. On the other hand, some useful improvement was achieved with a configuration which was not stressed beyond reasonable aerodynamic bounds. The effect of vortex generators in combination with inlet distortion has not yet been evaluated. It is plausible that they might offer some benefits in this environment.

Suction and Blowing. Suction or blowing as a means of boundary-layer control differs from the use of slots, tandem airfoils, or vortex generators in that it is an active means rather than a passive means. Thus some energy must be expended to accomplish it and it is therefore considered less attractive than the passive approaches. However, it also has a history of successful application to some situations. Hence, it is not surprising that the comprehensive NASA program exploring applications of boundary-layer control to increase diffusion limits in axial-flow compressors also included suction and blowing.

This program was pursued under a NASA contract by the General Electric Company. All tests were performed in combination with a compressor stage having a rotor tip speed of 341 m/s (1120 ft/s), an inlet hub/tip radius ratio of 0.5, and a rotor aspect ratio of 4.5. The rotor had a part-span shroud in order to retain aeromechanical stability. The design rotor tip diffusion factor was 0.45. The design is described by Griffen and Smith (1966).

The blowing configuration was described by Koch and Smith (1968a). A casing insert contained three rows of tapered holes oriented with their axes at a 20 degree angle from the tangential direction and 30 degrees from the axial direction such that the jets blew in a direction opposite to rotor rotation, producing counterswirl. The first two rows of holes discharged forward of the rotor leading edge; the third row discharged over the rotor tip. The area of the holes was chosen such that approximately 4 percent of design flow would pass through the holes when they were just choked.

The results were mixed. With uniform inlet flow, blowing had a negligible effect on stall margin. However, it was deduced that rotating stall was initiated in the vicinity of the part-span shroud so it is not surprising that blowing on the casing had little effect. On the other hand, with distorted inflow, either radial or circumferential, the area of stall initiation shifted to the outer casing and in this case blowing did produce an appreciable increase in range. A more interesting result was that even with the blowing flow turned off, the presence of the blowing holes and the plenum behind them produced an increase in stall margin relative to the clean casing for both undistorted and distorted inflow. The effect was more pronouced with distortion than without.

The suction configuration was described by Koch and Smith (1968b). The bleed insert over the rotor tip was made of hexagonal honeycomb extending from just aft of the rotor's leading edge to just aft of the trailing edge. The axes of the honeycomb cells were tilted 70 degrees from the radial direction in the tangential direction in order better to recover the energy of the tangential component of the flow at the tip of the rotor. The bleed flow area was sized such that up to 4 percent of the compressor design weight flow could be extracted.

The results were again mixed. With undistorted inflow, bleed accomplished little for the same reason that blowing was unsuccessful. On the other hand, with distorted inflow, bleed was successful in improving stall margin, although not quite to the same degree as blowing. It had relatively little effect with a radial distortion but it had a pronounced effect with circumferential distortion. With zero bleed flow, the presence of the honeycomb and plenum had virtually no effect relative to the plane casing with a radial inlet distortion. However, with a circumferential distortion, even with zero bleed, the honeycomb/plenum configuration showed a significant improvement in stall margin. The success of both blowing and suction configurations in improving stall margin under distorted inflow conditions even with zero inflow or outflow is what triggered much of the subsequent work on compressor casing treatment.

Newer Developments in Dealing With Higher Mach Number

Through-Blade Design Methods. A through-blade design method is a design approach wherein computations of the radial equilibrium flow field are made at several axially distributed locations within each blade row as well as at leading and trailing edges and in free spaces. The streamline curvature computational method is the approach used most frequently. Within a blade row, the presence of the blades is

introduced into the momentum equation in terms of spatially distributed body forces and blade lean angles, which introduce radial force terms. In the continuity equation, the presence of blades is introduced in the form of blockages due to the metal thickness, stagger angle, and boundary layers and wakes. Assumptions must be made for the distribution of loss and deviation angle within the interior of each blade row. Blades of arbitrary geometry may be defined by specifying work distributions within rotors and angular momentum distributions within stators. Alternatively, the geometry of blades of some prescribed form can be assumed and the radial equilibrium flow solution calculated by prescribing the internal distribution of relative flow angle.

The above-described method was used for design of a production fan by General Electric before 1960 as described by Wright and Novak (1960). However, it did not come into widespread use by the rest of the industry until after 1970. As a result, most of the earlier supersonic stages designed did not have the benefit of this level of sophistication in their design. Considering how sensitive the performance of high Mach number blading is to the blade configuration, the widespread adoption of through-blade design methods during the 1970s can be considered a major advancement in the ability to deal with higher Mach numbers successfully.

Application of Counterswirl. Counterswirl, meaning a swirl velocity in the opposite direction to rotor rotation, is sometimes introduced upstream of a rotor to increase its potential work capacity. Its value is obvious from equation (1). However, it has the inevitable result of increasing the Mach number relative to the following rotor. It has been widely applied to low-speed machinery with great success. However, its application to compressors operating at supersonic Mach numbers has been very limited and has also met with very limited success.

The point I wish to make here is that the lack of success in exploiting counterswirl at higher Mach numbers in the past had more to do with our poor capabilities to design for higher Mach number than it did with any properties inherent in the use of counterswirl. This was amply demonstrated by the success of a more recent design using contemporary design methods described by Law and Wennerstrom (1987). The application of counterswirl allows tradeoffs to be made between Mach number and diffusion level. With today's technology, it is often easier and more successful to design for higher Mach numbers in a core compressor than to attempt to achieve the same objective with exceptionally high diffusion levels.

The Use of Sweep. The concept of using swept wing theory to reduce shock losses was introduced into aircraft wing technology in the 1950s with considerable success. However, its application to turbomachinery was both sporadic and unsuccessful within that period. A variety of attempts were made to exploit this concept within the 1950s and 1960s. None met with notable success. One problem was that a number of attempts simply swept a leading edge in a linear manner. Conditions tended to get better in the region where the leading edge intersected a wall at an obtuse angle; the opposite sometimes occured where a leading edge intersected a wall at an acute angle. The first more positive results were achieved in combination with a curved stator leading edge where obtuse leading-edge/wall intersection angles were employed at both end walls and the leading edge was swept back from one wall and then curved forward again to meet the opposite wall. The first example of this was reported by Wennerstrom (1984) in which a slightly supersonic Mach number was sustained at a stator hub with no loss in performance. The geometry is illustrated in Fig. 11. This same technique was applied to another stator described by Law and Wennerstrom (1987) illustrated in Fig. 12. This second design was inadvertently operated at stator hub Mach numbers up to 1.2 and yet performed with loss coefficients equivalent to subsonic values associated only with the diffusion level. All evidence of shock loss was eliminated by the use of sweep.

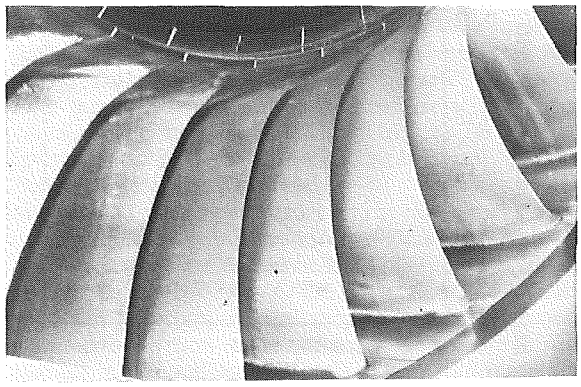

Fig. 11 Swept stator with integral end-wall shrouds

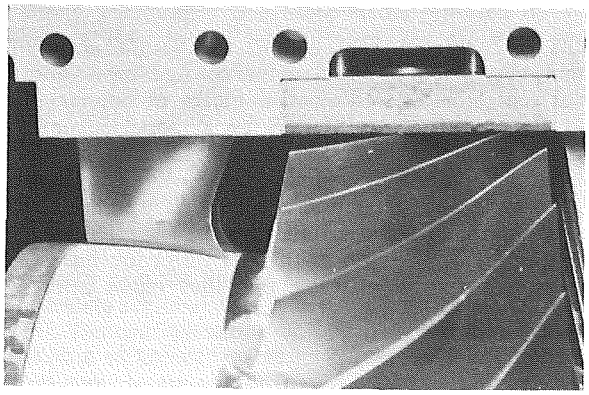

Fig. 12 Cantilevered variable unshrouded swept stator

The first real recognition of the significance of sweep to shock losses in high Mach number rotors was by Prince (1980). He observed that, although near peak efficiency shock waves appear approximately normal to the incoming flow on streamsurfaces, when one considers the three-dimensional surface formed by these shock waves, this surface can be highly swept in the spanwise direction at low aspect ratios. An example used by Prince is shown in Fig. 13. In this manner he explained the exceptional performance of some stages he examined and also the fact that the shock pressure rise measured by high response pressure transducers on the outer casing was often much lower than the shock position would indicate when this section was considered as a two-dimensional cascade.

Prince's observations led to the creation of the three-dimensional shock loss model of Wennerstrom and Puterbaugh (1984). This model has one major flaw in that the shock sweep is considered to be solely a function of the blade geometry. It ignores the fact that a strong oblique shock cannot intersect the outer casing of a compressor obliquely but must either become normal or bifurcate, the more likely condition. However, in spite of this weakness, the model does appear to be adequate to predict performance at modest levels of sweep. Several stages have been designed using this model and the results have been rewarding. However, it has been equally obvious that the model has its limitations. It is not yet clear exactly where the practical limits lie.

The Application of Computational Fluid Dynamics. One of the major advances in design technology in recent years has been the improvements achieved in computational fluid dynamics (CFD). In two-dimensional form, such methods

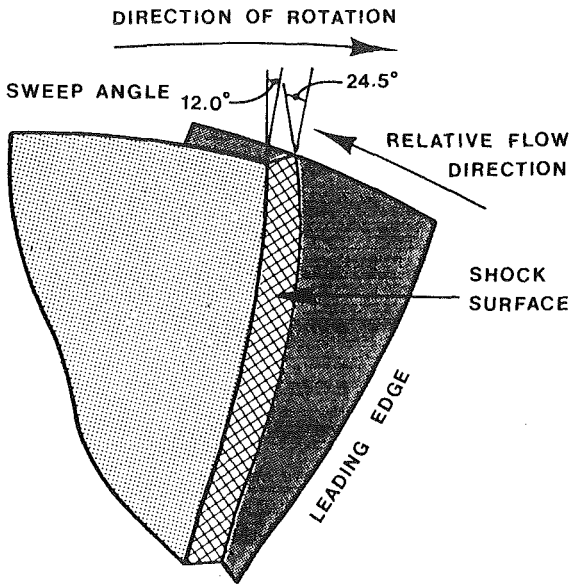

Fig. 13 Three-dimensional rotor shock surface illustrating spanwise sweep

have been very successful as inverse design tools in creating such things as controlled diffusion airfoils. However, in three dimensions, both inviscid and viscous methods remain analysis tools because a strategy is lacking for how to employ such a computation in three dimensions in some optimizational mode. They have been used to analyze complete three-dimensional designs and to guide their design revisions. One of the first examples of this was reported by Clemmons et al. (1983). However, the approach remains very iterative in that one must design a configuration using much more pedestrian means; it can then be analyzed in three dimensions. If one then observes something unattractive, the designer's problem is to come up with some intelligent revision, which he can introduce through the conventional design approach to rectify the problem he saw in a three-dimensional solution. It is not always obvious how to do this and herein lies one of the basic weaknesses of three-dimensional computational technology. Some of the three-dimensional computational codes have achieved a level of reliability that has rendered them quite useful for design analysis. However, we still need some sort of strategy that can translate the information obtained from such an analysis into direct guidance for design changes.

Newer Developments in Achieving Higher Diffusion Levels

Low Aspect Ratio. Of all things examined to increase diffusion limits, aspect ratio would appear to have the least to do with discouraging the separation of some boundary layers. However, when one looks back over all the efforts made to deal with boundary layers on local surfaces in turbomachinery, we have been monumentally unsuccessful in applying techniques useful for controlling external flow on aircraft surfaces to internal flow in turbomachinery. One of the conclusions frequently drawn is that the turbomachinery problem is uniquely related to the secondary flow, i.e., the nonaxisymmetric and non-two-dimensional characteristics, typical of diffusing and turning internal flows. This is precisely why aspect ratio has proven one of the more relevant parameters associated with compressor loading limits. This was described in some detail by Wennerstrom (1989). Schweizer and Garberoglio (1984) quantified this by relating aspect ratio to a diffuser of an equivalent cone angle and incorporating this into a preliminary design technique. A fundamental observation has simply been that lower aspect ratios are capable of sustaining higher diffusion limits before stall.

Fillet Geometry. It seems a fair assumption, based on the previously referenced experiments, that conventional airfoil surface boundary-layer control methods have a very limited capability to increase compressor diffusion limits. One of the few concepts derived from external aerodynamics that may still bear a significant relationship to diffusion limits is the treatment of airfoil/wall fillet geometry, in my opinion. Inasmuch as separation, and subsequently stall in a compressor, is almost always initiated in a corner between an airfoil and endwall, the treatment of this fillet geometry may be one of the few significant parameters still available with which to control diffusion limits. The work of Debruge (1980) gives some guidance in this direction. Early unpublished work indicated that, if a fillet were of uniform radius, smaller fillets gave better aerodynamic performance than large ones. On the other hand, Debruge showed that large fillets could handle the corner boundary layer much better under diffusion. A convenient rule of thumb that can be deduced from Debruge's results is that a fillet radius equal to approximately one quarter of the mean blade spacing is not far from optimum. The early experimental results combined with Debruge's results lead one to the conclusion that a variable fillet radius would provide the best aerodynamic result. The fillet should be small near the leading and trailing edge but should grow to substantial proportions over much of the chordwise extent. The aerodynamic opportunity anticipated here is small. The structural features of a large but variable fillet are attractive, but it does involve increased manufacturing complexity and cost. Insufficient aerodynamic experiments have been made from which to draw any firm conclusions concerning aerodynamic performance.

Splitter Blades and Vanes. Splitter blades and/or vanes have been used for many years in centrifugal compressors. A splitter is generally thought to consist of an airfoil dividing a flow passage, starting somewhere downstream of the inlet and continuing to the trailing-edge plane. Its first application to an axial compressor was described by Wennerstrom and Frost (1974). The cascade configuration employed is illustrated in Fig. 14 and the supersonic rotor incorporating them is shown in Fig. 15. It was originally conceived as a means of controlling the deviation angle under very severe conditions. It achieved this objective; however, in addition it showed an ability to perform at reasonable loss levels at very high diffusion factors. An example is shown in Fig. 16 drawn from Wennerstrom (1987), where both a cascade and a rotor are compared with a 1950s correlation of cascade data by Lieblein et al. (1953) of NACA. The most interesting feature of these data is that the cascade and rotor not only performed at loss levels comparable to past experience but this could be extrapolated to exceptionally high diffusion factors.

Possibilities for the 1990s

The Exploitation of Nonsteady Flow. One of the newest areas to arouse some interest is the possible exploitation of nonsteady flow as a means of increasing stall margin or allowable loading. The principal is based on the fact that an isolated airfoil or a cascade can accept much higher loading for short periods of time than it can under steady conditions. A time constant appears to be associated with most separation phenomena. This is a property that has been exploited in helicopter rotor design. This property for an isolated airfoil is illustrated in Fig. 17. In axial compressors this phenomenon is observed in the behavior of a compressor in the presence of a circumferential inlet distortion. If a zone of distortion is of sufficiently limited circumferential extent, a compressor can

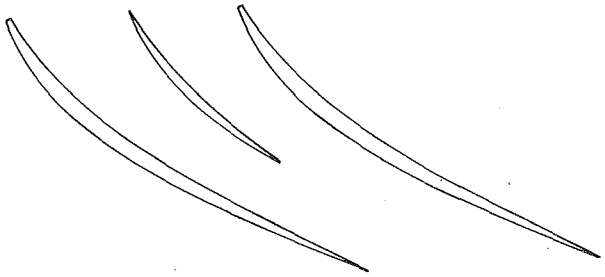

Fig. 14 Rotor cascade with splitters

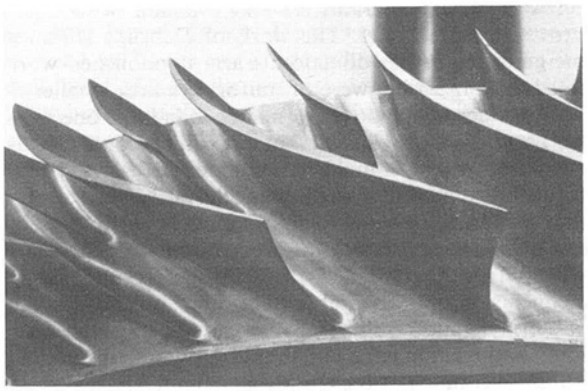

Fig. 15 Supersonic rotor including splitters

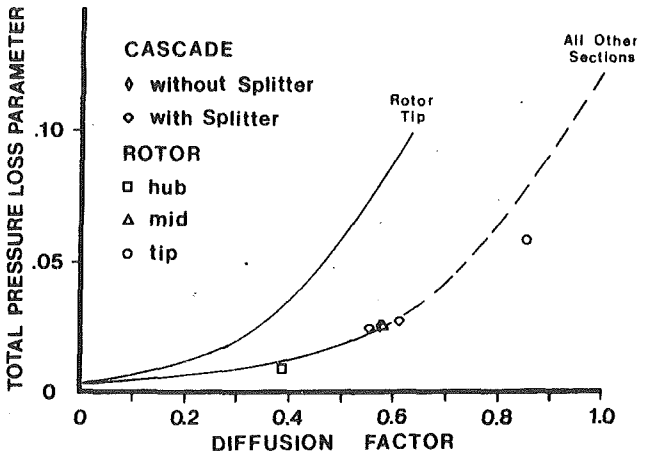

Fig. 16 Splittered rotor and cascade loss characteristics

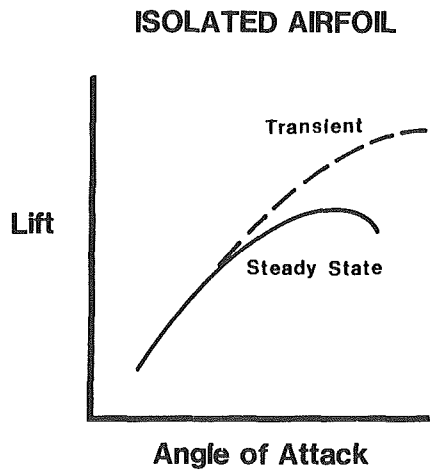

Fig. 17 Transient behavior of an isolated airfoil

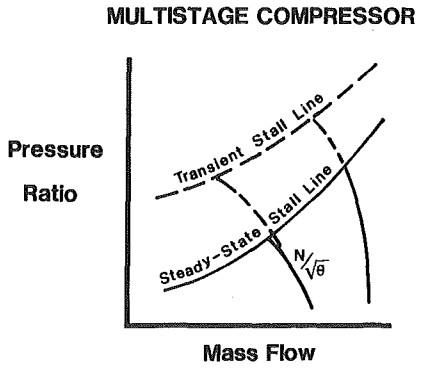

Fig. 18 Transient behavior of a compressor stage

often withstand a relatively severe distortion without stalling. However, as the angular extent of the distortion increases, the magnitude of the distortion it can withstand becomes less. This behavior in terms of a compressor map is depicted in Fig. 18.

The concept under consideration is deliberately to vary the stagger angle of the stationary blading in a multistage compressor in some periodic fashion around the periphery such that rotors would pass through periods of overloading followed by periods of relief during each revolution. The circumferential orientation of this in one stage relative to another would be varied such that a strong zone in one stage would make up for a weak zone in another stage. Although this will introduce forced vibrations at discrete frequencies, the recent trend toward compressors of much lower aspect ratio is likely to make this feasible from an aeromechanical point of view. This is currently under investigation in a multistage low-speed research compressor at Iowa State University.

A Reconsideration of Splitters. The work on splitters reported by Wennerstrom (1987) was concluded in 1974. Although the results were favorable, as shown in Fig. 16, it was also apparent from cascade tests conducted at the time that the losses could be much lower if more favorable pressure distributions could be achieved. An example of the very poor pressure distributions existing is shown in Fig. 19 as reported by Holtman et al. (1973) for nominal design conditions. The pressure on the suction surface of the splitter dips to a value so low that, remembering that it is behind the passage shock, it appears that the flow has reaccelerated to a Mach number of about 1.38, whereas the overall cascade inlet Mach number was 1.46. Efforts were made to improve this by restaggering the splitter as further reported by Holtman et al. (1973). These were unsuccessful. Another attempt was reported by Riffel and Fleeter (1977) in which the circumferential position of the splitter was adjusted within the passage. These tests were also unsuccessful in achieving much improvement in the flow field. A computational effort was made by Dodge (1975) using an inviscid code. It was ultimately concluded that the diffusion level was so high that viscous effects dominated the flow field and an inviscid code was incapable of providing useful guidance for an attempt to optimize splitter shape and position.

All further work on splitters for axial-flow compressors was terminated in the 1970s because at that time it appeared that no adequate viscous computational code existed that was capable of providing useful guidance for a design optimization. A trial-and-error experimental approach did not appear to be cost effective. Since then, considerable progress has been

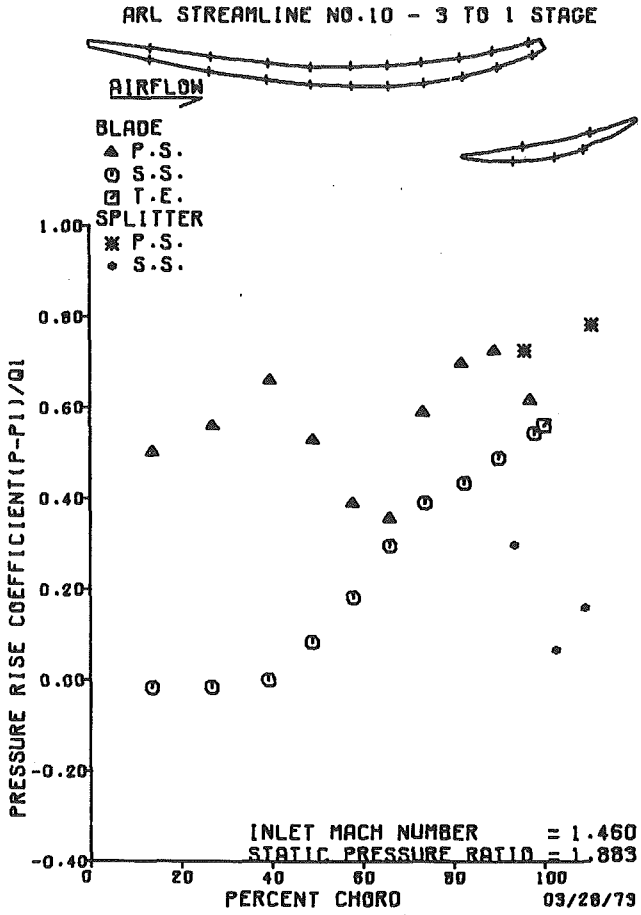

Fig. 19 Cascade pressure distribution with splitters

made in the computational arena. Both viscous/inviscid interaction schemes, such as described by Calvert (1983), and also Reynolds-averaged Navier–Stokes codes incorporating turbulence models such as described by Dawes (1986), have been developed and show some promise of being able to deal with this problem. Some ambitious designs are under consideration for which the use of splitters might prove the only practical approach to achieving the required diffusion levels. It now remains to be seen whether today's computational technology has improved to the extent that it can handle this very difficult optimizational problem.

Conclusions

The use of through-blade design methods and three-dimensional analysis codes has greatly enhanced our ability to deal with high Mach number designs. The use of lower aspect ratios has been the most important contributor to increases in diffusion levels. The use of all types of boundary-layer control, which have proven successful for control of the external aerodynamics of aircraft, has shown very limited applicability to axial flow compressors. The few positive results achieved have been small in magnitude and the areas of application appear very limited.

In fans it appears that further improvements in loading levels may be achieved by the use of splitters and some small further gains may be achieved by the use of variable-radius end-wall fillets. In core compressors, wider use of counterswirl to raise Mach numbers may be the most straightforward method of increasing average stage loading. The exploitation of nonsteady flow may offer additional opportunities, although at the present time I would view this as the alternative of highest risk.

References

Anonymous, 1965, "Fourth Quarterly Progress Report on Turboaccelerator Cycle Evaluation and Experimental Verification Program," Pratt & Whitney Aircraft, Report No. PWA-2569.

Blanton, J. W., 1989, Personal Communication.

Brent, J. A., 1970, "Single Stage Experimental Evaluation of Compressor Blading With Slots and Vortex Generators, Part III—Data and Performance for Stage 4," NASA CR-72741.

Brent, J. A., and Clemmons, D. R., 1974, "Single-Stage Experimental Evaluation of Tandem-Airfoil Rotor and Stator Blading for Compressors, Part VIII—Final Report," NASA CR-134713.

Burger, G. D., and Keenan, M. J., 1971, "Single-Stage Evaluation of Highly-Loaded High-Mach-Number Compressor Stages, III—Data and Performance Tandem Rotor," NASA CR-72772.

Calvert, W. J., 1983, "Application of an Inviscid-Viscous Interaction Method to Transonic Compressor Cascades," *Viscous Effects in Turbomachines*, AGARD Conference Proceedings No. 351, pp. 2/1-2/13.

Clemmons, D. R., Dodge, P. R., and Blackmore, W. L., 1983, "The Impact of Three-Dimensional Analysis on Fan Design," ASME Paper No. 83-GT-136.

Conliffe, C. H., 1971, "Demonstration of Direct Lift Components, Phase III Report," AFAPL-TR-71-48 Vol I and Vol II, Air Force Aero Propulsion Laboratory, Wright-Patterson Air Force Base, OH.

Dawes, W. N., 1986, "A Numerical Study of the 3D Flowfield in a Transonic Compressor Rotor With a Modeling of the Tip Clearance Flow," *Transonic and Supersonic Phenomena in Turbomachines*, AGARD Conference Proceedings No. 401, pp. 21/1-21/12.

Debruge, L. L., 1980, "The Aerodynamic Significance of Fillet Geometry in Turbocompressor Blade Rows," ASME *Journal of Engineering for Power*, Vol. 102, pp. 984-993.

Dodge, P. R., 1975, "Transonic Two-Dimensional Flow Analysis of Compressor Cascade With Splitter Vanes," Air Force Aero Propulsion Laboratory, Wright-Patterson Air Force Base, OH, AFAPL-TR-75-110, AD A025921.

Downs, W. D., 1953, "Development of the XJ55-FF-1 Engine," Power Plant Laboratory, Wright Air Development Center, Wright-Patterson Air Force Base, OH, WADC-TN-55-169, AD855980.

Erwin, J. R., 1964, "The Supersonic Compressor, Chap. 1: Early Work on Supersonic Compressors," *Aerodynamics of Turbines and Compressors*, Volume X, Section G, Princeton University Press, pp. 368-381.

Giffen, R. G., and Smith, L. H., Jr., 1966, "Experimental Evaluation of Outer Case Blowing or Bleeding of Single Stage Axial Flow Compressor, Part I—Design of Rotor and Bleeding and Blowing Configurations," NASA CR-54587.

Griepentrog, H. F. L., 1970, "Performance Prediction for High Turning Low Aspect Ratio Stator Cascades in the Transonic Regime," ASME *Journal of Engineering for Power*, Vol. 92, pp. 390-398.

Holtman, R. L., Huffman, G. D., McClure, R. B., and Sinnet, G. T., 1972, "Test of a Supersonic Compressor Cascade (Vol. II)," Aerospace Research Laboratories, Wright-Patterson Air Force Base, OH, ARL 72-0170, Vol. II, AD 756871.

Holtman, R. L., McClure, R. B., and Sinnet, G. T., 1973, "Test of a Supersonic Compressor Cascade With Splitter Vanes," Aerospace Research Laboratories, Wright-Patterson Air Force Base, OH, ARL 73-0142, AD 774549.

Klapproth, J. A., 1961, "A Review of Supersonic Compressor Development," ASME *Journal of Engineering for Power*, Vol. 83, pp. 258-268.

Koch, C. C., and Smith, L. H., Jr., 1968a, "Experimental Evaluation of Outer Case Blowing or Bleeding of Single Stage Axial Flow Compressors, Part III—Performance of Blowing Insert Configuration No. 1," NASA CR-54589.

Koch, C. C., and Smith, L. H., Jr., 1968b, "Experimental Evaluation of Outer Case Blowing or Bleeding of Single Stage Axial Flow Compressor, Part IV—Performance of Bleed Insert Configuration No. 3," NASA CR-54590.

Law, C. H., and Wennerstrom, A. J., 1987, "Performance of Two Transonic Axial Compressors Incorporation Inlet Counterswirl," ASME JOURNAL OF TURBOMACHINERY, Vol. 109, pp. 142-148.

Lieblein, S., Schwenk, F. C., and Broderick, R. L., 1953, "Diffusion Factor for Estimating Losses and Limiting Blade Loadings in Axial-Flow-Compressor Blade Elements," NACA RM E53D01.

Prince, D. C., Jr., 1980, "Three Dimensional Shock Structures for Transonic/Supersonic Compressor Rotors," AIAA *Journal of Aircraft*, Vol. 17, No. 1, pp. 28-37.

Riffel, R. E., and Fleeter, S., 1977, "The Effect of Splitter Vane Circumferential Location on the Aerodynamic Performance of a Supersonic Compressor Cascade," Air Force Aero Propulsion Laboratory, Wright-Patterson Air Force Base, OH, AFAPL-TR-77-20, AD A043860.

Rockenbach, R. W., 1968, "Single Stage Experimental Evaluation of Slotted Rotor and Stator Blading, Part IX—Final Report," NASA CR-54553.

Rockenbach, R. W., and Brent, J. A., 1970, "Single Stage Experimental Evaluation of Compressor Blading With Slots and Wall Flow Fences," NASA CR-72635.

Rockenbach, R. W., Brent, J. A., and Jones, B. A., 1970, "Single Stage Experimental Evaluation of Compressor Blading With Slots and Vortex Generators, Part I—Analysis and Design of Stages 4 and 5," NASA CR-72626.

Sabel, E. J., and Sabatiuk, A., 1957a, "Turbojet Engine Development: Design of Phase I Compressor," Curtiss-Wright Corporation, C. W. R. Report No. 501.

Sabel, E. J., and Sabatiuk, A., 1957b, "Turbojet Engine Development: Phase I Compressor Test Results," Curtis-Wright Corporation, C. W. R. Report No. 502.

Schweitzer, J. K., and Garberoglio, J. E., 1984, "Maximum Loading Capability of Axial Flow Compressors," AIAA *Journal of Aircraft*, Vol. 21, No. 8, pp. 593–600.

Sulam, D. H., Keenan, M. J., and Flynn, J. T., 1970, "Single Stage Evaluation of Highly-Loaded High-Mach-Number Compressor Stages, II—Data and Performance Multiple-Circular-Arc Rotor," NASA CR-72694.

Weise, A., 1937, "A Supersonic Axial Compressor," Lillienthal Society, Report No. 171.

Wennerstrom, A. J., 1984, "Experimental Study of a High-Throughflow Transonic Axial Compressor Stage," ASME *Journal of Engineering for Gas Turbines and Power*, Vol. 106, pp. 552–560.

Wennerstrom, A. J., 1987, "Some Experiments With a Supersonic, Axial Compressor Stage," ASME JOURNAL OF TURBOMACHINERY, Vol. 109, pp. 388–397.

Wennerstrom, A. J., 1989, "Low Aspect Ratio Axial Flow Compressors: Why and What It Means," ASME JOURNAL OF TURBOMACHINERY, Vol. 111, No. 4, pp. 357–365.

Wennerstrom, A. J., and Frost, G. R., 1974, "Design of a Rotor Incorporating Splitter Vanes for a High Pressure Ratio Supersonic Axial Compressor Stage," Aerospace Research Laboratories, Wright-Patterson Air Force Base, OH, ARL TR 74-0110, AD 786025.

Wennerstrom, A. J., and Puterbaugh, S. L., 1984, "A Three-Dimensional Model for the Prediction of Shock Losses in Compressor Blade Rows," ASME *Journal of Engineering for Gas Turbines and Power*, Vol. 106, No. 2, pp. 295–299.

Wright, L. C., and Novak, R. A., 1960, "Aerodynamic Design and Development of the General Electric CJ805-23 Aft Fan Component," ASME Paper No. 60-WA-270.

Aerodynamic Performance of a Scale-Model, Counterrotating Unducted Fan

T. J. Sullivan
General Electric Company,
Aircraft Engine Business Group,
Cincinnati, OH 45215

The aerodynamic performance of a scale-model, counterrotating unducted fan has been determined and the results are discussed herein. Experimental investigations were conducted using the scale-model propulsor simulator and uniquely shaped fan blades designed by the General Electric Company under contract to NASA. The blades, designed for a high disk loading at Mach 0.72, 35,000 ft altitude max climb condition, are aft-mounted on the simulator in a "pusher" configuration. Data are compared with analytical predictions at the design point and show good agreement.

1 Introduction

The unducted fan engine (UDF™) under development by the General Electric Company has evolved over the past four years from the need for a more fuel-efficient power plant. Conventional high bypass ratio turbofans, which were the engineering development creations of the 1960s and 1970s, have been pushed to practical limits of diameter and weight as thrust demands have grown to 60,000+ lb. Now, the technology advancements of the 1980s have lead to ultra-high bypass ratio fans with their potential for significant improvements in the fuel economy of modern jet aircraft. The unducted fan engine with high disk loading and counterrotating blades offers the industry the performance benefits of ultra-high bypass ratio without a large diameter duct and the associated weight penalty (Stuart, 1985). The direct-drive of the variable pitch fan blades from counterrotating power turbine stages further enhances the engine concept by eliminating the complexity, weight, and maintenance problems of a gearbox.

The General Electric UDF™ engine, which was flight tested on the Boeing 727 from Aug. 1986 through early 1987, and soon to be flight tested on the McDonnell-Douglas MD-80, operates with 11.67 ft diameter counterrotating fan blades. The demonstrator engine blades were designed in early 1984 and followed by an extensive scale-model wind tunnel test program aimed at developing the unducted fan technology needed to meet the engine requirements. Aerodynamic, acoustic, and aeromechanical performance aspects of several counterrotating blade configurations were investigated in the test program funded by NASA contract and also sponsored by General Electric independent research and development. Since 1984, scale-model testing of General Electric unducted fan designs has been conducted at the Boeing low-speed and transonic wind tunnels, the NASA-Lewis $8' \times 6'$ high speed tunnel, and the General Electric anechoic test chamber. NASA-funded programs, such as this, aimed at researching the counterrotating scheme and the development of thin swept, composite airfoils, have been the natural extension of the single rotation prop-fan program activity initiated by NASA in the mid-1970s (Mikkelson et al., 1984).

In the following discussion, aerodynamic performance results and analysis from wind tunnel testing of a scale-model counterrotating unducted fan configuration similar to the full-scale demonstrator engine configuration will be presented. The blade design, manufacture, test in the NASA $8' \times 6'$ wind tunnel, and data analysis of this configuration were funded through NASA Contract NAS3-24080. The Boeing transonic wind tunnel test and data analysis of the same configuration were funded through General Electric independent research and development.

II Test Rig Description

The Model Propulsion Simulator (MPS) is a counterrotating

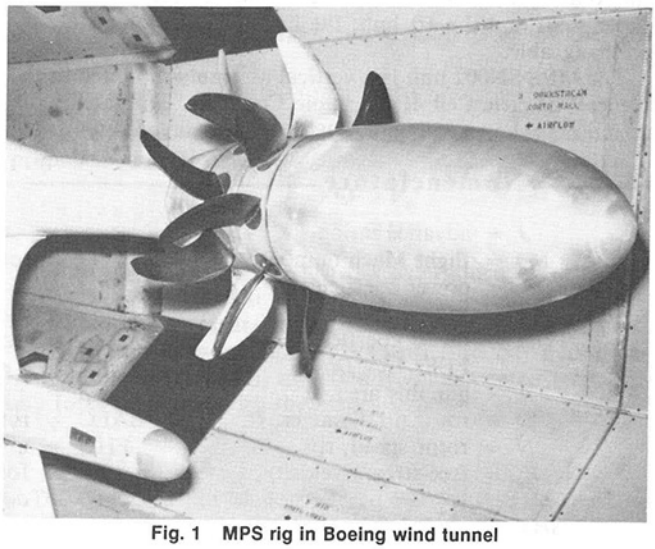

Fig. 1 MPS rig in Boeing wind tunnel

Contributed by the International Gas Turbine Institute and presented at the AGARD Conference, Paris, France, May 6, 1987. Manuscript received at ASME Headquarters April 1989.

unducted fan engine model propulsion system designed for testing "pusher" type fan blade configurations in either subsonic or transonic wind tunnels as described by Delaney et al. (1986). The overall length from the nacelle forebody nose to the aft end of the drive turbine housing is 119.3 in and the propulsor tip diameter is 24.5 in.

The MPS SN001 unit was used for testing in the $8' \times 12'$ Boeing Transonic Wind Tunnel (BTWT). The MPS SN003 unit was used for testing in the NASA-Lewis $8' \times 6'$ transonic wind tunnel and is nearly identical to the SN001 unit. A photograph of the MPS rig installed in the BTWT is shown in Fig. 1. In the wind tunnel, the MPS is mounted on a strut extending from the floor of the test section such that the MPS centerline coincides with the centerline of the test section. For this test, the wind tunnel walls were acoustically treated to allow for the measurement of the unducted fan noise at all critical operating points.

The MPS rig is shown with the pylon attached to a sting off the support strut. The strut is positioned on a turntable, which can be rotated to simulate angles of attack. The pylon is soft-mounted to the nacelle forebody and can be translated axially to two different positions relative to the forward blade leading edge. Testing in the BTWT was performed with and without the pylon installed. In the NASA transonic tunnel, all testing was performed without the pylon and at zero angle of attack.

The nacelle consists of two sections, the forebody and the afterbody. The forebody is an ellipsoid-shaped shell supported from the nonrotating center shaft of the MPS rig. Its shape represents the faired-over inlet and nacelle of an unducted fan engine and was designed to produce diffusion of the airflow just ahead of the counterrotating blade rows to reduce the shock strengths in the blading. The afterbody shape approximates the outer boundary of the turbine exhaust air exiting an actual engine; it has a short 6-in.-dia section before flaring to encompass the MPS drive turbine housing.

The flowpath hubs provide the attachment and locking mechanisms for the eight forward and eight aft rotor blades. The forward, or inner shaft, hub rotates counterclockwise (aft looking forward) while the aft, or outer shaft, hub rotates clockwise. A portion of the blade hub flowpath, as well as the blade plateforms, are dished to provide area-ruling for the blade root thickness where the throughflow Mach numbers would otherwise be the highest. The inner and outer hubs attach to the metric side of the rotating force balances, which, in turn, attach to the rotating shaft.

Propulsor loads are measured by rotating force balances gaged to measure thrust and torque. The rotating force balances incorporate strain-gaged flexure beams of thrust and torque load measurement. These balances are installed between the rotating inner shaft and the forward hub and the rotating outer shaft and the aft hub; the balances are completely interchangeable.

The MPS SN002 unit is a vertical assembly mounted in the General Electric Cell 41 Anechoic Chamber. The facility description is shown in Fig. 2. The propulsor is located 1.3 fan

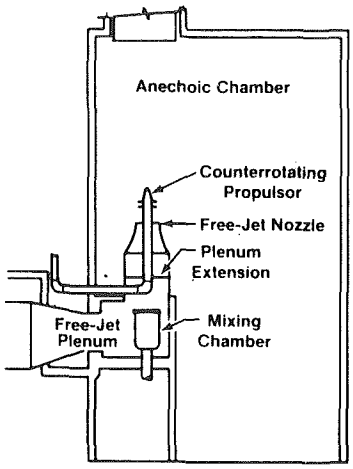

Fig. 2 Schematic of General Electric free-jet noise facility (cell 41)

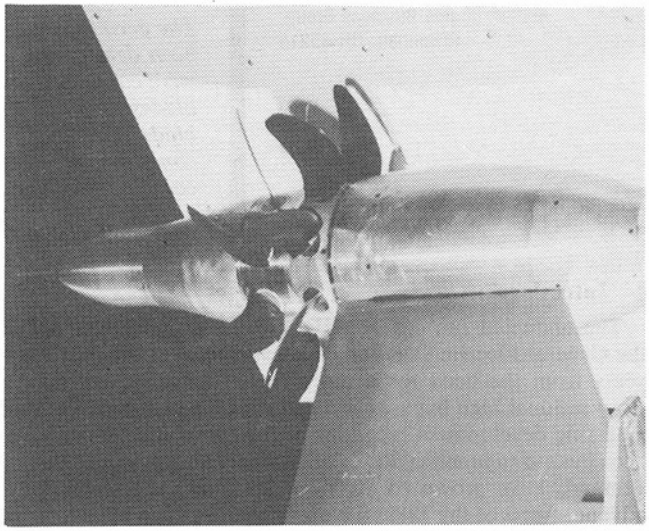

Fig. 3 MPS SN002 rig in GE Cell 41

diameters downstream of the free-jet nozzle exit. The Mach number capability of the free-jet facility for aerodynamic and acoustic testing is from 0 to 0.35. The shape of the MPS SN002 forebody and afterbody in the region near the propulsor blades is identical to the horizontal MPS SN001 and SN003 vehicles. Since the vehicle is driven by a shaft from the bottom and the flow is from bottom to top in the vertical assembly, the forebody does not close but blends into the turbine housing as shown in the photograph of Fig. 3. The afterbody contour is the same as the horizontal SN001 shape extending to the 6-in.-dia cylindrical section and then is closed out with an elliptical shape at the top of the model.

Data from the MPS SN001 and SN003 vehicles are presented herein.

Nomenclature

J = advance ratio
M_o = flight Mach number
PQA = power coefficient = $550\ \text{SHP}/A\rho N^3 D^3$
TQA = thrust coefficient = $\text{FEF}/A\rho N^2 D^2$
A = annulus area, ft^2
D = rotor tip diameter, ft
N = rotor speed, rps
V_o = free-stream velocity, fps
SHP = shaft horsepower
Q = rotor torque, ft-lb
β = blade angle at 3/4 radius, deg
η_{NET} = net efficiency = $J \times \text{TQA}/\text{PQA}$
ρ = air density, slugs/ft^3
FBALC = rotor balance force, lb
FHU = upstream face pressure force, lb
FHD = downstream face pressure force, lb
FH = tare-corrected hub force, lb
FFB = forebody force, lb
FAB = afterbody force, lb
FEF = effective thrust, lb
PT-RATIO = total pressure ratio
TT-RATIO = total temperature ratio

Subscripts

1 = forward rotor
2 = aft rotor

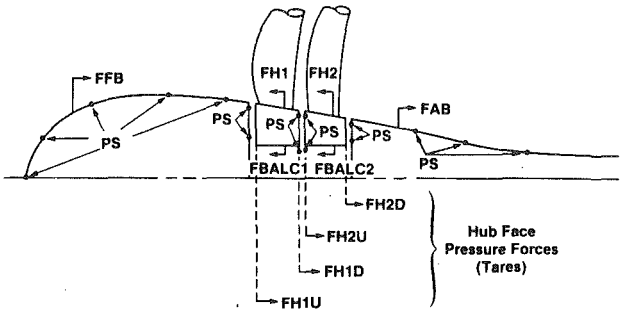

Fig. 4 Schematic description of MPS forces

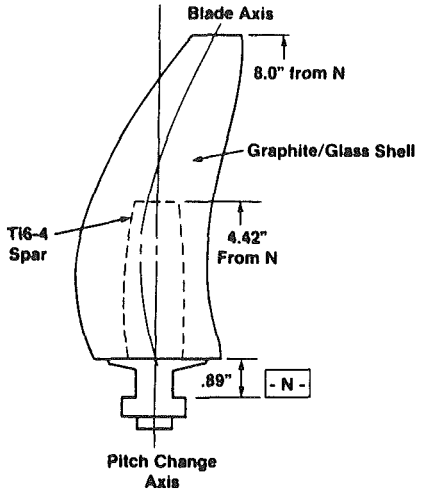

Fig. 5 MPS propeller blade design (F7)

III Instrumentation and Data Reduction

A data reduction program was set up to calculate the important performance parameters from the instrumentation measurements made during the wind tunnel testing of the MPS rig. Standard wind tunnel procedures were used to obtain free-stream total and static pressures and temperatures, tunnel Mach number, velocity, density, and Reynolds number. The basic MPS measurements included the blade angle, rotational speed, axial thrust, and torque for each of the counterrotating blade hubs. Force balance measurements were corrected for dynamic effects to get the true thrust and torque values. Four of the blades on each hub are instrumented with three strain gages each. Signals from these strain gages are routed through telemetry to a 14-track magnetic tape and monitoring equipment in the control room.

Five rows of thirteen static pressures are located on the nacelle forebody from the nose to the forward rotor leading edge. Four rows of twelve static pressures are located on the afterbody downstream of the aft rotor trailing edge to the point where the afterbody shape blends into the 6-in.-dia cylinder just ahead of the turbine housing and support strut. Static pressure measurements on the MPS forebody and afterbody as well as in the cavities between rotors were used to correct the forces measured by the hub balances, FBALC1 and FBALC2. A schematic of the MPS in Fig. 4 shows the location and direction of all the forces acting on the model. The body pressures are integrated over incremental projected areas assigned to each static pressure tap.

The resultant forces, FFB and FAB, are calculated for both the blades-on and blades-off configurations and used in the equations (below) to define the total effective blade thrust. The hub balance force data are corrected for the upstream and downstream hub face pressure integrals. Static pressure taps

Table 1

Mach No./altitude	0.72/35,000
Advance ratio, J	2.80
Power coefficient, PQA	4.17
Tip speed, ft/sec	780
Radius ratio	0.42
Total activity factor	2400
Aero tip sweep, FWD/AFT, deg	33/29

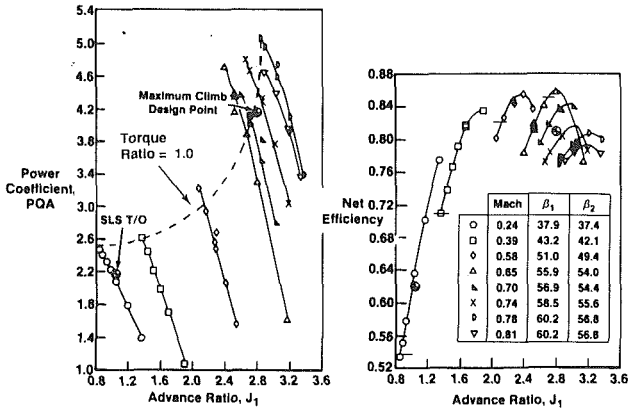

Fig. 6 F7A7 performance map

on the upstream and downstream faces of the rotors at different radial positions in the cavities beneath the flowpath are area-averaged and represent tare force corrections (FHU and FHD) to the hub balance thrust measurements. The hub forces measured with blades off (FH1 and FH2) are equal to or very nearly zero for both high-speed wind tunnel tests.

The MPS effective thrust includes the change in nacelle forces due to the action of the blading. Effective thrust can be calculated as the change in hub thrust, with-blades minus without-blades, plus the change in nacelle body forces (i.e., the forebody and afterbody pressure integrals) with and without blades. Each rotor thrust is credited (or debited) by half of the forebody-induced force and half of the afterbody-induced drag. The resultant equations for the effective thrust of each rotor are

$$\mathrm{FEF1} = \mathrm{FBALC1} + \mathrm{FH1U} + \mathrm{FH1D} - 1/2[\mathrm{FFB} + \mathrm{FAB}]^* - \mathrm{FH1}]^{**} \quad (1)$$

$$\mathrm{FEF2} = \mathrm{FBALC2} + \mathrm{FH2U} + \mathrm{FH2D} - 1/2[\mathrm{FFB} + \mathrm{FAB}]^* - \mathrm{FH2}^{**} \quad (2)$$

* Blades on minus blades off

** Blades off

The total propulsor effective thrust is the sum of the two individual rotor thrusts

$$\mathrm{FEF} = \mathrm{FEF1} + \mathrm{FEF2} \quad (3)$$

The total effective thrust (FEF) is then used to determine the propulsor net efficiency

$$\eta_{\mathrm{NET}} = \frac{\mathrm{FEF} \times V_o}{550\ \mathrm{SHP}} \quad (4)$$

In summary, the effective thrust is determined by using the blades-on rotor force, first corrected for the tare force (integrated hub face pressure), then corrected for blading induced body forces (blades-on versus blades-off forebody and afterbody pressure integrals), and finally, incremented from the hub force measured with the blades removed.

IV Blade Design

The unducted fan blades, named F7A7, were designed at the Mach 0.72, 35,000 ft altitude max climb flight condition.

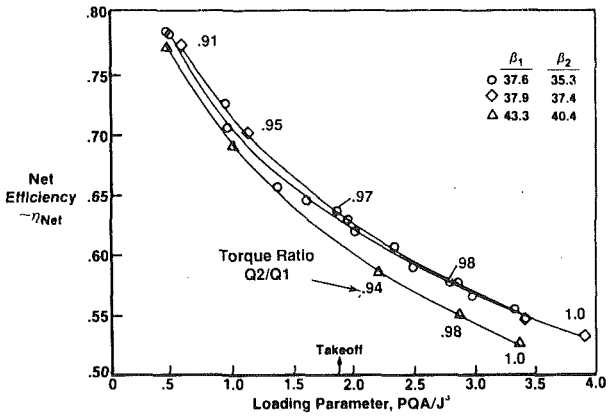

Fig. 7 F7A7 blade angle variations at Mach 0.24 efficiency versus loading parameter

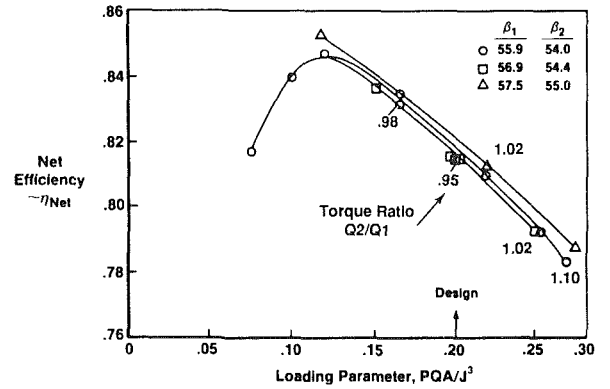

Fig. 8 F7A7 net efficiency versus loading parameter blade angle variations M = 0.70

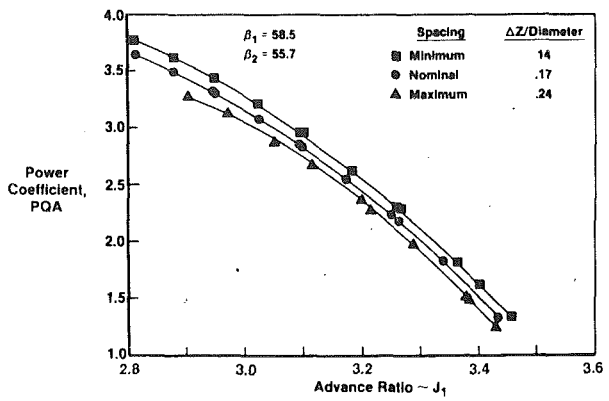

Fig. 9 NASA 8′ × 6′ F7A7 test results at M = 0.8 total power coefficient versus forward advance ratio

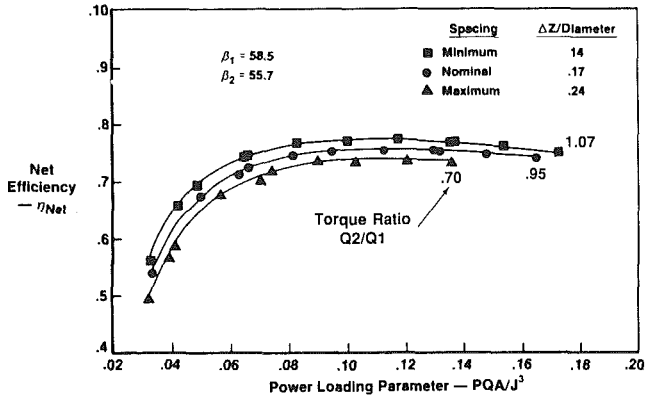

Fig. 10 NASA 8′ × 6′ F7A7 test results at M = 0.8 net efficiency versus power loading parameter

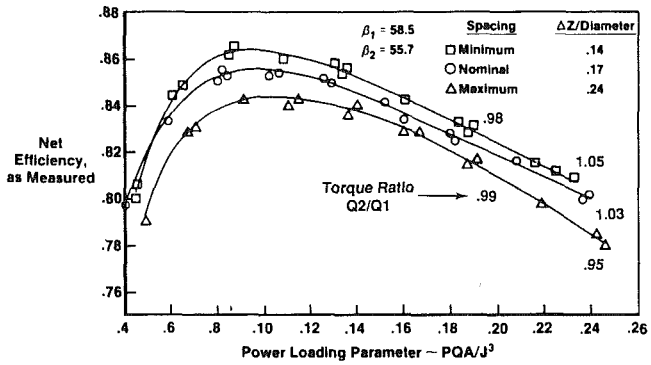

Fig. 11 NASA 8′ × 6′ rotor spacing effects at Mach 0.67

There are eight blades in the forward rotor and eight blades in the aft rotor, each having an activity factor of 150. The blades are designed at a high disk loading (SHP/A) of 86 to minimize the diameter and weight of the full-scale UDF™ engine. The aerodynamic design of the unducted fan blades was carried out using the general method described by Smith (1987). The design specified custom tailored airfoil and flowpath shapes designed to have favorable velocity distributions with minimum-strength shocks. The composite construction and moderate sweep cause the blades to deform substantially from the static to the running condition, and a finite-element elastic model was employed to account for this change. However, after the airfoil molds were made, the originally intended stiffness in the chordwise direction was increased, resulting in airfoils with 2–4 deg more camber than intended in the running condition. Subsequent analysis by GE and NASA (Celestina et al., 1986) have indicated that the tested airfoils might have relatively strong shocks at the trailing edge.

The blades are designed and manufactured in the 24.50-in.-dia scale-model size for wind tunnel testing at sea level atmospheric pressure. Table 1 show the aerodynamic design parameters of the F7A7 configuration.

A planform sketch of the MPS forward rotor blade F7 is shown in Fig. 5. The blade is made from a composite material of graphite fibers with a titanium shank and spar extending to approximately 50 percent of the blade span. The blades are designed with chord, thickness, and sweep distributions that will allow aeromechanical stability over the entire operating range.

V Wind Tunnel Test Data

Aerodynamic testing was conducted in the Boeing Transonic Wind Tunnel (BTWT), the NASA 8′ × 6′ Wind Tunnel, and the General Electric Anechoic Chamber, Cell 41. The BTWT was configured with acoustic wall panels and the vehicle was tested at tunnel speeds from Mach 0.24 to Mach 0.81. Testing was done with and without the pylon and at angles of attack. Forward-to-aft rotor spacing effects were evaluated and reverse thrust was measured. A circumferentially transversable rake was used to measure total pressure, total temperature, and yaw angle downstream of the aft rotor for certain key aerodynamic test points. Rotor spacing effects were also investigated in the NASA tunnel. Low-speed aerodynamic testing was performed in the GE anechoic chamber.

The F7A7 blades were tested in the high-speed wind tunnels over a wide range of Mach numbers, pitch angles, and rotor speeds. The blades were first set to pitch angles that would give equal rotor torques at design speed and the tunnel was brought up to the test Mach number with the blades wind-

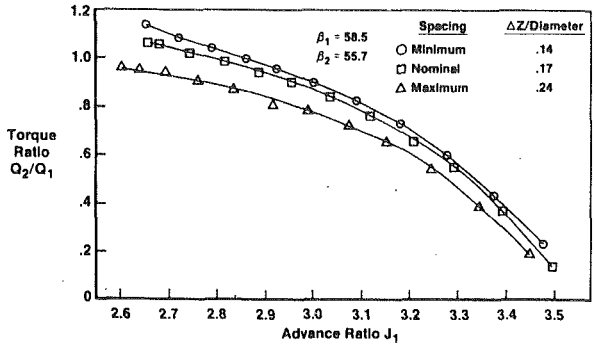

Fig. 12 NASA 8′ × 6′ F7A7 at Mach 0.72 rotor spacing effects on torque ratio

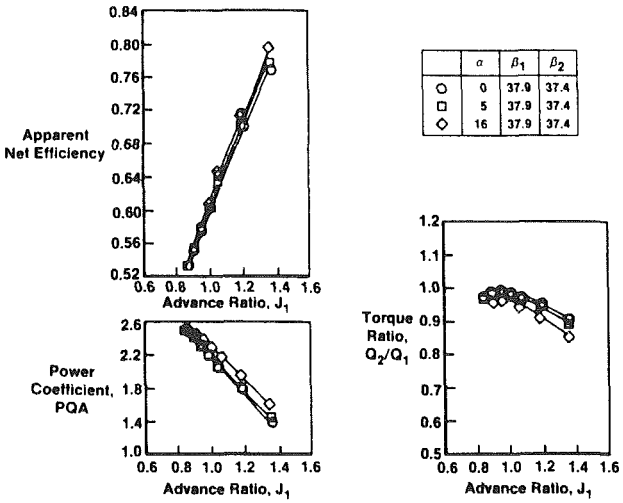

Fig. 13 Effect of angle of attack, F7A7, Mach 0.24, no pylon

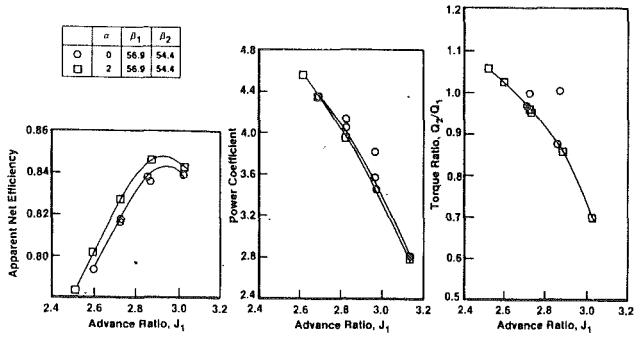

Fig. 14 Effect of angle of attack, F7A7, Mach 0.70, no pylon

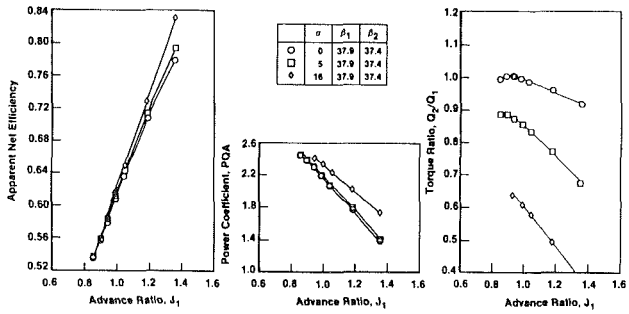

Fig. 15 Effect of angle of attack, F7A7 Mach 0.24, with pylon

milling. The rotors were powered to the minimum speed above windmill and data were taken with equal rotor speeds at several increments up to 110 percent design speed. The tunnel Mach number was then adjusted slightly up and down from the nominal setting and the test was repeated at the same equal rotor speed points. The initial pitch angles tested were chosen to produce the power required along the max climb flight path at 100 percent speed on both rotors and equal torques per stage.

(A) Overall Performance. In the Boeing transonic wind tunnel, the data were taken at tunnel speeds from Mach 0.24 to Mach 0.81 without the pylon and at zero angle of attack. The overall performance of the F7A7 blades for these conditions is presented in Fig. 6. The power coefficient, PQA, and net efficiency are plotted as a function of the advance ratio of the forward rotor, J1. The efficiencies plotted are as measured and do not account for strain gage effects or dynamic model calibration. When applied to the test data, these corrections will increase the net efficiency by 2–3 points at the high Mach numbers. Each power line represents a different tunnel Mach number with a different set of pitch angles. The max climb target design point at Mach 0.72 is shown on the performance map.

The net efficiency interpolated on the performance map from the measured data to the design point is 81 percent. The effects of increasing Mach number can be seen by tracing the fall-off of efficiency along a constant power loading line. The data trend shows that at Mach 0.65 the efficiency is 85 percent, dropping to 77 percent at Mach 0.81. At low speed, such as the takeoff condition at Mach 0.24, the net efficiency is 62 percent.

Blade pitch angle variations were made at the Mach 0.24 and Mach 0.70 test conditions and the performance data are shown in Figs. 7 and 8, respectively. The efficiency data when plotted versus the loading parameters, PQA/J^3, collapse to nearly a unique line for most of the pitch angles tested. When the loading differs greatly from the nominal value, the efficiency data will depart from a single line. This is the case at Mach 0.24 (Fig. 7) with both rotors open approximately 5 deg from nominal. The blade loading is significantly higher and the efficiency is 2–3 points less than nominal pitch angle data. At Mach 0.70 (Fig. 8), the three pitch angle settings vary only 1–2 deg from each other and produce efficiency levels within 0.5 point. The most open setting with the blades running slower for the same power absorbed gives slightly higher efficiency.

(B) Rotor Spacing Effects. Rotor spacing effects were investigated at Mach 0.80 with three different spacings of the rotor pitch-change axes. The spacings varied from the minimum axial distance to blade diameter ratio 0.14 to the maximum value of 0.24. The nominal distance for which most of the wind tunnel testing was conducted was 4.16 in. Figure 9 shows that for larger spacing between rotors, less power is absorbed by the rotors at the same advance ratio, even though the pitch angles are held constant. The spacing effect on efficiency is shown in Fig. 10 by plotting the data versus the power loading parameter, PQA/J^3. The minimum spacing gives the highest efficiency at all Mach 0.8 loading levels, approximately 1.0 to 1.5 points higher than the nominal spacing. The maximum spacing is 2 points worse in efficiency than the nominal spacing. Other F7A7 wind tunnel data (Fig. 11) show that at slightly lower Mach numbers, down to Mach 0.67, the nominal to maximum spacing effect is 1–2 points in net efficiency, while the minimum to nominal effect is less. At takeoff Mach 0.25, the test data indicate that rotor spacing has little or no effect on net efficiency.

The proximity of the downstream rotor to the upstream rotor has a pronounced effect on the torque split between rotors. Data are shown in Fig. 12 for three different spacings. At equal power and rpm, the total torque remains the same but the split between rotors is different. The torque ratio (Q_2/Q_1) decreases

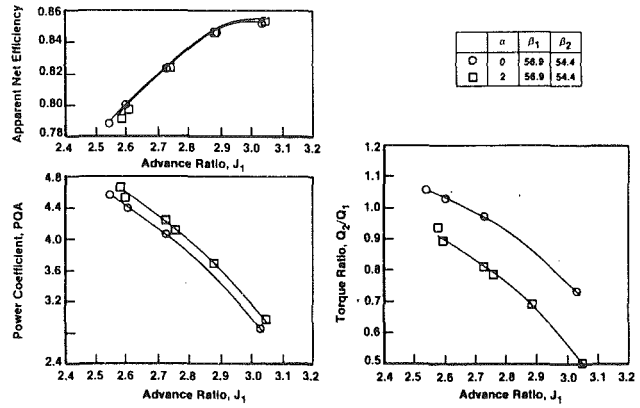

Fig. 16 Effect of angle of attack, F7A7, Mach 0.70, with pylon

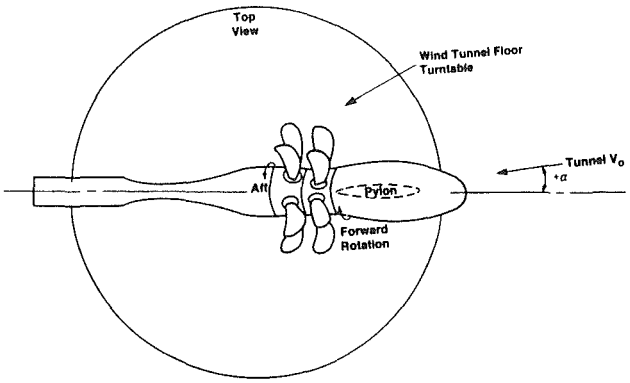

Fig. 17 Schematic of MPS in transonic wind tunnel at angle of attack, with pylon

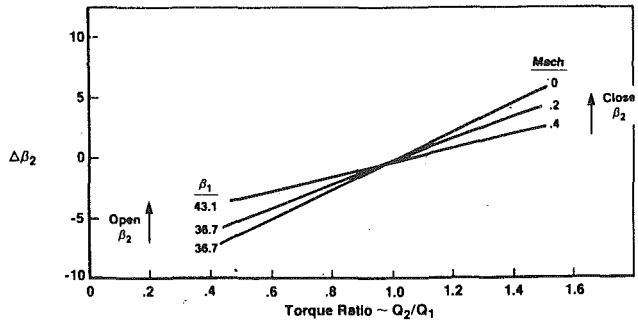

Fig. 18 Blade angle change required to match torques Mach 0–0.4 equal speeds, 100 percent N_c β_1 constant

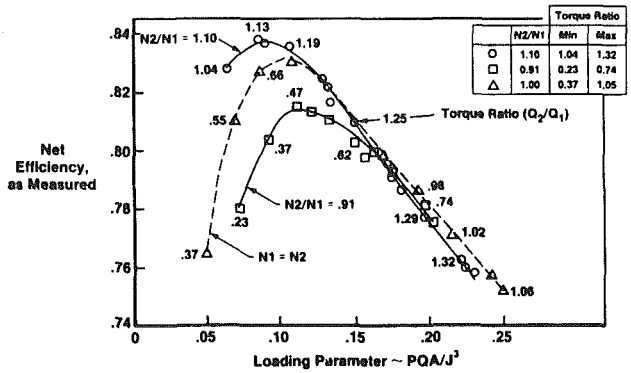

Fig. 19 NASA 8′ × 6′ F7A7 scale-model performance Mach 0.72: effect of mis-matched rotor speeds

as spacing increases since the induced effect of the downstream rotor is diminished. If the spacing were further increased, the effect would continue to lessen to the extreme condition where the downstream rotor is so far removed from the upstream rotor that it acts as an isolated blade row having no effect at all.

(C) Angle of Attack/Pylon Effects. Aerodynamic performance data taken in the transonic wind tunnel to assess the effect of angle of attack, with and without pylon, at Mach 0.24 and Mach 0.70, are shown in Figs. 13–16. The three graphs in Fig. 13 show the net efficiency, power coefficient, and torque ratio parameters as a function of advance ratio for the F7A7 configuration without pylon at Mach 0.24. Data are shown for three angles of attack, 0, 5, and 16 deg, with constant pitch angles. Similar data are shown in Fig. 14 at Mach 0.70 at 0 and 2 deg angle of attack. Since the model is rotated in the tunnel on a platform by the angle of attack (α), the free-stream velocity (V_o) in the direction of thrust is equivalent to V_o cos α. Correcting the advance ratio, J_1 by the cosine causes the data to collapse to one curve for all angles of attack on the power coefficient plot. The effect on the torque ratio lines is to spread them farther apart with increasing angle of attack.

The measured thrust is in the direction of the model centerline axis skewed from the free-stream tunnel direction by the angle of attack. The normal force on the blades as a result of the model direction relative to the airflow was not measured, and its streamwise component is therefore not accounted for in the efficiency calculation. The word "apparent" has been added to the efficiency label to indicate that it is not a true efficiency.

With the pylon installed at the bottom of the model, the test points are repeated at the same Mach numbers and blade pitch angles. The power coefficient, apparent net efficiency, and torque ratio data are shown in Figs. 15 and 16. Since the pylon drag is not measured by the rotor force balances and not otherwise accounted for in the overall thrust, the apparent efficiency values with pylon on are approximately the same as the pylon-off data, but slightly higher. Now, the free-stream velocity correction is no longer appropriate to collapse the power coefficient lines because of the angular momentum change caused by the pylon. The pylon effect is most noticeable in how it affects the level of torque ratio. With increasing angle of attack, the pylon acts like an inlet guide vane producing counterswirl into the forward rotor and loading it relative to the aft rotor. The schematic of the MPS in the wind tunnel, Fig. 17, shows that positive angles of attack produce counterswirl into the forward rotor; negative angles produce preswirl.

In Fig. 15 at Mach 0.24, the aft-to-forward rotor torque ratio (Q_2/Q_1) varies from 1.0 at zero angle of attack to 0.85 at 5 deg and 0.60 at 16 deg. The large split in torque per stage, observed from tests with constant pitch angles and constant speeds, will be corrected in the installed engine by varying blade pitch angles of maintaining equal speeds as the airplane climbs out from takeoff at some angle of attack. The direction of pitch angle change will also vary from right-hand engine to left-hand engine since the direction of forward rotation is down inboard on the airplane right side and up inboard on the left side. An estimate of the amount of angle change required to offset unequal torques is shown in Fig. 18. Data from low-speed tests at Mach 0, 0.2, and 0.4 were cross-plotted to obtain the amount of β_2 change, holding β_1 constant, as a function of torque ratio.

(D) Mismatched Rotor Speeds. Wind tunnel data were taken at Mach 0.72 with unequal rotor speeds over a wide range of rpm. Figure 19 shows the net efficiency plotted against the loading parameter, PQA/J^3, for two different speed ratio lines as well as equal rotor speed reference data. Testing was conducted with the aft rotor speed 10 percent higher and 10 percent lower than the forward rotor speed. Holding the pitch

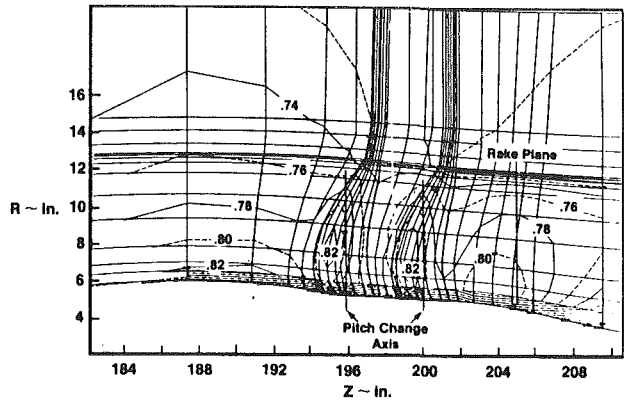

Fig. 20 F7A7 flowfield M = 0.70: meriodinal Mach number contours

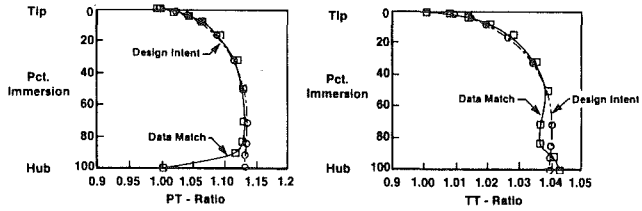

Fig. 21 F7A7 data match results: pressure and temperature profiles versus design intent; rotor 2 exit rake plane

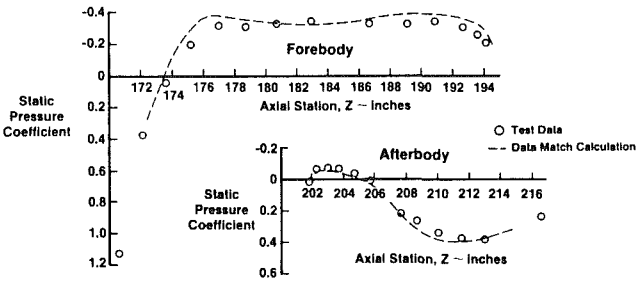

Fig. 22 F7A7 data match at Mach 0.74: static presure coefficient along forebody and afterbody

angles constant, as was necessary in this type of test, means the rotor torque splits are not equal as the rpm are increased. When rotor 2 is running 10 percent faster than rotor 1, the ratio of rotor 2 to rotor 1 torque varies between 1.04 and 1.32. When rotor 2 is running 10 percent slower, its torque varies between 23 and 74 percent of the rotor 1 torque. The data show that the net efficiency is higher at low loadings when the torques are within 25 percent of being equal. The lower efficiency line ($N_2/N_1 = 0.91$), at low loadings, shows torque ratios that are much less matched and consequently, lower efficiencies. At the high loading levels, however, the data show that when the torque ratios are within 25 percent of being matched, the speed ratio has little effect on the net efficiency. By comparing all the data shown in Fig. 19, the test points with torque ratios closest to 1.0 have the highest efficiencies.

(E) Design Point Data Match. Data were recorded in the high-speed wind tunnel near the design Mach 0.72 condition with a circumferentially traversable rake at the exit of the second rotor. The rake measured total pressure, total temperature, and swirl angle at 15 radial locations, which spanned from the rotor hub to an outer tip radius approximately 10 percent above the blade tips. The rake was traversable through an arc of 60 deg from 135 deg to 195 deg. Data were taken in five 15-deg increments, without pylon and at zero angle of attack, with the model operating at the tunnel Mach number of 0.70. In addition to the rake measurements, nacelle forebody and afterbody static pressures were measured. The rake and body pressure data were used to compare with the design analytical calculation of the circumferential average flowfield.

Detailed aerodynamic data-match studies were conducted using the test data to determine areas of the blade where improvements could be made to reduce losses. The data match analysis was performed by using a modified version of the circumferential-average flow calculation procedure that is used for designing and analyzing conventional high bypass turbofans. The data match test point was taken at Mach 0.70, design power coefficient of 4.17, and design advance ratio of 2.80. The procedure begins by inputting speed and torque for each rotor (measured from test) and adjusting the radial distributions of losses until the net thrust, body static pressure distributions, and the fan exit radial pressure profile are reasonably well matched.

The total airflow is adjusted so that the tip streamline matches the forward rotor blade tip diameter. Figure 20 illustrates the flow field that results when the data are matched. Meridional Mach number contours are superimposed on the chart with the flow streamlines and calculation stations; the rake plane location is also noted. The peak Mach number of 0.82 occurs inside the blades where the effects of thickness and lean are accounted for in the calculation. A hub boundary layer is specified to represent the flow losses near the hub surface. Figure 21 shows the data match of the pressure and temperature measurements at the discharge take plane. Since no data between the rotors were taken, it was necessary to assume the loss split. The symbols in these plots distinguish the aerodynamic design intent from the actual test data results. The data match analysis using the test data matches the original design intent quite well over most of the blade span. Locally in the hub region, where the boundary layer affects the test measurements, the blade total pressure falls off and the loss coefficients are higher than design intent.

The distribution of static pressure coefficient as a function of axial length along the forebody and afterbody of the MPS rig is shown in Fig. 22. The data match the theoretical expectations quite well and confirm the static pressure rise on the afterbody and where the hub necks down to a cylindrical body downstream of the blades.

VI Conclusions

The scale model, counterrotating unducted fan blades, F7A7, were tested in the Boeing and NASA high-speed wind tunnels and the aerodynamic performance has been demonstrated. The following are the most significant performance results:

- Aero data were obtained with several blade angle combinations up to Mach 0.81. The measured net efficiency at the max climb Mach 0.72 design point is 81 percent; at takeoff, the net efficiency is 62 percent.
- Large rotor spacings have a significant effect on net efficiency at high Mach numbers.
- Power coefficient lines at different angles of attack and constant pitch angles collapse to a single line when the advance ratio is corrected by cos α to account for the skewed thrust direction.
- The pylon, installed at an angle of attack, acts like an inlet guide vane, producing inlet swirl to the forward rotor. The swirl unloads or loads the forward rotor depending on the direction of rotation relative to the pylon. If pitch angles are held constant, unequal torque splits result.
- Data taken with unequal rotor speeds show very little effect on efficiency at loadings and torque ratios near the cruise design point. When the torque ratios are substantially different

from 1.0, the overall efficiency can be 2–5 points lower than nominal.

- The design point rake data were analyzed and showed good agreement with the design intent.

References

Celestina, M. L., and Mulac, R. A., and Adamczyk, J. J., 1986, "A Numerical Simulation of the Inviscid Flow Through a Counter-rotating Propeller," ASME JOURNAL OF TURBOMACHINERY, Vol. 108, pp. 187–193.

Delaney, B. R., and Balan, C., West, H., Humenik, F. M., and Craig, G., 1986, "A Model Propulsion Simulator for Evaluating Counter Rotating Blade Characteristics," presented as the SAE Aerospace Technology Conference and Exposition, Long Beach, CA.

Mikkelson, D. C., Mitchell, G. A., and Bober, L. J., 1984, "Summary of Recent NASA Propeller Research," presented at the AGARD Fluid Dynamics Meeting on Aerodynamics and Acoustics of Propellers, Toronto, Canada.

Smith, L. H., Jr., 1987, "Unducted Fan Aerodynamic Design," ASME JOURNAL OF TURBOMACHINERY, Vol. 109, pp. 313–324.

Stuart, A. R., 1985, "The Unducted Fan Engine," presented at the AIAA/SAE/ASME/ASEE 21st Joint Propulsion Conference, Monterey, CA.

Three-Dimensional Relief in Turbomachinery Blading

A. R. Wadia

B. F. Beacher

GE Aircraft Engines,
Cincinnati, OH 45215

The leading edge region of turbomachinery blading in the vicinity of the endwalls is typically characterized by an abrupt increase in the inlet flow angle and a reduction in total pressure associated with endwall boundary layer flow. Conventional two-dimensional cascade analysis of the airfoil sections at the endwalls indicates large leading edge loadings, which are apparently detrimental to the performance. However, experimental data exist that suggest that cascade leading edge loading conditions are not nearly as severe as those indicated by a two-dimensional cascade analysis. This discrepancy between two-dimensional cascade analyses and experimental measurements has generally been attributed to inviscid three-dimensional effects. This article reports on two and three-dimensional calculations of the flow within two axial-flow compressor stators operating near their design points. The computational results of the three-dimensional analysis reveal a significant three-dimensional relief near the casing endwall that is absent in the two-dimensional calculations. The calculated inviscid three-dimensional relief at the endwall is substantiated by airfoil surface static pressure measurements on low-speed research compressor blading designed to model the flow in the high-speed compressor. A strong spanwise flow toward the endwall along the leading edge on the suction surface of the airfoil is responsible for the relief in the leading edge loading at the endwall. This radial migration of flow results in a more uniform spanwise loading compared to that predicted by two-dimensional calculations.

Introduction

The continuing trend toward higher component efficiencies in gas turbine engines has historically demanded increasingly effective approaches to improve endwall flows. Current concepts to alleviate the losses due to blade/endwall interaction include stator end-bends in compressors and endwall contouring in turbines. Full realization of the performance gains accruing from improved endwall flows requires a detailed understanding of the complex flow structure in the endwall region.

The endwall flow field is characterized by an abrupt increase in the inlet flow angle, as shown in Fig. 1(*a*), for a low-speed compressor stator blading. While this local increase in inlet flow angle is well known, surprisingly little basic design information regarding the nature of the endwall flow with such inlet conditions seems to have been published in the open literature.

Generally, axially-flow compressor designs have been accomplished by assuming fairly uniform rotor exit total pressure and stator exit swirl angle distributions with the assumption of somewhat higher than average rotor and stator losses at the blade ends. The resulting "design" inlet flow angle distribution determined by conventional throughflow analyses that do not incorporate secondary flow and mixing effects is illustrated in Fig. 1(*a*). The difference between the smoothed design profile and the measured test profile is apparent in the figure. The leading edge metal angle distribution, also shown in Fig. 1(*a*), which had been designed using two-dimensional cascade analyses, follows the design air angle distribution closely.

The development of analyses that empirically model the viscous and secondary flow effects in an axisymmetric throughflow calculation (e.g., Adkins and Smith, 1982; Behlke, 1985) provides the designer with the additional analytical capability of modeling the inlet and exit vector diagrams more accurately. A typical result of the throughflow calculation with secondary flow and mixing (CAFMIX) as developed by Adkins and Smith (1982) is illustrated in Fig. 1(*b*) for high-speed compressor stator blading. The calculated inlet flow angle distribution is in good agreement with test data.

Now that the designer can calculate realistic air angles with CAFMIX, he is presented with the choice of either using the full radial profile illustrated in Fig. 1(*b*) or continuing to use a smoothed inlet flow angle distribution, as shown in Fig. 1(*a*), for detailed design of the blading. Two-dimensional cascade analyses (CASC) of the endwall section with inlet flow angle profiles, calculated by CAFMIX, would indicate the blading designed with the smoothed inlet flow angle distribution to operate at high incidence with considerable leading edge loading relative to the other spanwise sections. Based on such CASC results, the designer would be inclined to close the leading edges of the endwall sections considerably to align the blade with the inlet flow conditions. However, this would produce

Contributed by the International Gas Turbine Institute and presented at the 34th International Gas Turbine and Aeroengine Congress and Exhibition, Toronto, Ontario, Canada, June 4–8, 1989. Manuscript received at ASME Headquarters January 25, 1989. Paper No. 89-GT-151.

a very non-smooth distribution of leading edge metal angle that might be very difficult or expensive to manufacture. This is especially true in the case of high aspect ratio inlet stages (e.g., Figs. 1*a*, *b*) where the inlet air angle has a relatively large and uniform spanwise "core-flow" region but with regions of very high gradients from the endwalls to approximately 15 percent immersion. For lower aspect ratio middle stages (Fig. 1*c*), however, the viscous effects extend inward to 30 percent from either endwall, resulting in more gradual gradients in the flow angle distribution from the blade ends to the core-flow region.

Experimental data on low-speed compressor blading suggest, however, that cascade endwall leading edge loadings are not nearly as severe as those indicated by the two-dimensional-cascade analyses using the measured inlet flow angle distribution. This difference between the CASC calculations and experimental measurements has been attributed to three-dimensional relief, and may indicate that fully three-dimensional design methods may be required.

Objectives and Scope

This study was initiated to investigate the nature of endwall flows and to provide guidelines for the design of endwall sections. The present paper highlights some key analytical and experimental results that show the nature and causes of "three-dimensional relief" in endwall regions of turbomachinery blading.

In the following sections, vector diagrams, derived from an axisymmetric throughflow calculation with secondary flow and mixing effects that match data from a high-speed multistage compressor test are shown. The inlet and exit profiles are used with two-dimensional cascade analysis code (CASC) and a three-dimensional analysis code to determine the surface static pressure distributions on two stator configurations. Stator *A* was designed with the smoothed inlet profile in the casing endwall region, shown in Fig. 1(*c*), while stator *B* had leading edge metal angles set to meet the full endwall defect.

Comparisons of the two-dimensional and three-dimensional analytical results are presented for the pitchline and casing endwall sections, and a difference between the two-dimensional and three-dimensional calculations is observed near the endwalls. Secondary flow effects at the endwall that alleviate the leading edge loading for stator *A* in the three-dimensional calculations are illustrated. The differences in secondary flow calculated by the three-dimensional analysis between stator *A* and stator *B* are discussed. The effects of a thin casing endwall boundary layer at the inlet (over and above the effects of the highly skewed inlet air angle) on the secondary flow within the annulus are illustrated. Experimental verification of the three-dimensional analytical results is provided by detailed measurements of stator surface static pressures obtained in a low-speed research compressor.

Design Features of High-speed Compressor Stators

The analytical study was conducted on subsonic stator vanes typical of those in the middle stages of high-pressure compressors.

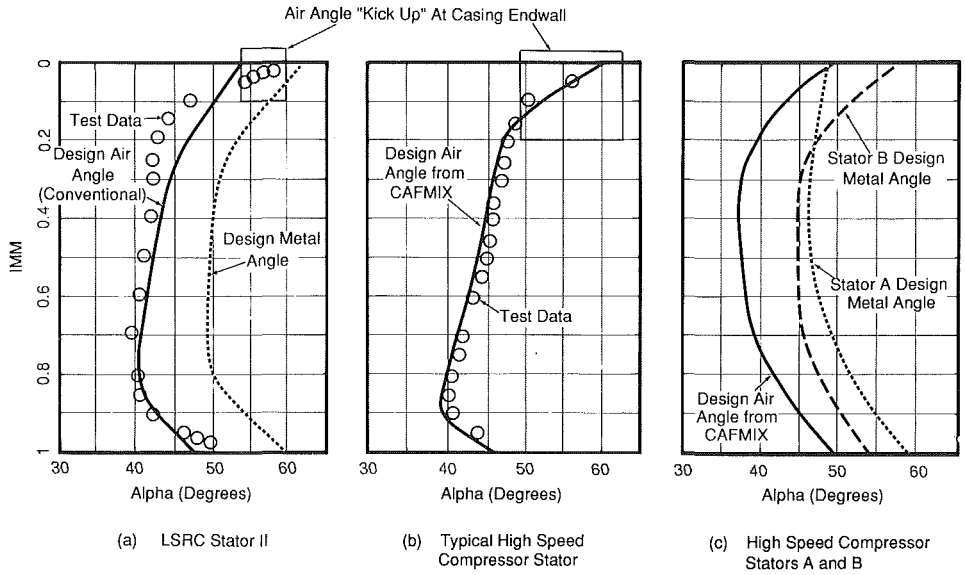

Fig. 1 Typical distributions of inlet absolute flow angle (both design and test) and metal angle for compressor stators

Nomenclature

ALPHA = absolute air angle
CASC = two-dimensional cascade analysis
CAFMIX = throughflow analysis with secondary flow and mixing
IMM = radial immersion (0 = tip and 1 = hub)
LE = leading edge
LSRC = low-speed research compressor
PS = pressure surface
R = radial distance
SS = suction surface
T = temperature
TE = trailing edge
V_s = blade surface secondary flow velocity normal to the axisymmetric Euler grid surface shown in the meridional plane in Fig. 3
2D = two-dimensional cascade analysis
3D = three-dimensional Euler analysis

Table 1 High-speed stator blading pitchline parameters

Parameter	Stator *A*	Stator *B*
Radius ratio	0.87	0.87
Solidity	1.34	1.34
Aspect ratio	1.48	1.48
Inlet Mach number	0.58	0.58
Stagger, deg	22.0	19.7
t_{max}/C	0.075	0.075

Stator *A* has airfoil sections that are conventional in design, with leading edge metal angles, shown in Fig. 1(*c*), being set by conventional throughflow analyses that do not incorporate secondary flow and mixing effects. These airfoil sections are conventional in the sense of having modified circular arc meanlines and NACA 65-series thickness distributions. The design philosophy is similar to that illustrated in Fig. 1(*a*) for the low-speed research compressor stator II.

Stator *B* sections are modern custom-tailored airfoils that give reduced profile losses and endwall loadings. Custom tailoring is accomplished by the appropriate selection of the meanline angle and chordwise thickness distribution to control the rate of surface velocity diffusion. Details of the various types of custom-tailored airfoils used in modern compressor designs can be found in the work of Wisler (1985). The leading edge metal angle distribution on stator *B* is set to follow the inlet flow angle distribution calculated by CAFMIX. The difference in the leading edge metal angle between stator *A* and stator *B* is apparent in Fig. 1(*c*).

Table 1 summarizes the salient features of the high-speed stators *A* and *B*.

Two-Dimensional Cascade and Three-Dimensional Euler Analyses

The two-dimensional cascade analysis code employed in this study is an updated version of the inviscid streamline curvature technique developed by Novak (1967). The two-dimensional cascade analysis accounts for the axial variation of radius and streamtube height. The three-dimensional Euler analysis was conducted using the computer program developed by Holmes and Tong (1985). Both codes have found wide usage within General Electric Company for compressor and turbine designs, are robust, and generally agree well with test data for cascades with unseparated boundary layers.

Conventional design practices generally utilize a throughflow circumferential-averaged solution, coupled to a two-dimensional cascade analysis, which feeds back into the throughflow analysis the average angular momentum distribution calculated by the two-dimensional cascade analysis. This iteration scheme between the circumferential-averaged throughflow analysis and the two-dimensional cascade analysis is essential for convergence to a unique surface velocity distribution in the design process. This process is inherent to the three-dimensional Euler analysis. The results of our investigation suggest that the quasi-three-dimensional design procedure (i.e., throughflow analysis coupled to two-dimensional cascade analysis) is not capable on a circumferential-averaged basis of adjusting the streamtube height as required in the cascade analysis to simulate the highly nonaxisymmetric nature of the flow at the endwall occurring with the three-dimensional relief.

Grid Description. Typical leading edge grids used to analyze the stator sections with the two-dimensional cascade analysis are shown in Fig. 2. Grid refinement in the leading edge region is automatically accomplished in the analysis.

The three-dimensional calculations were performed using the grid shown in Fig. 3. The grid consists of 97 nodes in the axial direction, of which 57 nodes were subdivided nonuniformly from the leading edge to the trailing edge, 49 nodes in blade-to-blade direction, and 21 nodes in the spanwise direction. A stretching parameter between 1.0 and 1.2 was used in all three directions to model the gradients in the flowfield near the endwalls and the blade surfaces. Special care was taken to obtain a fairly dense grid in the leading edge region near the casing endwall to model the details of the corner flow accurately.

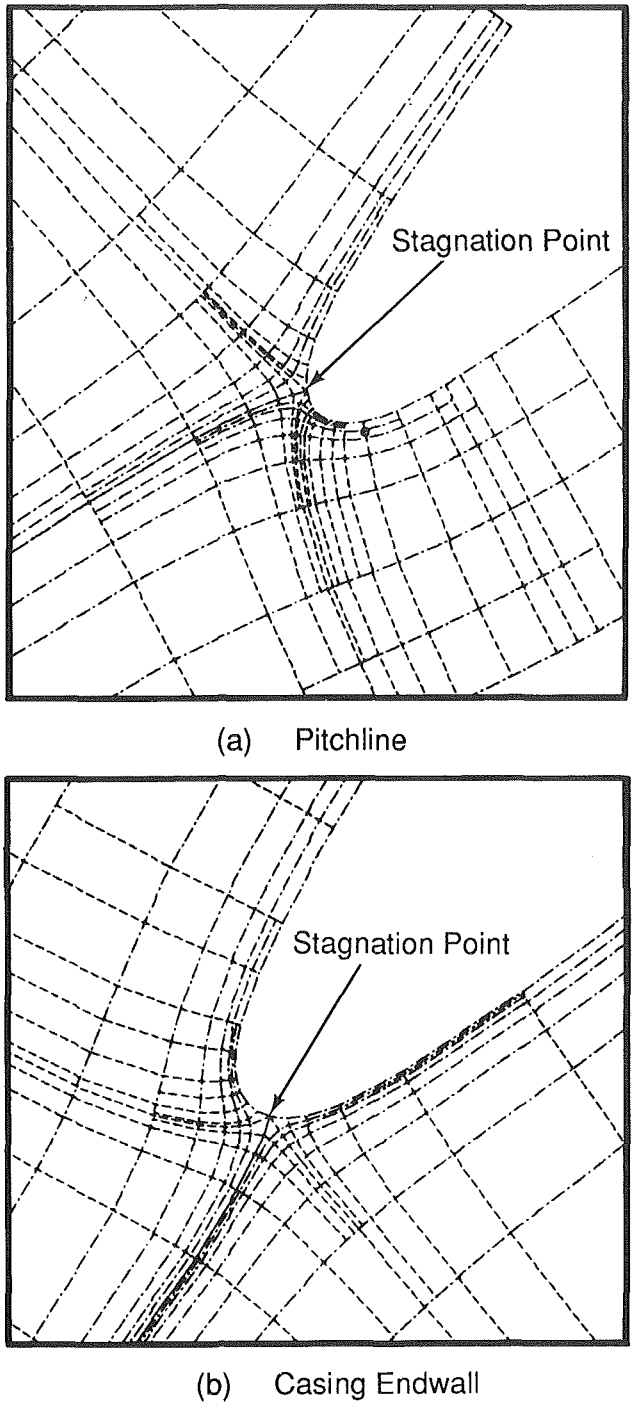

Fig. 2 Computational grid at the leading edge for two-dimensional cascade analysis (stator *A*); (note; the grid automatically adjusts itself to align with the flow, i.e., grid lines are streamlines)

Inlet Boundary Conditions. The inlet boundary conditions for the two-dimensional and three-dimensional analysis of the stators consisted of the inlet total pressure and temperature and the absolute flow angle. The inlet absolute flow angle distribution is illustrated in Fig. 1(*c*). The inlet total pressure

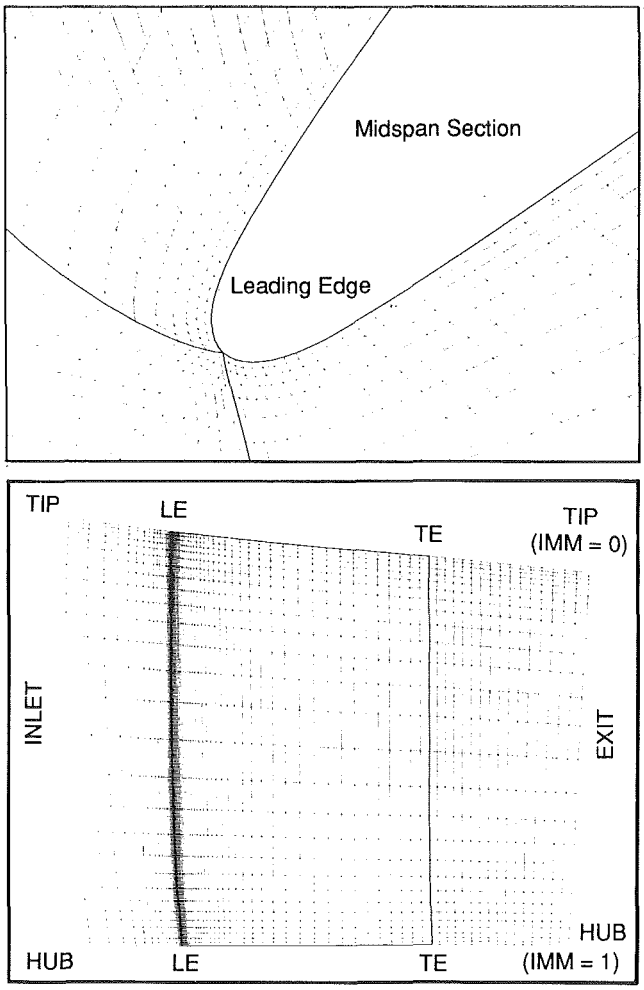

Fig. 3 Computational grid for three-dimensional Euler analysis of stator *A*

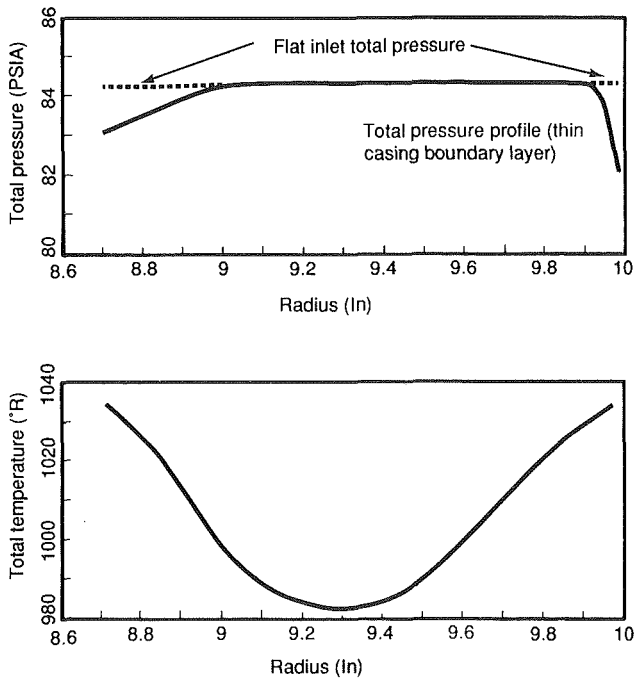

Fig. 4 Inlet total pressure and total temperature profiles for the analysis of stators *A* and *B*

and temperature distributions used in both analyses are presented in Fig. 4.

In order to understand better the effects of inlet flow angle skewing and inlet total pressure gradients, we will first examine a case where only flow angle skewing is present. This will be followed by calculations with an inlet total pressure distribution representing added inlet vorticity generated by incoming endwall boundary layers.

Comparison of Two-Dimensional and Three-Dimensional Calculations. The calculated pitchline and casing endwall surface static pressure distributions determined by the two and three-dimensional analyses with a uniform inlet total pressure profile for stator *A* and *B* configurations are presented in Figs. 5 and 6, respectively. The two-dimensional blade-to-blade and the three-dimensional calculations agree well at the pitchline. At the casing endwall, however, considerable differences in the shape and magnitude of the calculated distributions (Fig. 5*b*), are observed for the case of stator *A*. The two-dimensional cascade analysis shows a large leading edge loading that is nearly absent in the three-dimensional Euler analysis. It is recognized that some differences in the results between the two analytical techniques are introduced, due to grid spacing, smoothing, and artificial viscosity; however, the magnitude of these differences will not significantly alter the nature of the solutions presented.

For the casing endwall section in stator *A* (Fig. 5*b*), the suction surface static pressure near the leading edge calculated by the three-dimensional Euler analysis is considerably higher than the two-dimensional cascade analysis calculations. On the pressure surface, the surface static pressure calculated by the two-dimensional cascade analysis is relatively larger than the three-dimensional Euler calculations. The net result of this is a significant unloading of the leading edge region in the three-dimensional Euler results compared to the two-dimensional cascade analysis.

The casing endwall blade surface static pressure distribution for stator *B* illustrated in Fig. 6(*b*) shows good agreement between the three-dimensional Euler analysis and the two-dimensional cascade solution. Since the endwall section of stator *B* does not require any "help" because its incidence was designed to be low there, no significant three-dimensional relief is evident in the analysis.

Three-Dimensional Relief by Secondary Flow

The three-dimensional Euler analysis for both stators, described in the previous section, indicates the existence of three-dimensional relief that manifests itself through radial adjustment in the flow distribution at the leading edge. The fundamental flow mechanism that results in the unloading of the leading edge region at the casing endwall for stator *A* is the increased outward (toward casing) spanwise flow along the suction surface and the increased inward flow on the pressure surface relative to the amount of spanwise flow produced in stator *B*. At the trailing edge the spanwise flows for both stators are nearly the same because the overall turning angle distributions are approximately equal, requiring the same shed vortex sheet strengths.

Figure 7 shows the axial distribution of blade surface secondary flow velocities (V_s) normal to the axisymmetric Euler grid surface shown in the meridional view in Fig. 3. V_s is positive toward the outer wall. The magnitude of V_s on the suction surface of stator *A* is between 10 and 30 ft/sec larger relative to stator *B* along the grid surfaces close to the casing endwall (IMM = 0.009 to 0.063). This results in increased migration of flow toward the leading edge corner in stator *A* with respect to stator *B*. In addition, the shape of the normal velocity profiles, V_s, on the suction surface of stator *A* has peaks between 1 percent and 20 percent axial chord while the profiles for stator *B* are generally uniform from leading to trailing edge. This again indicates a stronger spanwise flow toward the

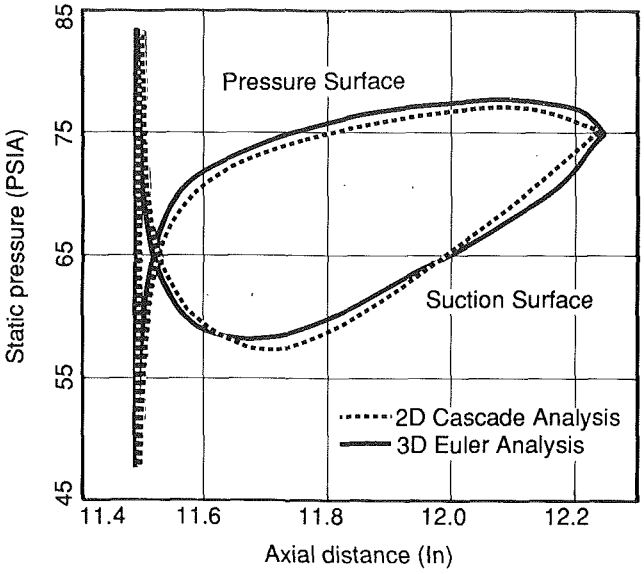

(a) Stator A Midspan

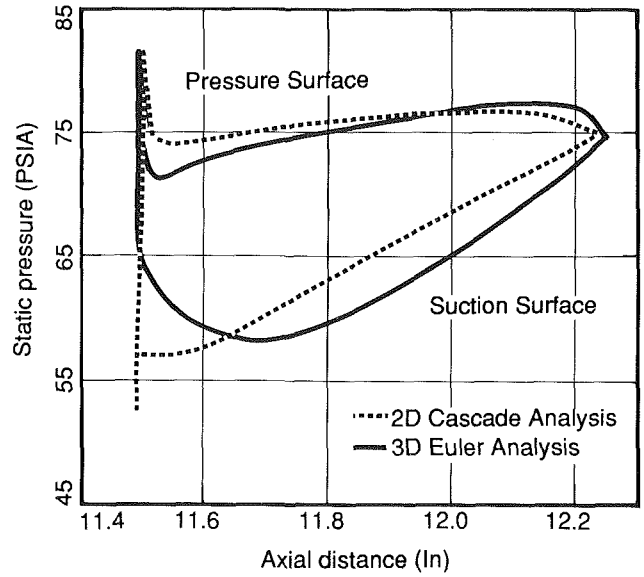

(b) Stator A Casing Endwall

Fig. 5 Comparison of two-dimensional and three-dimensional calculations of surface static pressures on stator *A* at midspan and casing endwall with flat inlet total pressure profile

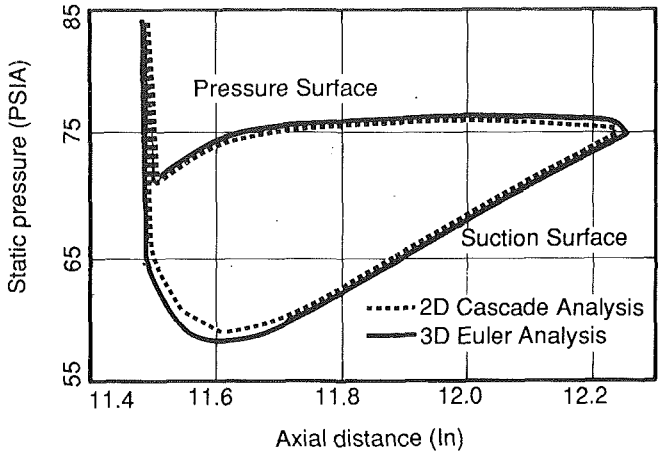

(a) Stator B Midspan

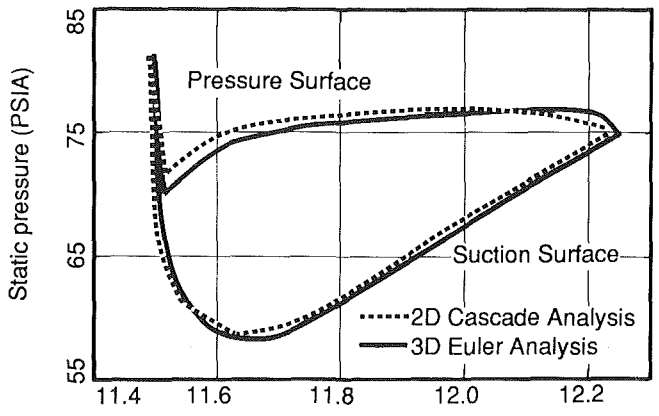

(b) Stator B Casing Endwall

Fig. 6 Comparison of two-dimensional and three-dimensional calculations of surface static pressures on stator *B* at midspan and casing endwall with flat inlet total pressure profile

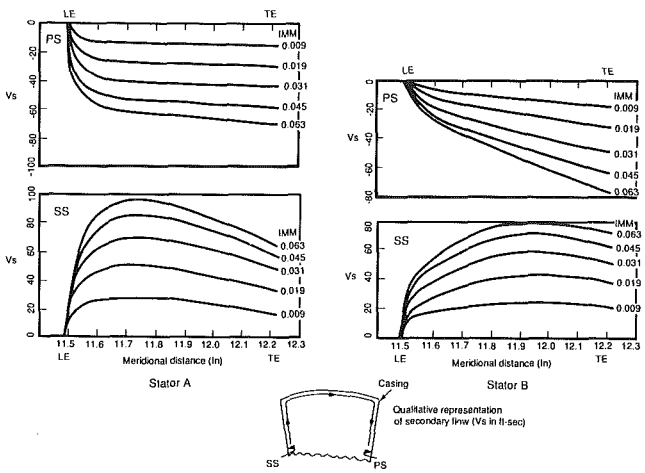

Fig. 7 Axial distribution of blade surface velocities normal to the grid surface in the meridional plane for compressor stators *A* and *B* with constant inlet total pressure profile

casing endwall along the leading edge on the suction surface of stator A relative to stator B.

On the pressure surface, the secondary flow velocities, V_s, are negative (inward from the casing endwall) for both stators A and B near the outer wall. In the case of stator B, the secondary flow velocities uniformly decrease from zero at the leading edge to a negative value at the trailing edge. For stator A, however, where the three-dimensional relief occurs, the secondary flow velocities decrease rapidly from zero at the leading edge to some negative value between 10–20 percent axial chord beyond which the value of V_s remains constant to the trailing edge.

The calculated secondary flow velocities, V_s, on the pressure and suction surfaces of stators A and B (Fig. 7) illustrate that the overall nature of the spanwise flow near the leading edge is much stronger in stator A, which displays a much higher degree of three-dimensional relief relative to stator B. The secondary flow in the annulus of stator B is mainly due to the spanwise gradient of the blade circulation, while for stator A the radial flow is a complex interaction between the components generated by the circulation gradient and the endwall flow adjustment resulting in the three-dimensional relief.

The three-dimensional relief is caused by the rapid deceleration that occurs as the radial flow approaches the surface boundary formed by the junction of the suction surface and

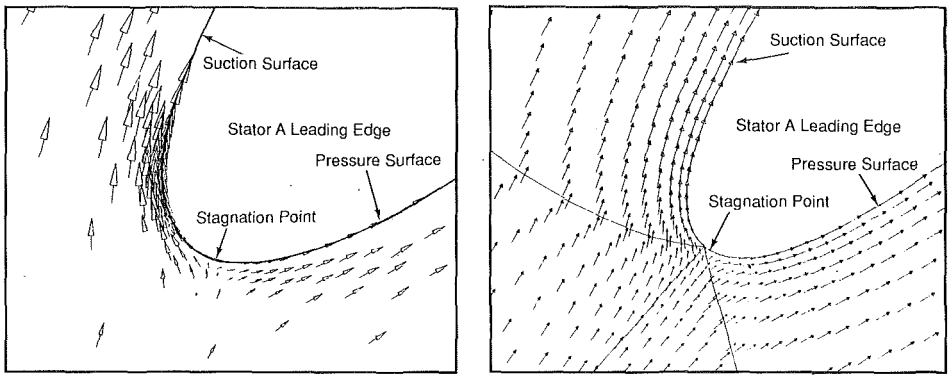

Fig. 8 Comparison of velocity vectors calculated by two-dimensional and three-dimensional analyses for high-speed stator *A* at the casing endwall

the casing endwall at the leading edge. This deceleration at the corner causes the static pressure to increase. The sketch at the bottom of Fig. 7 qualitatively illustrates the direction of the secondary flow in the vicinity of the leading edge corner on the suction surface of the stator. The secondary flow migrates up the suction surface, over the casing endwall, and down the pressure surface, as shown in Fig. 7. The net effect of the spanwise velocities on the suction surface static pressure distribution near the leading edge is to increase the pressure relative to the two-dimensional solution. While the circumferentially averaged air angle at the leading edge does not change between the two and three-dimensional solutions (input inlet boundary condition), the loading relief is provided by an adjustment in the suction surface static pressure in the three-dimensional calculations.

Figure 8 shows the comparison of the velocity vectors in the blade-to-blade view calculated by the two-dimensional and three-dimensional analyses at the casing endwall for stator *A* where three-dimensional relief exists. The two-dimensional cascade analysis shows the stagnation point to be on the pressure surface (high incidence), which results in the suction surface spike in the blade surface static pressure distribution, shown in Fig. 5(*b*). The three-dimensional Euler solution results in a stagnation point more in line with the mean camber line, consequently resulting in improved incidence and lower leading edge loading relative to the two-dimensional cascade analysis. This effect was illustrated by the surface static pressure distributions presented in Fig. 5(*b*).

Three-Dimensional Euler Analysis With Inlet Boundary Layer

With the flow mechanism for the three-dimensional relief established, we decided to investigate further the effects that the inlet boundary layer would have on the generation of spanwise flow and hence three-dimensional relief. For this study, a realistic profile of total pressure was employed, as shown in Fig. 4, which had deficits at both ends to simulate endwall boundary layers. The inlet temperature and absolute flow angle distributions were the same as before. The exit static pressure level was slightly modified so that the inlet pitchline Mach number would be the same as that obtained with the uniform inlet total pressure profile.

The resulting surface static pressure distributions, using the three-dimensional Euler analysis, were similar to those illustrated in Figs. 5 and 6 for both stators. Figure 9 is a typical comparison of the three-dimensional calculations with and without the inlet boundary layer at the casing endwall of stator *A* where three-dimensional relief was demonstrated in the previous section.

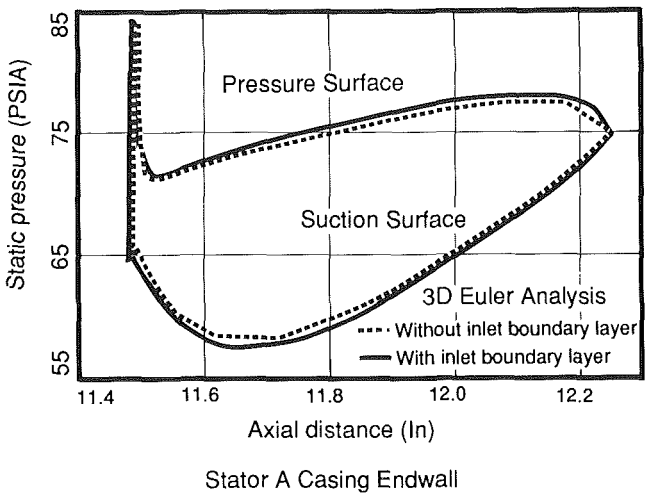

***Fig. 9 Comprison of three-dimensional Euler calculations of surface* static pressures on stator *A* at the casing endwall with and without inlet boundary layer profile**

Figure 10 shows the normal flow velocities, V_s, calculated for both stators with the inlet boundary layer. The normal flow velocities on the suction surface of both stators in Fig. 10 are generally similar to those calculated, using a uniform inlet total pressure profile, as shown in Fig. 7. The effect of the inlet boundary layer is most predominant on the pressure surface secondary flow velocities. With the inlet boundary layer, the pressure surface velocities at the leading edge close to the casing endwall are positive and remain positive to the trailing edge, contrary to those calculated without the inlet boundary layer (Fig. 7). The casing boundary layer extends approximately 3.5 percent into the annulus from the outer wall and this is reflected in the positive values of V_s for immersions between 0 and 0.031 in Fig. 10. For immersions below 0.031, the secondary flow velocities at the leading edge show behavior similar to that reported earlier in Fig. 7. The qualitative description of the secondary flow with inlet boundary layer is illustrated in the sketch at the bottom of Fig. 10. The calculation of V_s reveals a small recirculating region of secondary flow near the junction of the pressure surface and the casing endwall rotating in a direction opposite to that of the main secondary flow when a thin incoming boundary layer is used in the calculations.

Figure 11 shows typical blade-to-blade streamline patterns at the endwall section of stator *A* calculated by three-dimensional Euler analysis with and without the casing boundary layer. The streamlines in the meridional view on the pressure surface are also compared in the same figure. Without the inlet boundary layer, the streamlines remain attached to the pressure

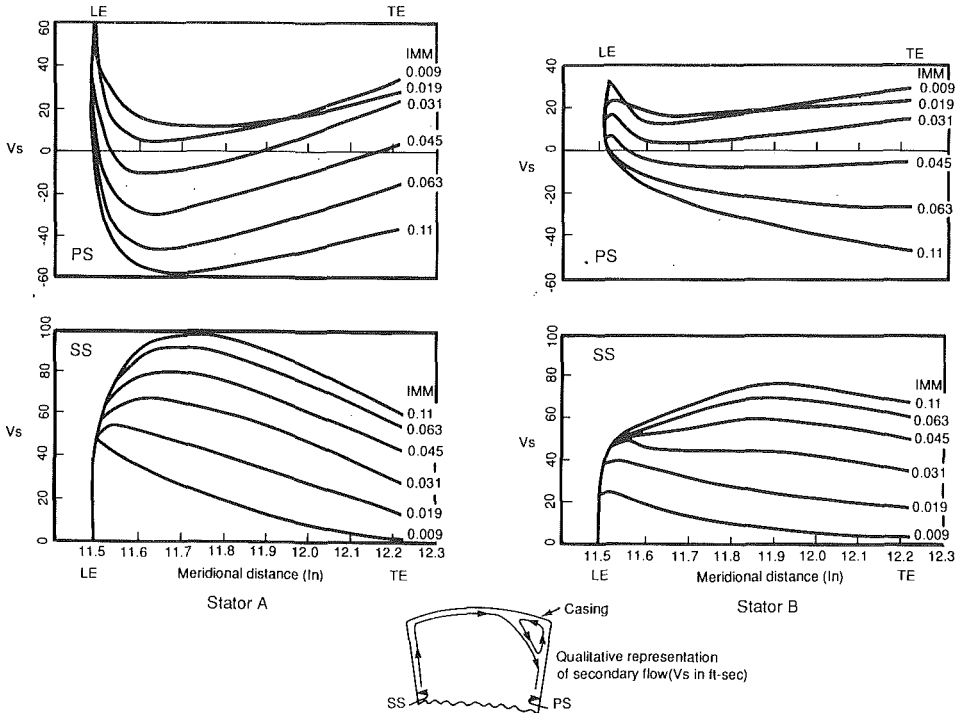

Fig. 10 Axial distribution of blade surface velocities normal to the grid surface in the meridional plane for stators *A* and *B* with inlet total pressure profile

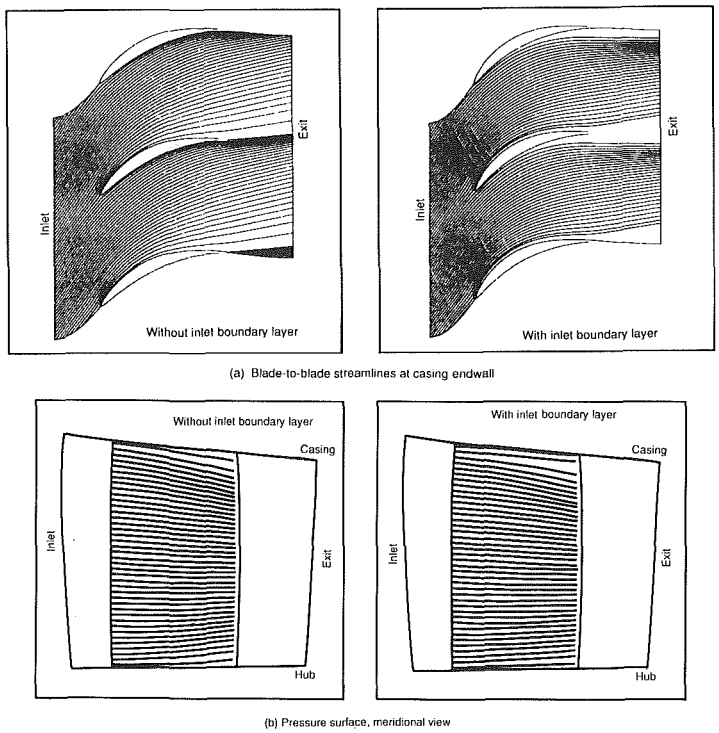

Fig. 11 Comparison of (a) casing endwall blade-to-blade streamlines and (*b*) pressure surface streamlines in the meridional plane with and without inlet boundary layer profile for stator *A*

surface in the blade-to-blade plane. The inlet boundary layer profile results in the streamlines moving away from the pressure surface toward the middle of the passage.

The meridional streamline patterns further strengthen the concept of a small recirculating region in the corner on the pressure surface with the inlet boundary layer. The streamlines for the no-inlet boundary layer case slope downward (away from the outer wall) from the leading edge to the trailing edge near the casing endwall. However, with the inlet boundary layer profile introduced in the three-dimensional Euler solution, the streamlines on the pressure surface are squeezed into the casing wall from the leading edge to the trailing edge. At approximately 10 percent immersion, the streamlines show trends similar to the case without the inlet boundary layer.

Design Features of Low-Speed Compressor Stators

Experimental verification of three-dimensional relief was observed on two low-speed stator configurations tested in Gen-

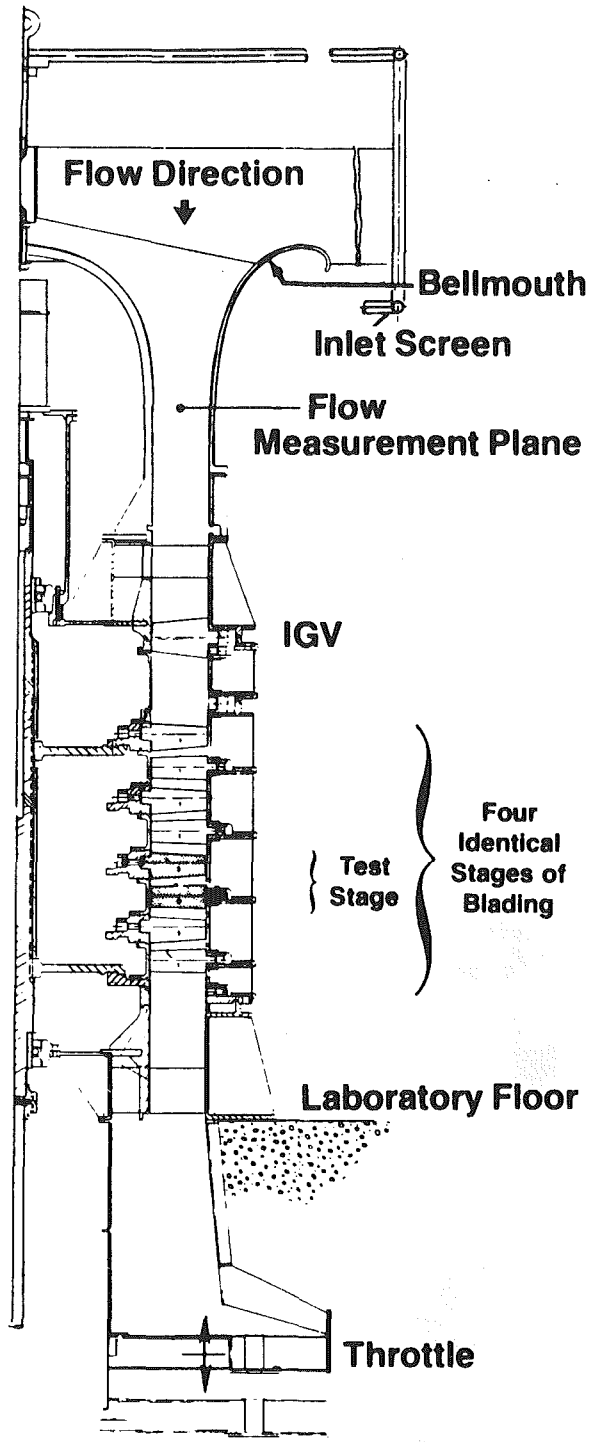

Fig. 12 Cross section of low-speed research compressor

eral Electric's Low-Speed Research Compressor (LSRC) facility illustrated in Fig. 12. The LSRC is set up in a four-stage configuration in order to simulate the repeating stage environment of high-speed multistage compressors. The third stage is the test stage where detailed internal performance data are obtained, including measurements of static pressure over the blade and vane surfaces. The facility is capable of simulating the aerodynamic performance of high-speed compressors by duplicating the essential features, which include realistic vector diagrams, blade surface velocity distributions, and clearance effects. Details of the test facility, operating procedures, instrumentation capabilities, and low-speed modeling techniques are described in Wisler's (1985) article.

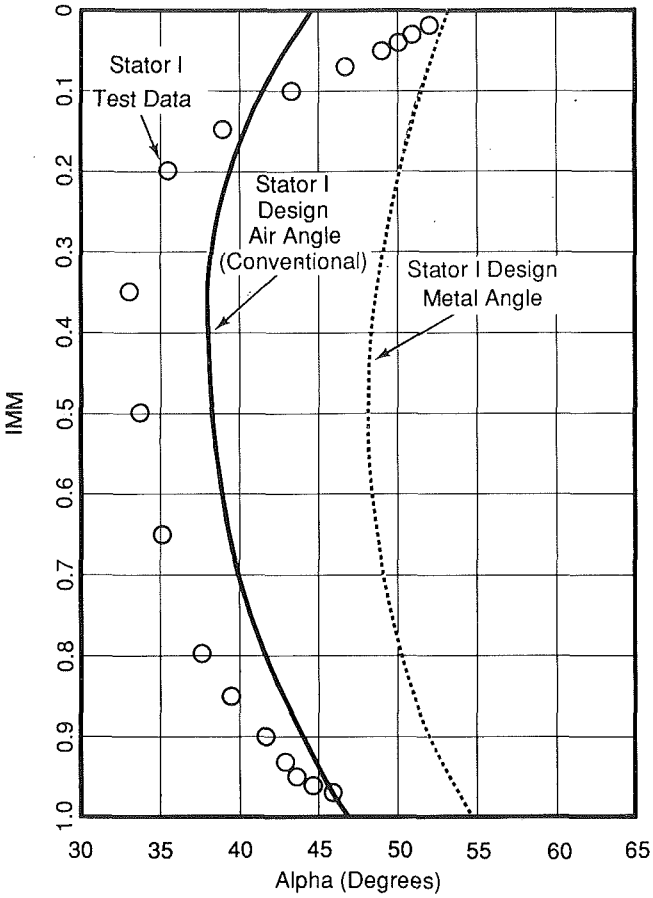

Fig. 13 Measured and design inlet swirl angle and metal angle distribution for low-speed compressor stator I

Table 2 Low-speed stator blading pitchline parameters

Parameter	Stator I	Stator II
Radius ratio	0.85	0.70
Solidity	1.32	1.15
Aspect ratio	1.45	1.80
Inlet Mach number	0.14	0.13
Stagger, deg	20.0	30.0
t_{max}/C	0.075	0.125

The experimental studies were conducted on two low-speed configurations, which modeled two types of subsonic stators found in the front and middle stages, respectively, of modern high-pressure compressors. The first configuration contains stator I, a low-speed model of the high-speed stator *A* described earlier. The airfoil sections are conventional (i.e., modified circular arc meanlines with NACA 65-series thickness distribution). The leading edge metal angle distribution (shown in Fig. 13) is set by conventional throughflow analyses (i.e., without the inclusion of secondary flow and mixing effects). The measured inlet flow angle distribution, also shown in Fig. 13, is similar to the inlet flow angle distribution calculated by CAFMIX for the high-speed stator *A* (Fig. 1*c*). The second configuration contains stator II, a low-speed model of a high-speed stator with higher aspect ratio than stator I. Stator II has airfoil sections that are custom-tailored, resulting in improved performance over conventional-shaped airfoils. Figure 1(*a*) illustrates the measured inlet flow angle and the leading edge metal angle distributions for stator II. Although it was not a model of the high-speed stator *B*, the design approach was similar, that is, the leading edge was closed somewhat at the casing to control endwall incidence better.

Table 2 summarizes some of the salient features of the low-speed stators I and II.

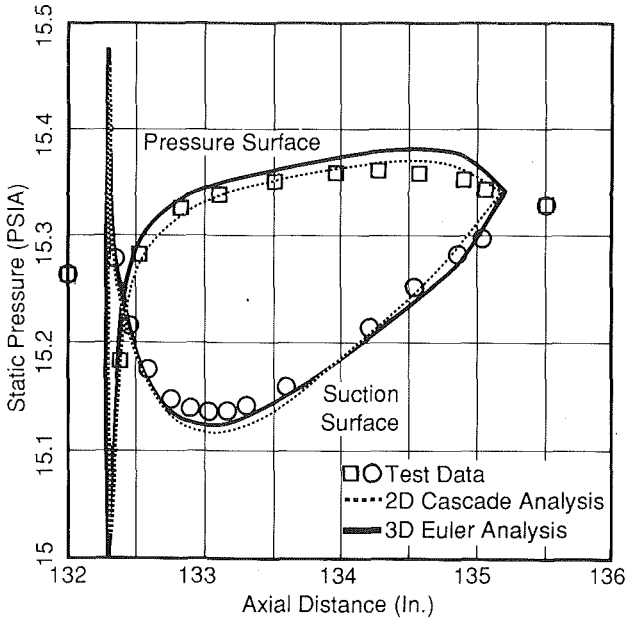

(a) Stator I Midspan

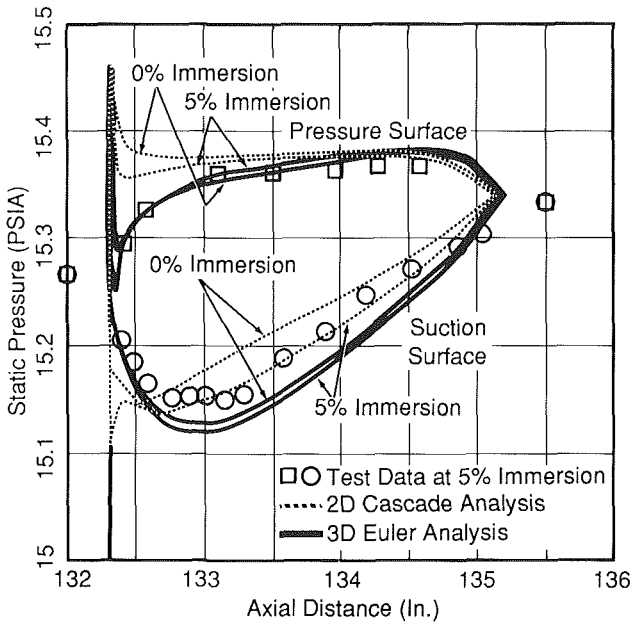

(b) Stator I Near Casing Endwall

Fig. 14 Comparison of measurements with two-dimensional and three-dimensional calculations of surface static pressures on the low-speed stator I

Experimental Verification of Three-Dimensional Relief

Three-dimensional relief was demonstrated on the low-speed stators by comparing the measured values of surface static pressure with those calculated by the two-dimensional cascade analysis and the three-dimensional Euler analysis. Although flow visualizations of the leading edge regions were not obtained, surface static pressures were measured sufficiently close to the leading edge so that the effect of three-dimensional relief could be identified.

Inlet Boundary Conditions. Detailed traverses, both radial and circumferential, of total and static pressures and flow angles were obtained upstream and downstream of the third-stage stator. These data were closely matched by throughflow

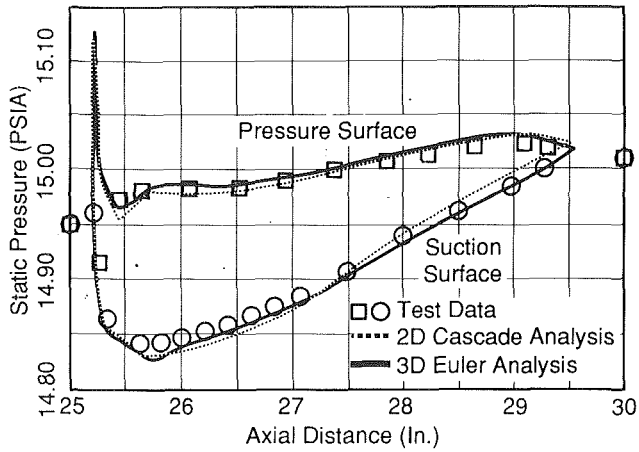

(a) Stator II Midspan

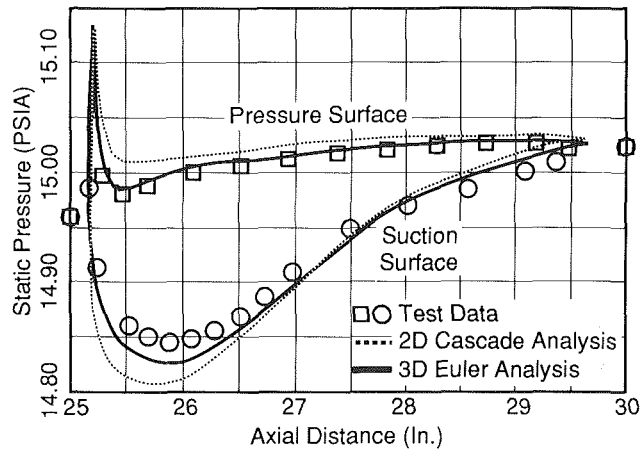

(b) Stator II Near Casing Endwall (5% Immersion)

Fig. 15 Comparison of measurements with two-dimensional and three-dimensional calculations of surface static pressures on the low-speed stator II

analyses (CAFMIX), which included the effects of secondary flow and mixing. The inlet total pressure and temperature and absolute flow angle distributions used in the three-dimensional Euler analyses were the same as those of the CAFMIX analyses. The exit static pressures were slightly modified so that the inlet flow would be the same as that obtained in the test. The inlet and exit conditions used in the two-dimensional cascade analysis were identical to those used in the three-dimensional Euler calculations.

Comparison of Two-Dimensional and Three-Dimensional Calculations With Test Measurements. Comparison of the measured and calculated surface static pressures is shown in Fig. 14(*a*) for the midspan section of stator I. At this location, the two-dimensional cascade and three-dimensional Euler solutions agree well with the measured data, in the same manner as the two-dimensional cascade and three-dimensional Euler solutions agreed in Fig. 5(*a*) at the midspan of the high-speed stator *A*. Thus it can be inferred that both two-dimensional cascade and three-dimensional Euler methods provide an adequate representation of the midspan flow where radial velocities and viscous effects are small. The measured surface static pressures implied no flow separation by virtue of the smoothly continuous rise in pressure exhibited along the suction surface, all the way to the trailing edge. In fact, a two-dimensional boundary layer analysis of this midspan section, using a turbulence intensity of 10 percent, also predicted no flow separation.

Comparison of the measured and calculated surface static pressures is shown in Fig. 14(*b*) for a section at 5 percent immersion from the casing endwall for stator I. Large differences are observed in the leading edge region where the two-dimensional cascade solution computes more loading than is implied by the three-dimensional Euler analysis and the data. The difference is similar to that observed between the two-dimensional cascade analysis and the three-dimensional Euler solution in Fig. 5(*b*), but of lesser magnitude because the comparison is made at 5 percent immersion where the measurements exist rather than at the casing. Because the inlet swirl angle continues to increase from 5 percent immersion to the casing endwall, the two-dimensional cascade analysis predicts a further increase in leading edge loading, as shown in Fig. 14(*b*). However, the three-dimensional Euler result at the endwall section is very similar to that calculated at 5 percent immersion. This suggests that the leading edge loading at the endwall is again influenced by secondary flow effects not adequately represented in the two-dimensional design procedure.

Comparisons of measured and calculated pressures for stator II are shown in Fig. 15. The comparisons in Fig. 15(*a*) show that stator II, like stator I, exhibits good agreement between the two-dimensional cascade and the three-dimensional Euler solutions and the measured data at the midspan location. The difference between the two-dimensional and three-dimensional solutions in Fig. 15(*b*) is less than for stator I because the leading edge is closed at the casing and the incidence gradient is less. The results are similar to those for the high-speed stator *B*.

The high-speed compressor stator *A* analyses and the low-speed compressor stator I test results imply that three-dimensional relief is associated with significant spanwise gradients of two-dimensional leading edge loading. This spanwise gradient is associated with a spanwise variation in "incidence," which is defined as the difference between the upstream circumferential-averaged air angle and the leading edge metal angle. Both the experimental measurements and the three-dimensional Euler solution of stator I indicate that, coinciding with the spanwise variation in incidence, there is three-dimensional relief, which reduces the spanwise gradient of leading edge loading in a manner similar to that computed by the three-dimensional Euler analysis of stator *A*.

Concluding Remarks

Both analytical and experimental results of an investigation of three-dimensional relief in several compressor stators has been presented. Comparisons of two-dimensional cascade analyses and three-dimensional Euler analyses show the presence of three-dimensional relief on the casing endwall of stator *A* and stator I. The unloading of the leading edge region at the casing is associated with the secondary flow velocities generated by the spanwise gradients of incidence. Experimental measurements on stators I and II verify the analytical results.

The analysis of stator *B* indicates that when large gradients in incidence do not exist at the endwalls, the need for flow migration to relieve the sections is reduced. This results in lower spanwise flow velocity components and less evidence of three-dimensional relief.

One implication of this study is that the designer can depend, to some extent, on radial velocities to adjust the spanwise flow distribution such that endwall leading edge loadings are acceptable, even with relatively conventional airfoil shapes. The need to align the inlet metal angle precisely with the skewed inlet flow angles at the endwall (at the risk of placing a significant spanwise twist gradient in the blade surface near the endwall) appears to be less than might be implied from two-dimensional analyses. It seems that, while some recognition of the high air angles that exist in the endwalls is desirable, extreme leading edge angle gradients may not be required.

Whether the increased secondary flows produced by high endwall incidence angles, as in stator *A*, themselves cause increased losses or a reduction in stall pressure rise capability was not clear from the experimental work reported herein, and is a subject that deserves additional research.

Acknowledgments

The authors would like to thank Roy Smith, Curt Koch, Peter Szucs, and Dave Wisler for the guidance during the course of the investigation and General Electric Company for permission to publish this paper.

References

Adkins, G. G., Jr., and Smith, L. H., Jr., 1982, "Spanwise Mixing in Axial-Flow Turbomachines," ASME *Journal of Engineering for Power*, Vol. 104, pp. 97–110.

Behlke, R. F., 1985, "The Development of a Second-Generation of Controlled Diffusion Airfoils for Multistage Compressors," ASME Paper No. 85-IGT-9.

Holmes, D. G., and Tong, S. S., 1984, "A Three-Dimensional Euler Solver for Turbomachinery Blade Rows," ASME *Journal of Engineering for Gas Turbines and Power*, Vol. 107, pp. 258–264.

Novak, R. A., 1967, "Streamline Curvature Computing Procedures for Fluid Flow Problems," ASME *Journal of Engineering for Power*, Vol. 89, pp. 478–490.

Wisler, D. C., 1985, "Loss Reduction in Axial-Flow Compressors Through Low-Speed Model Testing," ASME *Journal of Engineering for Gas Turbines and Power*, Vol. 107, pp. 354–363.

Comparison of the measured and calculated surface static pressures is shown in Fig. 14(*b*) for a section at 5 percent immersion from the casing endwall for stator I. Large differences are observed in the leading edge region where the two-dimensional cascade solution computes more loading than is implied by the three-dimensional Euler analysis and the data. The difference is similar to that observed between the two-dimensional cascade analysis and the three-dimensional Euler solution in Fig. 5(*b*), but of lesser magnitude because the comparison is made at 5 percent immersion where the measurements exist rather than at the casing. Because the inlet swirl angle continues to increase from 5 percent immersion to the casing endwall, the two-dimensional cascade analysis predicts a further increase in leading edge loading, as shown in Fig. 14(*b*). However, the three-dimensional Euler result at the endwall section is very similar to that calculated at 5 percent immersion. This suggests that the leading edge loading at the endwall is again influenced by secondary flow effects not adequately represented in the two-dimensional design procedure.

Comparisons of measured and calculated pressures for stator II are shown in Fig. 15. The comparisons in Fig. 15(*a*) show that stator II, like stator I, exhibits good agreement between the two-dimensional cascade and the three-dimensional Euler solutions and the measured data at the midspan location. The difference between the two-dimensional and three-dimensional solutions in Fig. 15(*b*) is less than for stator I because the leading edge is closed at the casing and the incidence gradient is less. The results are similar to those for the high-speed stator *B*.

The high-speed compressor stator *A* analyses and the low-speed compressor stator I test results imply that three-dimensional relief is associated with significant spanwise gradients of two-dimensional leading edge loading. This spanwise gradient is associated with a spanwise variation in "incidence," which is defined as the difference between the upstream circumferential-averaged air angle and the leading edge metal angle. Both the experimental measurements and the three-dimensional Euler solution of stator I indicate that, coinciding with the spanwise variation in incidence, there is three-dimensional relief, which reduces the spanwise gradient of leading edge loading in a manner similar to that computed by the three-dimensional Euler analysis of stator *A*.

Concluding Remarks

Both analytical and experimental results of an investigation of three-dimensional relief in several compressor stators has been presented. Comparisons of two-dimensional cascade analyses and three-dimensional Euler analyses show the presence of three-dimensional relief on the casing endwall of stator *A* and stator I. The unloading of the leading edge region at the casing is associated with the secondary flow velocities generated by the spanwise gradients of incidence. Experimental measurements on stators I and II verify the analytical results.

The analysis of stator *B* indicates that when large gradients in incidence do not exist at the endwalls, the need for flow migration to relieve the sections is reduced. This results in lower spanwise flow velocity components and less evidence of three-dimensional relief.

One implication of this study is that the designer can depend, to some extent, on radial velocities to adjust the spanwise flow distribution such that endwall leading edge loadings are acceptable, even with relatively conventional airfoil shapes. The need to align the inlet metal angle precisely with the skewed inlet flow angles at the endwall (at the risk of placing a significant spanwise twist gradient in the blade surface near the endwall) appears to be less than might be implied from two-dimensional analyses. It seems that, while some recognition of the high air angles that exist in the endwalls is desirable, extreme leading edge angle gradients may not be required.

Whether the increased secondary flows produced by high endwall incidence angles, as in stator *A*, themselves cause increased losses or a reduction in stall pressure rise capability was not clear from the experimental work reported herein, and is a subject that deserves additional research.

Acknowledgments

The authors would like to thank Roy Smith, Curt Koch, Peter Szucs, and Dave Wisler for the guidance during the course of the investigation and General Electric Company for permission to publish this paper.

References

Adkins, G. G., Jr., and Smith, L. H., Jr., 1982, "Spanwise Mixing in Axial-Flow Turbomachines," ASME *Journal of Engineering for Power*, Vol. 104, pp. 97–110.

Behlke, R. F., 1985, "The Development of a Second-Generation of Controlled Diffusion Airfoils for Multistage Compressors," ASME Paper No. 85-IGT-9.

Holmes, D. G., and Tong, S. S., 1984, "A Three-Dimensional Euler Solver for Turbomachinery Blade Rows," ASME *Journal of Engineering for Gas Turbines and Power*, Vol. 107, pp. 258–264.

Novak, R. A., 1967, "Streamline Curvature Computing Procedures for Fluid Flow Problems," ASME *Journal of Engineering for Power*, Vol. 89, pp. 478–490.

Wisler, D. C., 1985, "Loss Reduction in Axial-Flow Compressors Through Low-Speed Model Testing," ASME *Journal of Engineering for Gas Turbines and Power*, Vol. 107, pp. 354–363.

DISCUSSION

N. A. Cumpsty[1]

The authors have used effective computational techniques and accurate measurements to address and illuminate one of the more perplexing issues of compressor aerodynamics. It has been known for a long time that the pressure distribution and loading of blades in the endwall region, where the blades are operating in the casing or hub boundary layer, are similar to those in the midspan region. The blades do not normally show the high loading that would be expected on a two-dimensional basis at the high local incidence occurring near the endwalls. When blades were designed two dimensionally little attention was given to this, although the success of the design relied upon it occurring. When one wishes to take proper advantage of three-dimensional ideas and design tools now available it does become necessary to understand what is going on.

The absence of the severe loading near the hub and casing can be explained in one way by recognizing that the endwall regions are normally relatively small in the spanwise sense and the pressure field is established by the whole blade, most of which is outside the endwall boundary layer. The mechanism for this adaptation or relief has not normally been considered. It should be remembered that the low pressures around the leading edge of a blade at incidence are caused by the streamlines being made to follow a curved path of small radius. Thus, if the very low pressure in the leading edge region is to be removed, it requires that the effective streamline radius is increased; before the present paper by Wadia and Beacher, this writer had thought that the relief would probably be brought about by a three-dimensional separation bubble in the suction surface-endwall corner.

The authors have demonstrated very effectively that the relief can be predicted well by a three-dimensional Euler method. This dispels any idea that the relief is achieved by a

[1]Whittle Laboratory, University Engineering Department, Cambridge CB3 ODY England.

viscous process associated with a separation bubble, but indicates that the principal effect is inviscid. (The case is, of course, greatly strengthened by their comparison of the prediction with measurements in Figs. 14 and 15.) They have also shown that for compressor stators the principal effect in the endwall regions is the angle variation and not the stagnation pressure variation — an effect that would have been lost if attention were concentrated on cascade tests, as was the case with early work on secondary flow.

Having established that the relief mechanism is inviscid in character, it remains to be established what it is. The authors suggest relief is achieved by the spanwise velocities predicted by the three-dimensional code, but this cannot be a correct explanation for the whole effect. From Fig. 4, the density can be shown to be about 4 kg/m^3 and, from Fig. 7, the maximum velocity in the spanwise direction is about 30 m/s: an estimate of the maximum pressure difference that can be achieved by the spanwise velocity is $\frac{1}{2}\rho V^2$, which is around 1.8 kPa or 0.26 psia. The difference between two-dimensional and three-dimensional pressures in the leading edge region of Fig. 5(*b*) is much greater, around 7 psia. One might also notice that the peak spanwise velocities are predicted to occur for stator *A* at a meridional distance of about 11.75 in. in Fig. 7, well back from where the largest differences between two-dimensional and three-dimensional pressures were predicted. It is clear from the three-dimensional calculations and the measured results, shown in Fig. 14, that the spanwise gradients of pressure are very much less than the corresponding chordwise ones. In this sense, the flow in the endwall region of the blades is akin to a boundary layer flow and it is therefore more productive to regard the flow there as being determined by an imposed pressure distribution, which is established by the flow and around the blade as a whole. Given the relative sizes of the regions, the pressure field is established predominantly by the loading away from the endwall region.

High leading edge loading, such as that predicted by the two-dimensional method near the endwall, is a result of high velocity around the leading edge, because the flow is locally made to follow a path with a small radius of curvature. This occurs when the stagnation point is not on the leading edge but to one side (on the pressure side for positive incidence). The *only* way to avoid in three dimensions the very high loading near the leading edge, which the two-dimensional calculation predicts, is to remove the need for the flow there to follow a tight curve around the leading edge. The inviscid three-dimensional calculations have shown that this can be achieved without separation; instead what happens is that the stagnation point does not move away from the leading edge as much as the two-dimensional methods predict. In the midspan results of Wadia and Beacher the incidence is negative, the stagnation point is on the suction surface (Fig. 2*a*), and as a result the *pressure* surface has a velocity peak at midspan. In the endwall region, the local incidence is positive and the two-dimensional analysis predicts a stagnation point on the pressure surface, Figs. 2(*b*) and 8, giving a peak velocity on the suction surface and high leading edge loading; the three-dimensional analysis (which we have every reason to think is accurate) predicts the stagnation point in the endwall region to be just about on the leading edge, Fig. 8, so the velocity spike is greatly reduced.

To understand what is going on, it helps to step back and consider why in two dimensions the stagnation point does move around onto the pressure surface as incidence is increased. The stagnation streamline strikes the blade normal to the blade surface and the curving of this streamline must be accomplished by a static pressure field around and ahead of the blade. (One observes the same effect in ideal inviscid flow about a circular cylinder when the stagnation points move under the cylinder as the circulation is increased.) The stagnation point moves further around onto the pressure surface as the circulation and pressure field both gain in strength. In two dimensions, the

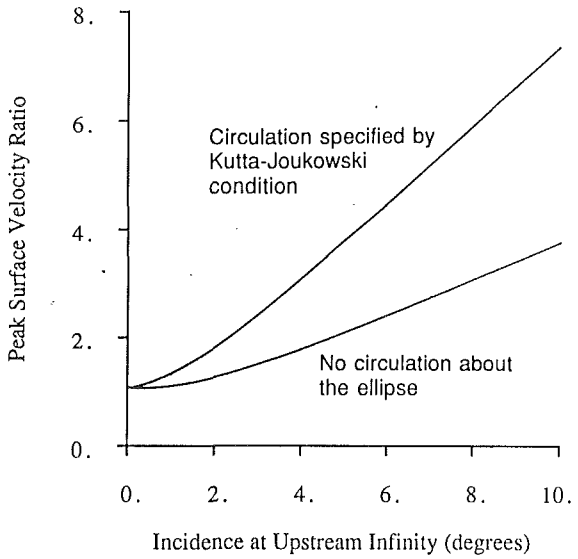

Fig. A1 Peak surface velocities about an isolated elliptic airfoil at incidence: Cases shown with and without Kutta-Joukowsky condition applied at trailing edge. Thickness-chord ratio 5 percent, incompressible flow; velocity nondimensionalized by free-stream velocity.

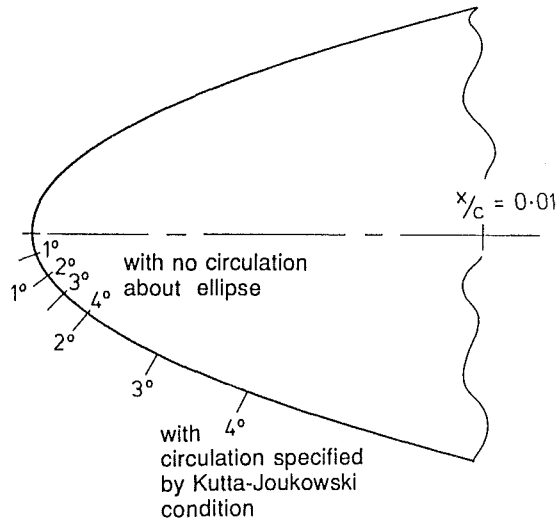

Fig. A2 Stagnation point positions at various incidences calculated with and without the Kutta-Joukowsky condition imposed at trailing edge. The front 1 percent of a 5 percent thick elliptic aerofoil is shown; calculations for isolated ellipse in incompressible flow.

circulation is proportional to the incidence for a given geometry, adopting the normal assumptions and neglecting changes due to compressibility and Reynolds number. Thus the position of the stagnation point and the level of the peak velocity near the leading edge are fixed for a particular aerofoil uniquely by the incidence. In three dimensions, this is no longer true because the pressure field and circulation can be varied independently of the local incidence.

To make the ideas about the independence of loading (i.e., the pressure field) and incidence a little more concrete, some inviscid, incompressible two-dimensional calculations have been carried out in which the pressure field about an aerofoil had been altered without change in incidence. In determining conditions about the leading edge in two-dimensional flow, the position of the stagnation point relative to the leading edge is crucial, and an isolated aerofoil, therefore, shows the same local effects as occur in cascades. The calculations have been performed about an isolated elliptic aerofoil at incidence, it being noted that the forward part of the NACA 65 aerofoil is

very similar to an ellipse. The peak velocity, nondimensionalized by the free-stream velocity, is shown in Fig. A1 of this Discussion. Two curves are shown. One is the "conventional" solution with the loading as set by the Kutta–Joukowsky condition at the trailing edge, giving circulation and net lift on the aerofoil proportional to the incidence. In the other solution, the Kutta–Joukowsky condition has been deliberately relaxed so that the aerofoil has no circulation and gives no net lift, even at incidence. This is a rather extreme example of altering the pressure field about an aerofoil, but it serves to show just how different the leading edge velocity peak and, therefore, the leading edge loading, can be at the same incidence when the overall pressure distribution is altered. The diagram in Fig. A2 of this Discussion shows the leading edge region of the ellipse, the front 1 percent of chord, on which are marked the stagnation points at four values of incidence with and without circulation. The importance of the overall pressure field, identified here with the circulation, on the position of the stagnation point is very apparent. The large changes in peak velocity with small movements of the stagnation point also can be seen by comparing Figs. A1 and A2 of this Discussion.

One can now understand more clearly why in three dimensions the stagnation point near the endwalls is not moved as far around the pressure surface, despite the high local incidence, and why there is not the very high peak velocity expected by applying two-dimensional calculation methods at the local incidence. First, it is because the pressure field is set up by the bulk of the flow, which is outside the endwall region, and this field is not as strong as that which would exist in a two-dimensional flow at the high local incidence. Second, it is because the position of the stagnation point is fixed not by the local incidence but by the whole pressure field. In other words, the predicted very high velocities in the leading edge region, due to high local incidence near the endwalls, are an artefact of two-dimensional reasoning and calculation. *It is not so much that the endwall flow is relieved by three-dimensional flow as that the two-dimensional flow is never established.*

Acknowledgment

The author is most grateful to J. A. Storer for carrying out the calculations and to T. P. Hynes for invaluable help in trying to clarify the argument.

Authors' Closure

The authors are grateful to Dr. Cumpsty for his discussion and share a similar desire to explain the physics behind the mechanism of three-dimensional relief in turbomachinery blading.

Cumpsty's argument that the stagnation point moves under a circular cylinder as the circulation is increased would seem to us to be not entirely applicable here. The two-dimensional and three-dimensional solutions presented in Figs. 5(*b*) and 14(*b*) show that the loadings of the two-dimensional cascade analysis and the three-dimensional Euler analysis are approximately the same (i.e., the areas bounded by the blade surface static pressure distributions or the lift forces are about equal between the two analyses). Therefore, there is *no net change* in the blade circulation of the endwall section between the analyses. Additionally, the three-dimensional Euler blade surface static pressure distribution is different *everywhere* relative to the two-dimensional cascade analysis and *not just locally* in the leading edge region. What has changed are the streamtubes near the endwall caused by the radial migration of the flow in three-dimensional. Due to their nonaxisymmetric nature, these streamtubes cannot be represented by a circumferential average variation that is required by the two-dimensional cascade analysis.

Dr. Cumpsty is correct to observe that the spanwise deceleration of velocity near the leading edge is not sufficient to explain the entire pressure difference between the two-dimensional and three-dimensional calculations. But at the casing, where spanwise velocities are zero, the secondary flow pattern (see lower part of Fig. 7) indicates a cross-passage flow that moves away from the suction surface and toward the adjacent pressure surface. This cross-passage flow pattern will also contribute to the opening of the endwall streamtube in the blade-to-blade plane near the suction surface and to the closing of the streamtube near the pressure surface. The streamtube opening on the suction side causes rapid reductions in streamline curvature along normals to the blade surface, with consequent reductions in the normal gradients of streamwise velocity and, therefore, through integrations along normals from midpassage, we are led to reductions in the surface velocities. One also could visualize how the secondary flow pattern could "drag" the stagnation streamline from its two-dimensional position on the pressure surface to its three-dimensional position closer to the suction surface as illustrated in Fig. 8. In our opinion, it is the warping of the streamtubes caused by both spanwise and cross-passage secondary flow velocities, which cannot be represented in a two-dimensional analysis, that is responsible for the endwall loading relief.

very similar to an ellipse. The peak velocity, nondimensionalized by the free-stream velocity, is shown in Fig. A1 of this Discussion. Two curves are shown. One is the "conventional" solution with the loading as set by the Kutta–Joukowsky condition at the trailing edge, giving circulation and net lift on the aerofoil proportional to the incidence. In the other solution, the Kutta–Joukowsky condition has been deliberately relaxed so that the aerofoil has no circulation and gives no net lift, even at incidence. This is a rather extreme example of altering the pressure field about an aerofoil, but it serves to show just how different the leading edge velocity peak and, therefore, the leading edge loading, can be at the same incidence when the overall pressure distribution is altered. The diagram in Fig. A2 of this Discussion shows the leading edge region of the ellipse, the front 1 percent of chord, on which are marked the stagnation points at four values of incidence with and without circulation. The importance of the overall pressure field, identified here with the circulation, on the position of the stagnation point is very apparent. The large changes in peak velocity with small movements of the stagnation point also can be seen by comparing Figs. A1 and A2 of this Discussion.

One can now understand more clearly why in three dimensions the stagnation point near the endwalls is not moved as far around the pressure surface, despite the high local incidence, and why there is not the very high peak velocity expected by applying two-dimensional calculation methods at the local incidence. First, it is because the pressure field is set up by the bulk of the flow, which is outside the endwall region, and this field is not as strong as that which would exist in a two-dimensional flow at the high local incidence. Second, it is because the position of the stagnation point is fixed not by the local incidence but by the whole pressure field. In other words, the predicted very high velocities in the leading edge region, due to high local incidence near the endwalls, are an artefact of two-dimensional reasoning and calculation. *It is not so much that the endwall flow is relieved by three-dimensional flow as that the two-dimensional flow is never established.*

Acknowledgment

The author is most grateful to J. A. Storer for carrying out the calculations and to T. P. Hynes for invaluable help in trying to clarify the argument.

Authors' Closure

The authors are grateful to Dr. Cumpsty for his discussion and share a similar desire to explain the physics behind the mechanism of three-dimensional relief in turbomachinery blading.

Cumpsty's argument that the stagnation point moves under a circular cylinder as the circulation is increased would seem to us to be not entirely applicable here. The two-dimensional and three-dimensional solutions presented in Figs. 5(*b*) and 14(*b*) show that the loadings of the two-dimensional cascade analysis and the three-dimensional Euler analysis are approximately the same (i.e., the areas bounded by the blade surface static pressure distributions or the lift forces are about equal between the two analyses). Therefore, there is *no net change* in the blade circulation of the endwall section between the analyses. Additionally, the three-dimensional Euler blade surface static pressure distribution is different *everywhere* relative to the two-dimensional cascade analysis and *not just locally* in the leading edge region. What has changed are the streamtubes near the endwall caused by the radial migration of the flow in three-dimensional. Due to their nonaxisymmetric nature, these streamtubes cannot be represented by a circumferential average variation that is required by the two-dimensional cascade analysis.

Dr. Cumpsty is correct to observe that the spanwise deceleration of velocity near the leading edge is not sufficient to explain the entire pressure difference between the two-dimensional and three-dimensional calculations. But at the casing, where spanwise velocities are zero, the secondary flow pattern (see lower part of Fig. 7) indicates a cross-passage flow that moves away from the suction surface and toward the adjacent pressure surface. This cross-passage flow pattern will also contribute to the opening of the endwall streamtube in the blade-to-blade plane near the suction surface and to the closing of the streamtube near the pressure surface. The streamtube opening on the suction side causes rapid reductions in streamline curvature along normals to the blade surface, with consequent reductions in the normal gradients of streamwise velocity and, therefore, through integrations along normals from midpassage, we are led to reductions in the surface velocities. One also could visualize how the secondary flow pattern could "drag" the stagnation streamline from its two-dimensional position on the pressure surface to its three-dimensional position closer to the suction surface as illustrated in Fig. 8. In our opinion, it is the warping of the streamtubes caused by both spanwise and cross-passage secondary flow velocities, which cannot be represented in a two-dimensional analysis, that is responsible for the endwall loading relief.

Tip Leakage Losses in a Linear Turbine Cascade

P. T. Dishart

J. Moore

Mechanical Engineering Department,
Virginia Polytechnic Institute and State University,
Blacksburg, VA 24061

An investigation of tip leakage flow and its effects on loss production was performed on a large-scale linear turbine cascade having a tip gap measuring 2.1 percent of the blade height. The flow exiting the tip gap was measured to determine the losses incurred within the tip gap and the secondary kinetic energy due to tip leakage. Additional measurements, 40 percent of an axial chord downstream of the blade trailing edges, showed the development of the leakage flow and the overall cascade losses. At the downstream location, the additional loss due to tip leakage was found to be the sum of the measured loss at the tip gap exit plane and the amount of tip gap secondary kinetic energy that had been dissipated by that downstream location.

Introduction

It is generally agreed that tip leakage flow has significant detrimental effects on turbine performance. The loss in efficiency and reduction of work due to tip leakage have been well documented (Kofskey, 1961; Roelke, 1973; Hourmouziadis and Albrecht, 1987). The details of tip leakage flow and the mechanisms involved in the production of tip leakage losses, however, are not yet fully understood.

The flow development within the tip gap has been considered by many workers (Rains, 1954; Booth et al., 1982; Wadia and Booth, 1982; Bindon, 1986, 1987, 1989; Moore and Tilton, 1988; Moore et al., 1989; Yaras et al., 1989), albeit mostly for incompressible flow; the emphasis of these studies has mostly been focused on velocity distributions and flow angles, and Bindon appears to be the only worker to consider the losses in the tip gap exit flow. Several experiments have shown the overall effects of tip leakage by detailed flow measurements downstream of turbine cascades (Hubert, 1963; Klein, 1966); and some of this data have been used to develop correlations for tip leakage loss (Dunham and Came, 1970). Many experiments have also revealed the details of the flow structure as the tip leakage flow mixes with the primary passage flow (Graham, 1985; Sjolander and Amrud, 1987; Yamamoto, 1988, 1989). In particular, tip leakage vortices have been observed; and (for compressors and turbines) loss production models have been developed in which "the kinetic energy associated with the induced flow field outside the vortex core gives a qualitative indication of the nature of the losses, but not necessarily their magnitude" (Lakshminarayana, 1985).

Present Contribution

In this paper, we adopt a different approach to understanding tip leakage losses. In a turbine cascade, we measure both the flow at the exit of the tip gap and the flow downstream, and we perform integrations of flow properties. The key questions motivating such a study are:

1 How much tip leakage loss is produced overall?
2 How much loss is already produced by the tip gap exit?
3 How much secondary kinetic energy is associated with the tip gap exit flow?
4 How much loss does the dissipation of this secondary kinetic energy produce?

We answer these questions for flow in the VPI&SU tip leakage turbine cascade (Moore and Tilton, 1988), we relate the results to existing correlations of tip leakage loss, and suggest a simple strategy for calculating this loss. No consideration is given to the possible effects of a moving endwall, such as in a rotating unshrouded blade row.

Apparatus

VPI&SU Cascade. A top view of two of the five blades in the six-passage blade row of the VPI&SU tip leakage turbine cascade is shown in Fig. 1. The blade shape is that of a reaction turbine having mean chamber line angles $\beta_1 = 43.99$ deg and $\beta_2 = 25.98$ deg measured relative to the blade-to-blade direction. The blades produce a velocity ratio of 1.6 through a nominal turning angle of 110 deg. The tip gap is 5 mm, 2.1 percent (± 0.1 percent) of the blade height. Also seen in Fig. 1 are the blade numberings and blade dimensions, as well as the locations of the downstream measuring plane and the endwall boundary layer bleeds. The endwall boundary layers were removed prior to the test section in order to reduce the secondary flows they produce within the blade passages. Thus, the effects of the tip leakage flow are not obscured by other three dimensionalities. In addition, the endwall and blade boundary layers were tripped to insure they were turbulent and uniform. A further description of the cascade can be found in Moore and Tilton (1988).

Measuring Equipment. All measurements in this study were made with pressure probes and static pressure tappings. A total pressure probe and a static pressure tap located upstream of

Contributed by the International Gas Turbine Institute and presented at the 34th International Gas Turbine and Aeroengine Congress and Exhibition, Toronto, Ontario, Canada, June 4–8, 1989. Manuscript received at ASME Headquarters January 13, 1989. Paper No. 89-GT-56.

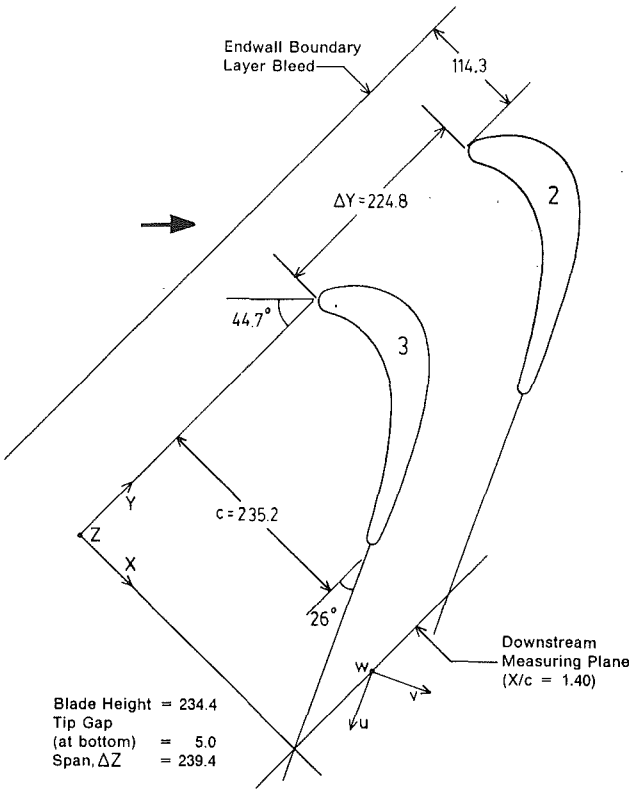

Fig. 1 Cascade geometry with coordinate system for the cascade (*X, Y, Z*) and showing primary and secondary flow velocities (*u, v, w*) downstream; linear dimensions in mm

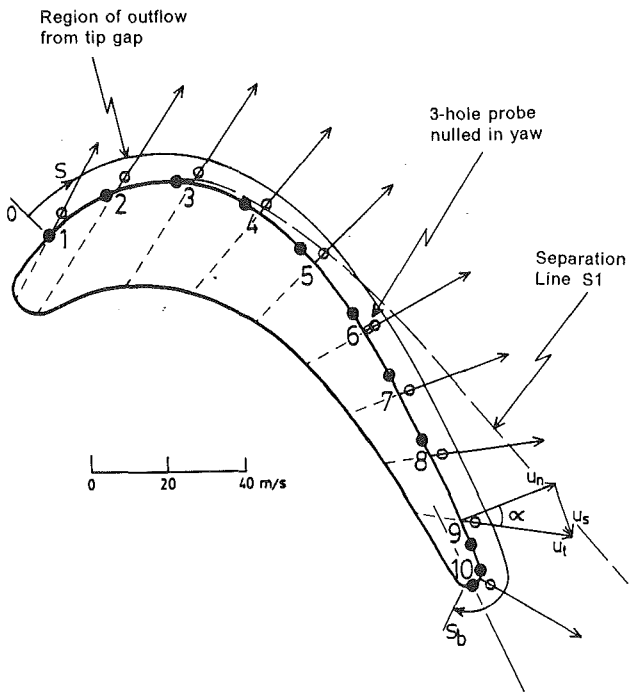

Fig. 2 Locations of tip gap exit flow measurements on blade 3: ○ three-hole probe traverse locations; ● endwall static pressure tappings. → mean tip gap exit velocities in direction of flow angle at midtip gap height; ---- tip gap flow paths from endwall flow visualization; —— endwall flow separation line S1

the blade row were used to measure the cascade inlet conditions. The tip gap measurements were made with a three-hole cobra probe constructed for this study; the thickness and width of the probe tip were 0.8 mm and 2.4 mm, respectively. A simple traversing gear that allowed spanwise movement and probe rotation was used for these measurements. The probe positioning was done by hand. A dial gage readable to 0.01 mm was used to measure spanwise position during each traverse. Cascade measurements downstream of the blade row were made with a United Sensor five-hole probe having a 3.18-mm (1/8-in.) tip diameter. The probe was calibrated to read total and static pressures as well as the three velocity components, u, v, and w; see Fig. 1. The five-hole probe was positioned by a traversing gear mounted above the cascade; this allowed pitchwise and spanwise traverses. The traversing gear also provided rotation, allowing the probe to be nulled in yaw. Because of its size, the five-hole probe could not be used near the passage endwalls. Therefore, the tip leakage probe and an additional but longer three-hole probe were used in these areas. Further details of the experimental equipment are given by Dishart (1987).

Measurements and Procedure

Tip Gap Exit Plane. To investigate the flow leaving the tip gap, static pressure tappings and holes for probe insertion were located in the cascade bottom endwall around blade 3; see Fig. 2. Using an endwall surface flow visualization as a guide, ten probe hole locations were chosen. All holes were

Nomenclature

C_D = discharge coefficient, equation (3)
C_{ps} = static pressure coefficient, equation (2)
C_{pt} = total pressure loss coefficient, equation (1)
P = static pressure
P_{s0} = cascade inlet static pressure
P_t = total pressure
P_{t0} = cascade inlet total pressure
Q = passage volume flow rate
S_b = tip gap exit length
u = velocity component in primary flow direction
U_0 = cascade inlet free-stream velocity
u_n = tip gap normal velocity, Fig. 2
u_s = tip gap streamwise velocity
u_t = tip gap total velocity
U_t = tip gap exit velocity based on potential flow
v = velocity component orthogonal to u and w
V = velocity at downstream measurement plane
V_n = velocity component normal to downstream measuring plane
w = velocity component in spanwise direction
X/c = axial distance from blade leading edge/axial chord
ΔY = blade pitch
ΔZ = blade span
β = flow angle with respect to pitchwise direction
δ_t = tip gap height
l/δ_t = leakage flow path/tip gap height
θ = flow angle with respect to axial direction
ρ = fluid density

Subscripts

0 = upstream of cascade, reference
d = mixed-out plane
ex = tip gap exit plane
x = axial direction
y = pitchwise direction

Superscripts

$\bar{}$ = area average, average
$\bar{\bar{}}$ = mass average

positioned such that when the probe was inserted and nulled in yaw, its tip would be in the tip gap exit plane, i.e., between the suction surface at the blade tip and the bottom endwall. Eleven static tappings were used, one corresponding to each probe location and an additional one at the trailing edge. The tappings were set in the tip gap exit plane, just to the side of the probe tip location. At each traverse location, a total of 18 measurements were made over the 5 mm tip gap height. At each traverse point, measurements of total pressure and flow angle were made. The static pressure was assumed uniform (in the z direction) at the local endwall value—an assumption supported by the blade tip and endwall static pressure measurements of Moore and Tilton (1988). The flow direction was determined by nulling the probe in yaw.

Downstream. The flow from the passage between blades 2 and 3 was measured at a distance of 0.4 axial chords downstream of the blade trailing edges. The measurements were made in an area defined by the extension of the mean camber lines from the trailing edges of blades 2 and 3 (see Fig. 1). The five-hole probe was used over most of the passage height; but within 6 mm of the bottom endwall and 15 mm of the top endwall, the three-hole probes were used.

Results, Analysis, and Discussion

Flow Conditions. The average inlet free-stream velocity was $U_0 = 20.5$ m/s at the standard test conditions of 94.9 kPa and 299 K. With an average air density of 1.10 kg/m^3 and a viscosity of 0.0000188 kg/ms, the Reynolds number based on the blade axial chord and an exit velocity of 32.7 m/s was 4.5×10^5. The inlet boundary layers were 2.2 mm thick, as reported earlier by Moore and Tilton. This gave a mass-averaged total pressure loss coefficient, $\bar{C}_{pt}$, of 0.0035 at the blade row entrance, where

$$C_{pt} = \frac{P_{t0} - P_t}{\frac{1}{2}\rho U_0^2} \tag{1}$$

Flow Visualization. A flow visualization study was performed to gain a qualitative understanding of the tip leakage flow. Following the procedure described by Moore and Tilton, surface flow visualizations were done on the suction surface of blade 3, the pressure surface of blade 2, and on the bottom endwall between the two blades. Also, to look at the leakage jet and vortex development within the blade passage, a smoke visualization technique was used. By heating diesel oil, smoke was generated and then injected into the tip gap. The injection was made parallel to the tip gap flow direction in order to minimize disturbances. The high flow velocities within the tip gap, however, could not be attained with the smoke generation equipment; only half the flow rate required for isokinetic injection could be achieved. To illuminate the smoke particles, the beam of a 5 mW laser was spread into a sheet by projecting it through a cylindrical glass rod. With the light sheet positioned in the blade passage where the injected smoke exits the tip gap, a cross section of the tip leakage vortex (perpendicular to the endwall) was revealed.

The smoke visualization of the leakage fluid, which exits the tip gap at 75 percent of the blade's axial chord, is superimposed on the endwall and suction surface visualizations in Fig. 3. This gives a three-dimensional perspective of the tip leakage flow as viewed from downstream of the blade trailing edge looking back upstream into the blade passage. The suction surface of blade 3 is seen on the left with smoke marking the leakage flow as it comes from under the blade. The entire leakage vortex is not illuminated because the smoke diffuses very quickly in the highly turbulent fluid. Traces of the leakage jet can be seen emerging from the tip gap and then separating from the endwall at the separation line S1 as the leakage fluid

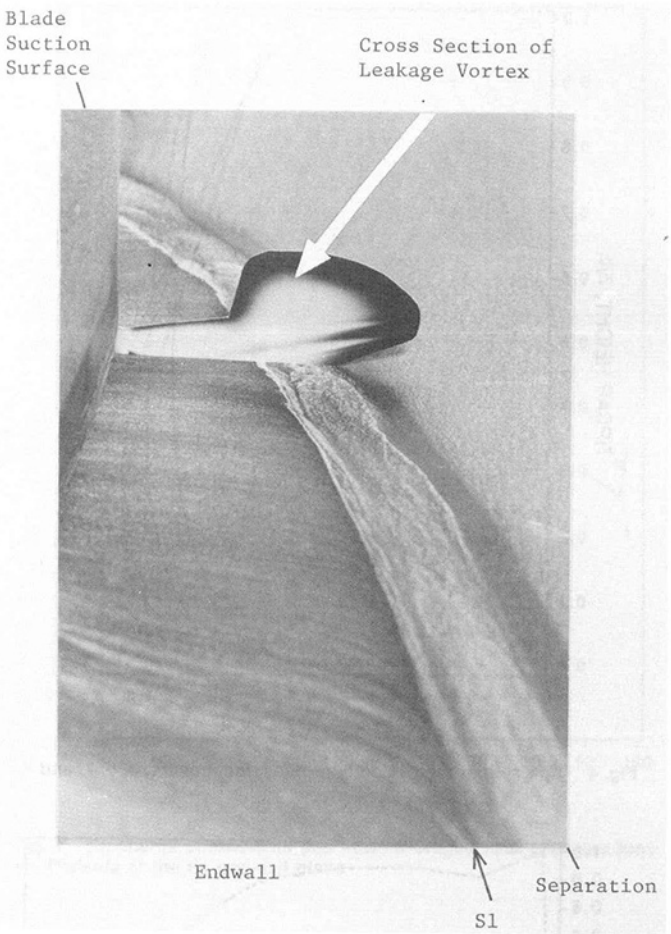

Fig. 3 Smoke and endwall flow visualization of tip leakage vortex in flow passage; viewed from downstream with blade suction surface on left

rolls up into a vortex. The separation line moves farther from the suction surface as the flow proceeds downstream toward the trailing edge, as shown also in Fig. 2.

Flow Measurements at the Tip Gap Exit

Velocity Profiles. The tip gap exit velocity profiles were determined from measured values of static and total pressure. Under the assumption that the spanwise velocity component was negligible (in the tip gap exit plane), the static pressure was considered locally uniform at the endwall value. The tip gap exit velocity profiles at locations 1, 3, 5, 7, and 9 of Fig. 2 are shown in Fig. 4. The profiles were extrapolated to the bottom endwall using $1/n$th power law approximations for turbulent boundary layers, which fit well. Appropriate choices for n could not be determined for the blade tip boundary layer profiles from the measured data, so the profiles were simply extrapolated linearly to a slip velocity at the blade tip.

The velocity profiles correspond to a flow through a vena contracta followed by flow mixing to fill the tip gap, as discussed by Moore et al. (1989). The extent of the mixing can be qualitatively judged by the shape of the velocity profile. The profiles at locations 1 and 3 are quite uniform compared with the curved profiles found toward the blade trailing edge (locations 5, 7, and 9), which show less evidence of mixing. The peak tip gap exit velocities are of the same order as the cascade exit velocity, approximately 1.6 U_0.

Static Pressure. The static pressures at the tip gap exit plane along with the blade pressure and suction surface pressures at

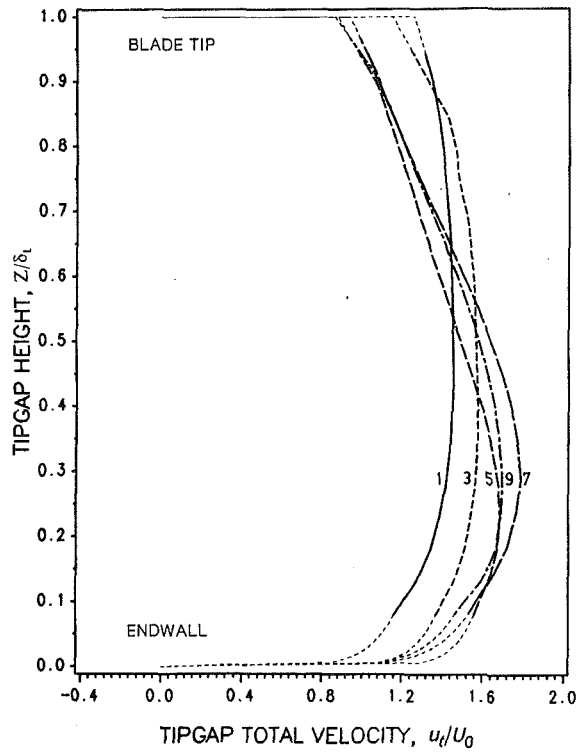

Fig. 4 Tip gap exit total velocity profiles, locations 1, 3, 5, 7, and 9

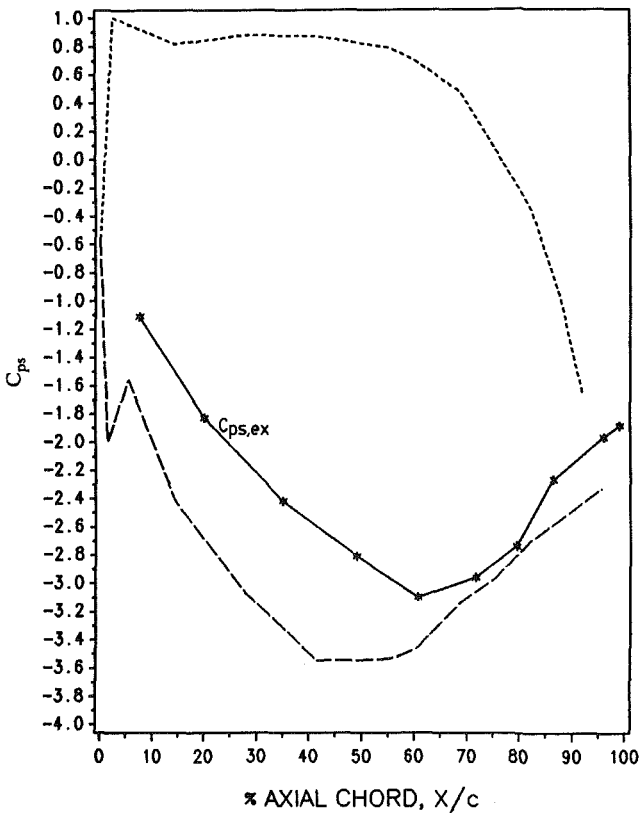

Fig. 5 Tip gap exit static pressure coefficients compared with blade loading at 45 percent span

45 percent span are shown as static pressure coefficients (C_{ps}) in Fig. 5. Here

$$C_{ps} = \frac{P - P_{s0}}{\frac{1}{2}\rho U_0^2} \tag{2}$$

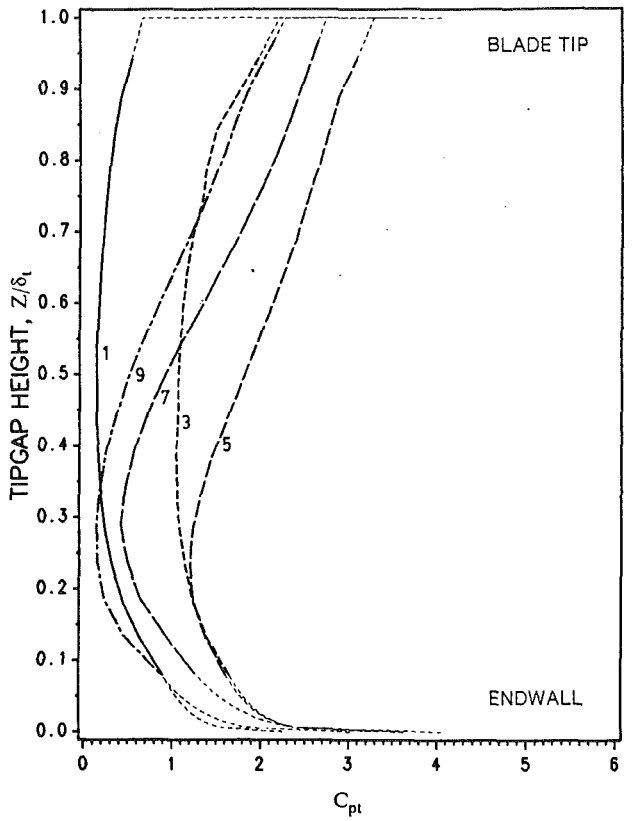

Fig. 6 Distribution of total pressure loss coefficient at tip gap exit locations 1, 3, 5, 7, and 9

The lowest exit plane static pressures are seen to exist near midaxial chord.

Total Pressure. The distributions of total pressure loss coefficient (equation 1) at the tip gap exit plane for measurement locations 1, 3, 5, 7, and 9 are shown in Fig. 6. The values near the endwall and the blade tip were calculated from the extrapolated values of velocity. After plane 3, the highest losses are seen near the blade tip where the flow is mixing to fill the tip gap; in the bottom half of the tip gap the losses are generally much lower. Again, the degree of mixing can be seen by the profile uniformity. The extent of the mixing is dependent on the length-to-tip-gap height ratio, l/δ_t, of the leakage flow path. Using the measured exit plane flow angles and the bottom endwall flow visualization, the length of the flow path within the tip gap for each measurement location was determined. The relative magnitudes of these lengths can be seen in Fig. 2. In general, a greater l/δ_t allows more complete mixing to occur within the tip gap. Near the blade leading edge, where l/δ_t is greatest (15.6 at location 2), the mixing appears to be fairly complete in the top half of the tip gap but apparently little loss was produced near the blade tip. Further downstream, more loss is produced near the blade tip, but l/δ_t decreases and the degree of mixing is seen to decrease as the trailing edge is approached. In particular, the profile at location 9 shows evidence of less mixing and seems still to possess a potential flow core at about 0.25 tip gap heights.

Directional Velocities. By measuring the direction normal to the blade surface at each probe location and comparing it to the measured flow direction, the tip gap velocities were resolved into normal and streamwise components. The streamwise direction is defined tangent to the blade surface and positive in the direction of the primary flow. The flow angles were found to remain essentially constant across the tip gap height.

Vectors representing the mean flow velocity at each measurement location are given in Fig. 2. Their directions are those of the flow at midtip gap height. Near the blade leading edge (location 1) the flow is primarily in the streamwise direction. The normal component of the velocity is small, therefore, and relatively little flow is discharging from the tip gap. Moving around the blade toward the trailing edge, the flow direction becomes more and more normal to the blade; by 54 percent axial chord (location 4) the flow is essentially normal to the blade. The flow direction continues to change and at 65 percent axial chord (location 5) the flow actually leaves the tip gap with a velocity component in the negative streamwise direction. As the trailing edge is approached, the streamwise velocity component turns positive again and then continues to increase.

The abovementioned behavior can be qualitatively explained by the variation of tip gap exit plane static pressure. As seen in Fig. 5, the exit static pressure is highest near the blade leading edge, providing little driving force for leakage flow. It drops down quickly toward midaxial chord, creating a strong, flow-inducing gradient from the pressure to the suction side of the blade. As the exit plane pressure then rises toward the trailing edge, the strength of the leakage flow diminishes and its path turns more in the streamwise direction.

Discharge Coefficient. Following the procedure of Moore and Tilton, a discharge coefficient was calculated for each of the ten tip gap measurement locations.

$$C_D = \frac{\bar{u}_n}{U_t} \tag{3}$$

$\bar{u}_n$ is the area-averaged normal velocity at each measurement location, and U_t is the tip gap exit velocity from potential flow analysis based on the cascade inlet free-stream total pressure P_{t0} and the local tip gap exit static pressure $P_{s,ex}$. The calculated values of discharge coefficient around the blade profile are plotted in Fig. 7. As expected, the highest values are seen to exist just past midaxial chord where the tip gap exit plane static pressure is lowest and the flow is most normal to the blade surface.

It may be noted that the discharge coefficient of 0.74 found from the present test at $X/c = 0.72$ does not agree with the value of 0.843 given by Moore and Tilton (1988). The difference is explained by a numerical error of +18 percent in the earlier evaluation of the tip gap flow. Therefore, the simple model of two-dimensional potential flow plus mixing used by Moore and Tilton to explain their discharge coefficient is only qualitatively correct.

Total Pressure Loss Coefficient. A mass-averaged total pressure loss coefficient was calculated for each of the measurement locations.

$$\bar{\bar{C}}_{pt} = \frac{\int_0^{\delta_t} \rho u_n C_{pt} dz}{\int_0^{\delta_t} \rho u_n dz} \tag{4}$$

The values are plotted versus percent axial chord in Fig. 7. These values represent the losses produced by the leakage flow up to the tip gap exit plane. The highest losses are seen to be between 40 and 80 percent axial chord, where Fig. 2 shows the flow exiting the tip gap nearly normal to the suction surface.

Overall Tip Leakage Coefficients. Various flow properties were integrated over the entire tip gap exit length to develop tip leakage coefficients. The coefficients and their definitions are given below.

Flow Coefficient:

$$\mathrm{FC} = \frac{\int_0^{S_b}\int_0^{\delta_t} \rho u_n dz ds}{\rho Q} \tag{5}$$

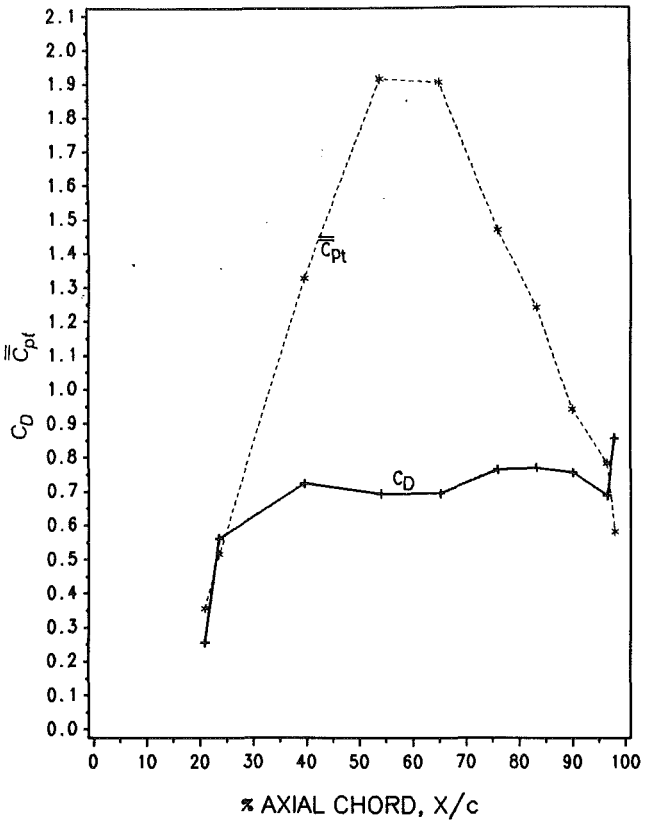

Fig. 7 Discharge coefficients and mass-averaged total pressure loss coefficients at the tip gap exit plane

Total Kinetic Energy Coefficient:

$$\mathrm{TKEC} = \frac{\int_0^{S_b}\int_0^{\delta_t} \rho u_n \left[\frac{u_n^2 + u_s^2}{2}\right] dz ds}{\rho Q \frac{U_0^2}{2}} \tag{6}$$

Normal Kinetic Energy Coefficient:

$$\mathrm{NKEC} = \frac{\int_0^{S_b}\int_0^{\delta_t} \rho u_n \left[\frac{u_n^2}{2}\right] dz ds}{\rho Q \frac{U_0^2}{2}} \tag{7}$$

Streamwise Kinetic Energy Coefficient:

$$\mathrm{SKEC} = \frac{\int_0^{S_b}\int_0^{\delta_t} \rho u_n \left[\frac{u_s^2}{2}\right] dz ds}{\rho Q \frac{U_0^2}{2}} \tag{8}$$

Total Pressure Loss Coefficient:

$$\mathrm{TPLC} = \frac{\int_0^{S_b}\int_0^{\delta_t} \rho u_n (P_{t0} - P_t) dz ds}{\rho Q \frac{\rho U_0^2}{2}} \tag{9}$$

The integrations around the blade profile (0 to S_b; see Fig. 2) were done to account for all flow exiting the tip gap. This required an estimate of the location where flow first began to exit the tip gap. The endwall flow visualization suggested the zero location to be at $X/c = 0.075$, a distance of 3.2 mm (1/8 in.) in front of location 1. The exact position of this location,

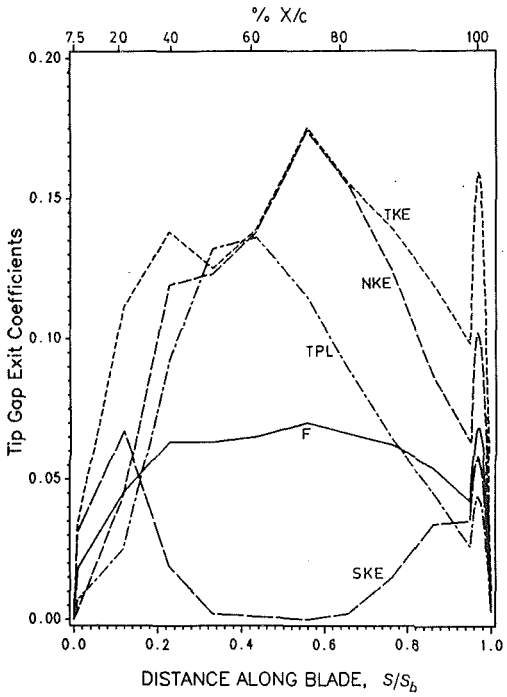

Fig. 8 Variations of flow rate F and fluxes of kinetic energy and total pressure loss at the tip gap exit; fluxes: TKE = total kinetic energy; NKE = normal kinetic energy; SKE = streamwise kinetic energy; TPL = total pressure loss; areas under the curves correspond to coefficients defined in equations (5)-(9)

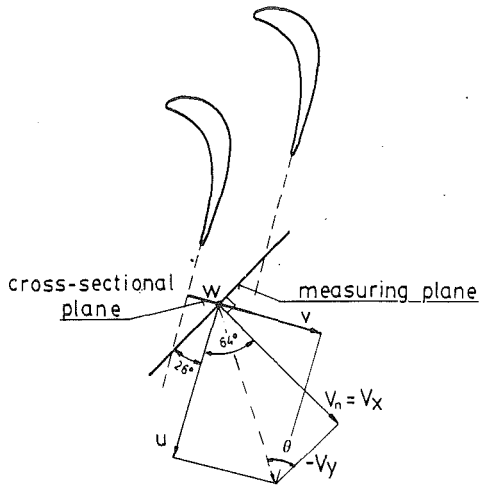

Fig. 9 Flow coordinate system at the downstream measuring plane

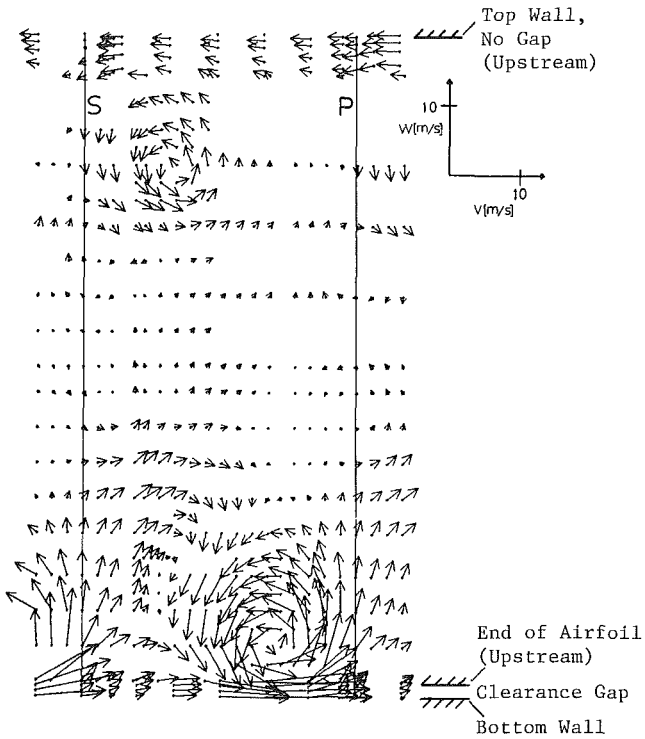

Fig. 10 Secondary velocity vectors in the cross-sectional plane at $X/c = 1.4$: —projections downstream of blades in direction of mean camber lines at trailing edges; S = downstream of blade 3; P = downstream of blade 2

however, was insignificant because the amount of flow exiting the tip gap at and before location 1 was so small. Flow continued to exit the tip gap for a distance of $S_b = 34.9$ cm around the blade profile. The blade geometry at the trailing edge required a slight modification to the integration procedure. Here, the streamwise and normal kinetic energies $u_n^2/2$ and $u_s^2/2$ were evaluated with the streamwise flow in the direction of the mean camber line at the trailing edge. Consulting the endwall flow visualization, the direction of the flow exiting the tip gap around the trailing edge circle appeared to be uniform, so the kinetic energies at any point on the trailing edge circle were calculated using the data measured at location 10. Also, the curvature of the trailing edge circle meant that the blade surface normal, and therefore the amount of flow exiting the tip gap, changed rapidly. Thus, integration points were chosen every 10 deg around the trailing edge, ending of the pressure side at S_b, 40 deg from the camber line, where the flow ceased to exit the tip gap. The integrated values of the tip leakage coefficients are presented below.

FC = 0.057
TKEC = 0.128
NKEC = 0.109
SKEC = 0.020
TPLC = 0.071

These coefficients reveal important information about the tip leakage flow. 5.7 percent of the passage flow is seen to pass through the tip gap. The total mass-averaged kinetic energy of this flow is 12.8 percent of the inlet kinetic energy on a per-passage basis. More importantly, the majority of this kinetic energy is exiting the tip gap in a direction normal to the primary passage flow. According to the work of Moore and Adhye (1985), it is therefore expected to dissipate as a loss as the flow travels downstream. The streamwise kinetic energy is small. A significant total pressure loss is seen to have occurred within the tip gap. The mass-averaged total pressure loss per passage is 7.1 percent of the inlet dynamic pressure.

A better understanding of the above coefficients can be gained by plotting the variations of the properties they represent as a function of the tip gap exit length (0 to S_b). The distribution of tip gap exit flow and the distributions of the fluxes of total kinetic energy, normal kinetic energy, streamwise kinetic energy, and total pressure loss are shown in Fig. 8. The plotted properties were normalized such that the areas under their distribution curves are equal to the coefficients defined in equations (5)–(9), respectively.

The flow exiting the tip gap is seen to be quite uniform from 30 percent axial chord to the trailing edge. The fluxes of total pressure loss and kinetic energy vary significantly, however. Consistent with Fig. 7, the flux of total pressure loss occurs largely between 40 and 80 percent axial chord. The flux of kinetic energy is mostly due to the normal "component" and

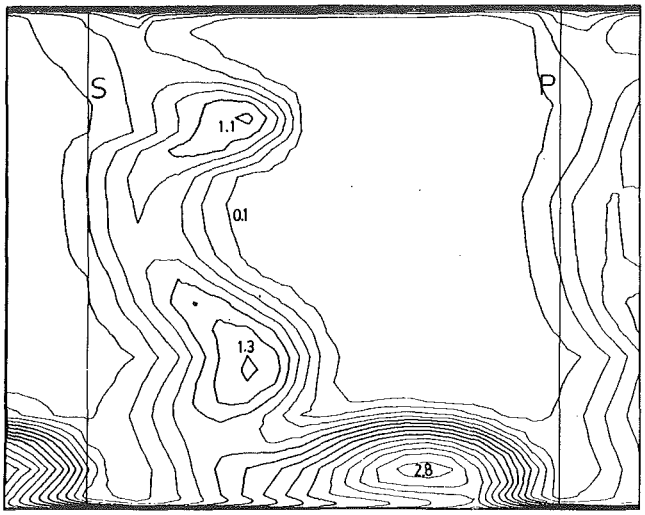

Fig. 11 Contours of constant total pressure loss coefficient at $X/c = 1.4$

again this is high from 30 percent axial chord to the trailing edge, peaking around 70 percent axial chord where Fig. 5 shows the tip gap exit static pressure to be near its minimum value.

Downstream Measurements

Secondary Flow Velocities. The primary flow direction at the downstream measuring plane ($X/c = 1.4$) is defined as the direction of the mean camber line at the blade trailing edge. The secondary velocities, v and w, lie in a plane perpendicular to the primary flow direction. This cross-sectional plane along with the three velocity components are illustrated in Fig. 9.

The secondary velocity vectors projected to the cross-sectional plane are presented in Fig. 10. Because the three-hole probes used for the near-wall measurements could not distinguish spanwise velocities, the w velocities from the near-wall five-hole probe measurements were imposed on the overlapping three-hole probe measurements. The w velocity was then assumed to vary linearly to zero at the endwalls.

Flow in the bottom half of the passage is dominated by the tip leakage vortex. At this downstream distance, it contains flow with secondary velocities reaching 11. m/s, 0.55 U_0. A small passage vortex with maximum secondary velocities of about 0.18 U_0 is seen in the top half of the passage. The rotation of a passage vortex is not clearly seen in the bottom half of the passage. The secondary velocity vectors do, however, show a clockwise rotation, but it appears to break down when it encounters the leakage vortex. This is probably a second passage vortex, which has its secondary velocities redirected upon interacting with the leakage vortex. Also in evidence is the expected overturning of the top endwall boundary layer.

Total Pressure. Contours of constant total pressure loss coefficient C_{pt} (equation (1)) are shown in Fig. 11. In addition to the blade wakes, three distinct regions of high loss are present. The strongest of these is the tip leakage vortex having a maximum C_{pt} of 2.8. The passage vortex in the top half of the passage is easily distinguished but considerably weaker, having a maximum loss coefficient of 1.1. The third high loss core has a maximum of C_{pt} of 1.3, slightly higher than that of the top passage vortex; the similar strength and symmetric location with the top passage vortex further suggest that this third loss core is the result of a second passage vortex.

The top endwall boundary layer is seen to be quite thin, extending only 6–7 mm into the passage. The boundary layer on the bottom wall appears even thinner, although its full extent is difficult to distinguish because of the presence of the leakage vortex and blade wakes. Estimates of its thickness range from less than 2 mm under the leakage vortex to 5 mm near the blade wakes.

A significant area of low loss ($C_{pt} < 0.1$) is seen to exist within the passage. This region, which covers about half the flow area, represents nearly two-dimensional flow. Near midspan, the blade wake seems undisturbed by the three loss cores and could be a measure of the blade profile loss.

Static Pressure. Over most of the downstream measuring plane, the static pressure is fairly uniform at a static pressure coefficient C_{ps} (equation 2) of approximately -2.0. The only significant zone of low pressure is near the center of the leakage vortex where C_{ps} drops to -2.25. An area of slightly depressed static pressure is also present near the center of the top passage vortex. Its small area of influence and minimum C_{ps} of only -2.1 is indicative of its lesser strength in relation to the leakage vortex. A similar but less distinct area corresponds to the location of the bottom half passage vortex.

Averaged Flow Properties. Flow properties were averaged over the downstream plane on mass and area bases. The area-averaged normal velocity is given by

$$\overline{V}_n = \frac{\int_0^{\Delta Y}\int_0^{\Delta Z} V_n dz dy}{\Delta Y \Delta Z} \tag{10}$$

The mass averaging for velocity components, total pressure loss, and kinetic energies takes the form

$$\overline{\overline{V}}_x = \frac{\int_0^{\Delta Y}\int_0^{\Delta Z} \rho V_n V_x dz dy}{\int_0^{\Delta Y}\int_0^{\Delta Z} \rho V_n dz dy} \tag{11}$$

The averaged flow angles were defined by

$$\overline{\beta} = \tan^{-1}\left[\frac{\overline{V}_x}{-\overline{V}_y}\right] \tag{12}$$

$$\overline{\overline{\beta}} = \tan^{-1}\left[\frac{\overline{\overline{V}}_x}{-\overline{\overline{V}}_y}\right] \tag{13}$$

Using the area-averaged normal velocity, $\overline{V}_n$, at the downstream measurement plane, a mass flow coefficient η was defined.

$$\eta = \frac{\overline{V}_n}{\overline{V}_{n,\text{cascade inlet}}} \tag{14}$$

The principle of mass conservation demands that η be 100 percent for incompressible flow. However, it is very sensitive to variations in measured yaw angle. A systematic yaw correction of 1.85 deg was needed to lower η from 106 to 100 percent. This correction was applied to each data point and the integrations were repeated. The resulting changes in the integrated values appeared only in the third significant figure but were retained to satisfy continuity over the flow field.

The various properties averaged over the flow field are presented in Table 1.

The mass-averaged total pressure loss coefficient $\overline{\overline{C}}_{pt}$ is 0.375, which represents the overall cascade loss at $X/c = 1.4$. An indication of the importance of tip leakage flow in loss production can be gained by comparison with the earlier work of Moore and Adhye (1985). On a geometrically similar cascade a mass-averaged total pressure loss coefficient of 0.347 was recorded for the same downstream measuring plane. In their case, however, the inlet boundary layers were significantly thicker, measuring approximately 38. mm compared to the present 2.2 mm. Their large inlet boundary layers contributed significant loss ($\overline{\overline{C}}_{pt} \sim 0.07$) at the cascade inlet and produced extreme secondary flows within the blade passage. Even with

Table 1 Averaged flow properties

$\overline{V}_n$ (m/s)	14.4
$\overline{\overline{V}}_x$ (m/s)	14.6
$\overline{\overline{V}}_y$ (m/s)	-29.3
$\overline{\beta}$ (°)	26.1
$\overline{\overline{\beta}}$ (°)	26.6
$\overline{\overline{C}}_{pt}$	0.375
$\frac{\overline{\overline{u^2}}}{U_0^2}$	2.597
$\frac{\overline{\overline{v^2}}}{U_0^2}$	0.010
$\frac{\overline{\overline{w^2}}}{U_0^2}$	0.006
$\frac{\overline{\overline{v^2 + w^2}}}{U_0^2}$	0.016
$\overline{\overline{C}}_{pt} + \frac{\overline{\overline{v^2 + w^2}}}{U_0^2}$	0.391

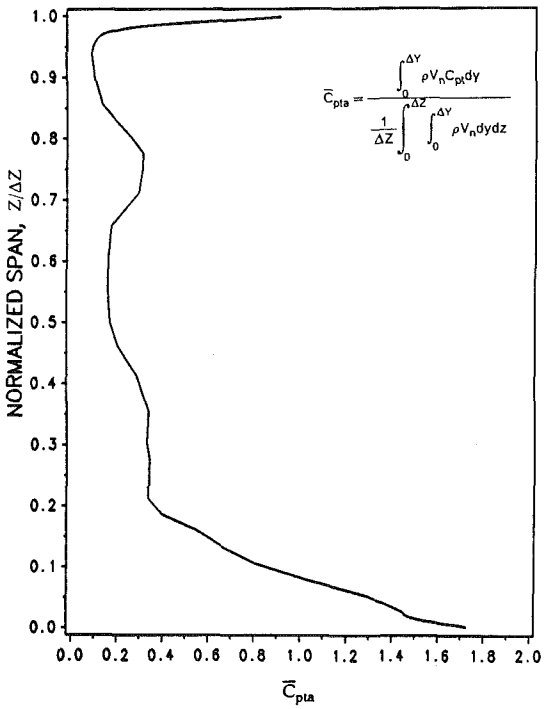

Fig. 12 Pitchwise-averaged total pressure loss coefficient, $\overline{C}_{pta}$, at $X/c = 1.4$

the large high-loss passage vortices created from these boundary layers, the mass-averaged loss at $X/c = 1.4$ was less than that of the present cascade with a leakage vortex and two small passage vortices.

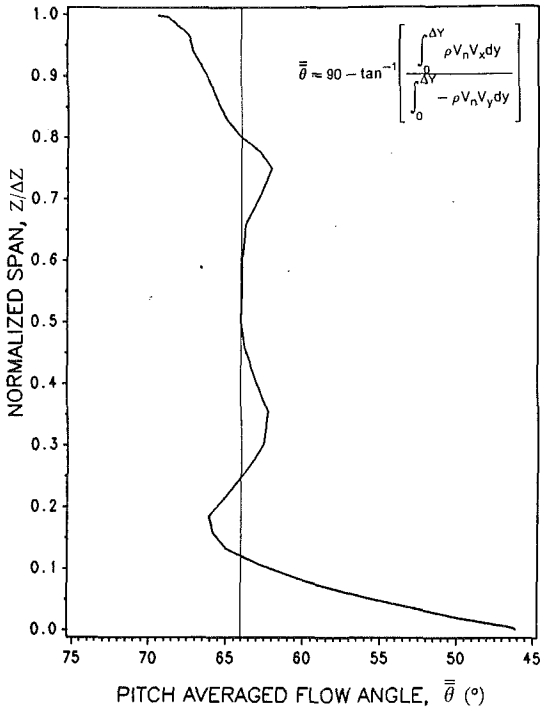

Fig. 13 Pitchwise-mass-averaged flow angle at $X/c = 1.4$

Better insight to the loss distribution within the passage can be gained from values of the pitchwise-averaged total pressure loss coefficient $\overline{C}_{pta}$. From Moore (1983)

$$\overline{C}_{pta} = \frac{\int_0^{\Delta Y} \rho V_n C_{pt} dy}{\frac{1}{\Delta Z}\int_0^{\Delta Z}\int_0^{\Delta Y} \rho V_n dy dz} \tag{15}$$

Note that $\overline{C}_{pta}$ is defined such that the area under its distribution curve is $\overline{\overline{C}}_{pt}$.

The distribution of $\overline{C}_{pta}$ along the passage height is shown in Fig. 12. The high loss of the leakage flow is seen extending to about 20 percent of the blade span. The smaller loss accumulation near 75 percent span is due to the top passage vortex. The thin high loss area of the top endwall boundary layer is also evident. In addition, an area of uniform loss is seen near midspan. This relatively constant pitchwise-averaged total pressure loss coefficient of 0.16 from 50 to 60 percent of the span could be a measure of the profile loss (for this blade with tripped boundary layers).

The distribution of pitchwise-mass-averaged flow angle was also found to be of interest. Figure 13 shows the spanwise variation of pitchwise-mass-averaged flow angle defined as

$$\overline{\overline{\theta}} = 90 - \tan^{-1}\left[\frac{\int_0^{\Delta Y} \rho V_n V_x dy}{\int_0^{\Delta Y} -\rho V_n V_y dy}\right] \tag{16}$$

for a particular spanwise location. Note that $\theta = 90$ deg $- \beta$. $\overline{\overline{\theta}}$ of 64 deg corresponds to the direction of the blade trailing edge mean camber lines. Near the bottom endwall, the tip leakage vortex produces significant underturning of the flow. The underturning due to the passage vortices as well as the overturning of the top endwall boundary layer are also clearly evident. The flow is seen to be essentially uniform at the exit blade angle between 50 and 60 percent of the span.

Mixing Analysis. As an estimate of the maximum possible

Table 2 Mixed-out flow properties

$\overline{V}_{x,d}$ (m/s)	14.4
$\overline{V}_{y,d}$ (m/s)	-29.3
$\overline{\beta}_d$ (°)	26.1
$\overline{C}_{ps,d}$	-1.968
$\overline{C}_{pt,d}$	0.427

Table 3 Comparison of the top and bottom halves of the flow passage

	Top Half Passage	Bottom Half Passage
$\overline{\overline{C}}_{pt}$, x/c = 1.4	0.199	0.555
$\frac{\overline{\overline{v^2 + w^2}}}{U_0^2}$, x/c = 1.4	0.005	0.027
$\overline{\overline{C}}_{pt} + \frac{\overline{\overline{v^2 + w^2}}}{U_0^2}$, x/c = 1.4	0.204	0.582
$\overline{C}_{pt,d}$	0.206	0.643

loss for this cascade, the measured flow at $X/c = 1.4$ was "numerically" mixed with constant area to uniform conditions. This was done by solving the continuity and momentum equations over a control volume for one passage flow. The control volume extended from the measurement plane to an arbitary distance downstream where the flow was considered mixed out. Further details on the mixing procedure can be found from Moore and Adhye (1985). The mixed-out flow properties (subscripted d) are presented in Table 2.

The flow angle $\overline{\beta}_d$ is 26.1 deg, showing that the mixed-out flow is essentially following the exit blade angle. The mixed-out total pressure loss coefficient is 0.427. This is an increase from the value of 0.375 at the measurement plane.

In the earlier work of Moore and Adhye (1985), it was noted that the increase in total pressure loss coefficient due to flow mixing was almost entirely explained by the dissipation of secondary kinetic energy. For this cascade with tip leakage, it is not the case. The sum of $\overline{\overline{C}}_{pt}$ and $\overline{\overline{(v^2+w^2)}}/U_0^2$ at the actual measurement plane is 0.391 (Table 1), which is lower than the mixed-out $\overline{C}_{pt,d}$ of 0.427. Thus, the mixing process of the tip leakage vortex seems to involve the dissipation of primary as well as secondary kinetic energy.

In order to investigate this further, the top and bottom halves of the passage were treated as entirely different flows. The losses of each half were mass averaged and then mixed out as if each half existed separately. The results of this analysis are presented in Table 3.

In the case of the top half passage, with only a passage vortex, the dissipation of secondary kinetic energy can account for the small increase in loss due to mixing, which agrees with the finding of Moore and Adhye. However, in the bottom half passage, the increase in loss at the mixed-out plane is significantly larger than the secondary kinetic energy at $X/c = 1.4$. This is the result of the residual distortion of the primary flow profile, which occurs when the leakage flow enters the blade passage.

Additional Losses Due to Tip Leakage. The presence of a region of nearly two-dimensional flow near midspan at $X/c = 1.4$ led to the splitting up of the passage flow into two parts, the bottom half being dominated by the leakage flow and the top half containing a passage vortex. If, as suggested by Figs. 10–13, the secondary flows of each half do not interact, then the difference between the mass-averaged total pressure loss coefficients of the top and bottom halves is a measure of the extra loss resulting from tip leakage.

The portions of the overall mass-averaged total pressure loss coefficient produced in the top and bottom halves of the flow passage were calculated. These values and their difference are shown below:

$$\text{Bottom half:}\quad \overline{\overline{C}}_{pt} = 0.275$$
$$\text{Top half:}\quad \overline{\overline{C}}_{pt} = 0.101$$
$$\text{Difference:}\quad \overline{\overline{C}}_{pt} = 0.174$$

The difference, $\overline{\overline{C}}_{pt} = 0.174$, represents an additional loss due to tip leakage of 87 percent. That is, the present cascade would have a mass-averaged total pressure loss coefficient that is 87 percent greater than that of a similar cascade having identical inlet conditions, but no tip gap.

Another estimate of the additional tip leakage loss can be made from secondary kinetic energy considerations and the flow measurements at the tip gap exit plane. By treating the flow in the bottom half of the passage as a symmetric reflection of the top half flow with the tip leakage flow superimposed upon it, the following analysis can be made. At the tip gap exit, a mass-averaged total pressure loss coefficient of 0.071 already exists and the normal or secondary kinetic energy coefficient is 0.109. At the downstream plane, the amount of the tip gap normal kinetic energy that has not yet been dissipated may be estimated from the difference between the portions of the total secondary kinetic energy in the bottom and top halves of the passage. The difference, $\delta\overline{\overline{(v^2+w^2)}}/U_0^2 = 0.013 - 0.002 = 0.011$, is the residual tip leakage secondary kinetic energy at $X/c = 1.4$. Therefore, by this estimate, the amount of tip gap secondary kinetic energy dissipated by $X/c = 1.4$ is $0.109 - 0.011 = 0.098$. The extra loss due to tip leakage at $X/c = 1.4$ is then:

$$\text{Tip gap exit:}\quad \overline{\overline{C}}_{pt} = 0.071$$
$$\text{Dissipated tip gap ske:}\quad \frac{\overline{\overline{v^2+w^2}}}{U_0^2} = 0.098$$
$$\text{Extra tip leakage loss:}\quad \overline{\overline{C}}_{pt} = 0.169$$

This is very close to the value of $\overline{\overline{C}}_{pt} = 0.174$ reached by the previous method. It suggests that the addition of the loss incurred within the tip gap and the amount of dissipated tip leakage secondary kinetic energy is a reasonable procedure for estimating the additional loss.

Comparison With Tip Leakage Loss Correlations. Several correlations for the extra loss due to tip leakage are available in the literature. Dunham and Came (1970), for example, give two correlations expressed in terms of a tip clearance loss coefficient Y_k, where

$$Y = \frac{P_{t1} - P_{t2}}{P_{t2} - P_2} \tag{17}$$

and the subscripts 1 and 2 refer to cascade inlet and exit conditions, respectively.

For the present test, Y_k has the value 0.067, at $X/c = 1.4$, and a mixed-out value of 0.087. The correlation of Ainley and Mathieson (1957) gives 0.089 and the modified correlation of Dunham and Came (1970) gives 0.203.

Conclusions

An experimental study of incompressible flow through a large-scale turbine cascade with a tip gap measuring 2.1 percent of the blade height has been performed. The Reynolds number based on axial chord and cascade exit velocity was 4.5×10^5. The flow exiting the tip gap was measured and its effects on the flow at 0.4 axial chords downstream of the blade trailing edges were documented.

A total of 5.7 percent of the passage flow passed through the tip gap, developing a mass-averaged total pressure loss coefficient $\bar{C}_{pt}$ of 0.071 (based on inlet dynamic pressure) by the tip gap exit plane. This leakage flow contributed secondary kinetic energy measuring 0.109 of the inlet kinetic energy on a per passage basis. Flow measurements at 0.4 axial chords downstream of the blade trailing edges revealed an overall mass-averaged total pressure loss coefficient of 0.375 for the cascade.

At $X/c = 1.4$, the effects of the tip leakage flow were limited to the bottom half of the passage. Therefore, the overall cascade loss at $X/c = 1.4$ can be considered to be twice the loss in the top half of the passage plus the additional loss due to tip leakage. The additional loss was found to be the sum of the internal tip gap losses and the tip leakage secondary kinetic energy that had been dissipated. Thus, this secondary kinetic energy adds to the tip leakage loss in nearly a one-for-one correspondence as it dissipates downstream of the blade row.

This simple physical picture of tip clearance loss may be helpful in further developing loss correlations. The Ainley and Mathieson correlation, however, agreed well with the additional tip clearance loss in the mixed-out downstream flow in the present test.

Acknowledgments

The authors wish to thank Rolls-Royce plc, Aero Division, for supporting this work under a cooperative agreement with Virginia Polytechnic Institute and State University.

References

Ainley, D. G., and Mathieson, G. C. R., 1957, "A Method of Performance Estimation for Axial Flow Turbines," British ARC, R&M 2974.

Bindon, J. P., 1986, "Pressure and Flow Field Measurements of Axial Turbine Tip Clearance Flow in a Linear Cascade," Report No. CUED/A-Turbo TR123.

Bindon, J. P., 1987, "Measurement of Tip Clearance Flow Structure on the End-Wall and Within the Clearance Gap of an Axial Turbine Cascade," I. Mech. E. 1987-6, pp. 43-52, Int. Conf. on Turbomachinery—Efficiency Prediction and Improvement, Cambridge, United Kingdom.

Bindon, J. P., 1989, "The Measurement and Formation of Tip Clearance Loss," ASME JOURNAL OF TURBOMACHINERY, Vol. 111, pp. 257-263.

Booth, T. C., Dodge, P. R., and Hepworth, H. K., 1982, "Rotor-Tip Leakage. Part 1—Basic Methodology," ASME *Journal of Engineering for Power*, Vol. 104, pp. 154-161.

Dishart, P. T. , 1987, "Tip Leakage Losses in a Linear Turbine Cascade," M.S. Thesis, Virginia Polytechnic and State University, Blacksburg, VA.

Dunham, J., and Came, P. M., 1970, "Improvements to the Ainley-Mathieson Method of Turbine Performance Prediction," ASME *Journal of Engineering for Power*, Vol. 92, pp. 252-256.

Graham, J. A. H., 1985, "Investigation of a Tip Clearance Cascade in a Water Analogy Rig," ASME Paper No. 85-IGT-65.

Hourmouziadis, J., and Albrecht, G., 1987, "An Integrated Aero/Mechanical Performance Approach to High Technology Turbine Design," AGARD Conference Proceedings No. 421 on Advanced Technology for Aero Gas Turbine Components, Paris, France.

Hubert, G., 1963, "Untersuchungen uber die Sekundarverluste in Axialen Turbomaschinen," VDI Forschungsheft 496, pp. 5-18.

Klein, A., 1966, "Untersuchungen uber den Einfluss der Zustromgrenzschicht auf die Sekundarshtromungen in den Beschaufelungen von Axialturbinen," *Forschung Ing.-Wes.*, Vol. 32, No. 6, pp. 175-188.

Kofskey, M. G., 1961, "Experimental Investigation of Three Tip-Clearance Configurations Over a Range of Tip Clearance Using a Single-Stage Turbine of High Hub to Tip Radius Ratio," NASA TM X-472.

Lakshminarayana, B., 1985, "Compressor Loss Correlations and Analysis and Effects on Compressor Performance," von Karman Institute for Fluid Dynamics, Lecture Series 1985-05 on Tip Clearance Effects in Axial Turbomachines.

Moore, J., 1983, "Flow Trajectories, Mixing and Entropy Fluxes in a Turbine Cascade," AGARD Conference Proceedings No. 351 on Viscous Effects in Turbomachines, Copenhagen, Denmark.

Moore, J. and Adhye, R., 1985, "Secondary Flows and Losses Downstream of a Turbine Cascade," ASME *Journal of Engineering for Gas Turbines and Power*, Vol. 107, No. 4, pp. 961-968.

Moore, J., Moore, J. G., Henry, G. S., and Chaudhry, U., 1989, "Flow and Heat Transfer in Turbine Tip Gaps," ASME JOURNAL OF TURBOMACHINERY, Vol. 111, pp. 301-309.

Moore, J., and Tilton, J. S., 1988, "Tip Leakage Flow in a Linear Turbine Cascade," ASME JOURNAL OF TURBOMACHINERY, Vol. 110, pp. 18-26.

Roelke, R. J., 1973, "Turbine Design and Application," A. J. Glassman, ed., NASA SP-290, pp. 125-131.

Sjolander, S. A., and Amrud, K. K., 1987, "Effects of Tip Clearance on Blade Loading in a Planar Cascade of Turbine Blades," ASME JOURNAL OF TURBOMACHINERY, Vol. 109, pp. 237-245.

Wadia, A. R., and Booth, T. C., 1982, "Rotor-Tip Leakage: Part II—Design Optimization Through Viscous Analysis and Experiment," ASME *Journal of Engineering for Power*, Vol. 104, pp. 162-168.

Yamamoto, A., 1988, "Interaction Mechanisms Between Tip Leakage Flow and the Passage Vortex in a Linear Turbine Rotor Cascade," ASME JOURNAL OF TURBOMACHINERY, Vol. 110, pp. 329-338.

Yamamoto, A., 1989, "Endwall Flow/Loss Mechanisms in a Linear Turbine Cascade With Blade Tip Clearance," ASME JOURNAL OF TURBOMACHINERY, Vol. 111, pp. 264-275.

Yaras, M., Zhu, Y., and Sjolander, S. A., 1989, "Flow Field in the Tip Gap of a Planar Cascade of Turbine Blades," ASME JOURNAL OF TURBOMACHINERY, Vol. 111, pp. 276-283.

Development of the Tip-Leakage Flow Downstream of a Planar Cascade of Turbine Blades: Vorticity Field

M. Yaras
Graduate Research Assistant.

S. A. Sjolander
Associate Professor.
Assoc. Mem. ASME

Department of Mechanical and Aeronautical Engineering,
Carleton University,
Ottawa, Ontario,
Canada K1S 5B6

The paper presents detailed measurements of the tip-leakage flow emerging from a planar cascade of turbine blades. Four clearances of from 1.5 to 5.5 percent of the blade chord are considered. Measurements were made at the trailing edge plane, and at two main planes 1.0 and 1.56 axial chord lengths downstream of the cascade. The results give insight into several aspects of the leakage flow, including the size and strength of the leakage vortex in relation to the size of the tip gap and the bound circulation of the blade, and the evolution of the components of vorticity as the vortex diffuses laterally downstream of the blade row. The vortex was found to have largely completed its roll-up into a nearly axisymmetric structure even at the trailing edge of the cascade. As a result, it was found that the vortex could be modeled surprisingly well with a simple model based on the diffusion of a line vortex.

Introduction

This paper presents further experimental data from an ongoing study of the tip leakage flow in a planar cascade of turbine blades. Earlier papers have examined the effect of the leakage flow on the blade loading (Sjolander and Amrud, 1987) and the behavior of the flow within the gap itself (Yaras et al., 1989). The data are quite extensive and are available in tabular form for use as a test case for computational methods (Yaras and Sjolander, 1988). The present paper focuses on the development of the vorticity field downstream of the trailing edge. The total pressure losses will be examined in a separate paper, which is in preparation.

A knowledge of the strength and downstream evolution of the tip leakage vortex is useful in a number of ways. It gives insight into the losses since it appears that a significant fraction of the tip leakage losses occur through the diffusion, or mixing out, of the vortex. Also, it gives information about the cross flows that will be experienced at the inlet to a downstream blade row, and the influence of the axial blade spacing on the magnitude of these crossflows. The data are of course also useful for verifying the predictions of the modern, three-dimensional viscous flow calculation methods that are now being applied to blade passage flows with tip leakage (e.g., Hah, 1986; Dawes, 1987).

The formation of the tip leakage vortex appears to have been documented first in the early 1950s through the measurements and flow visualization of Dean (1954) and Rains (1954). Subsequently, Lakshminarayana and Horlock (1962, 1965) made extensive measurements of the leakage flow for an isolated compressor blade and a compressor cascade. Their studies revealed the structure of the vortex as it appears close to the trailing edge but they did not follow its development downstream. Later studies of the mean velocity and turbulence fields behind a compressor rotor (e.g., Davino and Lakshminarayana, 1982; Pandya and Lakshminarayana, 1983a, 1983b) provide further information, although the vorticity again was not determined directly. Recently, Inoue and his co-workers have presented very detailed measurements of the flow field behind an axial compressor rotor (Inoue and Kuroumaru, 1984, 1989; Inoue et al., 1986). They did obtain the components of the vorticity vector and present the decay characteristics to a distance of 1.25 chord lengths downstream of the trailing edge. As evident, most previous studies of the tip leakage vortex have been conducted in compressor cascades and rotors.

It has been argued that not all the bound circulation in the blade is shed downstream in the tip leakage vortex, unlike the case of a wing tip vortex. Instead, part of the vorticity is believed to jump the gap between the blade tip and the endwall in the form of a vortex sheet. This modified lifting-line model appears to have been suggested first by Lakshminarayana and Horlock (1962) and it subsequently formed the basis for Lakshminarayana's (1970) analysis of the tip vortex behavior. The model is also used by Inoue and his co-workers to interpret their measurements. The modified lifting-line model implies that the fluid in the annulus between the tip and the endwall will effectively experience a lift force directly related to the circulation in the vortex sheet that crosses the gap. Values of this "retained lift" were obtained by Lakshminarayana and Horlock (1962, 1965) for an isolated compressor blade and compressor blades in cascade from pressures measured at the tip of the blade. Later, Lewis and Yeung (1977) measured the

Contributed by the International Gas Turbine Institute and presented at the 34th International Gas Turbine and Aeroengine Congress and Exhibition, Toronto, Ontario, Canada, June 4–8, 1989. Manuscript received at ASME Headquarters January 13, 1989. Paper No. 89-GT-55.

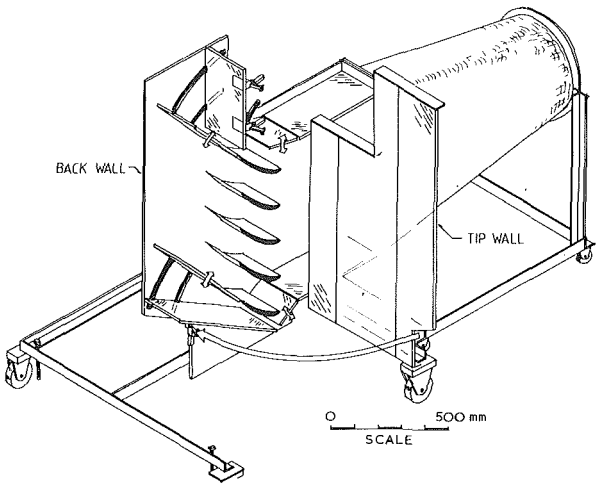

Fig. 1 Cascade test section

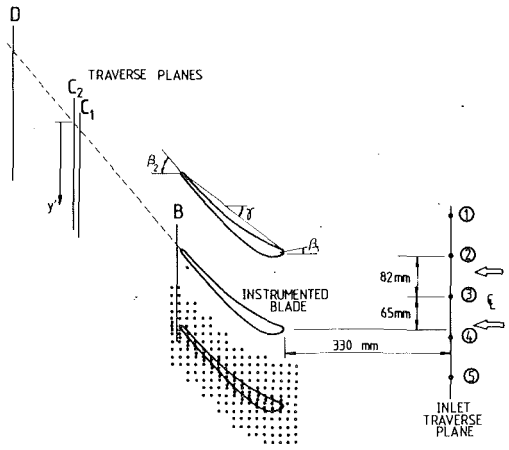

Chord Length, c	:	250 mm
Blade Thickness, t_{MAX}	:	24.6 mm
Blade Span, h	:	203 mm
Blade Spacing, S	:	150 mm
Aspect Ratio, h/c	:	0.812
Solidity, c/S	:	1.667
Stagger Angle, γ	:	37.2 ± 0.2 deg.
Blade Inlet Angle, $ß_1$	:	11.1 ± 0.2 deg.
Blade Outlet Angle, $ß_2$	:	49.6 ± 0.2 deg.

Fig. 2 Summary of cascade geometry

static pressure on the endwall above an isolated compressor blade using an array of taps, which followed the blade contour. Based on these data, correlations for the retained lift as a function of clearance were proposed (see Fig. 8). However, the correlations probably need further refinement to account for the effects of rotation.

If a broadly applicable correlation can be developed, the concept of retained lift appears useful since it provides a basis for estimating the circulation in the tip leakage flow from the blade lift, a known quantity. The data presented here are therefore examined and discussed partly in the context of this conceptual model.

As indicated, most previous studies of the downstream behavior of the tip vortex have considered compressor flows. The present study broadens the scope of the available data by examining the behavior of the tip leakage vortex in the higher-turning flow of an axial turbine. The experiment is of course still rather idealized. The effect of rotation, which acts in opposite directions on the gap flow in compressors and turbines, is not taken into account. Also, the flow was essentially incompressible and had a low level of free-stream turbulence.

Nomenclature

s_s = Squire's eddy viscosity constant (equation (8))
A = area
c = blade chord length
c_x = blade axial chord length
C_P = $(P-P_{CL})/(1/2\rho V_{CL}^2)$ = static pressure coefficient
C_{P_o} = $(P_o-P_{o_{CL}})/(1/2\rho V_{CL}^2)$ = total pressure loss coefficient
H = δ^*/θ = boundary layer shape factor
K = $1-\Gamma_{TV}/\Gamma_B$ = retained lift coefficient
L = lift force
P = static pressure
P_o = total pressure
r = radial coordinate
Re = $\rho V_{CL} c/\mu$ = Reynolds number based on blade chord
Re_d = $\rho V d/\mu$ = Reynolds number based on probe diameter
s = streamwise coordinate (Fig. 4)
S = blade spacing
t = time
$t_{\max}$ = blade maximum thickness
u, v, w = components of velocity in the x, y, and z directions
u' = root-mean-square velocity fluctuation in the x direction
v_θ = tangential component of velocity
V = resultant velocity
V_m = mean velocity through the cascade
x, y, z = coordinate in axial, tangential, and spanwise directions
x' = coordinate in chordwise direction
y' = local pitchwise coordinate (Fig. 2)
α = flow angle, measured from the axial direction
β = blade metal angle (Fig. 2)
γ = blade stagger angle (Fig. 2)
Γ_B = bound circulation
Γ_{TV} = circulation of the tip leakage vortex
Γ' = nondimensional circulation = (Γ/cV_1)
δ = boundary layer thickness
δ^* = $\int_0^\delta \left(1-\frac{V}{V_e}\right) dz$ = boundary layer displacement thickness
θ^* = $\int_0^\delta \left(1-\frac{V}{V_e}\right)\frac{V}{V_e} dz$ = boundary layer momentum thickness
Λ = Owen's eddy viscosity constant (equation (9))
μ = viscosity
ν = kinematic viscosity = μ/ρ
ν_e = eddy viscosity
ρ = density
σ = blade row solidity = c/S
τ = tip gap
ω = vorticity
ω' = nondimensional vorticity = $\omega c/V_1$

Subscripts

cl = vortex centerline value
CL = undisturbed centerline value
e = boundary-layer edge value
min, max = minimum and maximum values
x, y, z, s = component in x, y, z, and streamwise direction
1, 2 = cascade inlet, outlet

Table 1 Test matrix and inlet flow conditions

			CLEARANCE (τ/c)			
			0.015	0.020	0.028	0.055
TRAVERSE PLANE		x/c_x				
	B	1.03	X	X	X	X
	C1	1.96	X	X	X	X
	C2	2.01	X	X	X	X
	D	2.56				X
τ (mm)			3.8	5.1	7.1	13.7
δ^*/τ			1.36	0.96	1.09	0.23
θ/τ			1.01	0.71	0.72	0.15
H			1.34	1.34	1.52	1.51

Nevertheless, we feel that the results give useful qualitative insights into some of the important aspects of the tip vortex behavior in actual turbines.

Experimental Apparatus and Procedures

Test Section and Test Cascade. The test section, which is shown schematically in Fig. 1, has been described in detail in the earlier papers. The clearance is varied by using shims between the tip wall and the side walls. The side flaps and tailboards are used to establish periodic flow within the cascade. The flow periodicity is determined from static pressure measurements on the endwall inside each blade passage and from measurements of the velocity vector at midspan downstream of the cascade. The periodicity is checked and adjusted for each clearance.

Figure 2 summarizes the geometry of the test cascade and shows the location of the downstream traverse planes. Measurements have been made at three main planes from the trailing edge to 1.56 axial chord lengths downstream. The probe can be moved easily to essentially any position in the x direction. This feature was used to obtain velocity measurements at two closely - spaced planes at main plane C. These data allow all the gradients in velocity, and hence the complete vorticity vector, to be determined. The combinations of clearance and downstream traverse planes examined are summarized in Table 1. As indicated, four clearances ranging from 1.5 to 5.5 percent of the blade chord were considered. The clearance heights were set to an estimated accuracy of ±0.2 mm using feeler gages.

In addition to the downstream flow field measurements, static pressures were measured on the blade surface and on the tip endwall. The middle blade in the cascade is instrumented with 14 rows of static taps extending from midspan to very close to the tip. Each row consists of 73 taps and thus gives a very detailed picture of the local loading on the blade. As indicated in Fig. 2, the tip endwall is instrumented with a rectangular array of taps spanning one blade pitch.

Instrumentation. All pressures were measured using capacitive-type pressure transducers. The pressure signals were converted to digital form, with 12-bit resolution, using a Sciemetric Instruments data acquisition system controlled by an IBM PC-compatible microcomputer.

For the downstream traverses reported here, the flow field was measured using a conical, seven-hole pressure probe. The probe is mounted on a stem that projects through slots in the back wall of the test section. The stem attaches to a motorized traverse gear, which allows the probe to be positioned at any point in a plane parallel to the trailing edges. It is estimated that the position of the probe is known to within ±0.25 mm in all three coordinate directions. The probe is aligned with the mean flow direction and then used in the non-nulling mode. This can lead to high angles of misalignment with the flow as the probe is traversed through the tip leakage vortex. The seven-hole probe was chosen since Everett et al. (1983) had indicated that this geometry is particularly suitable for high levels of flow misalignment, and our experience with the probe has been good. The probe is manufactured from seven tubes of equal diameter, which form a natural bundle, enclosed in a thin-walled outer tube. The interstices between the tubes are filled with solder and the measuring face is then machined to a conical or other suitable shape. Our probe has an outer diameter of 2.4 mm and the total cone angle of the face is 60 deg. A small radius was applied to the mouth of the center port to eliminate the sharp-edged shoulder at the tip of the probe.

As indicated, the probe was often severely misaligned with the flow. It was therefore calibrated, in steps of 5 deg, through all combinations of pitch and yaw out to 50 deg of misalignment for both angles. For measurements in flows where the resultant misalignment exceeds about 20 deg, only data from the four ports on the windward side of the probe are used to obtain flow information. This avoids using pressures measured in the separated region on the leeward side where fluctuations are larger and the port pressure tends to be less sensitive to changes in the flow direction. Based on the scatter observed in the calibration measurements and other repeatability checks that were made, we estimate that in a reasonably uniform flow the angles inferred from the probe measurements would, conservatively, be accurate to within ±2 deg and the total and dynamic pressures to within ±5 percent of the local dynamic pressure. In the cascade flow, the effect of strong shear and varying Reynolds number introduces some additional uncertainty.

There appears to be little information available on the effects of shear on five- and seven-hole pressure probes. In any event, it would be difficult to establish a laboratory flow with controlled levels of shear of the order of magnitude we encounter in the tip leakage flow. Thus, we have no basis for applying corrections to our measurements or estimating the magnitude of the errors that may have been introduced. From internal checks on the data, we believe that our measurements have not been seriously compromised. For example, the values of circulation obtained for a given clearance at successive downstream planes are in good agreement, although as discussed later the slightly higher circulation detected at the trailing edge plane may be partly explained by measurement errors due to shear.

It is a common experience that the aerodynamic characteristics of conical five-hole pressure probes are quite sensitive to changes in Reynolds number. The seven-hole probe was calibrated at a probe Reynolds number Re_d of about 4100, corresponding roughly to the average value encountered in the downstream flow. In addition, representative calibration measurements were made for the complete range of Re_d seen in the cascade. When the calibration curves were applied to the data, flow angles were found to vary with Re_d by at most ±1.5 deg and the inferred dynamic pressure by at most ±5.0 percent; for most combinations of pitch and yaw the errors were much smaller. Thus, our probe appears to be relatively insensitive to Re_d changes over the range we experience. This may be partly due to the rounding of the mouth of the center port.

Determination of Vorticity. The components of the vorticity vector were obtained in Cartesian coordinates using a coordinate system aligned as shown in Fig. 2

$$\omega_x = \frac{\partial w}{\partial y} - \frac{\partial v}{\partial z}$$

$$\omega_y = \frac{\partial u}{\partial z} - \frac{\partial w}{\partial x} \tag{1}$$

$$\omega_z = \frac{\partial v}{\partial x} - \frac{\partial u}{\partial y}$$

Thus the velocity gradients needed to determine ω_x can be obtained from flow field measurements made in a single plane parallel to the y–z plane. With some simplifying assumptions, approximate values of the other two components can also be obtained from such measurements. Assuming steady incompressible flow, neglecting the viscous terms, and substituting from equation (1), the momentum equation for the y direction can be rewritten as

$$\frac{1}{\rho}\frac{\partial P_o}{\partial y} + u\omega_z - w\omega_x = 0 \tag{2}$$

Solving for ω_z,

$$\omega_z = \frac{1}{u}\left[w\omega_x - \frac{1}{\rho}\frac{\partial P_o}{\partial y} \right] \tag{3}$$

and all quantities on the right-hand side of equation (3) are available from the measurements in the y–z plane. Similarly, from the momentum equation in the z-direction

$$\omega_y = \frac{1}{u}\left[\frac{1}{\rho}\frac{\partial P_o}{\partial z} + v\omega_x \right] \tag{4}$$

As a check on the accuracy of the values given by equations (3) and (4), flow field measurements were made, for each clearance, at two closely spaced planes about one axial chord length downstream of the trailing edge. This allowed all the expressions in equation (1) to be evaluated directly. The agreement between the vorticity components obtained directly and the approximate values was excellent. The largest differences occurred near the edge of the vortex core where the velocity gradient is changing most rapidly and the viscous effects are therefore most important. However, even here the two values differed by less than 10 percent of the centerline vorticity, which is comparable with the uncertainty in either value. We intend to use only the approximate method in the future.

The flow field measurements downstream of the trailing edge were made on grids of evenly spaced points extending one passage width and half the blade span. At the trailing edge, plane B, a grid space of 5 mm was used while at planes C1, C2, and D a spacing of 10 mm was found to be sufficient. All gradients in the y and z directions were obtained by central

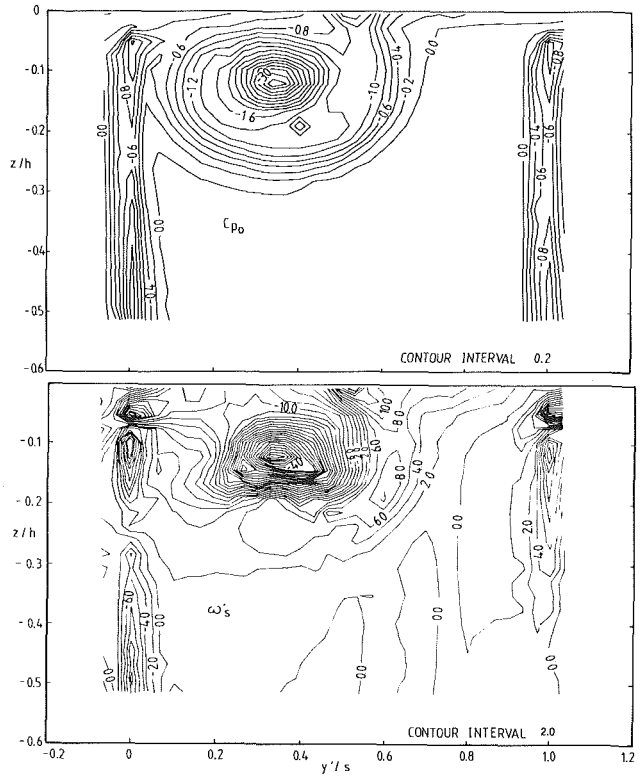

Fig. 3(*a*) Total pressure and streamwise vorticity distributions (r/c = 0.555, plane B)

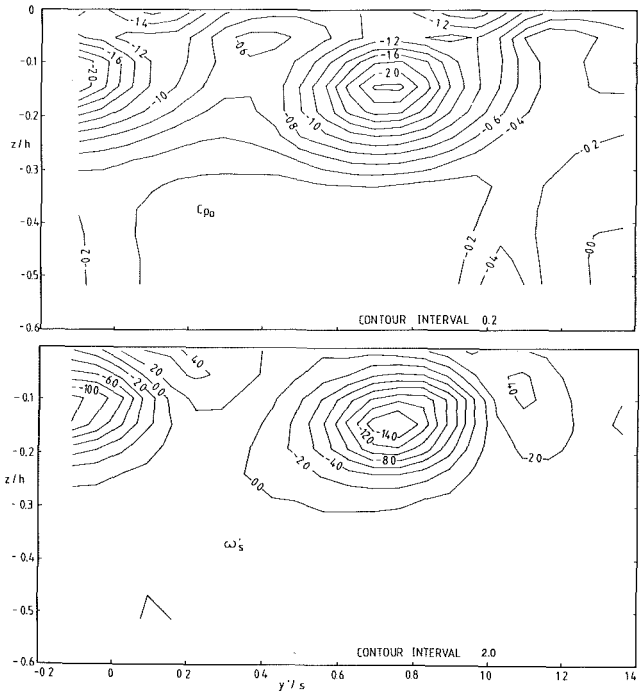

Fig. 3(*b*) Total pressure and streamwise vorticity distributions (r/c = 0.055 plane C2)

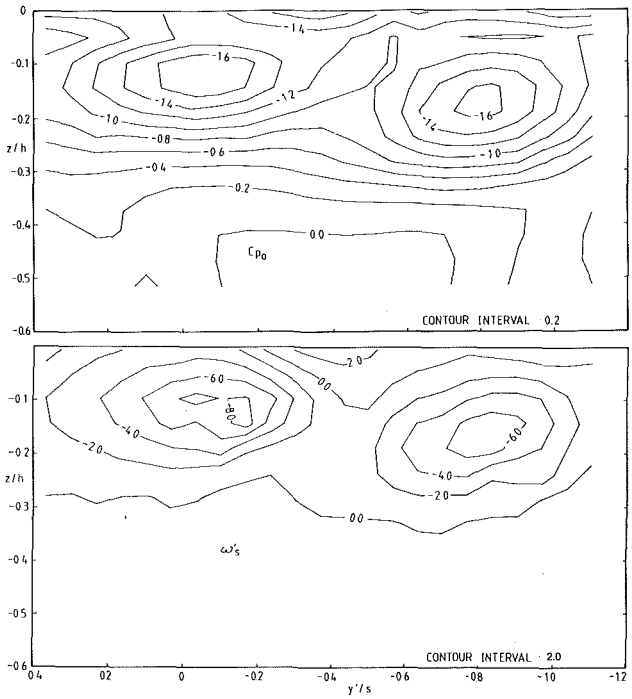

Fig. 3(*c*) Total pressure and streamwise vorticity distributions (r/c = 0.055, plane D)

differences while the x-wise gradients determined from the measurements in planes C1 and C2 were calculated by simple differences. No smoothing was applied to the flow field data beyond the time averaging performed during the data acquisition.

Experimental Results

Operating Conditions. As in the earlier studies, all measurements were made for a Reynolds number of $4.3 \times 10^5 \pm 2$ percent, where the Reynolds number is based on the blade chord and undisturbed upstream velocity. The corresponding inlet velocity was about 30 m/s so that conditions were essentially incompressible. The free-stream turbulence, u'/V_1, was about 1.5 percent at the inlet to the cascade for all cases. The integral parameters for the endwall boundary layer on the tip wall are given in Table 1. As the tip wall is moved outward to create the clearance, a ramp is inserted to provide the transition between the fixed upstream wall and the moveable section. This results in some variation in the boundary layer thickness with clearance. A similar trend was observed in the measurements reported by Yaras et al. (1989). As seen from the table, the displacement thickness of the tip wall boundary layer was roughly comparable with the smallest clearance.

The behavior of the tip leakage vortex was found to be very similar for the four clearances. Therefore, detailed results will be presented only for 5.5 percent clearance, the case for which the most extensive measurements are available.

General Downstream Development of the Tip-Leakage Vortex. The general downstream development of the tip leakage vortex is shown in Figs. 3(*a*, *b*, *c*), which present contour plots of streamwise vorticity and total pressure loss at planes B, C2, and D for 5.5 percent clearance. The total pressure plots are included to indicate the position of the tip leakage vortex relative to the blade wakes; since the blades are two dimensional, comparatively little vorticity is shed in the wake and the wake is not very evident on the vorticity plots, except right at the trailing edge. The same contour interval was used on successive contour plots, to give a visual impression of the rapid diffusion of the tip vortex.

Two vortices are evident from the plots for plane B. The tip vortex is clearly the dominant structure. However, at midpassage near the endwall there is also a small region of vorticity of the opposite sign, which is probably the passage vortex. Sjolander and Amrud (1987) had found evidence from the blade pressure distributions of the formation of multiple tip leakage vortices at larger clearances. Such multiple vortices are not apparent from the present vorticity plots, suggesting that the vortices quickly interact to form a concentric resultant vortex, as might be expected from their proximity and the fact that their rotation is in the same direction.

The roll-up of the tip vortex is clearly largely complete even at the trailing edge. Downstream of the trailing edge the vortex appears to migrate toward the pressure side of the passage flow. Inoue and his co-workers noted similar behavior for their compressor rotor flow. As seen from Fig. 3(*b*), at plane C2 the centerline of the vortex has moved three-quarters of the way across the passage flow and has begun to distort the next wake. The considerably smaller tip vortex for 2.0 percent clearance had moved to the middle of the pasage flow by the time it reached plane C. For the largest clearance, it is clear that adjacent tip vortices are beginning to interact significantly by plane D, 1.56 axial chord lengths from the trailing edge.

As indicated in Fig. 2, the traverse planes intersect the tip vortices at an oblique angle. When this angle was taken into account, it was in fact found that the tip vortex is quite close to being axisymmetric, even at the trailing edge. Therefore, the behavior of other flow quantities will be presented only for a representative line passing through the center of the vortex. The line parallel to the z axis was chosen since this line lies in the plane normal to the centerline of the vortex.

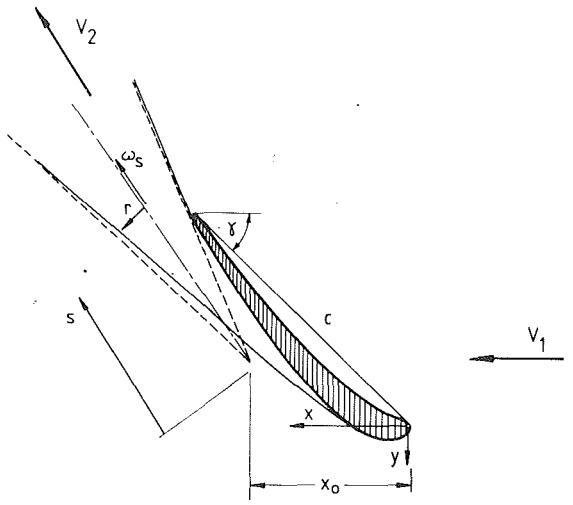

Fig. 4 Tip leakage vortex as a diffusing line vortex

Simple Model for the Tip Leakage Vortex. The rapid roll-up and near axisymmetry of the tip vortex suggested that it might be possible to model the vortex approximately with a fairly simple model. Such a model would, for example, allow the designer to estimate at the preliminary design stage the cross flows in the tip leakage vortex and their variation with downstream distance. Also, since the diffusion of the vortex is thought to contribute significantly to the total tip leakage loss, a simple vortex model might form a component of a semi-empirical method for estimating the losses.

The simplest starting point is the diffusion of a simple line vortex. For laminar flow and with the diffusion process beginning at time $t=0$, the solution for the tangential velocity in the flow at any time t is (Lamb, 1932)

$$v_\theta = \frac{\Gamma}{2\pi r}\left[1 - e^{-\frac{r^2}{4\nu t}}\right] \tag{5}$$

and the radial distribution of the vorticity is given by

$$\omega_s = \frac{\Gamma}{4\pi\nu t} e^{-\frac{r^2}{4\nu t}} \tag{6}$$

Thus, the vorticity on the centerline ($r=0$) is

$$\omega_{s_{cl}} = \frac{\Gamma}{4\pi\nu t} \tag{7}$$

This exact solution has been adapted, with some success, by Squire (1965) to prove a simple estimate for the diffusion with downstream distance of a turbulent wing-tip vortex. The vortex is assumed to start at some effective origin and then be convected downstream at the velocity of the surrounding stream V. Then at any distance s from the origin, the local section of the vortex will have been diffusing lateral for a time $t=(s/V)$. For the turbulent vortex, it is assumed that the turbulent momentum transport can be accounted for by a constant eddy viscosity ν_e. Neglecting longitudinal mixing along the vortex, the solution for the turbulent vortex is then assumed to be given by equations (4) and (5), with the viscosity replaced by $\nu_e + \nu$ and time replaced by (s/V). Squire suggested that the eddy viscosity should be a simple function of the circulation in the vortex

$$\frac{\nu_e}{\nu} = a_s\left(\frac{\Gamma}{\nu}\right) \tag{8}$$

with a_s a constant. Γ/ν can be interpreted as the vortex Rey-

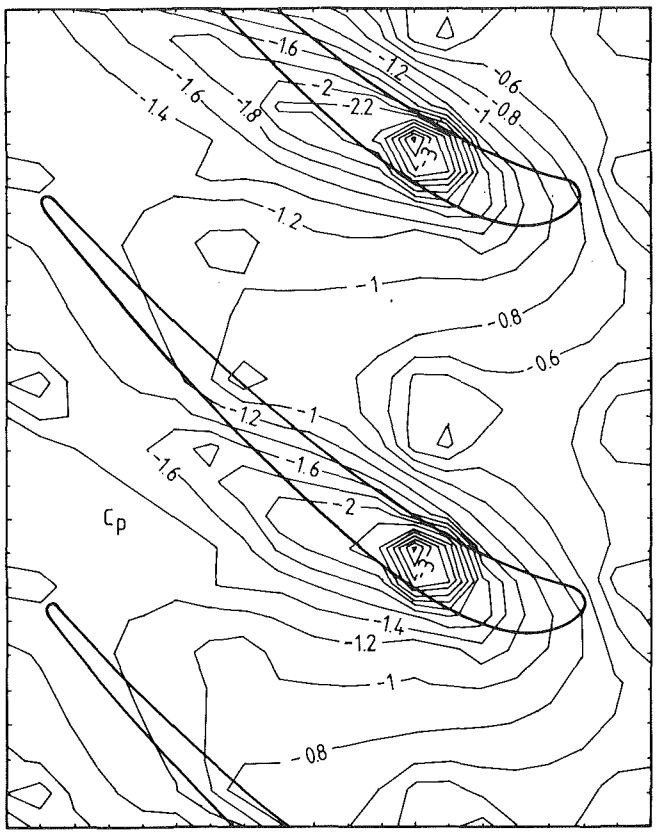

Fig. 5 Static pressure distribution on the tip endwall ($\tau/c = 0.055$)

nolds number. Subsequently, Owen (1970) developed a somewhat similar model but argued that the eddy viscosity should depend on the circulation according to

$$\frac{\nu_e}{\nu} = \Lambda^2 \left[\frac{\Gamma}{\nu}\right]^{1/2} \tag{9}$$

with Λ a constant. Data from a variety of laboratory and flight experiments show that Λ varies from about 0.7 to 1.2, whereas a_s was found to vary over a range of nearly 10 (El-Ramly, 1972).

The simple line vortex model was applied to the tip leakage vortex using the nomenclature defined in Fig. 4. The vortex is assumed to be convected downstream from its effective origin at $x = x_0$ at the downstream mean velocity V_2. It is also assumed that the centerline of the vortex is aligned with V_2, and that the axial velocity is constant so that V_2 can be replaced by $V_1/\cos\alpha_2$. Then equation (7) can be written in terms of the geometric and flow parameters of the cascade flow as follows:

$$\omega_s' = \frac{\Gamma'}{4\pi} \frac{\mathrm{Re}_c}{\left[\frac{\nu_e}{\nu} + 1\right] \cos\gamma \left[\frac{x}{c_x} - \frac{x_o}{c_x}\right]} \tag{10}$$

Using equation (10), experimental values of the eddy viscosity and the effective origin can be determined from the measured streamwise vorticity, on the centerline of the vortex, at two x-wise locations.

To apply the model, the designer would need to know the circulation of the tip leakage vortex, the eddy viscosity, and the axial position of the effective origin of the leakage vortex. Then from equation (5) the tangential velocity distribution through the vortex could be determined for any downstream position. The diffusion of the vortex as well as its diameter is completely defined for any position. The circulation for the tip vortex is examined next and correlations for the eddy viscosity and effective origin obtained for our cases are presented in later sections.

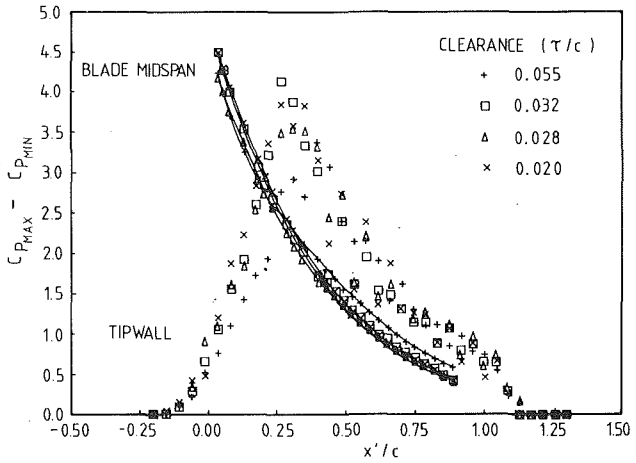

Fig. 6 Comparison between blade midspan pressures and driving pressure differences at endwall

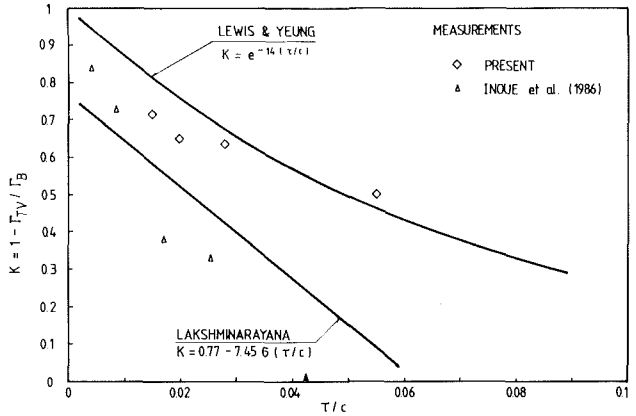

Fig. 7 Variation of retained lift coefficient with clearance

Retained Lift. As noted in the Introduction, Lakshminarayana and Horlock (1962) and Lewis and Yeung (1977) had suggested that only part of the blade's bound vorticity would be shed downstream in the tip leakage vortex. They inferred this from the effective blade loading at the endwall as obtained from static pressure measurements on the wall or from extrapolated blade surface pressures. The only direct measurements of the circulation in the tip leakage vortex, of which we are aware, are the data of Inoue et al. (1986) for a compressor rotor. They likewise found that for smaller clearances a fraction of the blade lift was "retained" at the endwall.

Indirect support for the concept of retained lift was presented by Yaras et al. (1989). Endwall static pressure measurements for clearances up to 3.2 percent showed that fluid near the endwall would experience a cross-channel pressure difference very similar to the undisturbed blade-to-blade pressure difference down inside the blade passage. These data are repeated in Fig. 6 along with the new data for 5.5 percent clearance. The values of driving pressure difference in Fig. 6 were obtained from contour plots such as Fig. 5. The pressure coefficient at the blade suction peak is about -3.5. From Fig. 5 it is seen that the minimum pressure coefficient on the endwall is about -3.0 for our largest clearance. There is thus beginning to be a noticeable attenuation of the driving pressure near the endwall. This is further evident from Fig. 6, which shows pressure differences on the endwall along lines that are approximately normal to the blade chord line and compares them with the blade midspan values. Although the pressure differences are reduced, it is nevertheless evident that fluid near the endwall will experience a significant cross-channel force, effectively a lift force, even for the 5.5 percent clearance.

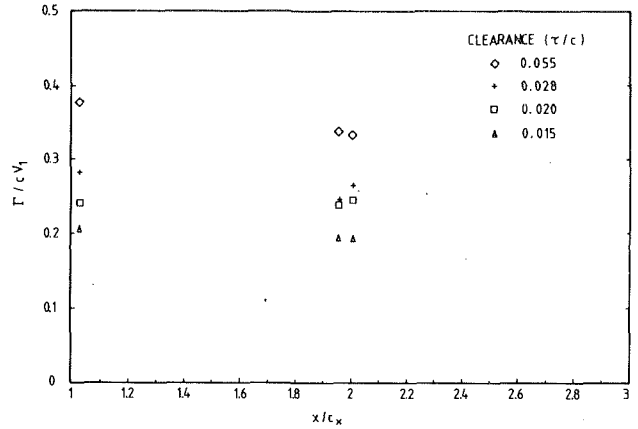

Fig. 8 Variation of tip vortex circulation with clearance and downstream distance

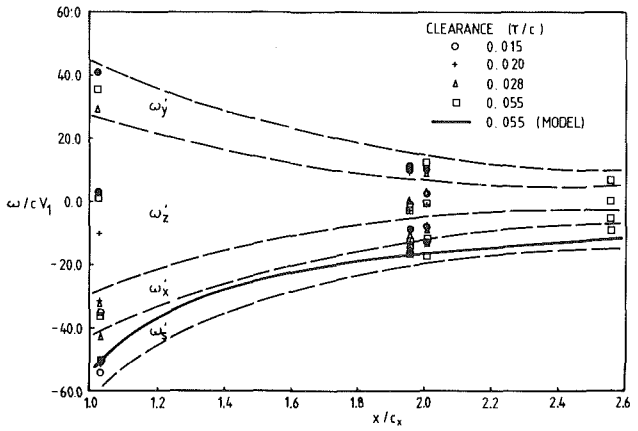

Fig. 9 Variation of components of vorticity on vortex centerline

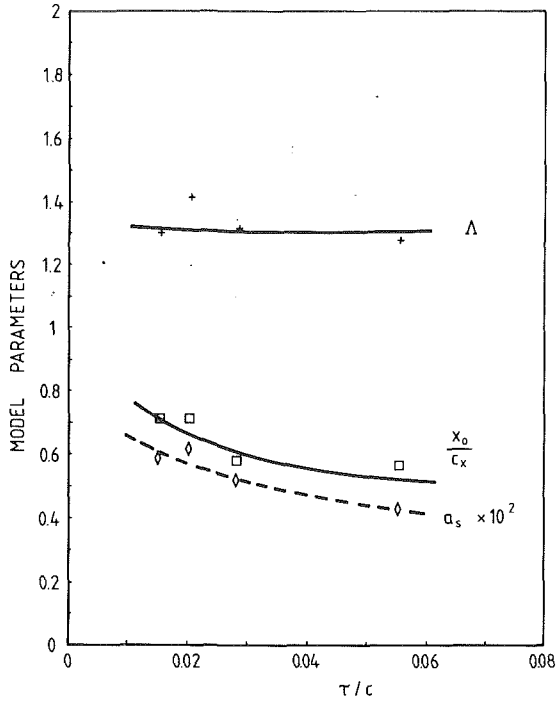

Fig. 10 Variation with clearance of parameters for line vortex model

To quantify the retained lift effect, values of the shed and the bound circulation were obtained for each of the clearances. The circulation in the tip leakage vortex, Γ_{TV}, was obtained, from Stokes' theorem, by integrating over the area the component of the vorticity normal to the traverse planes. The shed circulation was calculated for all traverse lanes and the values for a given clearance were in good agreement, as shown in Fig. 8. For present purposes, the average of the values obtained at planes C1 and C2 was used. The bound circulation was calculated from $\Gamma_B = L/\rho V_m$, where L is the lift obtained from the midspan blade pressures and V_m is the mean velocity through the blade row.

Figure 7 shows the measured variation of the retained lift coefficient, $K = 1 - \Gamma_{TV}/\Gamma_B$, with clearance for our experiment as well as for the compressor rotor experiment of Inoue et al. (1986). The correlations for retained lift proposed by Lakshminarayana and Horlock (1962) and Lewis and Yeung (1977) are also shown. As seen, our results are in reasonably good agreement with the correlation of Lewis and Yeung. However, it should be recalled that their correlation is based on lift values inferred from a ring of static taps, which followed the blade profile on the endwall. As evident from Fig. 5, such measurements for our flow would have led to much lower pressure differences than are in fact available to drive fluid either through the tip gap or across the passage. The agreement with Lewis and Yeung may therefore be somewhat fortuitous. In any event, it is clear that even for our largest clearance less than half the bound vorticity was shed downstream in the tip leakage vortex. For a given clearance, a much larger fraction of the bound vorticity was shed in the experiment of Inoue et al. This suggests that in a compressor the rotation increases the vortex shedding as well as increasing the mass flow rate through the gap; the two effects are probably connected. It remains to be determined whether the reduced leakage mass flow rate that occurs in a turbine rotor also results in a weaker tip leakage vortex.

Downstream Variation of Circulation and Vorticity. Figure 8 shows the circulation for the tip leakage vortex as determined at planes B, C1, and C2 for each of the clearances. As seen, the values for a given clearance are in good agreement except that the value at the trailing edge plane tends to be a little higher. Physically, the circulation in the vortex could only be changing as a result of vorticity production or destruction at the endwall. Such production can in turn only be occurring if there is a pressure gradient at the wall. From Fig. 5 it appears that endwall pressure gradients are very weak downstream of the trailing edge and the vorticity production should therefore by quite small. It seems likely therefore that the higher circulation obtained at plane B is mainly due to probe measurement errors arising from the effects of shear, which are strongest at this plane.

Figure 9 shows the variation of the three Cartesian components of vorticity as well as the streamwise component for the centerline of the vortex. To accommodate the growth of the vortex, its centerline should be inclined slightly relative to the endwall. Thus, one would expect a small negative component of vorticity in the z direction. As seen from the figure, the z component did tend to be negative. At main plane C, the values of ω_z were scattered over a range of about ± 3 nondimensional vorticity units or about ± 20 percent of the centerline value of the streamwise vorticity. This probably gives a reasonable indication of the uncertainty present in all of the quoted vorticity values. Figure 9 shows that the tip leakage vorticity diffuses quite rapidly: the components on the centerline decline to about one quarter of their trailing edge value over the first axial chord length.

Figure 9 also shows the variation in the streamwise vorticity component for 5.5 percent clearance as calculated from the line vortex model. As discussed earlier, the model parameters are obtained from the measurements at two axial stations. The data from planes B and C were used here and thus only the

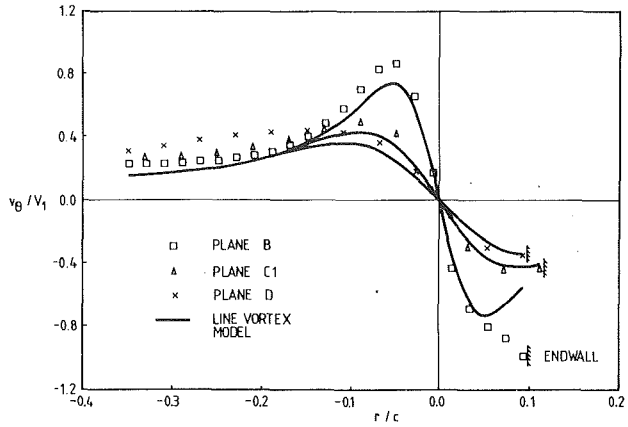

Fig. 11 Spanwise distribution of tangential velocity through center of ($\tau/c = 0.055$)

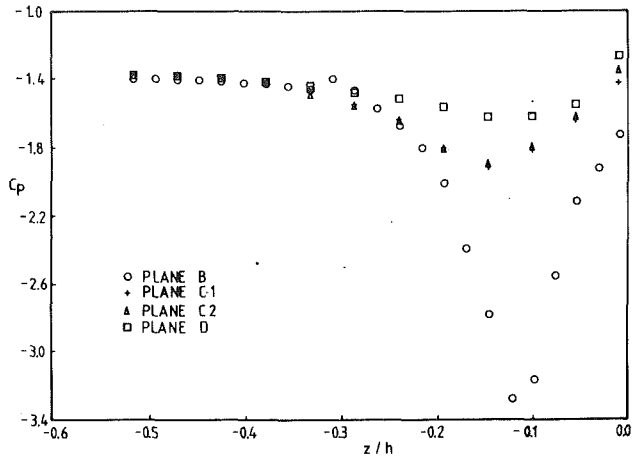

Fig. 12 Spanwise static pressure distribution through center of vortex ($\tau/c = 0.055$)

comparison at plane D tests the model's predictive capability. As seen, the predicted streamwise component agrees reasonably well with the measured value, bearing mind the uncertainty in the measurement. The ability of the model to predict the tangential velocity distribution through the vortex and the effective diameter of the vortex is examined in the next section.

To allow the vortex model to be applied to other blade rows, the correlations must be developed for the eddy viscosity and effective origin of the vortex. Figure 10 summarizes the values of the parameters obtained here. As a matter of interest, the eddy viscosity was found to be about 500 to 650 times the molecular viscosity. As seen, Squire's eddy viscosity constant, a_s, decreases noticeably with increasing clearance. On the other hand, Owen's constant, Λ, seems to be scattered around a mean value of about 1.32. This is slightly above but close to the upper end of the range of Λ observed in wing tip vortices. The results for the tip leakage vortex thus appear to support Owen's function (equation (9)) as a basis for obtaining the eddy viscosity, in agreement with the results for wing tip vortices. The effective origin of the tip vortex is seen to move forward with increasing clearance from about 72 percent of the chord length to about 55 percent for the range of clearances considered.

The correlation is of course incomplete in the sense that the important effects of rotation are not explicitly identified. The key to this may be the effect of the rotation on the shed circulation. The plot for the retained lift, Fig. 7, gives an indication of the effect of rotation on the shed vorticity and thus on the tip-vortex Reynolds number, Γ_{TV}/ν. From equation (9), the eddy viscosity is simply a function of Γ_{TV}/ν and it would therefore implicitly vary with rotation. Likewise, it might be more appropriate to correlate the position of the effective origin with the vortex Reynolds number, rather than with the clearance as was done here. Additional data, for cases with actual or simulated rotation, are needed to confirm this.

Variation of Flow Parameters Through the Vortex. Finally, the variation through the vortex of a few selected parameters is presented.

Figure 11 shows the spanwise variation of the tangential component of velocity for 5.5 percent clearance. Also shown are the distributions calculated from the line vortex model. The results are presented with the vortex centers coincident; the relative position of the endwall is indicated. As seen, the measurements and the simple line vortex model are in surprisingly good agreement. Both indicate very strong crossflows through the vortex at the trailing edge, plane B; the measured direction of the velocity vector varied through a range of about 75 deg, and the peak-to-peak variation through the model was only slightly smaller. Both show a core of nearly solid-body

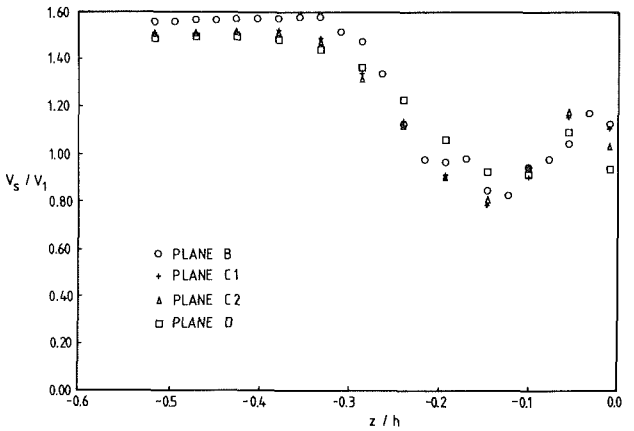

Fig. 13 Spanwise distribution of axial velocity through center of vortex ($\tau/c = 0.055$)

rotation and the core diameters, as indicated by the peaks in the crossflow velocity distributions, are also very similar. Both likewise show a similar decay in the crossflow velocities with downstream distance. The differences in the far field are explained by the fact that the velocities induced by the other tip vorticies in the cascade are neglected in the model calculations. Their effect could easily be included.

The model assumes that all of the fluid in the vortex is convected downstream at the mean velocity of the surrounding stream. However, the diffusion of the actual vortex implies that there will be a rise in the static pressure along the centerline. Figure 12 shows the static pressure distributions through the vortex as obtained from the seven-hole probe measurements. As shown, a very substantial rise does indeed occur. The static pressure rise also leads to relative flow up the center of the vortex. Figure 13 shows that the axial velocity is in fact reduced by almost half at the center of the vortex. The presence of this relative axial flow, which is neglected in the line vortex models, makes it even more remarkable that the simple model works as well as it does.

Conclusions

Detailed data have been obtained for the development of the tip leakage flow downstream of a turbine cascade. It was found that the circulation in the tip leakage vortex was substantially less than the bound circulation for the blade. Even at the largest clearance of 5.5 percent of the blade chord, the shed circulation was less than half the bound circulation. This

supports Lakshminarayana and Horlock's modified lifting-line model, which indicates that for a turbomachinery blade with clearance, part of the bound circulation can jump the tip gas in the form of a vortex sheet and only the balance is shed downstream. The tip vortex itself appeared to have essentially completed its roll-up by the time it reaches the trailing edge plane, and even here the structure was nearly axisymmetric. These characteristics make the tip leakage vortex amenable to a simple approximate analysis.

Although it only contains a fraction of the available circulation, the tip leakage vortex is nevertheless a powerful structure. At the trailing edge plane, it was found that the direction of the velocity vector varied by about 75 deg through the vortex. On the other hand, the vortex diffuses rapidly with distance. Over the first axial chord length, the components of vorticity on the centerline were found to decrease by a factor of about four.

The present data are extensive and detailed and can thus be used as a test case for modern turbomachinery viscous flow prediction codes. In addition, it was shown that a very simple model based on the diffusion of a line vortex can be used to obtain reasonable estimates of the lateral diffusion of the line vortex, the crossflow velocities through it, and the growth of its diameter with downstream distance. Correlations are presented for the two parameters needed to calculate the vortex development, namely the location of its effective origin and the eddy viscosity in the vortex. Further data on the effects of rotation are needed to verify the general validity of the correlations.

Acknowledgments

Financial support for this study provided by the Natural Sciences and Engineering Research Council of Canada under Grant No. A1671 and by Pratt & Whitney Canada Inc. is gratefully acknowledged.

References

Davino, R. M., and Lakshminarayana, B., 1982, "Characteristics of Mean Velocity in the Tip Region of Turbomachinery Rotor Exit," *AIAA Journal*, Vol. 20, No. 4, pp. 528–535.

Dawes, W. N., 1987, "A Numerical Analysis of the Three-Dimensional Viscous Flow in a Transonic Compressor Rotor and Comparison With Experiment," ASME JOURNAL OF TURBOMACHINERY, Vol. 109, No. 1, pp. 83–90.

Dean, R. C., 1954, "The Influence of Tip Clearance on Boundary-Layer Flow in a Rectilinear Cascade," M.I.T. Gas Turbine Laboratory, Report No. 27-3.

El-Ramly, Z., 1972, "Aircraft Trailing Vortices: A Survey of the Problem," Report No. ME/A 72-1, Carleton University, Ottawa, Canada, Nov.

Everett, K. N., and Gerner, A. A., and Durston, D. A., 1983, "Seven-Hole Cone Probes for High Angle Flow Measurement: Theory and Calibration," *AIAA Journal*, Vol. 21, No. 7, pp. 992–998.

Hah, C., 1986, "A Numerical Modeling of Endwall and Tip Clearance Flow of an Isolated Compressor Rotor," ASME *Journal of Engineering for Gas Turbine and Power*, Vol. 108, No. 1, pp. 15–21.

Inoue, M., and Kuroumaru, M., 1984, "Three-Dimensional Structure and Decay of Vortices Behind an Axial Flow Rotating Blade Row," ASME *Journal of Engineering for Gas Turbines and Power*, Vol. 106, No. 3, pp. 561–569.

Inoue, M., and Kuroumaru, M., 1989, "Structure of Tip Clearance Flow in an Isolated Axial Compressor Rotor," ASME JOURNAL OF TURBOMACHINERY, Vol. 111, pp. 250–256.

Inoue, M., and Kuroumaru, M., and Fukuhara, M., 1986, "Behavior of Tip Leakage Flow Behind an Axial Compressor Rotor," ASME *Journal of Engineering for Gas Turbines and Power*, Vol. 108, No. 1, pp. 7–13.

Lakshminarayana, B., 1970, "Methods of Predicting the Tip Clearance Effects in Axial Flow Turbomachinery," ASME *Journal of Basic Engineering*, Vol. 92, pp. 467–480.

Lakshminarayana, B., 1986, "Tip Clearance Effects in Turbomachines," von Karman Institute/Pennsylvania State University Lecture Course on Tip Clearance Effects in Axial Turbomachines, Apr.

Lakshminarayana, B., and Horlock, J. H., 1962, "Tip Clearance Flow and Losses for an Isolated Compressor Blade," ARC R.&M. 3316.

Lamb, H., 1932, *Hydrodynamics*, 6th ed., Cambridge University Press, London, United Kingdom.

Lewis, R. I., and Yeung, E. H. C., 1977, "Vortex Shedding Mechanisms in Relation to Tip Clearance Flows and Losses in Axial Fans," ARC R.&M. 3829.

Owen, P. R., 1970, "The Decay of a Turbulent Trailing Vortex," *Aeronautical Quarterly*, Vol. XX, pp. 69–78.

Pandya, A., and Lakshminarayana, B., 1983a, "Investigation of the Tip Clearance Flow Inside and at the Exit of a Compressor Rotor Passage—Part I: Mean Velocity Field," ASME *Journal of Engineering for Power*, Vol. 105, No. 1, pp. 1–12.

Pandya, A., and Lakshminarayana, B., 1983b, "Investigation of the Tip Clearance Flow Inside and at the Exit of a Compressor Rotor Passage—Part II: Turbulence Properties," ASME *Journal of Engineering for Power*, Vol. 105, No. 1, pp. 13–17.

Rains, D. A., 1954, "Tip Clearance Flows in Axial Flow Compressors and Pumps," Rept. No. 5, Hydrodynamics and Mechanical Engineering Laboratories, California Institute of Technology.

Sjolander, A., and Amrud, K. K., 1987, "Effects of Tip Clearance on Blade Loading in a Planar Cascade of Turbine Blades," ASME JOURNAL OF TURBOMACHINERY, Vol. 109, pp. 237–244.

Squire, H. B., 1965, "The Growth of a Vortex in Turbulent Flow," *Aeronautical Quarterly*, Vol. XX, pp. 302–306.

Yaras, M., and Sjolander, S. A., 1988, "Measurements of the Tip Clearance Flow in a Rectangular Cascade of Turbine Blades: A Test Case for Computational Methods," Tech. Rept. M&AE 88-1, Carleton University, Ottawa, Canada, Apr.

Yaras, M., Zhu, Y,. and Sjolander, S. A., 1989, "Flow Field in the Tip Gap of a Planar Cascade of Turbine Blades," ASME JOURNAL OF TURBOMACHINERY, Vol. 111, pp. 276–283.

Secondary Loss Generation in a Linear Cascade of High-Turning Turbine Blades

S. Harrison
Whittle Laboratory,
Cambridge University,
Cambridge, United Kingdom

Flow through a linear cascade of high-turning, low aspect ratio turbine blades has been measured in great detail at five planes within the cascade and two downstream in order to trace the generation of stagnation pressure loss in the passage. Five-hole probes were used in the main flow, but as it is important to resolve the boundary layers accurately, three-hole and single flattened probes were used near the endwall and blade surfaces, respectively. Endwall shear stresses have been measured using a hot-film probe and an oil-drop viscosity balance technique. Numerical predictions and simple aerodynamic models are used in conjunction with the experimental data to estimate the relative importance of different loss mechanisms, including boundary layer shear stresses and mixing processes.

Introduction

The structure of secondary flows in turbine blade passages is now reasonably well understood (see for example Sieverding, 1985) but for turbine design understanding of the mechanisms of loss generation is equally important. Although existing loss correlations such as those of Dunham (1970) and Sharma and Butler (1987) are useful in the early stages of design, their usefulness is limited when considering, for instance, detailed stacking geometry and radial variation of loading.

Of course, all loss mechanisms in a blade row are interdependent so it is impossible to categorize them precisely. However, simple assumptions have yielded promising results. For instance, Salvage (1974) and Gregory-Smith (1982) have both used two-dimensional boundary layer predictions to estimate endwall losses and Gregory-Smith based his estimate of downstream mixing losses on an inviscid prediction of the exit secondary flow. Denton and Cumpsty (1987) suggest a simplified model of entropy generation in a boundary layer, which the present paper will consider further.

The work described in this paper aims to examine in detail the mechanisms of loss generation in a large-scale, low-speed turbine cascade and forms the first phase of a project investigating the effect of dihedral on losses.

Experimental Details

A linear cascade was used for the experiments with four low aspect ratio, high-turning aerofoils. The blade profile, which was constant over the full span, was designed especially for the project in order to perform well at low Mach numbers and is typical of a modern turbine blade, except that it has a thin trailing edge in order that trailing edge losses do not mask other losses. The measured surface pressure distribution is given in Fig. 1.

Brief details of the cascade are given in Table 1. The blades were machined from aluminum alloy with slots into which hypodermic tubing was laid for static pressure tappings. The cascade (Fig. 2) was of wood with a sliding Perspex endwall section through which probes were inserted. This arrangement gave complete freedom of movement of the traversing probes and also allowed endwall static tappings or a hot-film gage to be traversed through the blade row when required.

Periodic flow was achieved by adjusting aluminum endplates at the top and bottom of the cascade and was checked using blade surface static pressure tappings on the center pair of blades, endwall static tappings in the Perspex window, and oil flow visualization on both endwalls. Finally a five-hole probe traverse over 1.4 pitches at $x/C_x = 1.03$ (not presented here) confirmed that the flow was periodic.

Area traverses were performed at seven locations ($x/C_x = 0.03$, 0.22, 0.45, 0.67, 0.83, 1.03, and 1.23) using 3.2-mm-dia five-hole probes in the main flow. This relatively large probe size was necessary in order to maintain a satisfactory probe Reynolds number (5300 based on probe diameter and inlet free-stream flow). The probes were calibrated up to ± 40 deg in pitch and yaw, but whenever possible the probe yaw was set to keep the probe incidence less than 20 deg. In general only one half span was covered, although a full area traverse was performed at $x/C_x = 1.23$ to ensure that the flow was symmetric. The spacing of five-hole probe measurement points was varied between 2 mm and 20 mm so as to resolve flow features well without recording excessive amounts of unnecessary data. Since much of the loss flux occurs in the boundary layers, it is important to resolve these accurately, so a 0.6 mm $\times$ 1.8 mm three-hole cobra probe was used near the endwall, always keeping the probe incidence below 8.5 deg. A 0.4 mm $\times$

Contributed by the International Gas Turbine Institute and presented at the 34th International Gas Turbine and Aeroengine Congress and Exhibition, Toronto, Ontario, Canada, June 4–8, 1989. Manuscript received at ASME Headquarters January 10, 1989. Paper No. 89-GT-47.

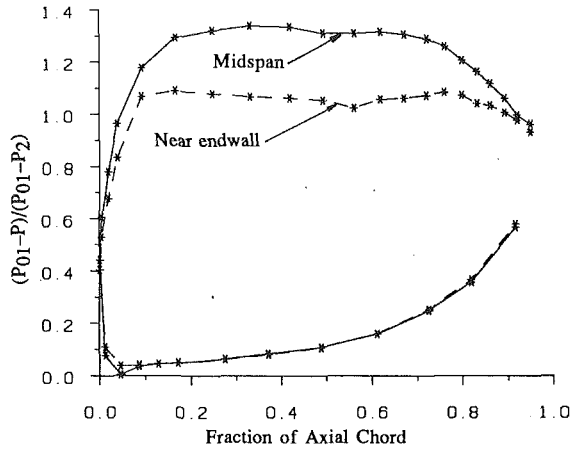

Fig. 1 Measured blade surface static pressures

Table 1

True chord	278.0 mm
Axial chord	222.0 mm
Pitch	230.0 mm
Span	300.0 mm
Trailing edge thickness	2.2 mm
Trailing edge included angle	5.8°
Inlet blade/flow angle (from axial)	40.0°
Exit blade angle (from axial)	–66.8°
Mean exit flow angle (from axial)	–65.5°
Exit Mach number	0.14
Blade chord Reynolds' number (based on true chord and exit flow)	8.7×10^5
Midspan Zweifel coefficient	1.10
Inlet boundary layer ($x/C_x = -0.56$) :	
Displacement thickness	2.6 mm
Momentum thickness	1.9 mm
Kinetic energy thickness	3.3 mm

1.2 mm flattened Pitot probe was used to traverse the blade surface boundary layers. In both blade and endwall boundary layers static pressure was obtained by interpolation between five-hole probe and endwall data.

Pressures are all measured relative to upstream stagnation pressure and nondimensionalized by exit-free stream dynamic head ($P_{01} - P_2$). Velocities are calculated assuming incompressible flow

$$u = \sqrt{\frac{P_0 - P}{0.5\rho}} \tag{1}$$

and nondimensionalized by exit free-stream velocity. The local stagnation pressure loss coefficient Y and the mass-averaged loss coefficient $\bar{Y}$ are thus defined as

$$Y = \frac{P_{01} - P_0}{P_{01} - P_2} \tag{2a}$$

$$\bar{Y} = \frac{\int Y u_x dA}{\int u_x dA} \tag{2b}$$

(integrals are evaluated over the entire flow area).

Two techniques have been used to measure endwall shear stress. The first was a conventional hot-film gage (Dantec 55R47). A relationship of the form

$$E^2 - E_0^2 = k\tau_w^{1/3} \tag{3}$$

is assumed (Hanratty and Campbell, 1983), where E is the anemometer output voltage and E_0 is the zero-flow voltage (whose variation with temperature is taken into account). The constant k is determined from the upstream shear stress coefficient, obtained by a law-of-the-wall (Clauser) plot of the upstream boundary layer profile. For a number of reasons, notably the single-point calibration and the difficulty of accurately determining E_0, the accuracy of mean shear stress by this method is estimated to be only ±30 to ±40 percent, but it has the advantage that unsteady shear stress can also be measured.

Results are also presented from work done by Camus et al. (1988) as part of an undergraduate project. Their method was based on the oil drop viscosity balance method of Tanner and Blows (1969). Mean shear stresses are determined from the rate of change of thickness of an oil drop, measured by laser interferometry, and accuracies of ±10 percent are claimed. There was good agreement between mean shear stresses measured by the two methods, but only mean shear stresses obtained by the more accurate oil drop method are presented here.

Shear stresses on the blade could not be measured by the oil drop method because of lack of access for the laser, and a hot-film gage was out of the question due to difficulty of calibration and much higher heat conduction into the alloy blade than the Perspex endwall.

Flow Structure

Oil flow visualization, showing clearly the lift-off lines associated with the horseshoe vortex and the suction surface corner vortex, is shown in Fig. 3. (The term "lift-off line" is used in this context because the term "separation line" can be misleading by implying that there is some similarity with two-dimensional boundary layer separation.) Probe transverse results, projected onto a plane perpendicular to the mean flow direction so that flow vectors represent secondary velocities, are presented in Fig. 4. Each plot covers one half span and either the full passage width ($x/C_X < 1.0$) or one blade pitch ($x/C_x > 1.0$). Whereas some workers have reported more than one horseshoe vortex at the leading edge, it is clear that in this case only a single vortex forms. The passage vortex, formed

Nomenclature

A = area
C_x = blade axial chord
C_F = skin friction coefficient = $\tau_w / 0.5\rho U^2$
H = boundary layer shape factor (displacement thickness/momentum thickness)
P = pressure
Re = Reynolds number
T = temperature
u = local velocity
U = free-stream velocity
x = axial direction (coordinates measured from leading edge plane)
Y = loss coefficient
y = pitchwise direction
z = spanwise direction
δ = boundary layer overall thickness
θ = boundary layer momentum thickness
μ = dynamic viscosity
ρ = density
τ_w = surface shear stress
Ω = vorticity

Subscripts

0 = stagnation
1 = cascade inlet (free stream)
2 = cascade exit (free stream)
M = fully mixed-out flow

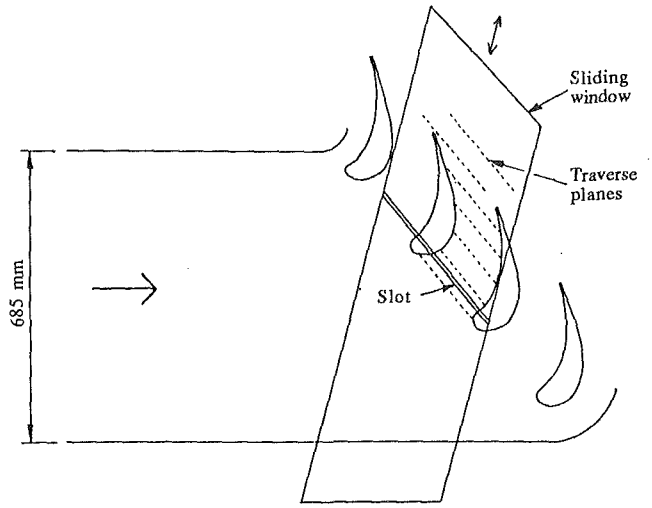

Fig. 2 Cascade arrangement (to scale)

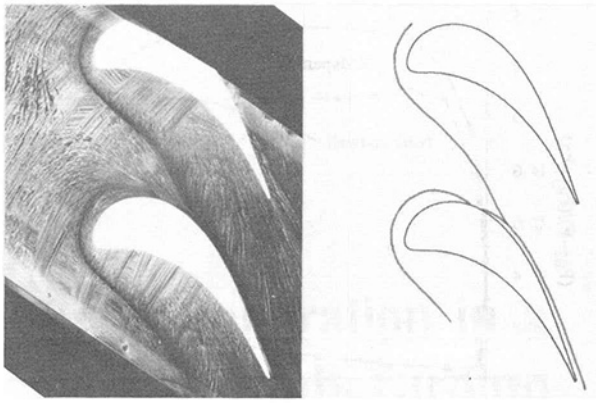

Fig. 3(*a*) Oil flow visualization on endwall

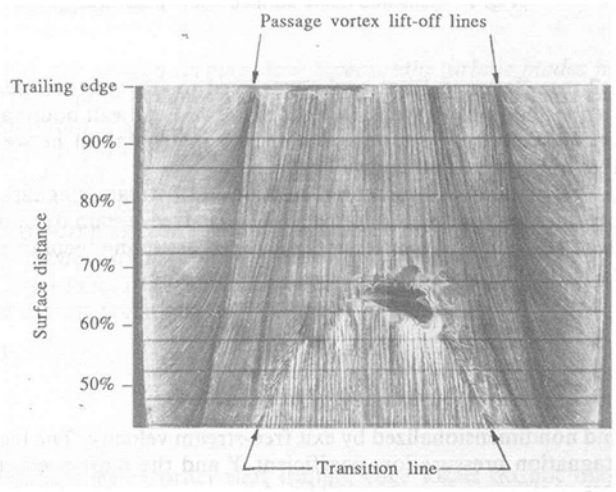

Fig. 3(*b*) Oil flow visualization on blade suction surface

by the action of the pitchwise pressure gradient on the inlet boundary layer, is indistinguishable from the pressure side leg of the horseshoe vortex.

The five-hole and three-hole probes show the position of the main endwall lift-off line (although this is not clear in the small-scale plots of Fig. 4) and these positions agree with the surface flow visualization. The position of this line is therefore not influenced by probe interference. For much of its length, the passage vortex lies directly over the lift-off line rather than to one side, as might be expected. This suggests that not only will the boundary layer downstream of the lift-off line be entirely new, but the presence of the vortex will also strongly influence the boundary layer upstream of the line. It also illustrates how misleading endwall flow visualization can be if used alone to deduce the flow structure away from the solid walls.

Vorticity has been calculated from the transverse results without smoothing (see Appendix) and contours of streamwise vorticity at $x/C_x = 1.23$ are presented in Fig. 5. The passage vortex is clearly visible and some of the trailing filament vorticity is concentrated in a discrete vortex above this. (Trailing filament vorticity is defined by Hawthorne (1955) and Came and Marsh (1974) but may crudely be regarded as resulting in the wake because there is a large component of spanwise flow near the suction surface but hardly any near the pressure surface.) These two vortices coincide with the two loss peaks at $x/C_x = 1.23$ seen in Fig. 4.

Boundary Layers

Boundary layer transition on the suction surface can be heard distinctly using a flattened probe and stethoscope. It occurs at 68 percent surface distance at midspan and progressively earlier nearer to the endwalls. It occurs abruptly (over about 10 mm surface length), indicating that it is possibly caused by a small laminar separation bubble. Flow of oil along this bubble makes the start of transition visible by flow visualization (Fig. 3*b*). There are no major regions of separated flow anywhere in the passage (the mark at midspan in Fig. 3(*b*) is where accumulated oil had to be wiped away to prevent it from running back down the blade when the flow was turned off).

The state of the boundary layer on the endwall is not so easy to deduce using the stethoscope, largely because it is extremely thin and more highly skewed than the blade boundary layer. It must therefore be deduced from boundary layer traverses and hot-film traces.

An endwall boundary layer thickness cannot be defined near the suction surface because it overlaps the main loss core. Away from the passage vortex, however, it can be determined from three-hole probe traverses. A momentum thickness is calculated based on only the magnitude of velocities, i.e., neglecting skew, and it is seen from Fig. 6 that over a large part of the endwall the Reynolds number Re_θ based on this thickness is less than 200. It is therefore virtually certain that the boundary layer is laminar in this region (see Schlichting, 1978, pp. 455–463) and the hot-film traces confirm this to be the case. (The traces shown in Fig. 6 are taken from a total of 130 over the whole endwall.) Transition to turbulence occurs near the trailing edge plane. Note that in the early part of the passage the thin boundary layer even extends upstream of the lift-off line, confirming that the presence of the passage vortex has a profound effect on the endwall boundary layer on both sides of this line.

Mean endwall shear stresses measured by the oil drop method are presented in Fig. 7. The shear stress is very low near the saddle point and there is an increase as the main lift-off line is crossed. This increase is a result of the sudden thinning of the endwall boundary layer by the passage vortex and is the opposite effect to that seen at a two-dimensional separation, where the mean shear stress falls rapidly. Shear stress coefficients (Fig. 8) have been calculated from the oil drop data by using upstream stagnation pressure and local endwall static pressure to derive a "free-stream" dynamic head. The very high values near the pressure surface in the first half of the passage correspond to the thin, laminar boundary layer there. Farther downstream C_F continues to fall gradually as the boundary layer thickens but remains higher near the lift-off line, where the boundary layer is turbulent. The slight rise in C_F at the trailing edge plane (which is also seen in the hot-film

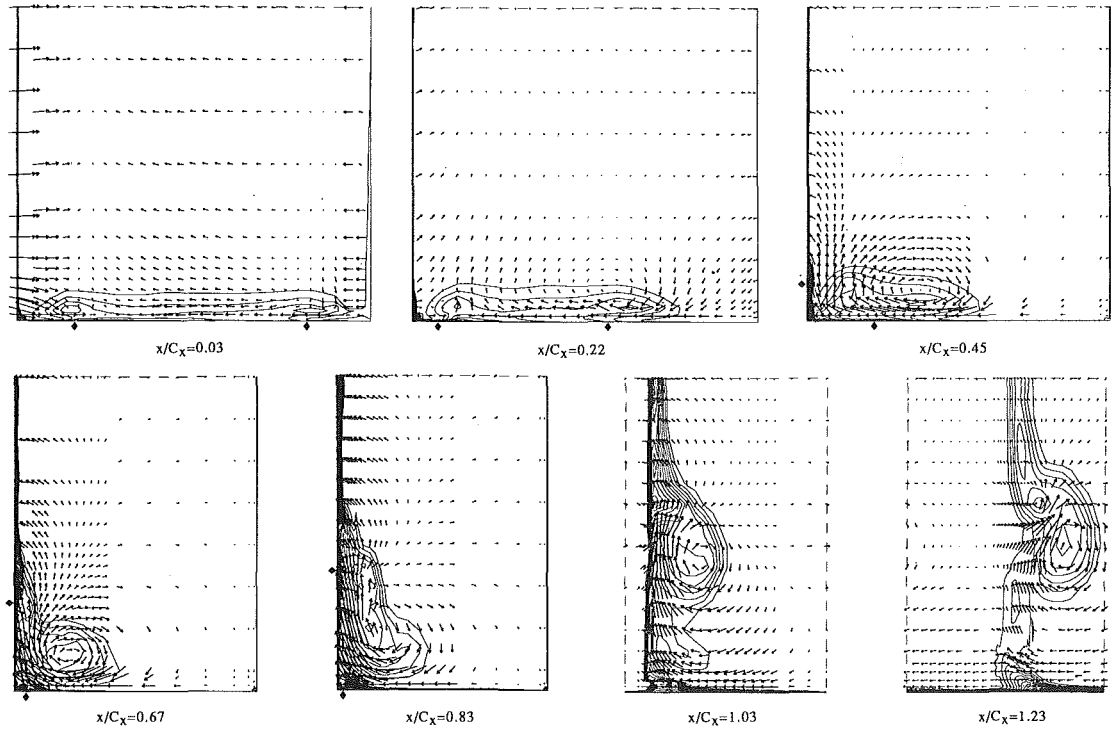

Contours of loss coefficient at intervals of 0.05
Secondary velocity vector scale: U_2 = ⟶
♦ indicates positions of horseshoe/passage vortex lift-off lines.

Fig. 4 Traverse results

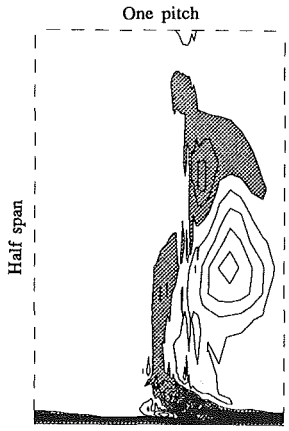

White areas : Clockwise (passage vortex)
Shaded areas : Anticlockwise (corner vortex and trailing filament vorticity)

Fig. 5 Streamwise vorticity ($x/C_x = 1.23$)

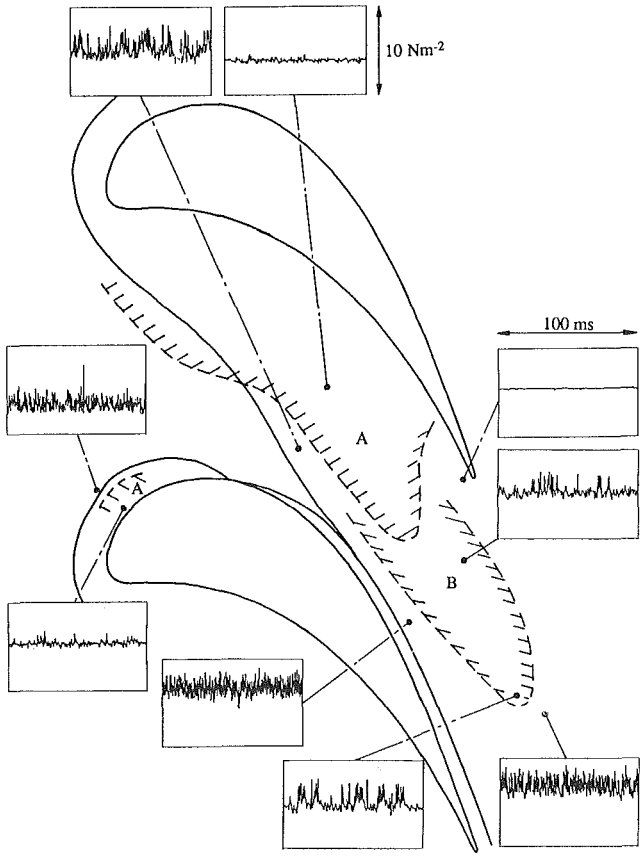

——— Horseshoe/passage vortex and suction surface corner vortex lift-off lines
A Reθ<200 (boundary layer laminar)
B Intermittent hot film signal indicates transition

Fig. 6 Endwall boundary layer hot-film traces

data, although these are not presented here) may be a result of transition.

Measured Loss

The suction surface boundary layer at midspan was predicted using Thwaites' method for the laminar part of the boundary layer and Green's lag entrainment method for the turbulent part (Herbert and Calvert, 1982) based on measured surface static pressures and the known transition point. The predicted trailing edge momentum thickness was 0.63 mm compared with 0.80 mm derived from measurements. The discrepancy is probably largely due to the fact that secondary flows cause suction surface streamlines to converge slightly at midspan, thickening the boundary layer. The measured loss coefficient at midspan

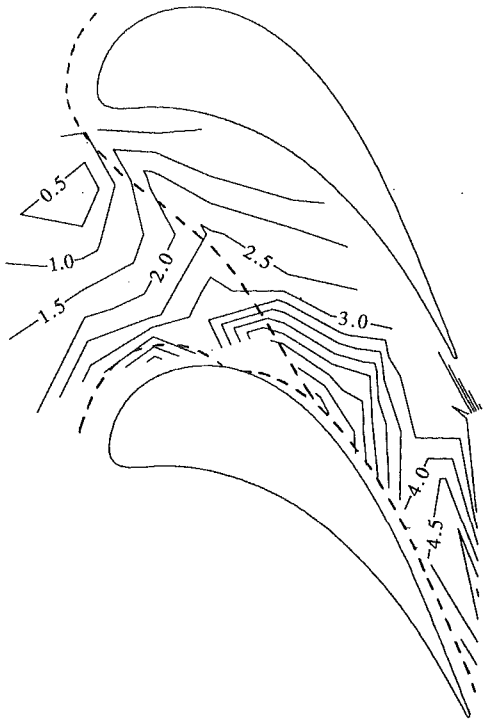

Fig. 7 Mean endwall shear stress (Nm^{-2})

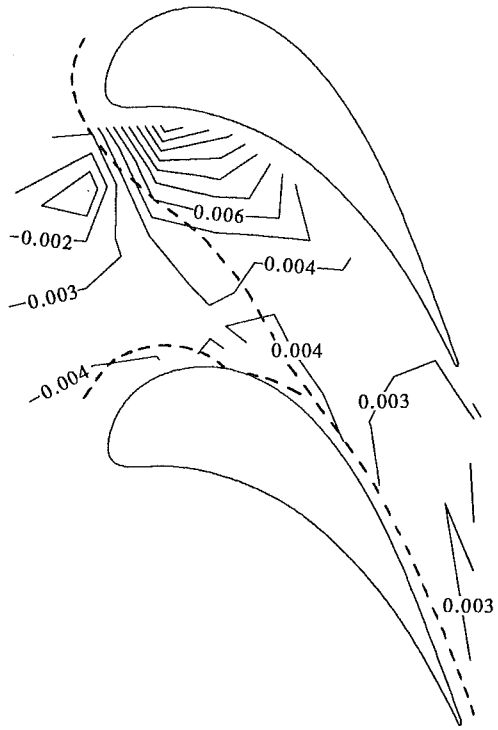

Fig. 8 Mean shear stress coefficient

is 2.0 percent and taking this value as the "profile" loss, Dunham's (1970) secondary loss correlation for turbine cascades predicts an overall loss coefficient of 6.0 percent. In fact the measured overall loss coefficient at the exit plane ($x/C_x = 1.23$) is only 4.8 percent.

Two quite different approaches may be used to divide the exit loss roughly into components (see Fig. 9). The first is to divide the loss into inlet boundary layer loss and "new" loss, then use the conventional definition of "secondary" loss as

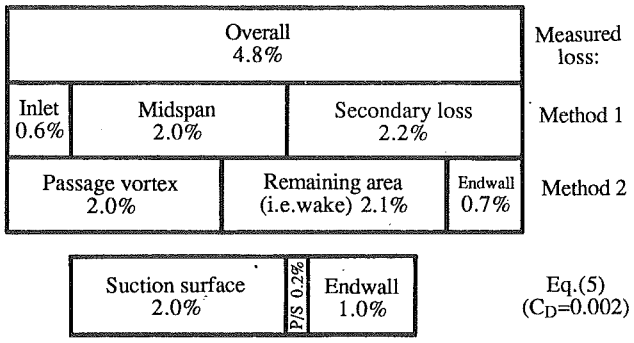

Fig. 9 Schematic breakdown of measured and predicted loss at $x/C_x = 1.23$

the overall "new" loss less midspan loss coefficient. As is to be expected from a low aspect ratio blade row, nearly half of the overall loss is so-called "secondary loss." The second method entails limited area integrations at $x/C_x = 1.23$. Although the division between the endwall boundary layer and the passage vortex loss core (Fig. 4) is clear, that between the passage vortex and trailing filament loss cores is not, so this method is very approximate. However, Fig. 9 does demonstrate that the main (i.e., passage vortex) loss core contains much more than just inlet boundary layer fluid but also includes a large part of the wake loss (see Fig. 4).

The area of flow that can clearly be recognized as the endwall boundary layer only represents about a third of the "secondary loss" (as defined above) and only about 17 percent of the total "new" loss. This is despite the fact that the area of endwall downstream of the lift-off line, i.e., the area covered by "new" boundary layer, represents 23 percent of the total solid surface area within $-0.56 < x/C_X < 1.23$. The remainder of the secondary loss will rise from a number of sources, notably:

(*a*) Increased suction surface boundary layer loss away from midspan due to earlier transition. The additional loss predicted at midspan if the suction surface boundary layer were fully turbulent from the leading edge is 0.7 percent. In an engine, where Reynolds number and free-stream turbulence would be higher than in this cascade, suction surface transition would probably occur earlier in any case, so this effect would be less significant.

(*b*) Loss generated on the endwall but swept away by the passage vortex before $x/C_x = 1.23$.

(*c*) Increased mixing upstream of $x/C_x = 1.23$ caused by the secondary flow.

Boundary Layer Dissipation

The dissipation integral C_D for a boundary layer may be defined as

$$C_D = \frac{d_1}{\rho U^3} = \frac{T\xi}{\rho U^3} \tag{4}$$

where d_1 is the shear work done in the boundary layer (Schlichting, 1968) and ξ is the rate of entropy generation per unit solid surface area (Denton and Cumpsty, 1987). Taking the flow through the cascade to be incompressible, the cascade loss coefficient (neglecting any dissipation occurring outside the boundary layers, e.g., through mixing in the wake or passage vortex) may be expressed as

$$\bar{Y} = \frac{2\rho}{mU_2^2}\int U^3 C_D dA \tag{5}$$

where m is the mass flow and the integral is evaluated over all solid surfaces. Schlichting (1968, p. 635) shows that for a two-dimensional, turbulent boundary layer, although the skin friction coefficient C_F is highly dependent upon shape factor, the

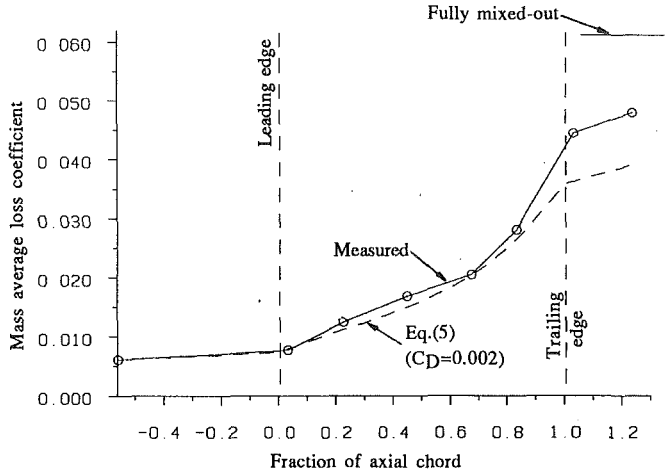

Fig. 10 Growth of loss through cascade

dissipation integral C_D is not. For turbulent boundary layers with $1.2<H<2.0$ and $10^3<\mathrm{Re}_\theta<10^5$ a good approximation for C_D is

$$C_D \approx 0.0056\ \mathrm{Re}_\theta^{-1/6} \quad \text{(turbulent)} \tag{6}$$

Denton and Cumpsty (1987) suggest that, since the dependence upon Re_θ is weak for a turbulent boundary layer, a further simplification that $C_D=0.002$ is acceptable as a rough approximation when Re_θ is not known. This approximation allows a loss coefficient to be predicted easily using equation (5) without the need for detailed knowledge of the boundary layers.

The approach has two major sources of error apart from its neglect of variations of Re_θ and its restriction to boundary layer loss. The first is the fact that turbulent boundary layers are assumed throughout, whereas in practice laminar boundary layers cover the entire pressure surface and much of the suction surface and endwall. For a laminar boundary layer C_D is more dependent upon shape factor and boundary layer thickness. Denton and Cumpsty quote the relation

$$C_D \approx 0.2\ \mathrm{Re}_\theta^{-1} \quad \text{(laminar)} \tag{7}$$

A laminar boundary layer will therefore have a dissipation integral greater than the assumed value of 0.002 if $\mathrm{Re}_\theta<100$ and less if $\mathrm{Re}_\theta>100$. Thus if $C_D=0.002$ is assumed throughout then the loss due to the thin boundary layers near the leading edge on the blade surface and on the endwall near the pressure surface will be higher than predicted by equation (5), whereas equation (5) will overestimate the loss generated in the thicker laminar boundary layers farther downstream. (N.B. Transition on the suction surface at midspan occurs at $x/C_X=0.80$, where $\mathrm{Re}_\theta \approx 640$.)

The second shortcoming of this approach is that it is based on relations for collateral boundary layers. If a boundary layer is characterized by velocity magnitudes only, then addition of skew will always increase velocity gradients, hence shear stresses, hence C_D. The magnitude of this error may be estimated by considering the rate of dissipation in a laminar boundary layer (e.g., Schlichting, 1968)

$$d_1=\rho U^3 C_D=\int_0^\delta \tau\frac{\partial u}{\partial y}dy=\mu\int_0^\delta\left(\frac{\partial u}{\partial y}\right)^2 dy \tag{8}$$

If the right-hand side of equation (8) is evaluated for a skewed laminar boundary layer by expressing the velocity u as a vector, then this would give the true dissipation integral C_D. If, on the other hand, it is evaluated by considering only velocity magnitudes, then a smaller value of C_D is obtained, which represents the dissipation integral of a boundary layer with the same velocity profile but which is collateral. The ratio of these two quantities will give an idea of the error due to the neglect of skew. (Although this argument is strictly only applicable to laminar boundary layers, one would expect a similar relationship for turbulent boundary layers.) Evaluating this ratio from endwall boundary layer traverses suggests an error less than 3 percent in most cases and below 10 percent in nearly all cases, despite boundary layer skew in excess of 50 deg.

Equation (5) has been used to predict boundary layer losses in the cascade, using equation (1) with upstream stagnation pressure and surface static pressures to derive local "free-stream" velocities. These predictions have been superimposed onto the measured inlet boundary layer loss and are presented in Fig. 10. The sudden increase in measured loss just after the trailing edge is due to a high rate of mixing in the wake, but this is not taken into account by equation (5), which considers only boundary layer loss. Otherwise the predictions match the measurements remarkably well, despite the shortcomings described above.

Comparing measurements with predictions in Fig. 9 it seems that equation (5) predicts the components of loss reasonably well, too. Further investigations on different bladerows will tell whether equation (5) could be incorporated into a viable loss prediction technique.

Mixing Loss

The dissipation integral C_D represents the local rate of entropy generation in a boundary layer. However, as a boundary layer grows, flow nonuniformities increase, and these have the potential to generate further entropy downstream as a result of mixing to a uniform flow. The increase in loss coefficient downstream of $x/C_x=1.23$ due to mixing at constant area with no external forces would be 1.3 percent, i.e., over one quarter of the measured loss coefficient (4.8 percent) at that plane, so it is important that any loss prediction method does not neglect mixing loss.

The mixing loss that would occur downstream of any plane may be calculated by applying momentum and continuity equations to a control volume with uniform flow at exit and periodic side boundaries (so that mass and momentum flux through the side boundaries may be ignored). If net external forces F_x and F_y are applied during mixing, the fully mixed-out stagnation pressure is given by

$$P_{0M}=\frac{1}{A_M}\left\{F_x+\int(P+\rho u_x^2)dA\right\} + \frac{\rho}{2}\left\{\left(\frac{F_y+\rho\int u_x u_y dA}{\rho\int u_x dA}\right)^2-\left(\frac{\int u_x dA}{A_M}\right)^2\right\} \tag{9}$$

where A_M is the flow area at the exit plane of the control volume, measured perpendicular to the axial (x) direction, and the integrals are evaluated over the entire inlet plane of the control volume.

If F_x and F_y can be assumed to be zero, for instance when considering mixing at constant flow area downstream of the measurement plane at $x/C_x=1.23$ with no following blade row, then equation (9) is easily applied. However, if there is a blade row downstream or if a measurement plane within the blade row is to be considered, then F_x/A and F_y/A are of the same order of magnitude as the dynamic head. Since the mixing loss is one or two orders of magnitude smaller than this, then F_x and F_y must be known very accurately. In practice this means that mixing loss cannot be calculated reliably in this way except for constant area mixing outside of blade rows. It must therefore be realized that the mixed-out loss often used to compare and correlate secondary losses is only a convenient value, which is easily calculated. It is not necessarily the loss that would occur in a turbine.

Even in a hypothetical case when the flow through the blade row could be considered inviscid, the inlet boundary layer

would still roll up into a passage vortex and so there would still be flow nonuniformities downstream, which would lead to mixing losses. Part of the 1.3 percent mixing loss actually observed, then, is attributable to the inlet boundary layer rather than to viscous effects within the blade row. However, the fact that the passage vortex contains fluid not only from the inlet boundary layer but also from the boundary layers on the blade suction surface and the endwall within the cascade suggests that inviscid effects are not responsible for the majority of the mixing loss.

To give an estimate of the amount of mixing loss attributable to the inlet flow, an inviscid calculation of the three-dimensional flow through the blade row, with the inlet boundary layer included, has been performed using Denton's (1985) time-marching program. The mixing loss coefficient for $x/C_x = 1.23$ based on this prediction is 0.47 percent. This figure is much higher than the value of 0.08 percent, which would have been incurred if the flow had mixed out to a uniform flow before entering the blade row, but is only roughly one third of the mixing loss calculated from measurements at $x/C_x = 1.23$, so it seems that a significant proportion of the exit mixing loss is indeed attributable to viscous effects within the blade row.

Conclusions

The passage vortex lies over the endwall lift-off line rather than to one side, so acts to thin the endwall boundary layer upstream as well as downstream of the line.

There is a laminar boundary layer over much of the endwall within the blade passage, and although the wall shear stresses are high, this boundary layer is not of overriding significance in the generation of secondary loss. In the cascade tested only about one third of the secondary loss arises in the "new" endwall boundary layer downstream of the lift-off line.

Loss predictions based on Denton and Cumpsty's approximation that the boundary layer dissipation integral is constant are surprisingly accurate given their simplicity. Wake mixing losses are entirely neglected by the method, but further investigation will determine whether the approximation could be incorporated into a viable loss prediction technique.

The downstream mixing loss is significant (in this case just over one quarter of the measured loss at $x/C_x = 1.23$) but an inviscid numerical prediction indicates that only about a third of this is attributable to mixing of the upstream boundary layer.

Acknowledgments

Particular thanks are due to Dr. J. D. Denton, who supervised this project, and to Dr. J.-J. Camus for the oil-dot endwall shear stress measurements. This work has been carried out with the support of the Procurement Executive, Ministry of Defence, and the Science and Engineering Research Council.

References

Came, P. M., and Marsh, H., 1974, "Secondary Flows in Cascades: Two Simple Derivations for the Components of Vorticity," *Journal of Mechanical Engineering Science*, Vol. 16, pp. 391–401.

Camus, J.-J., Starling, I., and Lam, E., 1988, Cambridge University, private communication.

Denton, J. D., 1985, "The Calculation of Fully Three-Dimensional Flow Through Any Type of Turbomachine Blade Row," *3D Computation Techniques Applied to Internal Flows in Propulsion Systems*, AGARD lecture series 140, Paper 9.

Denton, J. D., and Cumpsty, N. A., 1987, "Loss Mechanisms in Turbomachines," IMechE Paper No. C260/87.

Dunham, J., 1970, "A Review of Cascade Data on Secondary Losses in Turbines," *Journal of Mechanical Engineering Science*, Vol. 12, pp. 48–59.

Gregory-Smith, D. G., 1982, "Secondary Flows and Losses in Axial Flow Turbines," ASME *Journal of Engineering for Power*, Vol. 104, pp. 819–822.

Gregory-Smith, D. G., Graves, C. P., and Walsh, J. A., 1988, "Growth of Secondary Losses and Vorticity in an Axial Turbine Cascade," ASME JOURNAL OF TURBOMACHINERY, Vol. 110, pp. 1–8.

Hanratty, T. J., and Campbell, J. A., 1983, "Measurement of Wall Shear Stress," *Fluid Mechanics Measurements*, R. J. Goldstein, ed., Hemisphere/Springer-Verlag, Chap. 11.

Hawthorne, W. R., 1955, "Rotational Flow Through Cascades," *Quarterly Journal of Mechanics and Applied Mathematics*, Vol. VIII, pp. 266–292.

Herbert, M. V., and Calvert, W. J., 1982, "Description of an Integral Method for Boundary Layer Calculation in Use at NGTE, With Special Reference to Compressor Blades," NGTE Memorandum M82019.

Salvage, J. W., 1974, "Investigation of Secondary Flow Behaviour and the End Wall Boundary Layer Development Through Compressor Cascades," VKI TN 107.

Schlichting, H., 1968, *Boundary Layer Theory*, 6th ed., McGraw-Hill, New York.

Sharma, O. P., and Butler, T. L., 1987, "Predictions of Endwall Losses and Secondary Flows in Axial Flow Turbine Cascades," ASME JOURNAL OF TURBOMACHINERY, Vol. 109, pp. 229–236.

Sieverding, C. H., 1985, "Recent Progress in the Understanding of Basic Aspects of Secondary Flows in Turbine Blade Passages," ASME *Journal of Engineering for Gas Turbines and Power*, Vol. 107, pp. 248–257.

Tanner, L. H., and Blows, L. G., 1969, "A Study of the Motion of Oil Films on Surfaces in Air flow, With Application to the Measurement of Skin Friction," *J. Phys. E.*, Vol. 2, pp. 194–202.

APPENDIX

The components Ω_x, Ω_y, and Ω_z of the vorticity Ω are derived from experimental data as follows. Ω_x is obtained directly from velocity gradients

$$\Omega_x = \frac{\partial u_z}{\partial y} - \frac{\partial u_y}{\partial z} \tag{10}$$

Following the method of Gregory-Smith et al. (1988), Ω_y and Ω_z are obtained by making use of Crocco's equation

$$\mathbf{u} \times \Omega = \frac{1}{\rho} \nabla P_0 \tag{11}$$

Taking the y and z components of equation (11), we obtain

$$\Omega_y = \frac{1}{u_x}\left(u_y \Omega_x + \frac{1}{\rho}\frac{\partial P_0}{\partial y}\right) \tag{12}$$

$$\Omega_z = \frac{1}{u_x}\left(u_z \Omega_x - \frac{1}{\rho}\frac{\partial P_0}{\partial z}\right) \tag{13}$$

Comparison of Steady and Unsteady Secondary Flows in a Turbine Stator Cascade

G. J. Hebert

W. G. Tiederman

School of Mechanical Engineering,
Purdue University,
West Lafayette, IN 47907

The effect of periodic rotor wakes on the secondary flow structure in a turbine stator cascade was investigated. A mechanism simulated the wakes shed from rotor blades by passing cylindrical rods across the inlet to a linear cascade installed in a recirculating water flow loop. Velocity measurements showed a passage vortex, similar to that seen in steady flow, during the time associated with undisturbed fluid. However, as the rotor wake passed through the blade row, a large crossflow toward the suction surface was observed in the midspan region. This caused the development of two large areas of circulation between the midspan and endwall regions, significantly distorting and weakening the passage vortices.

Introduction

A major source of inefficiency in turbine blade passages is the secondary flow that develops due to the turning of the endwall boundary layers. Several investigators, such as Bardon et al. (1975) and Gregory-Smith (1982), have presented models for the prediction of secondary flows. Based on comparisons with experimental results, it is generally believed that these models reasonably predict the exit secondary flow patterns (though not losses) for steady flow through turbine blade passages. However, the relative motion of the rotor and stator blades and their wakes in a real turbomachine result in a highly unsteady flow. It is known that wake-generated unsteadiness has a significant effect on component aerodynamic efficiency, heat transfer, and structural loading. Therefore, it would be highly desirable to incorporate unsteady effects into the design procedure. To do this, a much better understanding of the unsteady flowfield, including secondary effects, is required.

Only in recent years has there been a significant research effort in turbomachinery unsteady flow. Several experimental investigations have been conducted by Joslyn et al. (1982, 1986), as well as Binder et al. (1989), and Hodson (1985b), resulting in a fairly thorough description of the wake-generated unsteady flow and turbulence in the midspan plane of a turbine blade passage. Sharma et al. (1985) also presented measurements made over the entire exit plane of a rotating blade row operating in the wake-effected flowfield behind a stator blade row. Data were presented for two time periods. The first corresponded to the flow of free-stream, undisturbed fluid through the rotor passage. The exit flowfield at this time was very similar to that found in steady flow cascade tests. The second time period corresponded to the time at which the fluid from the upstream vane wake occupied the rotor exit measurement plane. At this time, the passage vortices were weaker and more diffused, with the vortical motions spread over the entire passage. Additionally, a low static pressure, high loss region appeared near the midspan of the rotor blade wake. The presence of this region could not be explained. Sharma et al. concluded that the "... data revealed some interesting aspects of the flowfield, the impact of which is difficult to assess because of their complexity and the lack of comparable data."

The objective of the present study was to produce additional unsteady flow data similar to those of Sharma et al., but in a test section of less complex geometry. The experiments were conducted in a linear cascade to eliminate the effects of the radial pressure gradient. This study also used rotor wakes shed from moving cylindrical rods, acting on a downstream stator blade row. Since the stator blades were sealed at both endwalls, the tip leakage vortex was also eliminated. By reducing the geometric complexity it was hoped that the details of the exit flowfield would be more easily understood. The intent was not to duplicate exactly the conditions of an actual turbine, but to provide a carefully controlled study of the effect of periodic wakes on the secondary flows. These results will be useful for comparisons with prediction from analytical models using the same inlet and boundary conditions in a manner similar to that of Hodson (1985a, 1985b).

The tests were conducted using a water flow that matched the Reynolds number and reduced frequency of typical axial-flow turbine nozzles. For obvious reasons the Mach number could not be duplicated. Velocity measurements were obtained using a laser-Doppler velocimeter. By using water as the fluid medium, problems associated with particle seeding and data rates were greatly reduced.

As it is well known that the upstream boundary layer plays a major role in the development of secondary flows, measurements of the inlet flowfield were obtained as well as meas-

Contributed by the International Gas Turbine Institute and presented at the 34th International Gas Turbine and Aeroengine Congress and Exhibition, Toronto, Ontario, Canada, June 4-8, 1989. Manuscript received at ASME Headquarters January 17, 1989. Paper No. 89-GT-79.

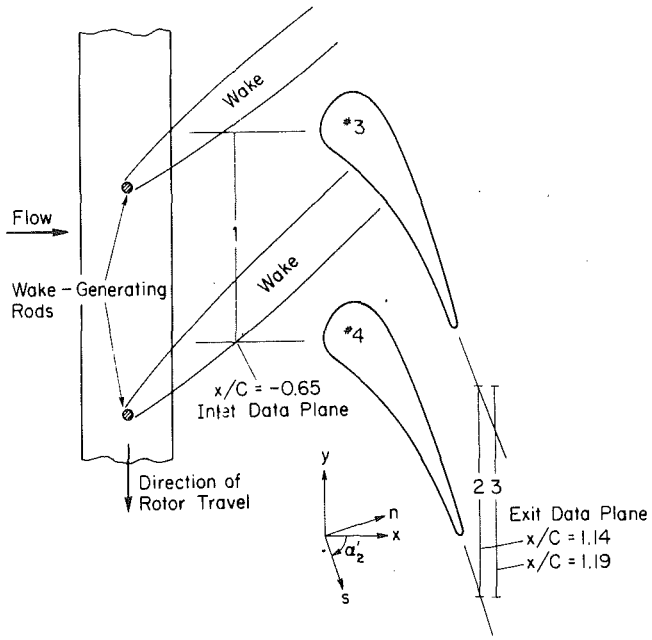

Fig. 1 Stator blades and wake-generating rods

urements in the exit flowfield. Phase-averaged axial and tangential boundary layer profiles were obtained at the inlet of the cascade for four separate time windows. All three velocity components in the exit flowfield were also obtained for four corresponding time windows. Using the exit velocity measurements, the streamwise vorticity distribution at the exit of the cascade was calculated and plotted, giving an indication of the strength of the secondary flow at various times within the cycle.

Apparatus and Procedures

Turbine Cascade. A five-blade, linear cascade of turbine stator vanes was installed in a recirculating water flow facility. Figure 1 shows two of the stator blades along with the location of the inlet and exit measuring planes, the wake generating rods, and the coordinate system. Note that the origin of the coordinate system is at the intersection of the leading edge ($x=0$) and the trailing edge of blade #4 ($y=0$). The blade profile is an advanced, high-pressure turbine nozzle vane designated "C3X" (Hylton et al., 1983). This profile is characterized by a large radius leading edge with the majority of the turning occurring in the first one-third of the blade chord. All of the pertinent cascade dimensional parameters are given in Table 1.

Table 1 Cascade geometry (Hylton et al., 1983)

Blade inlet angle	0 deg
Blade exit angle	−72.4 deg
True chord	145 mm
Axial chord	78.2 mm
Span	76.2 mm
Pitch	118 mm

Table 2 Rotor mechanism

Number of rods	14
Rod diameter	6.35 mm
Rod spacing	127 mm
Rotor-stator axial gap	152 mm

Wake-Generating Mechanism. For unsteady flow, simulated rotor wakes were generated using a mechanisms consisting of cylindrical rods mounted perpendicularly on a toothed timing belt. The belt was stretched between two pulleys such that the rods on the upper pass of the belt protruded into the flow stream. The entire mechanism was enclosed in a housing filled with water. One of the pulley shafts was driven by a constant speed a-c induction motor. This caused the rods to traverse linearly across the entire inlet to the cascade, in contrast to Doorly and Oldfield (1985), who pioneered this wake-generation concept with bars protruding from a large rotating drum. The cycle period was 215 ± 5 ms, which results in a reduced frequency of 4.7, based on the true semi-chord and the average inlet free-stream velocity. This frequency is typical of axial flow turbines and indicates that the flow is truly unsteady rather than quasi-steady. A small, permanent magnet was attached at the tip of each of the rods so that an electromagnetic pickup, mounted in the housing cover, could provide a signal for synchronizing the data acquisition to the rotor cycle. The details of the rotor mechanism geometry, which was designed to simulate rotor wakes reported by Dring et al. (1982), are given in Table 2.

Laser Velocimeter Measurements. All velocity measurements were obtained in an axial tangential-spanwise (x, y, z) coordinate system using a four-beam, two-component laser-Doppler velocimeter (LDV). The axial and tangential velocities (u, v) were obtained simultaneously with the LDV system in the two-component, forward-scatter configuration. The span-

Nomenclature

C = stator blade chord
h = stator blade span
k = rotor-wake reduced frequency = $\omega C/2(\overline{u_1})_{fs}$
$q^2/2$ = turbulent kinetic energy
Re_C = Reynolds number based on chord
s, n, z = Cartesian coordinates in the streamwise, normal, and spanwise directions
S = stator pitch (spacing)
t = time with respect to sync pulse
T = period of rotor-wake cycle
Tu = turbulence intensity in the axial direction
u, v, w = instantaneous velocity components in the x, y, z directions
u', v', w' = fluctuating velocity components in the x, y, z directions
V = total velocity
V_{nz} = secondary velocity (resultant of V_n and V_z)
x, y, z = Cartesian coordinates in the axial, tangential, and spanwise directions
α = fluid flow angle in the x-y plane, with respect to the positive x axis
α' = stator blade angle
δ = 99 percent boundary layer thickness
σ = standard deviation
ω = rotor-wake angular frequency
Ω = vorticity

Subscripts

1 = inlet measurement plane
2 = first exit measurement plane
3 = second exit measurement plane
fs = free-stream
rms = root-mean-square

Superscripts

— = time-averaged
~ = phase-averaged

wise velocity component (w) was obtained only at the exit of the cascade using the LDV system in the one-component, backward scatter mode. In both exit planes, an unevenly spaced 8×8 grid of measurement locations was used with the finest spacing in the suction surface endwall region. Measurements were made only in the lower half of the exit plane because the inlet conditions and the cascade were symmetric. Measurements in the exit region were transformed to a streamwise-normal-spanwise (s, n, z) coordinate system. This system is defined with the streamwise direction parallel to the endwall and the blade exit angle of -72.4 deg. the normal direction is then perpendicular to the streamwise and spanwise directions. For all subsequent analysis, the streamwise component is considered the primary velocity, while the normal and spanwise components are the secondary velocities.

For the steady flow measurements, each data set contained a minimum of 4000 velocity realizations per component. Using the statistical theory presented by Donohue et al. (1972) and the measured turbulence levels, a maximum error or 0.005 m/s was calculated for each component of the mean velocity, at a 95 percent confidence level. In the unsteady flow case, since data were obtained in 5 ms windows, the time required to obtain 4000 realizations at each location became prohibitively long. Consequently only 1500 realizations were obtained for each component, yielding a maximum error of 0.009 m/s in the phase-averaged mean velocity components at a 95 percent confidence level.

In unsteady flow, phase-averaged velocity data were obtained using a window technique. The rotor sync-pulse generator was connected to the LDV signal processor. The data acquisition software was then able to determine the time at which each velocity realization was acquired, with respect to the rotor sync pulse. Each realization not acquired at a time within one of the four programmed windows was discarded. The window width for all of the unsteady measurements was 5 ms. With a $\pm$ 5 ms uncertainty in the sync pulse the effective window width was approximately 6.2 percent of the period.

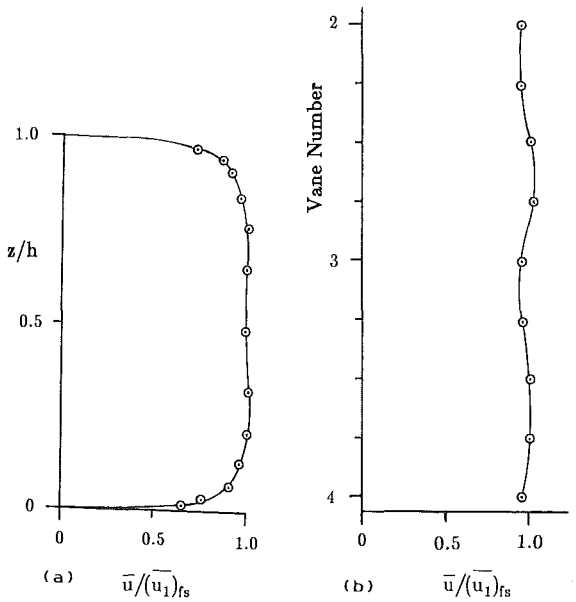

Fig. 2 Inlet axial velocities: (*a*) spanwise profile (midpitch); (*b*) pitchwise profile (midspan)

Data Reduction

Velocity Measurements. The velocity at each point in steady flow was assumed to consist of three mean velocity components ($\bar{u}$, $\bar{v}$, $\bar{w}$) and three corresponding fluctuating components (u', v', w'), such that the velocity at any given time is defined by

$$\begin{aligned} u &= \bar{u} + u' \\ v &= \bar{v} + v' \\ w &= \bar{w} + w' \end{aligned} \tag{1}$$

In the unsteady flow case, it was assumed that a mean periodic velocity existed at each location in the flowfield. This is a velocity that varied with time within each cycle, but was repeatable from cycle to cycle. Superimposed on this mean periodic velocity ($\tilde{u}$, $\tilde{v}$, $\tilde{w}$) were random turbulent fluctuations (u', v', w'). The velocity at any given time in unsteady flow could then be described using

$$\begin{aligned} u &= \tilde{u} + u' \\ v &= \tilde{v} + v' \\ w &= \tilde{w} + w' \end{aligned} \tag{2}$$

In unsteady flow, data were obtained for four different time windows within each cycle. Each of the four resulting data sets was then reduced, in the same manner as the steady flow data, to obtain the phase-averaged mean periodic velocity and the rms of the fluctuating component at their respective times in the rotor cycle.

Streamwise Vorticity. In the x, y, z, coordinate system, the individual components of the vorticity vector are

$$\begin{aligned} \Omega_x &= \frac{\partial w}{\partial y} - \frac{\partial v}{\partial z} \\ \Omega_y &= \frac{\partial u}{\partial z} - \frac{\partial w}{\partial x} \\ \Omega_z &= \frac{\partial v}{\partial x} - \frac{\partial u}{\partial y} \end{aligned} \tag{3}$$

The streamwise component of vorticity is then given by

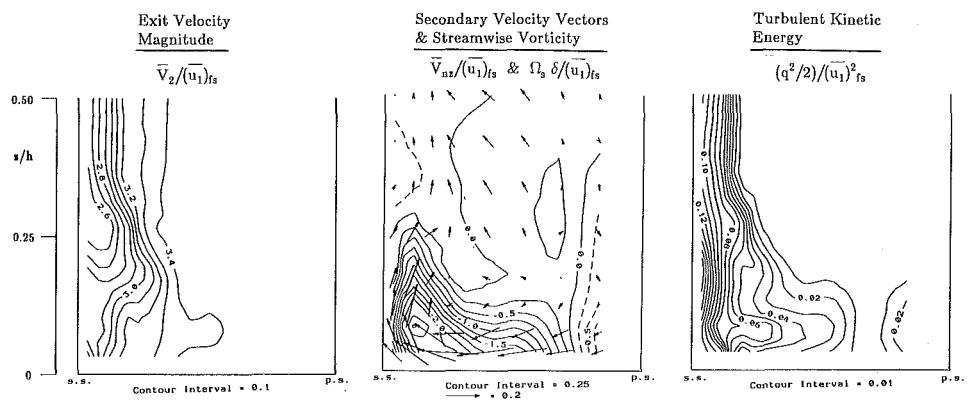

Fig. 3 Steady flow exit data

$$\Omega_s = \Omega_x \cos \alpha_2' + \Omega_y \sin \alpha_2' \quad (4)$$

The partial derivatives in equation (3) are determined from the exit velocity data, using simple finite difference approximations. A first-order approximation was used for the $\partial w/\partial x$ term since data were taken in only two axial planes. First-order approximations of the other derivatives were also used for points on the boundaries of the measurement grid. However, second-order approximations of these derivatives were used for all interior points.

Turbulent Kinetic Energy. To compare the turbulence levels of the steady flow and the various time windows in unsteady flow, the turbulent kinetic energy (per unit mass), $q^2/2$, was calculated using

$$\frac{q^2}{2} = \frac{1}{2}(\overline{u'^2} + \overline{v'^2} + \overline{w'^2}) \quad (5)$$

It is important to note that the spanwise component of velocity was deduced from measurements made at an angle of 5.8 deg from the spanwise direction. The mean velocities were easily resolved to obtain the true $\bar{w}$. However, without the mixed term, $\overline{u'w'}$, the true fluctuating component, w', could not be resolved. Because the measurement angle was small, and because the turbulence was reasonably isotropic, it was judged that $\overline{w'^2_{\text{meas.}}}$ could be used in equation (5) with reasonable accuracy.

Contour Plots. The exit velocity magnitude, streamwise vorticity, and turbulent kinetic energy data from measurement plane 2 are presented in the form of contour plots. The plots show the bottom half of the blade passage exit as viewed in the spanwise-normal plane looking upstream. The plotting software used the data from the unevenly space measurement locations to generate a uniform grid of values using triangulation followed by bivariate interpolation with a fifth-degree polynomial. The contour lines were generated using a splines-under-tension curve-fitting routine. The tension was adjusted so that the lines appeared smooth, while not allowing any local minima or maxima that were not represented by at least one original data point.

Results

Steady Flow. The axial velocity profile at the inlet to the passage between vanes #3 and #4 is shown in Fig. 2(*a*). The free-stream velocity was 0.444 m/s, corresponding to a Reynolds number of 0.7×10^5 based on blade chord. The boundary layers were turbulent, with a thickness of 14.4 mm or 19 percent of the blade span. The inlet conditions are summarized in Table 3. Velocity measurements were made at several locations across the inlet to the cascade to ensure that the flow was periodic. These measurements, plotted in Fig. 2(*b*), indicated less than 2 percent variation for any two corresponding locations in the passages between vanes #2, #3, and #4.

Figure 3 shows a plot of the isocontours of total velocity magnitude, normalized with the inlet free-stream velocity, at the exit of the passage (plane 2). The dominant feature of the plot is the suction side blade wake. Here, the lowest velocity fluid is concentrated in a small area at the center of the wake, halfway between the endwall and midspan. Velocity measurements were not made close enough to the pressure side of the passage to show the pressure side wake.

Secondary velocity vectors are also plotted in Fig. 3. The small spanwise velocities at midspan show that the exit flow is not perfectly symmetric about the midspan. The highest velocities are seen along the endwall toward the suction side, and in the positive z-direction along the suction side of the passage near the endwall. The flow pattern in the endwall corner does have the appearance of a vortex, although it is not yet fully developed this close to the trailing edge of the vane.

Isocontours of streamwise vorticity at the cascade exit, normalized with inlet boundary layer thickness and inlet free-stream velocity, are plotted along with the secondary velocity vectors. An area of concentrated negative vorticity is found in the suction side endwall corner. This vorticity, due to the presence of the passage vortex, has a peak value of -2.75. Areas of positive vorticity are shown along the pressure side of the passage and just below the midspan on the suction side. This is the vorticity of the stator wake. The free-stream and

Table 3 Steady flow inlet conditions

Freestream axial velocity	0.444 m/s
Reynolds No. (chord)	0.7×10^5
Freestream turbulence intensity	2.3 percent
Boundary layer thickness	14.4 mm
Displacement thickness	1.61 mm
Momentum thickness	1.23 mm

Table 4 Cycle-averaged inlet conditions for unsteady flow

Free-stream velocity	0.450 m/s
Reynolds No. (chord)	0.7×10^5
Boundary layer thickness	15.1 mm
Displacement thickness	1.24 mm
Momentum thickness	1.11 mm
Rotor velocity	0.59 m/s
Flow coefficient	0.76
Reduced frequency	4.7

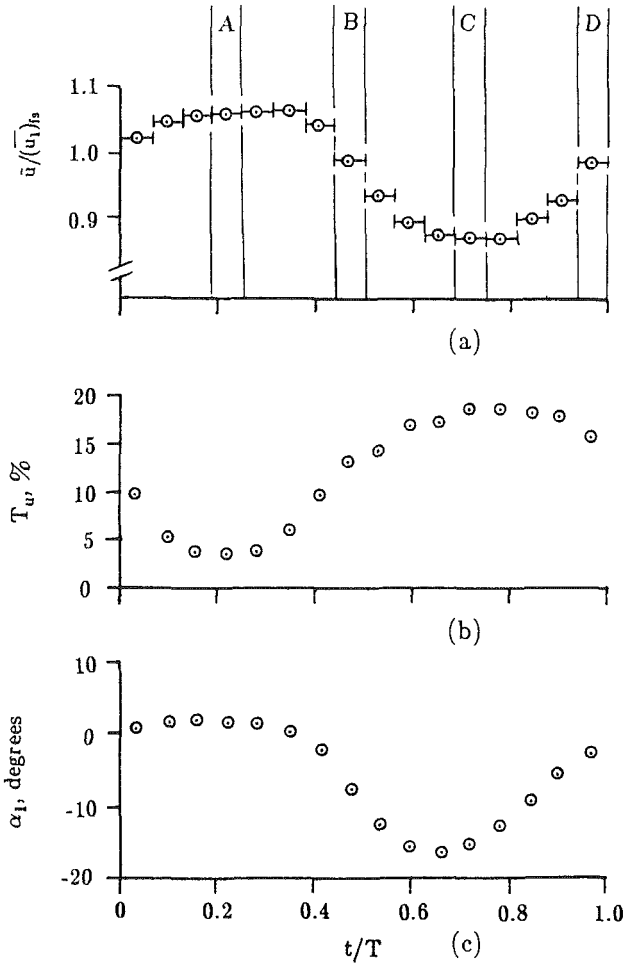

Fig. 4 Phase-averaged rotor-wake data at inlet midspan location; (*a*) axial velocity, (*b*) turbulence intensity, (*c*) flow angle.

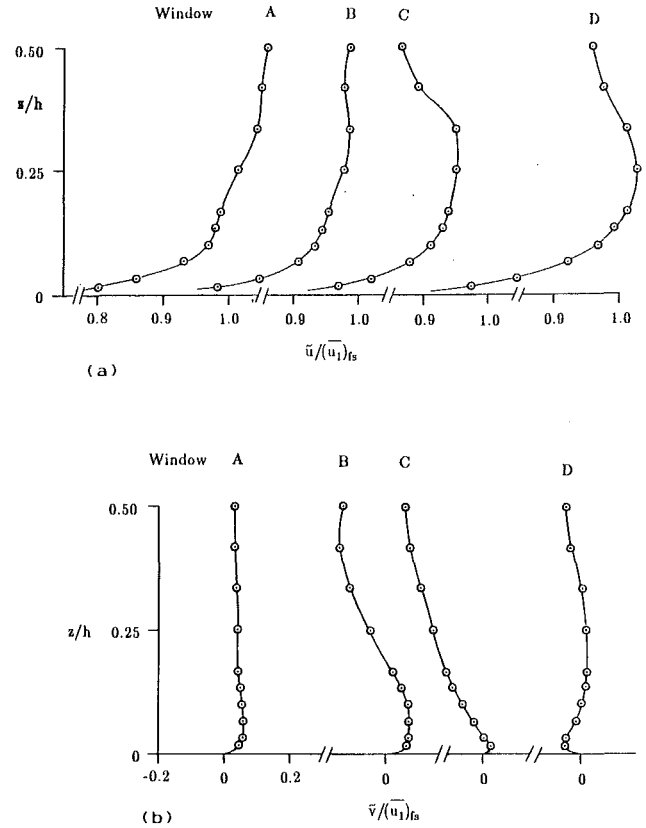

Fig. 5 Phase-averaged inlet boundary layers; (*a*) axial velocity profiles; (*b*) tangential velocity profiles

midspan areas show near zero vorticity, as would be expected, lending credibility to the method for calculating vorticity from the velocity data.

Figure 3 also contains a plot of the isocontours of turbulent kinetic energy normalized with the square of the inlet free-stream velocity. Turbulence levels less than 0.01 are seen in the majority of the passage. This is a small increase over the inlet free-stream level. The highest turbulence occurred in the suction side wake, where the contours are clearly spaced and nearly vertical. The peak value of the normalized turbulent kinetic energy is 0.166, located in the center of the blade wake approximately $0.18h$ from the endwall. The plot also shows a large bulge in the contour lines in the suction side endwall corner, indicating increased turbulence levels associated with the passage vortex.

Unsteady Flow. Flow visualization was performed at the exit of the blade passage using air bubble tracer particles and a high-speed video system. During that portion of the cycle when the flow was unaffected by the rotor wake, passage vortices, similar in size to those in steady flow, were observed. As the wake fluid passed through the exit plane, a strong crossflow toward the suction side was observed near midspan. This fluid, as it neared the suction surface, was turned toward the endwalls developing two counterrotating areas of rotation in the central portion of the passage. While the effect of the wake on the passage vortices was difficult to assess, it appeared as though they were destroyed or, at least, decreased in size and very distorted.

The cycle-averaged inlet axial velocity profile, measured in unsteady flow, was nearly identical to the steady flow profile. The average free-stream velocity was 0.450 m/s and the average boundary layer thickness was 15.1 mm. The time-averaged inlet conditions for unsteady flow are summarized in Table 4. Figure 4 shows the phase-averaged rotor-wake data at the inlet midspan location. A 20 percent velocity defect is observed in the wake at 71 percent of the rotor period. Figure 4(*b*) shows that the turbulence intensity increases from 4 percent in the free stream to 17 percent in the wake. The variation in the inlet flow angle as the rotor wake passes is plotted in Fig. 4(*c*). The free-stream fluid shows an inlet angle of 1.5 deg, while at the center of the wake the flow angle is -16.5 deg. Using Fig. 4(*a*), four time windows, A–D, were chosen, as indicated in the figure, for additional measurements. The windows are equally spaced at 1/4 period intervals and correspond to the free stream, wake leading edge, wake center, and wake trailing edge.

Phase-averaged boundary layer profiles at the cascade inlet are plotted in Fig. 5 for each of the time windows. The axial velocities indicate that the near wall region is much less affected by the rotor wake than is the free stream. In examining the tangential velocity profiles, the wake fluid should be marked by significant negative velocities since this is the direction of the rotor travel. The profile for window A shows a near constant and slightly positive v velocity. This time window is clearly in the freestream. The profile for window B indicates that the fluid from the endwall to $z=0.2h$ is in the free stream, and the fluid from $0.2h$ to midspan is in the rotor wake. This suggests that the leading edge of the wake is bowed at the midspan toward the $-y$ direction. The profile for window C indicates that the measurements were entirely within the rotor wake, with the exception of the first data point at $0.01h$. At window D, the tangential velocities have returned to near-zero levels. The bowing of the rotor wake would explain the inflection in the axial velocity profile of window A, and the unexpectedly high velocity in window D at $0.25h$. Because of the bowing, the peak in the free-stream velocity at $0.25h$ has shifted from window A to window D.

A phase-averaged profile of the rotor wake was also obtained at the exit of the passage (plane 2, midspan, 40 percent pitch from the suction side). A second set of four time windows was chosen at $t/T=0.34$, 0.59, 0.84, and 0.09 to correspond to the free stream, wake leading edge, wake center, and wake trailing edge.

The isocontours of total velocity magnitude are shown in the first column for each time window in Fig. 6. The results are quite similar to each other and to the steady flow case with the lowest velocity concentrated in a small area near the center of the suction side blade wake. The minimum velocity and the spanwise location of the area varied slightly. This low-velocity region is probably due to convection of low-momentum fluid from the endwall corner by the passage vortex. In time window B, when the spanwise velocities along the suction surface due to the passage vortex are the greatest, the velocity defect in this area is also a maximum.

Secondary velocity vectors for each of the four time windows are shown in the second column. The flow pattern for time window A is similar to the steady flow pattern. There is clearly an area of circulation in the endwall region due to the passage vortex, which appears to be slightly farther away from the suction side of the passage. The velocity vectors for the time window B show that the passage vortex has moved toward the suction side of the passage, to the approximate position observed in steady flow. The pressure side of the vortex, however, appears to be flattened out, with increased velocities toward the pressure side of the passage at the top of the vortex. Some of this fluid, as it nears the pressure side, is turned toward the midspan region, where there is significant flow back toward the suction side, forming a large area of circulation opposite to that of the passage vortex. In time window C, as the center of the wake passes through the measurement plane, the velocity vectors show a more pronounced area of rotation between midspan and the endwall region. This causes the endwall region to become distorted. It is pinched down near the middle of the passage, dividing the passage vortex into two separate

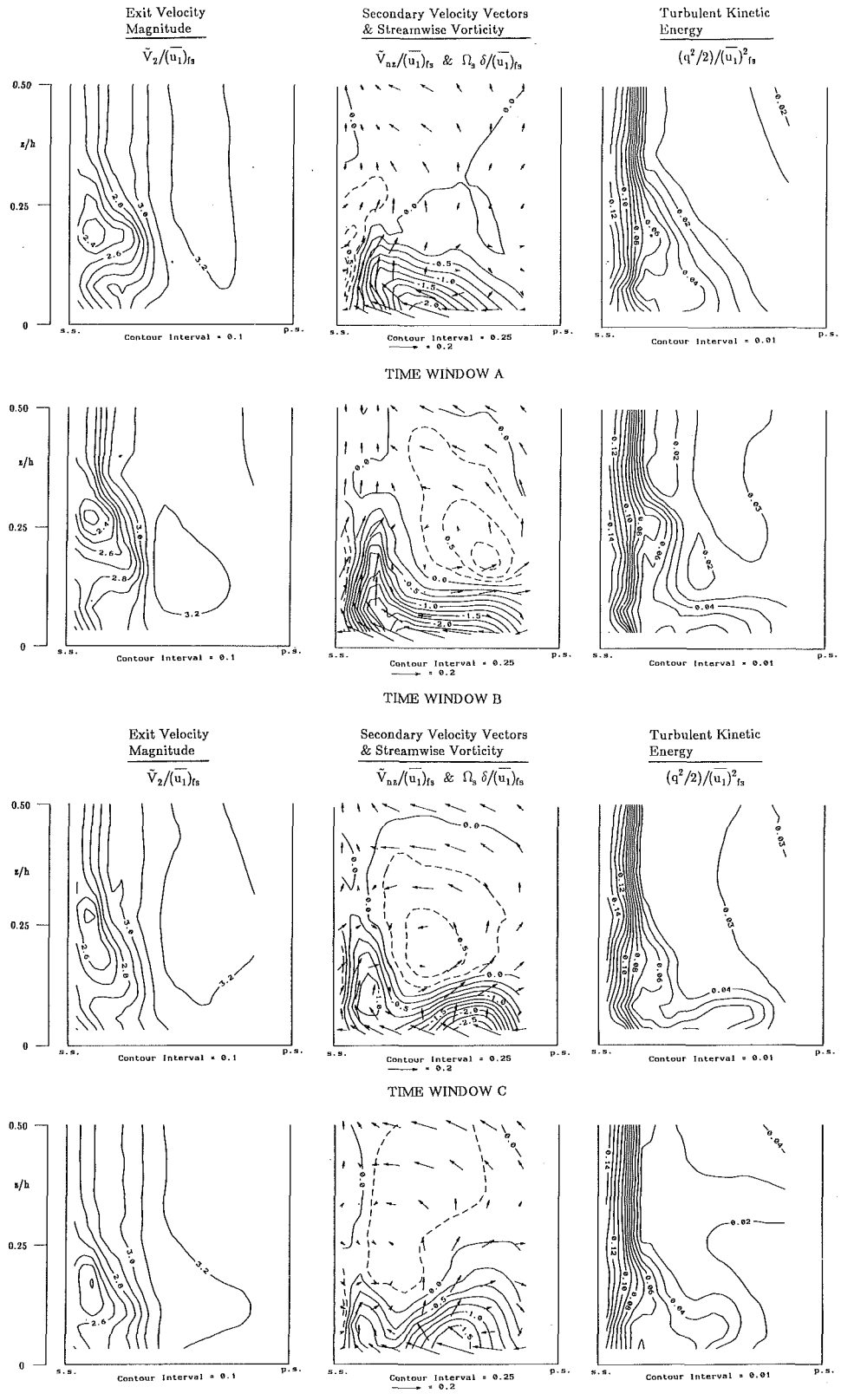

Fig. 6 Unsteady flow exit data

areas, each with lower secondary velocities. The circulation caused by the rotor wake is still clear at time window D. However, the velocities have decreased slightly and the center of rotation has moved farther toward the suction side of the passage. In the endwall region, the velocities of the fluid in the suction side corner are reduced even further and show only slight evidence of rotation. However, in the pressure side of the endwall region, the rotation (in the same sense as the original passage vortex) has become more pronounced, with increased velocities over those of window C.

Isocontours of streamwise vorticity are shown on the same plots as the secondary velocity vectors. The plot for time win-

dow A show a negative peak in the normalized vorticity of −2.48 at the endwall, near the center of the passage. This corresponds to the passage vortex location as indicated by the secondary velocity vectors. There is also a positive peak in the vorticity of 0.92 in the suction side blade wake. This vorticity of the stator wake is seen in all of the time windows, though the magnitude of the peak varies. The majority of the passage, however, has near-zero vorticity. At time window B, the negative peak in vorticity is now situated in the suction time endwall corner and has a maximum value of −2.58. This structure is nearly identical to that seen in the steady flow case. The reason that this occurs in window B rather than window A is because of the rotor wake bowing at the exit of the cascade as reported by Hodson (1985b) and Joslyn et al. (1986). Although window A corresponds to the free-stream fluid at the center of the passage, the suction side of the passage is still affected by the previous rotor wake. While window B is associated with the rotor wake leading edge, the suction side of the passage contains the free-stream fluid. It is obvious from the contour plot that the area outside of the suction side endwall region is very different from the steady flow case. There is now a large area of positive vorticity, with a peak value of 0.83, that has developed between the endwall region and midspan. At time window C, this area of positive vorticity has moved to the center of the passage and appears to be distorting the passage vortex. There are now two negative peaks of vorticity in the endwall region. The peak in the suction side corner has dropped to −1.21, while the one at the endwall, toward the pressure side of the passage, is still −2.62. The large area of positive vorticity is still present during time window D, though it has moved farther toward the suction side of the passage. The negative vorticity contours in the endwall region are similar in appearance to those of window C, but both peaks show decreased vorticity. The peak in the suction side corner has a value of −0.87 and the one nearer the pressure side is −1.98.

The third plot for each time window shows the isocontours of turbulent kinetic energy (per unit mass). A large area of the passage at time window A is low-turbulence free-stream fluid with a normalized turbulent kinetic energy level less than 0.01. This is the same level of turbulence seen in the free stream of the steady flow case. High turbulence levels are indicated in the suction side blade wake. This is typical for all time windows in unsteady flow, though the magnitude of the peak varies slightly. The vertical contour lines of the suction side blade wake protrude farther into the passage near the endwall, indicating increased turbulence levels in the passage vortex. At time window B, as the rotor-wake fluid begins to enter the measurement plane, the area at the center of the passage shows turbulence levels three times that of the free-stream fluid in the previous time window. Still, small areas of lower turbulence remain. The plot for time window C shows a large area of fairly uniform turbulence at the center of the passage. This turbulence level is three to four times that of the free stream in window A. The highest turbulent kinetic energy level in the blade wake is reached at time window C with a value of 0.157. As the trailing edge of the rotor-wake fluid comes through the measurement plane (time window D) the center of the passage becomes less uniform. The upper portion remains at levels of 0.03 to 0.04, while the lower portion near the pressure side has dropped to 0.02.

Complete data sets as well as a more comprehensive description of the experimental techniques and instrumentation are given by Hebert (1988).

Conclusions

Velocity measurements in steady flow confirmed the presence of a strong passage vortex, with a corresponding negative peak in streamwise vorticity, in the suction side endwall corner of the passage. The lowest velocity fluid at the exit was contained in a small region within the suction side blade wake near the top of the passage vortex. Low-momentum fluid from the endwall corner region was convected to this location by the passage vortex. The highest turbulence levels were also observed in the suction side blade wake. The turbulent kinetic energy within the passage vortex was approximately 35 percent of the maximum in the blade wake, while the turbulence in the free stream was only 5 percent of the maximum.

In unsteady flow, the passage vortex was reduced in strength and significantly distorted by the passing of the rotor wake. When the suction side of the passage was in the free stream, the passage vortex structure was very similar to that of the steady flow case, reaching approximately 90 percent of the steady flow streamwise vorticity. At the same time, the leading edge of the rotor wake entered the measurement plane in the center of the passage creating two large counterrotating areas of rotation, one on each side of the midspan. As this area of positive vorticity (in the lower half of the passage) moved across the passage, the endwall region was pinched down near the midpitch location dividing into two areas of negative vorticity. The vorticity in the suction side of the endwall region decreased dramatically, while the vorticity in the pressure side region decreased only to about 77 percent of the original peak. The vorticity in the suction side of the endwall region continued to decrease while the pressure side began to increase in strength and move toward the suction side of the passage to repeat the cycle.

By traversing the wake-generating rods linearly across the inlet to the cascade, the distribution of the wake velocity, relative to the free stream, was symmetric in the spanwise direction, with its peak at midspan. This caused the development of two counterrotating areas of circulation. However, in an annular turbine the velocity distribution in the wake would not be symmetric. Instead, the peak would occur near the outer casing because of the higher rotor speed at the tip. This would probably cause the development of only one large area of circulation in the stator passage, with the same rotational sense as the tip endwall passage vortex. This might cause the vortex and its low-momentum fluid to move away from the casing endwall, producing a high loss region near the midspan as reported by Sharma et al. (1985). At the same time, the hub endwall passage vortex, whose vorticity is opposite to the rotor-wake rotation, would be distorted and weakened.

Turbulent kinetic energy levels in the suction side stator blade wake and endwall corner region remained fairly constant throughout the cycle at levels comparable to those in steady flow. Turbulence levels in the rest of the passage, however, closely followed the periodically varying levels measured at the inlet to the cascade.

Acknowledgments

The authors would like to thank Prof. Sanford Fleeter for his guidance and suggestions. The support of this work by the Air Force Office of Scientific Research through the Air Force Research in Aero-Propulsion Technology program and by NASA Lewis Research Center is also gratefully acknowledged. A portion of the instrumentation was acquired with an Office of Naval Research Grant No. N00014-87-G-0040.

References

Bardon, M. F., Moffat, W. C., and Randall, J. L., 1975, "Secondary Flow Effects on Gas Exit Angles in Rectilinear Cascades," ASME *Journal of Engineering for Power*, Vol. 97, pp. 93–100.

Binder, A., Förster, W., Kruse, H., and Rogge, H., 1985, "An Experimental Investigation Into the Effect of Wakes on the Unsteady Turbine Rotor Flow,"

ASME *Journal of Engineering for Gas Turbines and Power*, Vol. 107, pp. 458–466.

Donohue, G. L., McLaughlin, D. K., and Tiederman, W. G., 1972, "Turbulence Measurements With a Laser Anemometer Measuring Individual Realizations," *Physics of Fluids*, Vol. 15, No. 11, pp. 1920–1926.

Doorly, D. J., and Oldfield, M. L. G., 1985, "Simulation of Wake Passing in a Stationary Turbine Rotor Cascade," AIAA *Journal of Propulsion*, Vol. 1, pp. 316–318.

Dring, R. P., Joslyn, H. D., Hardin, L. W., and Wagner, J. H., 1982, "Turbine Rotor–Stator Interaction," ASME *Journal of Engineering for Power*, Vol. 104, pp. 729–742.

Gregory-Smith, D. G., 1982, "Secondary Flows and Losses in Axial Flow Turbines," ASME *Journal of Engineering for Power*, Vol. 104, pp. 819–822.

Hebert, G. J., 1988, "Comparison of Steady and Unsteady Secondary Flows in a Turbine Stator Cascade," MSME Thesis, Purdue University, West Lafayette, IN.

Hodson, H. P., 1985a, "An Inviscid Blade-to-Blade Prediction of a Wake-Generated Unsteady Flow," ASME *Journal of Engineering for Gas Turbines and Power*, Vol. 107, pp. 337–344.

Hodson, H. P., 1985b, "Measurements of Wake-Generated Unsteadiness in the Rotor Passages of Axial Flow Turbines," ASME *Journal of Engineering for Gas Turbines and Power*, Vol. 107, pp. 467–476.

Hylton, L. D., Mihelc, M. S., Turner, E. R., Nealy, D. A., and York, R. E., 1983, "Analytical and Experimental Evaluation of the Heat Transfer Distribution Over the Surfaces of Turbine Vanes," NASA CR-168015, May.

Joslyn, H. D., Caspar, J. R., and Dring, R. P., 1986, "Inviscid Modeling of Turbomachinery Wake Transport," AIAA *Journal of Propulsion*, Vol. 2, No. 2, pp. 175–180.

Joslyn, H. D., Dring, R. P., and Sharma, O. P., 1983, "Unsteady Three-Dimensional Turbine Aerodynamics," ASME *Journal of Engineering for Power*, Vol. 105, pp. 322–331.

Sharma, O. P., Butler, T. L., Joslyn, H. D., and Dring, R. P., 1985, "Three-Dimensional Unsteady Flow in an Axial Flow Turbine," AIAA *Journal of Propulsion*, Vol. 1, pp. 29–38.

Inlet Skew and the Growth of Secondary Losses and Vorticity in a Turbine Cascade

J. A. Walsh
Logica Space and Defense Systems Ltd.
London, W1A 4SE United Kingdom

D. G. Gregory-Smith
School of Engineering and Applied Science,
University of Durham,
Durham, DH1 3LE United Kingdom

This paper presents results of an experimental investigation into the effects of inlet skew on the flow field of a large-scale axial flow turbine cascade. The results are presented in terms of the development of the streamwise vorticity since, in classical terms, the streamwise vorticity generates the transverse velocity components that cause the generation of the secondary losses. Inlet skew is shown to have a profound effect on the distribution and magnitude of the generated losses. A number of correlations for the secondary losses are compared with the measured values and it is shown that the correlations are not adequate for accurate loss prediction purposes.

Introduction

The term "secondary flow" is used to describe transverse velocity components that are produced when a nonuniform flow is turned, such as in the case of a shear flow through a turbomachine blade row. In the classical sense secondary flows may be thought of as being produced by the streamwise vorticity in the flow field, which is itself produced as a result of the turning of the inlet vorticity vector through the blade passage. The resulting so-called secondary losses may be a major proportion of the total losses that are generated within the blade row of a low aspect ratio turbine. Downstream of the blade row the streamwise vorticity is assumed by the classical theory to be made up of three components; the distributed secondary vorticity that generates the secondary velocities in the blade passage, and the shed vorticities (trailing filament and trailing shed) that appear in the blade wake. It is important to link the quantitative development of the streamwise vorticity with the classical results so that the use of the results and the theory can be qualified.

A complete review of the current understanding of experimental secondary flows has been presented by Sieverding (1985). The inlet boundary layer is currently perceived to play an important part in the initiation of the loss generation process in a blade row. Although there is a large literature concerning the effects of inlet boundary layer thickness (e.g., Gregory-Smith and Graves, 1983; Chen and Dixon, 1986), there is very little reported work on the effects of inlet skew. Inlet skew is introduced into the flow field of a turbomachine as a result of the flow field undergoing a change in frame of reference between the stator and the rotor blades.

Bindon (1979, 1980) found that inlet skew reduced the losses in an annular cascade of low aspect ratio, low turning angle turbine blades. However the geometry of his cascade means that is is difficult to judge the effect of skew alone. In particular the rotating hub extended to a slot immediately upstream of the leading edges of the blades; this slot was found to have an apparently larger effect than the skew by effectively sucking off the inlet boundary layer before the fluid reached the blade row. Klein (1966) also used an annular cascade (of steam turbine blades with a very thick leading edge) but found that the losses increased in the presence of inlet skew. Boletis et al. (1983) and Boletis (1984) presented the results of a major investigation of the flow field in annular cascades of nozzle blades. Two cases of inlet skew were investigated by having different upstream conditions. For the first case the inlet conditions were produced using a rotating hub and for the second case a complete stage. It was found that the first case was not a good model of the flow downstream of a complete stage. This was not a surprising result since the flow downstream of a stage will be highly unsteady and the flow field at inlet to the blade row would be very complex. However it was found that inlet skew has a significant effect, in particular reinforcing the suction surface endwall flows.

There are three studies reported that have used linear cascades to study the effects of skew. Moore and Richardson (1957) used air jets to produce a cross flow profile to simulate the skewing effect in compressors. Although they were unable to report on the effect of inlet skew on the secondary losses (no measurements were made in the exit plane) they did find that the skewed case showed reduced blade pressure forces near the endwall. Carrick (1977) investigated the effect of inlet skew in a cascade of turbine impulse blades using a moving belt upstream of the cascade to simulate the skew. It was shown that the secondary flows were intensified and that the secondary losses were increased in the presence of skew. Kingcombe (1976), using a Beltrami flow at inlet to a similar cascade, found that for very low levels of skew, classical secondary flow theory could be adapted to describe the behavior of the flow through the cascade adequately.

In order to use experimental data obtained from cascades in the design process for turbomachinery, a number of correlations for loss generation in blade rows have been developed.

Contributed by the International Gas Turbine Institute and presented at the 34th International Gas Turbine and Aeroengine Congress and Exhibition, Toronto, Ontario, Canada, June 4–8, 1989. Manuscript received at ASME Headquarters January 13, 1989. Paper No. 89-GT-65.

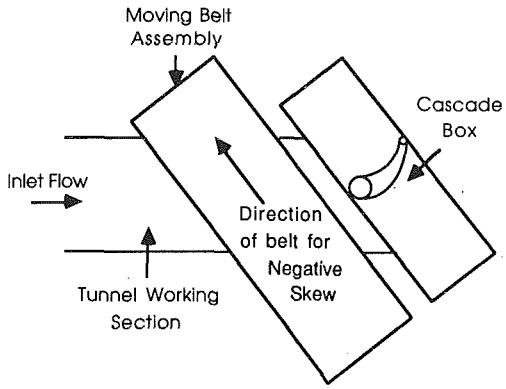

Fig. 1 Skewed boundary layer rig

Methods of correlating the secondary losses were reviewed by Dunham (1970) who found that using the Ainley and Mathieson (1951) blade loading parameter gave the best results. More recently Dunham and Came (1970), Came (1973), Morris and Hoare (1975), and Chen and Dixon (1986) have all provided amended forms of the basic equation. Numerous other correlations have been critically reviewed by Hirsh and Denton (1981) and by Sieverding (1984).

The complexity of the fluid flow processes in a turbomachine means that detailed information can often only be obtained by studying components in isolation so that the test conditions can be carefully controlled. The linear cascade can be used to investigate blade row fluid phenomena and loss generation mechanisms. Detailed measurements can be made relatively easily in the blade passage without the complexities of the radial pressure gradients that are found in annular cascades.

A program of work is currently under way at Durham University with the aim of obtaining detailed experimental data to aid the understanding of the fundamental processes associated with the generation of secondary flows and losses in axial flow turbines. It is hoped that such detailed data will provide a good test case for the validation and further development of computer codes for use in the design process of turbomachinery. Early results of the investigation into the effects of inlet skew have been presented by Walsh and Gregory-Smith (1987). This paper presents further results for inlet skew and examines the validity of some commonly used correlations.

Apparatus

The experimental measurements were carried out in a low-speed linear cascade. A moving belt was placed upstream of the blades, with its downstream edge placed 15 percent of an axial chord from the leading edges of the blades, to simulate the effect of skew. The belt was 800 mm wide and ran on two pulleys that had a maximum diameter of 150 mm on the crown. The upper pulley was driven by a 4-kW thyristor-controlled motor via a timing belt to give the required pulley speed. The lower pulley was mounted onto sliding adjusters to allow the belt to be tensioned. The belt was mounted so that it formed one endwall of the working section of the wind tunnel upstream of the cascade box (Fig. 1). Upstream of the belt there was a short length of false wall to allow the boundary layer to develop fully before reaching the belt.

Table 1 Cascade design data

Flow Inlet Angle	42.75°
Blade Exit Angle	-68.60°
Blade Chord	224 mm
Blade Axial Chord	181 mm
Blade Span	400mm
Blade Pitch	191mm
Zweifel Loading Coefficient	0.97
Cascade Reynolds Number (based on Chord and Exit Velocity)	4×10^5

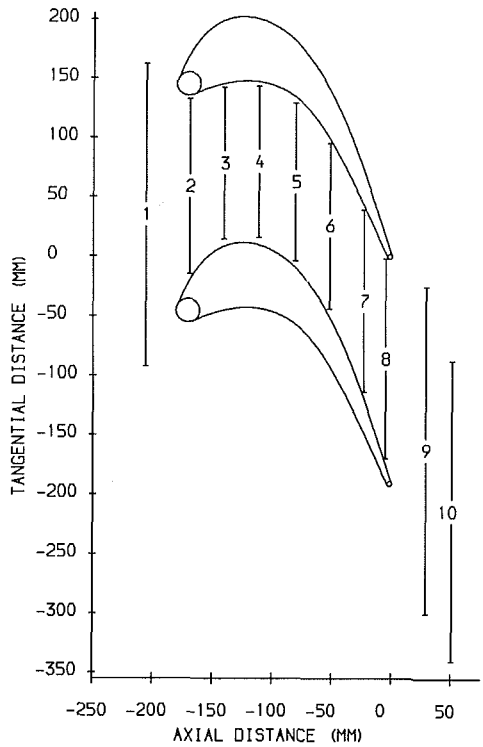

Fig. 2 Cascade and traverse slots

The blade profile that was used was based on the root section of a high-turning turbine blade. The blade profile was modified, using a quasi-three-dimensional streamline curvature blade design program, to minimize the effects of the large suction surface diffusion reported for a similar blade by Gregory-Smith et al. (1988). The cascade design and construction are described in detail by Walsh (1987); the main geometric parameters are summarized in Table 1.

Experimental Results

The direction and belt speed required to produce the skewing effect were determined by reference to a typical nozzle flow exit angle of 70 deg. Measurements were made for three cases of inlet skew: negative (corresponding to the flow in a turbine without secondary flows in an upstream nozzle), colateral (zero

Nomenclature

C_{ax} = axial chord
H = boundary layer shape factor
K = relative effect of skew
n = boundary layer power law index
s = pitch
Y = gross secondary loss
α = rotor air angle
β = stator air angle
δ = boundary layer thickness
δ^* = displacement thickness
ζ_s = streamwise vorticity
θ = momentum thickness

belt speed corresponding to the usual cascade situation), and positive (partially simulating the effect of secondary flows in an upstream nozzle but without the change in frame of reference). The cascade flow field was traversed using three and five-hole pressure sensing probes of the cobra type. The measurements were made at slots 1, 3, 5, 8, and 10, whose axial locations can be seen from Fig. 2. The measurements were recorded using a microcomputer and then analyzed using the university's mainframe computer.

Area plots of the total pressure loss coefficient and the secondary velocity vectors have been presented in an earlier paper (Walsh and Gregory-Smith, 1987). This paper presents results for the development of the streamwise vorticity through the cascade. Classical secondary flow theory uses the distribution of the streamwise vorticity to generate the transverse velocity components for the cascade and thereby the secondary losses. The experimental values of the streamwise vorticity have been derived using the method described by Gregory-Smith et al. (1988). They showed that by using the incompressible Helmholtz equation, the axial and tangential components of the vorticity vector (required for the streamwise vorticity) can be found from the gradients of velocity and stagnation pressure on a given traverse plane. We have used the same approach of fitting a least-squares bi-cubic spline surface to the data and calculating the required gradients from the resulting surface. The values of vorticity obtained were nondimensionalized by the upstream velocity and the blade pitch. Negative streamwise vorticity is taken in the sense of the passage vortex in the cascade.

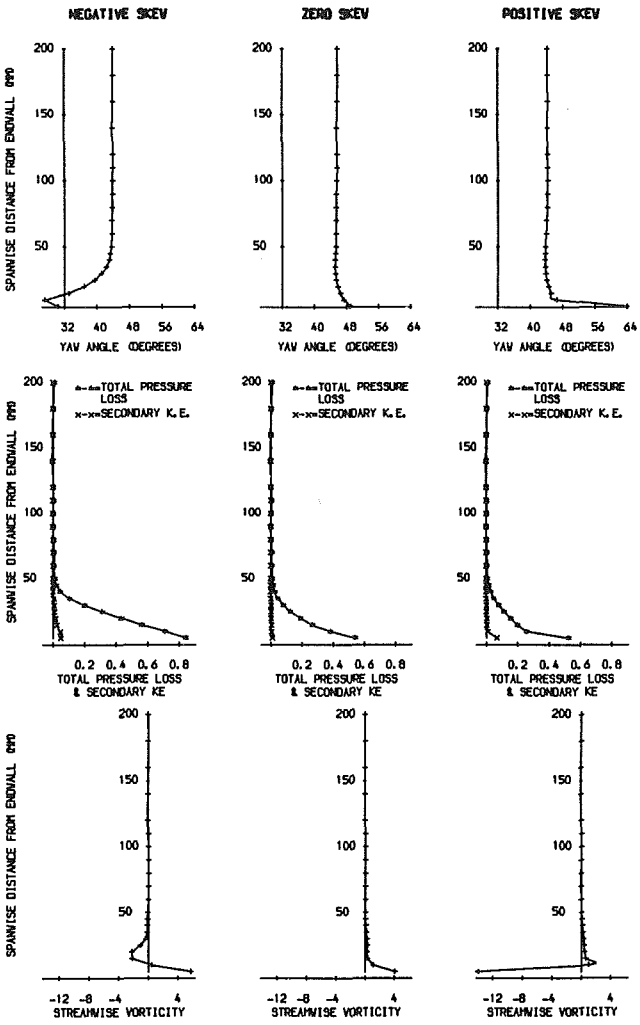

Fig. 3 Pitch-averaged results for slot 1

Inlet Flow. The inlet conditions for the cascade are obtained by pitch averaging the results for slot 1 (Fig. 3). The loss coefficients are defined with respect to the inlet dynamic pressure and are for the cascade frame of reference. Table 2 shows the boundary layer parameters; the exponent n was obtained from a logarithmic plot and the values of θ and δ^* from integration. The boundary layer thicknesses are defined relative to the moving belt frame of reference in the streamwise direction, which is assumed to be the same as the midspan flow direction. This is a valid assumption since the secondary flows appear to have little effect on the midspan flows. For each of the skew cases an effective velocity profile is deduced from the pitch-averaged total pressure loss results by assuming

Table 2 Inlet boundary layer data

	Inlet Skew Type		
	Negative	Colateral	Positive
n	0.153	0.147	0.126
δ	43.3	39.6	41.3
δ^*	5.9	6.0	5.7
θ	4.6	3.6	3.5
H	1.3	1.7	1.6
$\bar{Y}$	0.077	0.041	0.031

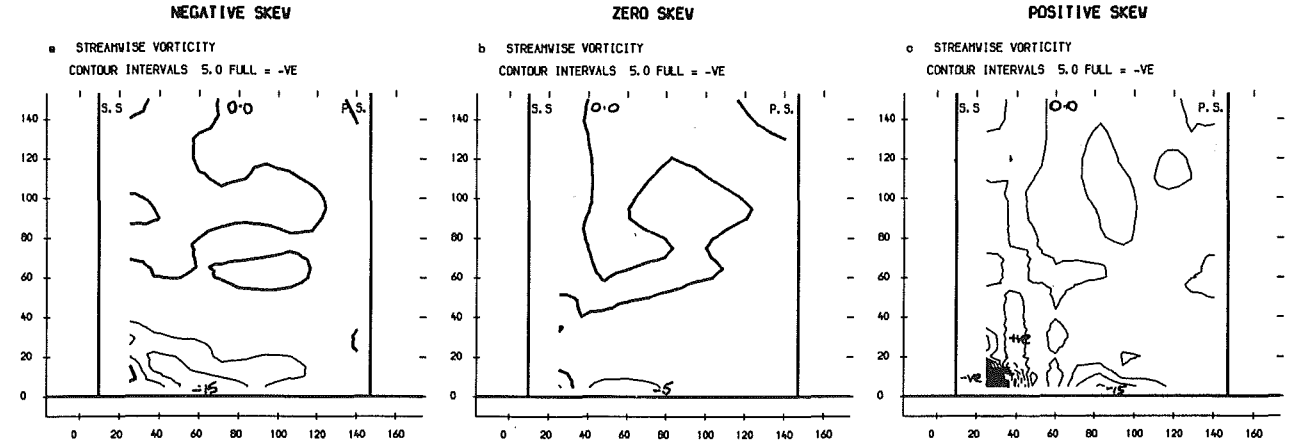

Fig. 4 Area plots for slot 3

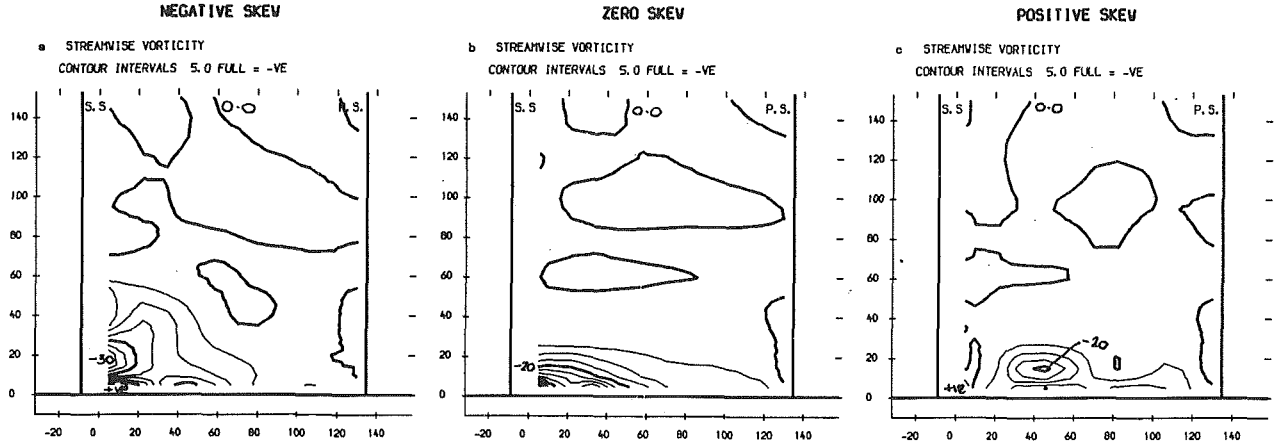

Fig. 5 Area plots for slot 5

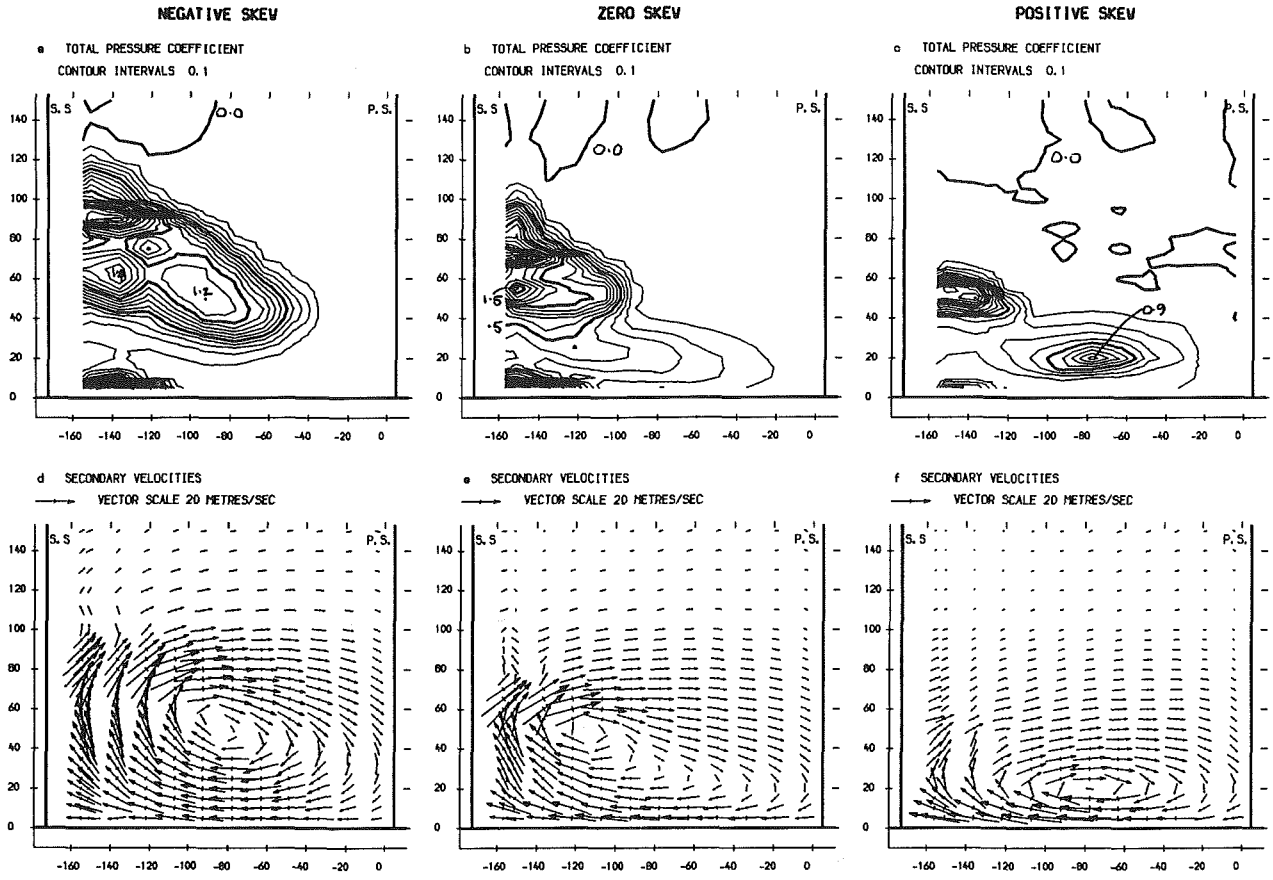

Fig. 6 Area plots for slot 8

that the static pressure is constant in the working section of the tunnel, upstream of the cascade.

Through-Passage Flow. The results for slot 3, presented in Fig. 4, show the major portion of the axial plane to have a zero value of streamwise vorticity for all three cases of skew. In the colateral case there is a small amount of negative vorticity on the endwall, and also a small peak close to the suction surface of the blade due to the presence of the pressure-side leg of the horseshoe vortex. For the case of negative skew, the negative vorticity is spread along the whole of the endwall and also up to the lower part of the suction surface of the blade to about 40 mm in the spanwise direction. The case of positive skew shows an important region of negative skew close to the endwall that is associated with the pressure-side leg of the horseshoe vortex.

The results for slot 5 are presented in Fig. 5. The main feature of the results is the development of the passage vortex. The negative skew case shows a more rapid development of the flow field than either of the other two cases. In the colateral case the vorticity appears to be concentrated on the endwall rather than on the suction surface of the blade, as in the case of negative skew. In the case of positive skew the flow field shows a concentration of vorticity remaining in the center of the passage. This appears to result from a combination of the pressure-side leg of the horseshoe vortex and a small passage vortex.

The results for slot 8, Figs. 6 and 7, include area plots of total pressure loss contours and secondary velocity vectors. It is appropriate to present these additional results since slot 8 is very close to the exit plane of the cascade and the effects of inlet skew on flow field are shown very clearly. The total

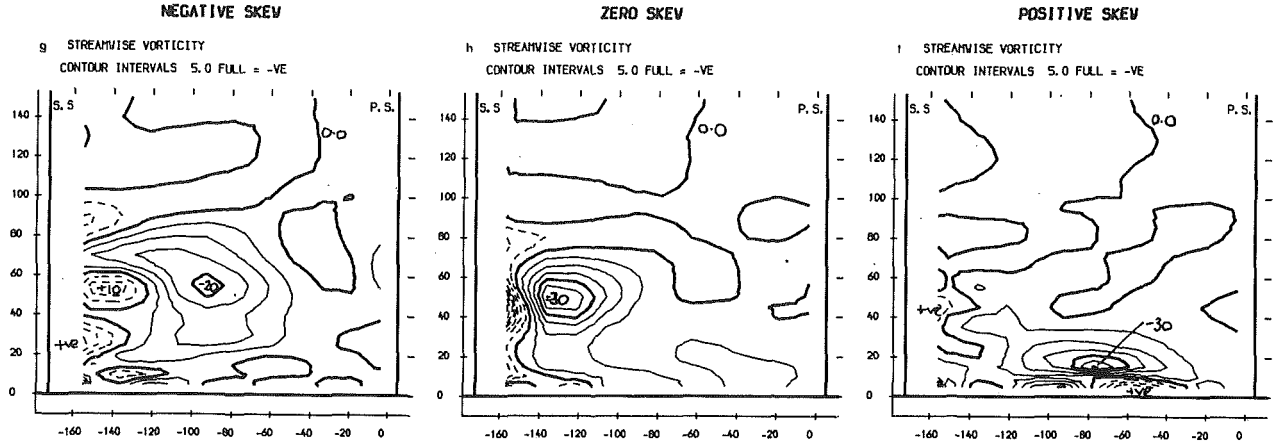

Fig. 7 Area plots for slot 8

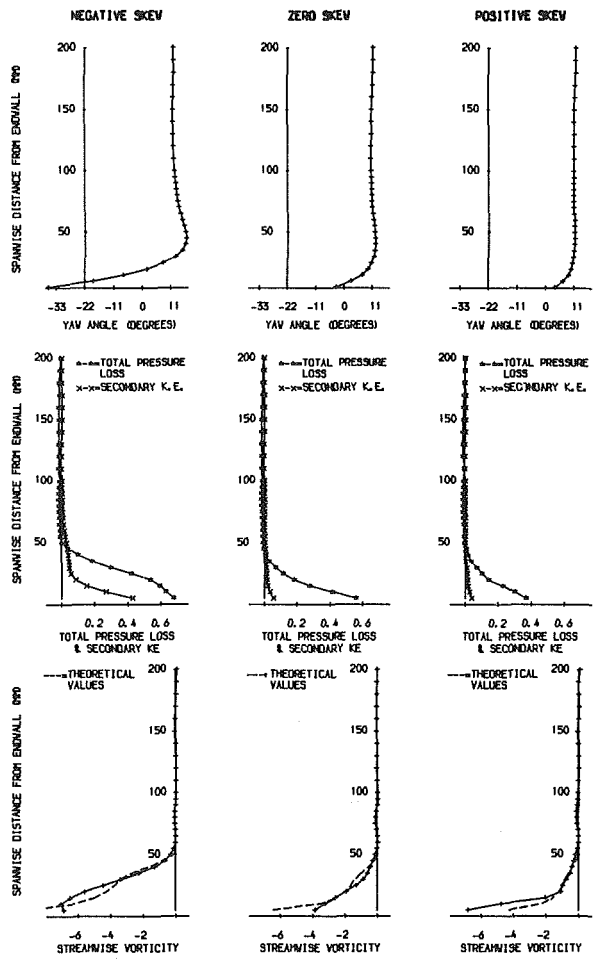

Fig. 8 Pitch-averaged results for slot 3

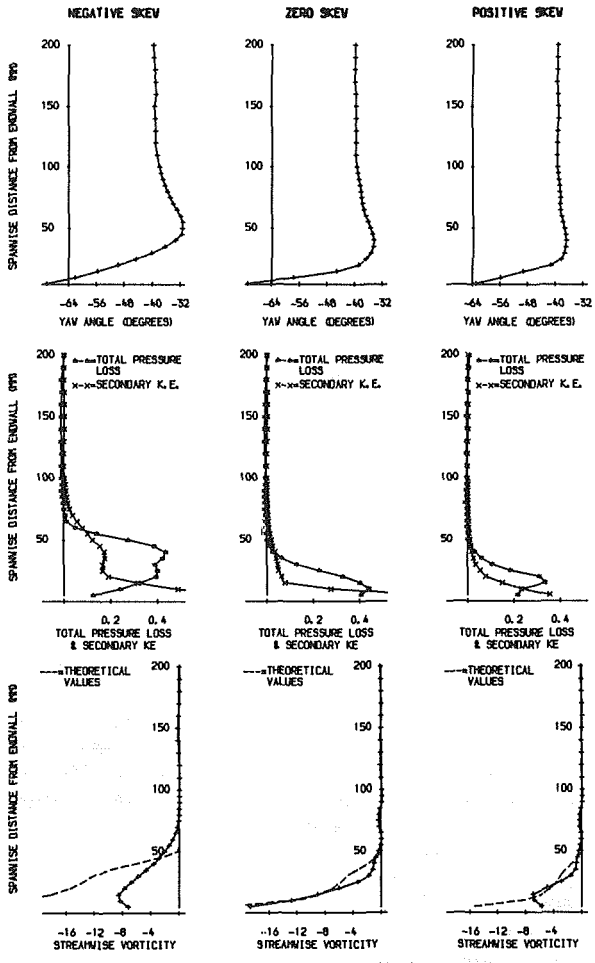

Fig. 9 Pitch-averaged results for slot 5

pressure loss contours (Fig. 6) show the pressure surface side of the passage to be covered by low loss free-stream fluid. In the colateral case three regions of loss can be identified. Close to the endwall is a region of loss that is due to the presence of the endwall countervortex; this vortex is formed as a result of the rolling up of the new endwall boundary layer that is formed and grows downstream of the cross-passage separation line that marks the movement of the pressure-side leg of the horseshoe vortex and the passage vortex. The second region of loss is farther from the endwall and develops as a consequence of the action of the passage vortex. These contours show the endwall flow being swept into this loss core. Further still from the endwall is another region, attached to the passage vortex region, that is caused by the presence of the suction-side leg of the horseshoe vortex as it travels up the suction surface of the blade. In the negative skew case a similar, but more developed, picture of the flow field is obtained. The loss core associated with the passage vortex has grown by sweeping most of the endwall flow into the loss core. As a consequence the loss core has taken on a distended shape and extends across the passage toward the pressure surface side. This region appears to have two peaks giving the impression of the loss core breaking into two, with one half staying close to the suction surface of the blade and the other moving out into the passage.

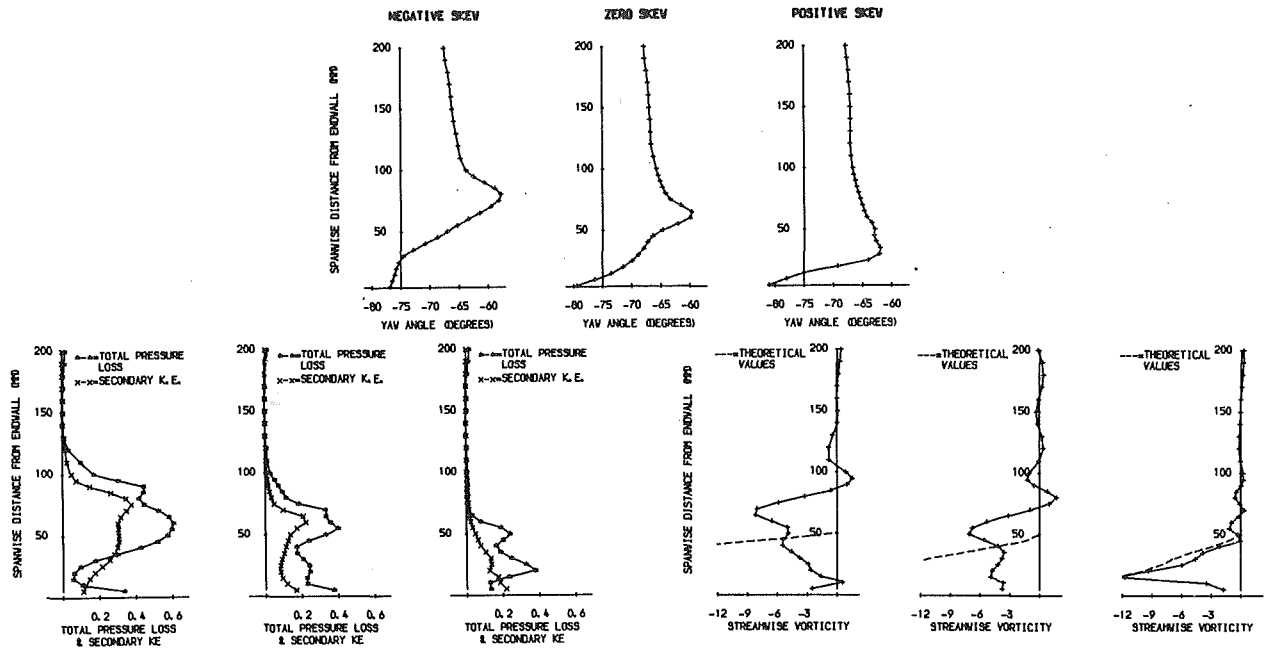

Fig. 10 Pitch-averaged results for slot 8

As in the colateral case there is a region of loss close to the suction surface of the blade attached to the midspan side of the loss core associated with the passage vortex. Due to the absence of the suction-side leg of the horseshoe vortex in this case (Walsh, 1987), this region of loss is associated with a region of positive vorticity that appears on the midspan side of the passage vortex separation line. In the case of positive skew the two regions of high total pressure loss seem to be almost separate. Close to the endwall there is a region of loss associated with the endwall countervortex, but at a lower magnitude than detected in the other skew cases. There is a loss core close to the suction surface of the blade that is associated with the separation line marking the edge of the passage vortex. There is also a loss core close to the midpitch position, which is associated with the combined passage vortex and pressure-side leg of the horseshoe vortex. The secondary velocity vectors appear to show fully developed passage vortices in all three skew cases that have expanded to their boundaries in the pitchwise direction. In the positive skew case the vectors show the effect of this mid-pitch vortex structure extending to the suction surface side of the passage. The passage vortex is closest to the suction surface side of the passage in the colateral case. In the case of negative skew the movement of the passage vortex away from the suction surface side is a result of the increased size of the passage vortex. The distance of the passage vortex from the endwall is very similar for both the colateral and negative skew cases. In the case of positive skew the center of the passage vortex is significantly closer to the endwall. The area plots of streamwise vorticity (Fig. 7) show that in all three skew cases the flow field is dominated by the presence of strong streamwise vorticity. The passage vortex is marked in the colateral and negative skew cases by the contours of negative vorticity. In the case of positive skew the contours of the negative vorticity remain in the center of the passage and are concentrated around the combined pressure-side leg of the horseshoe vortex and the passage vortex. The region of positive vorticity close to the suction surface of the blade corresponds to the separation line that marks the edge of the passage vortex. This region is also present in the colateral case where there are additional regions of positive vorticity. These regions mark the presence of the countervortex in the suction surface endwall corner and also the suction-side leg of the horseshoe vortex on the midspan side of the passage vortex. These regions of positive vorticity are seen even more clearly in the case of negative skew. An important additional feature is that the regions of positive vorticity have developed farther into the flow field away from the suction surface of the blade.

Averaged Through-Passage Results. The results of averaging in the pressure probe measurements across the blade pitch are presented in Figs. 8, 9, and 10. For comparative purposes the theoretical streamwise vorticity, calculated using the formula of Came and Marsh (1974), has been plotted onto the pitch-averaged streamwise vorticity results.

For slot 3 (Fig. 8), the pitch-averaged yaw angle results clearly show that the presence of inlet skew has a significant effect on the flow. The introduction of negative skew at inlet results in an increased level of overturning of the flow when compared to that produced in the colateral case. By contrast the introduction of positive skew results in the apparent removal of the overturning to give the appearance of a uniform flow. The results of pitch averaging the total pressure loss and the secondary kinetic energy show that the flow field, in the case of negative skew, has undergone a substantial development. The growth of loss falls away close to the endwall and there is a corresponding increase in the secondary kinetic energy, which is consistent with the rolling up of the Bernoulli surfaces as the passage vortex develops. The main feature of the experimental results is the early development of the passage vortex in the negative skew case, as shown by the increased negative vorticity. In the colateral case there is also a significant region of negative vorticity due to the pressure-side leg of the horseshoe vortex.

For slot 5 (Fig. 9), the pitch-averaged yaw angles show a significant overturning of the flow in all three skew cases. The total pressure loss results show the magnitude of the loss decreasing as the endwall is approached. This is a result of the movement of the loss core away from the endwall in the spanwise direction. The secondary kinetic energy is seen to grow as the endwall is approached with the negative skew and colateral cases having similar maximum values. The overall distribution shows similar trends for positive skew with a significantly lower maximum value. The negative skew case shows significantly more secondary kinetic energy in the spanwise

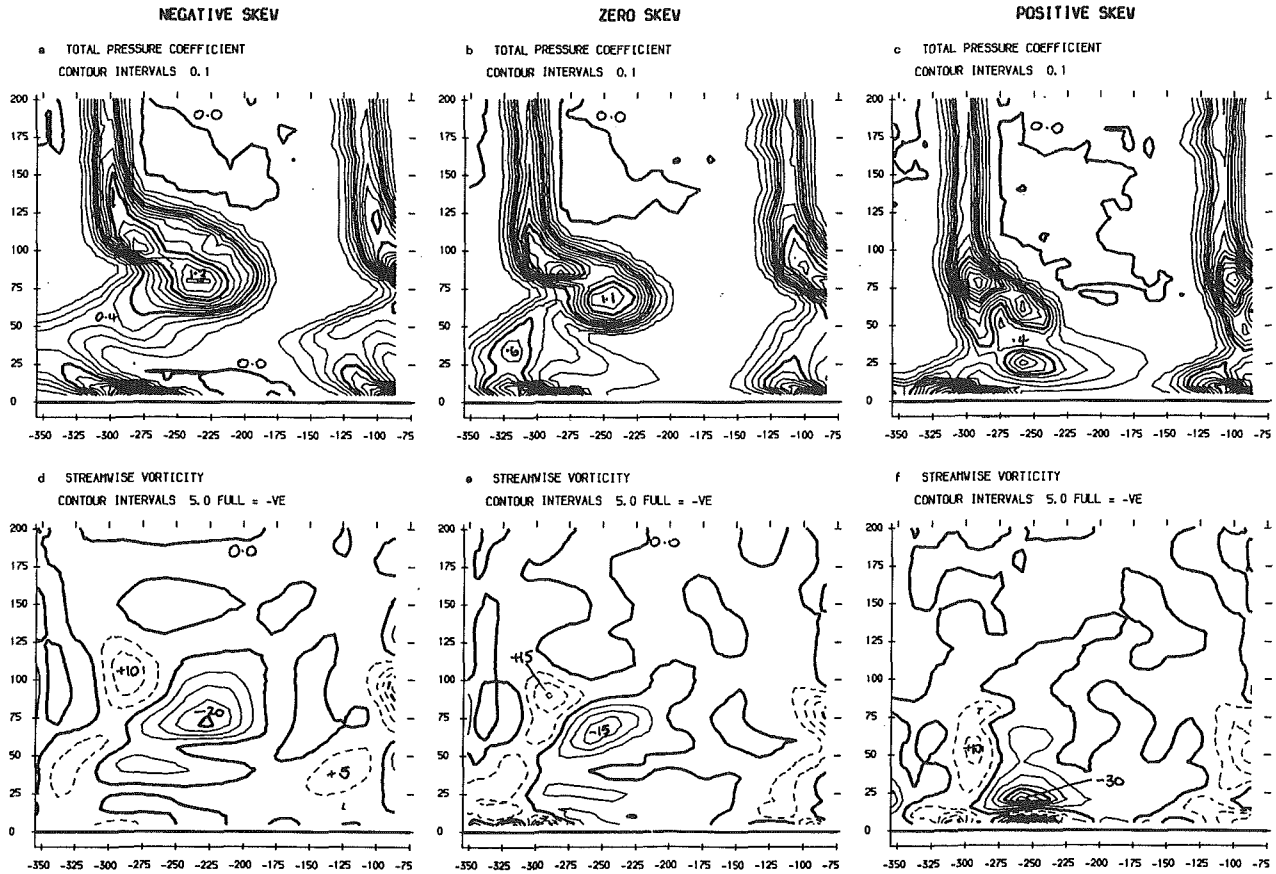

Fig. 11 Area plots for slot 10

region associated with the passage vortex, which is consistent with higher secondary velocities. For the streamwise vorticity, the cases of positive and negative skew both show regions of high negative vorticity at approximately the same spanwise distance from the endwall. The peak value in the case of negative skew is, however, approximately twice the peak value detected in the case of positive skew.

The pitch-averaged results for slot 8 (Fig. 10) show that the development for the flow field is dominated by the passage vortex in all three skew cases. The yaw angles show that the levels of overturning and underturning of the flow are generally increased. The underturned region has developed into a distinct peak, which has moved away from the endwall consistent with the movement of the passage vortex. The peak is farthest from the endwall in the case of negative skew and closest to the endwall in the case of positive skew. The total pressure loss results show that the magnitude of the maximum peak has remained virtually unchanged from that at slot 5. In the colateral and negative skew cases the loss is seen to grow on the endwall indicating the increasing importance of the growth of the countervortex. All three skew cases now have the double peak in the distribution of total pressure loss. The peak on the midspan side is associated with a region of positive vorticity on the suction surface of the blade, as seen in Fig. 7. In the cases of negative and positive skew this coincides with the separation line marking the edge of the passage vortex on the suction surface of the blade. These two cases of skew also have a peak in the distribution of secondary kinetic energy. In the case of negative skew the endwall growth of secondary kinetic energy is no longer present. In the other two cases the endwall growth of secondary kinetic energy is present but at a reduced level. The streamwise vorticity results show that in the noncolateral cases there is a large peak of negative vorticity associated with the passage vortex. The colateral case shows two smaller peaks separated by a region of positive vorticity as a result of the positive vorticity seen near the suction surface of the blade in the area plots. On the midspan side of the negative peak there is a small region of positive vorticity due, in the colateral case, to the suction side leg of the horseshoe vortex. In the other two cases this region appears to coincide with the separation line that marks the edge of the passage vortex.

Downstream Flow. The results for slot 10, 28 percent of an axial chord downstream of the cascade, are presented in Fig. 11. The contours of total pressure loss coefficient are included to illustrate several important effects of skew on the downstream flow field. The blade wakes are immediately obvious and, as expected, they are in a similar position and of a similar size for all three skew cases. The loss on the endwall associated with the countervortex shows interesting differences in the presence of skew. In the negative skew case this region is highly skewed, in the colateral case this region is pulled around to point at the wake centerline, and in the positive case the region is relatively unskewed. In this latter case the development of the countervortex may have been inhibited by other more dominant flow features. In the negative skew and colateral cases there appear to be two distinct peaks within the loss core. Although the positive skew case also has two peaks within the loss core, one of them is of a significantly lower value. In the positive skew case there is also a separate loss core associated with the passing of the combined passage vortex and pressure-side leg of the horseshoe vortex through the cascade. The streamwise vorticity contours show the regions of positive vorticity on the endwall and in the blade wakes for all three skew cases. The region closest to the endwall and extending into the wakes in all three skew cases is associated with the endwall countervortex. The core of positive vorticity

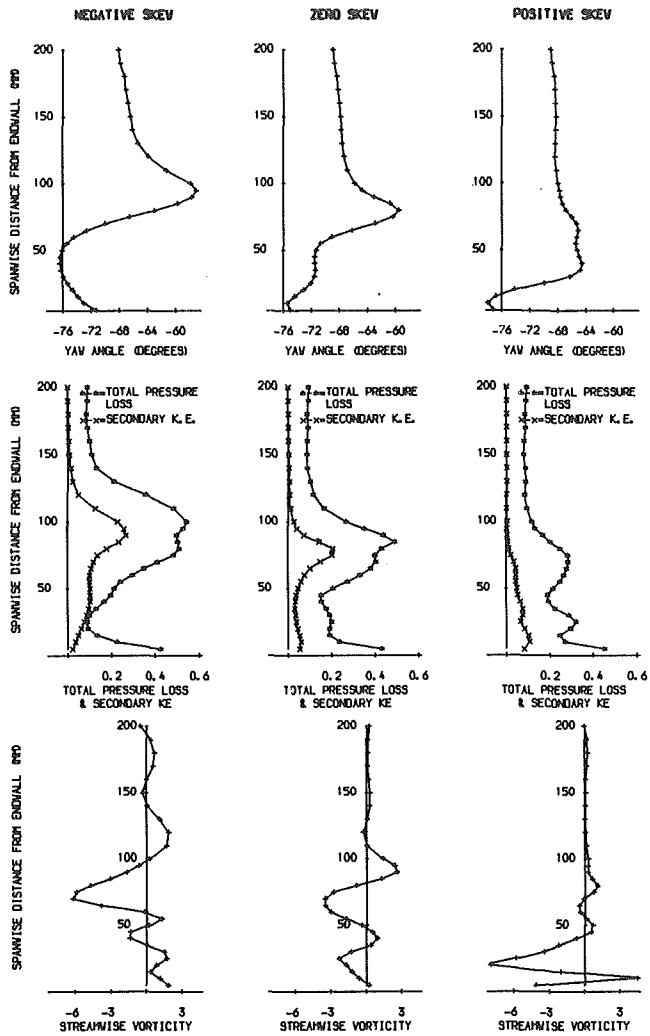

Fig. 12 Pitch-averaged results for slot 10

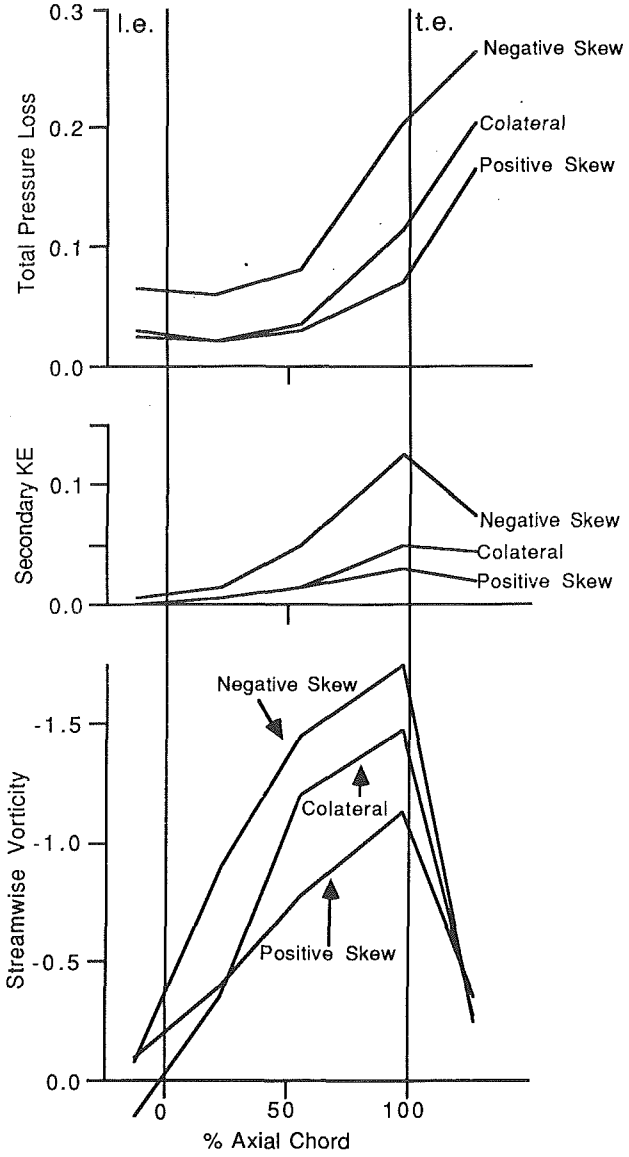

Fig. 13 Area-averaged results

that appears above this region in the spanwise direction in all three skew cases is the shed vorticity. This corresponds to the trailing filament and trailing shed vorticity of classical secondary flow theory. In the colateral and negative skew cases the passage vortex is marked by the presence of high negative vorticity. In the case of positive skew there appears to be a small peak of negative vorticity at the point where the passage vortex might have been expected to be centered. However this region is swamped by the attached stronger region of negative vorticity that is associated with the pressure-side leg of the horseshoe vortex.

Averaged Downstream Results. The pitch-averaged results are presented in Fig. 12. The yaw angle results show the continued development of the flow field for all three skew cases. The negative skew case shows a typical picture of the overturning and the underturning of the flow due to the action of the secondary flows. The distributions in the colateral and positive skew cases appear to have remained similar to those measured at slot 8. However a peak of underturning has developed close to the endwall in both cases. In all three skew cases the peak of overturning is found to have moved farther from the endwall, consistent with the movement of the passage vortex. The secondary kinetic energy results show a significant reduction in secondary kinetic energy for all three skew cases compared to slot 8. This is particularly noticeable close to the endwall. The total pressure loss results show that loss associated with the blade wakes appears in the distributions. The averaged vorticity results confirm the reduced strength of the passage vortex since the magnitudes of vorticity are lower than those measured at slot 8. All three skew cases show an increase in positive vorticity on the midspan side of the passage vortex due to the presence of the trailing shed and trailing filament vorticity components.

Area-Averaged Results. Mass meaned results for the growth of total pressure loss, secondary kinetic energy, and streamwise vorticity through the cascade are shown in Fig. 13. In the blade passage the averaging was carried out over the data boundaries. Upstream and downstream of the cascade the results were averaged over one pitch (data were collected over an area of about 1.5 times the pitch).

The results for the total pressure loss show that in the case of positive skew the inlet boundary layer appears to be re-energized, resulting in a lower value of loss. This is the reason that the colateral and positive skew cases have similar levels of loss at inlet to the cascade; the loss measured in the case of negative skew is much higher. In the colateral and positive skew cases the loss stays approximately constant in the first half of the blade passage when compared to the slight increase shown for the case of negative skew. In all three cases the loss is then seen to increase dramatically to the trailing edge of the

Table 3 Gross secondary loss correlations

Correlation	Inlet Skew Type		
	Negative	Colateral	Positive
Dunham (1970)	0.130	0.082	0.069
Dunham and Came (1970)	0.151	0.116	0.104
Came (1973)	0.097	0.056	0.049
Morris and Hoare (1975)	0.061	0.042	0.039
Gregory-Smith (1982)	0.519	0.151	0.050
Chen and Dixon (1986)	0.095	0.057	0.046
Experimental Results	*0.204*	*0.122*	*0.069*

blades with a further increase downstream of the cascade. The secondary kinetic energy and vorticity results show growth (more negative in the case of vorticity, which corresponds to the growth of the passage vortex) all the way through the cascade with a decay downstream of the cascade. In all of the area plots the difference due to the introduction of skew, in particular negative skew, is very significant.

Correlations

Secondary Losses. A number of correlations have been used to predict the effect of inlet skew on the magnitude of the secondary losses in the cascade. the results obtained with them are summarized in Table 3. In the cases of Dunham (1970) and Dunham and Came (1970) it has been assumed that the correlations are for the net secondary loss. The results in the table are for the gross secondary loss, and where appropriate the correlation has been corrected by adding on the measured inlet total pressure loss. The experimental results are for slot 8, the exit axial plane of the blades.

Of the correlations tested, Dunham and Came (1970) and Gregory-Smith (1982) gave reasonable estimates for the colateral case. Although all of the correlations predict the correct trend of loss with skew, none of them gave the correct relative change in the magnitude of loss due to the introduction of skew. Although the correlations do not provide any information about the physics of the flow or the fundamental nature of the loss generation process, they do highlight what are thought to be the most important parameters affecting the magnitude of the losses; aspect ratio, blade loading, inlet boundary layer thickness, and blade geometry. However their generality must be questionable since in reality all correlations rely on blade profile similarity.

Theoretical Comparison. Classical secondary flow theory has been used to calculate the distribution of streamwise vorticity in the cascade. The results are presented graphically with the pitch-averaged results. It can be seen that early in the cascade, up to slot 5, reasonably good results are obtained for the colateral case. The results are worse at slot 8 due to the distortion of the Bernoulli surfaces by the large secondary flows. The same is found for the case of negative skew, except that the earlier development of the strong secondary flows means that the agreement is worse at slot 5. The case of positive skew shows improvement on progression through the cascade due to the reduction in prominence of the endwall effects.

An interesting application of secondary flow theory has been proposed by Kingcombe (1976) in which a factor can be derived to show the relative effect of inlet skew, in the absence of shear, on the secondary vorticity at exit from a cascade. The formula here has been modified to ensure that in the colateral and skewed cases the relative flow to the cascade is the same (Walsh, 1987). The resulting factor is

$$K = \frac{\zeta_{S2[\text{skewed}]}}{\zeta_{s2[\text{colateral}]}} = 1 - \frac{\tan(\alpha_1 - \beta_2)}{2\tan\alpha_1 - \tan\alpha_2\left(1 + \dfrac{\cos^2\alpha_2}{\cos^2\alpha_1}\right)}$$

where all angles are measured from the axial direction. The formula predicts a ratio of 1.10:1.00:0.82 for the ratio of streamwise vorticity at the exit from the blade row for the skew cases negative:colateral:positive. The area-averaged experimental results for slot 8 (the exit plane of the cascade) give the ratio as 1.19:1.00:0.77. For slot 5 the formula predicts a ratio of 1.14:1.00:0.70; the ratio obtained from the experimental data is 1.20:1.00:0.64. These are surprisingly good results since it would be expected that the presence of high shear at inlet, and the high levels of skew, would play a large role in determining the levels of streamwise vorticity and therefore the secondary losses. However the pitch-averaged results presented in this paper have show that secondary flow theory is not able to predict the correct magnitude of the streamwise vorticity or of the secondary losses.

Discussion

The streamwise vorticity calculation technique that was used for this work calculates a bivariate surface fit to the data, which is then differentiated using numerical techniques. As long as the absolute values and the contour plots are interpreted with caution the results are acceptable. This caution is required in regions of high velocity gradient, such as close to the endwall, since the errors associated with the numerical schemes may be significant. The regions where the technique had difficulty are particularly apparent in the case of positive skew, where there are large velocity gradients close to the boundaries (e.g., the suction surface endwall corner of slot 3, and on the endwall at slots 8 and 10). However the technique has allowed informative pictures of the growth of streamwise vorticity to be produced.

The experimental results show that inlet skew is a very important factor in determining both the structure of the flow field in the blade row and the magnitude of the generated losses. Gregory-Smith et al. (1988) presented the results of a study of the growth of vorticity in a cascade similar to the one used in this work. They found good agreement with classical secondary flow theory predictions only for the early part of the passage. This agrees with our findings for, in particular, the colateral case. However we have shown that the modification of the distribution of the inlet vorticity by the introduction of skew has a profound effect on the secondary flows and losses in the cascade. The importance of the inlet vorticity, rather than the normal component due to the growth of the new endwall boundary layer within the passage, explains why some inviscid calculation methods are able to predict the exit angle variations caused by the presence of secondary flows.

The introduction of negative skew, at a level typical of the conditions in a modern turbomachine, intensified the secondary flows by appearing to cause the earlier development of the flow field. When compared to the colateral case the whole flow field is significantly altered. In particular the increased vorticity at inlet is seen to result in a larger passage vortex and loss core at the blade row exit. In terms of the gross secondary losses, the introduction of negative skew was found to increase them significantly. This large increase of loss agrees with the findings of Carrick (1977) for a turbine impulse cascade, and Boletis et al. for a rotating row of nozzles. This contrasts with the small changes in loss obtained by Atkins (1985), Gregory-Smith and Graves (1983), and others, who showed that the variation of inlet boundary layer thickness has only a small effect on the losses. Atkins (1985) also obtained only small changes in loss by endwall profiling. This then is a clear indication of the importance of inlet skew in the generation of losses within a blade row. The results are only strictly valid

for the simple case of a linear cascade and other factors will also be important in the cases of annular cascades and real machines. However the qualitative, if not the quantitative, effects of skew will be unchanged.

The introduction of positive skew was also found to have a profound effect on the flow field. The passage vortex that was formed was found to be much reduced in strength compared to the other cases. When compared to the other cases, the cross-passage movement of the pressure-side leg of the horseshoe vortex was delayed until much later in the blade passage. The result was that an intense region of loss was formed in the center of the passage close to the endwall. In terms of the secondary loss, the effect of positive skew was to halve approximately the magnitude of the gross secondary loss compared to the colateral case. While this results appears intuitively reasonable, there are no other comparable data.

The pitch-averaged results have been compared with predictions using classical secondary flow theory. Early in the blade passage there is a reasonable level of agreement although, in general, the classical secondary flow theory is not adequate for this high-turning cascade. However the formula derived from that of Kingcombe (1976) does give reasonable predictions for the relative magnitudes of the streamwise vorticity when skew is introduced into the inlet flow field.

A series of correlations have been used to predict the losses in the cascade. All of them are clearly limited in their application and should be applied with caution in the design process of turbines.

Conclusions

- This paper has presented the results of a detailed experimental investigation into the fundamental flow and loss generation processes of a large scale linear cascade of turbine blades.
- The experimental results have shown that the presence of inlet skew modifies the whole of the flow field and in particular modifies the distribution of vorticity at exit from the cascade.
- Inlet skew significantly alters the magnitude of the measured losses in the cascade. The effects of inlet skew appear to be more significant than variations in inlet boundary layer thickness or the reductions in loss than can be obtained by endwall profiling.
- In general correlations are unable to predict accurately the magnitude of the secondary losses or even the relative change due to the presence of inlet skew.
- Predictions obtained with secondary flow theory only appear to hold for the early part of the blade passage where the distortion of the Bernoulli surfaces by the secondary flows is small.
- Secondary flow theory can be used to provide reasonably good estimates of the relative effect of inlet skew on the averaged streamwise vorticity.

Acknowledgments

The authors thank Dr. J. Denton of the Whittle Laboratories for the loan of equipment from Cambridge University. This work has been carried out with the support of the Procurement Executive of the Ministry of Defence. We gratefully acknowledge additional support from Rolls-Royce plc and their permission to publish this paper. The authors also acknowledge the support that they received from the Science and Engineering Research Council.

References

Ainley, D. G., and Mathieson, G. C., 1951, "An Examination of the Flow and Pressure Losses in Blade Rows of Axial-Flow Turbines," ARC R&M, No. 2891.

Atkins, M. J., 1985, "Endwall Profiling in Axial Flow Turbines," Ph.D. Thesis, Cambridge University, United Kingdom.

Bindon, J. P., 1979, "The Effect of Hub Inlet Boundary Layer Skewing on the Endwall Shear Flow in an Annular Turbine Cascade," ASME Paper No. 79-GT-13.

Bindon, J. P., 1980, "Exit Plane and Suction Surface Flows in an Annular Cascade With a Skewed Inlet Boundary Layer," *International Journal of Heat and Fluid Flow*, Vol. 2, pp. 57–66.

Boletis, E., 1984, "Experimental Research on Secondary Flows in Annular Turbine Cascades at VKI," VKI-LS 1984-05.

Boletis, E., Sieverding, C. H., and Van Hove, W., 1983, "Effect of a Skewed Inlet Endwall Boundary Layer on the 3-D Flow Field in an Annular Turbine Cascade," AGARD CP 315, *Viscous Effects in Turbomachines*, Paper No. 16.

Came, P. M., 1973, "Secondary Loss Measurements in a Cascade of Turbine Blades," IMechE Conference Publication No. 3, *Heat and Fluid Flow in Steam and Gas Turbine Plant*, pp. 75–83.

Came, P. M., and Marsh, H., 1974, "Secondary Flow in Cascades: Two Simple Derivations for the Components of Vorticity," *Journal of Mechanical Engineering Science*, Vol. 16, pp. 391–401.

Carrick, H. B., 1977, "Secondary Flows and Losses in Turbine Cascades With Inlet Skew," AGARD CP 214, *Secondary Flows in Turbomachines*, Paper No. 9.

Chen, L. D., and Dixon, S. L., 1986, "Growth of Secondary Losses Downstream of a Turbine Blade Cascade," ASME *Journal of Engineering for Gas Turbines and Power*, Vol. 108, p. 270.

Dunham, J., 1970, "A Review of Cascade Data on Secondary Losses in Turbines," *Journal of Mechanical Engineering Science*, Vol. 12, pp. 48–59.

Dunham, J., and Came, P. M., 1970, "Improvements to the Ainley Mathieson Method of Turbine Performance Prediction," ASME *Journal of Engineering for Power*, Vol. 92, pp. 252–256.

Gregory-Smith, D. G., 1982, "Secondary Flows and Losses in Axial Flow Turbines," ASME *Journal of Engineering for Power*, Vol. 104, pp. 819–822.

Gregory-Smith, D. G., 1984, "Secondary Flow Theory in Straight and Annular Cascades," VKI-LS 1984-05.

Gregory-Smith, D. G., and Graves, C. P., 1983, "Secondary Flows and Losses in a Turbine Cascade," AGARD CP 315, *Viscous Effects in Turbomachines*, Paper No. 17.

Gregory-Smith, D. G., Graves, C. P., and Walsh, J. A., 1988, "Growth of Secondary Losses and Vorticity in an Axial Turbine Cascade," ASME JOURNAL OF TURBOMACHINERY, Vol. 110, pp. 1–8.

Hirsch, Ch., and Denton, J. D., 1981, *Throughflow Calculations in Axial Flow Turbomachines*, AGARD AR 175.

Kingcombe, R. C., 1976, "Skew and Shear in Cascades," PhD Thesis, Cambridge University, United Kingdom.

Klein, A., 1966, "Investigation of the Effect of the Entry Boundary Layer on the Secondary Flows in the Blading of Axial Flow Turbines," *Forshung Ing.-Wes.*, Vol. 32, p. 175 (translation: BHRA T1104, 1969).

Morris, A. W., and Hoare, A. G., 1975, "Secondary Loss Measurements in a Cascade of Turbine Blades With Meridional Wall Profiling," ASME Paper No. 75-WA/GT-13.

Sieverding, C. H., 1984, "Axial Turbine Performance Prediction Methods," *Proceedings of the NATO ASI on Thermodynamics and Fluid Mechanics of Turbomachinery*, Paper No. 5.3.

Sieverding, C. H., 1985, "Recent Progress in the Understanding of Basic Aspects of Secondary Flow in Turbine Blade Passages," ASME *Journal of Engineering for Gas Turbines and Power*, Vol. 107, pp. 248–252.

Walsh, J. A., 1987, "Secondary Flows and Inlet Skew in Axial Flow Turbine Cascades," PhD Thesis, Durham University, United Kingdom.

Walsh, J. A., and Gregory-Smith, D. G., 1987, "The Effect of Inlet Skew on the Secondary Flow and Losses in a Turbine Cascade," *Proceedings of IMechE International Conference Turbomachinery—Efficiency Prediction and Improvement*, Paper No. C275/87.

Mach Number Effects on Secondary Flow Development Downstream of a Turbine Cascade

A. Perdichizzi
Professor,
Department of Mechanical Engineering,
University of Brescia,
Brescia, Italy

The results of an investigation of the three-dimensional flow downstream of a transonic turbine cascade are presented. The investigation was carried out for a wide range of Mach numbers, extending from $M_{2is}=0.2$ up to 1.55. Measurements were made in five planes at different axial locations downstream of the trailing edge (covering more than one chord length), by using a miniaturized five-hole probe especially designed for transonic flows. The results are presented in terms of local loss coefficient, vorticity, and secondary velocity plots; these plots give a detailed picture of the secondary flow development downstream of the cascade and show how flow compressibility influences the vortex configuration. As Mach number increases, the passage vortex is found to migrate toward the endwall and secondary flow effects are more confined in the endwall region. The pitchwise mass averaged loss and flow angle distributions along the blade height appear to be affected by the expansion ratio; at high Mach number both underturning and overturning angles are found to be smaller than in low velocity flows. Overall losses, vorticity, and secondary kinetic energy versus Mach number are also presented and discussed.

Introduction

In the development of modern gas turbines, significant efficiency gains have recently been obtained, and in the near future even larger improvements are expected, through increase of the firing temperature and of the overall pressure ratio. Therefore, in the design of advanced gas turbines, there is a trend toward the adoption of highly loaded turbine stages characterized by high Mach number flows. Especially in the low and medium-power range, first turbine stages have low aspect ratios and secondary flow phenomena may become important, affecting blade row performance in a significant way. Most of the published data on secondary flows refer to low-velocity flows, and limited information about secondary flow effects in high velocity cascades are available; some data were published by Sieverding and Wilputte (1981) for a nozzle cascade and by Bassi and Perdichizzi (1987) for a rotor cascade.

A great deal of experimental work has been performed recently by several authors on secondary flow in linear cascades, aiming to clarify the basic aspects of this phenomenon: Among these Gregory-Smith et al. (1988a) and Moore and Adhye (1985) have investigated the complex three-dimensional flow field evolution respectively within and downstream of linear cascades. Hodson and Dominy (1987) have shown the influence of various parameters involved in secondary flow development, such as inlet boundary layer, Reynolds number, incidence, and pitch-to-chord ratio. Moore et al. (1987) carried out turbulence measurements by hot-wire anemometer; they were able to clarify the loss generation mechanism by measuring Reynolds stresses downstream of the cascade. More recently Zunino et al. (1987, 1988) and Gregory-Smith et al. (1988b) have found that high-turbulence regions are associated with total pressure loss cores, suggesting that turbulence plays an important role in mean kinetic energy dissipation.

An aspect that has not yet been adequately investigated is the influence of Mach number; the effects of compressibility on secondary flows and related losses at the moment are not fully clear. This paper presents data on secondary flow downstream of a linear transonic cascade for different expansion ratios, ranging from subsonic incompressible flow up to supersonic flow, aiming to provide information about Mach number influence on vortex configuration, secondary loss prediction, and vorticity distribution.

Apparatus and Instrumentation

The experimental results were obtained in the C.N.P.M. (Centro Nazionale pez Ricerche sulla Propulsione e sull'Energetica, Milano) transonic wind tunnel for turbine cascades; it is a blowdown type facility with a high-pressure air storage capacity of 3100 kg and a maximum air flow rate of 12 kg/s. The test section, 400 mm wide and 50 mm high, can accept a rather large number of blades. The cascade consists of 12 blades scaled from a midspan section of a steam turbine rotor. The blade profile and the cascade geometry are presented in Fig. 1. The relatively large number of blades, together with an adjustable tailboard, contributed to minimize flow peri-

Contributed by the International Gas Turbine Institute and presented at the 34th International Gas Turbine and Aeroengine Congress and Exhibition, Toronto, Ontario, Canada, June 4–8, 1989. Manuscript received at ASME Headquarters January 1989. Paper No. 89-GT-67.

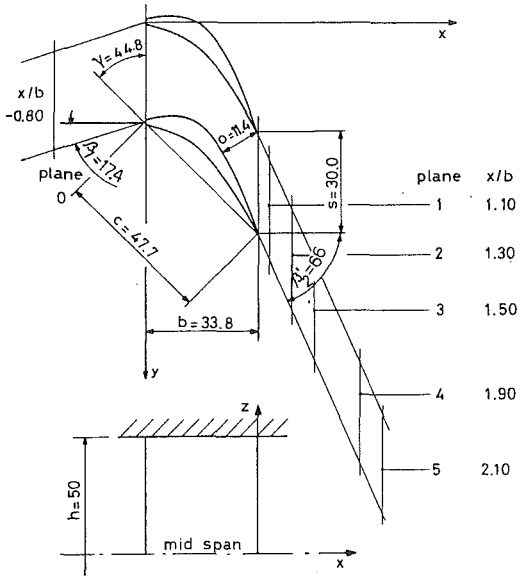

chord lenght	c = 47.7 mm.
pitch to chord	s/c = 0.63
aspect ratio	h/c = 1.05
inlet blade angle	β'_1 = 2.6 deg.
outlet blade angle	β'_2 = 66. deg.
incidence angle	i = 20. deg.
stagger angle	γ = 44.8 deg.
number of blades	z = 12

Fig. 1 Cascade geometry and measuring planes

odicity problems due to the reflection of shocks and expansion waves from the side boundary of the flow downstream of the trailing edge.

Downstream measurements were made by a miniaturized 30 deg conical pressure probe especially designed and manufactured for these tests. As can be seen from Fig. 2, the probe head has a diameter of only 1.5 mm and is 50 mm advanced from the probe stem; these characteristics were selected to minimize the blockage effects induced by the probe in the transonic regime. Meant to be used in fixed direction mode, the probe was calibrated for yaw and pitch angles ranging from −24 to +24 deg in 2-deg steps; calibration was obtained through a fully automated calibration system for Mach numbers ranging from 0.2 up to 1.8 in 0.1 steps. Downstream traverses were made in the same flow channel (the middle one) at different distances from the trailing edge, and covered 1 and 1/2 pitch so as to have a better check of the flow periodicity. The flow field within the blade passage could not be

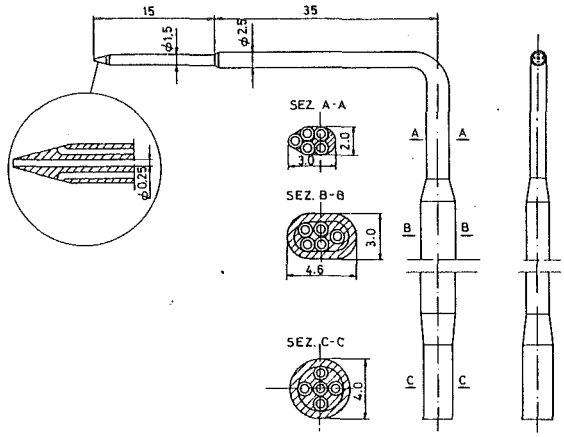

Fig. 2 Five-hole probe

Table 1 Estimated experimental uncertainties

Pitchwise position	±0.1 mm
Spanwise position	±0.1 mm
Inlet flow angle	±0.2 deg
Outlet flow angle	±0.2 deg
Stagnation pressure	±0.01 $(p_{t1}-p_{s2})$
Static pressure	±0.01 $(p_{t1}-p_{s2})$

investigated since in transonic regime the probe blockage introduces unacceptable disturbances in the flow.

Owing to the blowdown-type test facility and to the large air consumption connected to high Mach number tests, the time for a complete test on the measuring plane was severely limited. Therefore a large portion of the effort was devoted to minimizing the time required for each operation. The response time of the probe transducer system was reduced to 80 ms, locating 5 miniaturized pressure transducers just at the end of the probe stem. Probe traversing both in pitchwise and spanwise directions was achieved by stepping motors; probe position along the pitch was given by an encoder connected with the traversing carriage. Data acquisition and probe traversing were accomplished in a fully automated way by means of a microcomputer and the total time needed for a complete measuring plane (210 data points, i.e., 1900 measurements) was limited to about 150 s. Further details about the tunnel and the experimental procedure can be found in Bassi and Perdichizzi (1987).

The estimated experimental uncertainties are given in Table 1.

Generally the error in the local Mach number is estimated to be less than 0.01; for the transonic tests in planes close to

Nomenclature

a = speed of sound, m/s
b = axial chord, mm
c = chord length, mm
h = blade height, mm
H = form factor
i = incidence angle
M = Mach number
o = throat, mm
p = pressure, Pa
q = velocity, m/s
Re = qc/ν
s = pitch, mm
SKE = secondary kinetic energy
u, v, w = fluctuating velocity components, m/s
U = primary velocity, m/s
V, W = secondary velocities, m/s
x, y, z = cascade coordinates
β = flow angle
β' = blade angle
$\Delta\beta$ = secondary flow angle deviation
γ = heat capacity ratio
δ_1 = displacement thickness, mm
ζ = energy losses
θ = momentum thickness, mm
ν = dynamic viscosity
Ω = vorticity, s^{-1}

Subscripts

1 = upstream
2 = downstream (mixed out conditions)
is = isentropic
s = static
S = secondary
t = total
MS = midspan

Superscripts

$\bar{}$ = pitchwise averaged
$\bar{\bar{}}$ = pitch and spanwise averaged

Table 2 Inlet boundary layer

M_{2is}	0.32	0.50	0.72	1.02	1.23	1.38
δ_1	2.10	2.06	1.90	1.95	1.77	1.70
θ	1.61	1.68	1.51	1.56	1.37	1.37
H	1.30	1.28	1.25	1.25	1.28	1.23
$Re_2 \times 10^6$	0.35	0.59	0.84	1.23	1.55	1.61

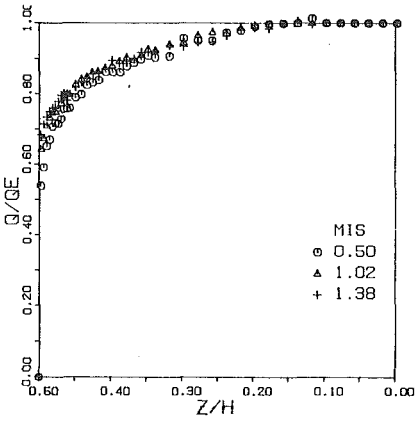

Fig. 3 Inlet boundary layer profiles

the trailing edge, larger inaccuracies occur because of probe blockage effects; also in these planes, for highly supersonic tests, probe measurements are affected by larger uncertainties, since high gradients in pitchwise direction are present. In both situations the error in the Mach number may be estimated at about 0.02–0.03, with consequent effects on the loss estimation.

Another source of inaccuracy in supersonic tests is due to the fact that, far downstream of the trailing edge, flow periodicity is more difficult to obtain and is generally worse than in the planes closer to the trailing edge; as a result much more attention had to be paid both in the setting of the tunnel and analysis of results.

Results and Discussion

Upstream Boundary Layer. The inlet boundary layer profile was determined by traversing the inlet flow at $x/b = -0.8$, by a flattened pitot probe (0.1×0.4 mm). Static pressure was obtained from wall static pressure tappings and it was assumed constant along the span. In Table 2 are presented the integral parameters of the boundary layer for the considered outlet isentropic Mach numbers; for some of these the velocity profile is shown in Fig. 3, while in Fig. 4 is presented the inlet isentropic Mach number. The boundary layer is always turbulent and the velocity profiles are almost similar.

These data show that inlet vorticity, nondimensionalized to the inlet free-stream velocity (and to a cascade reference length), is almost the same for all the cases, even if the free-stream velocity increases significantly up to the choked flow condition.

Downstream Flow Field. To show compressibility effects on secondary flows related to Mach number variation, a complete set of measurements was carried out over a wide range of expansion ratios, i.e., from $M_{2is} = 0.2$ up to 1.55 in roughly 0.2 steps. For each of the considered expansion ratios, measurements were taken in five planes downstream of the cascade, covering more than one chord from the trailing edge, as shown in Fig. 1.

Among these tests, three are presented as the most representative of different flow conditions:

$M_{2is} = 0.32$, corresponding to subsonic incompressible flow;

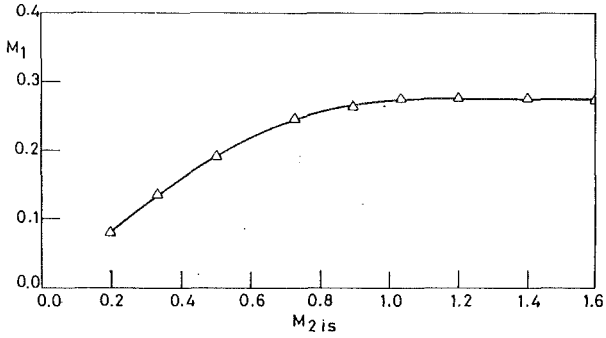

Fig. 4 Inlet Mach number

$M_{2is} = 0.92$, corresponding high subsonic/transonic flow;

$M_{2is} = 1.23$, corresponding to supersonic flow.

The results are presented in terms of kinetic energy loss coefficient, secondary velocity, and streamwise vorticity plots. The local kinetic energy loss coefficient is defined as

$$\zeta = \frac{q^2_{is(y,z)} - q^2_{2(y,z)}}{\bar{q}^2_{2isMS}} = \frac{(p_{s(y,z)}/p_{t(y,z)})^{\frac{\gamma-1}{\gamma}} - (p_{s(y,z)}/p_{t1(y,z)})^{\frac{\gamma-1}{\gamma}}}{1 - (\bar{p}_{sMS}/\bar{p}_{t1MS})^{\frac{\gamma-1}{\gamma}}}$$

The secondary velocity is defined as the projection of the velocity vector onto a plane normal to the velocity vector at midspan for a given tangential position; the velocity vector at midspan defines the primary velocity direction.

The streamwise vorticity Ω_s, i.e., the component of $\nabla x \bar{q}$ in the primary direction may be evaluated from Ω_x and Ω_y, being Ω_z perpendicular to the primary velocity direction in a linear cascade. The experimental results on each measuring plane allow a direct estimate of Ω_x, but Ω_y must be evaluated in an indirect way; following the indications of Gregory-Smith et al. (1988a), use has been made of the z component of the Crocco relation with the assumption of constant total enthalpy

$$\Omega_y = \frac{1}{q_x}\left(q_y \Omega_x + \frac{\alpha^2}{y}\frac{\partial(\ln p_t)}{\partial z}\right)$$

The vorticity values presented in the following are nondimensionalized by using inlet free-stream velocity and the blade chord.

Tests at $M_{2is} = 0.32$. The results for subsonic incompressible flow in different measuring planes are presented in Fig. 5. In the first plane downstream of the trailing edge ($x/b = 1.1$), a clear vortex configuration, typical of secondary flows, can be observed; most of the flow field is dominated by the passage vortex as indicated by the secondary velocity plot and by the large negative vorticity region on the suction side of the wake. The narrow band of positive vorticity just along the wake reveals the presence of the trailing filament and shed vortices, which, in terms of classical secondary flow theory, are related to the stretching of the vortex lines around the blades, and to the spanwise change of circulation. In the upper part of the wake. close to the endwall, there is a counterclockwise rotating flow (i.e., positive vorticity) corresponding to the corner vortex.

The loss contour plot has two peaks: a first one in the middle of the wake, where passage and shed vortices interact with each other, and the second in the corner vortex region. No loss core related to the passage vortex is found; however, there is a wide, relatively low loss region on the suction side to the wake, where low-energy fluid coming from inlet boundary layer is convected.

As the distance from the trailing edge increases, the flow field undergoes significant changes. Under the action of shear stress and turbulence the passage vortex decays, leaving an

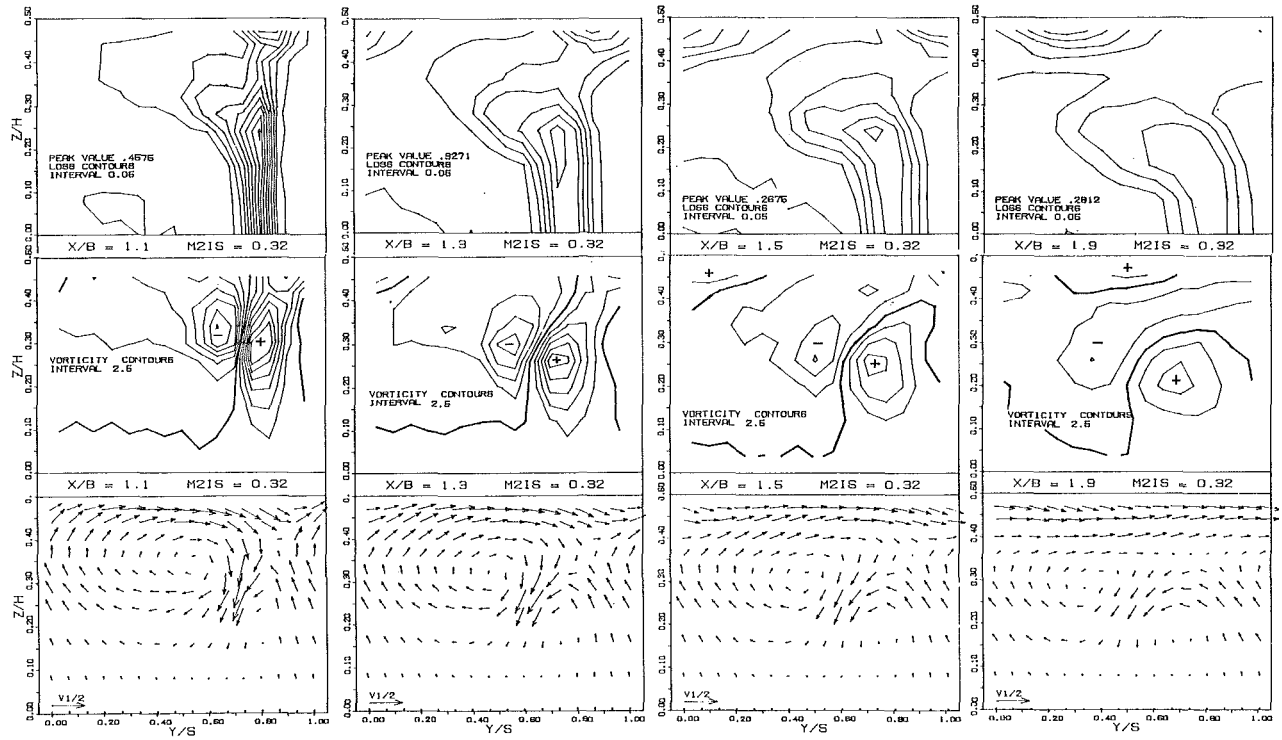

Fig. 5 Secondary velocity vectors, loss, and vorticity contours $M_{2is} = 0.32$

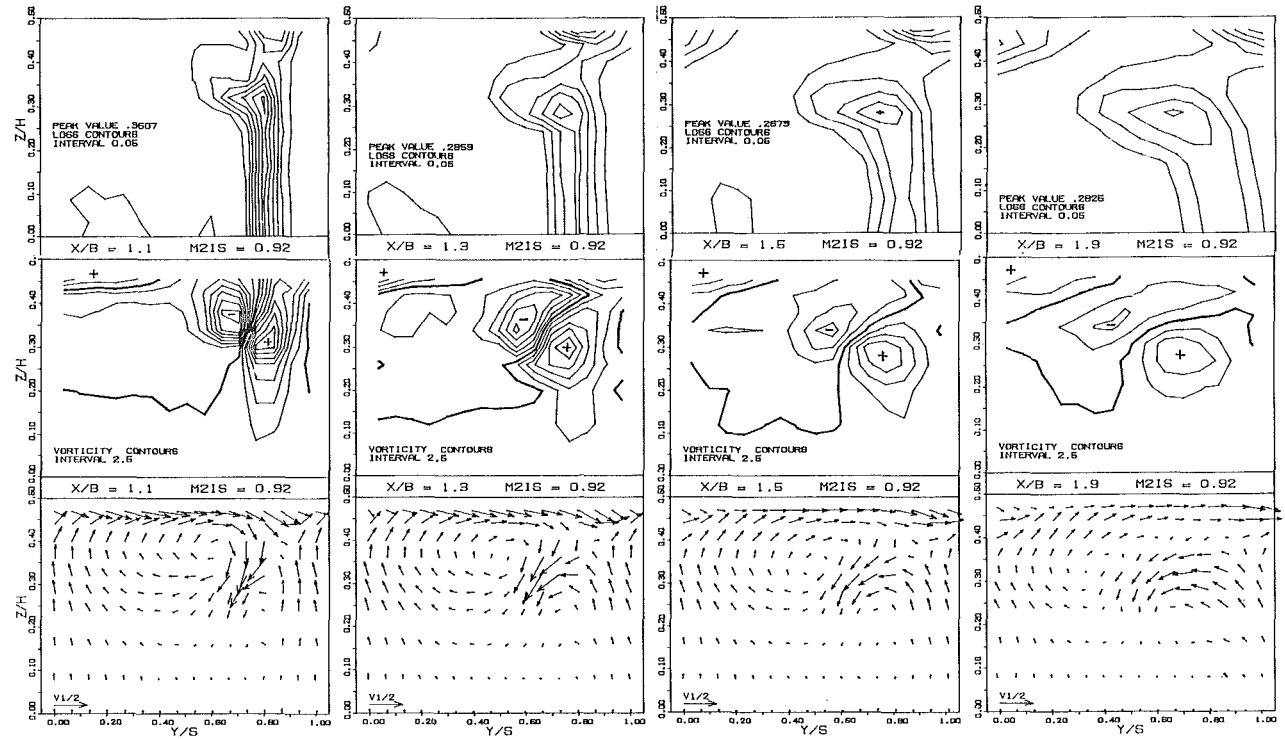

Fig. 6 Secondary velocity vectors, loss, vorticity contours for $M_{2is} = 0.92$

intense crossflow at the endwall. The trailing shed vorticity spreads over a wider zone, mostly in tangential direction; however, in the last plane, the shed vortex surpasses in intensity the passage vortex. The vorticity contours show that the passage vortex is squeezed between the shed and corner vortex, which are moving in opposite directions. Also the loss distribution changes in a significant way: Loss contours are rolled up because of the action of the passage vortex that conveys low-energy fluid toward midspan into the loss core. This loss core is found to move away from the suction side of the wake toward the middle of the channel; this is in agreement with the results of Moore and Adhye (1985). The second loss core, produced by the corner vortex and by the endwall shear stress, is convected in a pitchwise direction by the endwall crossflow and at the same time it widens considerably along the pitch and toward midspan.

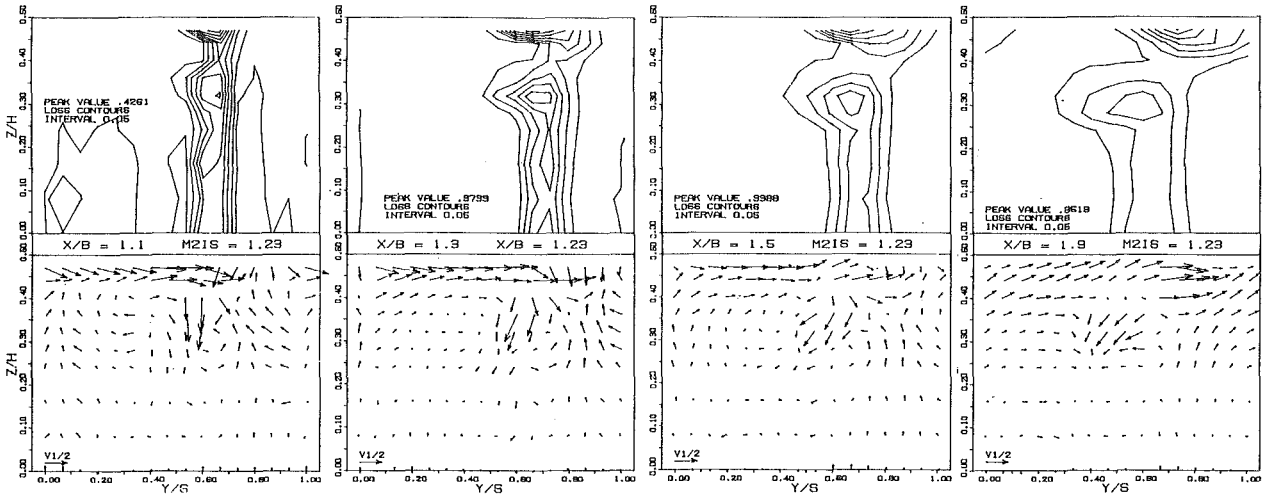

Fig. 7 Secondary velocity vectors and loss contours for $M_{2is} = 1.23$

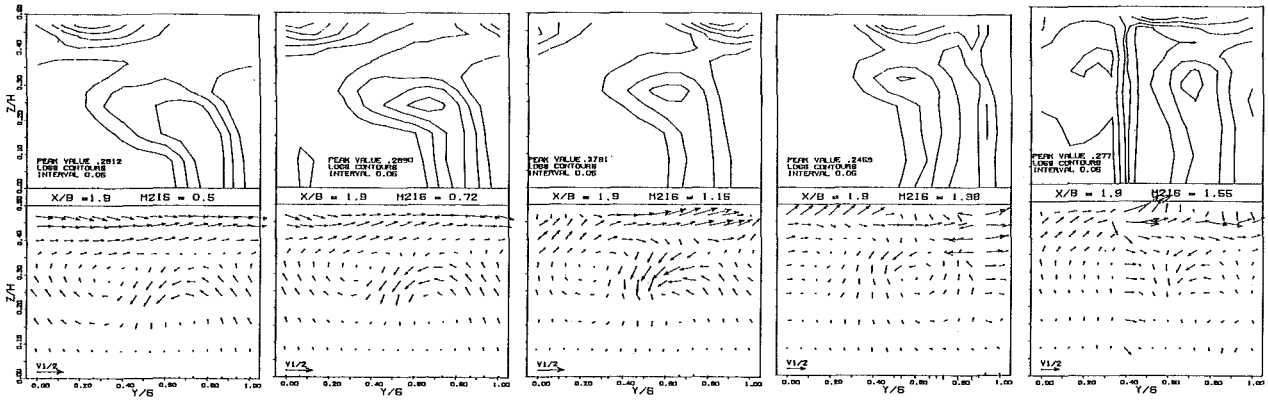

Fig. 8 Results at $x/b = 1.9$ for different M_{2is}

Tests at $M_{2is} = 0.92$. The results for high subsonic compressible flow case are presented in Fig. 6. The most interesting feature, compared to the low-velocity case, is that the passage vortex positions itself closer to the endwall and therefore the flow is two dimensional for a larger extent of the blade height. This feature is clearly shown by secondary velocities as well as by vorticity and loss contour plots. It has to be noted that only the negative vorticity core related to the passage vortex is located closer to the endwall, while the trailing shed vorticity core remains roughly in the same position as the low subsonic case. In plane 1 the vorticity distribution is similar to that of the low-velocity flow, with higher peak values (about 10–15) found both for positive and negative vorticity; as the inlet vorticity is almost the same, this means that compressibility (i.e., the larger density variation across the blade) affects the streamwise vorticity produced throughout the cascade, only slightly.

With regard to the loss distribution, a generally lower level is found, both in peak values and extent of loss region; the loss variation with the Mach number will be discussed later. The development of the flow field downstream of the cascade is similar to the previous case, but at the endwall, the corner loss core moves much less in the pitchwise direction and remains closer to the wake, because of a weaker crossflow produced by the passage vortex.

Tests at $M_{2is} = 1.23$. The secondary velocity field and the loss contour plots for the supersonic flow case are shown in Fig. 7; the vorticity distribution is not presented since its evaluation from experimental data in supersonic flows provided unrealistic results, due to an overly coarse measuring grid. In the first plane the secondary velocity field appears quite distorted, if compared to the previous cases; indeed the typical passage vortex pattern cannot be easily recognized; this is mainly caused by the high gradients (i.e., expansion and shock waves) always present in supersonic flows, especially in the trailing edge region. Moreover in the endwall region there are important effects due to the interaction of shock waves with endwall boundary layer, which produce large inward/outward secondary velocities.

Increasing the distance from the trailing edge, the mixing process reduces all the gradients, and the typical secondary flow field appears more clearly. Also the loss core on the suction side of the wake, which in plane 1 practically does not exist, grows significantly until it assumes the usual configuration. The passage vortex appears to be weak and less intense than the shed vortex. Conversely, the intensity of the corner vortex is quite large, as can be seen both from the secondary velocity and the loss contour plot; indeed the loss peak value at each measuring plane is located just in the corner vortex region. This feature is probably an effect of the three-dimensional interaction of the shock wave with endwall and blade suction side boundary layers.

In order to provide a more complete picture of the Mach number effects on the secondary flow field, a selection of results for other expansion ratios, up to very high supersonic flows ($M_{2is} = 1.55$), is presented in Fig. 8. These plots refer to plane 4, which is located at $x/b = 1.9$. As the expansion ratio is raised, the abovementioned trend of the passage vortex positioning itself closer to the endwall appears clearly. Consis-

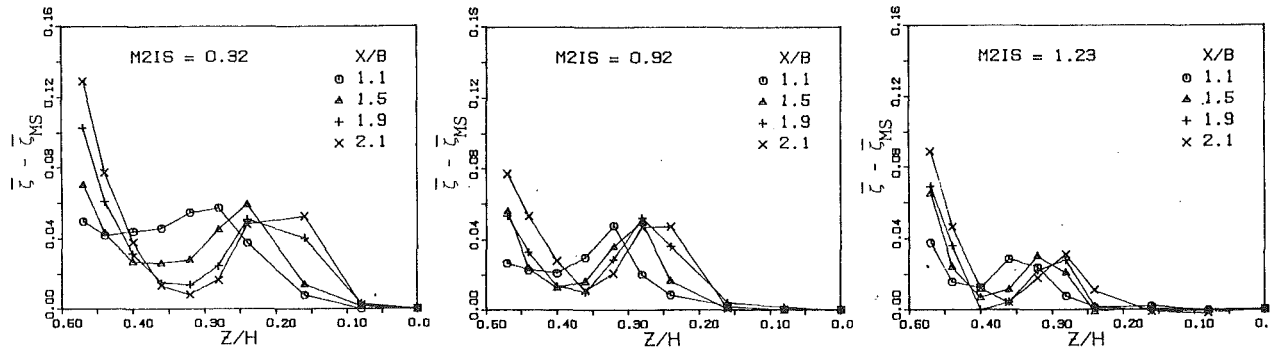

Fig. 9 Spanwise loss distribution at different planes

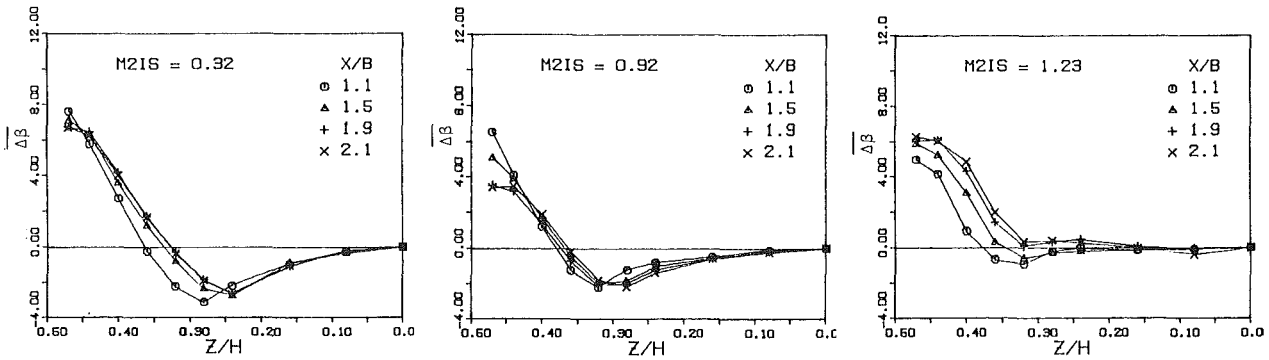

Fig. 10 Spanwise flow angle deviation at different planes

tently, the two-dimensional flow region extends progressively away from midspan and the loss core associated with the shed and passage vortices migrates toward the endwall: At $M_{2is}=0.5$ it is located at about $z/h=0.2$, while at $M_{2is}=1.38$ it is found at $z/h=0.3$.

Worthy of notice are the results for $M_{2is}=1.38$ and 1.55. They present one more loss region, just parallel to the wake, that is associated with the shock wave generated in the base pressure region. For $M_{2is}=1.38$ the shock wave bends in the tangential direction as it approaches the wall because of interaction with the boundary layer; also the secondary velocity pattern is heavily affected by the presence of the shock. For $M_{2is}=1.55$ the loss level in the endwall region is much higher since at high Mach numbers the shock loss is larger and the interaction more intense.

These results show that in supersonic flows, especially at high Mach numbers, the secondary flows in the classical sense (i.e., passage and trailing shed vortex) are less important than the three-dimensional effects connected with shock waves.

Pitch-Averaged Results. The data were mass averaged across the pitch to obtain the spanwise distributions of the loss coefficient and the flow angle deviation, defined as

$$\bar{\zeta}=\frac{\bar{q}_{2is}^2-\bar{q}_2^2}{\bar{q}_{2isMS}^2} \qquad \overline{\Delta\beta}=\bar{\beta}_2-\bar{\beta}_{2MS}$$

The results for different measuring planes are presented in Figs. 9 and 10.

As the distance from the trailing edge increases, the loss distribution undergoes significant changes and similar behavior is found for all the expansion ratios; as an example, for $M_{2is}=0.32$, at plane 1 the secondary loss is almost uniformly distributed in the region from $z/h=0.25$ up the wall; flowing downstream, low-energy fluid is accumulated toward the midspan under the rolling action of the passage vortex. At the endwall there is a significant loss increase caused by the shear stress at the wall and by the corner vortex decay. This indicates, in agreement with Sieverding and Wilputte (1981), that, once the flow is outside the blade passage, the endwall boundary layer undergoes a rapid reorganization since the low-energy fluid is no more removed from the endwall by the passage vortex.

No significant change in the deviation angle distribution except a slight migration of the underturning toward the midspan is noted downstream of the trailing edge. For $M_{2is}=0.92$, a decrease of the overturning angle can be observed close to the wall; it seems related to the larger vorticity decay downstream of the cascade occurring for compressible flows, as shown in Fig. 16.

Figures 11 and 12 show a selection of the results in plane 5 ($x/b=2.1$), showing the variation of the loss coefficient and the deviation angle versus Mach number. As the expansion ratio increases, the peak of the loss tends to move closer to the endwall, consistently with the passage vortex behavior. Beyond $M_{2is}=1.15$, i.e., after choking is reached, this trend ceases and the loss core remains almost in the same position. The peak value of the loss distribution decreases as M_{2is} rises, and for $M_{2is}=1.55$ the loss core is almost absent. In the endwall region a minimum loss value is found for transonic flows, while for higher expansion ratios a steep loss increase occurs due to the abovementioned shock wave boundary layer interaction effects.

As far as the flow angle deviation is concerned, the maximum underturning and overturning angle for the incompressible flow case are found to be about 3 and 7 deg, respectively; as the Mach number increases a progressive reduction both of the underturning and overturning angle can be observed: For $M_{2is}=1.55$ the underturning almost disappears, while the overturning reduces to about 3 deg. The reduction of the flow deviation is a consequence of the larger magnitude of primary velocities relative to the secondary ones, which takes place when the expansion ratio is increased, and especially after the choking condition is reached. At the endwall the smaller overturning is related to the larger importance assumed by the corner vortex in highly velocity flows.

These data show that the yaw angle distribution is heavily

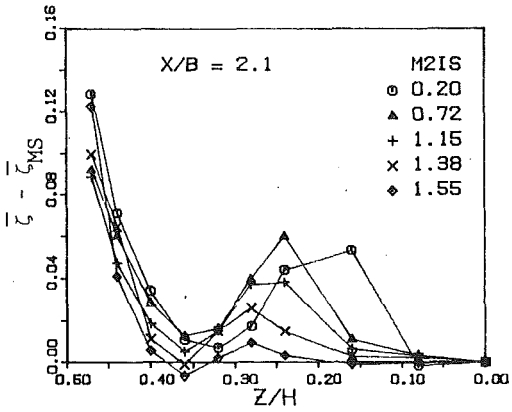

Fig. 11 Spanwise loss distribution at different M_{2is}

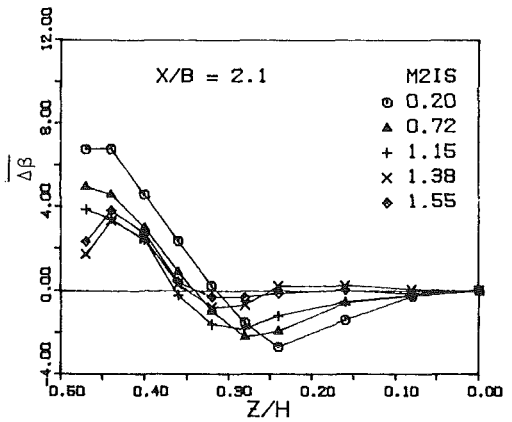

Fig. 12 Spanwise flow angle deviation at different M_{2is}

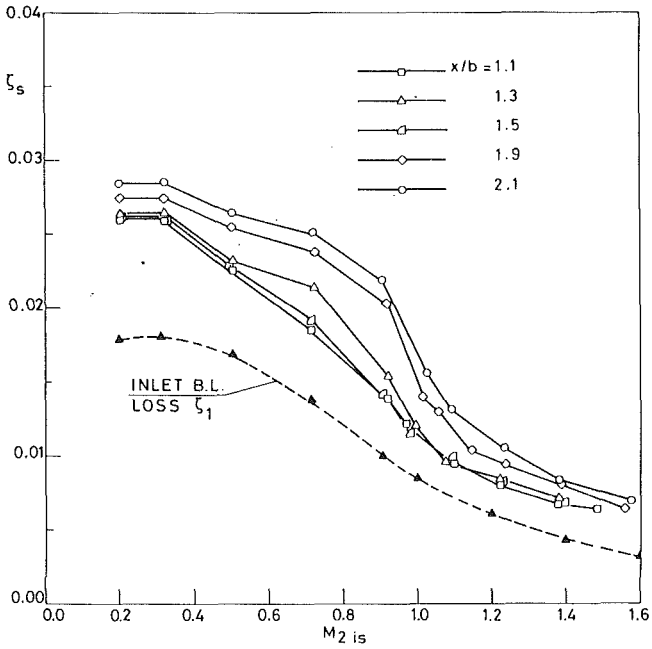

Fig. 13 Secondary losses

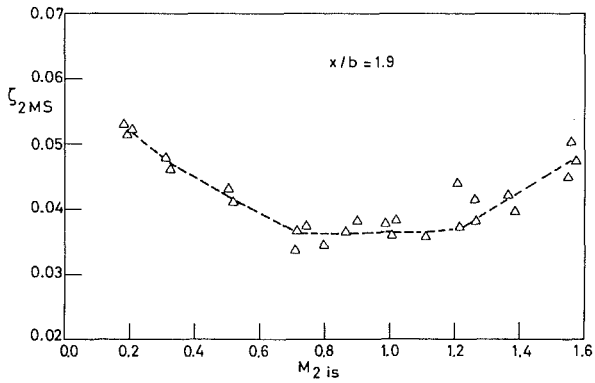

Fig. 14 Midspan loss

influenced by flow compressibility; therefore, in order to provide reliable results, a correlation for the prediction of the secondary flow angle deviation must explicitly take Mach number into account.

Area-Averaged Results. The growth of the secondary loss downstream of the cascade, versus Mach number, is shown in Fig. 13. The secondary loss was obtained by subtracting the two-dimensional loss (presented in Fig. 14) from the total loss, which was evaluated from the mass mean of the flow properties over the measuring plane. It appears that, as Mach number increases, the secondary loss undergoes a marked reduction, and for supersonic flows is is about one third of the one occurring at low Mach number. Such a reduction is mostly an effect of the huge variation in dynamic head, since the loss is referred to the outlet flow conditions. However, these results show that in transonic and supersonic flows, secondary losses, if compared to profile losses, are less important than in low subsonic flows. The results of Fig. 14 show that for $M_{2is} > 1.2$ the two-dimensional loss undergoes a significant increase; this is due to the stronger shocks generated in the base pressure region by the larger expansion occurring at the trailing edge.

To point out compressibility effects on secondary loss production, the net secondary loss produced throughout the cascade should be examined; such a loss, for all measuring planes, can be evaluated from Fig. 13 subtracting from the secondary loss the inlet loss due to the incoming boundary layer. For completeness, since usually in secondary flow analysis losses are commonly referred to inlet flow conditions, the net secondary loss in plane 5, referred to the inlet dynamic head, is also presented in Fig. 15; it should be noted that by this definition the loss is not affected by the variation of the outlet dynamic head and therefore it represents the actual energy dissipation. Both representations indicate that no appreciable variation of the net secondary loss is present up to $M_{2is} = 0.5$, i.e., in the incompressible flow range; then an important increase of energy dissipation takes place just when flow compressibility becomes significant (Fig. 15). The loss stops increasing at about $M_{2is} = 0.9$ and beyond this Mach number, i.e., in the transonic flow range, a marked reduction of the loss was found. For supersonic flows, beyond $M_{2is} = 1.2$, the loss increases again (in Fig. 13 it remains roughly constant) because of the larger importance assumed by shock wave effects.

Figure 13 shows also that in low subsonic flows, at plane 1 (i.e., at $x/b = 1.1$), most of the net secondary loss has already taken place and only a small amount is produced downstream of the trailing edge. When increasing the Mach number, a minor part of the loss is produced inside the blade passage, with the major portion generated downstream of plane 1. One can think that this feature might be related somehow to the smaller number of revolutions undergone by fluid particles involved in the passage vortex when the expansion ratio is increased.

However, it has to be pointed out that it is not clear why more energy dissipation occurs in the compressible flow range and why it is then reduced in the transonic range; an attempt to clarify this aspect was made by considering the streamwise vorticity and the secondary kinetic energy development down-

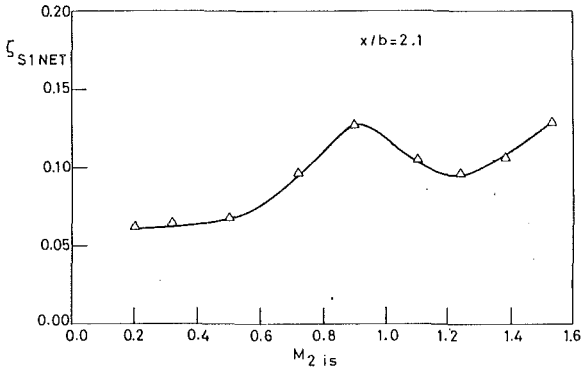

Fig. 15 Net secondary loss at $x/b = 2.1$, referred to inlet dynamic head

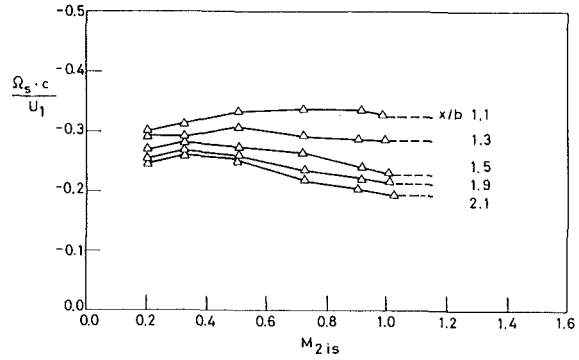

Fig. 16 Streamwise vorticity

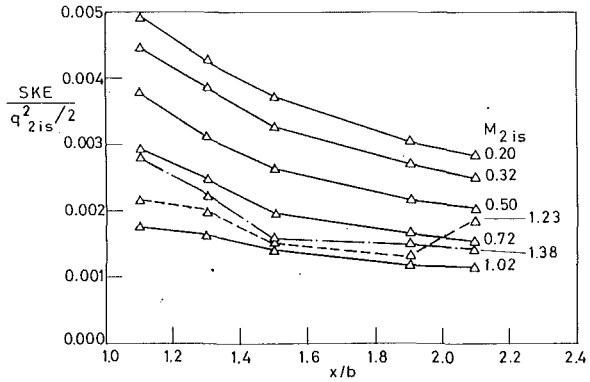

Fig. 17 Secondary kinetic energy

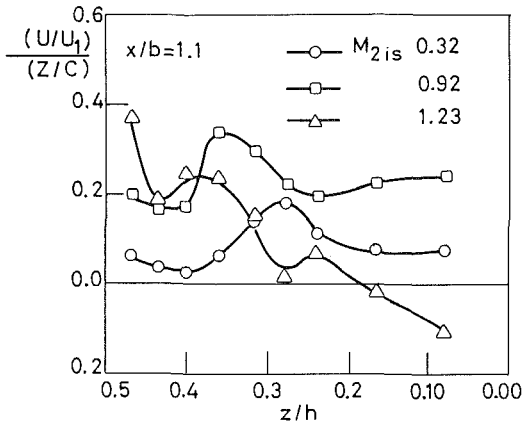

Fig. 18 Spanwise distribution of $\frac{\partial(U/U_1)}{\partial(z/c)}$

stream of the blades (Figs. 16 and 17). The secondary kinetic energy coefficient is defined as

$$\mathrm{SKE} = \int \frac{V_S^2 + W_S^2}{\bar{q}^2_{2isMS}} dydz$$

The streamwise vorticity evaluated in the first plane downstream of the trailing edge seems not to be much affected by Mach number variation; indeed slightly lower vorticities were found only in low subsonic cases. With regard to the vorticity development downstream of the cascade, it should be noted that a large vorticity decay takes place in compressible flows, while at low velocities it is much less. This trend is similar to the one observed for the net secondary loss raise (even if the rates are different); therefore a connection between loss production and vorticity decay seems to exist.

Figure 17 shows that for $M_{2is} \leq 0.3$ the SKE decay is roughly of the same order of magnitude as the loss increase between planes 1 and 5. These data are in agreement with the results of Moore and Adhye (1985) for a low-velocity cascade. For compressible flows a quite different situation occurs. The loss increase is found to be much more than the SKE decay (e.g., up to about eight times, for $M_{2is} = 1.02$). This indicates that a significant dissipation of the primary kinetic energy occurs between planes 1 and 5; part of this loss is certainly due to endwall boundary layer fluid fed into the bulk flow; however, it is the author's opinion that turbulence is mainly responsible for this loss production. Referring to the turbulent flow analysis carried out by Moore et al. (1987) in a low-velocity cascade, it seems that the opposite situation had occurred, that is mean kinetic energy could have been converted to turbulent kinetic energy through the work of deformation of the mean motion operated by Reynolds stresses. In the primary flow direction the deformation work, which contributes directly to changes in primary velocity, is expressed by

$$\frac{uu_j}{U_1^2} \frac{\partial(U/U_1)}{pt(x_j/c)}$$

This hypothesis, which could explain the higher loss production in the compressible flow cases as well as the subsequent reduction in the transonic field, is supported by the data of Fig. 18; larger values of

$$\frac{\partial(U/U_1)}{\partial(z/c)}$$

were actually found in the loss core region away from the endwall, just for $M_{2is} = 0.92$. However, it should be said that the decreasing trend noted for $0.9 < M_{1is} < 1.2$ might also be affected by the Reynolds number increase, since in these tests the variation of the Mach number involved significant Reynolds number variation (Table 3). In conclusion, a detailed investigation of the turbulent flow through hot-wire anemometry needs to be done in order to clarify the role played by turbulence in the loss production mechanism for compressible flows. This further investigation will be carried out in the near future.

Conclusions

The flow field downstream of a linear turbine cascade has been investigated over a wide range of expansion ratios. It has been found that secondary flow vortex configuration is influenced by the flow compressibility. With increasing Mach number, the passage vortex as well as the loss core on the wake suction side are found to move closer to the endwall; moreover the shed and, especially, the corner vortices tend to assume a larger importance relative to the passage vortex. In supersonic flows significant three-dimensional effects due to shock wave boundary layer interaction are superimposed on the secondary flow field. The pitch-averaged data clearly indicate a significant influence of Mach number upon the flow angle deviation dis-

tribution; smaller underturning and overturning were found at high expansion ratios.

The importance of secondary losses, compared to profile losses, is found to be diminishing as the Mach number rises. The net secondary loss increases just when flow compressibility also increases, i.e., for $M_{2is} > 0.5$, and, then, in the transonic field, undergoes a marked reduction. The data suggest that turbulence might be responsible for this trend.

Acknowledgments

The author wishes to thank Franco Tosi Industriale s.p.a., which provided the blade cascade and the permission to publish these data. The author is also grateful for the appreciated support received by C. De Ponti and G. B. Daminelli.

References

Bassi, F., and Perdichizzi, A., 1987, "Secondary Flow Development Downstream of a Transonic Cascade," *Proceedings 1987 Tokyo Gas Turbine Congress*.

Gregory-Smith, D. G., Graves, C. P., and Walsh, J. A., 1988a, "Growth of Secondary Losses and Vorticity in an Axial Turbine Cascade," ASME JOURNAL OF TURBOMACHINERY. Vol. 110, pp. 1–8.

Gregory-Smith, D. G., Walsh, J. A., and Graves, G. P., and Fulton, K. P., 1988b, "Turbulence Measurements and Secondary Flows in a Turbine Rotor Cascade," ASME JOURNAL OF TURBOMACHINERY, Vol. 110, pp. 479–485.

Hodson, H. P., and Dominy, R. G., 1987, "The Off-Design Performance of a Low-Pressure Turbine Cascade," ASME JOURNAL OF TURBOMACHINERY, Vol. 109, pp. 201–209.

Laksminarayana, B., 1975, "Effects of Inlet Temperature Gradients on Turbomachinery Performance," ASME *Journal of Engineering for Power*, Vol. 97, pp. 64–71.

Langston, L. S., Nice, M. L., and Hooper, R. M., 1977, "Three Dimensional Flow Within a Turbine Cascade Passage," ASME *Journal of Engineering for Power*, Vol. 99, pp. 21–28.

Moore, J., and Adhye, R. Y., and 1985, "Secondary Flow and Losses Downstream of a Turbine Cascade," ASME *Journal of Engineering for Gas Turbines and Power*, Vol. 107, No. 4, pp. 961–968.

Moore, J., Shaffer, D. M., and Moore, J. G., 1987, "Reynolds Stresses and Dissipation Mechanisms Downstream of a Turbine Cascade," ASME JOURNAL OF TURBOMACHINERY, Vol. 109, pp. 258–267.

Sieverding, C. M., and Wilputte, P., 1981, "Influence of Mach Number and End Wall Cooling on Secondary Flows in a Straight Nozzle Cascade," ASME *Journal of Engineering for Power*, Vol. 103, pp. 257–263.

Sieverding, C. M., 1985, "Recent Progress in the Understanding of Basic Aspects of Secondary Flow in Turbine Blade Passages," ASME *Journal of Engineering for Gas Turbines and Power*, Vol. 107, pp. 248–257.

Zunino, P., Ubaldi, M., and Satta, A., 1987, "Measurements of Secondary Flows and Turbulence in a Turbine Cascade Passage," ASME Paper No. 87-GT-132.

Zunino, P., Ubaldi, M., Satta, A., and Peisino, E., 1988, "A Comparison Between Measurements and Turbulence Models in a Turbine Cascade Passage," ASME Paper No. 88-GT-226.

APPENDIX

Blade Profile Coordinates

	X s.side	Y s.side		X p.side	Y p.side
1	0.0000	0.0000	28	33.7849	33.1481
2	0.0369	-0.2681	29	33.7396	33.3125
3	0.3118	-0.7228	30	33.6167	33.4307
4	0.7816	-0.9708	31	33.4506	33.4694
5	1.4686	-1.1336	32	33.2881	33.4177
6	2.9382	-1.4211	33	33.1749	33.2902
7	4.4068	-1.6197	34	32.3163	31.5498
8	5.8754	-1.7318	35	30.8467	28.7687
9	7.3450	-1.7584	36	29.3781	26.1495
10	8.8136	-1.6999	37	27.9095	23.6707
11	10.2823	-1.5419	38	26.4408	21.3164
12	11.7518	-1.2271	39	24.9713	19.0728
13	13.2204	-0.7450	40	23.5027	16.9148
14	14.6891	-0.0761	41	22.0340	14.6665
15	16.1577	0.8298	42	20.5645	12.8399
16	17.6272	1.9712	43	19.0958	11.2290
17	19.0958	3.3256	44	17.6272	9.7943
18	20.5645	4.9536	45	16.1577	8.5080
19	22.0340	6.9634	46	14.6891	7.3520
20	23.5027	9.5430	47	13.2204	6.3106
21	24.9713	12.5564	48	11.7518	5.3726
22	26.4408	15.6716	49	10.2823	4.5284
23	27.9095	18.8933	50	8.8136	3.7716
24	29.3781	22.2330	51	7.3450	3.0961
25	30.8467	25.7025	52	5.8754	2.4964
26	32.3163	29.3176	53	4.4068	1.9696
27	33.7634	33.0338	54	2.9382	1.5119
			55	1.4686	1.1203
			56	0.7790	0.9589
			57	0.3080	0.7192
			58	0.0355	0.2631

A Secondary Flow Calculation Method for Single-Stage Axial Transonic Flow Compressors, Including Shock-Secondary Flow Interaction

J. Kaldellis
Assistant.

D. Douvikas
Assistant.

National Technical University of Athens,
Athens, Greece

F. Falchetti
Engineer,
SNECMA, Villaroche, France

K. D. Papailiou
Professor,
National Technical University of Athens,
Athens, Greece

A secondary flow calculation method is presented, which makes use of the meridional vorticity transport equation. Circumferential mean flow quantities are calculated using an inverse procedure. The method makes use of the mean kinetic energy integral equation and calculates simultaneously hub and tip secondary flow development. Emphasis is placed upon the use of a coherent two-zone model and particular care is taken to describe adequately the flow inside an unbounded (external), semi-bounded (annulus), and fully bounded (bladed) space. Along with the velocity field, the losses, the defect forces, and the corresponding additional work realized inside the viscous wall shear layer are calculated for stationary and rotating flow. An approximate model for the interaction of the viscous shear layers and the external flow is used, which takes into account the meridional and peripheral blockage. When shock waves are present in the external flow, an approximate interaction model is used, additionally, which calculates the static pressure field resulting from the interaction of the shock wave and the corresponding wall shear layer. The method has been applied to two single-stage transonic flow compressors and the results of the comparison between theory and experiment are presented and discussed.

1 Introduction

Some recent attempts to calculate the secondary flow development in turbomachines solve the Navier–Stokes equations directly (see, for instance, Moore and Moore, 1985; Birch, 1987; Dawes, 1988; Hah and Laylek, 1987; Manchu, 1987). While this is ultimately bound to happen, both their turbulent modeling shortcomings and important computer time favor, for the present time, simpler methods for industrial applications.

This is particularly true of compressor secondary flow computations, where methods using circumferentially averaged equations, compatible with the meridional flow model, have proved particularly successful. The corresponding published work (see, for instance, Papailiou et al., 1977; Comte et al., 1981; Papailiou, 1983; Douvikas et al., 1987; Kaldellis et al., 1988; Leboeuf and Naviere, 1983; Brochet and Falchetti, 1987; Adkins and Smith, 1982; Gallimore, 1986; and Horlock, 1971, to mention only those methods that calculate the flow inside the blading) has been favored by industrialists and the number of approaches used reflects only the difficulty of the problem.

Contributed by the International Gas Turbine Institute and presented at the 34th International Gas Turbine and Aeroengine Congress and Exhibition, Toronto, Ontario, Canada, June 4–8, 1989. Manuscript received at ASME Headquarters February 1, 1989. Paper No. 89-GT-210.

The present work is a continuation of that presented by Papailiou et al. (1977), Comte et al. (1981), Papailiou (1983), Douvikas et al. (1987), and Kaldellis et al. (1988). It is also based on the same principles and methodology as those of Leboeuf (1984), Bario et al. (1982), and De Ruyck and Hirsch (1983). The corresponding improved two-zone model, which is the basis of the present calculation method, is now applied to the case of one transonic and one supersonic single-stage compressor. Various aspects as well as the implications of the improved flow model are presented briefly in Section 2. In Section 3 the equations are presented in the form in which they will be used. There, an approximate procedure is described, which is used to compute the shock/secondary flow interaction. In Section 4 the computational algorithm is presented, along with pertinent remarks concerning the numerical procedure. Section 5 is devoted to the comparison of theoretical calculations and experimental results and the method's possibilities are discussed. Section 6 presents the conclusions.

2 Qualitative Description of Flow Model

As was mentioned above, a two-zone model is adopted in the present work, as has been done previously by the authors Papailiou (1983), Douvikas et al. (1987), and Kaldellis et al.

(1988). This model has been used successfully to calculate the secondary flow development in a highly loaded compressor cascade (Kaldellis et al., 1988) and, now, it is applied to rotating machinery and transonic flow. For completeness the whole model will be presented below, although the aspects already described elsewhere will be only briefly mentioned here.

According to this model the flow is divided into an "inviscid" part (in which the profile losses are included) and a viscous part, which deals with the secondary flow. The analysis of the flow is realized in the meridional and the peripheral directions and, consequently, the corresponding velocity profiles are considered. As in previously presented work, it is assumed that the longitudinal velocity profile makes sense physically and may be represented in its reduced form by a velocity profile family borrowed from the classical compressible boundary layer theory. Although this is done for convenience, it is not necessary and is by no means part of the two-zone model underlying the present work. In fact, the integral approach adopted here for the longitudinal direction could be substituted by a differential one.

The analysis concerning the longitudinal profile, when the external flow, used as reference, changes in magnitude and direction from hub to tip, may be found in Mellor's work (Mellor et al., 1971) in most of the references cited above, which adopted it as a standard tool. In the present work, any information coming out of the longitudinal profile analysis is injected in the meridional and peripheral directions, along which the calculation is carried out. The transverse velocity profile is not directly considered, as in previous methods, but is an outcome of the calculation procedure. Instead, the peripheral velocity profile is used along with the corresponding meridional vorticity component. Thus, instead of the classical secondary vorticity transport equation, the meridional one is adopted in the present analysis.

This way of looking at things eliminates difficulties that are encountered when one considers the transverse velocity profile near the entrance and exit regions of a staggered blade row, not having a clear case of either a free duct or a bladed duct.

Before discussing things any further, we think it useful to give a general qualitative description of our model, so that the information to come fits into a specific frame. In doing this, we shall follow the flow as it moves downstream in an annular duct, then as it enters and proceeds downstream inside a rotor blading and, finally, as it leaves the rotor and enters the next annular duct region. Although this situation is not the most general considered in this paper, it may illustrate how things are viewed in the present calculation method. We shall assume that the "inviscid" external flow is given and calculated without any wall shear layer blockage effects.

In the calculation procedure presented below, the two wall shear layers (hub and tip) will be allowed, through a simplified calculation procedure (described by Papailiou, 1983, in detail and briefly in Section 4), to interact with the external flow. As a consequence, the meridional velocity of the external flow will be modified according to the blockage requirements at the considered station and the external flow angle will be modified according to a combination of the meridional and, as we shall see, the peripheral blockage effects.

Considering now the first annular duct space, we assume for simplicity that, at the entrance, we have a collateral shear layer. This introduces a meridional blockage effect and the external meridional flow is accordingly modified. As the calculation proceeds downstream, the external velocity field is modified at each step according to the blockage introduced by the two wall shear layers. Each shear layer development calculation is performed using the modified velocity field as one of the boundary conditions.

When a change in radius occurs for the external flow streamlines, a simultaneous change in direction takes place. The corresponding development of secondary vorticity indicates a

Nomenclature

a = speed of sound
b = blockage factor
B = $b \cdot R$
c_D = dissipation factor
$\mathbf{D}_1$ = deficit force vector
$\mathbf{f}$ = viscous force per unit mass
h = enthalpy
h_t = total enthalpy
h^* = passage height
k = peripheral striction parameter
k_m = curvature of m lines
k_n = curvature of n lines
m_s = mass flow ratio
p = static pressure
p_t = total pressure
q^2 = turbulent kinetic energy
R = radius
U = blade peripheral velocity
u_T = friction velocity
$\mathbf{V}$ = absolute velocity vector
$\mathbf{W}$ = relative velocity vector
(u, v, w) = components of velocity fluctuations with time
(ϑ, m, n) = coordinates of an orthogonal axisymmetric coordinate system
β = angle between meridional direction -m and longitudinal direction s
β', δ' = blade geometry angles
δ = boundary layer thickness
$\Delta\tau_{ij} = \tau_{eij} - \tau_{ij}$
δ_m^* = meridional displacement thickness
ϵ_D = defect force parameter
μ = meridional striction parameter
ξ = vorticity vector
ρ = density
φ = angle between meridional direction and machine axis
ω = angular velocity vector
μ_T = total viscosity coefficient
τ_{ij} = tensor of total viscous stresses

$$\Delta_{m_w}^* = \int_{n_w}^{n_{w'}} B(\bar{\rho}_e \bar{W}_{m_e} - \bar{\rho}\bar{W}_m)dn$$

$$\Theta_{mm_w} = \int_{n_w}^{n_{w'}} B\bar{\rho}\bar{W}_m(\bar{W}_{m_e} - \bar{W}_m)dn$$

$$\Theta_{mu_w} = \int_{n_w}^{n_{w'}} B\bar{\rho}\bar{W}_m(\bar{W}_{u_e} - \bar{W}_u)dn$$

$$\Theta_w^{**} = \int_{n_w}^{n_{w'}} B\bar{\rho}\bar{W}_m(\bar{W}_e^2 - \bar{W}^2)dn$$

$\bar{\xi}_i = b\xi_i \ (i = u, m, n)$

Subscripts

(u, m, n) = components in curvilinear axisymmetric orthogonal coordinate system (peripheral, meridional, normal)
(s, N, n) = components in intrinsic coordinate system (longitudinal, transverse, normal)
e = external flow
w, w' = value at hub and tip walls, respectively
t = total value
T = value at tip
H = value at hub
o = undisturbed external flow quantity in the shock/secondary flow interaction region
δ = boundary layer edge

Superscripts

$(\overline{})$ = mean peripheral value
$(\hat{\ })$ = initial external flow field
$\langle\ \rangle$ = time-averaged value
$*$ = theoretical meridional shock position

change in the direction of the mass flux from the meridional to the peripheral direction inside the wall shear layer under consideration. This modification of the mass flow rate in the peripheral direction exerts in the same direction a blockage to which the external peripheral flow field reacts due to the geometric confinement (limited passage height). It is expected, consequently, that the external flow will be modified not only by the meridional blockage, but by this peripheral blockage as well.

The peripheral blockage presence and the viscous peripheral velocity profile associated with the distribution of the meridional component of vorticity constitute an important aspect of the present calculation method. Details concerning these topics are presented by Kaldellis (1988) and Douvikas (1988). Here we shall only state results of the analysis realized in these references, which help to understand the present calculation method.

When a meridional (peripherally averaged) vorticity component distribution in the n direction is specified, then the corresponding peripheral velocity profile depends only upon the boundary conditions, that is upon the degree of geometric confinement. Expressions for the external aerodynamics case (unbounded), the annular duct space (semi-bounded), and the bladed case (fully bounded) have been developed by Douvikas et al. (1987). These expressions, identical in form for the three cases mentioned above, are used in the present calculation method. They take into account any practical situation, and they can describe the triangular velocity profile of Johnston, as well as the one resulting from the blade passage vortices inside the blading and downstream of it in the corresponding annular duct space. In this way the two cases of internal and external aerodynamics are bridged together on a common basis.

In order to arrive at the wall shear layer peripheral velocity profile we shall be using in this work, the total peripheral velocity field is divided into two parts. The first one takes into account the reaction of the external flow to the peripheral blockage. It is, finally, considered as part of it and modifies the external flow angle. The second one belongs to the viscous shear layer and is the one we have been talking about. The resulting viscous shear layer now has the same thickness in both longitudinal and transverse directions. At the same time, the S-shaped profiles used by Comte et al. (1981) and Papailiou (1983) are no longer necessary. This particular aspect is very useful when the change of coordinates (absolute to rotating frame of reference or vice versa) is operated.

An additional important feature of this analysis is that it renders to the two-zone model its coherence, in considering displacement effects in the same way both in the meridional and peripheral directions. More precisely, the static pressure field, which is the common basis of the "external" and viscous flow parts, becomes identical for both real and inviscid flow. A direct consequence of the coherence of the flow model is that negative losses are no longer encountered during the calculation procedure.

Two remarks have to be added to what has been described above. The first one concerns the usual meridional flow calculation methods. These have to be modified in order to be able to take into account the peripheral blockage effects.

The second remark concerns the analysis of experimental results according to the present model. It is necessary to perform this analysis using iteratively the present calculation method and that dealing with the external flow, as was explained above. Otherwise, it seems rather difficult to separate the experimental results into an "inviscid" and a viscous part.

With these remarks one may proceed inside the annular duct region until one finds the rotating blading. It is easy to pass from an absolute to a relative frame of reference and consider how the flow enters the blades.

As the flow enters the rotating blading, it must adapt to the blading in two ways. First, the external flow must adapt its direction to the one imposed by the blade presence. Second, any recirculating flow inside the duct must accept the confinement imposed by the presence of the blades. This situation imposes a zero total mass flow rate in the transverse direction (for a zero tip clearance). Consequently, at the blade entrance, there exists, generally, a nonzero defect force, which can be specified through the matching conditions.

There is nothing to remark here in connection with the calculation procedure, which will be described in Section 4 for the flow inside the rotating blading. At the exit, a change of coordinates occurs and the calculation continues in the absolute frame of reference. Entering the next annular duct region presents no problems as the defect force terms have been zeroed at the trailing edge. Inside the annular duct region the calculation is realized as will be described in Section 4.

With the above remarks we shall proceed to develop the equations that will be solved by the present calculation method.

3 Governing Equations

In our analysis we use the mass conservation equation, the momentum conservation equation, the energy conservation equation, and the vorticity transport equation in order to describe the flow field of a steady, viscous, and compressible fluid.

In these equations the gravity terms are neglected (gas flow) and the flow field is supposed adiabatic (zero heat exchange).

In order to develop the equations in scalar form, we use an orthogonal curvilinear axisymmetric coordinate system (m, n, ϑ). After a peripheral integration from suction to pressure surface of the blade (see Douvikas et al., 1987, for details), we get the following set of differential equations, written in deficit form (difference between the equations for the "external" and the real flow fields). These equations have been developed in detail by Kaldellis (1988) and Douvikas (1988).

In fact, the peripheral integration (which renders our formulation compatible with the one used for the calculation of the flow in the meridional plane) results in a loss of information. This loss manifests itself with the appearance of the classical (Papailiou et al., 1977; Comte et al., 1981; Horlock, 1971), additional unknowns (terms) of the defect forces and the peripheral fluctuations. In the frame of the present analysis the peripheral fluctuation terms have been neglected.

Momentum Equation in the Peripheral Direction (ϑ)

$$\frac{\partial}{\partial m}\left[B(\bar{\rho}_e \bar{W}_{m_e} \bar{W}_{u_e} - \bar{\rho}\,\bar{W}_m \bar{W}_u)\right] + \frac{\partial}{\partial n}\left[B(\bar{\rho}_e \bar{W}_{n_e} \bar{W}_{u_e} - \bar{\rho}\,\bar{W}_n \bar{W}_u)\right] = D_{1_u} + \frac{\partial}{\partial n}(B\Delta\bar{\tau}_{nu}) - b\cos\varphi[(\bar{\rho}_e \bar{W}_{u_e} \bar{W}_{n_e} - \bar{\rho}\,\bar{W}_u \bar{W}_n) + 2\omega R(\bar{\rho}_e \bar{W}_{n_e} - \bar{\rho}\,\bar{W}_n)] - b\sin\varphi[(\bar{\rho}_e \bar{W}_{u_e} \bar{W}_{m_e} - \bar{\rho}\,\bar{W}_u \bar{W}_m) + 2\omega R(\bar{\rho}_e \bar{W}_{m_e} - \bar{\rho}\,\bar{W}_m)] - B[k_n(\bar{\rho}_e \bar{W}_{u_e} \bar{W}_{m_e} - \bar{\rho}\,\bar{W}_u \bar{W}_m) + k_m(\bar{\rho}_e \bar{W}_{u_e} \bar{W}_{n_e} - \bar{\rho}\,\bar{W}_u \bar{W}_n)] + b(\cos\varphi \cdot \Delta\bar{\tau}_{nu} + \sin\varphi \cdot \Delta\bar{\tau}_{mu}) \quad (1)$$

where D_{1_u} is the peripheral component of the deficit force.

Momentum Equation in the Normal Direction (n)

$$R \cdot \frac{\partial[b(\bar{p}_e - \bar{p})]}{\partial n} = -\frac{\partial}{\partial n}\left[B(\bar{\rho}_e \bar{W}_{n_e}^2 - \bar{\rho}\,\bar{W}_n^2)\right] - \frac{\partial}{\partial m}\left[B(\bar{\rho}_e \bar{W}_{m_e} \bar{W}_{n_e}\right.$$

$$- \bar{\rho}\bar{W}_m\bar{W}_n)] + D_{1_n} + \frac{\partial(B\Delta\bar{\tau}_{nn})}{\partial n} + b\cos\varphi[(\bar{\rho}_e\bar{W}^2_{u_e} - \bar{\rho}\bar{W}^2_u)$$
$$+ 2\omega R(\bar{\rho}_e\bar{W}_{u_e} - \bar{\rho}\bar{W}_u) + \omega^2R^2(\bar{\rho}_e - \bar{\rho})]$$
$$- b\Delta\bar{\tau}_{uu}\cos\varphi + Bk_m[(\bar{\rho}_e\bar{W}^2_{m_e} - \bar{\rho}\bar{W}^2_m)$$
$$- (\bar{\rho}_e\bar{W}^2_{n_e} - \bar{\rho}\bar{W}^2_n)] - 2Bk_n(\bar{\rho}_e\bar{W}_{n_e}\bar{W}_{m_e} - \bar{\rho}\bar{W}_n\bar{W}_m) \quad (2)$$

Mass Conservation Equation

$$\frac{\partial[B(\bar{\rho}_e\bar{W}_{m_e} - \bar{\rho}\bar{W}_m)]}{\partial m} + \frac{\partial[B(\bar{\rho}_e\bar{W}_{n_e} - \bar{\rho}\bar{W}_n)]}{\partial n}$$
$$+ Bk_n(\bar{\rho}_e\bar{W}_{m_e} - \bar{\rho}\bar{W}_m) + Bk_m(\bar{\rho}_e\bar{W}_{n_e} - \bar{\rho}\bar{W}_n) = 0 \quad (3)$$

Energy Conservation Equation

$$\frac{\partial}{\partial m}[B(\bar{\rho}\bar{V}_m\bar{h}_t - \bar{\rho}_e\bar{V}_{m_e}\bar{h}_{t_e})] + \frac{\partial}{\partial n}[B(\bar{\rho}\bar{V}_n\bar{h}_t - \bar{\rho}_e\bar{V}_{n_e}\bar{h}_{t_e})] =$$
$$= - UD_{1_u} + B[k_n(\bar{\rho}_e\bar{V}_{m_e}\bar{h}_{t_e} - \bar{\rho}\bar{V}_m\bar{h}_t) + k_m(\bar{\rho}_e\bar{V}_{n_e}\bar{h}_{t_e} - \bar{\rho}\bar{V}_n\bar{h}_t)]$$
$$+ \frac{\partial}{\partial n}(B\bar{V}_u\bar{\tau}_{nu}) + \frac{\partial}{\partial n}(B\bar{V}_m\bar{\tau}_{mn}) + \frac{\partial}{\partial n}(B\bar{V}_n\bar{\tau}_{nn}) \quad (4)$$

Transport of Vorticity Equation in the m Direction

$$\bar{\rho}\bar{W}_m\frac{\partial\bar{\xi}^*_m}{\partial m} + \left(\bar{\rho}\bar{W}_n - 2\mu_\tau\frac{\cos\varphi}{R}\right)\frac{\partial\bar{\xi}^*_m}{\partial n} + \bar{\xi}^*_m\Bigg[\frac{\partial(\bar{\rho}\bar{W}_n)}{\partial n}$$
$$+ \bar{\rho}\bar{W}_m\frac{\sin\varphi}{R} + \bar{\rho}\bar{W}_n\frac{\cos\varphi}{R}$$
$$+ \bar{\rho}\bar{W}_mk_n - \bar{\rho}\bar{W}_m\frac{\partial\ln b}{\partial m}\Bigg] = \frac{\partial(\bar{\rho}\bar{W}_m)}{\partial n}(\bar{\xi}^*_n - 2\omega b\sin\varphi)$$
$$+ \bar{\xi}^*_n\left(\bar{\rho}\bar{W}_m\frac{\partial\ln b}{\partial n} - \bar{\rho}\bar{W}_mk_m - 2\mu_\tau\frac{\cos\varphi}{R}\frac{\partial\varphi}{\partial n}\right)$$
$$- 2\omega\Bigg[\cos\varphi\frac{\partial(b\bar{\rho}\bar{W}_n}{\partial n}$$
$$+ b\bar{\rho}\bar{W}_m\left(\frac{\sin\varphi}{R} + k_n\right)\cos\varphi + b\bar{\rho}\bar{W}_n\left(\frac{\cos^2\varphi}{R} - k_n\sin\varphi\right)$$
$$- b\bar{\rho}\bar{W}_m\frac{\partial\ln b}{\partial n}\sin\varphi\Bigg]$$
$$+ \mu_\tau\frac{\partial^2\bar{\xi}^*_m}{\partial n^2} + \mu_\tau b\bar{W}_u\frac{\cos\varphi}{R}\left(\frac{\partial\varphi}{\partial n}\right)^2 \quad (5)$$

In order to arrive at these equations we have neglected terms that contain the derivatives of the total shear stresses in the meridional direction and the (viscous stresses) × (curvature) terms.

Additionally, using the three components of the momentum equation written in deficit form, we may derive by simple integration from hub to tip along (n), the following set of integral equations

Momentum Equation in the Peripheral Direction (ϑ)

$$DU_1 = \frac{\partial}{\partial m}(\bar{W}_{u_{e_w}}\Delta^*_{m_w})$$
$$+ \frac{\partial}{\partial m}(\Theta_{mu_w})$$
$$+ \frac{\partial}{\partial m}\int_{n_w}^{n_{w'}} B(\bar{W}_{u_e} - \bar{W}_{u_{e_w}})(\bar{\rho}_e\bar{W}_{m_e} - \bar{\rho}\bar{W}_m)dn$$
$$- B_w\bar{\rho}_{e_w}\bar{W}_{u_{e_w}}\bar{W}_{n_{e_w}} - B_w\bar{\tau}_{nu_w} + \int_{n_w}^{n_{w'}} b\bar{\tau}_{nu}\cos\varphi\, dn$$
$$+ \int_{n_w}^{n_{w'}} b\bar{\tau}_{mu}\sin\varphi dn$$
$$+ 2\omega\int_{n_w}^{n_{w'}} B\sin\varphi(\bar{\rho}_e\bar{W}_{m_e} - \bar{\rho}\bar{W}_m)dn + 2\omega$$
$$\int_{n_w}^{n_{w'}} B\cos\varphi(\bar{\rho}_e\bar{W}_{n_e} - \bar{\rho}\bar{W}_n)dn$$
$$+ \int_{n_w}^{n_{w'}} b\sin\varphi(\bar{\rho}_e\bar{W}_{m_e}\bar{W}_{u_e} - \bar{\rho}\bar{W}_m\bar{W}_u)dn$$
$$+ \int_{n_w}^{n_{w'}} b\cos\varphi(\bar{\rho}_e\bar{W}_{u_e}\bar{W}_{n_e} - \bar{\rho}\bar{W}_u\bar{W}_n)dn$$
$$+ \int_{n_w}^{n_{w'}} Bk_n(\bar{\rho}_e\bar{W}_{u_e}\bar{W}_{m_e} - \bar{\rho}\bar{W}_u\bar{W}_m)dn$$
$$+ \int_{n_w}^{n_{w'}} Bk_m(\bar{\rho}_e\bar{W}_{u_e}\bar{W}_{n_e} - \bar{\rho}\bar{W}_u\bar{W}_n)dn \quad (6)$$

where

$$DU_1 = \int_{n_w}^{n_{w'}} D_{1_u}dn \quad (7)$$

This equation is used for the calculation of the peripheral striction parameter k (defined in equation (11) of this work) for semi-bounded regions (see Douvikas et al., 1987), where the deficit forces are nonexistent.

Momentum Equation in the Meridional Direction (m)

$$\frac{\partial}{\partial m}(\bar{W}_{m_{e_w}}\cdot\Delta^*_{m_w}) + \frac{\partial}{\partial m}(\Theta_{mm_w})$$
$$+ \frac{\partial}{\partial m}\int_{n_w}^{n_{w'}} B(\bar{W}_{m_e} - \bar{W}_{m_{e_w}})\cdot(\bar{\rho}\bar{W}_{m_e} - \bar{\rho}\bar{W}_m)dn$$
$$= B_w\bar{\rho}_{e_w}\bar{W}_{m_{e_w}}\bar{W}_{n_{e_w}} + \int_{n_w}^{n_{w'}} D_{1_m}dn - \frac{\partial}{\partial m}\int_{n_w}^{n_{w'}} B(\bar{p}_e - \bar{p})dn$$
$$+ \int_{n_w}^{n_{w'}} b(\bar{p}_e - \bar{p})\sin\varphi dn + B_w\bar{\tau}_{nm_w}$$
$$+ \int_{n_w}^{n_{w'}} b\bar{\tau}_{uu}\sin\varphi dn + \omega^2\int_{n_w}^{n_{w'}} BR\sin\varphi(\bar{\rho}_e - \bar{\rho})dn$$
$$+ 2\omega\int_{n_w}^{n_{w'}} B\sin\varphi(\bar{\rho}_e\bar{W}_{u_e} - \bar{\rho}\bar{W}_u)dn$$
$$+ \int_{n_w}^{n_{w'}} \mathrm{b}\sin\varphi(\bar{\rho}_e\bar{W}^2_{u_e} - \bar{\rho}\bar{W}^2_u)dn$$
$$+ \int_{n_w}^{n_{w'}} Bk_n[(\bar{\rho}_e\bar{W}^2_{n_e} - \bar{\rho}\bar{W}^2_n) - (\bar{\rho}_e\bar{W}^2_{m_e} - \bar{\rho}\bar{W}^2_m)]dn$$
$$- 2\int_{n_w}^{n_{w'}} Bk_m(\bar{\rho}_e\bar{W}_{n_e}\bar{W}_{m_e} - \bar{\rho}\bar{W}_n\bar{W}_m)dn \quad (8)$$

Total Kinetic Energy Integral Equation

$$\frac{\partial}{\partial m}(\Theta^{**}_w) = \int_{n_w}^{n_{w'}} B\bar{\rho}\left(\bar{W}_m\frac{\partial\bar{W}^2_e}{\partial m}\right.$$
$$\left. + \bar{W}_n\frac{\partial\bar{W}^2_e}{\partial n}\right)dn - 2\int_{n_w}^{n_{w'}} B\bar{\rho}_e\Bigg[\bar{W}_u\left(\bar{W}_{m_e}\frac{\partial\bar{W}_{u_e}}{\partial m}\right.$$
$$\left. + \bar{W}_{n_e}\frac{\bar{W}_{u_e}}{\partial n}\right) + \bar{W}_m\left(\bar{W}_{m_e}\frac{\partial\bar{W}_{m_e}}{\partial m} + \bar{W}_{n_e}\frac{\partial\bar{W}_{m_e}}{\partial n}\right)$$

$$+\bar{W}_n\left(\bar{W}_{m_e}\frac{\bar{W}_{n_e}}{\partial m}+\bar{W}_{n_e}\frac{\partial \bar{W}_{n_e}}{\partial n}\right)\Bigg]dn$$

$$+2\int_{n_w}^{n_{w'}}(\bar{W}_u D_{1_u}+\bar{W}_m D_{1_n}+\bar{W}_n D_{1_m})dn$$

$$-2\frac{\partial}{\partial m}\int_{n_w}^{n_{w'}}B\bar{W}_m(\bar{p}_e-\bar{p})dn+2\int_{n_w}^{n_{w'}}b(\bar{p}_e-\bar{p})$$

$$\frac{\partial(R\bar{W}_m)}{\partial m}dn+2\int_{n_w}^{n_{w'}}b(\bar{p}_e-\bar{p})\frac{\partial(R\bar{W}_n)}{\partial n}dn$$

$$+2\omega^2\int_{n_w}^{n_{w'}}bR^2(\bar{W}_n\cos\varphi+\bar{W}_m\sin\varphi)(\bar{\rho}_e-\bar{\rho})dn$$

$$+4\omega\int_{n_w}^{n_{w'}}B\bar{\rho}_e\bar{W}_{u_e}(\bar{W}_n\cos\varphi+\bar{W}_m\sin\varphi)dn$$

$$-4\omega\int_{n_w}^{n_{w'}}B\bar{\rho}_e\bar{W}_u(\bar{W}_{n_e}\cos\varphi$$

$$+\bar{W}_{m_e}\sin\varphi)dn+2\int_{n_w}^{n_{w'}}b\bar{\rho}_e\bar{W}_{u_e}(\bar{W}_{u_e}\bar{W}_m$$

$$-\bar{W}_u\bar{W}_{m_e})\sin\varphi dn+2\int_{n_w}^{n_{w'}}b\bar{\rho}_e\bar{W}_{u_e}$$

$$(\bar{W}_{u_e}\bar{W}_n-\bar{W}_{n_e}\bar{W}_u)\cos\varphi dn+2\Bigg\{\frac{\partial}{\partial m}\int_{n_w}^{n_{w'}}B\bar{\rho}\bar{W}_m\frac{\langle\overline{q^2}\rangle}{2}dn$$

$$+\frac{1}{2}c_D B_w\bar{\rho}_{e_w}\bar{W}^3_{s_{e_w}}$$

$$+\frac{\partial}{\partial m}\int_{n_w}^{n_{w'}}B\bar{\rho}[(\bar{W}_u+\bar{W}_m)\langle\bar{u}^2\rangle+\bar{W}_n\langle\overline{uw}\rangle]dn$$

$$-\int_{n_w}^{n_{w'}}b\bar{W}_u\bar{\tau}_{nu}\cos\varphi dn\Bigg\}$$

$$-\int_{n_w}^{n_{w'}}Bk_m\bar{\rho}\bar{W}_n(\bar{W}_e^2-\bar{W}^2)dn-\int_{n_w}^{n_{w'}}Bk_n\bar{\rho}\bar{W}_m(\bar{W}_e^2-\bar{W}^2)dn$$

$$-2\int_{n_w}^{n_{w'}}Bk_m\bar{\rho}_e\bar{W}_{m_e}(\bar{W}_m\bar{W}_{n_e}$$

$$-\bar{W}_n\bar{W}_{m_e})dn+2\int_{n_w}^{n_{w'}}Bk_n\bar{\rho}_e\bar{W}_{n_e}(\bar{W}_m\bar{W}_{n_e}-\bar{W}_n\bar{W}_{m_e})dn \quad (9)$$

Note that the total kinetic energy integral equation as written above has been derived by considering the mean kinetic energy integral equation and the circumferential mean turbulent kinetic energy equation, neglecting in it the pressure fluctuation terms. The final equation is derived when the production term is substituted by its expression from the turbulent kinetic energy equation.

The mean kinetic energy integral equation is developed by multiplying the three momentum equations in deficit form (equations for the external flow minus equations for the real flow) by $2\bar{W}_u$, $2\bar{W}_m$, and $2\bar{W}_n$, respectively, and summing them up. Then we integrate the resulting equation along (n) from hub to tip.

Global Mass Flow Rate Equation

$$\frac{\partial\mu}{\partial m}\left(\frac{m_s}{2\pi}+\hat{\Delta}^*_{m_H}+\hat{\Delta}^*_{m_T}\right)+\mu\frac{\partial}{\partial m}(\hat{\Delta}^*_{m_H}+\hat{\Delta}^*_{m_H})$$

$$+\frac{\mu}{2\pi}\cdot\frac{\partial m_s}{\partial m}-\frac{\partial}{\partial m}(\hat{\Delta}^*_{m_H}+\hat{\Delta}^*_{m_T})$$

$$+\int_{n_w}^{n_{w'}}B(k_n\bar{\rho}_e\bar{W}_{m_e}+k_m\bar{\rho}_e\bar{W}_{n_e})dn=0 \quad (10)$$

where μ is the meridional striction parameter and m_s the mass flow rate of the machine. The global mass equation, along with the total kinetic energy integral equation and the momentum equation in the meridional direction written twice (for the hub and the tip shear layers) constitute a nonlinear system of ordinary equations, which is used to calculate the shear layer thicknesses (δ_H, δ_T) and the friction velocities (u_{T_H}, u_{T_T}) simultaneously for both the hub and tip shear layers, as well as the meridional striction parameter μ.

4 Calculation Procedure

The calculation procedure may be divided into three parts. The first one makes use of equations in differential form and provides distributions along normals (n) of certain flow parameters. These are the following: (a) the meridional vorticity (and the corresponding peripheral velocity profile); (b) the total enthalpy, (c) the static pressure; (d) the three components of the deficit force; and finally, (e) the normal velocity.

The equations are used in deficit form, except for the one concerning meridional transport of vorticity.

The second part makes use of the developed integral equations (meridional momentum integral equation, energy integral equation for both hub and tip shear layers, and the global mass flow rate equation) and essentially computes the longitudinal velocity profiles and related quantities. Hub and tip shear layers are calculated simultaneously and a two-parameter velocity profile family is used for closure (Kuhn and Nielsen, 1973). In fact the two independent parameters chosen are the shear layer thickness δ and the wall friction velocity u_T, while additional quantities needed, such as the dissipation factor c_D, are limited to these two parameters through the same relations used for classical boundary layers (see for details Assassa and Papailiou (1979) and Papailiou (1981).

The last part concerns the correction of the external flow field using the meridional (parameter μ) and peripheral (parameter k) blockage influence.

The corresponding procedure, which is an approximate viscous/inviscid interaction one, relates modifications of the external flow to the growth of the two wall shear layers. it is described in detail by Kaldellis (1988) and Douvikas (1988) and assumes that the distribution along a normal (n) of the quantity $\bar{\rho}_e\bar{W}_{m_e}$, resulting from an "inviscid" meridional calculation method, is conserved as far as its first derivative is concerned. It is displaced, however, in order to accommodate the blockage effects of the two shear layers.

Recapitulating in order to render things clearer, we may say that the independent variables of our calculation procedure are the two striction parameters $\mu(m)$ and $k(m)$, the two shear layer thicknesses $\delta_H(m)$ and $\delta_T(m)$, the friction velocities at hub and tip $u_{T_H}(m)$ and $u_{T_T}(m)$, the distribution of real meridional vorticity $\bar{\xi}_m(m, n)$, and real total enthalpy $\bar{h}_t(m, n)$.

For computational purposes, the calculation domain is divided into subspaces according to the corresponding boundary conditions. As we have referred to in our previous work (Douvikas et al., 1987); Kaldellis et al., 1988), three different cases of subspaces may be specified: the unbounded case (external aerodynamics case), the semi-bounded case (annular duct case), and the fully bounded case (bladed space).

As the calculation proceeds from subspace to subspace, the inlet conditions for each one of them have to be specified. Details concerning the matching conditions are presented by Kaldellis (1988) and Douvikas (1988).

With these remarks we proceed to the description of the computational algorithm. The geometry of the machine and the initial external flow field of the previous iteration step, as well as the real flow quantities up to the previous station j (see Fig. 1), are supposed known. The procedure will be described for the calculation of the quantities at station (j + 1). The algorithm possesses the following steps:

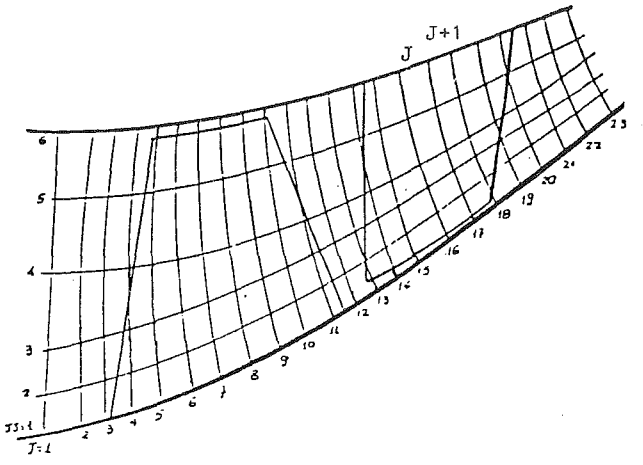

Fig. 1 Schematic representation of the computational grid

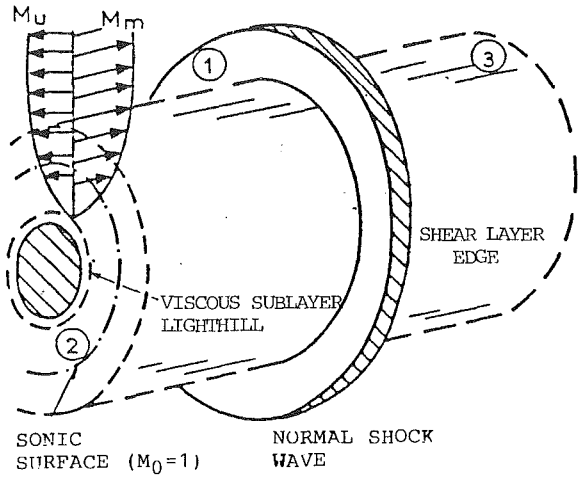

Fig. 2 Schematic presentation of the axisymmetric model used for the calculation of the shock wave/secondary flow interaction region

STEP 1 Apply equations (4) and (5) in order to obtain a first estimate of the real total enthalpy $\bar{h}_t(n)$ and real meridional vorticity distribution $\bar{\xi}^*_m(n)$, respectively, at $(j+1)$ for both hub and tip shear layers. The wall values $\bar{h}_{t_w}$ and $\bar{\xi}_{m_w}$ cannot be calculated in this step. They will be calculated later.

STEP 2 Assume an initial set of values for the independent shear layer parameters δ_H, δ_T, u_{T_H}, u_{T_T}, and μ at $(j+1)$.

STEP 3 Calculate the value of the parameter k (peripheral striction), which is common to both hub and tip wall shear layers. This calculation is performed using:

(*a*) For the unbladed region, the integral momentum equation in the peripheral direction (equation (6)), where both wall shear layers have been considered simultaneously.

(*b*) For the bladed region, the condition that the total recirculating mass flow rate in the transverse direction be zero (which is written in the system of coordinates attached to the blading).

From this value, the corresponding value of the meridional vorticity $\bar{\xi}_{m_w}$ at the wall can be computed from the following equation (Kaldellis et al., 1988):

$$k = \int_{n_w}^{n_w+\delta} R(\bar{\xi}^*_m - \bar{\xi}^*_{m_e})dn - B_w \hat{W}_{u_{e_w}} \tag{11}$$

where $(\hat{\ })_e$ denotes values of the intially given external flow field, and k is already known.

STEP 4 Compute the modification of the external flow field due to peripheral and meridional blockage effects using the values of k and μ.

In fact, using the analysis of Kaldellis (1988) and Douvikas (1988) by which the modification of the external velocity flow field in magnitude and direction can be computed, the distribution of the external total enthalpy $\bar{h}_{t_e}$, the static pressure $\bar{p}_e(n)$, and the total pressure $\bar{p}_{t_e}(n)$ are corrected.

STEP 5 Compute the distributions of the real flow field quantities in the n direction.

(*a*) The peripheral velocity is computed by a simple integration from the distribution of the meridional vorticity component as (Kaldellis et al., 1988)

$$\bar{W}_u = \hat{W}_{u_e} + \frac{k}{B} - \frac{1}{B}\int_n^{n_w+\delta} R(\bar{\xi}^*_m - \bar{\xi}^*_{m_e})dn \tag{12}$$

(*b*) The longitudinal velocity profile is computed using the expressions developed by Kaldellis (1988) and Douvikas (1988) (calculation of the reduced velocities and density profiles) and then the analysis of Mellor. An expression of the following form results:

$$\bar{W}_s = \bar{W}_s(\delta, u_T, \bar{W}_{s_e}, \bar{\rho}) \tag{13}$$

(*c*) Knowing the longitudinal and the peripheral velocity profiles, the meridional profile is computed.

(*d*) The normal velocity component is computed from the mass conservation equation (3).

(*e*) For the bladed region only, the peripheral component of the defect force is computed, using the momentum equation (1) in the peripheral direction. In order to compute the other two components of the deficit force the blade geometry and the evolution of the blade boundary layers are needed. We can generally write that

$$D_{l_m} = -D_{l_u}\tan(\beta' - \epsilon_D) \tag{14}$$

$$D_{l_n} = D_{l_u}\tan\beta' \cdot \tan\delta' \tag{15}$$

The parameter ϵ_D is zero, when the definite force vector is perpendicular to the blade mean surface.

(*f*) The real static pressure is computed from the momentum equation in the normal direction (2).

(*g*) The real density is computed from the total enthalpy, the static pressure and the velocity distributions using the gas state law.

STEP 6 Update the values of the meridional vorticity distribution $\bar{\xi}_m$ and the real total enthalpy $\bar{h}_t$ using the computed values of the flow field at station $(j+1)$, for both hub and tip shear layers. Repeat STEPS 3 to 5.

STEP 7 Having the values of all parameters at station $(j+1)$, we proceed to validate the system of our integral equations, which are:

(*a*) The integral momentum equation (8) in the meridional direction (two equations for hub and tip, respectively).

(*b*) The integral total kinetic energy equation (9) (two equations for hub and tip, respectively).

(*c*) The global mass conservation equation (10).

If the residuals of the integral equations are different from zero, we proceed to the calculation of a new set of shear layer parameters $(\delta_H, u_{T_H}, \mu, \delta_T, u_{T_T})$. A Gauss–Newton type iterative procedure is used in this respect. Then STEPS 3 to 7 are repeated until convergence is achieved.

Once the total computational algorithm has been described, we present below the computational algorithm used for the shock-secondary flow interaction case.

Calculation Procedure for Shock-Secondary Flow Interaction. For the calculation of the shock-secondary flow interaction flow field, we shall use a modified small-disturbance

theory similar to that of Panaras and Inger (1977) and Kallas and Papailiou (1987). In addition to what has been presented in these references, energy exchange and variable static pressure before and after the shock will be considered in the present case. Details of the development may be found from Panaras and Inger (1977) and Kallas and Papailiou (1987), while some additional information concerning the extension to the shock-secondary flow interaction may be found from Kaldellis (1988).

The simple model that describes the interaction region for an axisymmetric configuration is presented in Fig. 2. It consists of a three-dimensional shear layer (region 2) of constant thickness, of the outer part of the flow upstream of the shock wave (region 1) and of the outer part of the flow downstream at the shock wave (region 3). The shear layer is divided into two parts: the outer one in which the flow is transonic and rotational, and the inner one, in which there exists a subsonic region through which disturbances are transmitted upstream.

Following a small-disturbance approach, the flow field is decomposed into a basic flow field and a disturbance. The basic flow field consists of the real external pressure field upstream of the shock wave and a fictitious continuation of it in the region downstream of the shock. The basic flow field is continuous.

The disturbance consists of the shock wave induced pressure step, which, if added to the basic flow field downstream of the shock, will restore the real flow field.

The theoretical development is based on the Euler equations (Kaldellis, 1988). Denoting the basic external flow quantities with the subscript zero and disturbances with $\Delta(\ )$, we have

$$\hat{W}_{m_e} = W_{m_o}(m, n) + \Delta W_{m_e}(m, n) \tag{16}$$

$$\hat{W}_{u_e} = W_{u_o}(m, n) + \Delta W_{u_e}(m, n) \tag{17}$$

$$\hat{W}_{n_e} = W_{n_o}(m, n) + \Delta W_{n_e}(m, n) \tag{18}$$

$$\hat{p}_e = p_o(m, n) + \Delta p_e(m, n) \tag{19}$$

$$\hat{h}_{t_e} = h_{t_o}(m, n) + \Delta h_{t_e}(m, n) \tag{20}$$

$$\hat{\rho}_e = \rho_o(m, n) + \Delta \rho_e(m, n) \tag{21}$$

In order to compute the flow field of the interaction region, the external flow angle is considered unchanged through the shock wave, which is assumed normal to the flow direction. Consequently, we have

$$\hat{\beta}_e = \beta_{e_o} \tag{22}$$

Introduction of the above expressions (16) to (22) into the Euler equations yields, after manipulation and rearrangement (Kaldellis, 1988) the following equation, written in the coordinate system relative to the blades for the disturbance of the static pressure field:

$$\frac{\partial^2(\Delta\bar{p}_e)}{\partial n^2} + \left(\frac{1}{R} - \frac{2}{\bar{M}_{o_w}}\frac{\partial \bar{M}_{o_w}}{\partial n}\right)\frac{\partial(\Delta\bar{p}_e)}{\partial n} + (1-\bar{M}_{o_w}^2)\frac{\partial^2(\Delta\bar{p}_e)}{\partial m^2}\cos^2\bar{\beta}_o + \frac{\partial \bar{p}_o}{\partial n}\cdot\left[-\frac{1}{\bar{p}_o}\frac{\partial(\Delta\bar{p}_e)}{\partial n} - \frac{1}{\bar{\rho}_o a_o^2}\cdot\frac{\partial(\Delta\bar{p}_e)}{\partial n} + \left(\frac{2}{\bar{M}_{o_w}}\frac{\partial \bar{M}_{o_w}}{\partial n} + \frac{1}{\bar{p}_o}\frac{\partial \bar{p}_o}{\partial n}\right)\cdot\frac{(\Delta\bar{p}_e)}{\bar{\rho}_o \cdot a_o^3} + \frac{2(\Delta\bar{p}_e)}{\bar{\rho}_o \cdot a_o^3}\left(\frac{\partial a_o}{\partial m}\cos\bar{\beta}_o + \frac{\partial a_o}{\partial n}\right) - \frac{(\Delta\bar{p}_e)}{\bar{\rho}_o a^2 R} - \frac{1}{\bar{\rho}_o a_o^2}\cdot\frac{\partial(\Delta\bar{p}_e)}{\partial m}\cos\bar{\beta}_o\right] = 0 \tag{23}$$

For numerical analysis purposes, the above equation can be written as

$$\frac{\partial^2(\Delta\bar{p}_e)}{\partial n^2} + A\frac{\partial(\Delta\bar{p}_e)}{\partial n} + B\frac{\partial^2(\Delta\bar{p}_e)}{\partial m^2} + \Gamma = 0 \tag{24}$$

A first set of boundary conditions, which is considered valid inside all three regions of the model presented in Fig. 2, is imposed by demanding the equality of the pressure disturbance fields at the edge of the shear layer. Continuity of the streamline slope across the edge of the shear layer is used as an additional boundary condition.

The numerical solution of equation (24) is obtained through a Fourier transform. The pressure disturbance field may be calculated at any distance from the wall through equation (23).

Prior to presenting the steps of the computational algorithm, it is important to mention that the real jump of static pressure across the shock wave is needed as a boundary condition.

In order to obtain the real static pressure jump, a modified Rankine–Hugoniot condition is applied, taking into account the area variation across the shock wave, which results from the shear layer presence. Then, the real static pressure jump Δp_{e_r} can be expressed in relation to the theoretical one Δp_{e_o} given by the Rankine–Hugoniot conditions through the following equation:

$$\frac{\Delta p_{e_r}}{\Delta p_{e_o}} = 1 - \gamma\frac{\dfrac{p^*_{o_3}}{p^*_{o_1}}}{\left(\dfrac{p^*_{o_3}}{p^*_{o_1}} - 1\right)}\cdot\left[\frac{\left(\dfrac{\delta^*_{m_H} + \delta^*_{m_T}}{h^*}\right)M^{*2}_{o_3}}{1 - \left[1 + \left(\dfrac{\delta^*_{m_H} + \delta^*_{m_T}}{h^*}\right)\right]M^{*2}_{o_3}}\right] \tag{25}$$

This expression, introduced in the secondary flow interaction procedure described below, gives a good approximation of the pressure distribution under which the shear layers will develop. However, as the displacement thicknesses is not known beforehand with accuracy, an iterative procedure is necessary. Of course, the additional viscous–inviscid interaction procedure described in Section 4 must be used here also, in order to "protect" the shear layers from excessive positive pressure gradients.

At this point we shall present the shock-secondary flow interaction calculation algorithm.

STEP 1 Assume a distribution of the shear layer parameters for the interaction region.

STEP 2 Use equation (25) and calculate the real pressure jump across the shock wave, making use of the displacement thickness values. Then calculate the static pressure field $\Delta\bar{p}_e(m, n)$ inside the interaction region using equation (24).

STEP 3 Using the previously calculated static pressure field, calculate all the other pertinent parameters of the external flow field (velocity, total enthalpy, density).

STEP 4 Using the algorithm presented in Section 4 for the shear layer calculation, calculate the real flow field.

STEP 5 Compare the new values of the shear layer parameters with those of STEP 1. If convergence has not been achieved, repeat STEPS 2 to 5. Otherwise, proceed to the calculation of the shear layer downstream of the interaction region.

The abovedescribed algorithm is rather stable and converges rapidly (only three or four iterations are needed).

Once the two computational algorithm have been presented, we shall proceed and present comparisons of computational results with experiments.

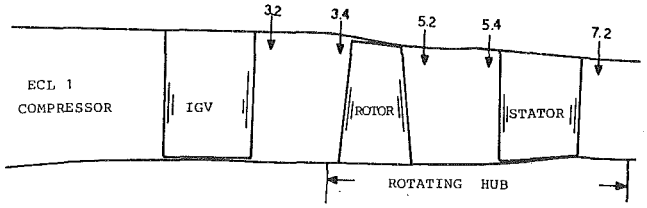

Fig. 3 Schematic representation of the ECL1 transonic axial compressor (meridional plane)

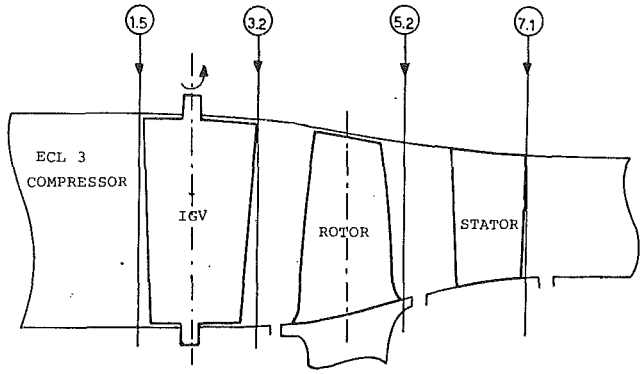

Fig. 4 Schematic representation of the ECL3 supersonic axial compressor (meridional plane)

5 Calculation Results, Comparison With Experiment, and Discussion

The calculation method described above was used to analyze the flow field through one transonic and one supersonic axial flow compressor stage, for which experimental results were available (Leboeuf and Naviere, 1983; Goutines and Naviere, 1987).

The transonic axial compressor stage ECL1, presented schematically in Fig. 3, possesses inlet guide vanes. On this figure are indicated the positions where measurements were taken (and comparisons between theory and experiment are performed). Due to limited space, comparisons will be presented only for stations (3.4), (5.4), and (7.2). No additional information about the experimental setup and the measurements will be presented here (it is already presented by Leboeuf and Naviere, 1983), other than the mass flow rate $m_s = 15.5$ kg/s, the stage pressure ratio $\pi = 1.35$, and the rotational speed $N = 10704$ rpm, which indicate the operating conditions characterizing the comparisons presented below.

The calculation was carried out using the meridional plane field issued from a meridional external flow calculation method with no wall shear layer presence.

The calculation results give the shear layer evolution along with the modified external flow field resulting from the approximate interaction procedure incorporated in the secondary flow calculation itself. No additional iteration using the external flow calculation method was performed. Figures 5–7 present comparisons between prediction and experiment for the spanwise evolution of W_m, a, p, p_t, and T_t. Solid lines on these figures represent the pitchwise-averaged flow field as computed by the present method. The "stars" represent the results of the external flow field calculated without wall shear layer presence and the squares represent the experimental results.

Overall agreement between computed and experimental results can be termed quite good at the inlet guide vanes exit (Fig. 5). The overall blockage is not yet important, but it is well predicted, as shown by the agreement of the external flow and real flow outside of the viscous shear layer regions. The total temperature increase near the hub, which is due to the rotating nacelle, fails to be predicted by the present method. In fact, in its present form this is not possible, although previously published work (Pavis et al., 1987) demonstrates how this could be done within engineering accuracy.

Again, at the exit of the rotor, agreement between computed and experimental results can be termed quite good (Fig. 6). The well-predicted overall blockage is quite important and one can remark the changes due to the peripheral blockage both upon the flow angle and the energy level at the rotor exit. The details of the shear layers are relatively well predicted, especially the exit flow angle. Still, the total temperature level inside the shear layers is underestimated, indicating that the computation of the lost work needs re-examination.

Finally, at the exit of the stator, agreement between computed and experimental results is good (Fig. 7). The external flow quantities agree well with the real ones inside the "inviscid" flow region, so that the same remark as before can be made for the overall blockage prediction. The details of the wall shear layers are well predicted (note that the longitudinal velocity profile has been presented here instead of the absolute angle profile, which is rather small).

We can observe the same discrepancy for the total temperature as for the rotor exit station. Although comparisons can only be made at the inlet and exit stations of the rotor, it is interesting to examine the evolution of the velocity field inside the rotor, relative to the blading. This evolution is presented in Fig. 8 for four successive stations (entrance, 33 percent of axial chord, 66 percent of axial chord, and rotor exit). Good inlet and outlet flow field agreement gives a good chance that the evolution presented in Fig. 8 represents reality.

The comparisons presented up to now concern the meridional and peripheral velocity fields, as well as the longitudinal one. In other approaches, the transverse velocity profile has played an important role, as the secondary vorticity is considered. A comparison of computed and experimental results for such a profile is presented in Fig. 9 for the rotor exit. The agreement is good, noting at the same time the important difference that exists between the initial and modified (by the combined meridional and peripheral blockage effects) external flow field.

The supersonic axial compressor stage ECL3, presented schematically in Fig. 4, possesses variable inlet guide vanes. On this figure, which presents a meridional section of the stage, are indicated the positions where measurements were taken (and comparisons between theory and experiment are performed). Due to limited space, comparisons will be presented only for stations (3.2), (5.2), and (7.1).

No additional information about the experimental setup and the measurements will be presented here either (it is already presented by Goutines and Naviere, 1987), other than the specific mass flow rate $m_s = 180$ kg/s/m^2, the stage pressure ratio $\pi = 1.84$, and the rotational speed $N = 15{,}965$ rpm, which indicate the operating conditions characterizing the comparison presented below.

The calculation was carried out using the meridional plane flow field issued form a meridional external flow calculation method with no wall shear layers.

The calculation results give the shear layer evolution along with the modified external flow field resulting from the approximate interaction procedure incorporated in the secondary flow calculation itself. No additional iteration using the external flow calculation method was performed here, as well.

Figures 10–12 present comparisons between prediction and experiment for the spanwise evolution of W_m, W_u, p, p_t, and T_t. The same symbols (as for the ECL1) are used for the present comparison.

Overall agreement between computed and experimental results can be termed quite good at the inlet guide vane exit (Fig.

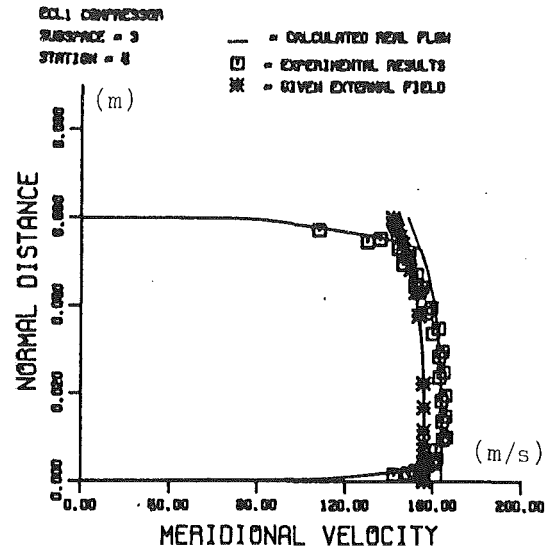

Fig. 5(*a*)

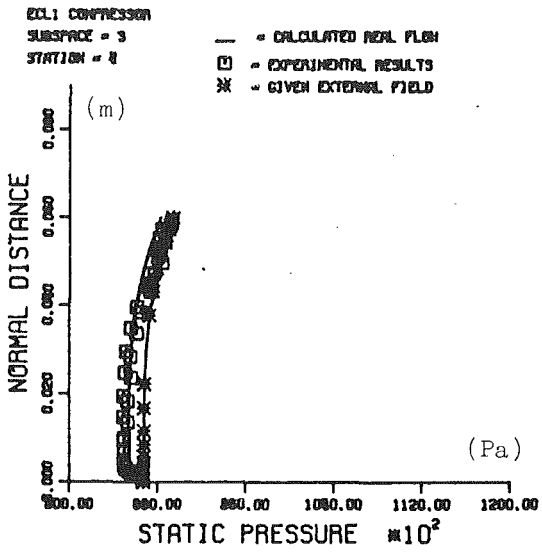

Fig. 5(*c*)

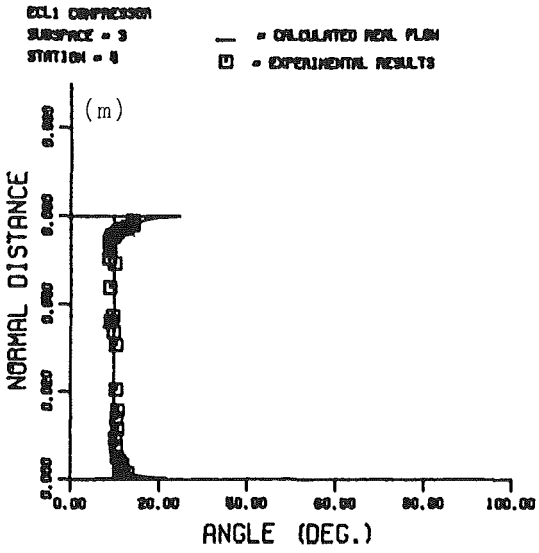

Fig. 5(*b*)

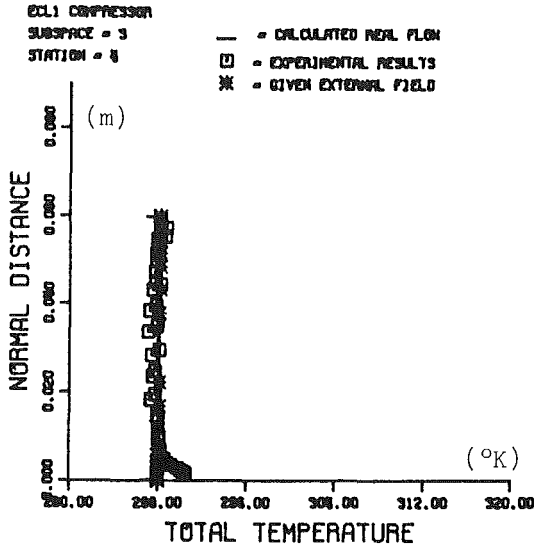

Fig. 5(*d*)

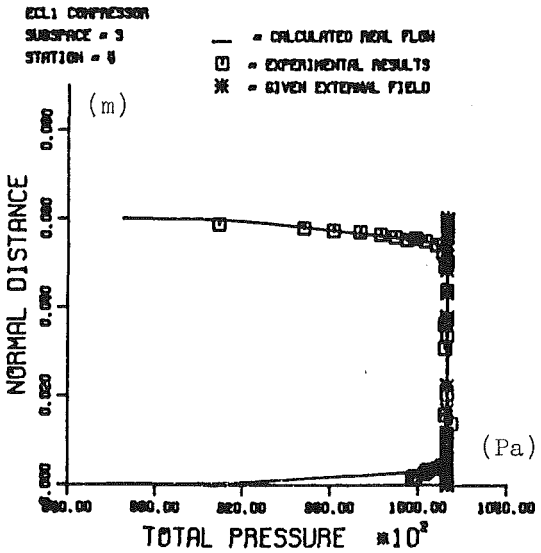

Fig. 5(*e*)

Fig. 5 Comparison between theory and experiment at exit of inlet guide vanes (Station 3.4, Fig. 3)

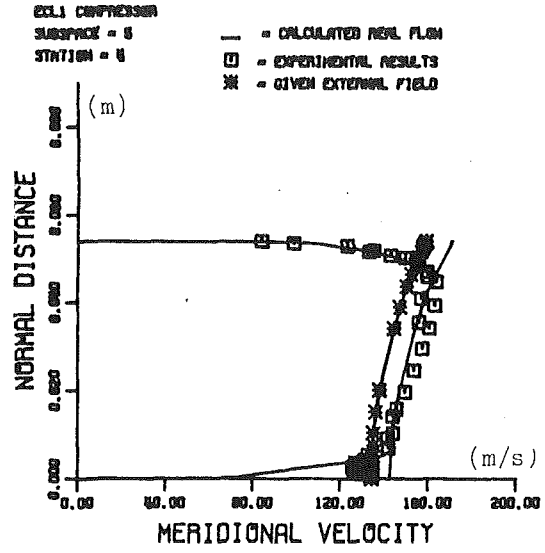

Fig. 6(*a*)

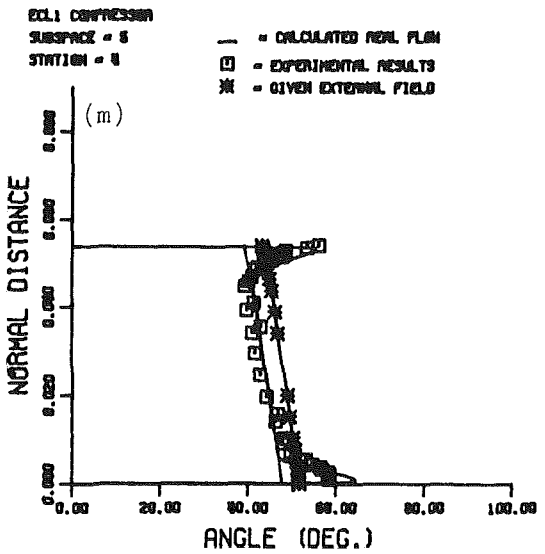

Fig. 6(*b*)

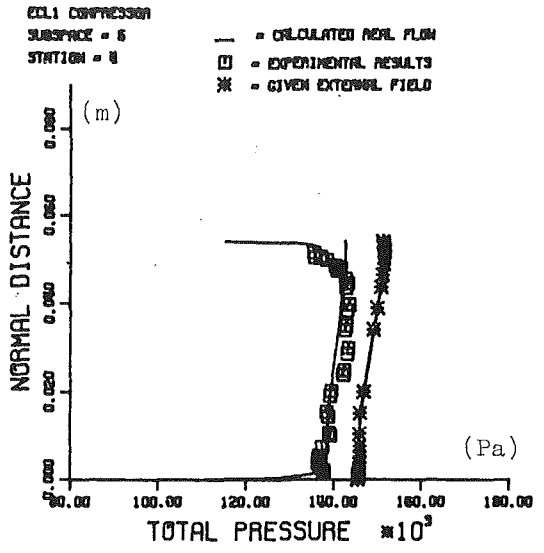

Fig. 6(*c*)

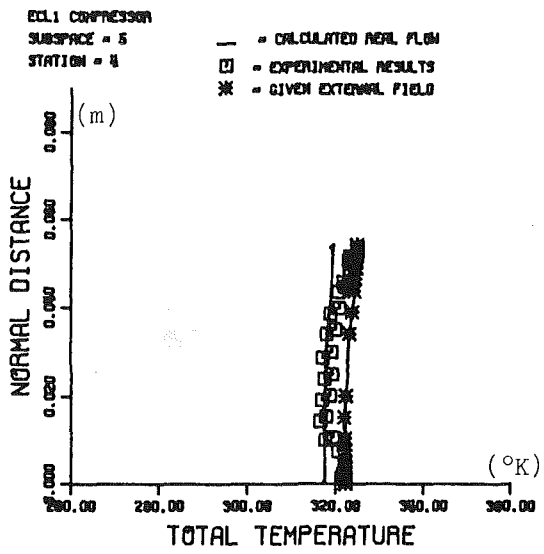

Fig. 6(*d*)

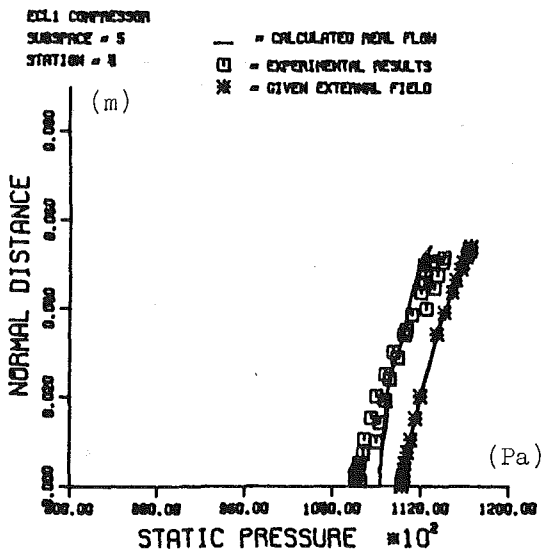

Fig. 6(*e*)

Fig. 6 Comparison between theory and experiment at exit of rotor (Station 5.4, Fig. 3)

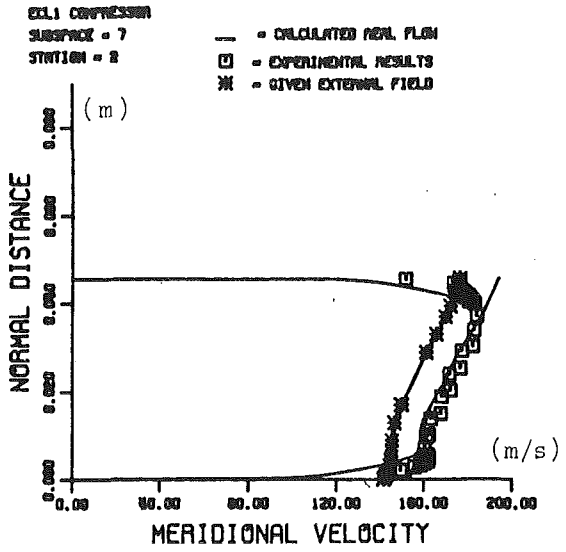

Fig. 7(*a*)

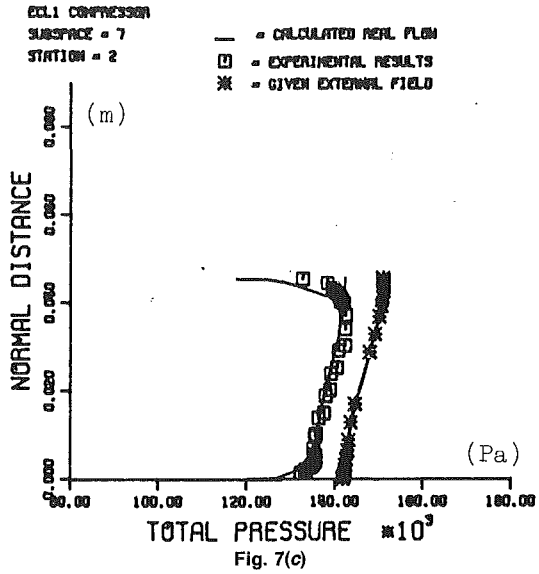

Fig. 7(*c*)

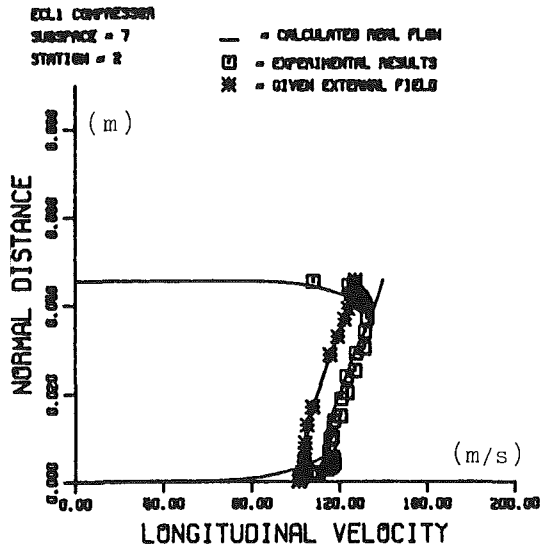

Fig. 7(*b*)

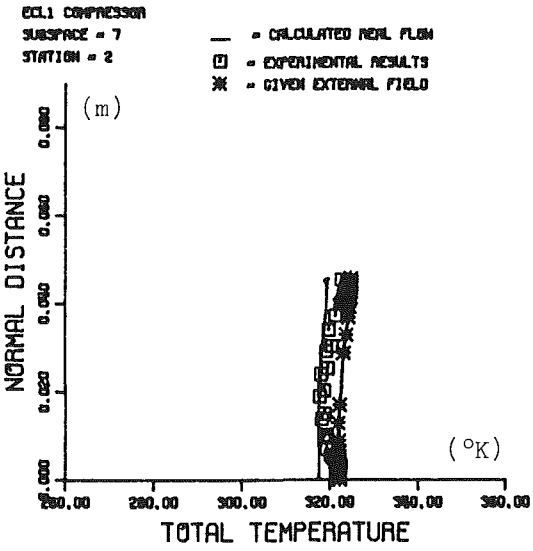

Fig. 7(*d*)

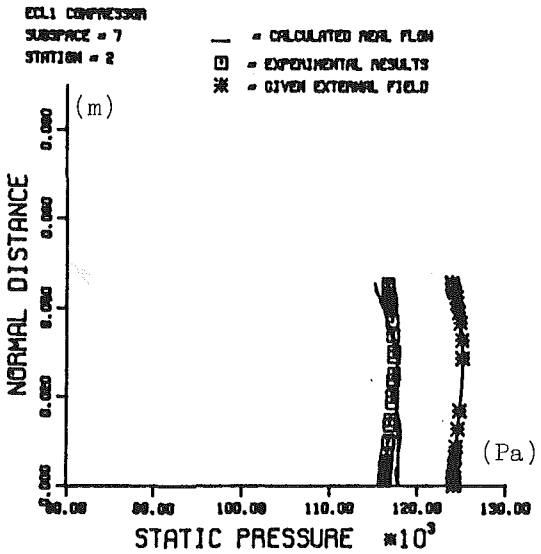

Fig. 7(*e*)

Fig. 7 Comparison between theory and experiment at exit of stator (Station 7.2, Fig. 3)

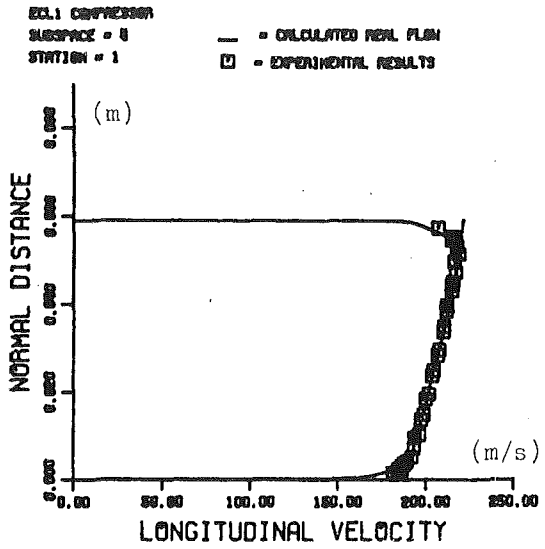

Fig. 8(*a*) Entrance

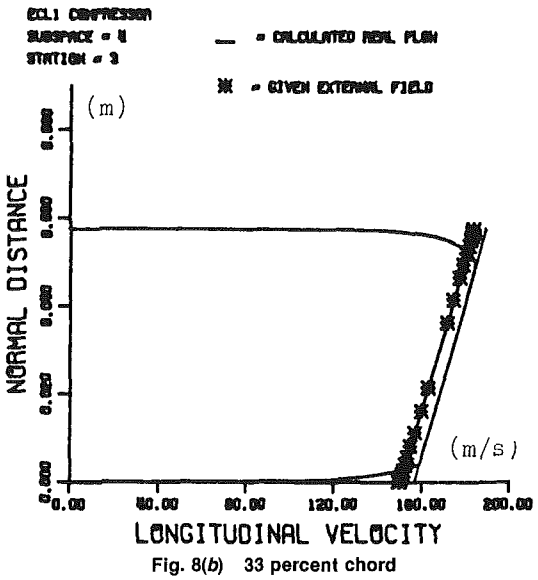

Fig. 8(*b*) 33 percent chord

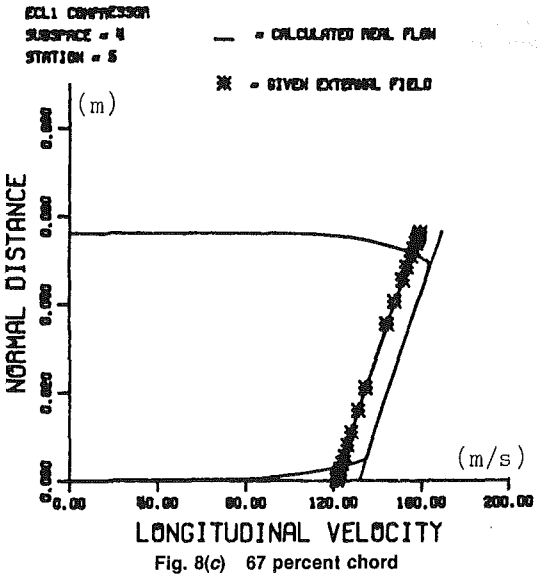

Fig. 8(*c*) 67 percent chord

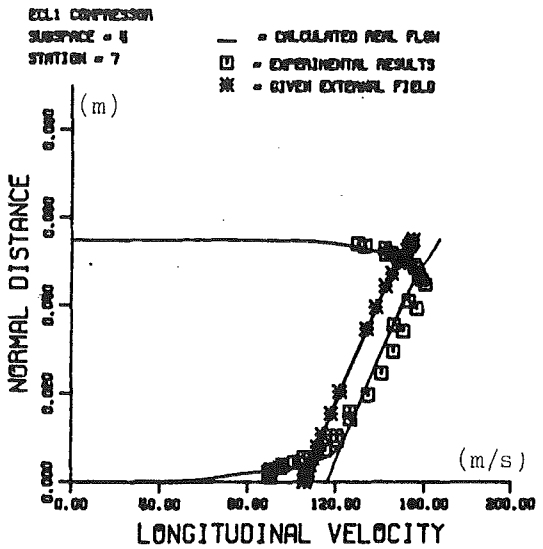

Fig. 8(*d*) Rotor exit

Fig. 8 Evolution of the longitudinal velocity profiles inside the rotor (relative to the blading coordinate system of reference)

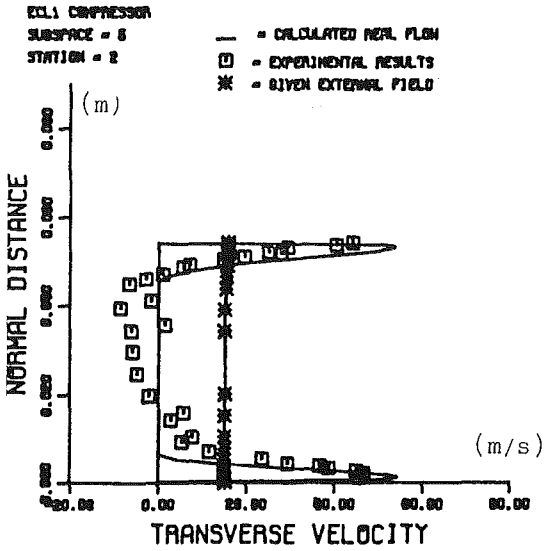

Fig. 9 Comparison between theory and experiment: transverse velocity profile at the exit of the rotor

10). The overall blockage, although it is rather small, is well predicted, as shown by the agreement of the external flow and real flow outside of the viscous shear layer regions. The total temperature profile demonstrates an increase not only near the hub as previously but also near the tip. We can find no explanation for this last increase.

Again, at the exit of the rotor, agreement between computed and experimental results can be termed good (Fig. 11). The overall blockage, which is relatively important only in the peripheral direction, is well predicted. One can remark the corresponding changes in the peripheral velocity distribution and the energy level at the rotor exit. The details of the shear layers are relatively well predicted, especially the exit total pressure. Still the total temperature level inside the hub shear layer is underestimated, indicating that the computation of the lost work needs re-examination.

Finally, at the exit of the stator, agreement between computed and experimental results is good (Fig. 12). The external flow quantities agree well with the real ones inside the external

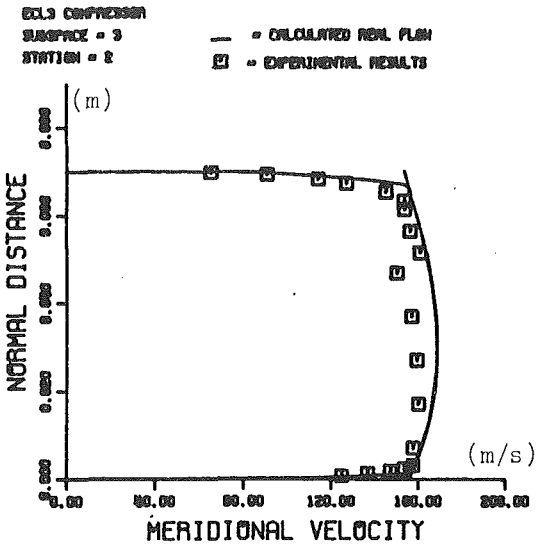

Fig. 10(*a*)

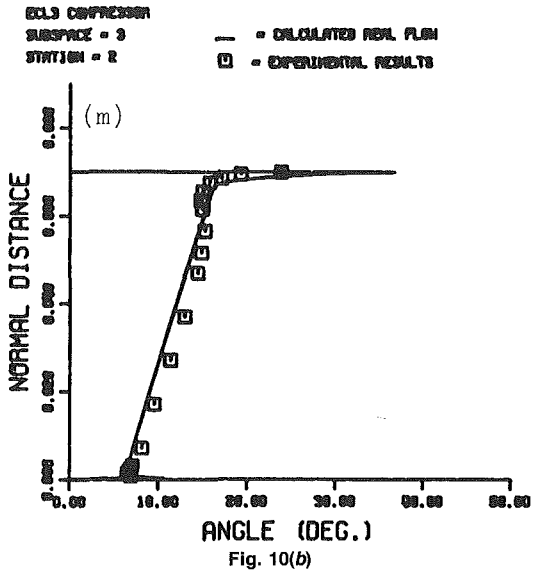

Fig. 10(*b*)

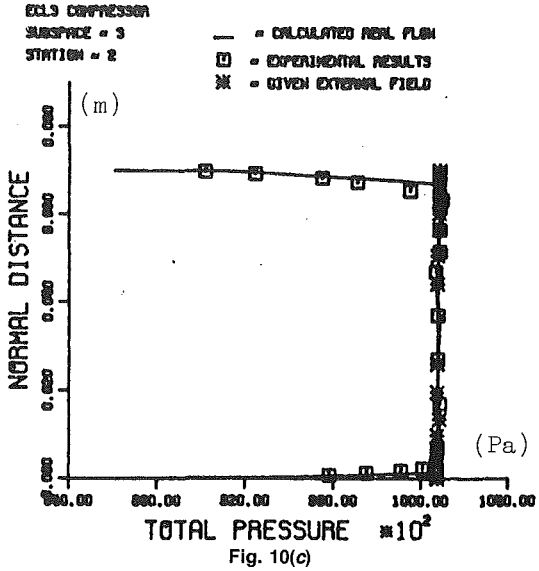

Fig. 10(*c*)

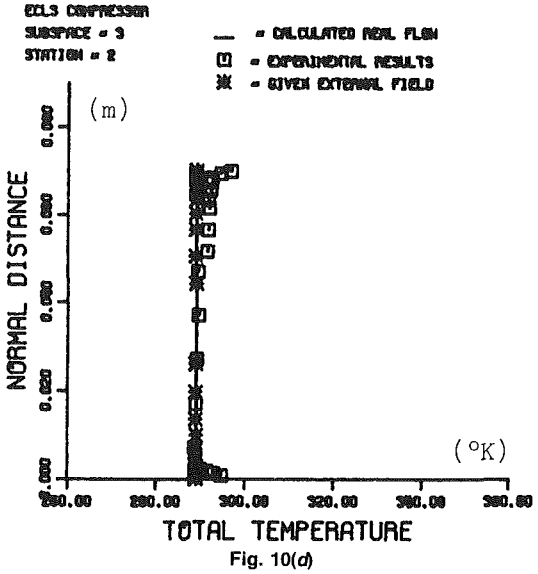

Fig. 10(*d*)

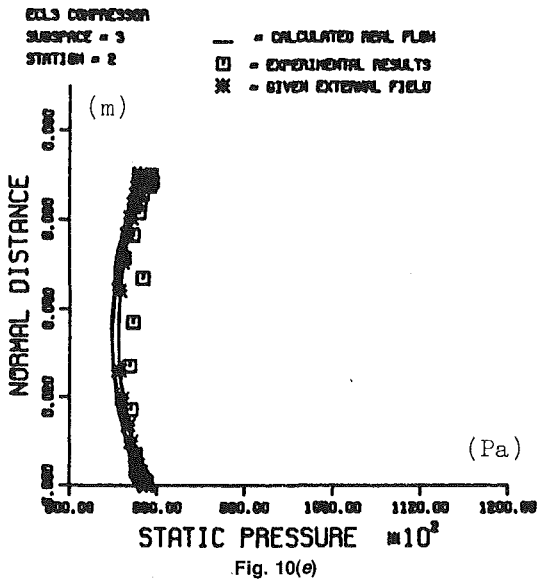

Fig. 10(*e*)

Fig. 10 Comparison between theory and experiment at exit of inlet guide vanes (Station 3.2, Fig. 4)

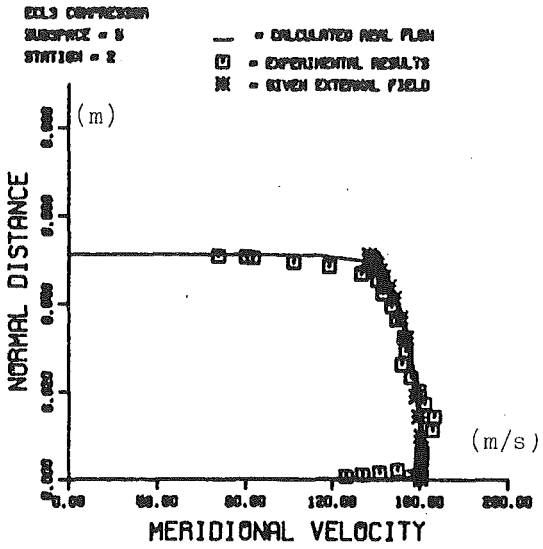

Fig. 11(*a*)

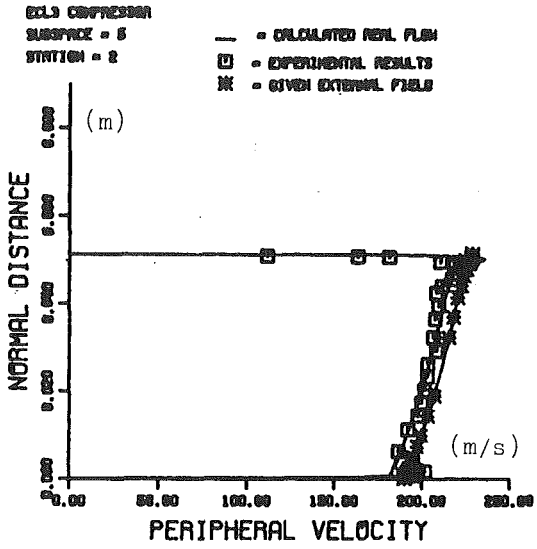

Fig. 11(*c*)

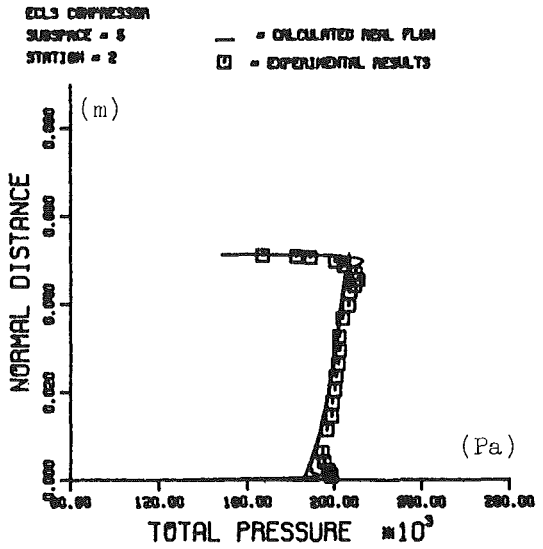

Fig. 11(*b*)

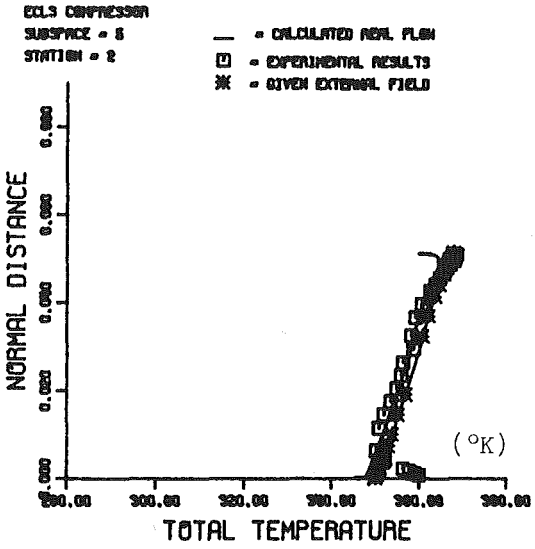

Fig. 11(*d*)

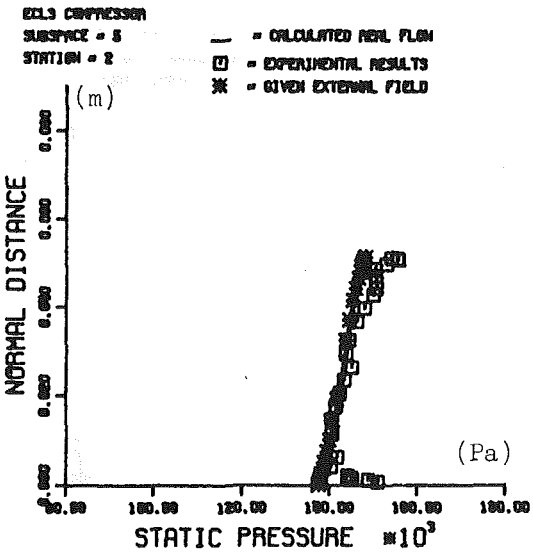

Fig. 11(*e*)

Fig. 11 Comparison between theory and experiment at exit of rotor (Station 5.2, Fig. 4)

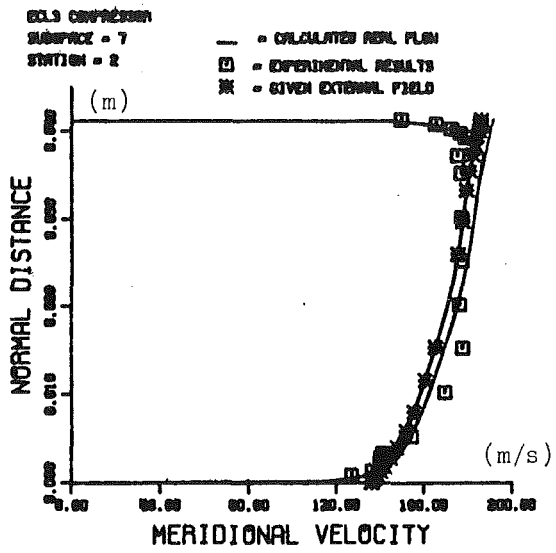

Fig. 12(*a*)

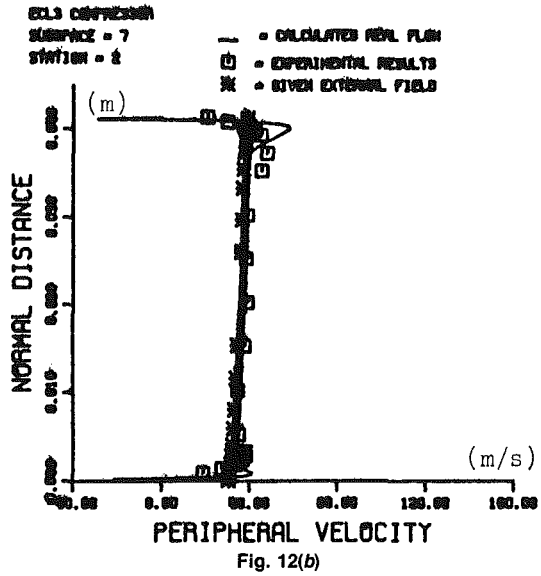

Fig. 12(*b*)

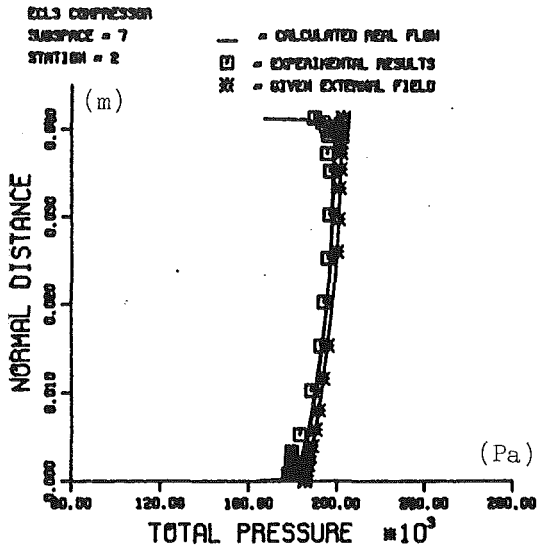

Fig. 12(*c*)

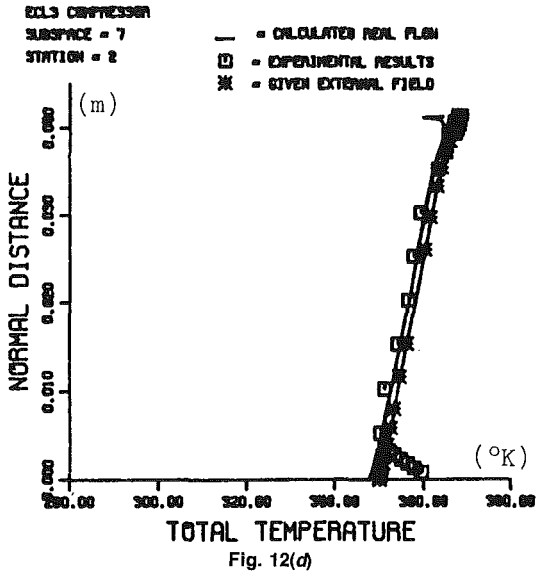

Fig. 12(*d*)

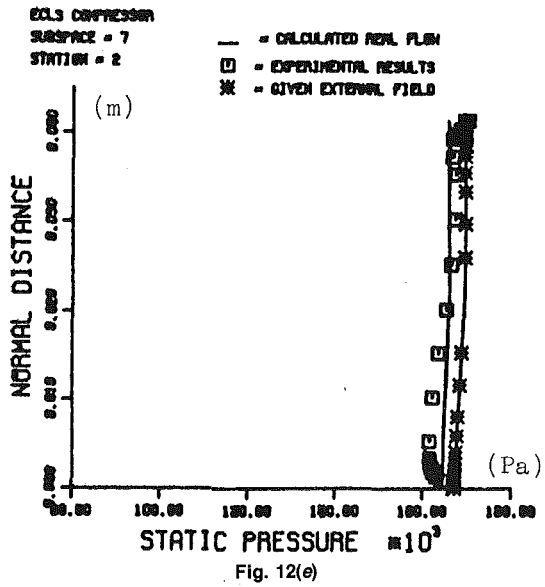

Fig. 12(*e*)

Fig. 12 Comparison between theory and experiment at exit of the stator (Station 7.2, Fig. 4)

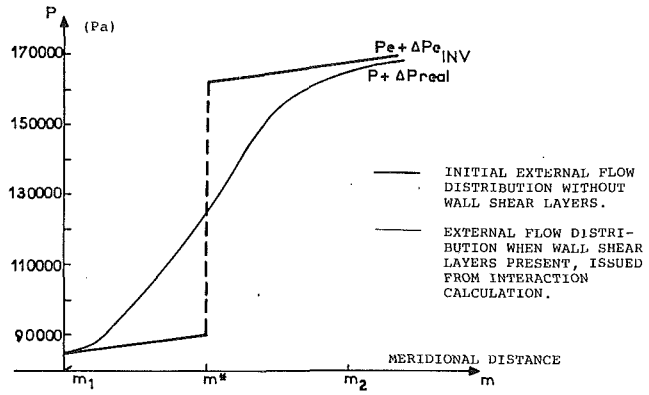

Fig. 13(*a*) Inviscid wall static pressure distribution inside shock-secondary flow interaction region near tip: $m = m_1$ at 25 percent axial chord; $m = m_2$ at 75 percent axial chord

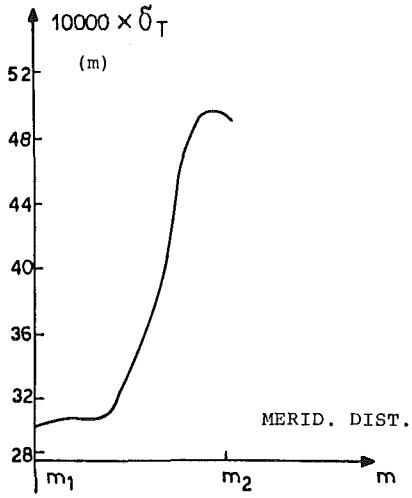

Fig. 13(*b*) Distribution of tip shear layer thickness inside interaction region (calculation results)

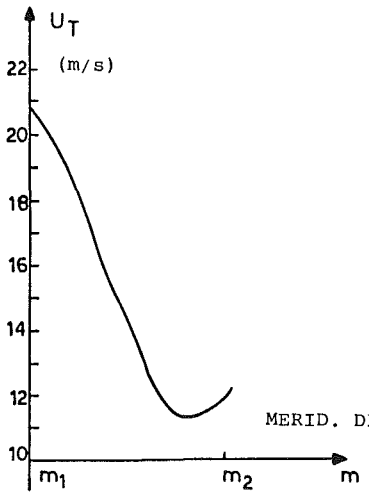

Fig. 13(*c*) Distribution of tip shear layer friction velocity inside interaction region (calculation results)

flow region, so that the same remarks as before can be made for the overall blockage prediction. The details of the wall shear layers are well predicted, except for the total temperature, for which we can observe the same discrepancy as for the rotor exit station.

In order to obtain the abovementioned results, the approximate procedure described above for the calculation of the shock secondary flow interaction field was used.

The shock position was calculated using a blade-to-blade calculation method along with the meridional external flow calculation one. In Fig. 13 some computational results are presented. Figure 13(*a*) presents the initial external flow static pressure distribution at the tip wall along with the distribution resulting from the combined effect of the interaction and the blockage. Note that the blockage is rather small, so that the decrease of the initial static pressure downstream of the shock due to the blockage is limited.

The shear layer thickness and the friction velocity distributions are presented on the same figure. No flow separation is present, while the interaction region extends itself to a good part of the blade axial chord. Unfortunately, no experimental data exist for comparison.

In addition to the comparisons presented above, we may add that the method is numerically well behaved and that the iterative procedure engaged in each calculation step converges in a few iterations. Although numerical aspects of the method have not been examined here, it may be interesting to state that quite a few numerical problems had to be solved. We may quote as an example the treatment of the vorticity transport equation and the calculation of the corresponding peripheral velocity profile, the prediction of which was controlled through an integral equation. In fact, we were obliged to start all integrations from the external flow field and derive the value of the meridional vorticity component at the wall through the peripheral blockage parameter.

6 Conclusions

A secondary flow calculation method was presented above, which solves the peripherally averaged flow equations and makes use of the two-zone model.

The method computes the hub and tip shear layers simultaneously and makes use of an approximate viscous/inviscid interaction calculation procedure, which modifies for blockage the initial external meridional flow field as the computation marches downstream. In fact, the viscous/inviscid approximate interaction procedure is incorporated in the wall shear layer calculation method, giving it the possibility to match with any external meridional flow calculation method, even when flow separation is present.

An improved two-zone model is used, which introduces the notion of the peripheral blockage. This is beneficial in more than one way, lifting in the first place certain incompatibilities existing before. External and internal flow problems are treated on a common basis and a clearer definition of each wall shear layer is possible, something that facilitates computations, when a change of coordinates takes place.

New matching conditions are developed and difficulties at inlet and exit of blade rows are avoided.

Instead of the traditional secondary vorticity, the meridional component is used, the transport of which is computed, taking into account viscous terms. The corresponding peripheral velocity profile is derived through a simple quadrature.

The total kinetic energy integral equation has substituted the entrainment equation used until now. Although this equation is not as easily applicable, it seems that its use produces better results and gives the possibility to treat the case of merging wall shear layers.

An approximate shock/shear layer interaction procedure was extended and adapted to the present calculation method in order to compute the shock wave/secondary flow interaction case whenever present.

The method was applied to the case of two single-stage axial flow compressors (one transonic and another supersonic), for which experimental results were available.

The wall shear layer calculation was performed using as external flow field, the one resulting from a meridional through flow calculation without wall blockage. Comparison between computed and experimental results was good. It made clear that the viscous shear layer calculation method was capable to compute correctly the blockage effects, demonstrating the importance of the peripheral part of the blockage. In addition, a good description of the details of the wall shear layers was obtained, except for the total temperature increase, which was underestimated.

Although the numerical aspects of the method were not discussed because of space limitations, the general behavior can be termed as stable and rapid.

It is hoped that the present work and comparisons will stimulate the work that has been done in recent years in the same field.

Acknowledgments

The authors wish to express their thanks to Sté SNECMA for the financial support they received for the accomplishment of the present work.

References

Adkins, G. G., Jr., and Smith, L. H., Jr., 1982, "Spanwise Mixing in Axial-Flow Turbomachines," ASME *Journal of Engineering for Power*, Vol. 104.

Assassa, G. M., and Papailiou, K. D., 1979, "An Integral Method for Calculating Turbulent Boundary Layer With Separation," ASME *Journal of Fluids Engineering*, Vol.101.

Bario, F., Leboeuf, F., and Papailiou, K. D., 1982, "Study of Secondary Flows in Blade Cascades of Turbomachines," ASME *Journal of Engineering for Power*, Vol. 104.

Birch, N., 1987, "Navier-Stokes Predictions of Transition, Loss and Heat Transfer in a Turbulent Cascade," ASME Paper No. 87-GT-22.

Brochet, J., and Falchetti, F., 1987, "Secondary Flow Computation in Multistage Axial Flow Compressors," presented at the 8th ISABE, Cincinnati, OH.

Comte, A., Ohayon, G., and Papailiou, K. D., 1981, "A Method for the Calculation of the Wall Layers Inside the Passage of a Compressor Cascade With and Without Tip Clearance," ASME *Journal of Engineering for Power*, Vol. 103, No. 3.

Dawes, W. N., 1988, "Development of a 3D Navier-Stokes Solver for Application to All Types of Turbomachinery," ASME Paper No. 88-GT-70.

De Ruyck, J., and Hirsch, C., 1983, "End-Wall Boundary Layers in Multistage Axial Compressors," AGARD 61th Specialist Meeting, *Viscous Effects in Turbomachines*, CP 351.

Douvikas, D., Kaldellis, J., and Papailiou, K. D., 1987, "The Circumferential Velocity Profile for Secondary Flow Calculations," ASME Paper No. 87-GT-255.

Douvikas, D., 1988, "Computation of Secondary Flows in Radial Compressors," Doctoral Thesis, Thermal Turbomachine Lab., National Technical University of Athens, Greece.

Gallimore, S. J., 1986, "Spanwise Mixing in Multistage Axial Flow Compressors: Part II—Throughflow Calculations Including Mixing," ASME JOURNAL OF TURBOMACHINERY, Vol. 103, pp. 10–16.

Goutines, M., and Naviere, H., 1987, "Conception et Essais d'un Etage de Tete d'un Compresseur HP Advancé," in: *Advanced Technology for Aero Gas Turbine Components*, AGARD-CP-421, Paris.

Hah, C., and Laylek, J., 1987, "Numerical Solution of Three-Dimensional Turbulent Flows for Modern Gas Turbine Components," ASME Paper No. 87-GT-84.

Horlock, J. H., 1971, "Cross Flow in Bounded Three-Dimensional Turbulent Boundary Layers," Cambridge Univ. GUED/A, Turbo/TR28, United Kingdom.

Kaldellis, J., Douvikas, D., and Papailiou, K. D., 1988, "A Secondary Flow Calculation Method Based on the Meridional Vorticity Transport Equation," ASME Paper No. 88-GT-260.

Kaldellis, J., 1988, "Computation of Shock/Secondary Flow Interaction," Doctoral Thesis, Thermal Turbomachine Lab., National Technical University of Athens, Greece.

Kallas, J., and Papailiou, K. D., 1987, "A Method for the Calculation of the Interaction of a Turbulent Boundary Layer With a Shock Wave," presented in the 8th ISABE International Symposium, Cincinnati, OH.

Kuhn, G. D., and Nielsen, J. N., 1973, "Prediction of Turbulent Separated Boundary Layers," AIAA Paper No. 73-663.

Leboeuf, F., and Naviere, H., 1983, "Etudes Experimentales et Theoriques des Couches Visqueuses Parietales dans un Compresseur Monoetagé Transonique," AGARD CP 351, Paper No. 20.

Leboeuf, F., 1984, "Computation of Secondary Flows in an Axial Flow Compressor Including Inviscid and Viscous Flow Computation," ASME Paper No. 84-GT-244.

Manchu, G. E., 1987, "The Performance Estimation of Transonic Turbine at Design and Off-Design Conditions," ASME Paper No. 87-GT-148.

Mellor, G. L., and Wood, G. M., 1971, "An Axial Compressor End-Wall Boundary Layer Theory," ASME *Journal of Basic Engineering*, Vol. 93.

Moore, J., and Moore, J. G., 1985, "Performance Evaluation of Linear Turbine Cascades Using Three-Dimensional Viscous Flow Calculations," ASME *Journal of Engineering for Gas Turbines and Power*, Vol. 107, pp. 969–975.

Panaras, A. G., and Inger, G. R., 1977, "Transonic Normal Shock Turbulent Layer Interaction in Pressure Gradient Flows," ASME Paper No. 77-GT-34.

Papailiou, K. D., Flot, R., and Mathieu, J., 1977, "Secondary Flows in Compressor Bladings," ASME *Journal of Engineering for Power*, Vol. 99.

Papailiou, K. D., 1981, "Le Foll's Method and the Calculation of Attached and Separated Two-Dimensional Boundary Layers," VKI LS 1981-1.

Papailiou, K. D., 1983, "A Contribution to the Calculation of Secondary Flows in an Axial Flow Compressor," presented at the 6th ISABE, Paris, pp. 439–446.

Pavis, S., Ktenidis, P., and Papailiou, K. D., 1987, "Boundary Layer Development Passing From a Stationary to a Rotating Axisymmetric Surface," presented at the 8th ISABE International Symposium, Cincinnati, OH.

Three-Dimensional Separated Flow Field in the Endwall Region of an Annular Compressor Cascade in the Presence of Rotor-Stator Interaction:

Part 1—Quasi-Steady Flow Field and Comparison With Steady-State Data

H. D. Schulz
Dipl.-Ing.

H. E. Gallus
Professor, Dr.-Ing.

B. Lakshminarayana[1]
Professor.

Institut für Strahlantriebe und
Turboarbeitsmaschinen,
RWTH Aachen,
D-5100 Aachen,
Federal Republic of Germany

An experimental study of three-dimensional flow field in an annular compressor cascade with an upstream rotor has been carried out at four different incidences to the stator blade. Blade boundary layers and the three-dimensional flow field at the exit are surveyed using a hot-wire sensor and a five-hole probe, respectively. The data on the blade boundary layer, passage flow, and separated corner flow are presented. The upstream rotor wake has a major influence on the transition, laminar separation bubble, extent of wall/corner flow separation, aerodynamic losses, secondary flow, and three-dimensional flow inside the passage. A detailed interpretation of the effects of upstream wakes on the entire passage flow is presented and compared with the data in the absence of a rotor.

Introduction

The flow in modern multistage compressors with high blade loading, low aspect ratio blading, and reduced blade row spacing is extremely complex. In many instances, separated regions exist both on the blade and in the hub wall region (corner stall separation). This feature, combined with the rotor-stator interaction, results in highly viscous, separated, and unsteady flow leading to decreased efficiency, decreased reliability, off-design operation, and enhanced rotor-stator interaction noise. A basic understanding of these phenomena is essential for the design and analysis of such turbomachinery. This is the major objective of the research presented in this paper.

Considerable progress has been made in understanding the nature and extent of wall separation and its dependency on blade loading in isolated blade rows such as cascades, annular cascades, and rotors. For example, Horlock et al. (1966), Salvage (1974), and Moore and Richardson (1957) provide a comprehensive understanding of the corner separation in a compressor cascade. Dring et al. (1982, 1983) and Wagner et al. (1985) published extensive measurements in a low aspect ratio isolated rotor with endwall flow separation. They observed separation up to 75 percent of the span at higher blade loading.

Murthy and Lakshminarayana (1987) found no major separation in a rotor hub region. They postulate that the centrifugal force due to rotation tends to reduce blade boundary layer growth on the blade near the hub wall through radial transport of boundary layer fluid in this region. In a stator, the situation is reversed. The blade boundary layer fluid has a tendency to move inward, resulting in large boundary layer growth in the hub wall region. This feature combined with the secondary flow will likely result in a separation region in the corner bounded by the hub wall and the blade suction surface in a stator. This is consistent with the results of Joslyn and Dring (1985) and Dong et al. (1987) who observed no separation in the rotor, but in the stator they observed endwall separation, both near the hub and the annular wall.

In order to gain a basic understanding of the extent and nature of separation in stators, Schulz and Gallus (1988) carried out detailed measurements of the flow and the pressure field in a stator alone configuration. The present paper (both Parts 1 and 2) is a continuation of this investigation to gain a basic understanding of the separation in the presence of rotor-stator interaction whose importance was emphasized by Evans (1977), Gallus and Hönen (1983), and Cyrus (1986). A simple config-

[1]Permanent address: Pennsylvania State University, University Park, PA 16802.

Contributed by the International Gas Turbine Institute and presented at the 34th International Gas Turbine and Aeroengine Congress and Exhibition, Toronto, Ontario, Canada, June 4–8, 1989. Manuscript received at ASME Headquarters February 14, 1989. Paper No. 89-GT-76.

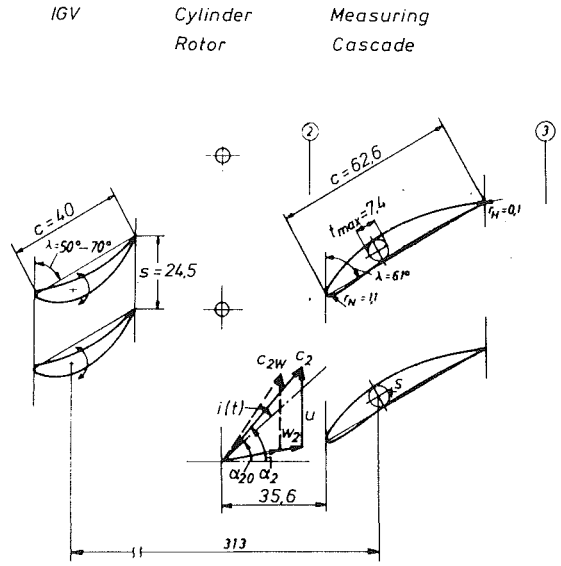

Fig. 1 Cascade geometry at midspan (units in mm)

uration was chosen to generate rotor-stator viscous wake interaction in the absence of potential flow effects. A moving row of cylinders was placed upstream of the annular cascade, and the following measurements are taken with almost identical inlet incidence and other inflow conditions, as those reported by Schulz and Gallus (1988):

1 Flow visualization;
2 Steady and unsteady blade pressure at various radial and chordwise location;
3 Five-hole probe measurements at the cascade exit;
4 Hot-wire measurements at various chordwise and radial locations, including passage flow, blade boundary layers, and separated regions.

The quasi-steady-state data are analyzed, interpreted, and compared with the data taken without the rotor. This comprises Part 1 of this paper. In Part 2 of the paper, the unsteady pressures and velocities both in the blade boundary layers and in the free stream are analyzed and interpreted from the point of view of wake transport, amplitude and phase of pressure fluctuations, and unsteady blade boundary layers. A brief review of the literature on unsteady aerodynamics is also given in Part 2 of the paper. The data are acquired at four different incidences and only representative results are given here in these papers. All the data will be presented in a Dr.-Ing. thesis by the senior author.

Experimental Facility and Inlet Conditions

The measurements were carried out in the annular compressor cascade described in detail by Schulz and Gallus (1988). The cascade consists of 24 untwisted blades, mounted on the hub (tip clearance 0.8 percent of blade height), with a hub-to-tip ratio of 0.75 and a tip diameter of 428 mm. The aspect ratio is 0.86 and the solidity at midspan is 0.78. Blade metal angles at inlet and exit are 44 and 15 deg, respectively (measured from axial); other geometric parameters are shown in Fig. 1. The blade profiles are radially stacked at their center of gravity. Forty-eight variable inlet guide vanes far upstream of the cascade provide an inlet swirl. In contrast to the former investigation with uniform and steady incoming flow, rotor-stator viscous wake interaction was generated by a rotor with rotating cylinders (simulating blades) located at 57 percent of chord or 7 cylinder diameters upstream of the cascade. The rotor incorporates 24 rods with a diameter of 5.3 mm. The rotational speed was kept constant for all investigations at 3000 rpm. Figure 1 shows the geometry of the cascade. All dimensions are in millimeters and the velocity triangle is drawn for an inlet angle of $\alpha_2 = 49.2$ deg. Rotating cylinders were chosen to achieve nearly identical inlet conditions as those in the case without rotor, at constant rotational speed of the rotor but different inlet angles. This could not have been achieved with a rotor incorporating blades.

The inlet angle and velocity distribution are shown in Fig. 2. These were taken at 10 percent chord upstream. The incidence angle is almost identical for both cases, with and without rotor. Even though the velocity profile differs slightly on the hub wall, the boundary layer thickness is almost identical in both cases, as shown in Fig. 3. The phase-locked-averaged velocity at cascade inlet has been measured with a hot-wire probe. Figure 4 shows the variation of the total velocity, the turbulence intensity, and the incidence variation with time in the absolute frame of reference for an inlet angle of $\alpha_2 = 49.2$ deg at midspan. Also indicated is the time-averaged incidence angle i. Velocity defects $\Delta C/\bar{C}$ of 15 percent and incidence

Nomenclature

c = blade chord
C = absolute flow velocity
C_{sec} = secondary velocity, equation (1)
C_p = pressure coefficient = $(P_{loc} - P_{cas})/(P_{t2} - P_{cas})$
i = incidence
H = blade height
LSB = laminar separation bubble
P = pressure
PS = pressure side
r = radius
s = blade spacing
S = center of gravity
SS = suction side
t = blade thickness
T = blade passing period
TS = location of turbulent boundary layer separation
Tu = turbulence level = $C_{RMS}/\bar{C}$
u = rotational velocity
v = flow velocity
w = relative velocity
x = axial direction
y = circumferential direction
z = spanwise direction
α = flow angle measured from axial direction
β = pitch angle
δ = boundary layer thickness
δ_2 = momentum thickness = $\int_0^\delta (1 - c/c_\infty)\ (c/c_\infty)\ dy$
ϵ = turning angle
θ = circumferential direction
λ = stagger angle
ρ = density
τ = shear stress
$\bar{\omega}$ = circumferentially mass-averaged loss coefficient = $(\bar{P}_{t2} - \bar{P}_{t3})/(\bar{P}_{t2} - \bar{P}_{s2})$
Ω = vorticity

Subscripts

0 = design flow angle
2 = upstream of the cascade
3 = downstream of the cascade
cas = casing
loc = local
m = blade midspan height
rms = root mean square
s = static
t = total
w = blade surface
w = wake
∞ = free stream

Superscripts

$\bar{(\ )}$ = mass averaged (circumferential)
$\underline{(\ )}$ = time averaged
$\bar{\bar{(\ )}}$ = averaged over the entire passage

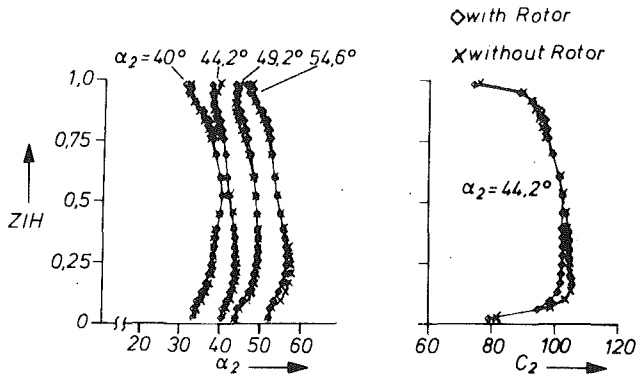

Fig. 2 Inlet angles α_2 (measured from the axial direction) and velocity distribution C_2 at cascade inlet (10 percent upstream)

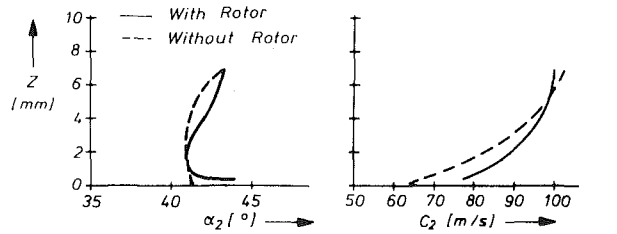

Fig. 3 Hub wall boundary layers 10 percent upstream of the cascade leading edge (α_2 = 44.2 deg)

changes from $\Delta i = -2$ deg to $\Delta i = +8$ deg were observed at $\alpha_2 = 49.2$ deg. The maximum turbulence intensity (inside the wake) was 13 percent and the mean turbulence intensity was 7 percent. These are much higher compared to 1.2 percent turbulence intensity measured in the no-rotor case.

Measurement Techniques

Flow Visualization. The flows on the blade and hub surfaces have been visualized using dye injection, oil film and titanium dioxide and tufts. Dye injection and oil film techniques have been described in detail by Schulz and Gallus (1988). To obtain some further information, one passage has been incorporated with about 100 very thin threads (tufts). All flow visualization studies have been filmed in motion with video camera equipment.

Wall Static Pressure Measurements. The wall static pressures were measured via a matrix array of 114 pressure taps at the hub and 34 pressure taps along the chord of the blade. The instrumented blade was radially traversed to 11 spanwise positions. The pressure taps were connected to a scanivalve. The accuracy of the transducer was 0.1 percent of the measured pressure difference with respect to the ambient pressure.

Five-Hole Probe Measurements. Detailed radial and circumferential measurements were carried out with a five-hole probe at the cascade exit plane (35 percent of chord downstream of the blade trailing edge). The probe head diameter is 2.6 mm and the uncertainty of the measurements was about ± 2 percent in C_p values and ± 1 deg in flow angle. Due to the high variation in flow angle, the probe had to be yawed at every measuring position in the exit plane. Measurements were taken at 22 radial and 21 circumferential positions. A description of the probe and its calibration is given by Bohn and Simon (1975).

Hot-Wire Measurements. The passage flow as well as the blade suction side boundary layers have been measured using a hot-wire probe. Since the boundary layers are very thin, only a single wire probe could be used. Thus the probe can only

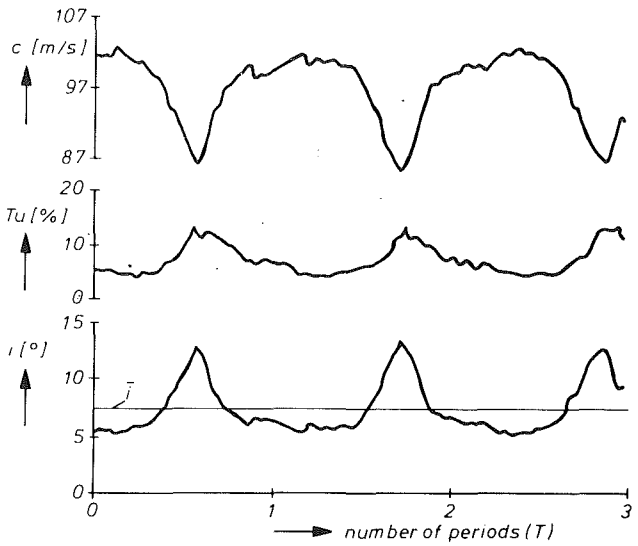

Fig. 4 Phase-lock averaged velocity (C), turbulence level (Tu), and incidence (i) variation with time 10 percent upstream of the cascade (midspan, α_2 = 49.2 deg)

Table 1 Test program

Measurement	Inlet Angle/Measurement Location
flow visualization	40.0° 44.2° 49.2° 54.6° 57.6°
five-hole probe	40.0° 44.2° 49.2° 54.6°
blade static pressure	40.0° 44.2° 49.2° 54.6° 57.6°
hub and casing wall static pressure	40.0° 44.2° 49.2° 54.6° 57.6°
passage flow	49.2° (midspan,6 axial positions)
blade suction surface boundary layer	49.2° (midspan and 13 percent span, 7 axial positions)

sense the value of the total velocity, and the flow direction could not be determined. The hot-wire probe incorporates an additional prong, which causes the traversing unit to stop if the prong touches the blade, thus positioning the probe at exactly 0.15 mm away from the surface. As described in more detail by Schulz and Gallus (1988), care has to be exercised in obtaining accurate data from a hot-wire probe in a highly turbulent flow. In general, the time-averaged flow velocity will be measured too high and the velocity fluctuation too small, if the local turbulence level exceeds 30 percent (Dengel and Vagt, 1983). This is particularly valid for separated flows in the presence of backflow events. Hence measurements in these regions should be viewed as qualitative. When turbulence level is below 20 percent and radial velocity is small (like in the midspan region of the passage), the error in total velocity is about ± 2 percent. Wall proximity effects are small at the high free-stream velocities of about 100 m/s, as discussed by Schulz and Gallus (1988). Since the given length-to-diameter ratio of the probe was 300 (wire diameter used is 5 μm), the frequency response of the probe was sufficient up to 30 kHz. The hot-wire data have been sampled at a rate of 80,000 samples/s. At a blade passing frequency of 1200 Hz, there are 67 samples per period. Turbulence quantities are derived from the rms values of the velocity fluctuations C_{rms} and nondimensionalized with the local time-averaged velocity $\bar{C}$.

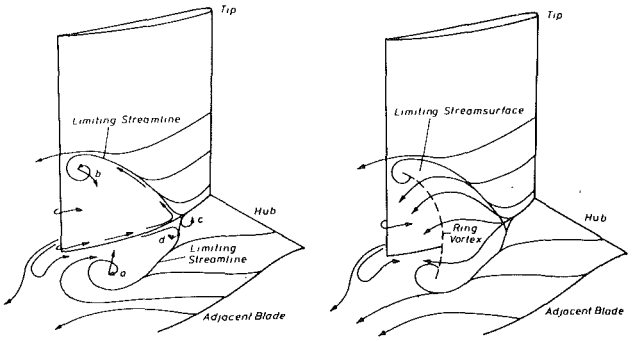

Fig. 5(*a*) Fig. (*b*)

Fig. 5 Flow structures on the surfaces and proposed topology of the hub corner stall (α_2 = 49.2 deg)

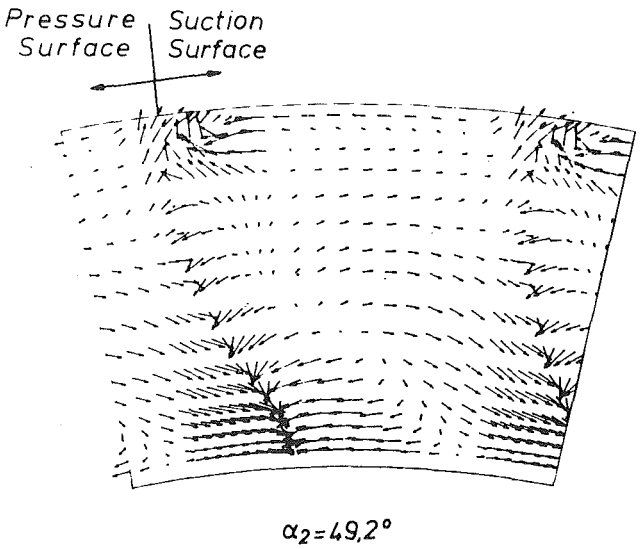

Fig. 6 Secondary flow vectors [C_{sec}, equation (1)] 35 percent downstream of the cascade (α_2 = 49.2 deg)

Test Program

The flow measurements in this rotor-stator interaction study were taken at the same inlet conditions as those carried out in the absence of a rotor. The points of operation are identified by the time-averaged yaw angle α_2 measured at midspan. All the steady-state measurements carried out in this program are summarized in Table 1, and only typical data are presented and interpreted in this paper.

Results and Discussion

Structure of Three-Dimensional Separation. Even though the objective of this investigation is to study the effect of rotor-stator interaction on the separated flow inside a compressor cascade, some further evaluation of the flow visualization tests in the case without rotor will be discussed first, to give some additional insight into the structure of the flow inside the separated region. Video movies of the dye injection test described in detail by Schulz and Gallus (1988) and of visualization through tufts have been studied. The structure derived from this study in the compressor cascade at α_2 = 49.2 deg is given in Figs. 5(*a*, *b*). The streamlines on the surfaces (Fig. 5*a*) show the presence of a vortex on the hub [marked (*a*) in Fig. 5(*a*)] and on the blade [marked (*b*) in Fig. 5(*a*)] toward the trailing edge, but away from the corner. In the core of these vortices, the flow is transported out normal to the surface, this has been substantiated by tufts at that location. Points (*a*) and (*b*) in Fig. 5(*a*) seem like saddle points. At the leading edge of the separated region a vortex (*c*) is formed by the main flow when the sudden obstruction is encountered. The backflow inside the separated regions moves upstream and coils up in another vortex (*d*). The separated region is closed off from the main flow by limiting streamlines at the hub and on the blade suction side. The presence of a vortex on the hub is clearly revealed in the flow visualization on the hub shown later (Fig. 8). The vortex axis is normal to the hub on the hubwall and normal to the blade on the blade surface. Hence, it is anticipated that a ring vortex is formed joining the blade suction surface and the hub somewhere near the blade trailing edge.

Even though Dallmann (1987) claims that there might be ambiguities when deducing the topological structure of separated regions from the surface streamlines, a possible three-dimensional structure is proposed in Fig. 5(*b*). The limiting streamsurface, bounded by the limiting streamlines on the hub and the suction side, is closed off by a ring vortex near the trailing edge. The downward motion of the fluid due to this vortex and a strong flow deflection downstream of the separated bubble can be seen in the secondary flow vectors derived from five-hole probe measurements at 35 percent of chord downstream of the cascade with rotor (Fig. 6). Since the blade is untwisted and the design features are identical at all spanwise locations, a mass-averaged velocity was used in the definition of secondary velocity vectors, given by

$$C_{sec} = C_{loc} - \bar{C}$$

$$\bar{C} = \int_{hub}^{tip}\int_{SS}^{PS} C\, C_x dr\, d\theta \Big/ \int_{hub}^{tip}\int_{SS}^{PS} C_x dr\, d\theta \qquad (1)$$

The vector $\bar{C}$ is then derived from the total velocity $\bar{C}$ and the mass-averaged flow angles $\bar{\alpha}$ and $\bar{\beta}$. The striking feature is the high deflection of the flow even in the mainstream. The separated region cannot be sustained downstream of the cascade and hence it closes off slightly upstream of the location where the probe has been traversed. The flow perceives the corner stall region as a solid body obstruction. The data indicate large flow turning around the trailing edge of the stalled region from both sides. Substantial deflection of the main flow occurs due to the blockage of the corner stall. The separation bubble at the hub becomes distorted downstream of the trailing edge because of different convection velocities at its edges. Imbalance between the radial pressure gradient and the centrifugal force results in downward flow (radial inward velocities), as shown in Fig. 6.

Since the clearance height is small (0.8 percent of blade height), the tip clearance flow is confined to a small region at the casing and has not penetrated the casing corner stall. Therefore, the leakage flow has not washed out the separation in the outer wall region. This is consistent with the observations by Lakshminarayana and Horlock (1965) and by Dong et al. (1987).

Comparison of Measurements With and Without Rotor

Surface Flow Visualization. The oil film method has been applied to the blade suction surface to detect regions of separated flow qualitatively. A comparison of the surface flow with and without the rotor is shown in Fig. 7 for all incidences under investigation.

Three major changes can be observed. First, the three-dimensional laminar separation bubble, found in the case without the rotor, disappears at all incidences at the suction and the pressure side (not shown here). Because of its elimination, the flow along the blade becomes more two dimensional upstream of the turbulent separation in the rotor case. Second, the regions of turbulent separated flow in the vicinity of the endwalls decrease in the rotor case, especially at smaller inlet angles (or blade loading). Third, at the trailing edge, the midspan boundary layer seems to separate earlier in the rotor case.

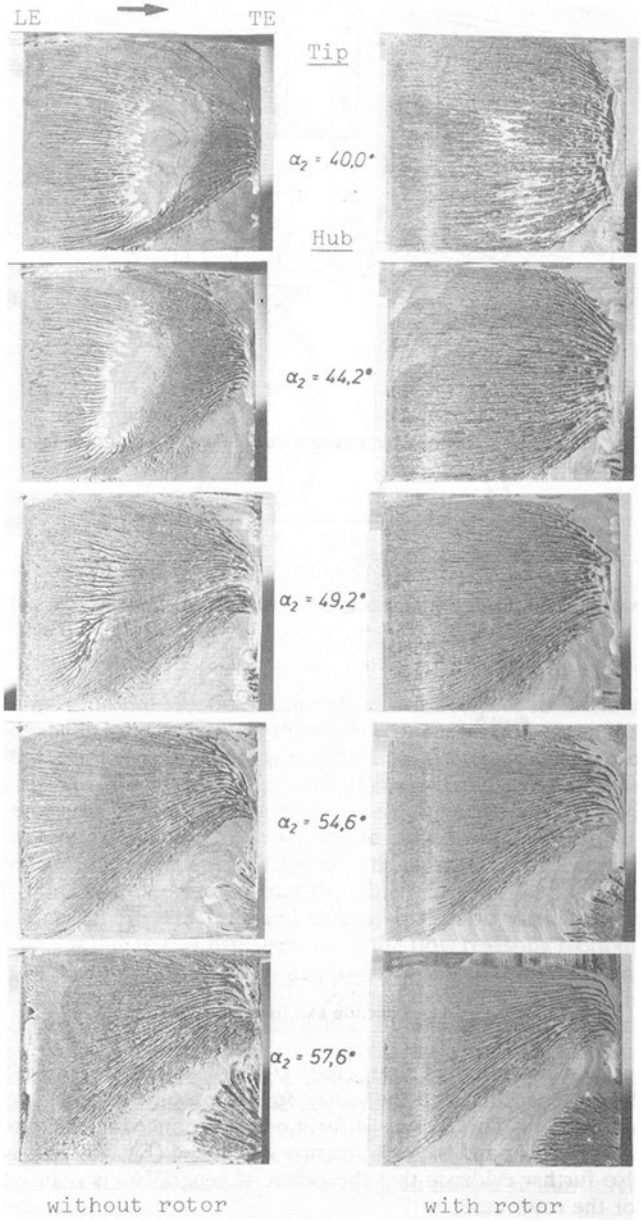

Fig. 7 Oil flow visualization on the blade suction side

The disappearances of the laminar separation bubble with free-stream turbulence levels higher than 3 percent have also been observed by Hoheisel and Kiock (1986) in turbine cascades. In their investigation, the location of boundary layer transition was weakly dependent on the turbulence level, even though the prediction of Dunham (1972) showed a much higher influence. Walker (1974) proposes that the periodic disturbances arising from the passage of rotor wakes have a major influence on the transition process, but they will only have a major effect on the location of the transition point when their scale is large compared with the boundary layer instability length or if their amplitude is high. Recent investigations by Hodson and Addison (1989) reveal that the wakes generate the formation of turbulent patches within an otherwise laminar boundary layer, which rapidly merge, thus causing the transition to occur earlier. It is therefore concluded that not only has the laminar separation bubble disappeared, but that transition starts very close to the blade leading edge. This also would account for the earlier turbulent separation of the boundary near midspan, since the boundary layer is growing more rapidly for the case with rotor. In order to corroborate these conclusions, we would expect the profile losses in the midspan of the blade to increase while in the endwall regions the losses should decrease.

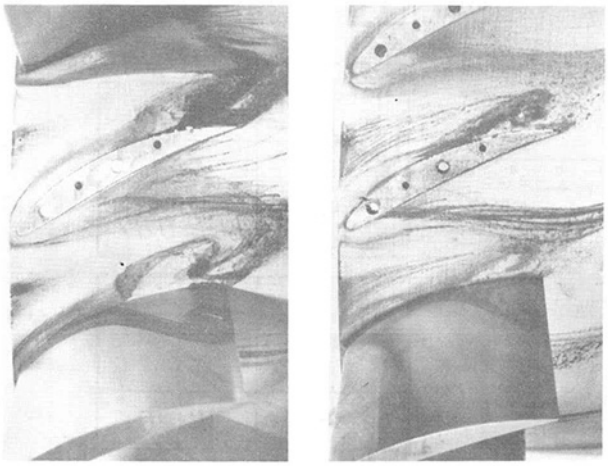

(*a*) Without rotor (*b*) With rotor

Fig. 8 Hub and blade suction side flow visualization (α_2 = 44.2 deg)

Figure 8 shows streamlines at the hub and the blade suction side, with and without rotor, at $\alpha_2 = 44.2$ deg. It can be seen that due to the presence of the rotor, not only on the blade but even more significantly on the wall, the separated region is reduced. This might result from the different hub boundary layers at the cascade inlet (Fig. 3).

Secondary flow is based on the well-known formula given by Squire and Winter (1951)

$$\Omega_{sec} = -2\epsilon\partial C/\partial z \tag{2}$$

Since for the rotor case $\partial C/\partial z$ is smaller inside the hub boundary layer but larger right at the wall, the secondary flow could be different with respect to the no-rotor case. This would influence the migration of low-momentum fluid toward the hub suction side corner region and hence the corner separation.

Since Fig. 8 shows no evidence of diminished secondary flow on the hub, it is felt that the unsteady flow field and the increase in overall turbulence level caused by the rotor are responsible for the reduced corner stall. Measurements by Takei and Masuda (1988) in a two-dimensional diffuser revealed that an enforced velocity oscillation significantly reduces the extent of a separated region. The oscillation enhances the formation of vortical structures in the separated shear layer and thus reenergizes the retarded flow near the wall. In their investigation, Takei and Masuda could relate the reduction in separated flow directly to the amplitude of the velocity fluctuation.

Even though the vortex on the hub (Fig. 5*a*) in the rotor case is not as strong as in the case without rotor, the structure of the separated region seems to be unchanged.

Surface Static Pressure Measurements. The effect of increased incidence and hence the blade loading on the static pressure distribution inside the flow channel has been discussed in detail by Schulz and Gallus (1988). Similar trends have been observed in the rotor case and will, therefore, not be presented here. The emphasis is placed in evaluating the effects of rotor on the blade and the wall static pressures. Figure 9 shows a comparison of the blade pressure distribution, with and without rotor, for $\alpha_2 = 44.2$ deg at four spanwise positions. Here the local pressures are measured relative to the casing wall static pressure at the inlet, normalized by the midspan dynamic head at the inlet. Since the static pressure remains constant downstream of the location where the flow separates, regions of separated flow can be identified by regions of constant pressure, and the flow separation on the blade can be detected by the "flattening" of the pressure distribution.

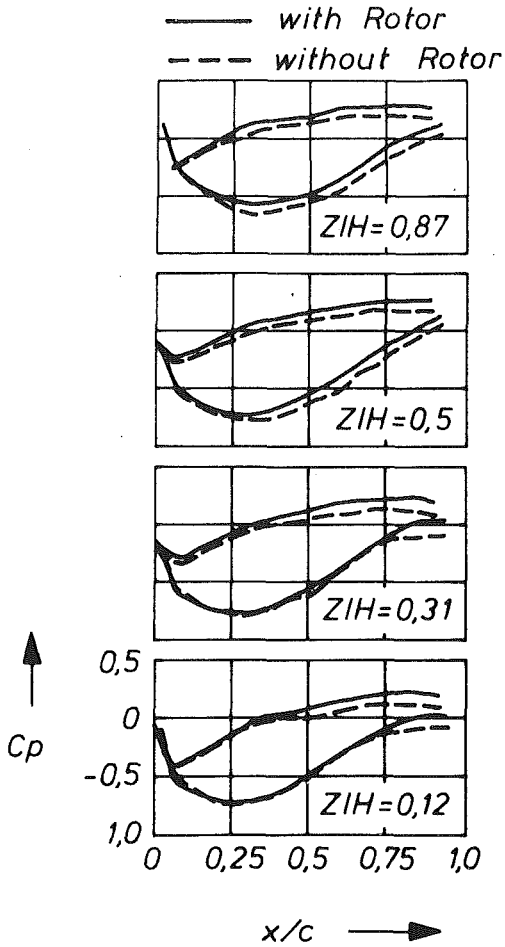

Fig. 9 Comparison of blade pressure distribution at various spanwise positions (α_2 = 44.2 deg)

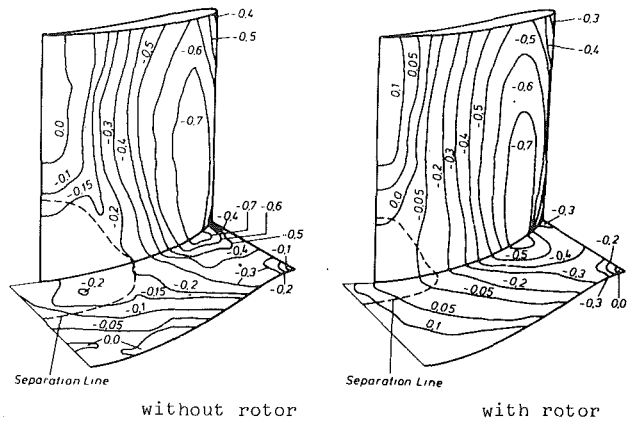

Fig. 10 Hub and blade static pressure coefficient (C_p) contours (α_2 = 44.2 deg)

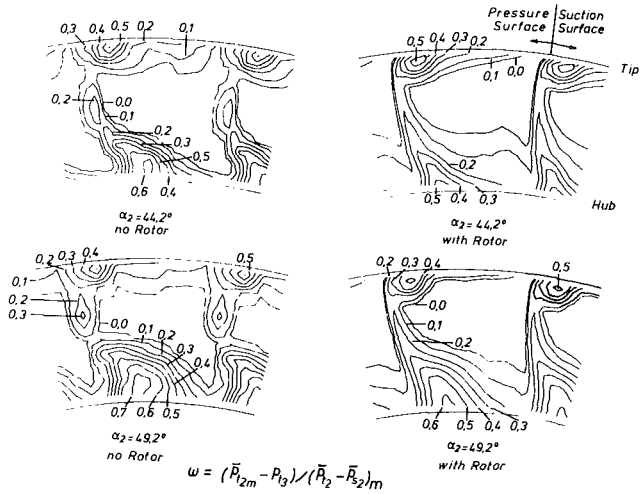

Fig. 11 Cascade exit loss contours

Separation is observed close to the hub (11.5 and 30.6 percent span from the hub) at about 75 percent of chord for the case without rotor. For the rotor case, the pressure distribution near the trailing edge (at 11.5 and 30.6 percent span) indicates either a mild separation or no separation, and the exit static pressure is generally higher. This is brought about by reduced separation in the rotor case and the associated reduction in blockage effect. The blockage due to separation tends to accelerate the fluid, thus decreasing the pressure rise. The pressure distribution at midspan indicates that there is no separation in either case. The shift in C_p distribution is also evident at midspan and near the tip (86.8 percent span). The blade static pressure distribution is consistent with the oil flow measurements shown in Fig. 7.

Since the separation occurring in the corner formed by the hub and the blade suction side is of great interest, the static pressure contours in these regions are compared in Fig. 10 for α_2 = 44.2 deg.

The lines along which the flow separates on the hub and the blade suction side, deduced from visualization and the C_p distribution, are also indicated. The extent of the separated corner region and its effect on the pressure distribution can be observed in Fig. 10. The isostatic pressure contours should be nearly vertical along the blade in the case of unseparated, uniform, and inviscid flow. Any deviation from this represents either a nonuniform incoming flow, profile boundary layer separation, or corner separation. The "shell-like" shape of the pressure contours in the front part of the blade is a result of a reduction in inlet swirl close to the walls, due to the development of the hub and casing boundary layers downstream of the inlet guide vanes (Fig. 2). In the rear part of the cascade, the contours clearly indicate the low-pressure regions due to separation and the vortex formation on the blade and hub surface. This feature is far more pronounced in the case without rotor and the exit pressure is reduced (Fig. 9). This is also further evidence that the extent of separation is reduced for the rotor case.

Flow Field and Losses at the Exit. Contour plots of the total pressure loss at the cascade exit plane are shown in Fig. 11. The loss coefficient is defined as the difference between the local stagnation pressure and the inlet stagnation pressure at midspan, normalized by the midspan dynamic head at inlet. The contour plots are compared with the measurements in the case without rotor. Due to the rotor, there is a slight positive total pressure gradient toward the casing at the cascade inlet. The region of zero loss, therefore, seems to be more confined in the upper part of the passage.

Several observations can be made by comparing the loss contours for the two cases shown in Fig. 11. The flow field near the tip, including separation and tip clearance flow, remains unchanged. The maximum losses as well as the extent of losses in the hub-blade suction side corner are reduced for the rotor case. As observed earlier, the corner separation is reduced with the rotor, and the loss contours confirm this trend. Furthermore, the wake losses are higher for the no-rotor case. This is probably caused by faster decay of the blade wake for the rotor case. Since the turbulence levels are higher, the wake decays much more rapidly and hence the observed trend. While the wake is clearly distinguishable for the rotor case, it is not a dominant feature for the case without rotor.

The spanwise distribution of circumferentially mass-aver-

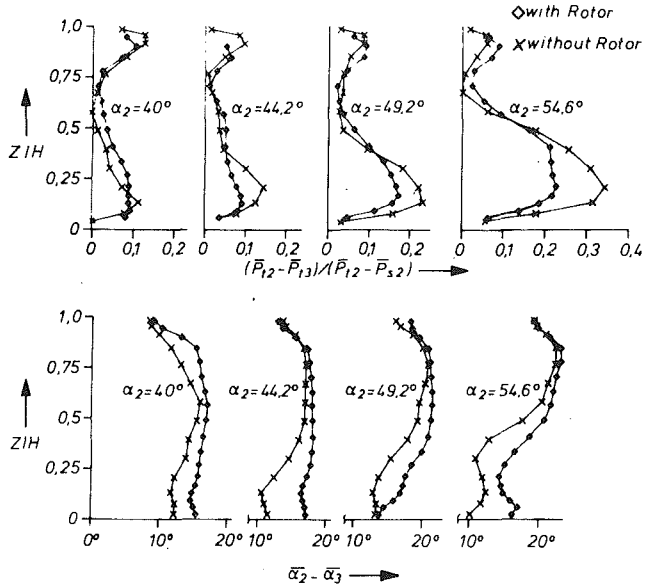

Fig. 12 Circumferential mass averaged total pressure loss and flow turning

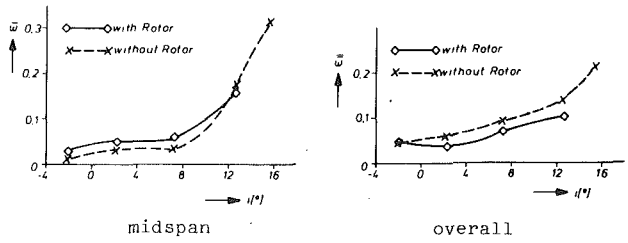

Fig. 13 Losses as a function of incidence (*i*)

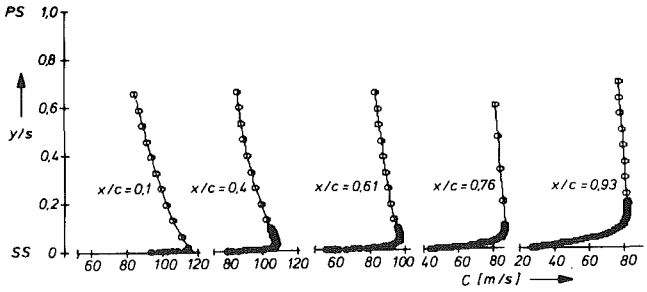

Fig. 14 Velocity distribution inside the flow passage (midspan, α_2 = 49.2 deg with rotor)

aged total pressure loss, normalized with respect to the local dynamic head at inlet, is shown in Fig. 12. It can be seen that the losses, due to separation at the hub, decrease for the rotor case at all angles of attack, while the loss at midspan increases, except at $\alpha_2 = 54.6$ deg where the hub corner stall extends beyond midspan. The losses at the casing with the rotor do not decrease with angle of attack as much as in the case without rotor. This is evidence that the observed decrease in casing corner stall (see Schulz and Gallus, 1988; Joslyn and Dring, 1985) is due to the displacement of the flow resulting from the severe blockage caused by the hub corner stall. The reduction in corner stall and blockage also has a major influence on the flow turning ($\bar{\alpha}_2 - \bar{\alpha}_3$), shown in Fig. 13. The flow turning is generally higher for the rotor case. Hence, the diffusion and the static pressure rise (not shown here also have increased. At lower loading ($\alpha_2 = 40$ deg and $\alpha_2 = 44.2$ deg) the flow turning is nearly constant across the span. Only the tip region shows a reduction in turning due to the tip clearance vortex and the flow separation, which seem to have a similar effect for both cases.

The secondary velocity vectors derived from the five-hole probe measurements are plotted in Fig. 6. An interpretation of these data including the presence of leakage flow, distortion of the separated zone, and radial flows is given in the section, "Structure of Three-Dimensional Separation."

The variation of the loss coefficient at midspan and the overall mass-averaged loss coefficient with incidence are shown in Fig. 13. The losses at midspan are taken directly from Fig. 12 and the overall losses are the spanwise mass averages of the radial distributions. As mentioned before, the losses at midspan increase in the case with rotor due to the early boundary layer transition, the resulting increased boundary layer thickness, and earlier trailing edge separation. This increase in losses is about 30 percent, which is in agreement with investigation by Zil'berman et al. (1973), Cyrus (1988), and Evans (1977). The overall losses ($\bar{\omega}$) decrease as much as 40 percent due to the decreased hub corner stall, except at the negative incidence, where the separation is small for both cases (Fig. 7). Here, higher profile losses and lower separation losses for the rotor case compensate to provide nearly the same values of $\bar{\omega}$ as in the case without rotor. These results are encouraging, since practical compressor stages always have rotor-stator interaction, and the data without an upstream rotor may not be valid for a practical stage. Performance measurements should not only include three-dimensional flow effects, but also the turbulence levels that exist in practical configurations.

Quasi-Steady Surface Blade Boundary Layers. The passage flow, as well as the blade boundary layers, have been measured using a single wire hot-wire probe. The development of the boundary layer, especially the variation in the location of transition and separation due to the presence of the rotor, is of great interest. Hot-wire measurements are a well-known technique to survey boundary layers, and it has been established by Hodson (1983) that it can also detect separated flow and boundary layer transition reliably.

The hot-wire probe was traversed at various chordwise and circumferential positions by a specially designed mechanism scanning through the suction surface boundary layer and the flow passage. Figure 14 shows the development of the velocity profiles from suction side (SS) to pressure side (PS) in the flow channel at midspan ($\alpha_2 = 49.2$ deg). Due to the geometric limitations, the probe could not be traversed close to the pressure side. The blade-to-blade flow data clearly reveal the continuous deceleration of the inviscid region and the rapid growth of the suction surface boundary layer from $x/c = 0.76$ to $x/c = 0.93$.

Figure 15 shows the development of the suction surface boundary layer (velocity C and turbulence Tu) at midspan for an angle of attack of $\alpha_2 = 49.2$ deg. The very thin boundary layer at the leading edge grows continuously and separates just upstream of the trailing edge (98 percent of chord). The hot-wire probe cannot sense the reversed flow, but very high turbulence intensities and very low velocities near the blade surface at 98 percent of chord are an indication that the flow is separated close to the trailing edge. The turbulence intensities, both in the boundary layer and in the free stream, are considerably higher than in the no-rotor case. Turbulence intensities in the free stream have increased by nearly 500 percent, while those near the wall have increased by 100 percent with respect to the no-rotor case.

The time-resolved velocities at 0.15 mm distance from the blade surface are shown in Fig. 16. The vertical scale in these traces is the same, ranging from the time-averaged velocity C + 20 m/s to C − 30 m/s. The time coordinate has been nondimensionalized with respect to the rotor wake passing period T. The data are taken at midspan at $\alpha_2 = 49.2$ deg at the same axial positions as the velocity profiles shown in Fig.

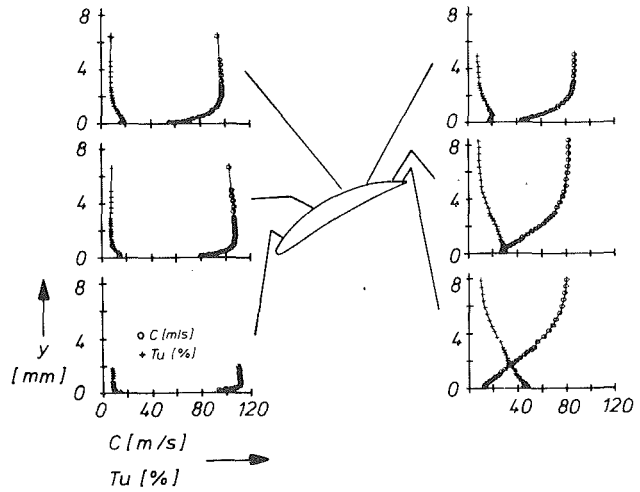

Fig. 15 Boundary layer development along the blade suction side (midspan, α_2 = 49.2 deg with rotor)

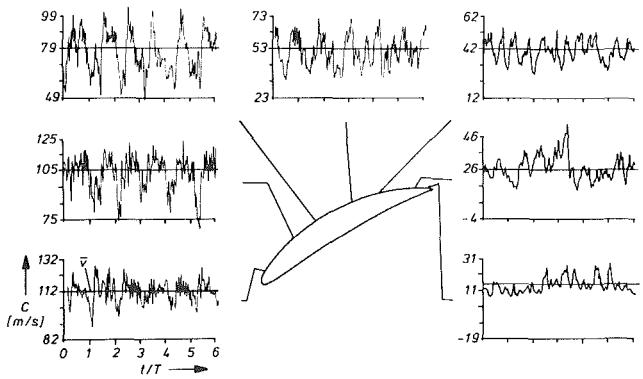

Fig. 16 Time resolved velocities at the blade suction surface (midspan, α_2 = 49.2 deg, with rotor)

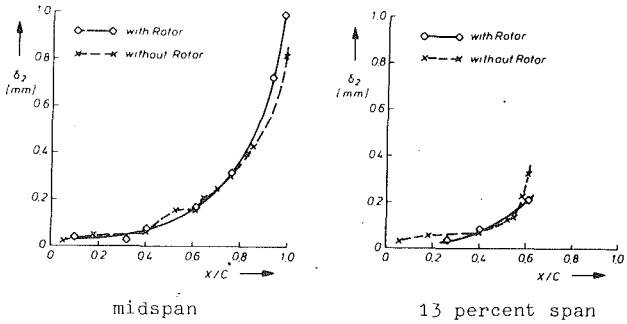

Fig. 17 Development of momentum thickness (α_2 = 49.2 deg)

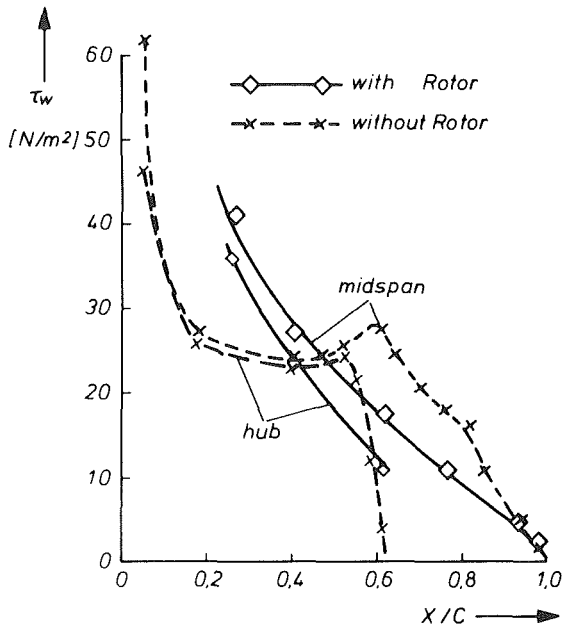

Fig. 18 Development of wall shear stress (α_2 = 49.2 deg)

15. The periodicity due to the rotor wakes is clearly visible in all traces, except near the trailing edge where the flow is separated. The wake signal is damped out there and does not reach the flow near the blade surface. This is also evident in the signal from a Fourier spectrum analyzer, which shows no peak at the blade passing frequency (not shown here). The minima of the velocity signal at the trailing edge go to zero. This is clear evidence that the flow is separated at this location.

The signal at the leading edge shows substantial random fluctuations, an indication that the boundary layer is already in a transient state very shortly downstream of the leading edge, most probably due to the impinging of the wake and the presence of high free-stream turbulence. No evidence of a transitional boundary layer on the blade suction side has been observed for the rotor case (compare Fig. 18 in Schulz and Gallus, 1988) showing that there is a continuous turbulent boundary layer growth. On the contrary, for the no-rotor case, the transition occurred at about 30 percent of chord length. This indicates substantial changes in boundary layer phenomena due to wakes impinging on the surface.

The development of the momentum thickness δ_2 along the suction side for both the rotor case and the no-rotor case is compared in Fig. 17. At midspan, presence of a rotor wake results in higher momentum thickness beyond 80 percent of chord and thus in higher profile losses. This is consistent with the observations made earlier. The hump at about 40 percent of chord has disappeared, indicating that the laminar separation bubble observed for the no-rotor case has disappeared. At 13 percent span from the hub, the distribution of δ_2 shows a sharp increase for the no-rotor case at about 60 percent chord, indicating the onset of turbulent separation. The separation is being delayed in the presence of the rotor. This is brought about by a combination of changes in local pressure gradient, transition, and free-stream turbulence and the absence of the laminar separation bubble. The precise mechanism causing the delayed separation can only be determined through a systematic variation of some of the causes mentioned.

The wall shear stresses have been deduced from the boundary layer measurements by approximating the profiles through a law of the wall, as described by Schulz and Gallus (1988). Close to the wall, the formulation by van Driest (1956) has been used to achieve more reliable values for the shear stress rather than extrapolating the measurements. The wall shear stress distribution is shown in Fig. 18. For the no-rotor case at midspan, the wall shear stress decreases rapidly because of the deceleration of the laminar boundary layer, then increases as it undergoes transition and decreases again due to effect of adverse pressure gradient on the turbulent boundary layer. In the rotor case, the distribution does not show a local minimum but rather a continuous decrease toward the trailing edge where it reaches a value of about zero. This again is an indication that the boundary layer is transient near the leading edge, and that the laminar region and separation bubble observed for the no-rotor case has disappeared.

Similar trends are observed near the hub. The higher value of the shear stress at x/c = 0.61 in the rotor case results from a delayed separation at the hub. The measurements downstream of x/c = 0.61 are not reliable due to large errors in the hot-wire data caused by high turbulence levels. The wall

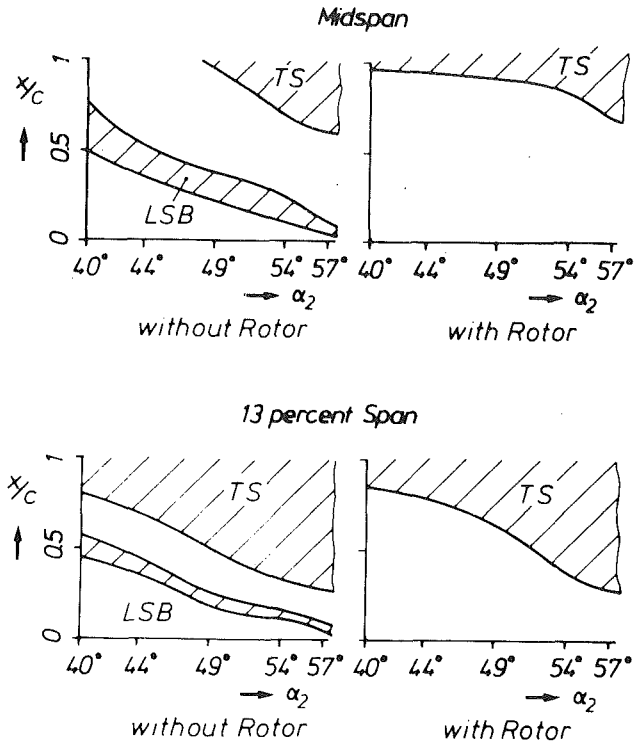

Fig. 19 Boundary layer history versus angle of attack

shear stress measurements are also consistent with the conclusions drawn from the flow visualization and the five-hole probe measurements and give a clear indication that the corner separation is delayed for the rotor case, causing decreased losses as observed earlier.

The results of the suction side profile boundary layer measurements are summarized in Fig. 19. The extent of separated flow in chordwise direction at various inlet angles at midspan and close to the hub (13 percent span) are shown. Regions of separated flow [laminar separation bubble (LSB) and turbulent separation (TS)] determined from the experiments are indicated. A comparison between the no-rotor case and the rotor case shows the disappearance of the laminar separation bubble at all incidences for the rotor case. In the rotor case, there is turbulent separation at midspan at lower inlet angles but TS is reduced at higher incidences as compared to the no-rotor case. The latter effect is due to the reduction of the corner stall region, which can be clearly seen from the data at 13 percent span. On the pressure side (not shown here), there is no evidence of a turbulent separation with or without the rotor. The laminar separation bubble visible at lower inlet angles in the case without rotor (see Fig. 20 and Fig. 21 in Schulz and Gallus, 1988) disappears in the rotor case. It is most likely that the transition on the pressure side also starts close to the leading edge.

Conclusions

The influence of rotor-stator interaction on the development of the blade suction surface boundary layer and endwall corner separation, and on the losses of an annular compressor cascade has been evaluated. The measurements provide a benchmark data base for code verification and correlations, taking into account unsteady, viscous, and three-dimensional flow effects.

At all angles of attack under investigation, the laminar separation bubbles observed at steady and uniform incoming flow have disappeared due to the presence of the rotor. This results in decreased three dimensionality in the flow field near the blade upstream of turbulent separation.

The measurements suggest that transition starts very close to the leading edge in the presence of rotor wakes. This results in a larger rate of boundary layer growth and, hence, in an earlier turbulent separation, at midspan.

With the rotor upstream, the hub corner stall and, hence, the losses near the hub have significantly decreased. This is mostly due to the wakes and the high turbulence level and partly due to the absence of the laminar separation bubble. It is not caused by the change in the hub wall boundary layer at the cascade inlet since the flow visualization on the hub does not show any change in secondary flow, which might influence the separated region.

Even though the losses at midspan increase up to 30 percent due to the unsteady boundary layer, the overall losses for the entire passage decrease up to 40 percent. This is primarily caused by decreased corner separation. The profile losses increase and the endwall losses decrease.

Evaluation of flow visualizations reveals a complex vortex structure of the separated corner region. It is proposed that the separated region is bounded by limiting streamlines on the hub and the blade suction side and by a ring vortex at its trailing edge. The flow perceives the corner stall as a solid obstruction, which ends shortly downstream of the blade trailing edge. Here the flows from both sides of the separated zone merge again.

Acknowledgments

The work reported herein was supported within the framework of research programs of the "Deutsche Forschungsgemeinschaft." Permission for the publication is gratefully acknowledged. The authors are also indebted to R. Loesch-Schloms for his assistance in carrying out these investigations and to C. Poensgen for his contribution to the analysis of the separated flow region. B. Lakshminarayana was a recipient of the Senior Professor Fulbright Award and partial support from U.S. National Science Foundation during his stay at the institute.

References

Bohn, D., and Simon, H., 1975, "Mehrparametrige Approximation der Eichräume und Eichflächen von Unterschall- bzw. Überschall-5Loch-Sonden," ATM *Messtechnische Praxis*, Lieferung 470.

Bradbury, L. J. S., 1976, "Measurements With a Pulsed Wire and a Hot-Wire Anemometer in the Highly Turbulent Wake of a Normal Plate," *Journal of Fluid Mechanics*, Vol. 77, Part 3, pp. 473–497.

Cyrus, V., 1986, "Experimental Study of Three-Dimensional Flow in an Axial Compressor Stage," ASME Paper No. 86-GT-118, Düsseldorf.

Cyrus, V., 1988, "Effect of the Inlet Velocity Profile in the Three-Dimensional Flow in a Rear Axial Compressor Stage," ASME JOURNAL OF TURBOMACHINERY, Vol. 110, pp. 434–440.

Dallmann, U., and Schewe, G., 1987, "On Topological Changes of Separating Flow Structures at Transition Reynolds Numbers," AIAA Paper No. AIAA-87-1266.

Dengel, P., and Vagt, J. D., 1983, "A Comparison Between Hot-Wire and Pulsed-Wire Measurements in Turbulent Flows," *Proceedings 4th Turbulent Shear Flow Conference*, Karlsruhe, Federal Republic of Germany.

Dong, Y., Gallimore, S. J., and Hodson, H. P., 1987, "Three-Dimensional Flows and Loss Reduction in Axial Compressors," ASME JOURNAL OF TURBOMACHINERY, Vol. 109, pp. 354–361.

Dring, R. P., Joslyn, H. D., and Hardin, L. W., 1982, "An Investigation of Compressor Rotor Aerodynamics," ASME *Journal of Engineering for Power*, Vol. 104, pp. 84–96.

Dring, R. P., Joslyn, H. D., and Wagner, J. H., 1983, "Compressor Rotor Aerodynamics," AGARD-CP-351, Reference 24.

Dunham, J., 1972, "Prediction of Boundary Layer Transition on Turbomachinery Blades," AGARDograph No. 164, pp. 55–71.

Evans, R. L., 1977, "Boundary Layer Development on an Axial-Flow Compressor Stator Blade," ASME Paper No. 77-GT-11.

Gallus, H. E., and Hönen, H., 1983, "Measurements of 3D Unsteady Flow Downstream of Rotor and Stator Blades in Axial-Flow Compressors," GTSJ Paper No. 83-Tokyo-IGTC-68.

Hodson, H. P., 1983, "The Detection of Boundary Layer Transition and Separation in High Speed Turbine Cascades," *Proceedings 7th Symposium on Measuring Techniques in Transonic and Supersonic Flow in Cascades and Turbomachines*, Aachen, Federal Republic of Germany.

Hodson, H. P., and Addison, J. S., 1989, "Wake-Boundary Layer Inter-

actions in an Axial-Flow Turbine Rotor at Off-Design Conditions," ASME JOURNAL OF TURBOMACHINERY, Vol. 111, pp. 181–192.

Hoheisel, H., Kiock, R., Lichtfuss, H. J., and Fottner, L., 1987, "Influence of Free-Stream Turbulence and Blade Pressure Gradient on Boundary Layer and Loss Behavior of Turbine Cascades," ASME JOURNAL OF TURBOMACHINERY, Vol. 109, pp. 210–219.

Horlock, J. H., Lewis, J. F., Percival, P. M. E., and Lakshminarayana, B., 1966, "Wall Stall in Compressor Cascade," ASME *Journal of Basic Engineering*, p. 637.

Joslyn, H. D., and Dring, R. P., 1985, "Axial Compressor Stator Aerodynamics," ASME *Journal of Engineeirng for Gas Turbines and Power*, Vol. 107, pp. 485–493.

Lakshminarayana, B., and Horlock, J. H., 1965, "Leakage and Secondary Flow in Compressor Cascades," Department of Mechanical Engineering, University of Liverpool, Reports and Memoranda No. 3483, United Kingdom.

Moore, X. X., and Richardson, Y. Y., 1957, "Skewed Boundary Layer Flow Near End Walls of a Compressor Cascade," *Trans. ASME*, Vol. 79, pp. 1789–1800.

Murthy, K. N., and Lakshminarayana, B., 1987, "The Hub Wall Boundary Layer Development and Losses in an Axial Flow Compressor Rotor Passages," 2., *Flugwiss. Weltraumforschung*, Vol. II, p. I–II.

Salvage, J. W., 1974, "Investigation of Secondary Flow Behaviour and End Wall Boundary Layer Development Through Compressor Cascades," von Karman Inst. TN 107.

Schulz, H. D., and Gallus, H. E., 1988, "Experimental Investigations of the Three-Dimensional Flow in an Annular Compressor Cascade," ASME JOURNAL OF TURBOMACHINERY, Vol. 110, pp. 467–478.

Squire, H. B., and Winter, K. G., 1951, "The Secondary Flow in a Cascade of Airfoils in a Nonuniform Stream," *Journal of Aeronautical Science*, 1951, pp. 271–277.

Takei, N., and Masuda, S., 1988, "Acoustic Control of Turbulent Separation in a Two-Dimensional Diffuser," presented at the Second European Turbulence Conference.

van Driest, E. R., 1956, "On Turbulent Flow Near a Wall," *Journal of Aerospace Science*, Vol. 23, pp. 1007–1036.

Wagner, J. H., Dring, R. P., and Joslyn, H. D., 1985, "Inlet Boundary Layer Effects in an Axial Compressor Rotor: Part I—Blade to Blade Effects," ASME *Journal of Engineering for Gas Turbines and Power*, Vol. 107, No. 2, pp. 374–380.

Walker, G. J., 1974, "The Unsteady Nature of Boundary Layer Transition on an Axial-Flow Compressor Blade," ASME Paper No.74-GT-135.

Zil'berman, A. S., Lopatitski, A. O., Nakman, Y. V., and Vol'fson, I. M., 1973, "Additional Energy Losses Due to Periodic Non-steadiness of the Flow in the Moving Blades of Turbine Stages," *Teploenergetika*, Vol. 20.

Three-Dimensional Separated Flow Field in the Endwall Region of an Annular Compressor Cascade in the Presence of Rotor-Stator Interaction:

Part 2—Unsteady Flow and Pressure Field

H. D. Schulz
Dipl.-Ing.

H. E. Gallus
Professor, Dr.-Ing.

B. Lakshminarayana[1]
Professor.

Institut für Strahlantriebe und
Turboarbeitsmaschinen,
RWTH Aachen,
D-5100 Aachen,
Federal Republic of Germany

An experimental study of the unsteady three-dimensional flow and pressure field in an annular compressor cascade with an upstream rotor has been carried out at several incidences to the stator blade. The distributions of the unsteady pressures at the blade surfaces are measured using fast response Kulite sensors. The unsteady blade boundary layers and the passage flow are measured with a hot-wire sensor. A detailed interpretation of the magnitude of unsteady pressures, phase angle differences, unsteady blade boundary layers, and wake transport through the stator passage is presented and analyzed in the paper. The unsteady pressures are found to be dominant near the blade leading edge. Substantially higher pressure fluctuations occur in this region as well as on the edge of the corner flow separation region.

Introduction

The recent trend toward closer blade row spacing in turbomachinery, especially in aircraft engines, introduces considerable unsteadiness in the flow field. Most of the present analysis and design of aircraft engines are based on steady aerodynamics. The unsteady flow associated with blade row interaction has a major influence on blade pressures, flow field, blade boundary layers, transition, turbulence intensities, corner separation, vibration, and noise. The objective of the investigation reported in this paper is to understand the effects of rotor-stator interaction on blade boundary layers. Of particular interest is its influence on the endwall separation in the corner formed by the suction surface and the hub wall. The quasi-steady results are presented in Part 1 of the paper, and the unsteady pressure and flow field data from the same facility are analyzed and interpreted in this paper.

There has been a large number of investigations on the unsteady aerodynamics associated with rotor-stator interaction. Greitzer (1985) and Gallus (1987) have provided comprehensive reviews on the effect of unsteady wakes on blade pressure and flow field. The groups at Purdue University (e.g., Capece and Fleeter, 1989), Aachen (e.g., Gallus et al., 1982), UTRC (e.g., Carta, 1983), and Penn State (e.g., Bruce and Henderson, 1975) have carried out extensive investigations. Most of these investigations are concerned with the unsteady blade pressures associated with a rotor or a stator upstream (both potential and viscous interactions). Recently, there have been several attempts made to understand the flow field (mainly inviscid flow field) by groups at Cambridge (e.g., Hodson and Addison, 1989), and DFVLR (e.g., Foerster and Mach, 1985). Detailed measurement of unsteady flow away from the blade surface using both a hot-wire and a laser two-focus system have been reported.

The investigation of unsteady boundary layers is mainly confined to simple configurations (e.g., Brendel and Mueller, 1988), and there has been no attempt made to understand the effect of upstream blade rows on flow separation associated with the blade boundary layers and the flow separation in the corner formed by the suction surface and the endwall. This is the major objective of the investigations reported in this paper.

The quasi-steady date are presented in Part 1 of this paper and will not be repeated here. The major emphasis of this paper is to present and analyze the unsteady pressures measured on the blade from hub to tip, leading edge to trailing edge, and the unsteady flow field in the entire passage of an annular cascade. A further emphasis is to derive information on the nature, magnitude, and phase angle associated with blade boundary layers, passage flow, and separated regions.

Measurement Technique and Test Program

A detailed description of the experimental facility is given

[1]Permanent address: Pennsylvania State University, University Park, PA 16802.

Contributed by the International Gas Turbine Institute and presented at the 34th International Gas Turbine and Aeroengine Congress and Exhibition, Toronto, Ontario, Canada, June 4-8, 1989. Manuscript received at ASME Headquarters February 14, 1989. Paper No. 89-GT-77.

in Part 1 of the paper and by Schulz and Gallus (1988) and will not be repeated here.

Unsteady Pressure Measurements. The unsteady blade pressure distribution was measured using 11 Kulite LQ-080 thin line series transducers, which provide a frequency response of at least 13 kHz. The maximum thickness of the transducers is 0.38 mm and the diameter of the pressure sensitive area is 0.97 mm. The transducers were installed in cavities such that the pressure sensitive area is flush with the profile contour. Figure 1 shows the chordwise distribution of the transducers: Six are mounted on the suction side and five on the pressure side of the blade. Since the blade is untwisted, it is designed to be traversed radially at different spanwise positions. Unsteady pressure measurements were always taken at the same speed of the cylinder rotor (3000 rpm), at three different inlet angles (α_2 = 44.2 deg, α_2 = 49.2 deg, α_2 = 54.6 deg) and at five radial positions (3.1, 11, 30, 50, and 88 percent of span, measured from the hub). Only representative results are given in this paper; a complete set of data is available from the senior author. The pressure transducers were statically calibrated, and a typical standard deviation to a straight line calibration curve is 0.1 percent. The temperature during the calibration was kept constant to the air temperature in the wind tunnel.

Unsteady Flow Field Measurements. The flow field in the entire passage and the blade suction surface boundary layer have been traversed using a single sensor hot-wire probe. The probe and the traversing unit are described in Part 1 of this paper. Major emphasis was placed on measuring the unsteady boundary layer and its response to the wake shed form the rotating cylinder. Since the profile boundary layers are very thin, only a single wire probe could be used in these investigations. In addition to measuring the properties of the boundary layers, the probe has been traversed circumferentially across the whole passage to derive the magnitude of the absolute velocity vector, even though the probe cannot resolve flow angles or the velocity components. It has been shown by Adachi and Murakami (1979), Murakami et al. (1981), and Hodson (1985) that the wakes have a major influence on the flow field inside the passage. Therefore, a knowledge of wake trajectory, wake transport, and unsteady flow are essential for a basic understanding of the rotor-stator interaction and interpretation of the pressure field.

The passage has been scanned at six axial positions corresponding to the location of the pressure transducers along the blade suction surface. The measurement closest to the blade suction surface was 0.15 mm away from the surface. Due to mechanical limitations of the probe, no measurements could be acquired close to the blade pressure side (the closest distance to the surface is 10 percent of blade spacing). The passage data (excluding boundary layers) were acquired at about 11 stations across the passage. The suction surface boundary layer has been measured at about 12 locations normal to the blade surface at 57, 74, and 98 percent of chord at midspan. All the measurements were carried out at an inlet angle of α_2 = 49.2 deg at midspan, where the flow separation occurs just upstream of the trailing edge. An estimate of the error in the hot-wire measurements is given in Part 1 of this paper.

To understand the effect of rotor wake on the flow inside the separated region, the passage has been additionally traversed at 11 percent of span and 74 percent of chord, where the separated region covers a major part of the flow channel. The measurements in this region should be viewed as qualitative as the hot wire cannot sense the direction, and the error due to high turbulence in the flow field is appreciable.

Data Analysis and Processing. The data from the high response pressure transducer and the hot-wire anemometer were acquired and recorded in digital form via a five-channel transient recorder and an anlog-digital converter. Each channel could be sampled at a rate of 1000 kHz and 89 kHz, respectively. The systems were operated in the external trigger mode so that data could be synchronized with the rotor. Two hundred samples were taken along one cylinder passage and averaged 128 times (N = 128). Also real-time data were stored to derive turbulent quantities (rms values). All data were processed to physical units after the tests.

The ensemble-averaged, time-averaged, rms values and the overall fluctuation are defined as follows:

$$\tilde{P} = \frac{1}{N}\sum_{i=1}^{N} P_i \tag{1}$$

$$\bar{P} = \frac{1}{T}\int_0^T \tilde{p}\, dt \tag{2}$$

$$P_{\text{rms}} = \sqrt{\frac{1}{N}\sum_{i=1}^{N} (p_i - \tilde{p})^2} \tag{3}$$

Nomenclature

BPf = blade passing frequency
c = blade chord
C = absolute velocity
ΔC = velocity fluctuation at a given time = $\tilde{C}(t) - \bar{C}$
ΔC_D = instantaneous drag coefficient = $\oint \tilde{P}\, d\eta/(q \cdot c)$
ΔC_L = instantaneous lift coefficient = $\oint \tilde{P}\, d\xi/(q \cdot c)$
C_p = pressure coefficient = $(P_{\text{loc}} - P_{2m})/q$
ΔC_p = unsteady pressure coefficient = P/q
f = frequency
i = incidence
P = pressure
PS = pressure side
q = inlet dynamic heat at midspan = $1/2\rho C_{2m}{}^2$
s = bladed spacing
SS = suction side
t = time
T = blade passing period
u = rotational velocity
W = relative velocity
x = axial direction
y = circumferential direction
α = flow angle measured from axial direction
β = pitch angle
δ = boundary layer thickness
δ_2 = instantaneous momentum thickness = $\int_0^\delta [(1 - C/C_\infty)(C/C_\infty)]dy$
η = coordinate normal to the blade chord
ξ = coordinate parallel to the blade chord
ρ = density
ϕ = phase

Subscripts

2 = upstream of the cascade
i = instantaneous
loc = local
m = blade midspan height
rms = root mean square
s = static
t = total
w = wake
∞ = free stream

Superscripts

$\bar{(\ )}$ = time averaged
$\tilde{(\ )}$ = periodic fluctuation
$(\ )'$ = overall fluctuation
$\hat{(\ )}$ = amplitude

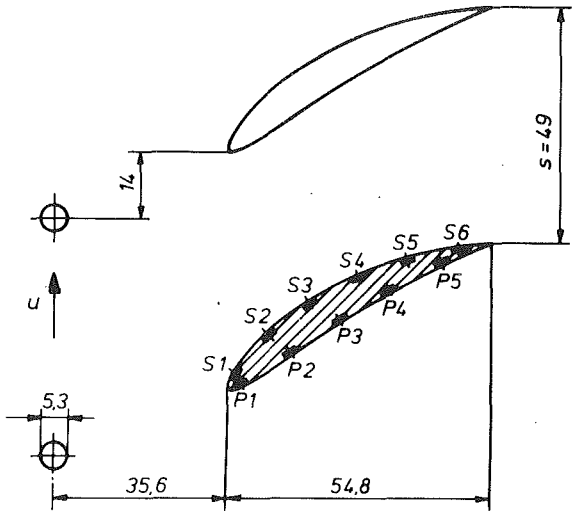

Fig. 1 Instrumented blade and cylinder position at $t = 0$ (midspan)

$$P' = \sqrt{\frac{1}{N}\sum_{i=1}^{N}(p_i - \tilde{p})^2} \tag{4}$$

where P_i is a function of x/c, y/s and represents instantaneous AC values, phase-locked to a constant angular position (t/T) of the rotor.

Similarly

$$\tilde{C} = \frac{1}{N}\sum_{i=1}^{N} c_i \tag{5}$$

$$\mathrm{Tu} = \sqrt{\frac{1}{N}\sum_{i=1}^{N}(c_i - \tilde{c})^2/\tilde{c}} \tag{6}$$

The analog digital converters used have a 12-bit resolution. The accuracy in conversion, therefore, is 0.024 percent of the measured value. Lakshminarayana and Poncet (1974) derived a relation for the random error occurring in an ensemble-averaging data reduction process, which includes the turbulence intensity and the number of ensemble-averages (N). The error in the present tests is estimated to be 1.4 percent in mean pressure and in mean velocity data.

Results and Discussions

Unsteady Blade Pressures. As mentioned earlier, the instantaneous pressures were measured at 5 radial and 11 chordwise locations. The ensemble (phase-locked)-averaged data as well as the values of the pressure fluctuations are presented in this section. In addition, the data are analyzed and interpreted to derive information on the amplitude, phase angle, and spectrum of these pressure fluctuations. The ensemble-averages, the rms values, and the overall pressure fluctuations are derived by equations (1), (3), and (4), respectively.

The data presented in this section, as well as the hot-wire data presented in the next section, have the same time base with respect to the rotor position, so that a direct comparison can be made between the blade pressure data and the flow field data. All the data are for $\sigma_2 = 49.2$ deg, and $t = 0$ corresponds to the rotor-stator relative position shown in Fig. 1 of this paper.

Periodic and Random Pressure History. The phase-lock averaged periodic pressure fluctuations at the midspan and at a location close to the hub (11 percent of span) at various

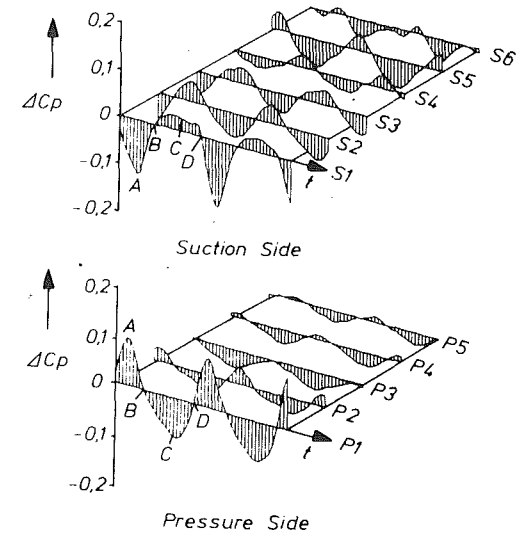

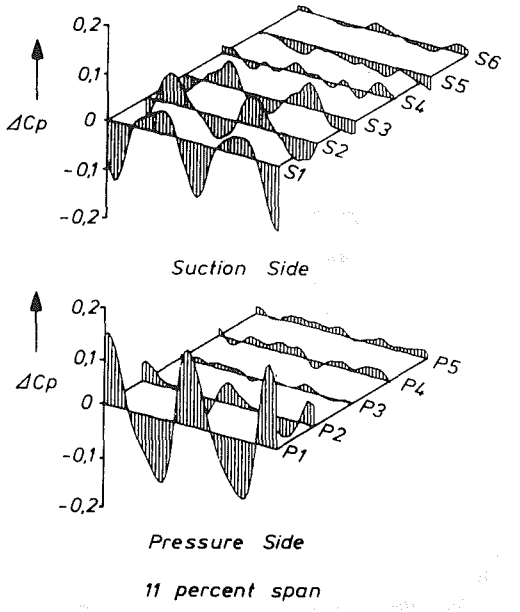

Fig. 2 Ensemble-averaged pressure fluctuation

chordwise locations are shown in Fig. 2. These data represent the fluctuating periodic component (difference between the ensemble-averaged values at any time t and the time averaged values $\bar{P}$) nondimensionalized with the inlet dynamic head at midspan q.

It is useful to relate the unsteady pressures with the wake trajectory. Referring to Fig. 1 of Part 1, the wake in both the absolute and the relative frame of reference will have a defect in velocity at the centerline. It should be noted that this is not always true. If W_2 and C_2 are in opposite directions, the shear layer from the cylinder will be a wake in the relative frame of reference, but can be a jet in the absolute frame of reference. In this particular configuration, shear layers viewed from both frames of reference will be wakes. Furthermore, the rotor wake in the absolute frame will be highly skewed, as shown in Fig. 1 of Part 1. The velocity vector $\mathbf{C}_{2W}$ will change in magnitude as well as direction. It is this phenomenon that causes a change in incidence $i(t)$. The wake trajectory, viewed from the stator, is along the $\alpha_2 + i(t)$ direction as shown. Knowing the angle,

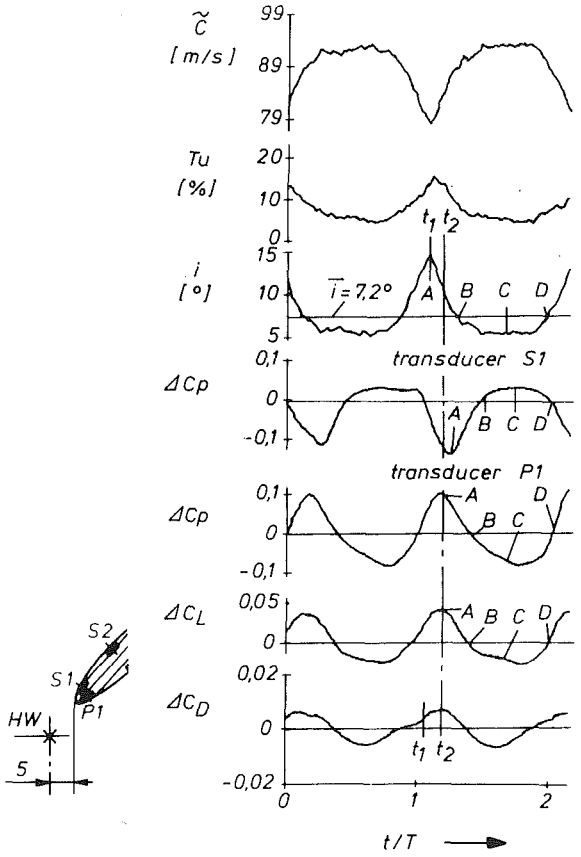

Fig. 3 Ensemble-averaged hot-wire and pressure signals (midspan)

and assuming that the wake is convected with the time-averaged velocity, the wake trajectory can be estimated.

The effect of rotor wake on unsteady blade pressure distributions can clearly be seen by data such as wake profile, instantaneous incidence angle, and ΔC_p distribution that are referred to the same time base as shown in Fig. 3. The hot-wire measurements were carried out at an upstream distance d = 5 mm from the leading edge of the blade. The location of the hot-wire probe, as well as the location of the Kulites near the leading edge, are given in the inset. The wake center (marked A) has the lowest velocity, highest turbulence intensity, and highest incidence change, all of which are time dependent in a stator frame of reference. Also shown in the figure are the time-dependent distribution of ΔC_L and ΔC_D, all of which refer to the same instant of time. The time lag $t_2 - t_1$ between the wake data and the unsteady pressure is the time taken for the wake to travel from the hot-wire location to S1 and P1 transducer locations, respectively. It is clear that peak suction pressure decreases (increasing the absolute negative value) and the peak pressure on the pressure surface increases at the instant of time when the wake impinges on the blade leading edge. The locations B in Figs. 2 and 3 correspond to zero incidence change, where the unsteady lift, pressures, and drag are nearly zero. The locations C in both these figures correspond to the minimum incidence, and also to reversal and negative values of ΔC_p, ΔC_L, and ΔC_D.

The highest perturbation in blade pressures (10 to 15 percent of q) occurred near the leading edge (Fig. 2) at all points of operation and span positions, except at the highest loading (α_2 = 54.6 deg) on the suction side, where there is a leading edge separation. The unsteady pressures are appreciable at locations (P2, S2) as well as (P3, S3), but not as severe as those near the leading edge (P_1, S_1) (Fig. 2). The magnitude of unsteady pressure decreases much more rapidly on the pressure side than on the suction side. This is consistent with measurements reported by Dring et al. (1982) and Zandbergen (1988).

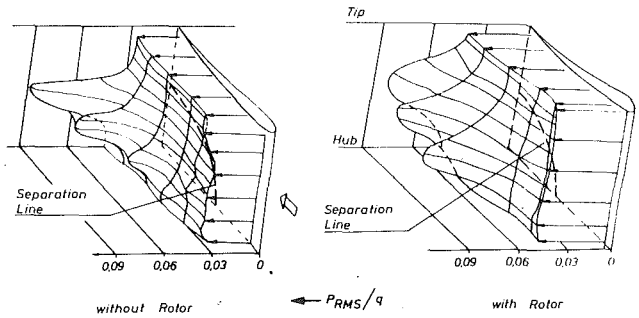

Fig. 4 Random pressure fluctuation at the blade suction side, α_2 = 54.6 deg

On the suction side at midspan, the decay in unsteady pressures occurs up to the transducer location S4 (Fig. 2). A sudden increase in the fluctuating unsteady pressures at transducer location S5 on the suction side can be attributed to unsteady separation near the trailing edge (Fig. 7, Part 1). The separation point on the blade may be time dependent, giving rise to the observed trend.

The decay of the unsteady pressures toward the trailing edge behaves quite differently at midspan and close to the hub. On the suction side at midspan, the fluctuation gradually decreases toward the trailing edge while at the hub, the fluctuations of P are high up to transducer S3 and then decrease rapidly farther downstream. It is known from flow visualization (Part 1 of this paper) that the last three transducers are inside the separated region at the spanwise position shown here. Therefore, it is concluded that the periodic fluctuation of the unsteady pressure P is damped, and the disturbance due to the wake has not been able to penetrate the separated zone. The ensemble-averaged pressure fluctuations in these regions are much smaller than at the corresponding location near midspan.

The unsteady pressures on the pressure side near the hub decay much more rapidly and are insignificant beyond transducer location P2. This may result from the reduced deceleration of the flow on the pressure side due to the blockage caused by the separated region. It is known from the experimental work of Hill et al. (1963) that the decay of a wake is slower in an adverse pressure gradient field. Likewise, the decay of shear layers (jets, wakes) is much more rapid in accelerating flow. This may account for negligible unsteady pressures on the pressure side beyond the leading edge compared to the values on the suction side.

The random fluctuations are amplified in the region close to the separation line. A comparison of the random pressure fluctuation P_{rms} as defined in equation (3), with and without rotor, illustrates this point. The results for α_2 = 54.6 deg are plotted in Fig. 4, as these features are more pronounced at this high inlet angle. The values of the fluctuations are higher in the rotor case due to higher free-stream turbulence intensities and periodic fluctuations in this case. The turbulent velocity fluctuations, which are most pronounced in the wake center (Fig. 3), are amplified by the deceleration of the flow near the leading edge resulting in high pressure fluctuation at this location. Beyond the leading edge, the acceleration of the flow, combined with diffusion and dissipation of the turbulent energy, results in a decrease of the random pressure fluctuation. High P_{rms} values are measured near the separation line caused by the high turbulence intensities that exist in these regions (Schulz and Gallus, 1988). The unsteady separation induces additional turbulence as described earlier.

Blade Pressure Frequency Spectra. The amplitudes of the first and second harmonics of the blade passing frequency (BPf) taken from the spectrum of an FFT-spectrum analyzer are shown in Fig. 5 at midspan and at 11 percent of span. The frequency spectra for some typical chordwise locations near

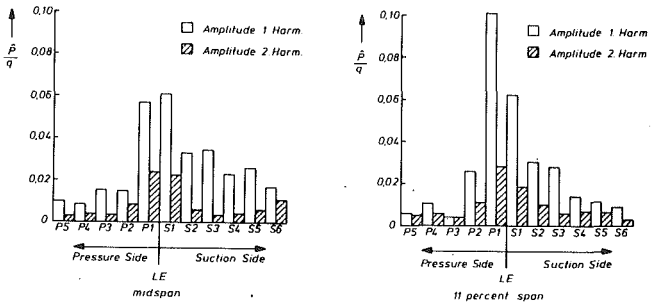

Fig. 5 Amplitudes of the first and second harmonics of the blade passing frequency

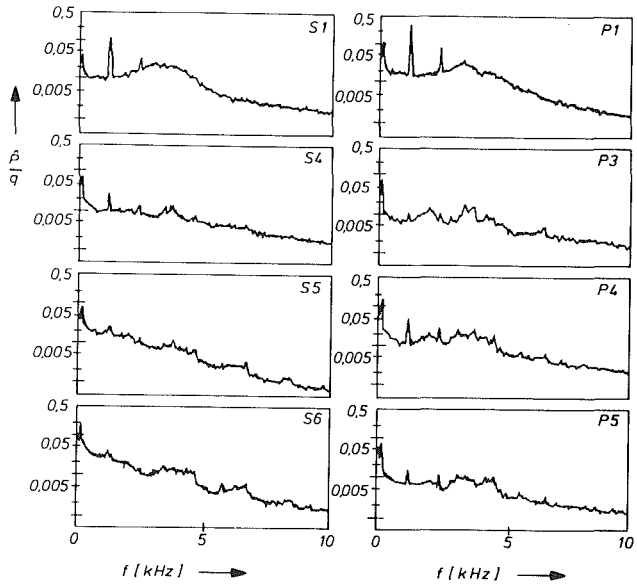

Fig. 6 FFT spectra of the pressure signals at 11 percent span

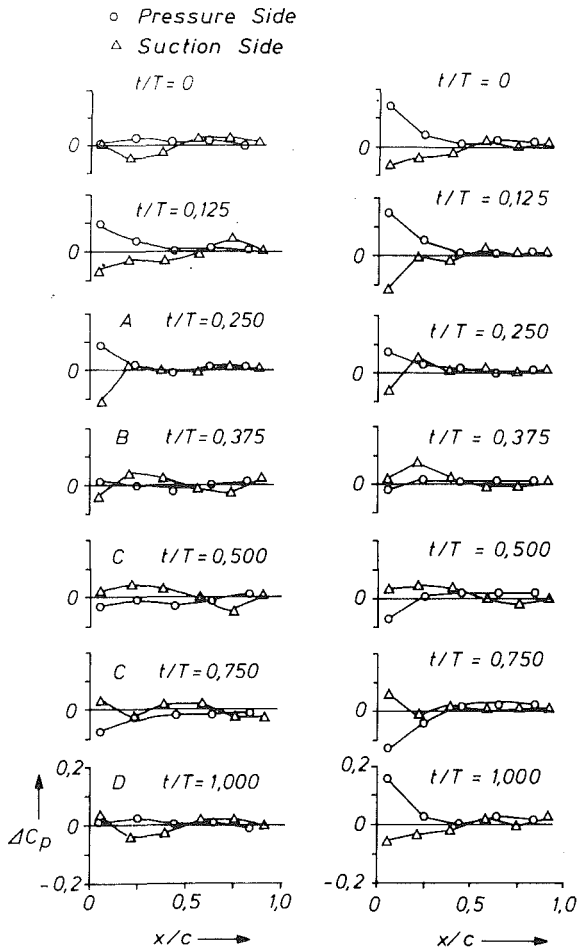

Fig. 7 PLA distribution of the fluctuating component of the pressure coefficient

the hub are given in Fig. 6. In these figures S1, P1, etc., denote the transducer S1, P1, as shown in Fig. 1. The amplitudes are nondimensionalized with the inlet dynamic head at midspan (q). Note the logarithmic scale of the ordinate in Fig. 6. Figure 5 indicates that the first harmonics are dominant at all locations, but the second harmonics also are considerable and approach values up to nearly 50 percent of the first harmonics, especially in the leading edge region. As can be seen in Fig. 6, the third harmonics do not exceed the noise level and are negligibly small. It is clear from Fig. 5 that the wake has a strong effect at the leading edge. At midspan, on the pressure side the wake decays rapidly toward the trailing edge but more gradually on the suction side. As discussed before, the wake persists longer in decelerating flow, and hence the observed effect.

At 11 percent span, the wake decays even more rapidly on the pressure side. On the suction side, the decay is similar with regard to midspan up to transducer S3, but the wake is already weak at S4 and nonexistent at S5 and S6. This is being confirmed by Fig. 6 showing that the amplitude of all BPf harmonics are smaller than the noise level beyond S4. This again is an indication that the wake cannot penetrate the separated region and that the rapid decay of the wake beyond the midchord location on the suction and the pressure side at 11 percent of span is brought about by the separated flow as explained earlier.

Unsteady Pressure and Lift Coefficients. The distribution of the ensemble-averaged pressure fluctuation (ΔC_p), at seven consecutive angular positions of the rotor (starting with t = 0 as shown in Fig. 1), are presented at midspan and at 11 percent span in Fig. 7. Here $t = T$ corresponds to one period of BPf. The periodicity is confirmed through almost identical ΔC_p distributions at $t = 0$ and $t = T$.

Figure 7 should be interpreted in combination with Fig. 3, where the instantaneous wake profile, incidence, and turbulence intensity are shown. The wake defect, incidence, and turbulence intensity are highest at the wake center, and the corresponding influence on C_p distribution can be interpreted as follows: Referring to Fig. 3, the points A, B, C, and D on the instantaneous incidence curve approximately represent the midspan pressure distribution at $t/T = 0.25$, 0.375, 0.66, and 1.0, respectively, taking into account the time lag $t_2 - t_1$ of 0.12 T. The wake impinges on the leading edge of the blade when t/T is about 0.2, giving rise to large increase in the magnitude of suction pressure and positive pressure on the pressure side. The disturbance at other chordwise locations is negligibly small.

Region B in Fig. 3 corresponds approximately to t/T = 0.375 in Fig. 7. Here the wake has moved downstream of the leading edge causing unsteady pressures near the midchord as well as the trailing edge regions. As the free stream is approached, a negative incidence change occurs (location C in Fig. 3), and the pressure decreases on the pressure side and the suction pressure decreases on the suction side. This represents a reversal of the ΔC_p curve as well as a minimum in ΔC_L in Fig. 3. As region D is approached, the incidence angle change again is zero and, as shown at $t/T = 1.0$, ΔC_p is nearly zero near the leading edge.

These results are consistent with the measurements by Zand-

bergen (1988), who investigated the acoustic and aerodynamic response of an unloaded stator vane to rotor wakes shed from cylindrical rods. The plots of ΔC_p in Fig. 7 show clearly how the instantaneous C_p distribution is changing with time, with maximum ΔC_p values occurring close to $t/T = 0.125$ and 0.250, and minima occurring close to $t/T = 0.5$ and $t/T = 0.75$.

The magnitude of ΔC_p close to the hub (11 percent span) is higher in the vicinity of the leading edge than at the midspan. Furthermore, it approaches its maximum value earlier (about 0.125 T). This can be attributed to the reduced inlet angle inside the hub wall boundary layer due to a loss in inlet swirl (compare Fig. 2 in Part 1). Thus the wake has to travel a shorter distance to approach the blade leading edge and, therefore, has also decayed less. This results in a higher incidence change and hence in a higher effect on the ΔC_p distribution, which can be seen in Fig. 7. The importance of wake decay and its impact on the unsteady blade pressure distribution has been discussed in more detail by Gallus et al. (1982) and Dring et al. (1982). While close to the leading edge, the pressure fluctuations are higher, it is clear from Fig. 7 that downstream of midchord the fluctuations are less than at midspan. This again is brought forth by the separated flow as explained earlier.

The unsteady changes in lift and drag coefficients for the entire blade at the midradius are plotted as a function of time in Fig. 3. The fluctuating lift coefficient was computed from the component normal to the blade chord of the instantaneous pressure difference across the blade. The drag is the blade force component parallel to the blade chord and hence includes only the pressure drag. Lift and drag are nondimensionalized by inlet dynamic head and chord length. The peak unsteady lift coefficient corresponds to the instant of time when the wake impinges on the leading edge. Here the wake centerline, with minimum velocity, is directed toward the leading edge, and the incidence change is maximum. The maximum change in drag coefficient also occurs at this instant of time. The interpretation of the effect of the wake on ΔC_L and ΔC_D is similar to that described for the instantaneous ΔC_p distribution. For example, at B in Fig. 3, where the incidence changes are small, both ΔC_L and ΔC_D go to nearly zero. At C, where there is a negative incidence change (with respect to the time-averaged incidence), negative changes in lift and drag coefficient are also observed. The maximum changes in lift and drag coefficients are about 10 percent and 2 percent of the steady-state value, respectively.

Unsteady Flow Field. The unsteady flow field was derived from the hot-wire measurements. The interpretation of the passage flow data and of the unsteady boundary layers is presented next.

Unsteady Passage Flow Field and Correlation With the Unsteady Pressure Field. There is a close correlation between the unsteady flow field and the unsteady pressure field. Hence, the unsteady flow field presented in this section should be viewed along with the unsteady pressure field shown in Figs. 2 and 7. Typical unsteady velocity profiles at midradius at two instants of time $t/T = 0.125$ and $t/T = 0.5$ are shown in Fig. 8. In this figure, the deviation of the ensemble-averaged velocity at a given time from the time-averaged velocity is plotted at different chordwise and circumferential positions. The zero-deviation lines (which correspond to the time-averaged velocity) are drawn as vertical lines. The magnitude of the deviation in velocity is indicated perpendicular to this origin at each position. The scale of the deviation and the instance of time the flow field is frozen are indicated in the figures. Since the flow is turned, accelerated or decelerated throughout the passage, the trajectory of the wake front at an instance of time is not straight but curved as indicated in the figure. When the wake center is at the leading edge (Fig. 8, $t/T = 0.125$), the

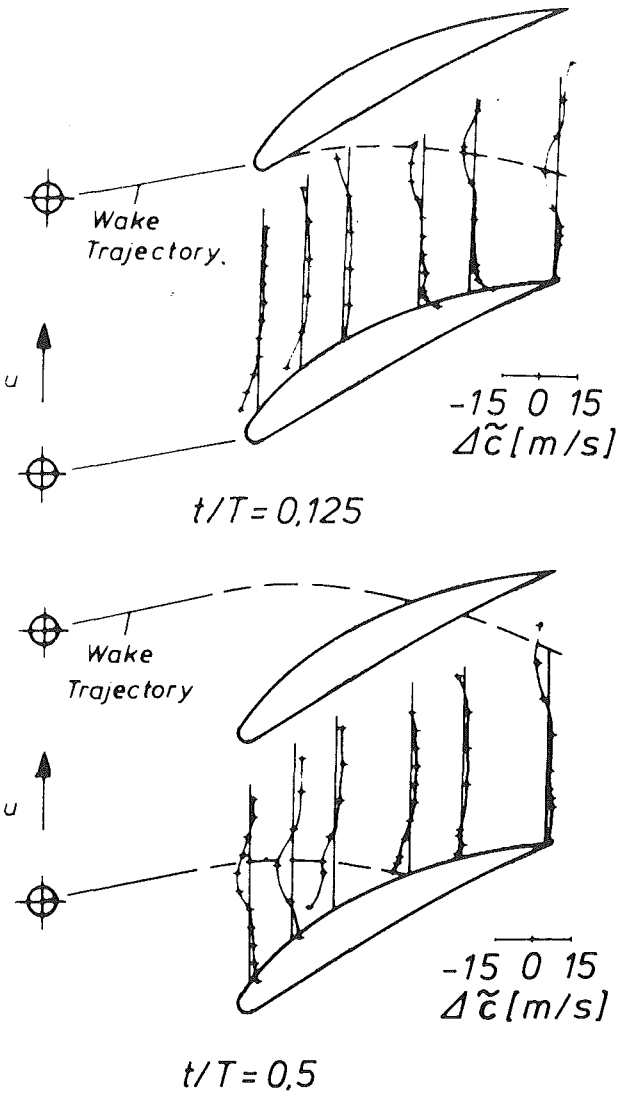

Fig. 8 Deviation between the ensemble-averaged velocity at a given time and the time-averaged velocity, $\Delta C = \tilde{C}(t) - \bar{C}$ (at midspan)

subsequent change in incidence creates an increase in the pressure on the pressure side and a decrease in pressure on the suction side. The C_p distributions (Figs. 2 and 7) clearly show an increase in blade loading. The wake is apparent on the first two stations of the leading edge, and Fig. 8 shows that another wake front is in the rear part of the flow passage. At $t/T = 0.5$, the wake is located at the leading edge station at about midpassage. At this time, the slight increase in velocity at the leading edge is probably due to the displacement by the wake.

Unsteady Pressure Wave and Flow Field Phases. It has been pointed out that the amplitudes of the unsteady pressures at the leading edge are by far the largest and have a most significant influence on the lift coefficient, but some contributions also come from a far extended region, notably the front 70 percent of the blade chord (Zandbergen, 1988). The wake shedding from the cylinder considerably influences the flow field in the passage and, on the other hand, the wake itself becomes distorted while traveling downstream (Adachi and Murakami, 1979). It also influences the stator blade wake, causing a flapping movement, which emits acoustic wakes traveling upstream. In fact, the total response of the blade pressure distribution is a mixture of the aerodynamic and the acoustic phenomena and one of them may dominate. Therefore, the phase behavior of unsteady pressures on the blade is very complicated.

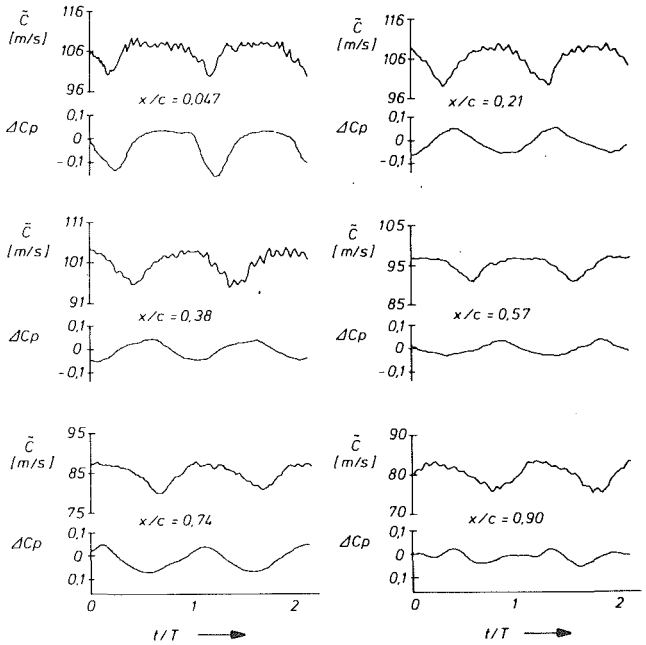

Fig. 9 PLA velocity and pressure at the blade suction side (midspan); the velocity scale is ± 10 m/s from the time-averaged velocity $\bar{C}$

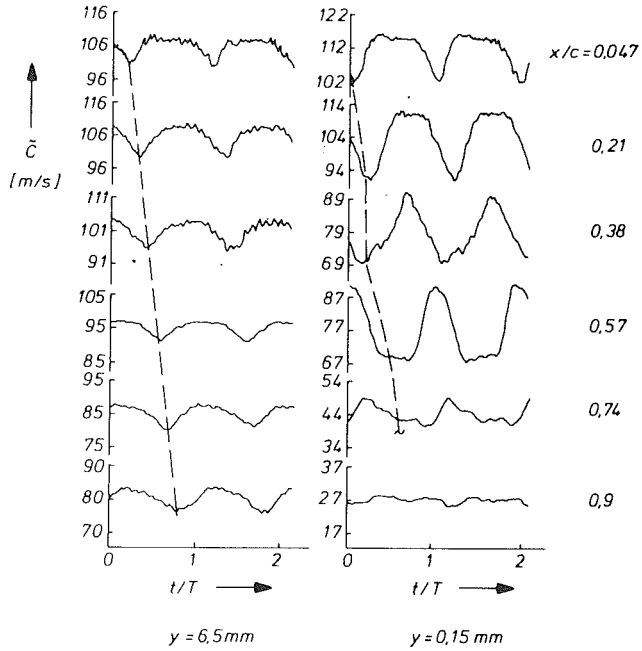

Fig. 11 PLA velocities at the blade suction surface and in the free stream (midspan); the velocity scale is ± 10 m/s from the time-averaged velocity $\bar{C}$

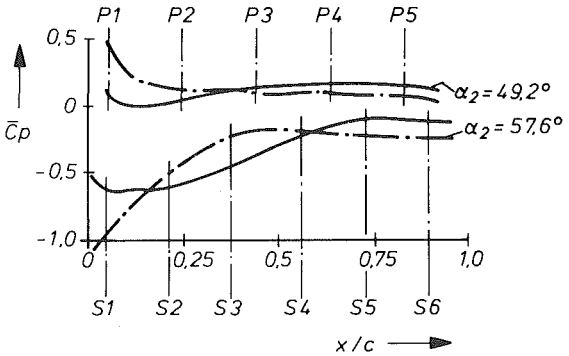

Fig. 10 Time-averaged static pressure distribution at midspan (from static pressure measurements)

Figure 9 shows a comparison of the ensemble-averaged velocity and pressure fluctuations at all transducer positions on the blade suction side at midspan. The velocities are measured outside the blade boundary layer at a constant distance of 13 percent of spacing (6.5 mm) away from the wall. It can be seen that there is a nearly constant phase shift in the velocity signals corresponding to the convection velocity of the free stream. The pressure fluctuations correlate with the velocity fluctuations but they are in-phase only at the leading edge, where the wake induces a high suction peak as discussed before.

At transducer locations S2 and S3 (x/c = 0.21 and x/c = 0.38) there is a difference in phase of little less than 180 deg between the velocity and the pressure. This suggests that the pressure disturbance is not convected with free-stream velocity. Therefore, in this case, they are not caused by the wake passage. From comparing the pressure minima at transducer location x/c = 0.047 and x/c = 0.21, one would deduce a convection velocity much smaller than the free-stream velocity, which is not sensible. For further discussion of this phenomenon, the time-averaged static pressure distribution is presented in Fig. 10. The pressure distributions at α_2 = 49.2 deg and at α_2 = 57.6 deg are shown here. The latter represents an increase in incidence of Δi = 8.4 deg, which closely corresponds to the increase in incidence due to the wake (compare Fig. 3). Due to the extent of the separated region at higher blade loading and its influence on the quasi-steady static pressure distribution, the C_p lines cross at about 15 percent of chord. Indicated in Fig. 10 are also the sites of the pressure transducers. It is clear that while transducer S1 realizes an increase in suction peak, transducers S2 and S3 experience an increase in static pressure due to the change in incidence.

When calculating the convection velocity of the pressure disturbance from the time difference of the pressure minimum at x/c = 0.047 and the pressure maximum at x/c = 0.21, the value found was close to the speed of sound, which seems to be reasonable. Figure 10 also provides an explanation for the relatively high pressure fluctuation at sensor S3 and the relatively low fluctuation at sensor S4. In an ongoing investigation on aerodynamic damping and flutter in the same test facility and the same cascade (Poensgen, 1988), it was found that the unsteady pressures lag the pressure changes due to incidence variation, but show the same tendencies. However, the amplitudes of the pressure fluctuations in the investigation reported in this paper are smaller by a factor of about 3 than the differences in static pressure deduced from Fig. 10. Therefore, even if the quasi-steady pressures exhibit the same trends, one cannot view the unsteady pressures in a quasi-steady manner only.

Transducer S5 is close to the edge of the separated region and, as mentioned before, this might explain the relatively high pressure fluctuation. Transducer S6 is inside the separated region and, therefore, showing a rapid decrease of the periodic unsteadiness, which seems to be in phase with the velocity fluctuation of the free stream (Fig. 9, x/c = 0.90).

It is apparent from Figs. 9 and 10 that the phase shift between the free-stream disturbances and the pressure fluctuations is mainly caused by the blade pressure distribution, responding to a change in incidence, and by the movement of the separation line, which will have an upstream influence on the pressure and the flow field. The flow and pressure field may respond differently, with regard to phase as well as amplitude. The free-stream unsteadiness has very little influence on the pressure in the separated region.

Unsteady Blade Boundary Layer and Corner Separation. A comparison of the unsteady flow field at midspan at 13 percent (6.5 mm) and 0.3 percent (0.15 mm) of passage

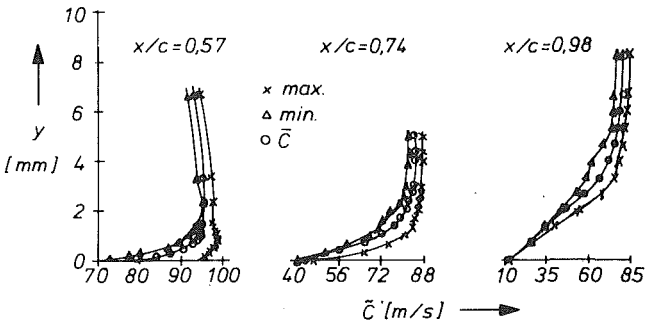

Fig. 12 Instantaneous and time-averaged velocity profiles at the blade suction side (midspan)

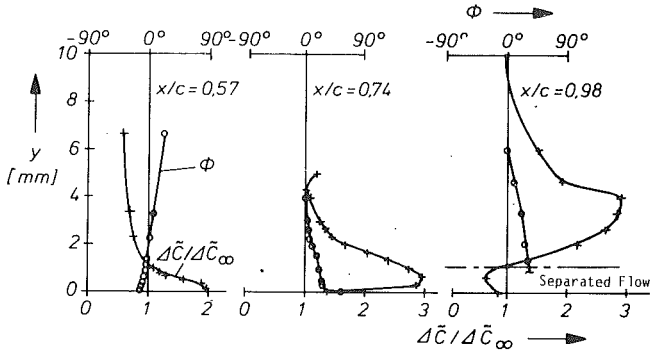

Fig. 13 Phase (ϕ) and amplitude (ΔC) of the velocity fluctuation in the suction side boundary layer with respect to the free stream (C_∞)

width away from the suction surface is shown in Fig. 11. Comparing phase angle and amplitude, the response of the free stream as well as the inner boundary layer to the wake upstream can be detected. Two major effects could be observed here. The amplitude of the velocity fluctuation inside the boundary layer or near the wall is much higher than those in the free stream up to $x/c = 0.57$, nearly the same at $x/c = 0.74$, and much lower in the separated region ($x/c = 0.9$). Furthermore, there is a phase shift in the flow field between $y = 6.5$ mm and $y = 0.15$ mm. This is consistent with measurements by Brendel and Mueller (1988) and Hodson (1983). At $x/c = 0.047$ and $x/c = 0.21$, the velocity in the region between the wakes is higher near the blade surface than that away from the blade ($y = 6.5$ mm). This is an inviscid effect caused by acceleration of the flow near the leading edge surface. There the boundry layer thickness is very small (less than 0.15 mm). Also, the wake defect in the wall region is higher than those in the free stream. One explanation for this behavior is that the flow near and along the stagnation streamline is decelerating rapidly upstream of the leading edge. Hence, the wake defect near the leading edge surface (upstream) would decay very slowly or even increase due to the adverse pressure gradient. Therefore, in the leading edge plane, the wake defect near the surface should be higher than that away from the surface. This history effect persists even beyond the leading edge region, as shown in Fig. 11, for $x/c = 0.047$ and $x/c = 0.21$.

At $x/c = 0.38$ and $x/c = 0.57$, the measuring stations are within the boundary layer ($d = 0.15$ mm). The amplitudes of the wakes in these regions are higher and wider than those in the corresponding free stream as well as those at $x/c = 0.21$, $y = 0.15$ mm. The flow near the surface is decelerating from 114 m/s at $x/c = 0.21$ to 90 m/s at $x/c = 0.57$. As explained earlier in this paper and by Hill et al. (1967), the defect in the wake centerline velocity may actually increase due to rapid deceleration, which accounts for the increased amplitudes in this region. The deceleration of the free stream ($y = 6.5$ mm) is comparatively smaller than those near the wall ($y = 0.15$ mm). Hence, the wake velocity defects decay gradually downstream of $x/c = 0.21$. Turbulent diffusion plays a major role in the decay of the wake in the free stream.

At $x/c = 0.74$, the amplitudes of the wake at $y = 0.15$ mm and at $y = 6.5$ mm are nearly the same. At this chordwise position and at $x/c = 0.9$, the quasi-steady pressure remains nearly constant as can be seen in Fig. 10, and the turbulence increases rapidly since the boundary layer flow approaches separation. This results in a considerable decay of the velocity fluctuation near the blade surface.

In the free stream, the wake is convected with the free-stream velocity, varying from about 110 m/s near the leading edge to about 80 m/s at the trailing edge (see Fig. 11, dotted line), but inside the blade boundary layer at $y = 0.15$ mm, the convection velocity varies considerably more. At $x/c = 0.047$ and $x/c = 0.21$, they are nearly the same as in the free stream, and thus the phase angle differences with respect to the free stream are also small, but beyond $x/c = 0.38$, these differences become considerable. This is clearly brought about by the boundary layer growth and a lower convection velocity close to the wall. Furthermore, the convection velocity inside the boundary layer does not vary in a linear fashion, giving rise to a distorted trajectory as shown for $y = 0.15$ mm.

The instantaneous and time-averaged boundary layer profiles at three different chordwise positions are shown in Fig. 12. These profiles are obtained by taking a "slice" at a given instant of time through a series of ensemble-averaged velocity records for the whole boundary layer. The instantaneous profiles shown were taken at the instant of time when the free-stream velocity is maximum and minimum. At different chordwise positions, these profiles represent the relative "breathing" of the boundary layer in response to the imposed oscillation. As pointed out by Lighthill (1954), the fluctuating pressure gradient acting on the slowly moving fluid inside the boundary layer is the same as the one influencing the free stream. Therefore, the same pressure fluctuation results in a larger relative change of velocity in the boundary layer than in the outer flow. This is even more evident in the ratio of the local fluctuation amplitude to the free-stream amplitude, shown in Fig. 13. It is apparent that the maximum amplitude ratio moves away from the wall as the flow moves downstream. It is also clear that close to the laminar sublayer and inside regions with separated flow the velocity fluctuation is damped. This is also noticeable in Fig. 11 in the data at $x/c = 0.90$. Similar observations have been reported by Evans (1973), Brendel and Mueller (1988), and Gostelow (1977).

The phase response of the boundary layer to the periodic flow is also shown in Fig. 13. The phase lead with a maximum of 12 deg occurring close to the wall at $x/c = 0.57$ is in agreement with observations by Karlson (1960). Again, this type of behavior is associated with the aforementioned effect that the low-momentum fluid responds to the externally imposed temporal pressure gradient with a greater velocity change than the free stream. Farther downstream, however, there is a phase lag when getting closer to the wall. This might be due to the distortion of the wake (Fig. 11), which also can be seen from the data of Hodson (1985) (compare Figs. 6 and 7 of this reference). A phase lag in a turbulent boundary layer was recently observed by Brendel and Mueller (1988), too.

The boundary layer profile in the separated region ($x/c = 0.74$, 13 percent span) is shown in Fig. 14. The data inside the separated region and with backflow events should be viewed as qualitative for reasons discussed earlier. The behavior here is quite different from that observed in the nonseparated region (Figs. 12 and 13). The velocity fluctuation near the wall is negligible and the maximum fluctuations occur just outside the region with backflow ($y = 7$ mm to $y = 12$ mm). Here, the increased amplitude is caused by the oscillation of the separated region. The phase angle change across the separated

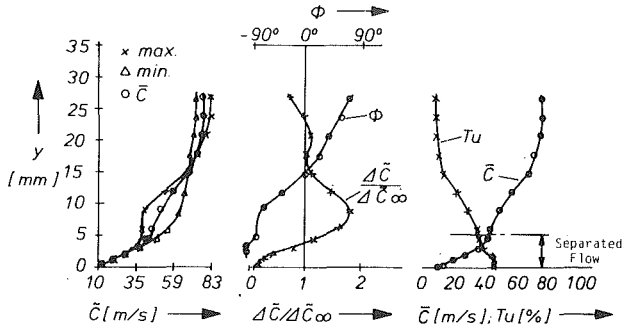

Fig. 14 Results of the passage survey at x/c = 0.74, 13 percent span

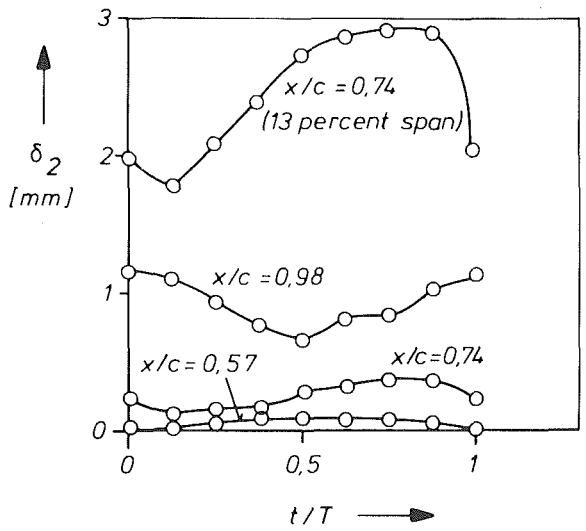

Fig. 15 PLA momentum thickness distribution at midspan and at 13 percent span (only at x/c = 0.74)

layer (about 20 mm thick) is nearly 180 deg. This indicates the complex response of the separated flow to the free-stream unsteadiness. Part or most of the phase shift may come from the difference in convection velocity in this layer, which is much smaller near the wall (ca. 10 m/s) compared to nearly 80 m/s at y = 25 mm. Within the backflow region, the phase angle and turbulence intensities are nearly constant, but these data may not be reliable. Here, the velocity fluctuation is caused mainly by the movement of the separation line. As indicated earlier, the pressure disturbance in this region (Fig. 2) is small, indicating little or no influence of the free-stream unsteadiness.

Unsteady Momentum Thickness Distribution. The instantaneous momentum thickness δ_2 is plotted in Fig. 15. The boundary layer momentum thickness varies considerably in most locations. Furthermore there is a phase lag between the instantaneous boundary layer momentum thickness at various chordwise locations. This is brought out mainly by the convection velocity of the disturbance. There is a close correlation between δ_2 at x/c = 0.98, midradius, and ΔC_L shown in Fig. 3. The minimum vlues of δ_2 and ΔC_L and the maximum values of δ_2 and ΔC_L occur at nearly the same instant of time. It is clear that even a small wake disturbance can cause large variation in momentum thickness, blade blockage, and profile losses.

The boundary layer data inside the separated zone should be viewed with caution due to reasons given earlier. Nevertheless, a plot of the instantaneous momentum thickness at 13 percent span provides qualitative information on the size of the separation bubble. The instantaneous momentum thickness at x/c = 0.74, both at midspan and at 13 percent span, are nearly in phase even though the amplitudes of the fluctuations are much higher at 13 percent span. This is clear from Fig. 15.

Conclusions

The influence of rotor-stator interaction on the development of the blade boundary layer and separated regions, the flow field in the passage, and the blade pressure distribution in an annular compressor cascade have been evaluated.

The incidence change caused by the velocity defect in the wake has a major impact on the unsteady pressure distribution along the blade. At the instant of time when the leading edge of the blade is near the wake centerline, a peak in suction pressure occurs on the suction side and a pressure maximum occurs on the pressure side, resulting in a peak in lift coefficient.

The pressure fluctuation has maxima at the blade leading edge and decays rapidly toward the trailing edge. The wake does not penetrate regions of separated flow and, hence, has only a minor influence on the static pressure there. A local maximum in pressure fluctuation occurs along the separation line caused by viscous interaction and the movement of the separated region.

The separated flow has an upstream influence on the pressure and the flow field, which may respond differently with regard to the phase as well as the amplitude. The phase angle and the amplitude of the pressure fluctuation are mainly influenced by the blade pressure distribution, which responds to a change in incidence caused by the upstream wake.

In the free stream, the rotor wake is convected with the free-stream velocity, and a large phase shift with regard to the pressure fluctuation was observed. The velocity fluctuation in the free stream is nearly conserved and its decay can be attributed mostly to turbulent diffusion.

Inside the boundary layer, the wake velocity defect is amplified by the large deceleration near the blade surface. Considerable variation in the convection velocity along the blade chord and the boundary layer growth result in a distorted wake trajectory and phase shift with respect to the wake in the free stream.

The blade boundary layer responds to the imposed velocity fluctuation by a relative breathing of its velocity profiles and its momentum thickness. The amplitude of local velocity fluctuation is maximum inside the boundary layer and reaches values of up to three times the amplitude in the free stream.

Inside the separated flow regions and close to the laminar sublayer, the rotor wake is damped and, hence, only small-velocity fluctuations were observed there.

Acknowledgments

The work reported herein was supported within the framework of research programs of the "Deutsche Forschungsgemeinschaft." Permission for publication is gratefully acknowledged. The authors are also indebted to R. Hagenguth and J. Peters for their assistance in carrying out these investigations. B. Lakshminarayana was the recipient of a Senior Professor Fulbright Award and partial support from the U.S. National Science Foundation during his stay at the institute.

References

Adachi, T., and Murakami, Y., 1979, "Three-Dimensional Velocity Distribution Between Stator Blades and Unsteady Force on a Blade Due to Passing Wakes," *Bulletin of the JSME*, Vol. 22, No. 170.

Brendel, M., and Mueller, T. J., 1988, "Boundary Layer Measurements on an Airfoil at a Low Reynolds Number in an Oscillating Free Stream," *AIAA Journal*, Mar., pp. 257-263.

Bruce, E. P., and Henderson, R. E., 1975, "Unsteady Pressures on Rotor Blade Row," AGARD CP 177.

Capece, V. R., and Fleeter, S., 1989, "Experimental Investigation of Multistage Interaction Gust Aerodynamics," ASME JOURNAL OF TURBOMACHINERY, Vol. 111, pp 409–417.

Carta, F. O., 1983, "Unsteady Aerodynamics and Gapwise Periodicity of Oscillating Cascaded Airfoils," ASME *Journal of Engineering for Power*, Vol. 105, No. 3, pp. 565–574.

Dring, R. P., Joslyn, H. D., Hardin, L. W., and Wagner, J. H., 1982, "Turbine Rotor-Stator Interaction," ASME *Journal of Engineering for Power*, Vol. 104, pp. 729–742.

Evans, R. L., 1977, "Boundary Layer Development on Axial-Flow Compressor Stator Blade," ASME Report No. 77-GT-11.

Foerster, W., and Mach, K., 1985, "Unsteady Flow in Turbine Rotor," *VDI Berichte*, 572.2, pp. 273–292.

Gallus, H. E., 1987, "Unsteady Aerodynamic Measurements on Rotors," AGARD-AG-298, Vol. 1.

Gallus, H. E., Grollius, H., and Lambertz, J., 1982, "The Influence of Blade Number Ratio and Blade Row Spacing on Axial-Flow Compressor Stator Blade Dynamic Load and Stage Sound Pressure Level," ASME *Journal of Engineering for Power*, Vol. 104, No. 3, pp. 633–641.

Gostelow, J. P., 1977, "A New Approach to the Experimental Study of Turbomachinery Flow Phenomena," ASME *Journal of Engineering for Power*, Vol. 99, pp. 97–105.

Greitzer, E. M., 1985, "An Introduction to Unsteady Flow in Turbomachines: In Thermodynamics and Fluid Mechanics of Turbomachinery," *Proceedings of a NATO Advanced Study Institute*, Martinus Nijhoss.

Hill, P. G., Schwab, U. W., and Senoo, Y., 1963, "Turbulent Wakes in Pressure Gradients," ASME *Journal of Applied Mechanics*, Vol.30, p. 518.

Hodson, H. P., 1983, "The Development of Unsteady Boundary Layers on the Rotor of an Axial-Flow Turbine," AGARD CP-351, Copenhagen.

Hodson, H. P., 1985, "Measurements of Wake-Generated Unsteadiness in the Rotor Passage of Axial-Flow Turbines," ASME *Journal of Engineering for Gas Turbines and Power*, Vol. 107, pp. 467–475.

Hodson, H. P., and Addison, J. S., 1989, "Wake-Boundary Layer Interactions in an Axial-Flow Turbine Rotor at Off-Design Conditions," ASME JOURNAL OF TURBOMACHINERY, Vol. 111, pp 181–192.

Karlson, S. K. F., 1960, "An Unsteady Turbulent Boundary Layer," *Journal of Fluid Mechanics*, Vol. 5, pp. 622–636.

Lakshminarayana, B., and Poncet, A., 1974, "A Method of Measuring Three-Dimensional Rotating Wakes Behind Turbomachinery Rotors," ASME *Journal of Fluids Engineering*, Vol. 96, pp. 87–91.

Lighthill, M. J., 1954, "The Response of Laminar Skin Friction and Heat Transfer to Fluctuation in Stream Velocity," *Proceedings Royal Society*, A, p. 224.

Murakami, Y., Hirose, T., Adachi, T., and Hiroshi, K., 1981, "Unsteady Force in a Cambered Blade Passing Through an Oblique Wake," *Bulletin of the JSME*, Vol. 24, No. 195.

Poensgen, C. A., 1988, Private Communication.

Schulz, H. D., and Gallus, H. E., 1988, "Experimental Investigation of the Three-Dimensional Flow Field in an Annular Compressor Cascade," ASME JOURNAL OF TURBOMACHINERY, Vol. 110, pp. 467–478.

Schulz, H. D., Gallus, H.E., and Lakshminarayana, B., 1990, "Three-Dimensional Separated Flow Field in the Endwall Region of an Annular Compressor Cascade in the Presence of Rotor-Stator Interaction: Part 1—Quasi-Steady Flow Field and Comparison With Steady-State Date," ASME JOURNAL OF TURBOMACHINERY, Vol. 112, this issue.

Zandbergen, T., 1988, "Stator Vane Response Due to the Impingement of the Wake of an Unloaded Rotor," AIAA Paper No. 88/2814, presented at the Joint Propulsion Conference, Boston, MA.

Capece, V. R., and Fleeter, S., 1989, "Experimental Investigation of Multistage Interaction Gust Aerodynamics," ASME JOURNAL OF TURBOMACHINERY, Vol. 111, pp 409-417.

Carta, F. O., 1983, "Unsteady Aerodynamics and Gapwise Periodicity of Oscillating Cascaded Airfoils," ASME *Journal of Engineering for Power*, Vol. 105, No. 3, pp. 565-574.

Dring, R. P., Joslyn, H. D., Hardin, L. W., and Wagner, J. H., 1982, "Turbine Rotor-Stator Interaction," ASME *Journal of Engineering for Power*, Vol. 104, pp. 729-742.

Evans, R. L., 1977, "Boundary Layer Development on Axial-Flow Compressor Stator Blade," ASME Report No. 77-GT-11.

Foerster, W., and Mach, K., 1985, "Unsteady Flow in Turbine Rotor," *VDI Berichte*, 572.2, pp. 273-292.

Gallus, H. E., 1987, "Unsteady Aerodynamic Measurements on Rotors," AGARD-AG-298, Vol. 1.

Gallus, H. E., Grollius, H., and Lambertz, J., 1982, "The Influence of Blade Number Ratio and Blade Row Spacing on Axial-Flow Compressor Stator Blade Dynamic Load and Stage Sound Pressure Level," ASME *Journal of Engineering for Power*, Vol. 104, No. 3, pp. 633-641.

Gostelow, J. P., 1977, "A New Approach to the Experimental Study of Turbomachinery Flow Phenomena," ASME *Journal of Engineering for Power*, Vol. 99, pp. 97-105.

Greitzer, E. M., 1985, "An Introduction to Unsteady Flow in Turbomachines: In Thermodynamics and Fluid Mechanics of Turbomachinery," *Proceedings of a NATO Advanced Study Institute*, Martinus Nijhoss.

Hill, P. G., Schwab, U. W., and Senoo, Y., 1963, "Turbulent Wakes in Pressure Gradients," ASME *Journal of Applied Mechanics*, Vol.30, p. 518.

Hodson, H. P., 1983, "The Development of Unsteady Boundary Layers on the Rotor of an Axial-Flow Turbine," AGARD CP-351, Copenhagen.

Hodson, H. P., 1985, "Measurements of Wake-Generated Unsteadiness in the Rotor Passage of Axial-Flow Turbines," ASME *Journal of Engineering for Gas Turbines and Power*, Vol. 107, pp. 467-475.

Hodson, H. P., and Addison, J. S., 1989, "Wake-Boundary Layer Interactions in an Axial-Flow Turbine Rotor at Off-Design Conditions," ASME JOURNAL OF TURBOMACHINERY, Vol. 111, pp 181-192.

Karlson, S. K. F., 1960, "An Unsteady Turbulent Boundary Layer," *Journal of Fluid Mechanics*, Vol. 5, pp. 622-636.

Lakshminarayana, B., and Poncet, A., 1974, "A Method of Measuring Three-Dimensional Rotating Wakes Behind Turbomachinery Rotors," ASME *Journal of Fluids Engineering*, Vol. 96, pp. 87-91.

Lighthill, M. J., 1954, "The Response of Laminar Skin Friction and Heat Transfer to Fluctuation in Stream Velocity," *Proceedings Royal Society*, A, p. 224.

Murakami, Y., Hirose, T., Adachi, T., and Hiroshi, K., 1981, "Unsteady Force in a Cambered Blade Passing Through an Oblique Wake," *Bulletin of the JSME*, Vol. 24, No. 195.

Poensgen, C. A., 1988, Private Communication.

Schulz, H. D., and Gallus, H. E., 1988, "Experimental Investigation of the Three-Dimensional Flow Field in an Annular Compressor Cascade," ASME JOURNAL OF TURBOMACHINERY, Vol. 110, pp. 467-478.

Schulz, H. D., Gallus, H.E., and Lakshminarayana, B., 1990, "Three-Dimensional Separated Flow Field in the Endwall Region of an Annular Compressor Cascade in the Presence of Rotor-Stator Interaction: Part 1—Quasi-Steady Flow Field and Comparison With Steady-State Date," ASME JOURNAL OF TURBOMACHINERY, Vol. 112, this issue.

Zandbergen, T., 1988, "Stator Vane Response Due to the Impingement of the Wake of an Unloaded Rotor," AIAA Paper No. 88/2814, presented at the Joint Propulsion Conference, Boston, MA.

DISCUSSION

N.A. Cumpsty[1] and Y. Dong[2]

The authors have presented a body of interesting measurements in a complicated flow fairly representative of an axial compressor. We would like to offer some comments based on our observations in a much simpler two-dimensional cascade with incident wakes.

Our experience showed that the *start* of transition was farther upstream with wakes present (or with high free-stream turbulence) but the *completion* of transition occurred further downstream. This has also been found on flat plate boundary layers, as reported by Pfeil et al. (1983). When laminar separation bubbles are present the flow is particularly complicated, with the separation disappearing when the flow is turbulent upstream of the separation point and reappearing when the flow reverts to laminar. The turbulent spot initiated by the wake is followed by a calmed region, and this calmed region is the cause of the completion of transition being delayed to further downstream when wakes are present. Conversely, at times between the wakes the undisturbed laminar boundary layer near the front of the blade may be caused to separate by the adverse pressure gradient. When separation occurs the shear layer becomes highly unstable and transition is rapidly completed.

We suspect that similar effects were taking place in the blade row tested by the authors, at least in the regions away from the effect of the endwalls. We also suspect that the flow was not fully turbulent from near the leading edge, as inferred from Fig. 16 of Part 1, but instead only intermittently turbulent. The clarification of this requires measurements very near to the surface (inside what would be the laminar sublayer of the turbulent boundary layer) with temporal resolution sufficient to show the various regimes that can occur over the period of one rod passing. If the flow were genuinely turbulent from near the leading edge it would be surprising if the momentum thickness growth were not substantially higher over the whole chord in the case with the rotor: Fig. 17 of Part 1 does not show this to be the case.

The interpretation of separation regions on the basis of time-mean measurements or oil flow visualization also needs to be very careful because these can convey the impression of fully attached flow in cases when it is only attached for part of the time. Schulz et al. are clearly aware of this, but may not have been aware of the curious unsteady behavior of transition and separation, which we found on the blade we tested.

The authors found that with the rods there was a turbulent separation toward the trailing edge near midspan in the case for $\alpha_2 = 49.2$ deg. They attribute this to the thicker turbulent boundary layer formed when the transition takes place sooner because of the rods. This seems implausible and the data of Fig. 17 of Part 1 do not bear it out. Instead we think that it is because of the larger static pressure recovery with the rods and, therefore, the greater deceleration to which the midspan boundary layer is exposed. For boundary layers near to separation, where the skin friction is small and the form parameter H is changing slowly, the momentum thickness δ_2 can be related to the free-stream velocity by

$$\frac{\delta_2}{\delta_{20}} \approx \left(\frac{U_0}{U}\right)^{(2+H)}$$

Using this with the free-stream pressures given for $\alpha_2 = 44.2$ deg (these pressures not being given for 49.2 deg, the angle used for the boundary layer measurements) would lead to an increase in momentum thickness at the trailing edge of about 10 percent. This should be compared with a difference of 20 percent shown in Fig. 17 of Part 1. The difference of about 10 percent attributable to the rotor wakes is near to the increase in trailing edge momentum thickness of 7 percent that we found when the wakes were present.

Could the authors explain what appears to be an inconsistency in the paragraphs surrounding Fig. 17 of Part 1? The transition with no rotor is first said to occur at 30 percent chord: 9 lines down the hump in the momentum thickness distribution is attributed to the separation bubble but this hump *begins* at about 40 percent chord. Would one not expect the transition in the no-rotor case to occur in the separated shear layer of the bubble?

Finally, a comment about the experiment. The rotor of rods is used to simulate an upstream blade row. The rods will generate a momentum deficit θ, which can be related to the drag coefficient of the rod, and at the Reynolds numbers used the drag coefficient will be about 1.0. The wake momentum thickness of a typical blade near its optimum incidence is between about 1 and 3 percent of the chord length (see, for example, Koch and Smith, 1976). It follows that the diameter of the rod should be between 2 and 6 percent of the blade chord it is intended to simulate. If the rotor chord is to be comparable

[1]Whittle Laboratory, University Engineering Department, Cambridge CB3 ODY England.

[2]New Products Division, Ruston Gas Turbines, Lincoln LN6 7AA England.

to the stator, in the present case 62.6 mm, this suggests a rod of *not more* than about 4 mm diameter would be appropriate. In fact the rod used was about 5.3 mm in diameter and so the effect of the rod wakes on the downstream blade row can be expected to be substantially more severe than those of an upstream blade. Would the authors care to comment on this?

References

Koch, C. C., and Smith, L. H., 1976, ASME *Journal of Engineering for Power*, Vol. 98, pp. 411–424.

Pfeil, H., Herbst, R., and Schröder, T., 1983, ASME *Journal of Engineering for Power*, Vol. 105, pp. 130–137.

R. L. Evans[3]

The authors are to be congratulated on a very thorough presentation of data concerned with the effects of rotor-stator interaction on flow in the endwall region and on blade boundary layers. There are only very limited experimental data available on the unsteady effects of rotor-stator interaction, and the authors have made an important contribution to our understanding of these complex flow phenomena in turbomachinery.

Recent calculations of unsteady boundary layer development may provide some further insight into the reported phase response of the blade boundary layers. In Fig. 13, there is seen to be a small phase lead in the boundary layer near midchord, while farther downstream a phase lag is shown. The authors indicate that the experiments of Karlsson would lead to the expectation of a phase lead, and suggest that one possible reason for the phase lag may be distortion of the wake. Karlsson's experiments, however, subjected the boundary layer to a standing-wave type of free-stream disturbance, which causes the boundary layer to respond quite differently from one subjected to a traveling-wave type of disturbance, such as occurs in turbomachinery.

Figures 1 and 2 of the Discussion show the results of unsteady laminar boundary layer calculations reported by Evans (1989) for both standing wave and traveling wave free-stream conditions. It can be seen that the calculations compare favorably with the theory of Lighthill (1954) for the standing wave case, which results in a phase lead in the boundary layer, and with the experiments of Patel (1975) for the traveling wave case, which results in a phase lag. Similar results were obtained for turbulent boundary layers, showing an increase in phase lag with increasing reduced frequency for the case of a traveling wave free-stream disturbance.

The experiments reported by Evans and Yip (1988) provide further confirmation of the phase lag to be expected from a traveling-wave type of disturbance resulting from rotor-stator interaction. Figure 3 of the Discussion shows the results of phase lag measurements made in a turbulent boundary layer developing on a flat plate in a wind tunnel downstream of a moving rotor row. The phase lag is seen to increase with distance from the leading edge, or with increasing reduced frequency, as predicted by the calculation results. The phase lag over the latter half of the blade, as reported by the authors, therefore appears to be consistent with other experimental data and with the results of calculations.

References

Evans, R. L., 1989, "Calculation of Unsteady Boundary Layer Development on Axial-Flow Turbomachinery Blading," *Proceedings of the 9th International Symposium on Air Breathing Engines*, Athens, Greece, Sept., pp. 837–846.

Evans, R. L., and Yip, R. S. K., 1988, "An Experimental Investigation of Unsteady Wake-Boundary Layer Interaction," *Journal of Fluids and Structures*, Vol. 2, pp. 313–322.

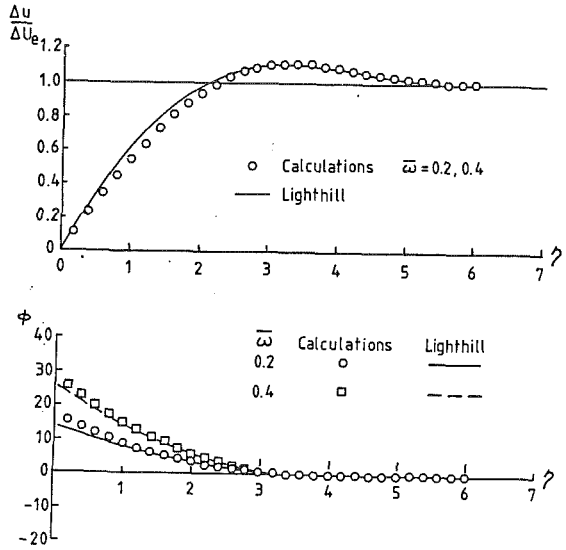

Fig. 1 Standing wave free-stream calculations compared to theory of Lighthill (1954)

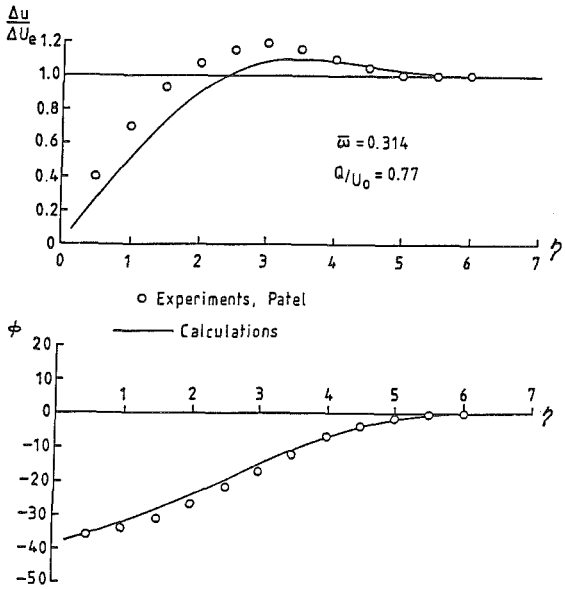

Fig. 2 Traveling wave free-stream calculations compared to experiments of Patel (1975)

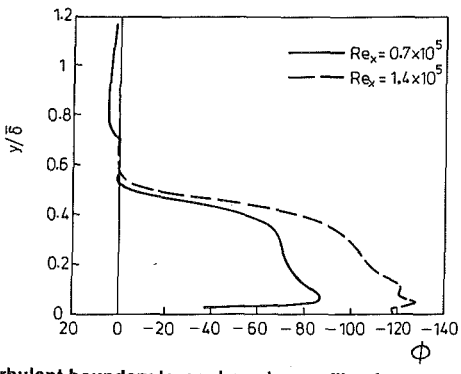

Fig. 3 Turbulent boundary layer phase lag profiles from Evans and Yip (1988)

Lighthill, M. J., 1954, "The Response of Laminar Skin Friction and Heat Transfer to Fluctuations in the Stream Velocity," *Proceedings of the Royal Society of London*, A, Vol. 224, June, pp. 1–23.

Patel, M. H., 1975, "On Laminar Boundary Layers in Oscillatory Flow," *Proceedings of the Royal Society of London*, A, Vol. 347, pp. 99–123.

[3]Department of Mechanical Engineering, The University of British Columbia, Vancouver, B.C., V6T IW5, Canada.

to the stator, in the present case 62.6 mm, this suggests a rod of *not more* than about 4 mm diameter would be appropriate. In fact the rod used was about 5.3 mm in diameter and so the effect of the rod wakes on the downstream blade row can be expected to be substantially more severe than those of an upstream blade. Would the authors care to comment on this?

References

Koch, C. C., and Smith, L. H., 1976, ASME *Journal of Engineering for Power*, Vol. 98, pp. 411–424.

Pfeil, H., Herbst, R., and Schröder, T., 1983, ASME *Journal of Engineering for Power*, Vol. 105, pp. 130–137.

R. L. Evans[3]

The authors are to be congratulated on a very thorough presentation of data concerned with the effects of rotor-stator interaction on flow in the endwall region and on blade boundary layers. There are only very limited experimental data available on the unsteady effects of rotor-stator interaction, and the authors have made an important contribution to our understanding of these complex flow phenomena in turbomachinery.

Recent calculations of unsteady boundary layer development may provide some further insight into the reported phase response of the blade boundary layers. In Fig. 13, there is seen to be a small phase lead in the boundary layer near midchord, while farther downstream a phase lag is shown. The authors indicate that the experiments of Karlsson would lead to the expectation of a phase lead, and suggest that one possible reason for the phase lag may be distortion of the wake. Karlsson's experiments, however, subjected the boundary layer to a standing-wave type of free-stream disturbance, which causes the boundary layer to respond quite differently from one subjected to a traveling-wave type of disturbance, such as occurs in turbomachinery.

Figures 1 and 2 of the Discussion show the results of unsteady laminar boundary layer calculations reported by Evans (1989) for both standing wave and traveling wave free-stream conditions. It can be seen that the calculations compare favorably with the theory of Lighthill (1954) for the standing wave case, which results in a phase lead in the boundary layer, and with the experiments of Patel (1975) for the traveling wave case, which results in a phase lag. Similar results were obtained for turbulent boundary layers, showing an increase in phase lag with increasing reduced frequency for the case of a traveling wave free-stream disturbance.

The experiments reported by Evans and Yip (1988) provide further confirmation of the phase lag to be expected from a traveling-wave type of disturbance resulting from rotor-stator interaction. Figure 3 of the Discussion shows the results of phase lag measurements made in a turbulent boundary layer developing on a flat plate in a wind tunnel downstream of a moving rotor row. The phase lag is seen to increase with distance from the leading edge, or with increasing reduced frequency, as predicted by the calculation results. The phase lag over the latter half of the blade, as reported by the authors, therefore appears to be consistent with other experimental data and with the results of calculations.

References

Evans, R. L., 1989, "Calculation of Unsteady Boundary Layer Development on Axial-Flow Turbomachinery Blading," *Proceedings of the 9th International Symposium on Air Breathing Engines*, Athens, Greece, Sept., pp. 837–846.

Evans, R. L., and Yip, R. S. K., 1988, "An Experimental Investigation of Unsteady Wake-Boundary Layer Interaction," *Journal of Fluids and Structures*, Vol. 2, pp. 313–322.

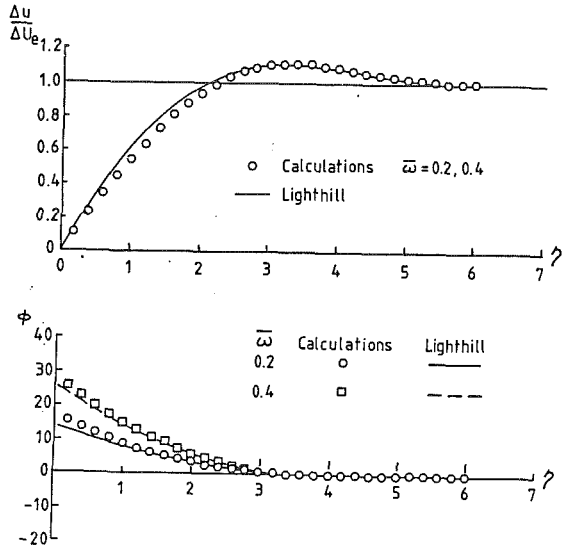

Fig. 1 Standing wave free-stream calculations compared to theory of Lighthill (1954)

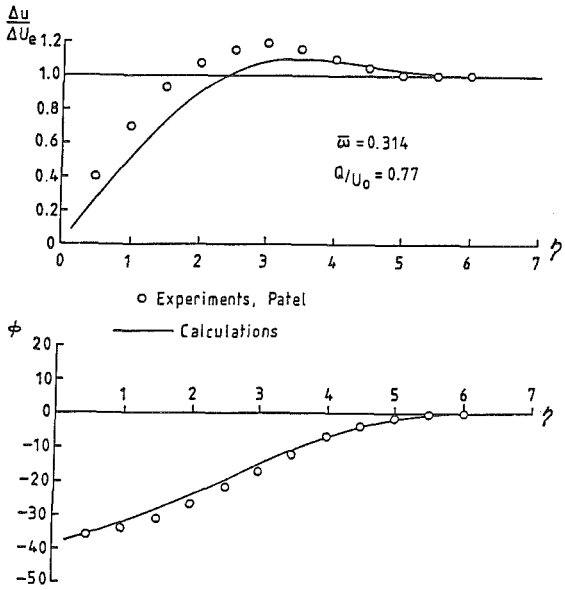

Fig. 2 Traveling wave free-stream calculations compared to experiments of Patel (1975)

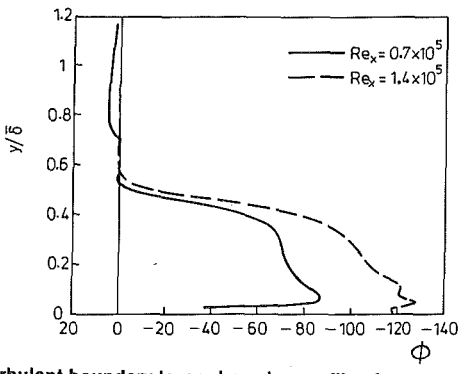

Fig. 3 Turbulent boundary layer phase lag profiles from Evans and Yip (1988)

Lighthill, M. J., 1954, "The Response of Laminar Skin Friction and Heat Transfer to Fluctuations in the Stream Velocity," *Proceedings of the Royal Society of London*, A, Vol. 224, June, pp. 1–23.

Patel, M. H., 1975, "On Laminar Boundary Layers in Oscillatory Flow," *Proceedings of the Royal Society of London*, A, Vol. 347, pp. 99–123.

[3]Department of Mechanical Engineering, The University of British Columbia, Vancouver, B.C., V6T IW5, Canada.

Authors' Closure

The authors would like to thank Dr. Cumpsty and Dr. Dong, as well as Dr. Evans, for the comments they have made and the questions they have raised.

The authors share the opinion of Dr. Cumpsty and Dr. Dong regarding the *transient behavior of the profile boundary layer*. Hot-film measurements along the profile surface, taken after these papers were submitted, revealed that while the onset of transition moved upstream the completion of transition on the suction side took place farther downstream, resulting in a transitional boundary layer over a large part of the blade surface. This has already been mentioned at the presentation of the paper and is discussed in great detail in the most recent paper by Schulz and Gallus (1990).

Indeed, to relate the increase in *momentum thickness at the trailing edge* in the case with rotor purely to the earlier onset of transition is some kind of oversimplification. The difference in the boundary layer growth can be attributed to several causes as there are:

- Increase in channel diffusion, because of the reduced corner stall regions;
- Increase in the free-stream turbulence level;
- Earlier boundary layer transition;
- Slightly earlier trailing edge separation with rotor (compare Fig. 7, Part 1).

Hence, this phenomenon is very complex, but the authors believe that all the aforementioned will account for the 20 percent increase in momentum thickness compared to 10 percent (7 percent) in a two-dimensional case.

There indeed is an inconsistency in the location of the transition as referred to in the paper and the hump in the *momentum thickness distribution*, and the authors are glad that Dr. Cumpsty and Dr. Dong have pointed that out. Transition occurs within the laminar separation bubble, which at this point of operation starts at 30 percent and continues to about 50 percent. This is hard to see on the oil flow (Fig. 7), but is has also been confirmed by the latest hot-film measurements (Schulz and Gallus, 1989). Anyway, the hot-wire measurements in this flow region are very difficult, since the boundary layer is very thin and backflow events are present. Since there is only one data point indicating the hump, one might want to be more careful with its interpretation.

Concerning the *rod diameter*: the Koch and Smith data are for a two-dimensional cascade. Moreover, the rotor-stator interaction depends strongly on *wake defect* and *wake width*, both of which are local properties. The wake profile, width, and defect measured by the authors (Fig. 4, Part 1) are close to the rotor wake data reported by Ravindranath and Lakshminarayana (1979, compare Fig. 14*a* of this reference). Thus the authors feel that the wake data generated are typical of those that exist in actual compressors, where profile wakes are growing with increasing incidence even more. Taking this into account, the chosen rod diameter of 5.3 mm was felt to be appropriate.

In an ongoing investigation, the flow field and the decay of the wakes downstream of the cylinder rotor have been studied (Poensgen and Gallus, 1990). It is planned to compare these results with measurements taken downstream of a rotor incorporating blades, to validate the previous arguments.

Since, at this state, the authors know more about the transient behavior of the profile boundary layer, they believe that the *observed phase lead* is related to its complex transitional state, and they are glad that Dr. Evans has commented on that. Over the latter half of the blade though, the boundary layer is fully turbulent, and thus the here observed lag can be explained numerically as shown by Dr. Evans.

References

Poensgen, C., and Gallus, H. E., 1990, "Three-Dimensional Wake Decay Inside of a Compressor Cascade and Its Influence on the Downstream Unsteady Flow Field—Part I: Wake Decay Characteristics in the Flow Passage," ASME Paper No. 90-GT-xx.

Ravindranath, A., and Lakshminarayana, B., 1979, "Mean Velocity and Decay Characteristics of the Near and Far-Wake of a Compressor Rotor Blade of Moderate Loading," ASME Paper No. 79-GT-202.

Schulz, H. D., and Gallus, H. E., 1989, "Experimental Investigation of the Influence of Rotor Wakes on the Development of the Profile Boundary Layer and the Performance of an Annular Compressor Cascade," AGARD CPP-468/469, Conference on Unsteady Aerodynamic Phenomena in Turbomachines, Luxemburg.

Modeling Unsteady Transition and Its Effects on Profile Loss

H. P. Hodson
Whittle Laboratory,
Cambridge University,
Cambridge CB3 0DY, United Kingdom

This paper considers the effects of wake interactions on the transition processes of turbomachine blade boundary layers. A simple model of unsteady transition is proposed, which is then used to identify a relationship between a new reduced frequency parameter and the profile loss of a blade row that is subjected to unsteady inflow. The value of this new parameter is also used to identify the nature of the boundary layer development on the blade surfaces. The influence of other parameters on the transition process is also discussed. The model is then extended to deal with the more general case. The validity of the models is demonstrated by a comparison with a correlation of the effects of wake-generated unsteadiness on profile loss that was originally proposed by Speidel. The effects of unsteady inflow on four idealized turbine blades are considered.

Introduction

It is known that in axial-flow turbomachines the efficiency of the midspan blade sections can be significantly different from that of equivalent cascades, which operate with steady inflow (e.g., Lopatitskii et al., 1970). It is only recently, however, that the details of the unsteady flow have received much attention.

The relative motion of adjacent blade rows in axial turbomachines gives rise to a variety of unsteady interactions. The potential influence of a blade extends both upstream and downstream. Wakes convect only downstream of the blades and their rate of decay is much less than that of the potential influence (Dring et al., 1982). In low aspect ratio machines, the secondary flow vortices also cause unsteadiness in succeeding blade rows (Binder, 1985). In transonic turbines, further interactions arise as the direct result of the impingement of the trailing shock waves on the downstream blade row (e.g., Doorly and Oldfield, 1985). Despite the increased awareness of the importance of unsteady flows very few publications (e.g., Speidel, 1957; Hodson, 1983; Tanaka, 1984; Hodson and Addison, 1989; Binder et al., 1989; Sharma et al., 1988) have concerned themselves with the effect of unsteady flows on the overall performance of axial machines.

Wake interactions are present in all turbomachine stages. The present paper is specifically concerned with wake interactions and their effect on profile loss. A simple model of unsteady transition is presented. This is used to explain the effects of periodic unsteadiness on the profile loss of turbomachine blade rows and to highlight the most important aspects. The model is then extended to deal with the more general case. Comparisons are made between results obtained using the model and available experimental data.

Previous Research Into Unsteady Boundary Layer Development

The majority of research concerned with the impact of wake interactions on blade surface boundary layers (e.g., Walker, 1974; Hodson, 1984; Doorly, 1988; Dong, 1988) has concluded that the most significant effect of the interaction is the periodic forcing of transition of the boundary layers. It is this forcing that is responsible for the changes in profile loss.

Distance–time diagrams are often used to illustrate how the state of a boundary layer varies with time over the blade surface. Figure 1 is a distance–time diagram based on those presented by Pfeil et al. (1983), Doorly and Oldfield (1985), LaGraff et al. (1989), Hodson and Addison (1989), Dong (1988), Addison and Hodson (1990a), and Addison and Dong (1989), who investigated the effects of wakes on the transition process. The abscissa is the nondimensional surface distance (s/s_{max}) while the ordinate is the nondimensional time ($t^* = t/T$) where T represents the wake passing period. In such

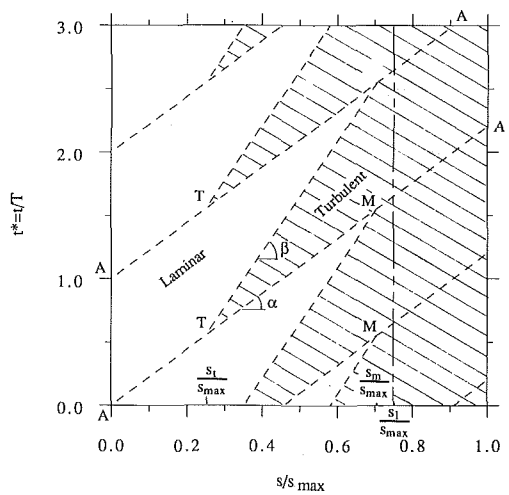

Fig. 1 Schematic distance–time diagram of boundary layer states showing end of forced transition before natural transition (assuming constant free-stream velocity)

Contributed by the International Gas Turbine Institute and presented at the AGARD PEP74a Meeting, Luxembourg, September 1989. Manuscript received at ASME Headquarters December 1989.

diagrams, a line parallel to the distance axis represents instantaneous propagation, while a line parallel to the time axis indicates a stationary phenomenon. The hatched area represents the turbulent flow.

In Fig. 1 the first occurrence of periodic transition from laminar to turbulent flow, which marks the creation of the turbulent patches, begins not at the leading edge but at a short distance beyond the point at which the response of the boundary layer to large disturbances in the free stream first becomes unstable (Addison and Hodson, 1990a, 1990b). Currently available data suggest that transition does not begin until the momentum thickness-based Reynolds number Re_θ exceeds a value of approximately 163, which is consistent with the known behavior of laminar boundary layers undergoing natural transition (e.g., Abu-Ghannan and Shaw, 1980). Having formed, the turbulent patch begins to grow as it convects along the blade surface. As a consequence, the front of the turbulent patch propagates at a velocity of similar magnitude to that of the free stream while the rear propagates at a speed much less than that of the leading edge but still in the downstream direction. Eventually, the leading edge of one patch catches up with and then merges with the trailing edge of the preceding patch thus forming a turbulent boundary layer. In several respects, these turbulent patches are equivalent to the individual turbulent spots that form during natural transition.

Table 1 lists the available data concerning propagation rates. The first six cases are concerned with the formation of individual turbulent spots. The table shows that in the majority of cases, the trailing edge of a turbulent patch or individual spot propagates at approximately half the free-stream velocity and that the quoted values vary very little. In contrast, the propagation rates of the leading edge differ considerably.

In the cascade simulations and turbomachine tests listed in Table 1, the leading edge propagation rate usually *appears* to be equal to or greater than that of the free stream. Addison and Hodson (1990a) explain that this is because although transition is most likely to occur near the centerline of the wake, where the turbulence is greatest, the undisturbed (i.e., laminar) part of the boundary layer continuous to develop so that it becomes capable of undergoing transition at the lower levels of free-stream turbulence, which are to be found away from the centerline of the wakes. Simultaneously, the wake itself travels at a speed approximately equal to that of the free stream and therefore at a faster rate than the leading edge of a conventional spot (e.g., Schubauer and Klebanoff, 1955). Thus, further spots can form ahead of the zone of influence of the single initial spot. Because the formation of spots is a stochastic process and the transition data are usually ensemble averaged, the above effects combine to produce an *apparent* propagation rate of the leading edges that is at least equal to the free-stream velocity. Though not necessarily a true propagation rate, the term will continue to be used for convenience. The extent to which this apparent propagation rate can exceed the free-stream velocity is dependent on the wake characteristics and Reynolds number (Addison and Hodson, 1990b). It is also more appropriate to refer to these periodically intermittent regions as transitional rather than turbulent. In the case of the trailing edge of the transitional patches, the effects mentioned above tend to cancel so that the propagation rate indiated by the ensemble-averaged data corresponds more closely to that associated with the rear of a single spot.

In order to be able to predict the effect of unsteady inflow on the profile loss of compressor or turbine blade rows, it is necessary to make an estimate (in the absence of a model) of the time-dependent "intermittent" state of the blade surface boundary layers. Ideally, the formation and growth rates of the individual turbulent spots that make up the transitional patches should be employed. Unfortunately, published data are not in a form that allows an estimate of these parameters to be made. However, the state of the boundary layers is also

Table 1 Comparison of propagation rates for leading and trailing edges of turbulent patches in transitional boundary layers

Authors/Configuration/Reynolds number/ Cause of transition	V_{le}/V (apparent)	V_{te}/V (apparent)
Schubauer and Klebanoff, flat plate, spark	0.88	0.5
Wygnanski et al., flat plate, spark	0.89	0.5
Obremski and Fejer, flat plate, oscillating external flow	0.88	0.58
Houdeville et al., flat plate, oscillating external flow	0.89	0.48
Pfeil et al., flat plate accelerating flows, wakes	0.75–0.9	0.54
Hodson et al., single-stage turbine rotor, $Re = 3.5 \times 10^5$, individual turbulent spots	~1.0	~0.5
Doorly and Oldfield, turbine rotor cascade, wakes, $Re = 2 \times 10^6$, ensemble-averaged data	≥1.0	0.5
LaGraff et al., turbine rotor cascade, wakes, $Re = 9 \times 10^5$, ensemble-averaged data	~1.0	0.5
Addison and Hodson, single-stage turbine rotor, $Re = 3 \times 10^5$, ensemble-averaged data	−1.0	0.3
Dong, supercritical compressor cascade, $Re = 3 \times 10^5$, wakes, ensemble-averaged data	0.76	0.56
Addison and Dong, supercritical compressor cascade, $Re = 1.5 \times 10^5$, wakes, ensemble averaged data	>1.0	~0.5

Nomenclature

C_x = axial chord of current blade row
p = pitch of upstream blade row
r = mean radius
Re_θ = Reynolds number based on local momentum thickness and free-stream velocity
s = surface distance
T = wake passing period
t = time
t^* = dimensionless time $= t/T$
U_b = mean blade speed
V = free-stream velocity
Y = profile loss coefficient
α = angle of trajectory of leading edge of transition zone in s–t diagrams
β = angle of trajectory of trailing edge of transition zone in s–t diagrams
γ = time-averaged intermittency factor (0 = laminar, 1 = turbulent)
θ = boundary layer momentum thickness
ϕ = flow coefficient
ω = radian frequency $= 2\pi/T$
$\bar{\omega}$ = reduced frequency parameter

Subscripts

ft = fully turbulent (see text)
l = laminar, end of attached laminar flow
le = leading edge
m = end of unsteady transition zone
max = maximum value
t = turbulent; start of turbulent flow
te = trailing edge
tr = transition
x = axial

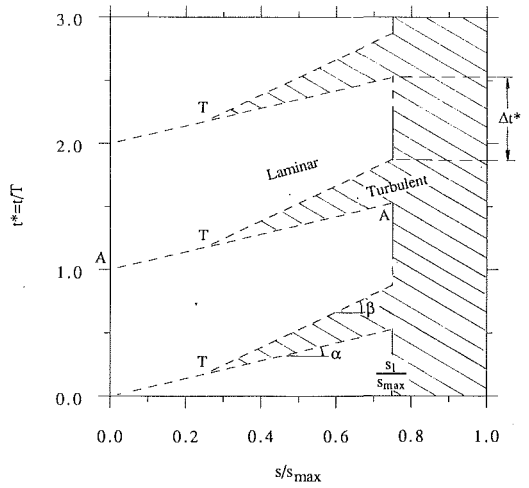

Fig. 2 Schematic distance-time diagram of boundary layer states showing combined forced and natural transition (assuming constant free-stream velocity)

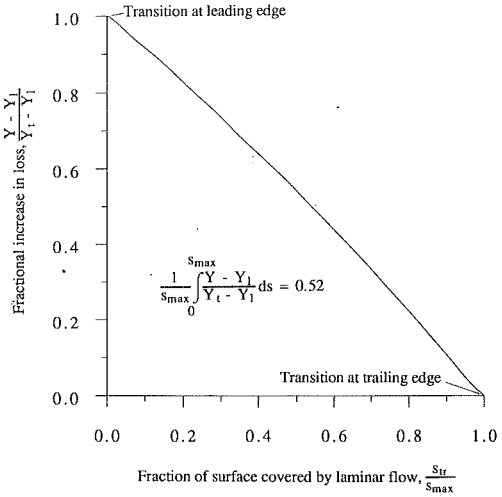

Fig. 3 Effect of transition location on profile loss of a flat plate with zero pressure gradient

related to the information presented in s–t diagrams and the analyses presented below rely on appropriate choices for the apparent leading and trailing edge propagation rates of the turbulent patches. Specifying these propagation rates is equivalent to specifying a certain combination of the average formation and growth rates of the individual turbulent spots.

A Simple Model of Unsteady Boundary Layer Transition and Development

The results of Speidel (1957) suggest that the profile loss of a blade row is dependent on a reduced frequency that defines the character of the wake-generated unsteady flow in relation to the development of the blade surface boundary layers. The simplest model of unsteady wake-induced boundary layer transition will be used to explain why this is so.

Figures 1 and 2 are idealized surface distance–time diagrams illustrating two possible modes of boundary layer transition. In the case of steady flow, natural transition or laminar separation takes place at a distance s_l from the leading edge. In the unsteady case, transition begins at a distance s_t from the leading edge where a turbulent and not a transitional patch begins to develop. The boundary layer state is assumed to be either laminar or turbulent. It is never intermediate between the two and transition occurs in a stepwise fashion. Thus, the hatched areas represent the turbulent flow. Figure 1 refers to the case where the turbulent (i.e., not transitional) patches generated by successive wakes merge at a surface location s_m (points M), which is upstream of the location of steady-state transition s_l. Figure 2 corresponds to the situation when only part of the wake passing cycle contains a moving transition "point." In either case, attached laminar flow may persist up to the trailing edge when operating with stationary inflow (i.e., $s_l = s_{max}$).

The transition process will be assumed to be quasi-steady. Justification for the quasi-steady assumption may be found in the discussion by Addison and Hodson (1990b). They argued that the most important time scales with regards to unsteady transition were those associated with the time it takes for the free-stream turbulence to diffuse into the boundary layer and the periodic time of the wake passing, which will generally be much greater than the diffusion time so that the process may be regarded as quasi-steady. Since values for the conventional forms of the reduced frequency parameter will therefore convey little or no information about the unsteady transition process, an alternative definition is required.

The coalescence of turbulent patches formed by successive wakes is related to the rate at which they grow as they move across the blade surface and the time interval between them. A new reduced frequency is therefore defined by the equation

$$\bar{\omega} = \omega \int_{s_t}^{s_l} \frac{ds}{V} \tag{1a}$$

where ω is the frequency of the disturbances and V is the free-stream velocity. Since, in the present simplified analysis, the latter will be assumed to be constant and equal to the average value over the surface between the points s_t and s_l, equation (1a) becomes

$$\bar{\omega} = \omega \frac{s_l - s_t}{V} \tag{1b}$$

The reduced frequency as defined above represents the ratio of convection to periodic time scales and relates specifically to the unsteady transition zone of the blade surface in question.

For the purposes of this simple model, it will also be assumed that the leading edge of a turbulent patch advances at the same rate as the free stream (lines AA in Figs. 1 and 2), while the trailing edge lags, convecting at a rate that is one half of the free-stream velocity. Therefore, the slope of the trailing edge of each patch is twice that of the leading edge in the distance–time diagrams, i.e.,

$$2 \tan \alpha = \tan \beta \tag{2}$$

The above assumptions are equivalent to specifying a linear variation of a time-averaged intermittency function γ between the locations s_t ($\gamma = 0$) and s_m ($\gamma = 1$) in the case of Fig. 1 and between the locations s_t ($\gamma = 0$) and s_l ($\gamma < 1$) with a step change to fully turbulent flow ($\gamma = 1$) at s_l, in the case of Fig. 2. None of the above assumptions are strictly necessary; they are made in order to simplify the analysis. The assumption of constant free-stream velocity is based on the premise that the unsteady transition zone will not occupy a large proportion of the surface length. Dring et al. (1982), Hodson (1983), and Ashworth et al. (1985) have all shown that unsteady transition of this type occupied no more than 40 percent of the surface length at typical reduced frequencies in axial turbines.

For transition of the type shown in Fig. 1, trigonometric considerations lead to the result that the physical length of the unsteady transition zone ($s_m - s_t$) is given by

$$1 + \tan \alpha \left[\frac{s_m - s_t}{s_{max}}\right] = \tan \beta \left[\frac{s_m - s_t}{s_{max}}\right] \tag{3}$$

so that by equation (2)

$$\left[\frac{s_m - s_t}{s_{max}}\right] = \frac{1}{\tan \alpha} \tag{4}$$

where

$$\tan \alpha = \frac{\omega}{2\pi} \frac{s_l - s_t}{V} \frac{s_{\max}}{s_l - s_t} = \frac{\bar{\omega}}{2\pi} \frac{s_{\max}}{s_l - s_t} \tag{5}$$

Figure 3 shows the results of a series of boundary layer calculations in which the laminar-turbulent transition point s_{tr} was varied from the leading to the trailing edge of a flat plate. The flat plate had a constant free-stream velocity. The ordinate in Fig. 3 is the increase in profile loss above the laminar value $(Y - Y_l)$ expressed as a fraction of the maximum possible change, the latter being the difference between the fully turbulent (Y_t) and fully laminar (Y_l) values. The results show that for the case of zero pressure gadient, the increment in loss varies almost linearly with the amount of surface $(s_{\max} - s_{tr})$ that is covered by turbulent flow. Therefore, it will be assumed that the profile loss varies linearly with the extra amount of blade surface, which is, on average, covered by turbulent flow. Evaluating the area under the curve of Fig. 3 reveals that, in the case of a transition point that slowly and cyclically moves back and forth between the leading and trailing edges of the flat plate in, say, a sawtooth fashion, the above assumption leads to an error in the average additional profile loss equal to 4 percent of the maximum change $(Y_t - Y_l)$.

When transition follows the pattern shown in Fig. 1, the above assumptions lead to the result that the profile loss associated with the blade surface in question is equal to the average of the values that correspond to transition at the points T and M, whence

$$Y = 1/2(Y_t + Y_m) \tag{6}$$

Furthermore, if transition occurs at s_l in the absence of wakes or free-stream turbulence, then

$$Y_m = Y_t (Y_l - Y_t) \left[\frac{s_m - s_t}{s_l - s_t} \right] \tag{7}$$

or

$$Y = 1/2 \left[2Y_t + (Y_l - Y_t) \left\{ \frac{s_m - s_t}{s_l - s_t} \right\} \right] \tag{8}$$

which on substitution from equation (2) can be rearranged to give

$$\frac{Y - Y_l}{Y_t - Y_l} = 1 - \frac{1}{2} \frac{2\pi}{\bar{\omega}} \tag{9}$$

The left-hand side of equation (9) represents the fractional increase in loss above the steady-state value. It approaches unity when the reduced frequency becomes very large.

In circumstances that give rise to transition of the type indicated in Fig. 2 and using the same assumptions as above, the profile loss coefficient is given by

$$Y = 1/2(Y_l + Y_t)(1 - \Delta t^*) + Y_l \Delta t^* \tag{10}$$

where Δt^* represents the fraction of the wake passing cycle for which laminar flow persists at the trailing edge of the attached laminar region $(s = s_l)$. Here, trigonometry and the abovementioned assumptions result in

$$(1 - \Delta t^*) = \left[\frac{s_l - s_t}{s_{\max}} \right] \tan \alpha \tag{11}$$

which, on substitution into the rearrangement of equation (10), gives

$$\frac{Y - Y_l}{Y_t - Y_l} = \frac{1}{2} \frac{\bar{\omega}}{2\pi} \tag{12}$$

Equations (9) and (12) are identical when the turbulent patches converge either at the steady-state transition point $(s_m = s_l)$ or at the trailing edge $(s_m = s_{\max})$. This equality corresponds to the special case

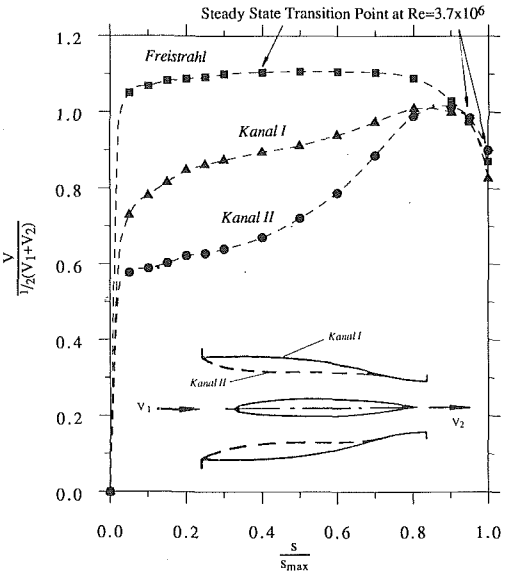

Fig. 4 Velocity distributions corresponding to Speidel's test cases

$$\frac{\bar{\omega}}{2\pi} = 1 \tag{13}$$

while equation (12) is valid for lower values of the reduced frequency $(\bar{\omega}/2\pi \leq 1)$. Thus,

$$\frac{Y - Y_l}{Y_t - Y_l} = \begin{cases} 1 - \dfrac{1}{2} \dfrac{2\pi}{\bar{\omega}}; & \dfrac{\bar{\omega}}{2\pi} \geq 1 \\ \dfrac{1}{2} \dfrac{\bar{\omega}}{2\pi}; & \dfrac{\bar{\omega}}{2\pi} \leq 1 \end{cases} \tag{14}$$

where $\bar{\omega}$ is defined by equation (1b).

Speidel's Unsteady Profile Loss Correlation: A Comparison With the Simple Model

The generalized effects of wake-generated unsteadiness on the time-averaged profile loss of a turbine blade row have been considered by Speidel (1951, 1952, 1953, 1957). A symmetric aerofoil was tested either in a free-stream or in two different but symmetric convergent ducts in order to create typical turbine blade surface velocity distributions. The measured distributions are presented in Fig. 4. Simulated wakes from an upstream blade row were generated using a steel wire aligned with the spanwise direction 0.15 chord lengths ahead of the aerofoil. The wire had a diameter of 0.02 chord lengths; above this diameter, the profile loss of the aerofoil was shown to be independent of the size of the wire. Unsteady inflow was created by oscillating the wire in the pitchwise direction. The amplitude of the oscillations was sufficient to ensure that the increase in profile loss was also independent of the amplitude. Since it is the turbulence in the wake that is largely responsible for the transition of the boundary layers, it is therefore unlikely that the experiment was compromised by the use of an oscillating wire. Indeed, the symmetry of the entire test configuration meant that the time-mean response of each surface of the aerofoil to the wakes was identical and that it was sufficient to measure the effects of the oscillating wire on the loss within the wake flow. The results obtained by Speidel, therefore, may be used to validate the proposed models.

Speidel found that the profile loss depended on a reduced frequency parameter that characterized the unsteady flow. He defined the reduced frequency parameter by the equation

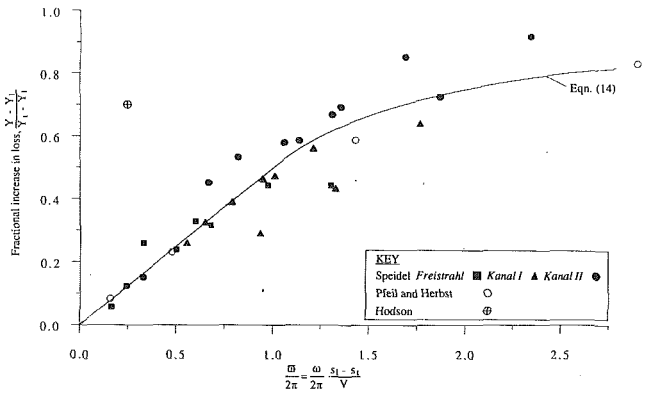

Fig. 5 Correlation after Speidel of effects of unsteadiness on profile loss showing comparison of simple model and experimental data

$$\bar{\omega}_{\text{Speidel}} = \omega \frac{s_l}{V} \tag{15}$$

where s_l is the distance along the surface from the leading edge to the end of attached laminar flow when the inflow is undisturbed, V is the average surface velocity over that length, and ω is the disturbance frequency of the wakes.

Speidel expressed the fractional increase in loss as the difference between the actual profile loss Y and that with steady inflow Y_l, expressed as a fraction of the difference between a maximum value Y_{ft} and the steady-state low turbulence value Y_l. He correlated this against the reduced frequency parameter $\bar{\omega}_{\text{Speidel}}$ so that the general form of the correlation

$$\frac{Y - Y_l}{Y_{ft} - Y_l} = f(\bar{\omega}_{\text{Speidel}}) \tag{16}$$

is similar to that of equation (14). The value of Y_{ft} in equation (16), which Speidel claimed was the value for fully turbulent flow, was deduced from measurements made with the wire positioned on the axis of the tunnel so that the wake continuously affected both surfaces of the aerofoil. In practice, it is unlikely that turbulent spots could have been sustained within the boundary layer close to the leading edge. However, the chord-based Reynolds numbers associated with Speidel's experiments are typically in the range from 1.6 to 3.7×10^6 and calculations show that $\text{Re}_\theta \approx 163$ when $s/s_{\max} \approx 0.05$ so that the stability point for large free-stream disturbances will be very close to the leading edge. Thus, it is not unreasonable to assume that wake-induced transition effectively commences at the leading edge (e.g., $s_t \ll s_t$) so that

$$\bar{\omega} \approx \bar{\omega}_{\text{Speidel}} \tag{17}$$

and

$$Y_t \approx Y_{ft} \tag{18}$$

Thus, equation (14) represents a more general form of Speidel's correlation.

Figure 5 shows Speidel's correlation together with equation (14) and some additional data. As the reduced frequency increases from zero, the profile loss increases (in practice, it may sometimes decrease) from the undisturbed level and asymptotically approaches a limit equal to that obtained with steady turbulent flow over the surface from s_l to $s_{\max}$. It should be noted that in some cases, the numerator and denominator of the ordinates are produced by the subtraction of very similar numbers so that some scatter of the data is inevitable. The reduced frequencies of the majority of turbomachine blade rows will lie in the range from 0.5 to 1.0. Given the simplicity of the model proposed above and the accuracy of the experimental data, the agreement between the data and equation (14) is very satisfactory.

The success of the simple model in predicting the observed

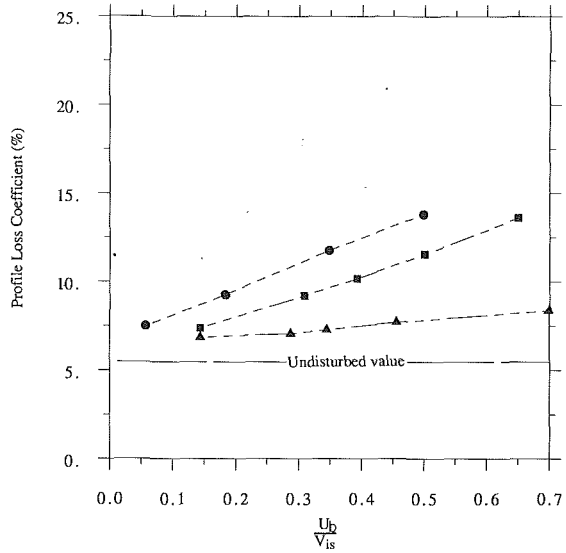

Fig. 6 Effect of wake passing frequency, axial spacing, and wake intensity on profile loss (after Yurinskiy and Shestachenko); blade chord = 30 mm, bar diameter = 1.5 mm; ● axial gap = 1/6 chord; ■ axial gap = 2/5 chord; ▲ axial gap = 1/2 chord

trends is essentially due to the recognition that the nature of the time-dependent unsteady transition, as illustrated by the s–t diagrams, dominates the generation of the additional loss. Figure 5 confirms the significance of the reduced frequency parameter $\bar{\omega}$ in relation to the generation of profile loss. This is because the quantity $\bar{\omega}/2\pi$ represents the ratio of the time it takes for a wake to convect across the transition zone $(s_t - s_l)$ at the free-stream velocity V to the periodic time of the disturbance $(\omega/2\pi)$. The agreement between the data and equation (14) shows that suitable choices have been generally made for the propagation rates of the leading $(V_{le} = V)$ and trailing edges $(V_{te} = 1/2V)$ of the turbulent spots, the data of the present author being the major exception, as will be discussed below. It is sufficient to assume that the state of the boundary layer is either laminar or turbulent.

The significance of the parameter $\bar{\omega}/2\pi$ extends beyond that indicated by equation (14) since its magnitude can be used to predict the unsteady nature of the blade surface boundary layers. For example, laminar separation is unlikely to occur if $\bar{\omega}/2\pi \geq 1$ (see Fig. 1) and in this case, the value of $\bar{\omega}/2\pi$ dictates the length of the unsteady transition zone (see equation (2)). Likewise, if $\bar{\omega}/2\pi \leq 1$ (see Fig. 2), then should laminar separation be predicted when the flow is steady, it is most probable that it will occur in the presence of unsteady flow. In this case, the value of $\bar{\omega}/2\pi$ determines the fraction Δt^* of the wake-passing period for which the laminar flow exists at the distance $s_l/s_{\max}$ from the leading edge (see equation (11)). In an axial turbine and compressor simulation, Binder et al. (1989), Dong (1988), and Addison and Dong (1989) have observed the periodic formation and decay of laminar separations in the presence of wake interactions. If $\bar{\omega}/2\pi \ll 1$, the profile loss may be satisfactorily determined from steady-state measurements or predictions.

Data of Yurinskiy and Shestachenko

The effects of wake-generated unsteady flow on profile loss have also been reported by Yurinskiy and Shestachenko (1974), who rotated a spoked wheel of radial, circular bars in front of a linear cascade of impulse blades. They investigated the effects of changing the axial distance between the bars and the cascade over a range of flow coefficients. The changes in axial distance resulted in differing wake strengths. The test rig was similar in principle to the later construction of Doorly and Oldfield (1985).

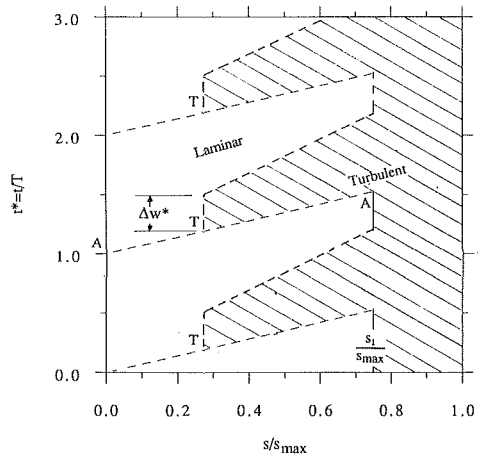

Fig. 7 Schematic distance-time diagram of boundary layer states showing combined forced and natural transition, with forced transition being initiated by a wake of width Dw^* (assuming constant free-stream velocity)

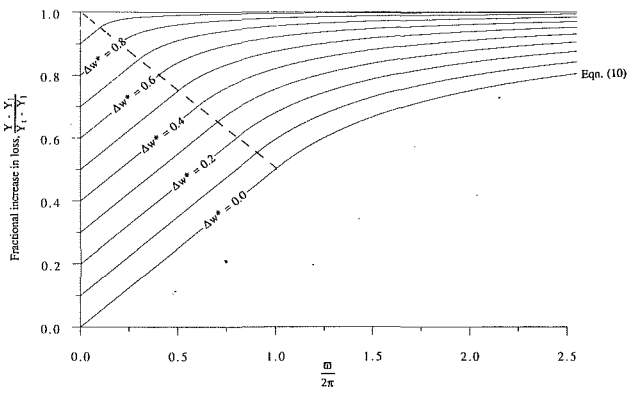

Fig. 8 Prediction, from equation (19), of effect of unsteadiness on profile loss showing effect of wakes of finite width Dw^* (see also Fig. 5)

It is not possible to add their data to the correlation of Fig. 5 because the asymptotic value Y_l is unknown. Instead, their data have been plotted in Fig. 6. The abscissa is the ratio of the bar speed U_b to the isentropic expansion velocity V_{is}, which, on substitution of the values quoted by the authors, is approximately one half of the ratio $\bar{\omega}/2\pi$ (i.e., $U_b/V_{is} \approx 1/2\bar{\omega}/2\pi$) when $s_t = 0$. Figure 6 shows that for the range of U_b/V_{is} investigated and a given axial spacing, the additional loss due to the unsteadiness increases linearly. This is consistent with equation (14) when $\bar{\omega}/2\pi \leq 1$.

Unfortunately, Fig. 6 also shows that the additional loss is also dependent on the axial gap between the rotating bars and the impulse cascade. The variation in gap is very large. This fact becomes particularly evident when it is noted that the inlet flow angle will be of the order of 70 deg (the actual value is not given). Therefore, the character of the inflow will vary from discrete wakes at the smallest gap to a virtually uniform flow, albeit with turbulence, at the largest gap. Transition correlations (e.g., Abu-Ghannan and Shaw, 1980) indicate that the critical value of the Reynolds number based on the momentum thickness of the boundary layer Re_θ is a strong function of the free-stream turbulence level when the level is of the order of a few percent. Therefore, the effect of these changes will be to alter the position s_t at which transition first occurs. The variation of loss with axial gap, which amounts to a factor of two at a given value of U_b/V_{is}, suggests a change in the maximum available transition length $(s_l - s_t)$ of the same magnitude (see equation (14) for example) that is not unreasonable. These results therefore support the case that it is inadequate to assume that transition begins immediately after the wakes touch the blade surface or, indeed, when Re_θ reaches a value of 163.

Effect of a Finite Wake Thickness

The simple model presented above is based upon the premise that transition is periodically initiated at a point corresponding to the centerline of the wake. In practice, the profile of turbulence within a wake is such that near the centerline, the intensity is relatively constant. If the wake is relatively thin, this is not important. When the wake width is large, however, as it might be in L.P. turbines if gross separation of the suction surface boundary layers were to occur, it is possible that transition will not be initiated at a point in time and space but, in effect, at a point in space over a finite period in time. The length of this period, when expressed as a proportion of the periodic time, is denoted by the quantity Δw^* as shown by Fig. 7. The s–t diagrams of Addison and Hodson (1990a) contain more than a suggestion of such a phenomenon.

Following the same lines as the simple analysis presented above, it can be shown that

$$\frac{Y - Y_l}{Y_t - Y_l} = \begin{cases} 1 - \dfrac{1}{2}\dfrac{2\pi}{\bar{\omega}}(1-\Delta w^*)^2; & \dfrac{\bar{\omega}}{2\pi} \geq 1 - \Delta w^* \\ \dfrac{1}{2}\dfrac{\bar{\omega}}{2\pi} + \Delta w^*; & \dfrac{\bar{\omega}}{2\pi} \leq 1 - \Delta w^* \end{cases} \tag{19}$$

which reduces to equation (14) when $\Delta w^* = 0$.

Equation (19) is plotted in Fig. 8. It shows that at low reduced frequencies, the fractional increase in profile loss is equal to Δw^*, the effect being reduced when the frequency exceeds the value given by

$$\frac{\bar{\omega}}{2\pi} = 1 - \Delta w^* \tag{20}$$

which also corresponds to the frequency at which the individual patches caused by successive wakes merge at the point where attached laminar flow would otherwise cease. The relationship (equation (20)) is plotted as a dashed line in Fig. 8 and shows that the reduced frequency at which this occurs is reduced in proportion to the wake thickness. Typical values of Δw^* are, as yet, unavailable but given the success of the simple correlation, they may generally be expected to be small at least at the higher Reynolds numbers found in turbomachines.

Effect of a Nonuniform Free-Stream Velocity: A More Exact Model

So far, it has been assumed that the free-stream velocity is equal to the mean value over the maximum possible extent of the unsteady transition zone (i.e., $s_t \leq s \leq s_l$). In practice, the velocity may not be constant over this distance so that the turbulent wedges shown in Figs. 1 and 2 are no longer bounded by straight lines. Figure 11 shows one such example. Nor is it correct to use the form of the reduced frequency given in equation (1*b*); the more general definition (i.e., equation (1*a*)) will be employed below.

It has already been noted that in Speidel's experiments, turbulent flow is unlikely to have been sustained near the leading edge and that the earliest transition could have occurred would have been near $s/s_{\max} = 0.05$, where $\mathrm{Re}_\theta \approx 163$. If it is assumed that this location represents the distance s_t and that s_l is equal to the values given by Speidel (1953), the data of Fig. 5 can be replotted against the reduced frequency parameter as de-

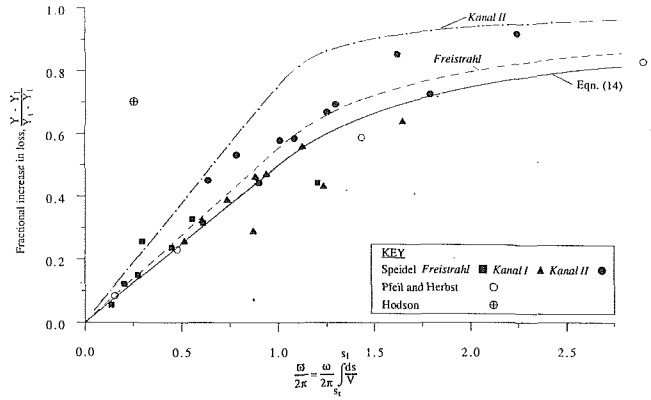

Fig. 9 Recorrelation of the effects of unsteadiness on profile loss showing comparison of models and experimental data (see also Fig. 5)

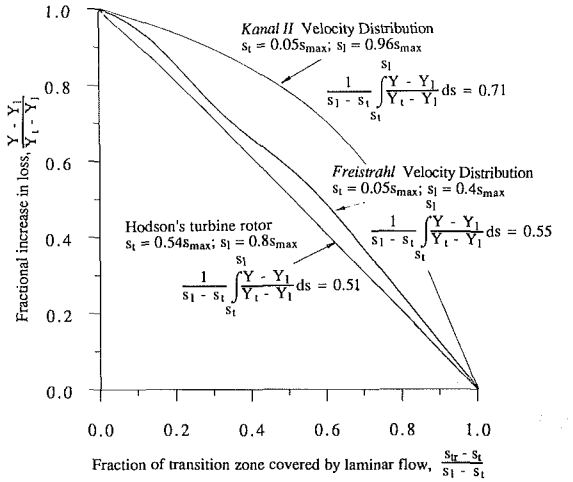

Fig. 10 Effect of transition location on profile loss for profiles with nonuniform velocity distributions

fined by equation (1*a*) to produce the correlation shown in Fig. 9. The data of Pfeil and Herbst (1979) ($s_t/s_{max} = 0.14$, $s_l/s_{max} = 1.0$) and the present author ($s_t/s_{max} = 0.54$, $s_l/s_{max} = 0.8$) are also shown. The differences between the positions of the data points in the two figures are very small, which helps to explain the success of Speidel's original correlation.

A nonuniform velocity distribution will also result in a growth rate of the laminar and turbulent boundary layers, which is different from that on a flat plate in a zero pressure gradient. Figure 10 shows the effect of changing the transition point upon the fractional increase in profile loss of the *kanal II* and *freistrahl* aerofoils. The calculations were carried out at the highest Reynolds number tested and the transition point was varied over the range shown in the figure. Unlike the case of the flat plate, the loss no longer varies linearly with the location of transition, particularly for the *kanal II* aerofoil. The results for the turbine rotor suction surface of the present author ($s_t/s_{max} = 0.54$, $s_l/s_{max} = 0.8$) are also shown in Fig. 10. Like the *freistrahl* aerofoil, there is less variation in the free-stream velocity in this case so that the variation of loss is nearly linear. Thus, the assumption that the additional loss produced by the wake interaction is proportional to the additional area of the blade, which is on average covered by turbulent flow, appears to be valid for the turbine rotor and the *freistrahl* aerofoil but not for the *kanal II* aerofoil.

In order to examine the significance of a nonuniform velocity distribution, the velocities measured by Speidel (Fig. 4) were used as input data to two calculation methods. The first part

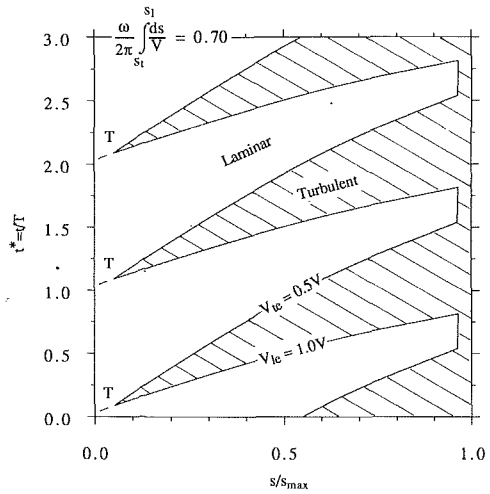

Fig. 11 Distance-time diagram of boundary layer states showing effect of nonuniform velocity distribution for Speidel's *kanal II* aerofoil

of each method consisted of a time-marching calculation, which traced the development of adjacent turbulent patches in s–t space and so determined their shape. The time-marching calculation produces s–t diagrams such as that of Fig. 11. Thus, it is possible to determine the relative proportion of time for which a boundary layer is turbulent at a given location in space, which is in effect the intermittency γ, or where and when transition begins for a parcel of boundary layer fluid that leaves the leading edge at a given time with a specified convection rate.

A Strip Calculation Method. In the first series of calculations, the s–t space was divided into small strips of equal width in time Δt running from the leading to the trailing edge of the blade. The width Δt was sufficiently small that the final solution was independent of the size of the strip. For each strip, it was assumed that the development of the boundary layer was quasi-steady and that the rate of convection of information (the mean propagation rate) was $0.72V$, though the precise value is of little significance. Thus, a series of steady-state boundary layer calculations (Cebeci and Carr, 1978) were performed for each strip using the information on boundary layer state derived from the s–t diagrams. The mean integral thicknesses of the boundary layer during its development beyond the start of unsteady transition were then determined by averaging the results obtained for all the strips.

The results obtained by this method are shown by the dotted and chain-dotted lines in Fig. 9. The line for the *kanal II* aerofoil ($Re = 3.6 \times 10^6$) shows that it should be significantly more sensitive to unsteady inflow than the *freistrahl* aerofoil, which has a flat-topped pressure distribution. This is consistent with the trends exhibited by the experimental data, though the prediction indicates a higher level of sensitivity than the data admits to. This discrepancy is not understood, although the margin of error in the experimental data relating to the *kanal II* aerofoil is known to be typically of the order $1/5(Y_t - Y_l)$: much greater than for the other two of Speidel's test cases. Nevertheless, the model and data suggest that a correlation based solely upon the reduced frequency parameter, while indicating the general trends, is not sufficient for an accurate prediction of the effects of unsteady inflow when there is a very large variation in the free-stream velocity over the potential transition zone. Under these circumstances, it is necessary to take account of the nonlinear relationship that exists between the profile loss and the location of transition. It will be shown below that the effect of varying free-stream velocity on the shape of the turbulent patches in the s–t diagrams (i.e., the intermittency) is much less important.

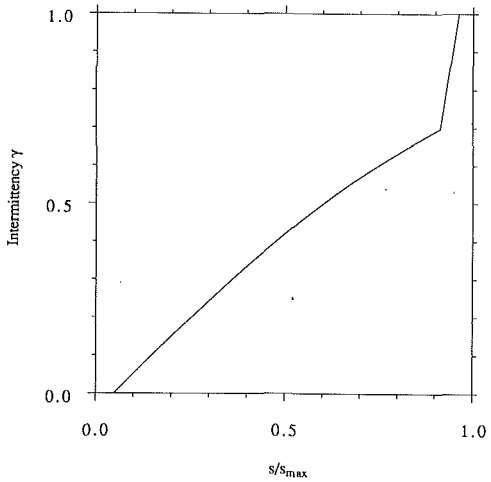

Fig. 12 Variation of time-averaged intermittency function based on results of Fig. 11 for Speidel's *kanal II* test case

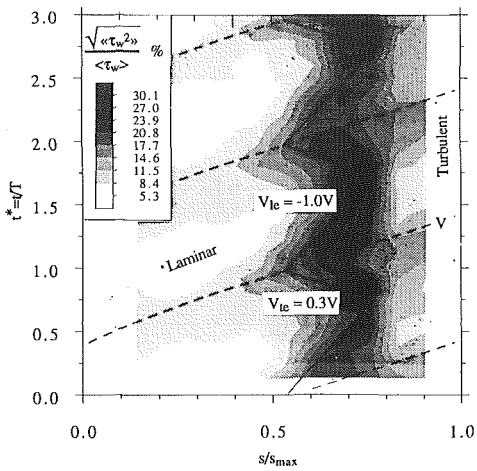

Fig. 13 Distance-time diagram of suction surface random unsteadiness derived from hot-film data acquired in axial flow turbine rotor (Addison and Hodson, 1990a): $\ll\tau_w^2\gg$ = ensemble variance, $<\tau_w>$ = ensemble mean of wall shear stress

Table 2 Comparison of predicted losses for the *kanal II* aerofoil for $\bar{\omega}/2\pi = 0.7$

Calculation method	$\frac{Y-Y_l}{Y_t-Y_l}$
Strip method	0.54
Average-intermittency method	0.63

In the case of the experiments conducted by Pfeil and Herbst and by Hodson, transition occurs in a region of essentially constant velocity so that the profile loss varies almost linearly with the location of the transition point along the surface over the potential transition zone. Therefore, the data of Pfeil and Herbst agree particularly well with the model. However, the model significantly underestimates the effect of unsteady inflow on the turbine rotor of the present author, a result that can be attributed to the very rapid spread of the turbulent patches (see below).

An Average Intermittency Model. The s–t diagrams, using the same assumptions as above, may be used to specify the time-averaged intermittency of the blade surface boundary layers. The boundary layer calculation employs a differential method using an eddy viscosity derived from mixing length arguments. For a given height within the boundary layer, the eddy viscosity was determined according to the relationship

$$\epsilon_{\text{eff}} = \epsilon_{\text{laminar}} + \gamma\epsilon_{\text{turbulent}} \tag{21}$$

where γ is the intermittency determined from the s–t diagrams.

A calculation was performed for the *kanal II* aerofoil, again at a Reynolds number of 3.6×10^6. This test case was chosen again since, of those investigated, it exhibits the greatest deviation from the "wetted area" assumption. The reduced frequency chosen corresponds to that of Fig. 11. The corresponding variation of intermittency is plotted in Fig. 12. It has a value of zero before the start of transition and unity after transition is complete. Over the unsteady transition zone, the variation of γ is virtually linear so that the effect of having a nonuniform free-stream velocity over the transition zone is slight.

Table 2 compares the losses predicted by the "strip" and "average-intermittency" models. The difference amounts to only approximately 16 percent of the fractional increase in the predicted loss.

A question remains as to which of the above two methods is more appropriate. At most low reduced frequencies (say, $\bar{\omega}\leq 1.0$) when, for example, separated flow or natural transition may persist for relatively long periods of time between the wakes, the quasi-steady method is clearly more applicable. The average-intermittency method denies the very existence of unsteady flow. However, at high reduced frequencies, the time scales for turbulent diffusion will be greater than those of the wake passing (Addison and Hodson, 1989b) so that the average-intermittency method may well be more appropriate.

Influence of the Formation and Growth Rates of the Turbulent Spots

So far, the unsteady transition process has been assumed to be periodic, with a single turbulent patch forming at a distance soon after the response of the boundary layer to large disturbances becomes unstable. The leading edge of the wedges has been assumed to propagate with the wake in the free stream. Figure 13 is based upon a figure presented by Addison and Hodson (1990a), who showed that the above may not always be the case; several turbulent spots may form underneath the footprint of a single wake and as a consequence, the apparent rate of propagation may be so great as to appear negative (see Table 1). The data in Fig. 13 were obtained on the suction surface of a turbine rotor blade using surface-mounted hot-film gages, which were calibrated for the measurement of wall shear stress. The figure shows the development of the phase-locked random unsteadiness. It indicates that turbulent flow begins near $s/s_{\max} = 0.45$, which is soon after $\text{Re}_\theta = 163$. The latest occurrence of transition is limited by a possible laminar separation at $s/s_{\max} \approx 0.8$. The free-stream velocity is relatively constant over the specified transition zone so that the variation of loss with transition location is almost linear (see Fig. 10).

To illustrate the importance of using the correct value of the (apparent) leading edge propagation rate, the strip calculation method was applied to the profile of Hodson (and of Addison and Hodson), and a variety of leading and trailing edge propagation rates were chosen. For the purpose of the calculation, due regard was given to the fact that the experimental data are ensemble averaged and that as a result, the start of transition at $0.45s_{\max}$ as indicated by Fig. 13 does not represent the start of fully turbulent flow within the wedges formed on the s–t diagram. Therefore, transition from fully laminar to fully turbulent flow was specified as beginning at $s_t/s_{\max} = 0.54$ rather than at $0.45s_{\max}$.

Figure 14 shows the results of the predictions, the information being presented in the same way as in Fig. 9. For the pur-

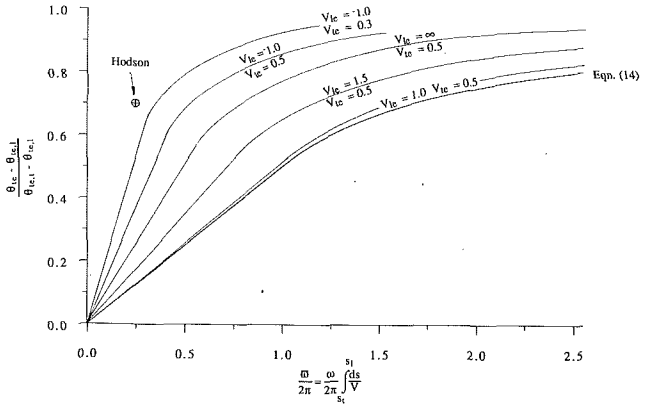

Fig. 14 Prediction of effect of spot leading and trailing edge propagation rates (V_{le} and V_{te}) on profile loss of Hodson's turbine rotor

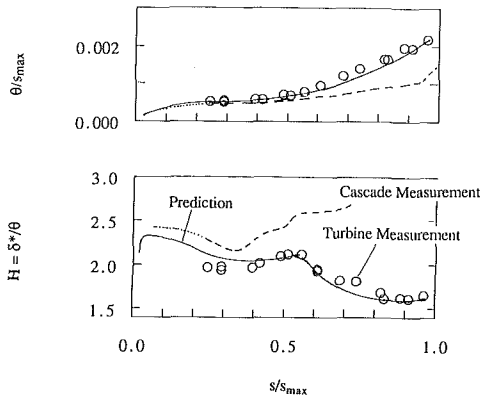

Fig. 15 Predicted and measured suction surface boundary layer development for the turbine rotor of Hodson

pose of plotting the experimental data point, the maximum and minimum values of the trailing edge momentum thicknesses are those given by the predictions. Figure 14 shows that the increase in profile loss is a strong function of the apparent leading edge propagation rate, which is in reality a combination of the spot formation rate and the propagation rate of the individual spots. The solid line drawn over the s–t diagram of Fig. 13 shows the start of transition employed by the calculation with the turbine operating at the condition corresponding to the measurements. The agreement between the prediction, based upon the measured propagation rates ($V_{le}=-1.0V$; $V_{te}=0.3V$), and the measured trailing edge momentum thickness is also encouraging, although the measured value is higher than that predicted. A comparison was also made between the predictions of the strip and average intermittency methods for the turbine rotor of Hodson. The maximum difference in the integral thicknesses of the boundary layers predicted by the two methods at any point on the blade surface was insignificant.

The surface distributions of the integral parameters of the suction surface boundary layer are also available for the above test case (Hodson, 1983). Figure 15 shows the measured variation of the momentum thickness θ and shape factor H ($=\delta^*/\theta$). The measured values for a laminar flow cascade of equivalent geometry to the turbine rotor (Hodson, 1983) are also shown. The data show that in the turbine rotor, the measured momentum thicknesses and shape factor are, respectively, higher than and lower than the cascade values. Addison and Hodson (1990a) argue that these differences suggest that the boundary layer ahead of transition is not fully laminar. Thus, an underprediction of the measured loss might be expected using the models so far described.

The average intermittency (equation (21)) model was

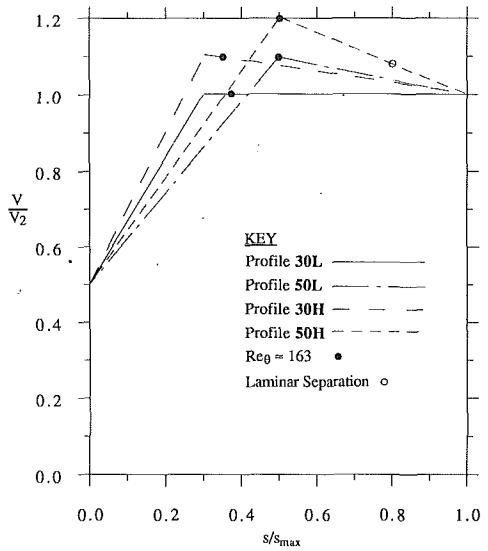

Fig. 16 Idealized velocity distributions for turbine suction surfaces

modified to take account of the facts noted above. The s–t diagram of Fig. 13 was again used as a basis for the predictions but with the simple alteration that the average intermittency γ was not allowed to be lower than 0.1. The resulting surface variations of the integral parameters that correspond to the operating point of the turbine are plotted in Fig. 15. The agreement between the predictions and measured data is self-evident, the further increase in trailing edge momentum thickness due to the change representing 7 percent of the predicted value. It is also noted that although the average intermittency varies almost linearly with surface distance, the shape factor falls more rapidly during the earlier stages of transition than toward the end, suggesting that care must be taken when using the shape factor to represent the "state" of the boundary layer.

Examination of Forward and Aft-Loaded Turbine Blades

In this section, the effects of unsteadiness upon two sets of idealized turbine blades are considered at a Reynolds number of 3×10^5. The profiles have not been optimized in any way, their distributions being chosen so as to permit a simple comparison of differing design philosophies.

The velocity distributions corresponding to the suction surfaces of the four profiles are shown in Fig. 16. Peak suction on the forward-loaded profiles **30L** and **30H** occurs at $s/s_{max}=0.3$ while it is found at $s/s_{max}=0.5$ on the aft-loaded profiles **50L** and **50H**. Profiles **30L** and **50L** have attached laminar flow over their entire surface length when the inflow is steady. They are relatively lightly loaded, the lift as defined by the line integral

$$\Gamma=\frac{1}{s_{max}}\int_0^{s_{max}}\frac{V}{V_2}\,ds \tag{22}$$

being equal to 0.925. Profiles **30H** and **50H** have a higher loading ($\Gamma=0.975$). As a result, laminar separation occurs at $s/s_{max}=0.8$ on profile **50H** in the absence of wakes. For the sake of simplicity, transition in the absence of unsteady inflow was specified at this location. Laminar separation will not occur in the case of profile **30H**. The location of the start of transition ($Re_\theta\approx163$) is also indicated in Fig. 16.

The strip calculation method described above was used to calculate the trailing edge momentum thickness for each of the four profiles over a range of frequencies. Two different leading edge propagation rates ($V_{le}=1.0V$, $V_{le}=\infty$) were investigated. Since the variation in velocity over the potential

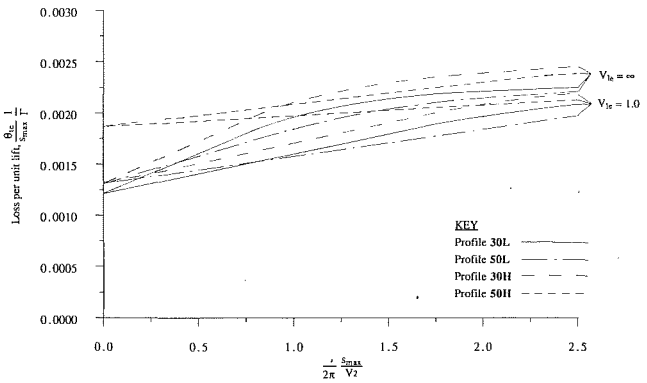

Fig. 17 Effect of unsteadiness on loss of idealized turbine suction surfaces

transition zone is relatively small, the four profiles appear to be equally sensitive to unsteady inflow when the results are plotted in a manner similar to previous figures. However, this disguises the fact that the upper (Y_t) and lower (Y_l) limits of the profile loss and the lengths of the transition zones ($s_l - s_t$) of the four profiles exhibit differences. Thus, the data are presented as in Fig. 17, where the abscissa represents the ratio of the convection time over the entire surface to the periodic time while the ordinate is the predicted trailing edge momentum thickness per unit lift. Usually, the abscissa will have a value in the range from 0.5 to 2.0. The loss typically rises by 50 percent over this range.

Figure 17 shows that the forward-loaded profiles **30L** and **30H**, respectively, present a lower time-averaged profile loss than the aft loaded profiles **50L** and **50H** at the lower frequencies. At the highest frequencies, the opposite is true. The change-over point for the more highly loaded profiles occurs at a much higher frequency. This is because profile **50H** has a higher profile loss in the absence of wakes and because it is much less susceptible to unsteady inflow since it has a shorter surface length over which unsteady transition can occur. The change-over point occurs at lower frequencies for higher values of V_{le} (i.e., when rate of formation and growth of the turbulent spots is higher).

If a turbine stage has significantly more rotor than stator blades, the stator blades will tend to lie to the right of the abovementioned change-over point and the rotors to the left. In such cases, the results of Fig. 17 suggest that the stator blades should be aft-loaded and that rotors should be forward-loaded. However, if laminar separation can be avoided between the wakes, the differences between the aft- and forward-loaded profiles is relatively small. In situations where the design constraints dictate that laminar separation will occur whatever the loading philosophy, the relative insensitivity of these profiles to incoming wakes suggests that steady flow calculations may well be sufficient. This might explain the relative success of some highly loaded L.P. turbine designs.

Further Discussion

This paper has attempted to present, by modeling, the most important features of wake-induced boundary layer transition. It has been shown that a new form of the reduced frequency parameter (equation (1)) can be used to characterize the boundary layer development and the additional profile loss associated with the unsteady transition, providing that a reasonable estimate is made of the rate of growth and the formation of the turbulent spots during transition. A linear variation (or nearly linear in the case of nonuniform free-stream velocities) of the time-averaged intermittency over the unsteady transition zone ($s_t \le s \le s_l$) has been found to be adequate for the present purposes. In practice, of course, the formation of spots within the so-called transitional patches is a stochastic process so that transition appears on the s–t diagrams to be gradual rather than instantaneous when ensemble averaged over many cycles (see Fig. 13). Similarly, natural transition to turbulent flow, which occurs between the wakes at low reduced frequencies, is also gradual. Nevertheless, the assumption that transition is stepwise in fashion also appears to be sufficient for the present purposes.

The models presented successfully predict the influence of wakes upon high Reynolds number blade profiles. This is because there is much less uncertainty over the growth rates of the turbulent patches (see Table 1). With reference to the last point, Addison and Hodson (1990b) have suggested that it is only at relatively low Reynolds numbers ($\mathrm{Re} \sim 3 \times 10^5$) that significant differences exist between the idealized processes of Fig. 1 or Fig. 2 and the true process. It is also important to recognize that transition does not necessarily commence close to the leading edge and that the wakes may be sufficiently broad so as to affect the shape of the s–t diagrams, particularly at these low Reynolds numbers. Though a start of transition criterion has been suggested ($\mathrm{Re}_\theta \approx 163$), evidence of later transition has also been presented. The success of all the analyses provides further evidence to suggest that the process of wake-induced transition can be considered to be quasi-steady at representative reduced frequencies.

The effects of wake-generated unsteadiness on the profile loss of a turbine blade were considered recently by Sharma et al. (1988) who also replotted and added to the earlier correlation of Speidel (1957). Sharma et al. chose to redefine the reduced frequency parameter as

$$f_{\mathrm{Sharma}} = \frac{\omega}{2\pi}\frac{C_x}{V_x} = \frac{U_b}{p}\frac{C_x}{V_x} = \frac{1}{\phi}\frac{C_x}{p} \tag{23}$$

which represents the ratio of the convection time of the wakes through the blade row (C_x/V_x) to the wake passing period ($\omega/2\pi$). Presumably, this form was chosen because it is a simple function of the flow coefficient ($\phi = V_x/U_b$) and the geometry. The above definition differs from that proposed by the present author (equation (1)) and by Speidel (equation (15)) and so does not admit to the possibility that it is the ratio of the time it takes for a wake to convect across the transition zone ($s_l - s_t$) at the free-stream velocity V to the periodic time of the disturbance ($\omega/2\pi$), which determines the transition process. Attention should be paid to the flow on each blade surface before the effect of wake-generated unsteady flow can be modeled.

In their current forms, the present models and the correlation are of limited use to the turbine designer during the initial stages of the design process. This is because the exact nature of the geometry ($s_{\max}$) and the limits for boundary layer transition (s_t and s_l) are unknown until a design nears completion. However, manufacturers of specific turbines tend to design within relatively narrow constraints so that relationships can be established, for example, between the chord and surface lengths and between, say, the Reynolds number and the distances $s_l/s_{\max}$ and $s_t/s_{\max}$. This approach, rather than using a form of the reduced frequency such as that proposed by Sharma et al., is to be preferred since the physical process of unsteady transition is embodied within the parameter $\bar{\omega}/2\pi$. Once a design nears completion, the location of first point of instability s_t can be determined, for example, by use of the transition correlations; the undisturbed transition length s_l may be found and it is no longer necessary to assume a constant free-stream velocity.

Although much of the above discussion has concerned itself with the effects of wake interactions on the profile loss turbine blades, compressors are not excluded from the model, but there is little available evidence to confirm this (e.g., Tanaka,

1984; Dong, 1988). Likewise, the influence of wake-induced transition of the time-averaged heat transfer characteristiccs of turbine blades might readily be modeled, though in such circcumstances, the assumption that transition occurs in a stepwise fashion will probably result in local errors.

Conclusions

A simple model of unsteady transition has been proposed. It has been used to identify a relationship between a new form of the reduced frequency parameter and the profile loss of a blade row subjected to unsteady inflow. The value of this new parameter not only determines the effect upon the profile loss but also the nature of the unsteady transition process. It describes, for example, whether forced transition ends before the location of either natural transition or laminar separation and the length of the resulting unsteady transition zone. The model is shown to be consistent with experimental observations. It successfully explains the correlation by Speidel of effects of wake-generated unsteadiness on the profile loss of turbine blade rows.

Extensions to the simple model show that the formation and growth rates of the turbulent spots have a major influence on the susceptibility of a profile to unsteady inflow and that further information is required regarding these matters and the stability of laminar boundary layers in the presence of unsteady, turbulent wake flows. The transition process may be considered to be quasi-steady and adequately represented by a step change in boundary layer state.

A simple investigation of four idealized turbine blade surface velocity distributions showed that, for a given loading, aft-loaded blades are to be preferred at the higher blade passing frequencies and that forward-loaded profiles are more suitable at the lower frequencies encountered in typical turbomachines. In the case of the more lightly loaded profiles, for which laminar separation was not predicted under steady flow conditions, the benefits of changing the loading distribution were slight. When the distance between the first possible occurrence of transition and the start of steady transition, whether via laminar separation or not, is small, then the profile will be relatively insensitive to unsteady inflow.

Acknowledgments

The author wishes to thank Dr. Stark of the Institut für Strömungsmechanik, Technische Universität, Braunschweig, who made copies of Speidel's internal reports available to him.

References

Abu-Ghannan, B. J., and Shaw, R., 1980, "Natural Transition of Boundary Layers—the Effects of Turbulence, Pressure Gradient and Flow History," *J. Mech. Eng. Sci.*, Vol. 22, No. 5, pp. 213–228.

Addison, J. S., and Dong, Y., 1989, "Unsteady Wake-Boundary Layer Interaction in a Compressor Cascade," *Proceedings of the 5th Symposium on the Unsteady Aerodynamics and Aerolasticity of Turbomachinery and Propellers*, Beijing, People's Republic of China.

Addison, J. S., and Hodson, H. P., 1990a, "Unsteady Transition in an Axial Flow Turbine: Part 1—Measurements on the Turbine Rotor," ASME JOURNAL OF TURBOMACHINERY, Vol. 112, pp. 206–214.

Addison, J. S., and Hodson, H. P., 1990b, "Unsteady Transition in an Axial Flow Turbine: Part 2—Cascade Measurements and Modeling," ASME JOURNAL OF TURBOMACHINERY, Vol. 112, pp. 215–221.

Ashworth, D. A., LaGraff, J. E., Schultz, D. L., and Grindrod, K. J., 1985, "Unsteady Aerodynamic and Heat Transfer Processes in a Transonic Turbine Stage," ASME *Journal of Engineering for Gas Turbines and Power*, Vol. 107, pp. 1022–1030.

Binder, A., 1985, "Turbulence Production Due to Secondary Vortex Cutting in a Turbine Rotor," ASME *Journal of Engineering for Gas Turbines and Power*, Vol. 107, pp. 1039–1046.

Binder, A., Schroeder, Th., and Hourmouziadis, J., 1989, "Turbulence Measurements in a Multistage Low-Pressure Turbine," ASME JOURNAL OF TURBOMACHINERY, Vol. 111, pp. 153–161.

Cebeci, T., and Carr, L. W., 1989, "A Computer Program for Calculating Laminar and Turbulent Boundary Layers for Two-Dimensional Time-Dependent Flows," NASA TM 78470.

Dong, Y., 1988, "Boundary Layers on Compressor Blades," PhD Thesis, Cambridge University, United Kingdom.

Doorly, D. J., and Oldfield, M. L. G., 1985, "Simulation of the Effects of Shock Wave Passing on a Turbine Rotor Blade," ASME *Journal of Engineering for Gas Turbines and Power*, Vol. 107, pp. 998–1006.

Doorly, D. J., 1988, "Modeling the Unsteady Flow in Turbine Rotor Passage," ASME JOURNAL OF TURBOMACHINERY, Vol. 110, pp. 27–37.

Dring, R. P., Joslyn, H. D., Hardin, L. W., and Wagner, J. H., 1982, "Turbine Rotor-Stator Interaction," ASME *Journal of Engineering for Power*, Vol. 104, pp. 729–743.

Hodson, H. P., 1984, "Boundary Layer and Loss Measurements on the Rotor of an Axial Flow Turbine," ASME *Journal of Engineering for Gas Turbines and Power*, Vol. 106, pp.

Hodson, H. P., 1983, "The Development of Unsteady Boundary Layers on the Rotor of an Axial-Flow Turbine," presented at the AGARD Conf. on Viscous Effects in Turbomachines, AGARD CP-351, Copenhagen, June.

Hodson, H. P., et al., 1990, unpublished data.

Hodson, H. P., and Addison, J. S., 1989, "Wake-Boundary Layer Interactions in an Axial Flow Turbine at Off-Design Conditions," ASME JOURNAL OF TURBOMACHINERY, Vol. 111, pp. 181–192.

LaGraff, J. E., Ashworth, D. A., and Schultz, D. L., 1989, "Measurement and Modeling of the Gas Turbine Blade Transition Process as Disturbed by Wakes," ASME JOURNAL OF TURBOMACHINERY, Vol. 111, pp. 315–322.

Lopatitskii, A. O., et al., 1970, "Energy Losses in the Transient State of an Incident Flow on the Moving Blades of Turbine Stages," *Teploenergetika*, Vol. 17, No. 10, pp. 21–23.

Obremski, H. J., and Fejer, A. A., 1927, "Transition in Oscillating Boundary Layer Flows," *Journal of Fluid Mechanics*, Vol. 29, pp. 93–111.

Pfeil, H., and Herbst, R., 1979, "Transition Procedure of Instationary Boundary Layers," ASME Paper No. 79-GT-128.

Pfeil, H., Herbst, R., and Schröder, T., 1983, "Investigation of the Laminar-Turbulent Transition of Boundary Layers Disturbed by Wakes," ASME *Journal of Engineering for Power*, Vol. 105, pp. 130–137.

Schubauer, G. B., and Klebanoff, P. S., 1955, "Contributions on the Mechanics of Boundary Layer Transition," NACA TN 3489; NACA Rep. 1289 (1956).

Sharma, O. P., Renaud, E., Butler, T. L., Milsaps, K., Dring, R. P., and Joslyn, H. D., 1988, "Rotor-Stator Interaction in Multi-stage Axial-Flow Turbines," AIAA Paper No. AIAA-88-3013, presented at the AIAA/ASME/SAE/ASEE 24th Joint Prop. Conf., Boston, MA, July.

Speidel, L., 1951, "Untersuchungen über die Verwendung von Laminarprofilen in einer Reaktionsturbine," Bericht 51/5, Institut für Strömungsmechanik der Technische Hochschule Braunschweig, Federal Republic of Germany.

Speidel, L., 1952, "Untersuchungen über die Verwendung von Laminarprofilen in einer Reaktionsturbine," Bericht 52/11, Institut für Strömungsmechanik der Technischen Hochschule Braunschweig, Federal Republic of Germany.

Speidel, L., 1953, "Untersuchungen über die Verwendung von Laminarprofilen in einer Reaktionsturbine," Bericht 53/14, Institut für Strömungsmechanik der Technischen Hochschule Braunschweig, Federal Republic of Germany.

Speidel, L., 1957, "Beeinflussung der laminaren Grezschicht durch periodische Strörungen der Zuströmung," *Z. Flugwiss. 5*, Vol. 9, pp. XX–OO.

Tanaka, S., 1984, "Influence of a Periodical Fluctuation on a Profile Loss of a Cascade—Part 1, Determination of the Total Pressure Loss Coefficient," *Bulletin of JSME*, Vol. 27, No. 226, pp. 660–666.

Walker, G. J., 1974, "The Unsteady Nature of Boundary Layer Transition on an Axial-Flow Compressor Blade," ASME Paper No. 74-GT-135.

Wygnanski, I., Sokolov, M., and Friedman, D., 1976, "On a Turbulent Spot in a Laminar Boundary Layer," *Journal of Fluid Mechanics*, Vol. 78, Pt. 4, pp. 785–819.

Yurinskiy, V. T., and Shestachenko, I. Ya., 1974, "Losses in an Impulse Turbine Cascade in an Unsteady Flow," *Fluid Mechanics—Soviet Research*, Vol. 3, No. 1, pp. 222–27.

On the Mechanism of Dangerous Blade Vibration Due to Blade Flow Interactions on Centrifugal Compressors

U. Haupt

D. F. Jin

M. Rautenberg

Institute for Turbomachinery,
University of Hannover,
Hannover 1, Federal Republic of Germany

Severe blade flow interactions at part-load operation conditions were investigated on a centrifugal compressor with a vaned diffuser leading to material stresses beyond the allowable values. By means of a number of measurement and analysis techniques it could be found, that a stationary periodic pressure field is produced on the circumference by the vibrating blade itself, which is induced at resonance conditions by the peripheral pressure nonuniformity due to the outlet tube. This peripheral pressure field of an integer wave number intensifies the blade resonance excitation from downstream leading to an additivity effect between wave amplitude and blade displacement. The significant role in this mechanism plays the reverse flow near the corner shroud/suction side in the impeller, occurring at part-load operation, which is controlled by the interaction of the tip angle of the vibrating blade and the flow angle at that location. It could be demonstrated that this dangerous blade vibration, in addition, is the source of a shift of the surge line toward higher mass flow, reducing the compressor operating range considerably in this operating zone.

Introduction

High operational reliability is an important demand in the design of high pressure ratio high mass flow centrifugal compressors. As a consequence efforts in the stress design of these turbomachines are generally intensified, regarding stresses due to the centrifugal forces on the rotating components. The static load on the blades, blade vibration, concerning questions arising from temperature problems and the right choice of the material. Among these, the question of blade vibration is of major concern, since this problem has often been the cause of severe failures of the impeller, the compressor and other connected components of a system.

Blade vibration is a traditional field of research on axial compressors due to the thin and flexible blades (Pearson, 1953; Legendre, 1954; Jäger, 1962, 1967; Leissa, 1981; Ishihara and Funakawa, 1980; Hagiwara et al., 1987). The problem arose only a few years ago on centrifugal compressors, when impeller designers reduced the blade thickness to obtain higher rotational speed and higher power concentration. Nowadays only few and mostly qualitative information exists for the design engineer concerning the blade excitation mechanism in a centrifugal compressor with thin blades (Naguib, 1977; Ellison et al., 1978; Haupt and Rautenberg, 1982, 1984a). The very complex flow in this type of machine, especially at part-load operation, is the major reason, which makes a collection of fundamental design material so difficult. In addition, not only the flow in the impeller is complex, but also the influences of adjacent components on the impeller flow, such as the semivaneless space, the vaneless or vaned diffuser or the type of scroll, have to be taken into account and aggravate a prediction of the flow conditions as well as an evaluation of the blade vibration strain.

Progress in this field has been attained in the past by carefully studying the blade excitation source—the flow characteristics on the compressor—simultaneously with the blade vibration response (Haupt et al., 1985a, 1985b). This procedure enables considerable insight in the blade excitation mechanism. It should be mentioned, that, in addition, blade vibration data for example also were used to determine the occurrence of reverse flow near shroud or rotating stall and thus were very useful to advance in the aerodynamic field of centrifugal compressor research.

Recent activities in the investigation of the blade excitation mechanism in centrifugal compressors were concentrated on compressor operating conditions with high levels of blade vibration strain:

- Blade resonance excitation caused by the pressure nonuniformity downstream of the impeller (Haupt and Rautenberg, 1984b),
- High frequency impeller vibrations with strong participation of the blades excited by downstream located diffuser vanes (Haupt et al., 1985b),
- Blade excitation by strong reverse flow in the impeller

Contributed by the International Gas Turbine Institute and presented at the 34th International Gas Turbine and Aeroengine Congress and Exhibition, Toronto, Ontario, Canada, June 4–8, 1989. Manuscript received at ASME Headquarters February 14, 1989. Paper No. 89-GT-291.

range near shroud in the part-load compressor operating zone (Haupt et al., 1988a),

- Blade excitation due to rotating stall (Haupt and Rautenberg, 1983; Haupt et al., 1985b, 1986, 1988b; Abdelhamid et al., 1987; Chen et al., 1989),
- Blade excitation due to surge (Haupt and Rautenberg, 1985; Haupt et al., 1987b, 1988c).

While different excitation sources turned out to be less dangerous, in this paper an additional unknown blade excitation phenomenon is described in detail, which was found to be extremely dangerous to the blading and, therefore, has necessarily to be taken into account in the blade stress design of highly loaded centrifugal compressors: blade vibration due to blade flow interactions in the part-load compressor operating range.

In the mechanism of this blade excitation phenomenon unsteady flow behavior in the impeller channels play a central role regarding the severe increase of this excitation toward lower mass flow. A great number of measurement techniques had to be used as follows, to analyze the complicated interactions between blade displacement and unsteady impeller flow characterizing this blade vibration:

- Strain gage measurements telemetered from the rotor,
- Unsteady flow measurements by means of high frequency response pressure transducers,
- Peripheral steady static pressure measurements,
- Telemetry/strain/frequency-calibration tests at rest,
- Flow visualization by oil injection in the flow channel during compressor operation.

The described blade excitation phenomenon has to be considered not only of high importance in the stress design due to its high levels of stress and the arising danger to the material. In addition, it could be found, that the compressor operating range is reduced considerably in the zone of the blade excitation due to blade flow interactions near the surge line. A reduction of the mass flow range of the compressor in many cases is an undesired limitation, since many attempts are generally made to increase the operating range of centrifugal compressors mainly toward lower mass flow.

Compressor Test Facility

Blade vibration and flow measurements were carried out on a single-stage centrifugal compressor test rig as shown in Figs. 1 and 2 operated with an open loop. The compressor is driven by a 1350 kW d-c motor coupled to a gear box. The maximum values of compressor pressure ratio and mass flow were $\pi \approx 5$ and $\dot{m}_{red} \approx 10$ kg/s, respectively. The flow enters the compressor in the axial direction through a short suction pipe from a setting chamber and passes through the impeller and a long radial diffuser. Configurations of the diffuser may be changed

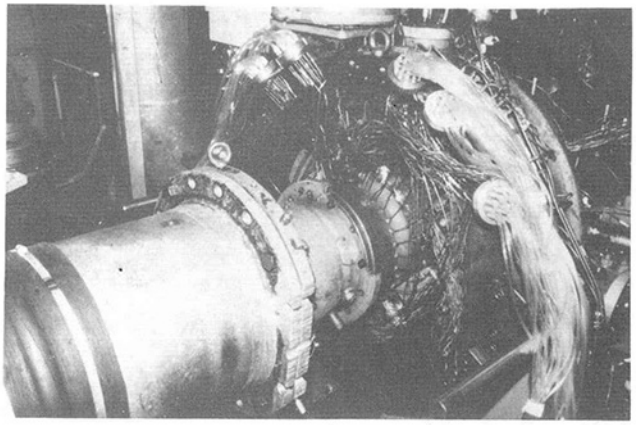

Fig. 1 Centrifugal compressor test facility for the investigation of blade vibration with the installation of peripheral static pressure measurements

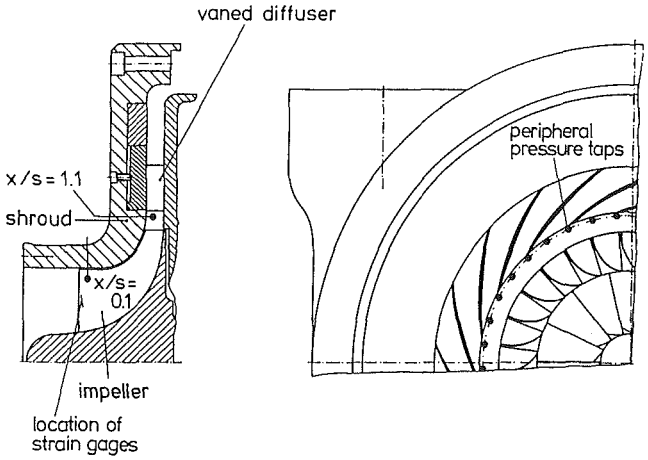

Fig. 2 Cross-sectional view of the test compressor with the vaned diffuser and indications to the locations of strain gages and peripheral pressure taps

Nomenclature

a = blade vibration amplitude at tip
A = maximum blade vibration amplitude
c = axial-flow velocity
f = frequency
$\dot{m}$ = mass flow rate
n = rotor speed
p = pressure
r = radius
s = blade length at tip
t = time
u = circumferential flow velocity
V = blade vibration velocity
W = relative flow velocity
x = coordinate along blade tip
α = relative inlet flow angle
λ = radius ratio = r/r_2
β = relative flow inlet angle
β' = relative flow inlet angle without blade vibration
ϵ = blade vibration strain amplitude
ζ = damping factor
θ = peripheral angle
θ' = blade inlet angle due to displacement
π = pressure ratio
σ = stress
φ = phase angle of vibrating blade
ψ = blade vibration phase angle

Subscript

1 = blade No. 1
1 = impeller inlet
2 = impeller outlet
5 = blade No. 5
I = first mode
0 = resonance
ba = alternating bending
c = axial direction
d = design condition
k = inlet plenum
max = maximum value
min = minimum value
red = reduced to reference conditions $T_K = 288.15$ k; $p_K = 1.01325$ bar
s = shaft rotation
stat = static
tot = stagnation
u = circumferential direction

Superscript

= amplitude value

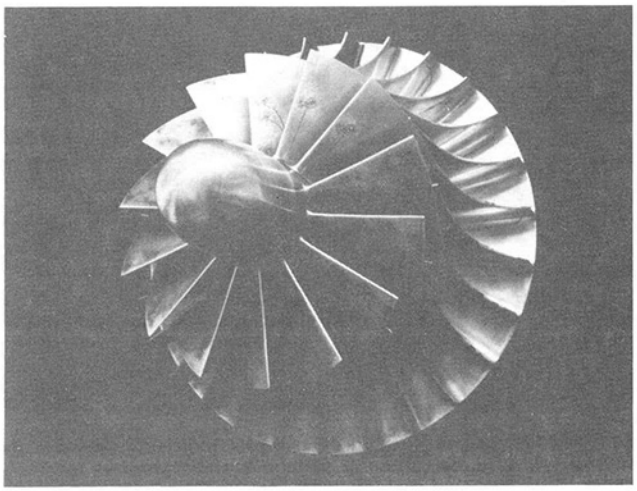

Fig. 3 Impeller used in the blade vibration and flow measurements with mounted eight-channel FM telemetry transmitter covered in the hollow impeller shaft

to operate as a vaneless diffuser with constant radial flow area, as it was described by Haupt et al. (1986, 1988a), or as a vaned diffuser with 19 vanes, as is demonstrated in Fig. 2. The flow downstream is collected in an annular collecting chamber and then leaves the compressor by the outlet tube which is tangential to the machine. As a consequence of this configuration of the outlet tube a certain peripheral nonuniformity of the flow in the compressor occurs, which represents the excitation source of blade vibration from downstream, as it was demonstrated by Haupt et al. (1984b).

The unshrouded impeller of the test compressor used for this investigation is shown in Fig. 3. It has characteristic thin blades of about 1 mm thickness at the inlet tip and 4 mm at the outlet. The impeller has an outer diameter of 400 mm and 28 radial ended blades with every second blade cut back at the inlet. The material is aluminum alloy.

Measurement and Analysis System

As was just mentioned, a detailed analysis of the flow characteristics as the blade excitation source is the precondition for an insight in the mechanism of blade excitation in the compressor. For this reason, various measurement techniques were used in this investigation as follows:

Steady Static Pressure Measurements. Peripheral nonuniformities of the flow in the compressor represent the excitation source for the blade, which passes these variable pressure conditions during its revolution. As a result, the blade is excited to resonance vibration by the different engine-orders. An investigation of this excitation source requires detailed measurements of the peripheral static pressures. Results of the frequency analysis of these data respond to the question, to what extent the different engine-orders contribute to various blade vibration stress levels especially at resonance conditions. Since such an excitation is of major concern in the present investigation, peripheral static pressure taps were installed in two planes in the compressor as is demonstrated in Fig. 2. A number of 36 static pressure holes are located at $x/s = 0.2$ (x/s = related blade length from inlet), in order to give information about the flow conditions in the impeller inlet zone, where the blade is extremely sensitive to the flow excitation forces. A second plane for peripheral pressure taps was chosen immediately downstream of the impeller at $x/s = 1.1$ with 38 holes, one located directly in front of the diffuser vane leading edge and every second one in the midchannel position as shown in Fig. 2.

In addition, conventional pressure and temperature probes were mounted in the test rig in order to determine the overall compressor performance as it is plotted in the compressor chart.

Unsteady Flow Measurements. Stationary high frequency response pressure transducers mounted in the compressor shroud were used to investigate the characteristics of unsteady flow, such as rotating stall, nonrotating stall and reverse flow. During compressor operation, these static wall pressure transducers were simultaneously recorded on a 14 channel magnetic tape, together with one blade vibration signal and a trigger pulses every shaft revolution. Before the tests, a careful calibration of the transducers had to be carried out after mounting them in a calibration setup. In this process, different amplifier values and characteristics of the whole measuring systems from the transducer to the tape were determined for various calibration pressures.

Blade Vibration Measurements. Among the different measuring methods to determine blade vibration during compressor operation, strain gage measurements were chosen. The use of this method needs considerable preliminary work concerning the right choice of the strain gage locations on the blades, which is dependent on knowledge of blade frequency, blade modes and stress distribution for different orders. This work has been carried out by means of finite element calculations and vibration tests at rest and it is described in detail by Haupt et al. (1985a). Semiconductor strain gages were fixed on nearly all blades of the impeller in the inlet zone at the locations of maximum stress and principal strain directions for the Nos. I and II blade mode as is indicated in Fig. 2. A dynamic calibration was considered to be necessary because sensitivity factors of the semiconductor strain gages showed considerable differences. The accuracy of the vibration measurements were ascertained by comparing the outputs of the semiconductor strain gages with data from adjacent foil strain gages during calibration runs.

Blade Vibration Signal Transmission. For the transmission of blade vibration signals from the rotating shaft a multichannel FM-telemetry system was selected due to the high rotational speed of the compressor. This transmission system is described in detail by Haupt and Rautenberg (1982) and it has proved to have good reliability up to maximum compressor speed. The eight-channel telemetry transmitter is situated in the bore of the hollow impeller shaft and is connected to the strain gages on the blades. The energy for this system is transmitted by an inductive power supply consisting of a coil system on the socket tube located between the gear box and the compressor. In the telemetry receiver, a reconversion process of the high frequency signal results in separation of channels, demodulation, filtering and amplifying. Results of a calibration for each channel of the transmission system had to be used in the analysis of the blade vibration signals, which are recorded on magnetic analog tapes during compressor test operation.

Flow Visualization by Colored Dye Injection. The difficulty of doing measurements in a rotating system generally prevents clear insight into the flow conditions in a rotating blade channel of a centrifugal impeller. Besides laser measurements, recent attempts were successful in this field by using a flow visualization method. Colored dye is injected from outside through a hole in the compressor shroud during operation, which is transported by the flow on its path in the rotating impeller channel and which forms traces in the channel and the inner shroud side. After the injection, the compressor is operated still 15 min under the same conditions before it is run down. After disassembly of the compressor shroud wall, the traces of the dye can be examined on the impeller and on the shroud. By means of this method, clear indications to a

reverse flow in centrifugal compressors from impeller outlet to inlet near the shroud could be obtained. This reverse flow plays a central role in the theory on the nature of rotating stall, which was recently published by Haupt et al. (1987b) and Chen et al. (1987, 1989).

Characteristics of Resonance Vibrations on the Compressor With a Vaneless Diffuser

Blade vibration measurements on the compressor with the vaned diffuser showed a very surprising result in the operating zone of approximately 70 percent design speed. Near the resonance between the No. I natural blade frequency and the No. 4 engine-order extremely high vibratory stress levels were measured when the compressor was operated at part-load conditions. This behavior is completely different from the corresponding blade excitation on the compressor with a vaneless diffuser, which is explained earlier in this chapter.

Detailed measurements of the flow behavior in the compressor as the source of broadband blade excitation accomplished by Haupt et al. (1988a, Fig. 7) showed, that the influence of the tangential positioned outlet tube results in a strong nonuniformity of the peripheral static pressure distribution at high mass flow operation. This nonuniformity measured at the shroud is strong in the diffuser and shows still considerable influence upstream in the impeller up to the blade inlet. Throttling the compressor to part-load operating conditions, the mentioned nonuniformity disappears completely to very uniform peripheral distributions at higher pressure levels. It was found in a detailed investigation, that the occurrence of reverse flow near shroud, bending from the blade pressure side at impeller outlet to the suction side and then directed upstream toward impeller inlet, is one of the reasons for this behavior at low mass flow operation.

Considering the excitation of the rotating blade, due to the two different flow characteristics mentioned, it can be expected that higher levels of vibratory stress occur in the blade resonance at higher mass flow, compared to part-load operation, where the uniform peripheral static pressure distribution represents an excitation source of much lower intensity. Figure 4 shows results of corresponding measurements of blade vibration during compressor operation from 14,500 to 12,000 rpm, with a resonance between the No. I natural blade frequency and the No. 4 engine-order at $n \approx 13{,}000$ rpm. At is was expected from the characteristics of the excitation source, the blade amplitude only increases in the resonance at high mass flow operation, while resonance characteristics completely disappear, when the compressor is throttled to part-load conditions. In this whole unsteady flow range, the measured absolute blade amplitudes are much higher, as the resonance peak value in the upper diagram for choke conditions, if one considers the different scales for the two curves. The reason for this behavior is demonstrated by means of the blade vibration spectra in Fig. 5 for various mass flow and constant rotational speed of $n_{red} = 13{,}000$ rpm, which is near the resonance in Fig. 4. As was expected, high mass flow operation with its first-order peripheral pressure distribution and the corresponding first engine-order excitation, the blade responds with a strong peak of shaft rotation frequency f_s. The fourth-order excitation is weak at high mass flow operation, but obvious due to the coincidence with the frequency range of the first blade mode. Moving the lower mass flow, the first-order excitation de-

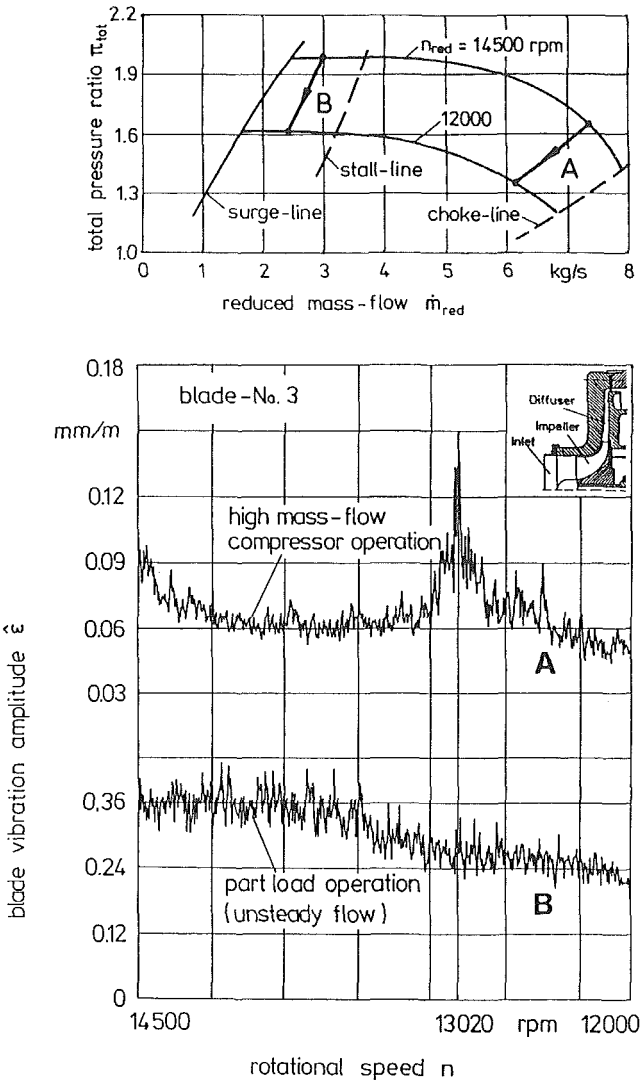

Fig. 4 Comparison of blade resonance behavior at high mass-flow and part-load operation of a centrifugal compressor with a vaneless diffuser; (coincidence between No. 1 natural blade frequency and No. 4 engine-order at $n = 13020$ rpm)

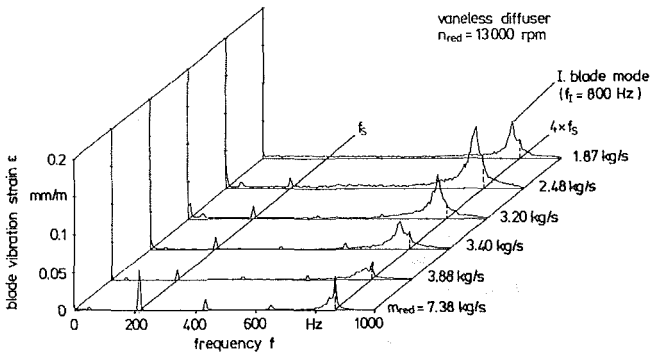

Fig. 5 Frequency analysis of blade vibration signals recorded during compressor operation at $n_{red} = 13{,}000$ rpm and various mass flow rates

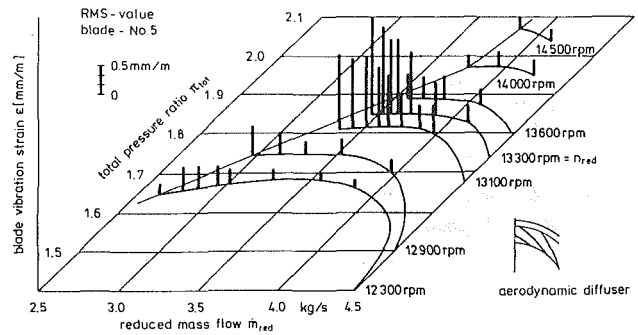

Fig. 6 Selected results of blade vibration measurements plotted in the compressor chart

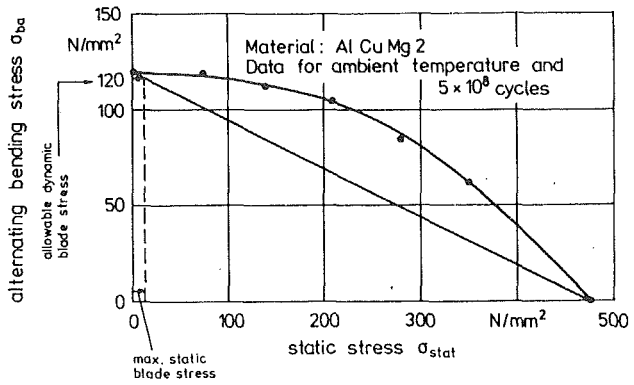

Fig. 7 Goodman-diagram for aluminum alloy showing allowable alternating bending stress values

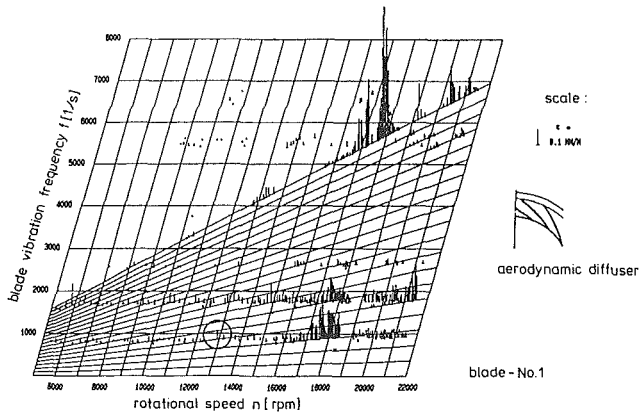

Fig. 8 Campbell diagram obtained from blade vibration measurements on the compressor with a vaned diffuser

creases, because the intensity of the excitation source weakens, when the peripheral pressure distribution becomes more and more uniform. In addition, the blade response in the first mode frequency range develops to a significant broadband behavior toward lower mass flow, while at the same time, the fourth-order excitation becomes less significant in the blade response in Fig. 5. The flow characteristics, as the source of this type of blade excitation, have been investigated by Haupt et al. (1987a) in detail. It was found that the broadband nature of the blade vibration is a response of a strong reverse flow near shroud, which has reached the impeller inlet zone on its way upstream. This reverse flow covers the whole circumference of the impeller inlet and feeds the toroidal ring vortex, known as "prerotation," located in the outer annulus section of the impeller inlet. At higher mass flow, this reverse flow splits into two zones of strong forward and strong reverse flow and begins to rotate, known as "rotating stall," according to the theory presented by Haupt et al. (1987b) and Chen et al. (1987, 1989).

The described blade excitation behavior, characterized by significant blade resonances at high mass flow and broadband excitation, due to reverse flow near the shroud at part-load operation, with the simultaneous disappearance of the multiple engine-order excitation, could be determined generally on the compressor with the vaneless diffuser and in the low speed range ($n < 0.6\ n_d$) of the compressor with a vaned diffuser.

Dangerous Blade Vibration During Compressor Operation With a Vaned Diffuser

Results of blade vibration measurements on the compressor with a vaned diffuser are shown in Fig. 6 plotted in the compressor chart. While the development of blade vibration amplitudes at $n_{red} = 12{,}300$ rpm was expected with its increase due to reverse flow toward lower mass flow, completely unexpected were the high vibration amplitudes in the part-load operating range and the speed zone between 13,100–13,600 rpm, with maximum stress values at this particular blade of $\epsilon_{max} = 1.7$ mm/m at 13,300 rpm and compressor operation immediately before surge. The danger of this blade vibration becomes evident, if the material data of the impeller is considered. According to the Goodman-diagram for the type of aluminum alloy of the impeller in Fig. 7, the degree of danger can be evaluated by a rough estimation. Since $\epsilon_{max} = 1.7$ represents blade stress of $\sigma \approx 120$ N/mm² for this material, the diagram shows that even for low values of static load on the blade, due to the centrifugal force, the considered vibration represents a case beyond allowable stress limits and beyond the safety margin.

The important question arises concerning the excitation cause and its mechanism, characterizing this unusual blade vibration with its significant occurrence in the unsteady flow compressor operating range. A response to this question will be given by the analysis of the blade signal and the flow characteristics in the following sections.

Analysis of the Blade Excitation Mechanism

Analysis of Blade Vibration Signals. Characteristics of blade vibration are shown for one particular blade in the Campbell diagram in Fig. 8, which was obtained from measurements in the high mass flow range. According to these results, significant blade stress was obtained in the speed range from 17,000–18,000 rpm, where the flexible impeller disk section near the outlet is excited to resonance vibration at $f \approx 5500$ Hz by the 19 diffuser vanes and where the blades participate in this vibration in a higher blade mode. In the speed range between 12,000 and 14,500 rpm, which is taken into consideration here, no significant blade vibration could be determined. Two resonance points in this speed range between the No. 1 blade mode and the No. 4 engine-order and between the second blade mode and the No. 8 engine-order are characterized by only low stress amplitude values.

To respond to the question, why much higher blade vibration amplitudes were obtained, when throttling the compressor to part-load operation, the frequency analysis of the blade signal had to be considered. These data are plotted in Fig. 9 for compressor operation at various mass flow for three selected constant rotational speed. For a comparison of these results, the differences in the ordinate scales have to be taken into account.

Regarding the diagram for $n_{red} = 12{,}300$ rpm first, low values of the No. 1 blade mode vibration strain ($f_1 \approx 800$ Hz) are obtained at higher mass flow rates. Throttling the compressor to lower mass flow, the No. 1 blade mode frequency curve develops to the typical broadband characteristic, which is due to the reverse flow excitation of the blade in the shroud zone, as it was demonstrated by Haupt et al. (1988a). Results of corresponding pressure measurements for the same operating points as in Fig. 9 ($n_{red} = 12{,}300$ rpm) are plotted in Fig. 10. It is demonstrated by these data, that broadband static pressure characteristics at low frequency could be determined at low mass flow conditions. This behavior represents the case, when the backflow, on its way upstream near the shroud has reached the position of the wall-mounted pressure transducer ($x/s = 0.55$). According to Haupt et al. (1987a), these phenomena could generally be observed for both configurations, the compressor with a vaneless and with a vaned diffuser.

Completely different to the behavior of blade vibration on the compressor with the vaneless diffuser, as shown in Fig. 5, is the development of the peak representing the No. 4 engine-order blade excitation being in the No. 1 mode frequency range. The amplitude of this particular blade frequency increases considerably toward lower mass flow, different from Fig. 5,

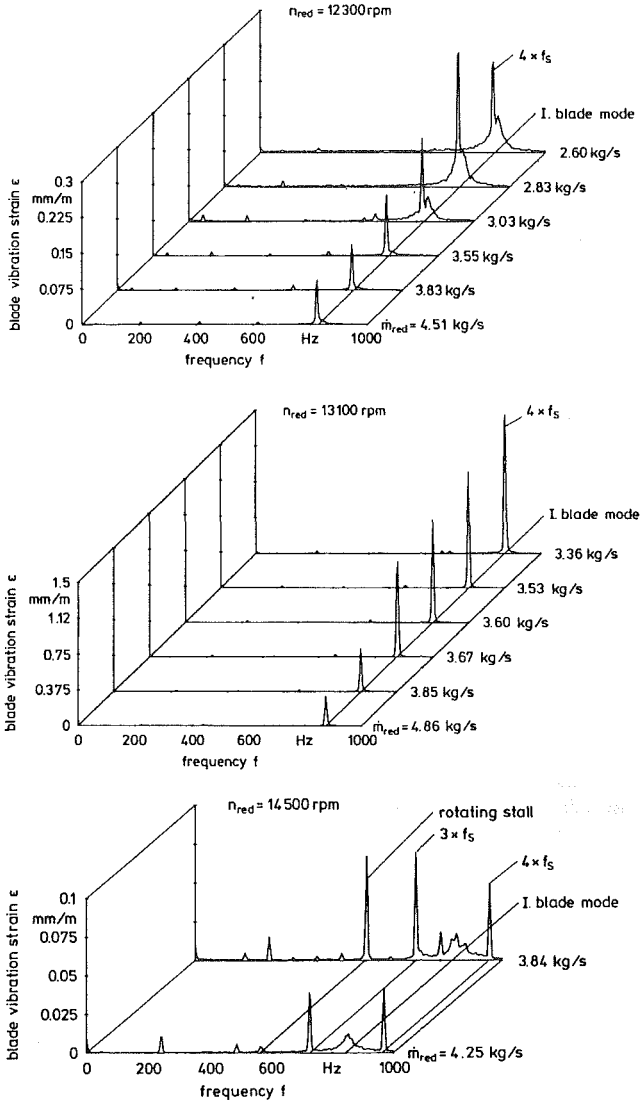

Fig. 9 Frequency analysis of blade vibration signals recorded during compressor operation at three selected rotational speeds and various mass flow rates, corresponding to data points in Fig. 6

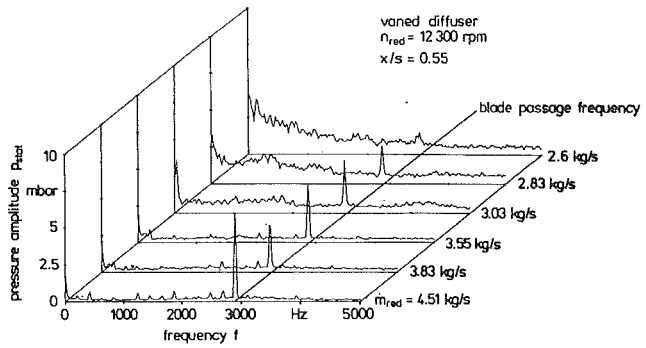

Fig. 10 Frequency spectra of pressure signals from a transducer in the impeller range at various mass flow and constant rotational speed

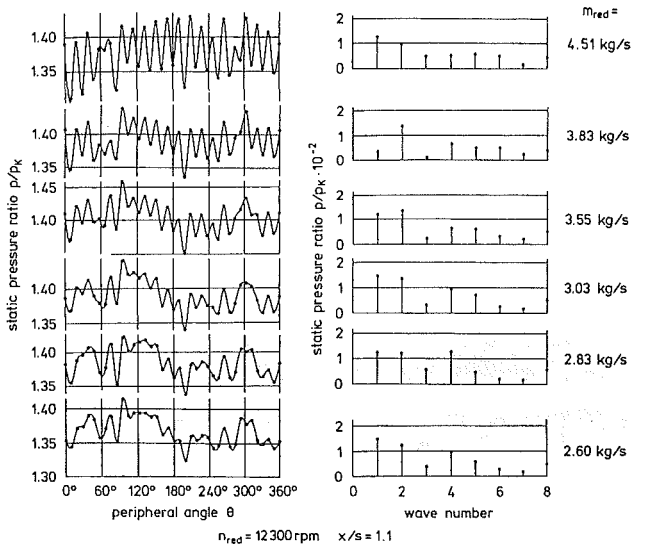

Fig. 11 Peripheral static pressure distribution downstream of the impeller at $n_{red} = 12{,}300$ rpm and frequency analysis of the data

and decreases only slightly to operating conditions immediately before surge. Obviously the reverse flow represents not only the cause for the broadband excitation but also an amplification of the No. 4 engine-order blade excitation.

This phenomenon is extremely significant at slightly higher rotational speed ($n_{red} = 13{,}100$ rpm) (see Fig. 9), characterized by still better coincidence between the No. 1 natural frequency of the considered blade and the No. 4 engine-order value. While broadband behavior in the first mode range at this speed is not evident, the peak representing the response to the No. 4 order excitation develops to unusual high stress values (see different ordinate scale), bearing a great danger of blade failure as demonstrated by means of the diagram in Fig. 7.

Conditions at higher rotational speed ($n_{red} = 14{,}500$ rpm) are plotted in the third diagram of Fig. 9 showing the Nos. 3 and 4 order excitation away from the No. 1 blade mode frequency range and thus, resulting in much lower values of blade strain. Rotating stall of two cells rotating against the impeller direction could be determined during operation immediately before surge. According to a detailed investigation on the same compressor by Abdelhamid et al. (1987), these unsteady flow patterns excite the blades to vibrate at $f \approx 560$ Hz, as shown in the spectrum in Fig. 9. Nearly no broadband excitation can be observed in the No. 1 blade frequency range, which is due to the fact that the present rotating stall represents a rotating reverse flow zone, as described by Haupt et al. (1987b) and Chen et al. (1987), extending only up to the leading edge of the splitter blade. Results of a corresponding investigation by Haupt et al. (1988a) show that significant broadband excitation of the blades occurs, when, as a precondition, the reverse flow near shroud reaches the sensitive inlet part of the long blade, whether this is due to a reverse flow, which covers the whole inlet circumference or a rotating stall with a rotating reverse flow zone, extending upstream to the long impeller blade leading edge.

An additional result is obtained from the third diagram in Fig. 9. The blade response to the third engine-order excitation increases toward lower mass flow, although it is far from the No. 1 blade frequency. The reason for this behavior will be explained among others by flow investigations as described in the next section.

Analysis of the Flow Characteristics as the Blade Excitation Source. Detailed flow measurements were accomplished to find a response to the question, why the fourth engine-order blade excitation increases so significantly in the unsteady flow operating range. For this reason, the compressor was equipped with a great number of peripheral static pressure taps in two planes in the shroud wall as already described (see Fig. 2) and as shown in the photo in Fig. 1.

Results of this investigation are plotted in Fig. 11 for compressor operation at 12,300 rpm showing the peripheral static pressure distribution downstream of the impeller, before diffuser inlet, together with the corresponding frequency analysis

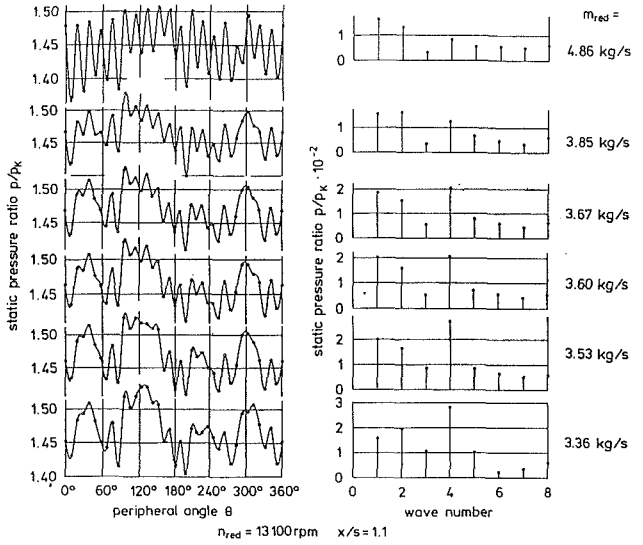

Fig. 12 Peripheral static pressure distribution downstream of the impeller at n_{red} = 13,100 rpm and frequency analysis of the data

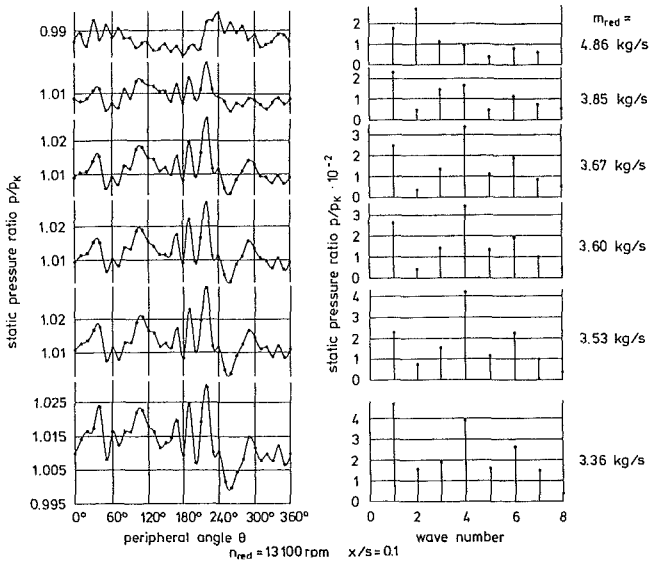

Fig. 13 Peripheral static pressure distribution at impeller inlet at n_{red} = 13,100 rpm and frequency analysis of the data

of each pressure distribution curve. At high mass flow, the alternating characteristic of the pressure data is due to the specific locations of the pressure taps, one hole in front of the diffuser vane leading edge and the adjacent hole at midchannel position. Throttling the compressor at this speed to lower flow rates, an increase of wave number 4 is evident, while the first and the second wave order are significant, for nearly the whole considered operating range. Wave number 1 is expected for all measurements due to the disturbance of the peripheral pressure uniformity of the tangential outlet-tube.

Corresponding results of measurements at 13,100 rpm in Fig. 12 representing the case of dangerous blade excitation, show a much more periodic behavior of the pressure distributions, now characterized by the growing dominance of wave number 4 toward lower mass flow. This interesting result demonstrates the occurrence of a steady static pressure wave of 4 maxima and minima along the circumference at these part-load operating conditions, being obviously the cause of the serious blade excitation, as shown in Fig. 6. The question concerning the origin of this steady wave produced by the rotating impeller is discussed in the next chapter.

Corresponding pressure measurements in a second plane,

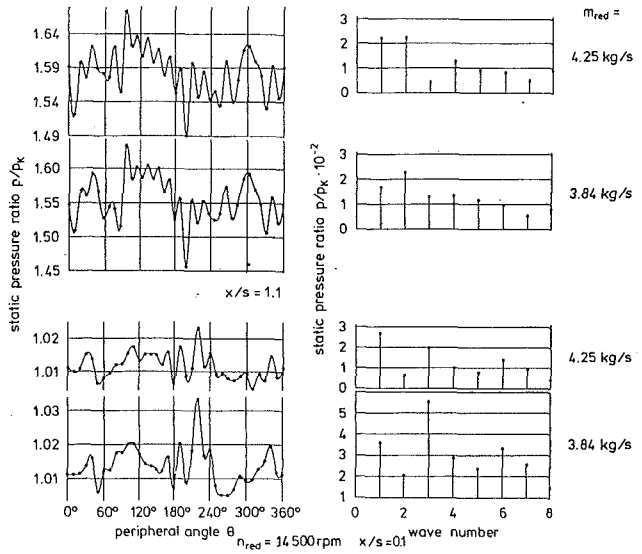

Fig. 14 Peripheral static pressure distribution at impeller inlet and downstream of the impeller at n_{red} = 14,500 rpm and frequency analysis of the data

near impeller inlet ($x/s = 0.1$), are plotted in Fig. 13 for the same operating conditions as in Fig. 12. It can be demonstrated clearly by these results, that the static pressure wave of four periods along the circumference even extends upstream to the impeller inlet zone, when the compressor is throttled to lower mass flow. This result explains the high levels of blade stress measured at these conditions, since obviously the periodic excitation forces even act in the blade inlet zone with its great sensitivity to vibration.

Interesting results were obtained when running the compressor at n_{red} = 14,500 rpm close to surge, as it is shown in the diagram in Fig. 14 for both planes. No significant wave number is obtained for the conditions at impeller outlet. In the inlet plane, a steady wave of order number 3 was analyzed, when the compressor is operated toward the surge line. This behavior explains the increase of the blade response to the No. 3 engine-order excitation, as shown in Fig. 9. The next chapter deals with the question, why these steady waves of the No. 4 and No. 3 order develop downstream and in the impeller as the source of dangerous blade vibration.

Investigation of the Blade Excitation Mechanism. Considering the most dangerous case of the described blade excitation, two arguments seem to be important concerning the question to the cause of the development of steady waves mainly downstream and in the impeller:

(*a*) The occurrence of significant steady waves and dangerous blade excitation could only be determined in the unsteady flow range close to surge,

(*b*) The dangerous excitation only happens in the resonance range of the No. 1 blade mode and the fourth engine order.

Diagrams in Fig. 12 are convenient to find out the mechanism of this steady wave occurrence. Regarding the peripheral pressure distributions at $\dot{m}_{red} = 3.53$ and 3.36 kg/s in this figure, these curves roughly change their characteristics four times along the circumference, showing two different particular behaviors. Four periodic short periods of these curves are signified by typical alternating behavior, which characterizes flow conditions at high mass flow rate (see curve $\dot{m}_{red} = 4.86$ kg/s). In between these periods, the peripheral static pressure increases and remains fairly constant.

It can be assumed that this pressure distribution is obviously produced by the vibrating blade itself (vibrating four times per

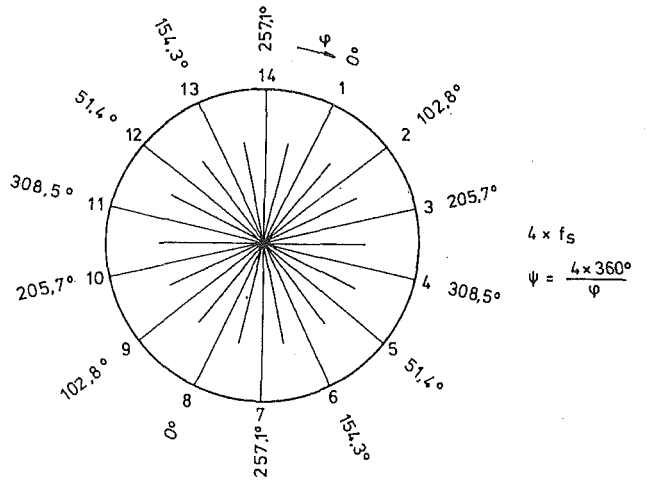

Fig. 15 Theoretical phase values of the different impeller blades against the reference blade No. 1 ($\varphi = 0$ deg) under the following assumptions: (1) Four vibration periods during one revolution and, (2) Zero point of the vibration for each blade at the location of blade No. 1

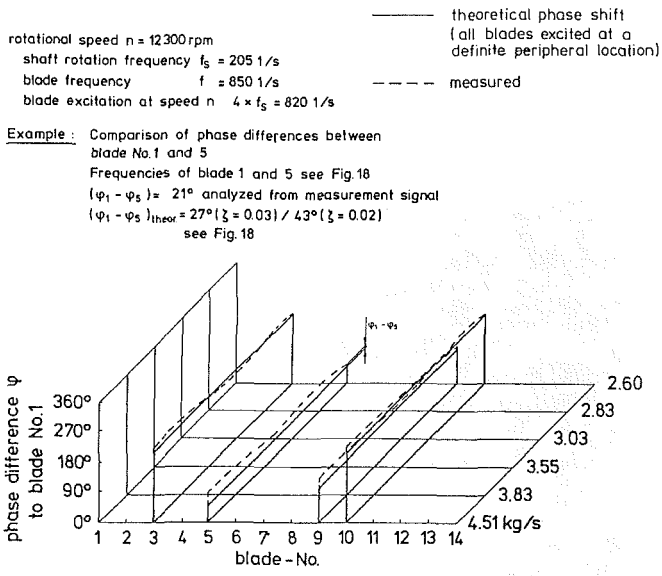

Fig. 16 Comparison of measured and theoretical phase values against the reference blade (No. 1) for four impeller blades at various mass flow rate $n_{red} = 12{,}300$ rpm

revolution), changing its blade inlet angle from high to low mass flow conditions and vice versa, during one period of vibration. The pressure characteristics, as shown in Fig. 12, represent a blade excitation from downstream leading to still higher blade amplitudes and thus, resulting in a more significant fourth-order pressure distribution. This excitation procedure is thus characterized by an accumulation or building-up process, which occurs due to the interactions between the blade displacement during resonance vibration on one side and the flow in the impeller channel being controlled by the alternating blade inlet angle during vibration on the other hand.

Two additional questions need a satisfactory response in order to confirm and to give an comprehensive explanation of this blade excitation mechanism as previously described.

(*a*) The peripheral pressure distribution of wave number 4 in Fig. 12 would only be produced by the impeller if the majority of the blades vibrate inphase at a particular position of the circumference. Vibration phases of different blades were analyzed in order to respond to this question and results are presented in the next chapter.

(*b*) The particular flow characteristics in the impeller channel during dangerous blade vibration compressor operation have to be investigated in order to find out, why relative small blade inlet angle variations during resonance influence the impeller outlet conditions in such a considerable consequence. A response to this question is given in an additional chapter.

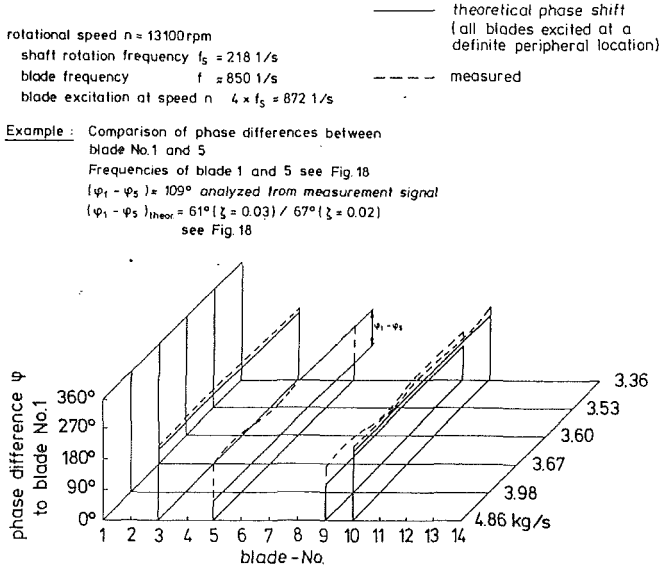

Fig. 17 Comparison of measured and theoretical phase values against the reference blade (No. 1) for four impeller blades at various mass flow rate $n_{red} = 13{,}100$ rpm

Phase-Relationship of the Impeller Blades. An investigation was accomplished to study the phase relationship of the impeller blades during dangerous vibration at $n_{red} = 13{,}100$ rpm at low mass flow. For this purpose, at first, the transmission system had to be investigated in a calibration test at rest concerning the phase shift between the input and output signal for each of the eight channels. Phase shifts were measured and taken into account in the following considerations.

Assuming the blades are excited significantly at one location on the circumference during their revolution in the compressor, they are forced to vibrate in a clear phase relationship to each other. Constant phase values of the vibrating blades at a particular location on the circumference represent the precondition for the occurrence of a steady pressure wave. In Fig. 15, the phase differences of the blades, vibrating four periods per revolution, are plotted when the system is observed at a time t in the moment of the phase shift 0 deg of blade No. 1 and if all blades have the same phase value at a particular position on the circumference. These data are considered as "theoretical values." An analysis of the phase shift of simultaneously recorded blade vibration signals was now accomplished, in order to find out if the phase values will confirm the model of an in-phase vibration of the blades at particular peripheral locations being the source of the steady pressure wave.

Results of an analysis of the blade vibration signals at $n_{red} = 12{,}300$ rpm and various mass flow concerning the phase configuration are plotted in Fig. 16 with the theoretical values, if all blades are excited at a definite peripheral location, and the measured phases given by the dotted line. Good agreement in this comparison was obtained for all blades except blade No. 5, showing slight differences in the phase. Similar results were obtained for compressor operation at $n_{red} = 13{,}100$ rpm, as shown in Fig. 17, with still more evident disagreement for blade No. 5.

Looking for reasons of the missing coincidence in the phase relationship of blade No. 5 against blade No. 1 it was found, that the differences in the natural blade frequencies have to be taken into account. Certain blade frequencies are lower, others are higher, leading to consequences concerning the

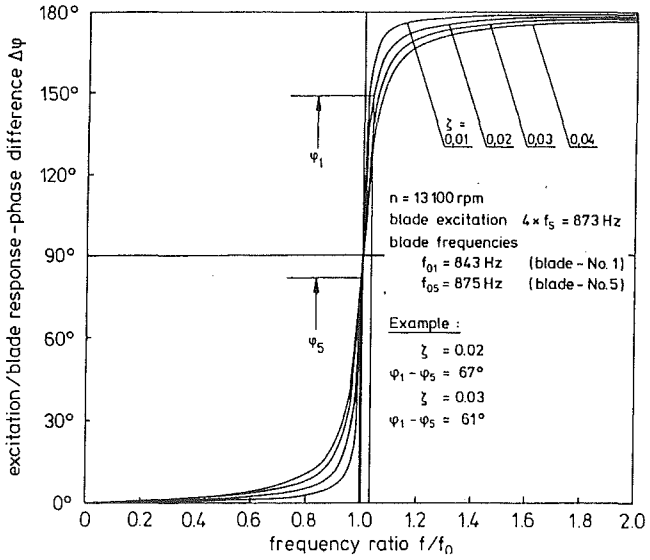

Fig. 18 Comparison of phase relationships in the phase diagram for blade Nos. 1 and 5, having different natural frequencies for a given excitation of $f = 873$ Hz

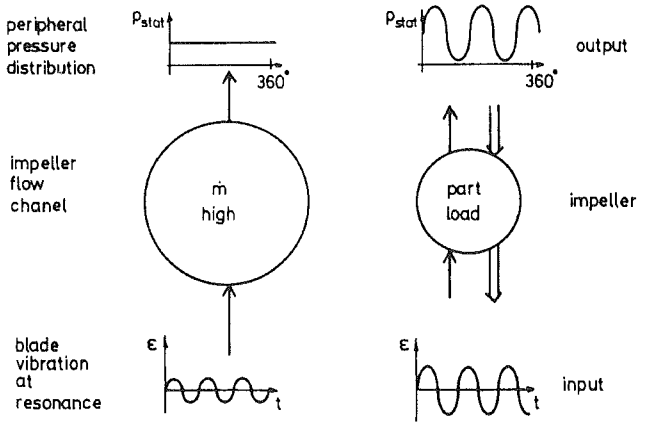

Fig. 19 Demonstration of the role of the flow in the impeller channel for the blade excitation

phases of the blade response. In the phase-diagram in Fig. 18, the particular case of blade Nos. 1 and 5 is considered showing theoretical phase differences $\varphi_1 - \varphi_5$ of 67 deg or 61 deg depending on the ζ value, due to the distinct blade frequency values towards the excitation frequency. If these conditions are taken into account in the phase considerations, the measured value of $\varphi_1 - \varphi_5 = 109$ deg is reduced to a much lower value and other phase results from Figs. 17 and 18 were generally corrected to still better coincidence.

Considering these small differences in the theoretical and measured values and the fact that there are considerable interactions between the blades of an impeller being connected to a system mainly by the outer ring section, it can be concluded that there is very good agreement. The result confirms the picture of a systematic vibration of the different impeller blades with constant phase angles at a fixed location in the compressor.

Major Role of the Impeller Flow in the Blade Excitation Mechanism. As shown in Fig. 6, the occurrence of dangerous blade vibration as previously described is limited to the low mass flow range near surge. Obviously, the particular flow conditions in the impeller channel play a significant role in this excitation mechanism. While resonance vibration of the blades at high mass flow operation does not influence the static

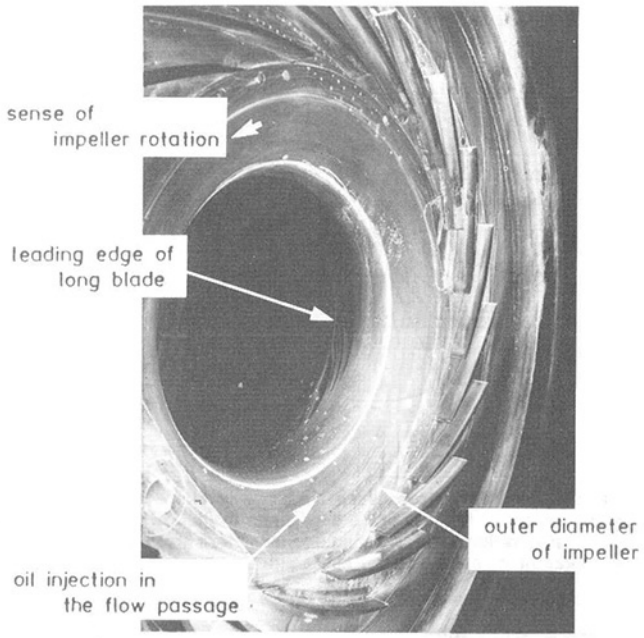

Fig. 20 Results of colored dye injection experiment and view to the shroud wall inside with flow traces showing the extension of the upstream directed reverse flow: $n_{red} = 13{,}100$ rpm; compressor operation close to surge

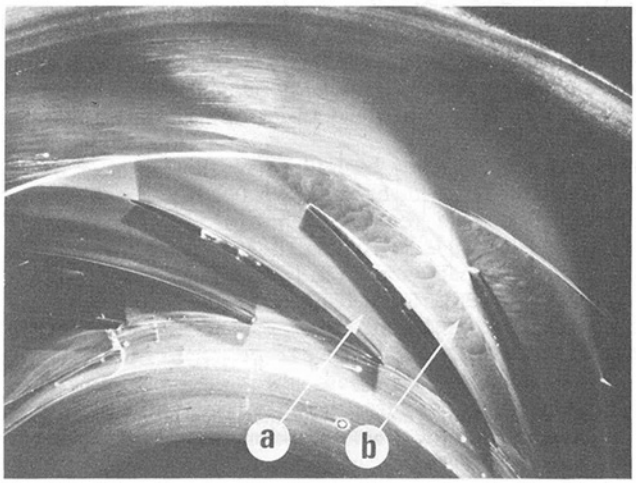

Fig. 20(*a*) Flow characteristics in the diffuser visualized by the dye injection experiment; operating conditions (see Fig. 20) and the differences in the throughflow conditions near shroud with uniform flow at channel (*a*) closer to the outlet tube and stalled flow at channel (*b*)

pressure distribution downstream of the impeller (see Figs. 11–14), at low mass flow the same vibrations are the source of a pressure characteristic, which is strongly dependent upon the angular position of the blade leading edge during vibration, as sketched in Fig. 19. Which properties characterize the impeller flow at these latter operating conditions?

Figure 20 shows results of a colored dye injection test, as described earlier in detail, when running the compressor at conditions of dangerous blade vibration. Regarding the traces on the shroud wall from inside and considering the direction of the impeller rotation, the flow near shroud, originating from impeller outlet, is obviously directed backward up to a meridional position of $x/s = 0.7$, where a ring of the dye is formed as a stagnation zone of this reverse flow, characterized by zero meridional flow velocity. The forward directed inlet flow also is visible in Fig. 20 from impeller inlet up to the ring. The approaching flow is here deflected by the stagnation to the radial and tangential direction. The colored dye of the reverse

flow is obviously carried into the forward flow, apparently by the narrow branch of the reverse flow along each of the innermost corners between the blade suction surfaces and shroud. A detailed analysis of the flow properties at these operating conditions is given by Chen et al. (1987).

The result of the flow visualization in Fig. 20 demonstrates that the flow in the impeller channel, at these operating conditions, is obviously dominated by strong reverse flow near the shroud and a stagnation front between forward and backward flow with strong fluid particle transportation in the radial direction. These flow conditions, represented obviously by a systematic well-formed vortex system in the impeller channels being in an unstable equilibrium, turned out to be very dependent from the angular position of the blade leading edge during vibration. This unstable equilibrium of the flow, occurring only near surge, when the reverse near shroud has reached a certain intensity, represents the precondition of the amplification effect in the impeller, leading to the dangerous blade vibration. It should be mentioned, in addition, that the described operating conditions are located in the intermediate zone between three and two cell rotating stall occurrences.

An important additional result from Fig. 20 has to be mentioned. There is a small zone on the circumference of the impeller inlet ($\theta \approx 240$ deg), where the dye traces indicate reverse flow up to the leading edge of the long blade. During impeller rotation, the sensitive inlet part of the blade passes this zone and a sudden change of the local flow conditions will surely result, like a pressure pulse, in a blade excitation. This phenomenon also can be determined in the pressure distribution at impeller inlet ($x/s = 0.1$) at $\theta \approx 240$ deg in Fig. 13, where an unusual pressure drop is evident between $\theta = 220$ deg and 250 deg. This local static pressure decrease is due to an increase of the flow velocity in the range of the outlet tube being on a streamline with the inlet position of $\theta \approx 200$ deg (see Fig. 12). This peripheral nonuniformity, which is extremely significant in the sensitive blade inlet zone, is very likely the reason for the in-phase vibration of the blades and thus another precondition for the occurrence of the steady waves downstream of the impeller.

In addition, this peripheral nonuniformity of the pressure due to the tangential position of the compressor outlet tube, also could clearly be determined in the diffuser range by means of the colored dye injection method. Figure 20(*a*) shows traces of the dye characterizing the flow properties near shroud in some impeller channels, after operating the compressor under conditions of Fig. 20. While the streamlines connected to the outlet tube (*a*) shows clear through flow lines, the channel immediately adjacent has completely different flow characteristics being stalled near the shroud. These different flow conditions represent considerable differences in the peripheral static pressures in this zone, as it is shown in the low mass flow diagrams in Fig. 12 at a peripheral angle of $\theta \approx 200$ deg. These significant differences of the throughflow characteristics of adjacent impeller channels in the part-load operating range can be considered as the source of the pressure nonuniformity in the impeller inlet and with this, one of the reasons for the in-phase blade vibration at particular peripheral positions.

Reduction of the Compressor Operating Range Due to the Described Blade/Flow Interactions

In order to complete the picture of the consequences of the described dangerous blade vibration, an additional aspect of great practical importance has to be mentioned. It has been observed in the experiments, that in the range of high blade strain occurrence the surge-line was shifted considerably toward higher mass flow. To understand the reason for this phenomenon, an investigation of the quantitative blade angle variation at impeller inlet was accomplished for the case of

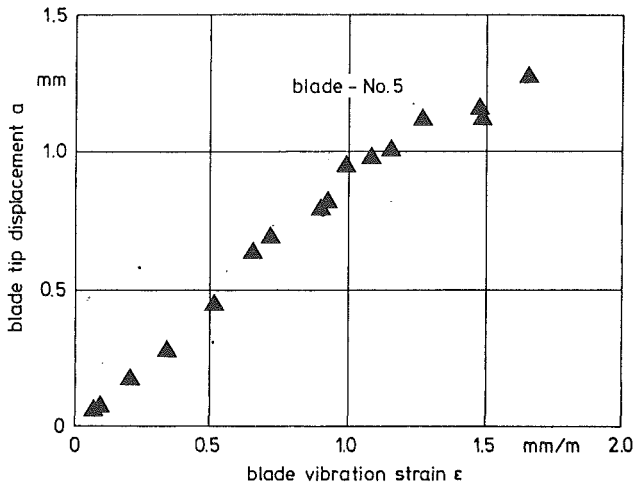

Fig. 21 Results of calibration test at rest showing the blade displacement as a function of blade strain ϵ, measured at inlet location

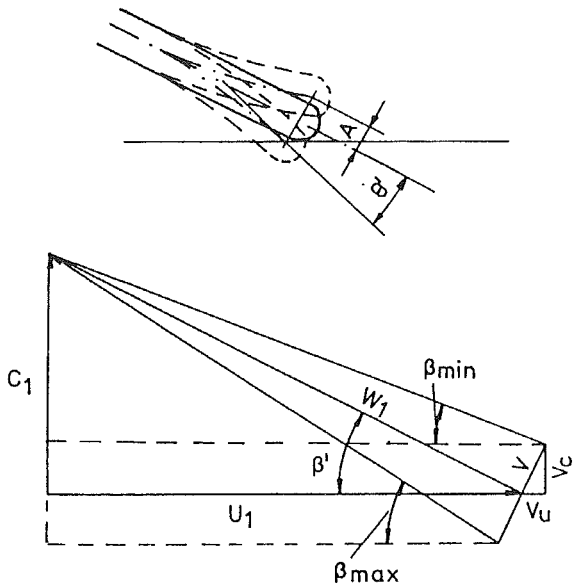

Fig. 22 Inlet-angle variation and velocity triangles at impeller inlet during vibration of the blade V = velocity of the blade tip during vibration

maximum blade amplitude. These values then were related to mass flow rates at steady compressor operation. Attempts were made by this study to find an answer to the question, if probably the low value of the periodic blade angle variation during vibration induces the surge cycle at operating points, where, at no blade vibration, steady compressor operation is still possible.

In a calibration test at rest, at first the blade displacement at tip was measured as a function of the stress value from the strain gage at blade inlet. Results of this experiment are plotted in the diagram in Fig. 21, with displacements of the blade 1 mm, when the stress has a value of about 1.0 mm/m.

Finite element calculations were accomplished to determine the blade tip angle at inlet as a function of the blade displacement a during vibration. As a result, the change of blade inlet angle is 1.09 deg, when the blade amplitude at tip A is 1.0 mm. When a is defined as

$$a = A \cdot \sin(2\pi ft),$$

then the inlet angle θ at blade tip (see Fig. 22) is

$$\theta = 1.09\ a = 1.09 \cdot A \sin\ (2\pi ft).$$

It has to be taken into account in this consideration, that the velocity of blade tip V during vibration influences the flow

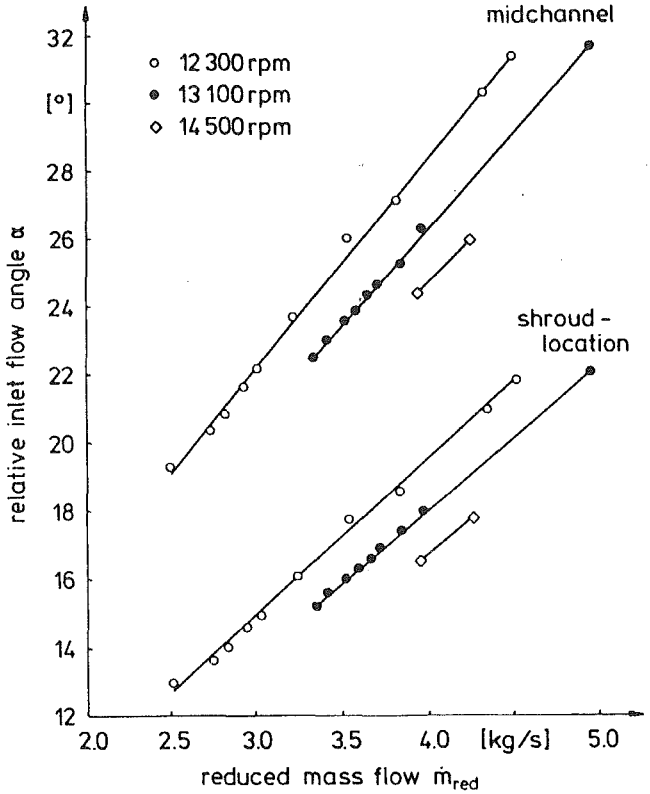

Fig. 23 Relative inlet flow angle at steady compressor operation for various rotational speed calculated from flow measurements

angle at inlet due to the alternative change of the velocity triangles at this location. V can be decomposed in a component in the circumferential and in the axial direction, according to Fig. 22 as follows

$$V = \frac{d_a}{d_t} = 2\pi f A \cos(2\pi f t)$$

$$V_u = V \cdot \sin \beta'$$

$$V_c = V \cdot \cos \beta'$$

As a consequence also different relative flow angles β occur, depending from the instantaneous values of V_c and V_u

$$\beta = \tan^{-1}\left(\frac{C_1 - V_c)}{U_1 - V_u}\right)$$

$$\beta = \tan^{-1}\left(\frac{C_1 - 2\pi f A \cos\beta' \cdot \cos(2\pi f t)}{U_1 + 2\pi f A \sin\beta' \cdot \cos(2\pi f t)}\right)$$

If β' represents the relative flow angle at no blade vibration, the change of the relative inlet flow angle due to the vibration is

$$\Delta\beta = \theta + \beta - \beta'$$

In this equation, the time-dependent changes of θ and of β' are not in-phase. Assuming a blade vibration stress amplitude ϵ of about 1.5 mm/m, as measured, for example, in Fig. 6, this results in a blade inlet variation θ of about 1.5 deg to both sides, according to the results in Fig. 21. Considering the described effect of velocity triangle variations during blade vibration, the term $\beta - \beta'$, being out-of-phase to θ, is added to the θ-value and results in a $\Delta\beta$, which is about 30 percent higher than θ. Concluding this example, 1.5 mm/m blade inlet amplitude during vibration is thus equal to a blade inlet angle amplitude of $\Delta\beta \approx 2.0$ deg and a peak-to-peak value of ≈ 4 deg.

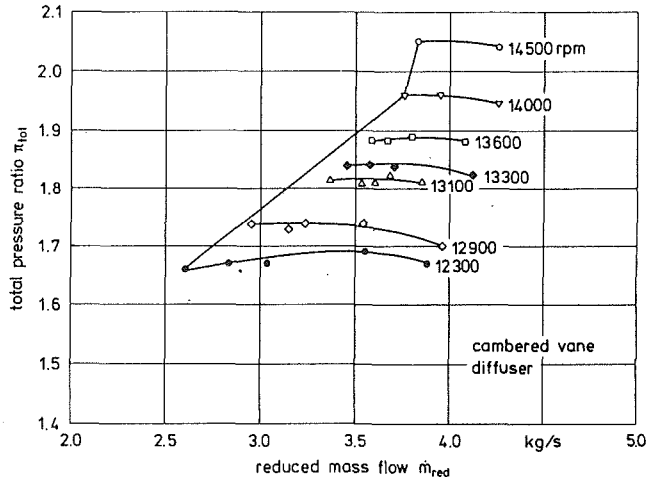

Fig. 24 Compressor chart with the reduction of the operating zone in the range of the dangerous blade vibration near surge at $n_{red} = 13{,}100$ rpm (cambered vane diffuser)

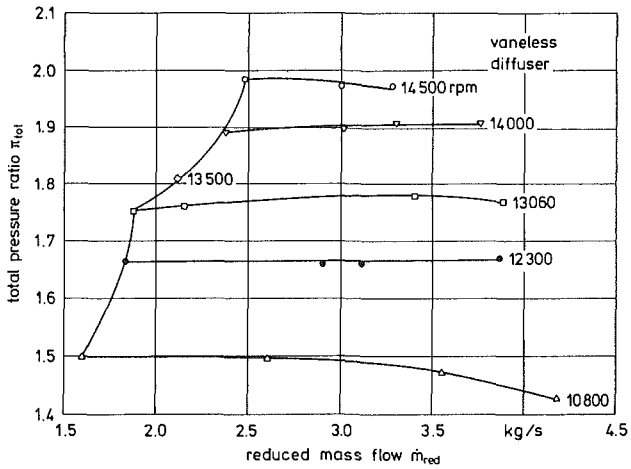

Fig. 25 Operating characteristics of the compressor with the vaneless diffuser in the chart without the reduction as shown in Fig. 24 in the range of the No. 4 engine-order No. 1 blade mode resonance near $n_{red} = 13{,}100$ rpm

Calculating now the flow angles at blade tip and midchannel from results of measurements assuming steady operation and plotting these values against the mass flow, the great influence of the blade vibration can be evaluated from Fig. 23. Assuming a blade inlet angle variation of $2 \times \Delta\beta$ for one cycle of the blade vibration, according to the example just mentioned, resulting in a change of the flow angle toward the blade inlet of the same value, this corresponding to mass flow conditions varying nearly $\Delta\dot{m} \approx 1.0$ kg/s at blade tip (shroud location).

This great chnge of the flow angle α toward the blade, together with the consideration of the corresponding mass flow values at steady operation, explains why steady compressor operation near surge is not possible in the range of dangerous blade vibration in the resonance zone with its center at $n_{red} = 13{,}100$ rpm, as it is shown in Fig. 24.

Throttling the compressor toward the surge-line, very low flow angles occur alternating during the vibration of the blade tip at inlet, initiating the surge cycle earlier, as it would happen at no vibration conditions. As it is demonstrated in Fig. 24, it has generally been taken into account that the surge line is considerably shifted toward higher mass flow in the blade resonance range, if the described blade/flow interactions occur in the unsteady flow operating zone. Compared to corresponding conditions on the same compressor with the vaneless dif-

fuser, where the phenomenon is not induced and blade resonance vibration stress values are low in the considered rotational speed range, the reduction of the operating zone in the chart cannot be observed, as shown in Fig. 25.

Conclusions

The mechanism of dangerous blade vibration in the resonance zone between the No. 4 engine-order and the No. 1 natural blade frequency, with its occurrence limited to the unsteady flow range has been investigated on a centrifugal compressor with a vaned diffuser. The major role in the mechanism of this blade excitation plays the flow in the impeller channel, characterized by strong reverse flow near the shroud from the impeller outlet upstream partly to the impeller inlet. These flow characteristics are controlled by the position of the blade inlet angle, leading to impeller outlet pressure conditions strongly dependent from the instantaneous position of the blade leading edge during vibration. Since the blades vibrate in-phase at particular constant locations on the circumference, a peripheral pressure distribution of alternative nonuniformity characterized by wave number 4 could be determined downstream and in the impeller being the cause for the intensification of the blade excitation and an accumulation effect. In addition, as an important practical aspect for the design of centrifugal compressors, the surge-line is shifted considerably toward higher mass flow in the range of dangerous blade resonance excitation and the operating zone of the compressor is reduced. No such phenomenon was found on the same compressor with a vaneless diffuser, obviously due to the fact, that reverse flow conditions in the impeller are different and not being so dependent from the instantaneous blade inlet angle.

Future work will be directed toward the question concerning the parameters, which determine the occurrence of the described blade/flow interactions in order to get some experience in the prediction of this dangerous phenomenon.

Acknowledgments

The research described in this paper was funded by the Deutsche Forschungsgemeinschaft (DFG) and the Forschungsvereinigung Verbrennungskraftmaschinen e.V. (FVV). The authors would like to thank them for their support. In addition, the advice of Dr. Jäger, Dr. Chen, and Professor Abdelhamid was appreciated in this work and is gratefully acknowledged. Many colleagues in the author's institute contributed to this investigation and in the completion of the paper. The authors wish to thank them for this support.

References

Abdelhamid, A. N., Haupt, U., and Rautenberg, M., 1987, "Unsteady Flow Characteristics in a Centrifugual Compressor With Vaned Diffuser," ASME Paper No. 87-GT-142.

Chen, Y. N., Haupt, U., and Rautenberg, M., 1987, "On the Nature of Rotating Stall in Centrifugal Compressors With Vaned Diffusers, Part II. Karman Vortices as the Controlling Mechanism," *Proceedings of the 1987 International Tokyo Gas Turbine Congress*, Vol. II, pp. 169–182, Paper No. 87-TOKYO-IGTC-23.

Chen, Y. N., Haupt, U., and Rautenberg, M., 1989, "The Vortex-Filament Nature of Reverse Flow on the Verge of Rotating Stall," ASME JOURNAL OF TURBOMACHINERY, Vol. 111, pp. 450–461.

Ellison, F. F., Miere, C. E., and Partridge, J. M., 1978, "Vane Vibration in Radial Flow Turbochargers," *Proc. I. Mech. E.*

Hagiwara, N., Yoneyama, M., Ishii, H., Matsuura, Y., and Kashiwabara, Y., 1987, "An Analysis of Blade Vibration of an Axial Flow Compressor During Rotating Stall," *Proceedings of the 1987 International Tokyo Gas Turbine Congress*, Vol. 111, pp. 349–355, Paper No. 87-TOKYO-IGTC-92.

Haupt, U., and Rautenberg, M., 1982, "Investigation of Blade Vibration of Radial Impellers by Means of Telemetry and Holographic Interferometry," ASME *Journal of Engineering for Power*, Vol. 104, No. 4, pp. 838–843.

Haupt, U., and Rautenberg, M., 1983b, "Blade Vibration on Radial Impellers Excited by Rotating Stall-Cells and During Surge," Paper No. 83-TOKYO-IGTC-124, International Tokyo Gas Turbine Congress.

Haupt, U., and Rautenberg, M., 1984a, "Blade Vibration Measurements on Centrifugal Compressor by Means of Telemetry and Holographic Interferometry," ASME *Journal of Engineering for Power*, Vol. 106, No. 1, pp. 70–78.

Haupt, U., and Rautenberg, M., 1984b, "Investigation of the Influence of the Nonuniformity of the Flow Downstream a Radial Impeller on the Excitation of Blade Vibration," presented at the Fifth International Conference for Mechanical Power Engineering, Cairo, Egypt.

Haupt, U., Bammert, K. and Rautenberg, M., 1985a, "Blade Vibration on Centrifugal Compressors—Fundamental Considerations and Initial Measurements," ASME Paper No. 85-GT-92.

Haupt, U., Bammert, K., and Rautenberg, M., 1985b, "Blade Vibration on Centrifugal Compressors—Blade Response to Different Excitation Conditions," ASME Paper No. 85-GT-93.

Haupt, U., and Rautenberg, M., 1985, "Investigation of Blade Vibration During Surge of a Centrifugal Compressor," presented at the 7th Symposium on Air Breathing Engines, Beijing, People's Republic of China.

Haupt, U., Abdelhamid, A. N., Kaemmer, N., and Rautenberg, M., 1986, "Excitation of Blade Vibration by Flow Instability in Centrifugal Compressors," ASME Paper No. 86-GT-283.

Haupt, U., Chen, Y. N., and Rautenberg, M., 1987a, "On the Nature of Rotating Stall on Centrifugal Compressors With Vaned Diffusers. Part 1: Detection of Reverse Flow," *Proceedings of the 1987 International Tokyo Gas Turbine Congress*, Vol. II, pp. 161–168, Paper No. 87-TOKYO-IGTC-22.

Haupt, U., Jin, D., Seidel, U., and Rautenberg, M., 1987b, "On the Mechanism of Blade Excitation Due to Surge on Centrifugal Compressors," *Proceedings of the 1987 International Tokyo Gas Turbine Congress*, Vol. 111, pp. 341–348, Paper No. 87-TOKYO-IGTC-91.

Haupt, U., Abdelhamid, A. N., and Rautenberg, M., 1988a, "Blade Excitation by Broadband Pressure Fluctuations in a Centrifugal Compressor," ASME JOURNAL OF TURBOMACHINERY, Vol. 110, No. 1, pp. 129–137.

Haupt, U., Seidel, U., Abdelhamid, A. N., and Rautenberg, M., 1988b, "Unsteady Flow in a Centrifugal Compressor With Different Types of Vaned Diffusers," ASME JOURNAL OF TURBOMACHINERY, Vol. 110, No. 3, pp. 293–302.

Haupt, U., Chen, Y. N., and Rautenberg, M., 1988c, "Rotating Stall in Radialverdichtern als umlaufende Karmansche Wirbelstraße," VDI-Tagung "Turbokompressoren im industriellen Einsatz," Essen, VDI-Bericht Nr.

Ishihara, K., and Funakawa, M., 1980, "Experimental Investigation on the Vibration of Blades Due to a Rotating Stall," *Bulletin of the JSME*, Vol. 23, No. 177, pp. 353–360.

Jäger, B., 1962, "Die Eigenfrequenzen einer Scheibe mit verwundenen Schaufeln," *Zeitschrift für Flugwissenschaften*, 10. Jahrg., Vol. 12, pp. 439–446.

Jäger, B., 1967, "Die Berechnung des Schwingungsverhaltens gedrungener Schaufeln nach der Schalen-theorie," VDI-Berichte No. 113, pp. 29–34.

Legendre, R., 1954, "Premiers éléments d'un calcul de l'amortissement aérodynamique des vibrations d'aubes de compresseurs," *La Recherche Aéronautique*, No. 37.

Leissa, A. W., 1981, "Vibrational Aspects of Rotating Turbomachinery Blades," *Applied Mechanics Reviews*, Vol. 34, No. 5, pp. 629–635.

Naguib, M., 1977, "Schwingungstechnische Entwicklung der Turbolader-Radialturbine," *Brown Boveri Mitteilungen* 4-77, pp. 205–209.

Pearson, H., 1953, "The Aerodynamics of Compressor Blade Vibration," *The Engineer*, Abstracts of the Fourth Anglo-American Aeronautical Conference.

An Euler Solution for Unsteady Flows Around Oscillating Blades

L. He
Whittle Laboratory,
Cambridge University,
Cambridge, United Kingdom

A time-marching Euler calculation for 2-D and quasi-3-D unsteady flows in oscillating blade rows is presented, based on a finite volume scheme with cell-vertex discretization in space and 2-step Runge–Kutta integration in time. Extra fluxes due to the deformation of the moving finite volumes are directly included in the conservation equations in the physical coordinate system. A zonal moving grid technique is used, in which only subregions near oscillating blades are moved to fit both the moving (blade) boundaries and fixed regions. For phase-shifted periodic conditions, the conventional "Direct Store" method is used as a basis for comparison. Two alternative methods to save computer storage are proposed and preliminary demonstrations of their usefulness are given in the present calculations. Calculated results for unsteady flows in an oscillating flat plate cascade are in good agreement with those from two well-established linear methods, LINSUB and FINEL. The unsteady pressure distribution and aerodynamic damping calculated by the present method for a turbine blade test case (Aeroelasticity Workshop Standard Configuration No. 4 cascade) agree well with the corresponding experimental data. Computations for an oscillating biconvex cascade in transonic flow conditions are performed, which show some strong nonlinear behavior of shock wave movement.

Introduction

One of the major concerns in the development of axial-flow turbomachinery is blade flutter, which has caused many problems with broken blades. In order to predict the blade flutter boundaries, calculations of unsteady aerodynamic forces (aerodynamic damping) in oscillating blades are required. So far, most of the available calculation methods for blade flutter are time linearized models in a global (e.g., Smith, 1971) or local sense (e.g., Verdon, 1982; Whitehead, 1982). In the latter case, a potential flow model is usually assumed. For subsonic flows without high loadings, the linear methods in some cases gave fairly good predictions compared with experiments. But under transonic conditions noticeable discrepancies have been observed (e.g., Bölcs and Fransson, 1986).

It is well known that, compared to the aeroelasticity condition of aircraft wings, the coupling between the aerodynamic and structural dynamic sides in blade flutter problems is usually very weak. Therefore, the Energy Method (Carta, 1967) has been widely used in predicting the flutter boundaries, in which the aerodynamic forces induced by a linear oscillating blading system, usually in its natural mode, are calculated. The point is, the unsteady flow field may not always respond to the linearly oscillated system, in a linear way. Strong nonlinear effects are quite likely to exist in unsteady transonic flows induced by oscillating blades at small amplitudes.

Recently, finite difference schemes (e.g., MacCormack, 1969; Beam and Warming, 1978) have been used to solve the Euler equations by the time-marching method for unsteady flows in oscillating blades (e.g., Joubert, 1984; Bölcs et al., 1987; Gerolymos, 1988). The time-marching Euler solutions can completely remove the time linearization and potential flow assumptions. But, an obvious extra expense is that much more computer time and storage are usually needed. So, in developing a time-marching method for blade flutter calculations, one should always pay attention to computing efficiency and/or simplicity, both of which are very important for engineering applications.

In addition to timewise accuracy of numerical schemes and boundary condition treatments, two aspects should be particularly addressed when using time-marching methods to solve unsteady flows induced by oscillating blades.

The first one is concerned with moving-grid techniques, which are required to ensure that computational grids always fit the blade surfaces when they are oscillated. For time-marching methods using finite difference schemes, this can be done by means of a transformation from the physical plane to a computational plane where rectangular meshes are fixed with time. The moving and deformed meshes in the physical plane are accounted for by updating the time-dependent transformation Jacobian at every time step. It is noted that the solution for the transformed Euler equations is more time-consuming and complicated, while the evaluation of the transformation Jacobian in time makes this feature more pronounced. On the other hand, the finite volume schemes (e.g., Denton, 1975, 1983; Jameson, 1981; Ni, 1981) have been widely used for steady flow calculations, and some of them have been extended

Contributed by the International Gas Turbine Institute and presented at the 34th International Gas Turbine and Aeroengine Congress and Exhibition, Toronto, Ontario, Canada, June 4–8 1989. Manuscript received at ASME Headquarters February 1, 1989. Paper No. 89-GT-279.

to calculating unsteady flows due to rotor-stator interactions (e.g., Hodson, 1984; Giles, 1987). One of the advantages, using the finite volume scheme, is that the discretization can be made directly in the physical coordinate system. This provides a possibility of dealing with the moving grid in a very simple way.

The second aspect is concerned with the conditions on the periodic boundaries of the blade passage. Usually upper and lower blades vibrate with an approximately constant phase difference (Inter-Blade-Phase-Angle, IBPA). When the IBPA is not zero, a phase-shifted periodic boundary condition has to be applied if the computation is performed in a single blade passage. A conventional way of implementing this phase-shifted condition is to store parameters on the periodic boundaries for a whole period, and update (or correct) current solutions according to the IBPA. This was first used by Erdos and Alzner (1978). This implementation method needs a large computer storage, especially for explicit numerical schemes in low-frequency conditions. In order to overcome similar problems in the calculations of unsteady flows, due to interactions between rotors and stators with unequal blade pitches, Giles (1987) proposed a method in which the computation time plane was inclined along the pitch direction. The inclination angle was determined in such a way that an ordinary periodic condition (zero phase shift) could be directly used and no extra computer storage was needed. However, because of the characteristics of the Euler equations, the inclination angle was restricted to certain values. An application of Giles' method to oscillating blade flow calculations was made by the present author, and the numerical tests showed a strong limitation on possible values of interblade phase angle and frequency (He, 1988). If this method is to be used for more general situations, multipassage computations (Giles, 1987) have to be performed.

The starting point of present work is a time-marching program for calculations of 2-D and quasi-3-D (with variations of radius and height of streamtube) unsteady flows due to rotor-stator interactions, which is under development by Hodson at the Whittle Laboratory. The basic scheme for the unsteady Euler equations consists of the cell-vertex finite volume discretization in space on a simple H mesh (Denton, 1983; Ni, 1981) and the 2-step Runge-Kutta integration in time (Jameson, 1981). The present paper describes an extension of the method to the calculations for unsteady flows induced by oscillating blades, with the main emphasis on the two aspects just mentioned.

Basic Discretization Scheme and Far-Field Boundary Condition

The Euler equations governing 2-D inviscid compressible flows can be written in a conservation form

$$\frac{\partial U}{\partial t}+\frac{\partial F}{\partial x}+\frac{\partial G}{\partial y}=0 \tag{1}$$

where

$$U=\begin{pmatrix}\rho\\ \rho u\\ \rho v\\ \rho E\end{pmatrix}\quad F=\begin{pmatrix}\rho u\\ \rho uu+p\\ \rho uv\\ (\rho E+p)u\end{pmatrix}\quad G=\begin{pmatrix}\rho v\\ \rho uv\\ \rho vv+p\\ (\rho E+p)v\end{pmatrix}$$

An integral form of equation (1) over a finite volume fixed with time is

$$\frac{\partial}{\partial t}\int\int U dxdy+\int (Fdy-Gdx)=1 \tag{2}$$

By using the cell-vertex discretization, fluxes are calculated from the computation points at corners of each cell. The calculated change of U in each cell is distributed equally to each corner point of the cell. In this scheme, the grid points on blade surfaces can be treated in the same manner as interior points. Therefore, the corresponding boundary conditions are remarkably simplified, especially when the surfaces are oscillated.

The time-marching process is performed by using the multistep Runge–Kutta integration (Jameson, 1981). Here only two steps are used, giving a second-order accuracy in time

$$U^{n+1/2}=U^n-0.5\frac{\Delta t}{\Delta s}\sum_{ij}(F_i\Delta y_i-G_j\Delta x_j-D_{ij})^n \tag{3a}$$

$$U^{n+1}=U^n-\frac{\Delta t}{\Delta s}\sum_{ij}(F_i\Delta y_i-G_j\Delta x_j-D_{ij})^{n+\frac{1}{2}} \tag{3b}$$

In equation (3), D_{ij} are dissipation terms, which are required for suppressing numerical oscillations. For the cell-centered scheme, Jameson (1981) proposed an adaptive dissipation form which consists of the second and fourth-order terms. However, it was found that if these adaptive dissipations were used directly for the cell-vertex scheme, some numerical difficulty could be involved in the pitchwise direction within the blade passage (He, 1988). So the author adopts a simple linear smoothing in the pitchwise direction, as used in Denton's method (Denton, 1983), while Jameson's adaptive dissipation is used in the streamwise direction.

At inlet and outlet boundaries with subsonic axial flow velocities, the 2-D approximate nonreflecting boundary conditions, proposed by Giles (1988), are used in the present calculations. For the inlet conditions, three time-dependent differential equations for perturbation characteristics (corresponding to three zero incoming waves) are centrally differenced in the pitchwise direction, and explicitly integrated simultaneously with the solution for interior cells. While at the outlet, one perturbation characteristics equation (corresponding to one zero incoming wave) is solved in the same way. In solving these equations, the phase-shifted periodic condition, as discussed later for the primitive variables, are applied for the perturbation characteristic variables on the

Nomenclature

A = amplitude
CP_1 = unsteady pressure coefficient
c = length of blade chord
f = frequency
k = reduced frequency = $\frac{\omega c}{U_{in}}$
M = Mach number
N_p = number of time steps in one period
P = pressure
P_0 = steady inlet stagnation pressure
R = gas constant
S = entropy
u = axial velocity
v = pitchwise velocity
ω = angular frequency
σ = interblade phase angle

Subscripts

L = lower blade
U = upper blade
in = inlet boundary
out = outlet boundary

Superscripts

0 = time-averaged value
n = number of time step; order of Fourier coefficients

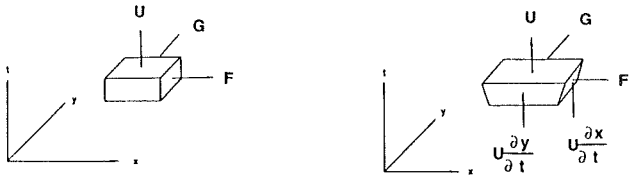

(a) Fixed in Time (b) Deformed (Moving) in Time

Fig. 1 Computational finite volume

intersecting points between the far-field and the periodic boundaries.

The use of the nonreflecting boundary conditions allows the inlet and outlet boundaries to be set closer to the blade row, and also gives a faster convergence rate.

Moving-Grid Method

Discrete Euler Equations for a Dynamic Finite Volume. As mentioned in the Introduction to this paper, for time-marching solutions, the computational grids have to be moved when blades are oscillated. By using a finite volume scheme, a moving grid can be easily realized in the physical coordinate system. This is briefly illustrated as follows.

Consider the primitive parameter U as a timewise vector. For the integral form of the equations over a fixed finite volume, Fig. 1(*a*), the change of the flux U across the finite area ΔS ($\Delta x \Delta y$) is equal to the net fluxes F across $\Delta x \Delta t$ and G across $\Delta y \Delta t$. When the finite area ΔS is changed in time, due to blade oscillations, the finite volume is deformed, as shown in Fig. 1(*b*). Now, there are two extra fluxes $U\frac{\partial x}{\partial t}$, $U\frac{\partial y}{\partial t}$, due to the inclination of corresponding areas along time. So the integral form of the Euler equations over a deformed moving finite volume becomes

$$\frac{\partial}{\partial t}\int\int U dx dy + \int\left[\left(F - U\frac{\partial x}{\partial t}\right)dy - \left(G - U\frac{\partial y}{\partial t}\right)dx\right] = 0 \tag{4}$$

In the two-step Runge–Kutta scheme, we have

$$U^{n+1/2} = U^n\left(2 - \frac{\Delta S^{n+1/2}}{\Delta S^n}\right) - 0.5\frac{\Delta t}{\Delta S^n}\sum_{ij}\left[\left(F - U\frac{\partial x}{\partial t}\right)_i \Delta y_i - \left(G - U\frac{\partial y}{\partial t}\right)_j \Delta x_j\right]^n \tag{5a}$$

$$U^{n+1} = U^n\left(2 - \frac{\Delta S^{n+1}}{\Delta S^n}\right) - \frac{\Delta t}{\Delta s^n}\sum_{ij}\left[\left(F - U\frac{\partial x}{\partial t}\right)_i \Delta y_i - \left(G - U\frac{\partial y}{\partial t}\right)_j \Delta x_j\right]^{n+1/2} \tag{5b}$$

Zonal Moving-Grid Technique. To solve equation (5), the movements of the grid points in time must be known. As in general blade flutter calculations, blade surface's harmonic vibration modes (frequency, amplitude and phase) are given as input. In order to save computing effort, a zonal moving-grid treatment is adopted, i.e., only the grids in local regions around oscillating blades are moved, as shown in Fig. 2. The deformations of cells in these zones are distributed in a first-order arithmetic progression, to fit both the fixed region and the moving blade boundaries. The number of cells moved can be chosen according to the vibration amplitudes of the blades, based on the requirement to guarantee numerical stability for the explicit scheme. In the present calculations, only one or two adjacent cells to the blades were moved. The procedure is quite simple.

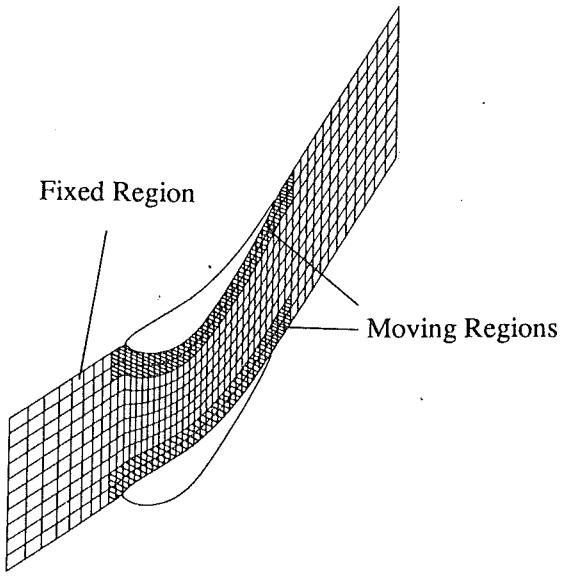

Fig. 2 Zonal moving grid

On blade surfaces, because the grids are moved with the blades, zero flow fluxes across the finite volume boundary on the surface are applied, while for the energy equation, work terms done by pressure due to the surface movement must be retained.

Phase-Shifted Periodic Condition

For a single blade passage with upper and lower periodic boundaries, as shown in Fig. 2, if the upper blade vibrates in an angular frequency ω and with a phase angle lead σ (IBPA) relative to the lower one, a phase-shifted periodic condition has to be applied

$$U_L(x,t) = U_u(x, t - \sigma/\omega) \tag{6}$$

Three different ways have been used to allow nonzero IBPA.

Direct Parameter Storage (Direct Store). The Direct Store method, first adopted by Erdos and Alzner (1978), has been widely used in the past, although it can be implemented in different manners. In the present case, four primitive variables at the periodic boundaries are stored for a period of oscillation. At every time step, parameters at the boundaries are updated by averaging the data obtained from the current time-marching solution and those stored, according to a given IBPA, and, at the same time, the stored parameters are corrected. The condition given in equation (6) can be completely satisfied, when the time-marching process converges to a periodic solution.

Because there is no other assumption than the phase-shifted condition itself, the Direct Store method can be used as long as the phase-shifted periodicity exists. Nevertheless, we have to face an unfavorable feature, large computer storage. For an explicit numerical scheme like that used here, the maximum time step is limited by the minimum spatial mesh size. Therefore, this feature becomes more pronounced when the frequency of blade vibration is lower. For example, on a mesh with 61 × 11 grid points the computer storage required by the Direct Store can be up to 2 ~ 5 mega-bytes in low-frequency conditions, while only 0.5 mega-bytes storage is needed if the IBPA is zero.

Sinusoidal Shape Correction. The first effort to avoid using large computer storage is started by assuming a form for the variations with time at the periodic boundaries.

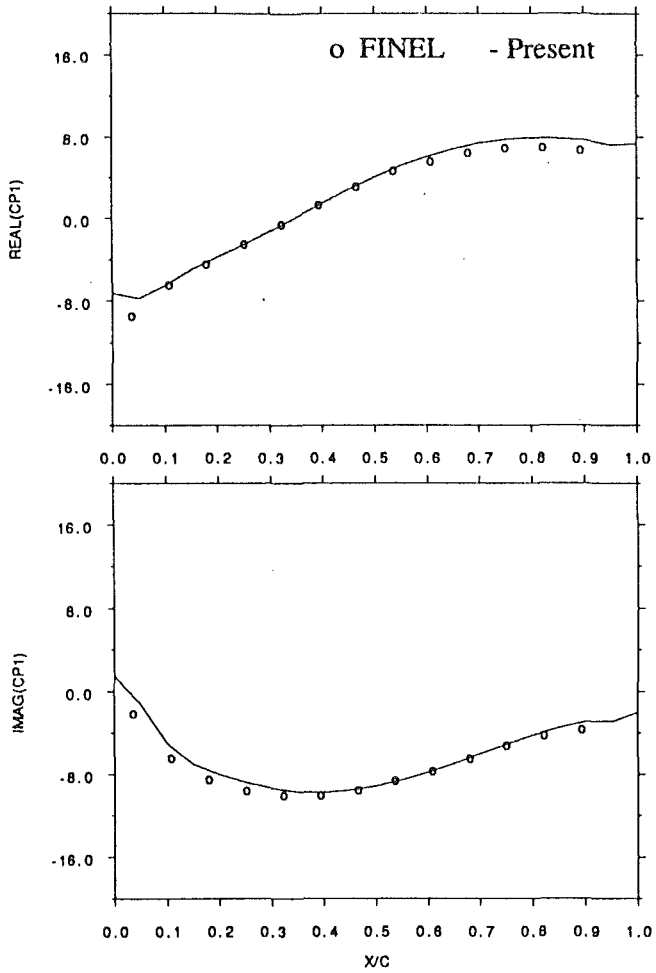

Fig. 3(a) Comparison of calculated real and imaginary parts of CP_1 for upper surface of a flat plate cascade (f = 1000 Hz)

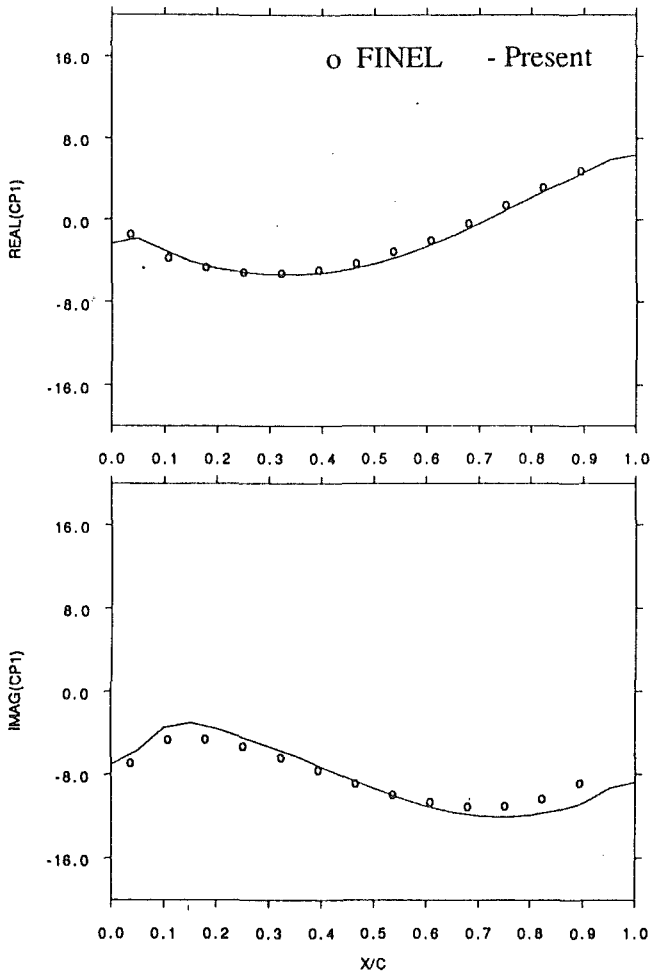

Fig. 3(b) Comparison of calculated real and imaginary parts of CP_1 for lower surface of a flat plate cascade (f = 1000 Hz)

For simplicity, parameters at the periodic boundaries are assumed to change in a sinusoidal form in time

$$f_L(x,t) = f^0(x) + A(x)\sin[\omega t + \phi(x)] \tag{7a}$$

$$f_u(x,t) = f^0(x) + A(x)\sin[\omega t + \phi(x) + \sigma] \tag{7b}$$

The corresponding derivatives in time are

$$\left(\frac{\partial f}{\partial t}\right)_L = \omega A\cos(\omega t + \phi) = d_L \tag{8a}$$

$$\left(\frac{\partial f}{\partial t}\right)_u = \omega A\cos(\omega t + \phi + \sigma) = d_u \tag{8b}$$

Solving these two equations, we get

$$\cos^2(\omega t + \phi) = \frac{\sin^2\sigma}{1 - 2\cos\sigma\left(\frac{d_u}{d_L}\right) + \left(\frac{d_u}{d_L}\right)^2} \tag{9}$$

The following procedure is used to implement the phase-shifted periodic condition governed by equations (7)–(9).

Step 0: Make an initial guess for $f^0(x)$ and $A(x)$ (usually $f^0(x)$ from steady solution and $A(x) = 0$). Then start the unsteady solution.

Step 1: At time step n, update the primitive variable $f(x, t)$ on the periodic boundary points from the current solution.

Step 2: Work out d_u and d_L using $f(x, t)$ from the current time step and that from a previous time step. Then store $f(x, t)$.

Step 3: Use d_u and d_L to get the phase and amplitude from equations (9) and (8), which are used to correct the previous phase and amplitude. The current solution is then corrected by using equation (7).

After each period, $f^0(x)$ can be corrected using the latest time-averaged value.

In this way, we correct the variables on the periodic boundaries at almost every time step [there might be some steps at which we can not get a solution from equation (9)]. An important thing to note is that only the solution at one previous time step needs to be stored for calculating the time derivatives d_u, d_L. Therefore, the computer storage needed is greatly reduced.

High-Order Shape Correction. The method just described is only suitable for situations where nonharmonic effects are negligible. In some conditions, such as transonic flows with unsteady shock wave movement, the harmonic distribution in time is a questionable assumption. To relax this limitation, a more general method is proposed.

At the lower and upper periodic boundaries, we write an Nth-order timewise Fourier series for primitive variables as

$$f_L(x,t) = f^0_L(x) + \sum_{n=1}^{N}[A^n_L(x)\sin(n\omega t) + G^n_L(x)\cos(n\omega t)] \tag{10a}$$

$$f_U(x,t) = f^0_U(x) + \sum_{n=1}^{N}[A^n_U(x)\sin(n\omega t + \phi) + B^n_U(x)\cos(n\omega t + \phi)] \tag{10b}$$

In this case, the phase-shifted condition manifests itself as

$$\phi = \sigma \tag{11a}$$

$$f_L^0(x) = f_U^0(x) \tag{11b}$$

$$A_L^n(x) = A_U^n(x) \tag{11c}$$

$$B_L^n(x) = B_U^n(x) \tag{11d}$$

The procedure of implementing equations (10) and (11) is similar to that for the Sinusoidal Shape Correction. The different parts are as follows:

Step 2: Use $f(x, t)$ to do the timewise integrations for the Fourier coefficients (e.g., at the lower boundary)

$$A_L^n(x) = \frac{\omega}{\pi} \sum_1^{Np} f_L(x,t)\sin(n\omega t)\Delta t \tag{12a}$$

$$B_L^n(x) = \frac{\omega}{\pi} \sum_1^{Np} f_L(x,t)\cos(n\omega t)\Delta t \tag{12b}$$

Step 3: The current solution is corrected using equation (10) with previous coefficients.

After each period of integration new values of the coefficients can be obtained from equation (12). Then the coefficients in equation (10) are updated by the new values, associated with equation (11).

For situations of general interest, the first few orders of Fourier coefficients are sufficient to approximate the timewise distributions; therefore, the whole implementation needs only minor extra computer storage. Because the timewise integrations for Fourier coefficients are very straightforward, the computer time is not greatly increased. In the present calculations, Fourier coefficients up to the 4th order were used. The total increase in CPU time was about 15 percent compared to the Direct Store method.

Numerical Results

Oscillating Flat Plate Cascade. The first check on the present method has been made by calculating unsteady subsonic flows induced by an oscillating flat plate cascade. For this case, the nonlinear effects are negligible. Therefore, the calculated results are compared with those using two well-established programs based on linear theories, LINSUB (Smith, 1971), and FINEL (Whitehead, 1982).

The cascade is of chord 0.076 m; solidity 1.3; stagger angle 0 deg. Parameters of inlet flow are Mach number 0.65; incidence 0 deg. It is oscillated with IBPA 90 deg, bending amplitude 1 percent chord.

Convergence of unsteady solutions can be estimated by

$$\text{Max}\left|\frac{u^n - u^{n-Np}}{u^n}\right| < \delta$$

A convergent solution, with $\delta = 0.001$, can be usually achieved by 5 ~ 10 periods of time-marching solution. When the solution converges, the amplitude and phase of the parameters are determined by taking a Fourier transformation.

First, the periodic condition was treated in the conventional way, Direct Store. The calculated unsteady pressure coefficients distributions in a relatively high-frequency condition (f = 1000 Hz, k = 2.285), are shown in Fig. 3. The real and imaginary parts correspond to in-phase and out-phase components, respectively. Overall comparisons with the results by FINEL are very good. The discrepancy near leading edge could be due to the singularity at the leading edge point.

Similar results were obtained in a lower frequency condition (f = 250 Hz, k = 0.57), as shown in Fig. 4. Calculated unsteady pressure jumps across blade are compared with those using LINSUB. For this case, the first alternative method, "Sinusoidal Shape Correction," for the phase-shifted condition also was used. It can be seen by the comparison that this simple

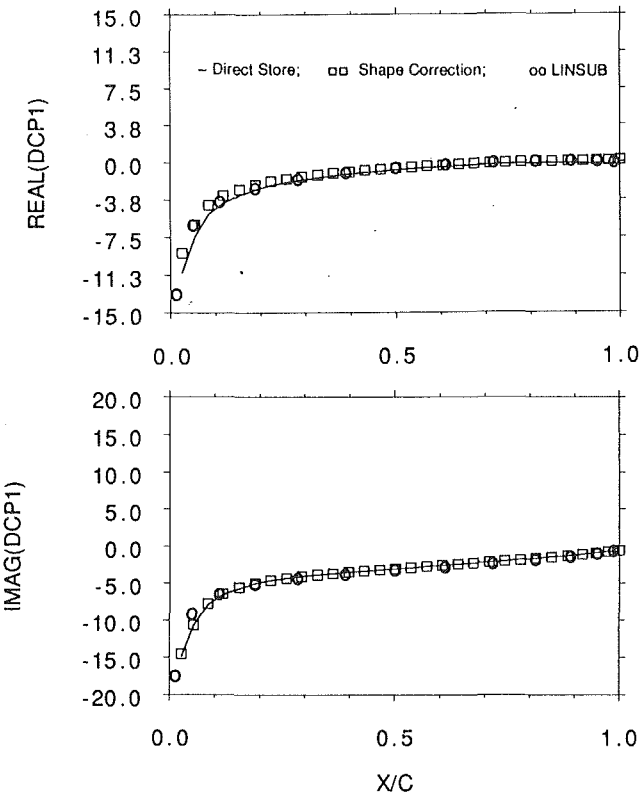

Fig. 4 Comparison of calculated real and imaginary parts of DCP_1 distributions for a flat plate cascade (f = 250 Hz)

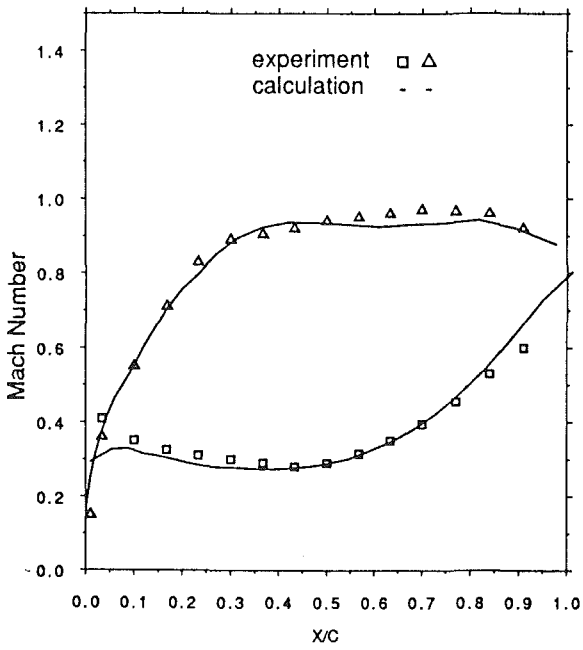

Fig. 5 Steady Mach number distribution for a turbine cascade

alternative method worked quite well. While for this calculation only about 1/4 of computer storage required by using the Direct Store was needed by using the Sinusoidal Shape Correction. It also should be mentioned that the foregoing calculations were carried out on a mesh with 61 × 11 grid points. Greater savings can be obtained for calculations using finer meshes.

Standard Configuration No. 4 Cascade (Aeroelasticity Workshop). This case is an annular turbine cascade flow for which experimental data are available. In the experiment, the

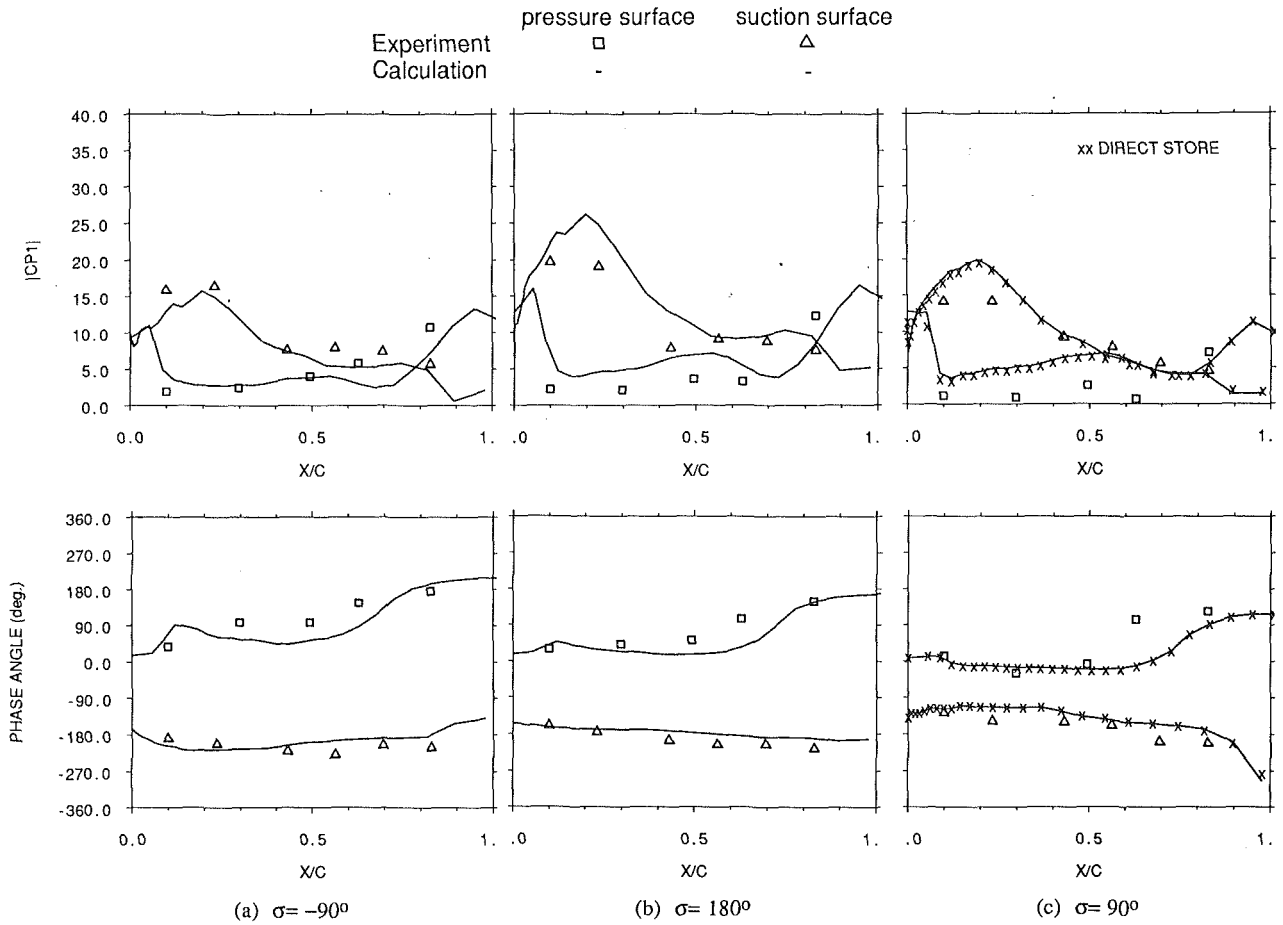

Fig. 6 Amplitude and phase of first harmonics of unsteady pressure coefficients at different IBPA

cascade was oscillated in a bending mode under high subsonic and transonic flow conditions. Detailed description of the geometry and working conditions was given by Bölcs and Fransson (1986). The present calculations were performed for different IBPA with a constant outlet Mach number (M_{out} = 0.9).

In order to match the experimental inlet and outlet flow conditions, the streamtube height (quasi-3-D effect) was linearly varied along the streamwise direction with a ratio (H_{out}/H_{in}) 1.1. The calculated steady Mach number distribution is compared with the experimental one in Fig. 5.

The phase-shifted condition was implemented by using the second-order Shape Correction for the unsteady calculations.

The calculated phase and amplitude distributions of the first harmonic unsteady pressure coefficient are shown in Fig. 6 for IBPA −90°, 180°, 90°. At the condition of −90 deg, the comparison with the experiment is quite good for both amplitude and phase angle. While at conditions of 180 and 90 deg, the amplitudes in the front part of suction surface were overpredicted. A calculation also was made for zero IBPA, in which very low amplitude levels, as found in the experiment, were predicted. The small amplitudes make it difficult to compare the phase distributions.

In Fig. 6(*c*), results calculated by using the Direct Store also are presented. The comparison shows that the Shape Correction method can work as well as the Direct Store and, in this case, only about 1/3.5 of the computer storage was needed for the former.

Figure 7 shows the variation of aerodynamic damping coefficients (nondimensional aerodynamic work per cycle of oscillation, as defined by Bölcs and Fransson (1986)) with IBPA. The sinusoidal trend was well predicted by the present method.

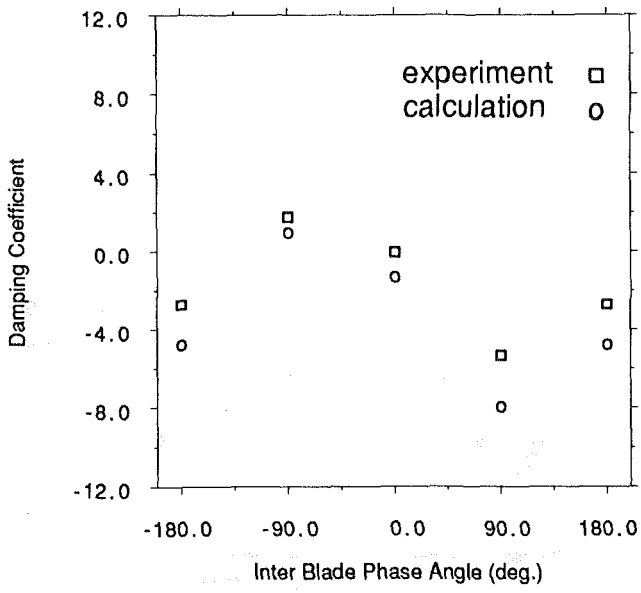

Fig. 7 Comparison of aerodynamic damping with IBPA

The larger differences between the experiment and calculation at IBPA, 90 and 180 deg are due to the amplitudes being overpredicted.

In spite of some discrepancies with the experiment, the aforementioned comparisons are quite encouraging, considering the state of the art of both computations and experiments on oscillating cascade flows (Bölcs and Fransson, 1986).

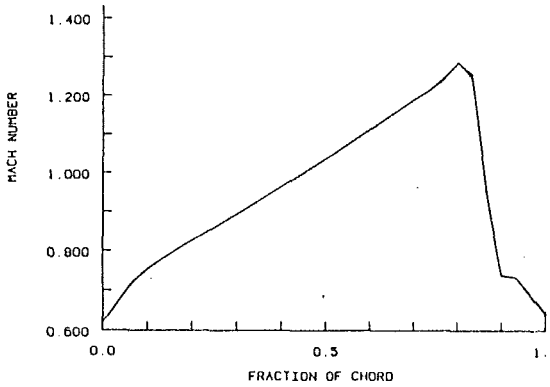

(a) Mach Number along Chord

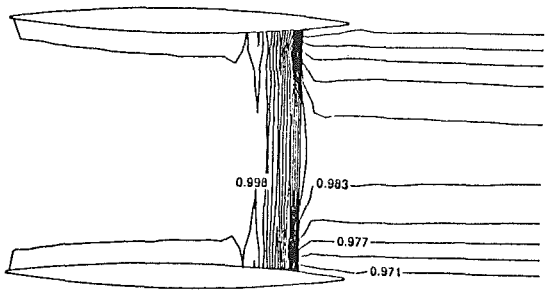

(b) Entropy Contour

Fig. 8 Steady flow distributions (P_{out}/P_0 = 0.708)

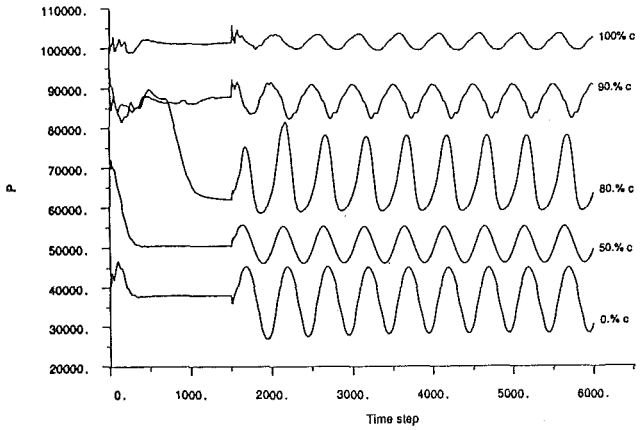

Fig. 9 Convergence history of static pressure at different locations on blade surface

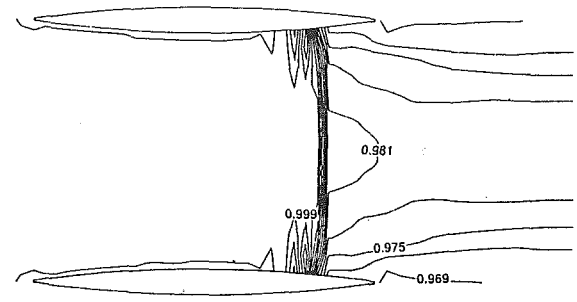

(a) $\omega t = 0$

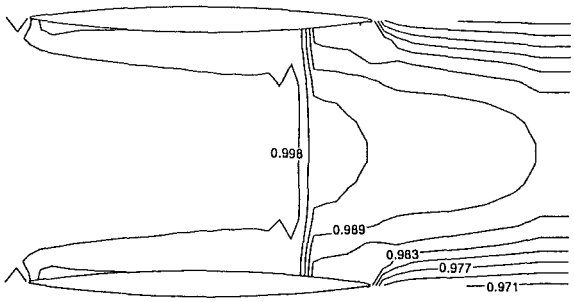

(b) $\omega t = \pi/2$

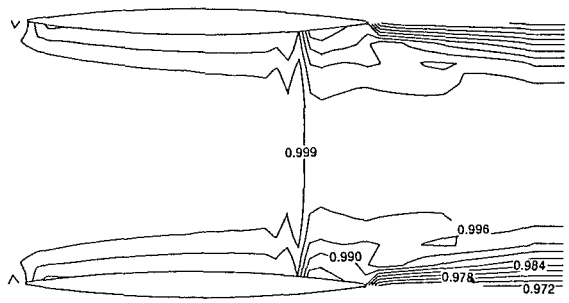

(c) $\omega t = \pi$

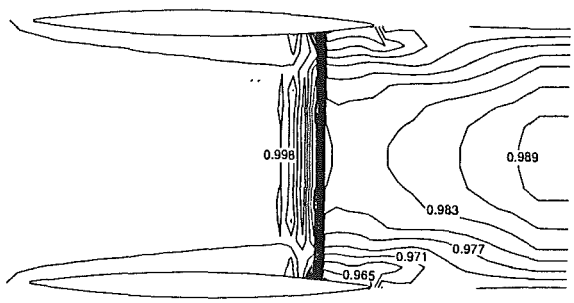

(d) $\omega t = 3\pi/2$

Fig.10 Entropy contours at different moments in one period

Oscillating Transonic Biconvex Cascade. In order to test the ability of present method handling unsteady transonic flows, an oscillating biconvex cascade flow with a shock wave in the passage was calculated.

The geometry of cascade is: stagger angle 0 deg; chord 0.1524 m; relative thickness 7.6 percent; solidity 1.3.

At the inlet condition with Mach number 0.68 and incidence 0 deg, the cascade was choked with a shock wave in the divergent part of the cascade. The location of the steady shock wave is determined by the downstream back pressure. The present calculations were performed in two different back pressure conditions:

Case A: $\frac{P_{out}}{P_0}$ = 0.708 (a strong shock at about 85 percent chord).

Case B: $\frac{P_{out}}{P_0}$ = 0.731 (a supersonic bubble near the throat).

When the steady state was established, the cascade was set to undertake a torsion motion around its leading edge. The angular displacement of the lower blade was given by

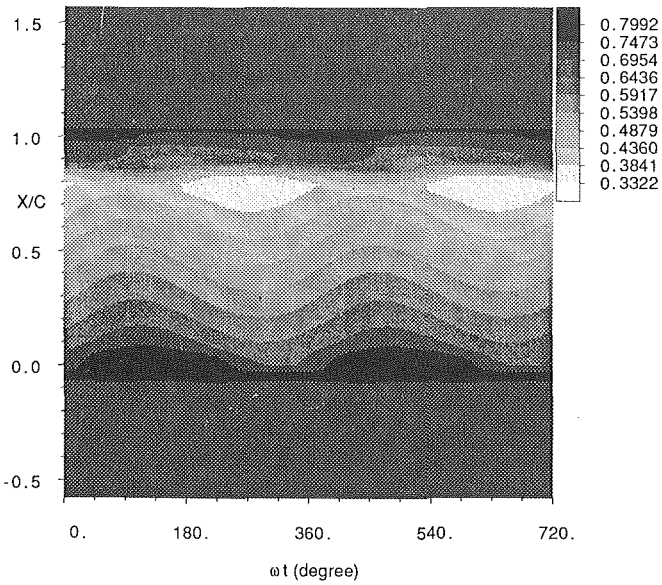

Fig. 11 Space-time contour of relative static pressure (P/P_0) in two periods (P_{out}/P_0 = 0.708; σ = 180 deg)

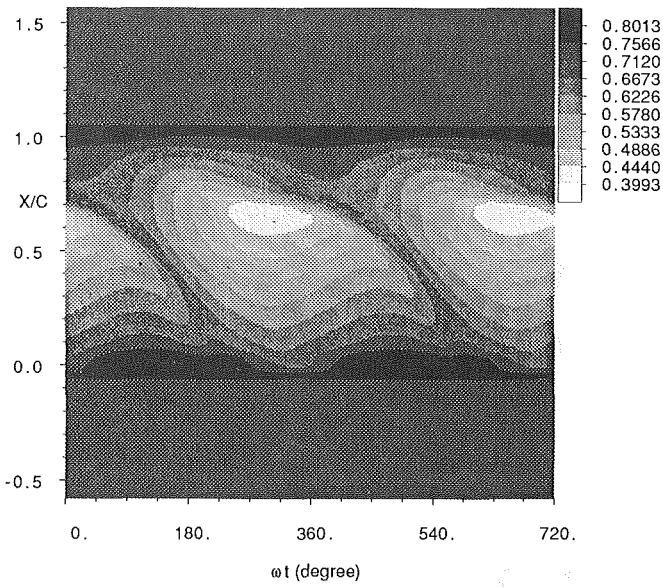

Fig. 13 Space-time contour of relative static pressure (P/P_0) in two periods (P_{out}/P_0 = 0.731; σ = 180 deg)

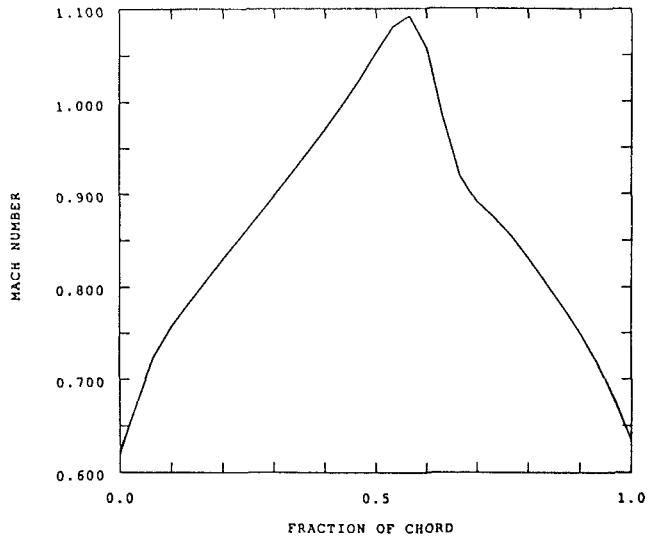

Fig. 12 Steady Mach number distribution (P_{out}/P_0 = 0.731)

$$\alpha = A_\alpha \sin(\omega t)$$

with the anticlockwise as the positive direction. For both cases, the same oscillation amplitude and frequency were specified as follows:

$A_\alpha = 2$ deg
$f = 300$ Hz; $(k = 1.3)$

In Case A, the upper and lower blades were vibrating symmetrically. So the IBPA is 180 deg. While in case B, both 90 deg and 180 deg IBPA were used.

Case A: Figure 8 shows the calculated steady Mach number distribution and entropy contour in terms of exp(s/R), which can be usefully compared with the unsteady results given later.

The unsteady calculations were performed by using the fourth-order Shape Correction. The convergence history of static pressure at different locations of blade surface is given in Fig. 9. (The scale is true for all of the data but the absolute value is only correct for those at 50 percent chord.) After the first period of vibration, well-defined periodic shapes can be observed at all the locations except for that at 80 percent chord, where the shock wave movement took a longer time to achieve a periodic solution.

Figure 10 shows entropy contours at 4 instants in the 10th period of oscillation: (*a*) $\omega t = 0$; (*b*) $\omega t = \pi/2$; (*c*) $\omega t = \pi$; (*d*) $\omega t = 3\pi/2$.

It seems that the unsteady behaviors of flow during the first part of the period can be roughly traced in a quasi-steady way. The distribution of the flow field at time (*a*) is similar to that in the steady state (Fig. 8). While from time (*a*) to (*b*), because of the increased angular displacement, the rear part of the cascade became less divergent. Therefore, the velocity in front of the shock wave was decreased and also the pressure behind it was increased to match the downstream condition and trailing edge pressure disturbance from neighboring blade passages. Both of these two factors made the shock move upstream. At the same time, it was weakened. The changed circulation of the cascade, at this time, manifested itself as vorticity shedding at the trailing edge to maintain the Kutta condition, which can be observed in Fig. 10(*b*).

However, the quasi-steady explanation cannot be carried far. The vorticity shedding process lasted for at least 1/4 period, Fig. 10*c*, and the distribution at time (*c*) is quite different from the steady state. The phase-lag feature also is reflected by the contour at time (*d*), which is similar to that at time (*a*).

The space-time contour of relative static pressure along the lower blade surface distance in two successive periods is plotted in Fig. 11. Here $x/c < 0$ and $x/c > 1$ correspond to the distances from leading edge to inlet boundary and from trailing edge to outlet boundary, respectively. It can be seen from the plot that the shock wave movement was confined in a small range over the blade surface, while in the region which was not disturbed by the moving shock, well-established pressure waves were almost in the same phase.

Case B: Steady surface Mach number distribution is shown in Fig. 12. In this case, a supersonic bubble occurring near the throat was ended by a very weak shock.

First, in order to make a comparison with Case *A*, the unsteady calculation was performed with 180 deg IBPA and also the fourth-order Shape Correction was used. The *S–T* static pressure contour is shown in Fig. 13. It is interesting to note that, in this case, the shock wave moved in quite a different way from that in Case *A*. When the shock arrived at the throat, it didn't decay into a complete compression wave, as expected

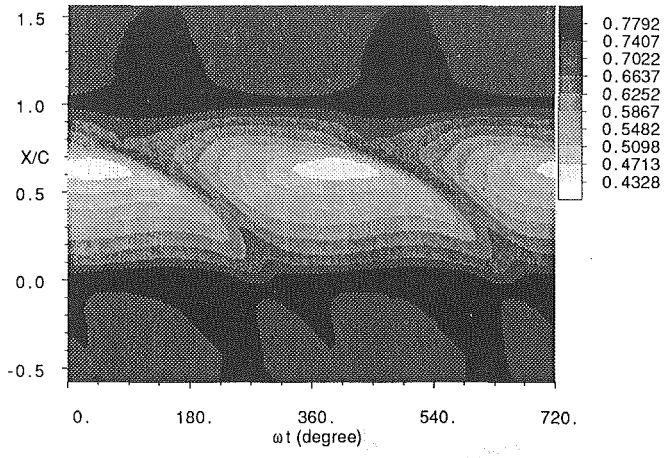

Fig. 14 Space-time contour of relative static pressure (P/P_0) in two periods (4th-order Shape Correction)

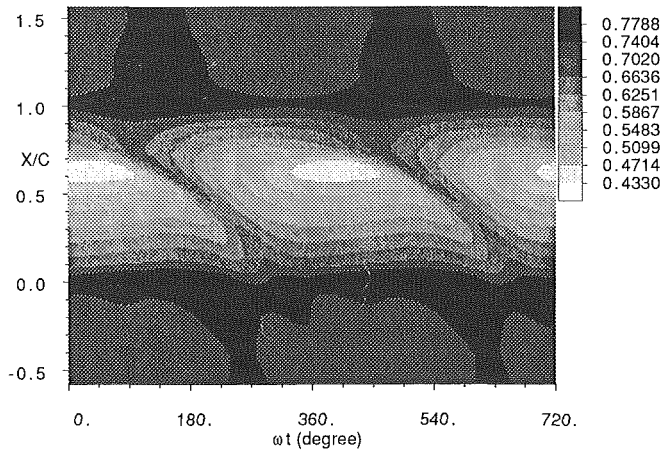

Fig. 15 Space-time contour of relative static pressure (P/P_0) in two periods (Direct Store)

in a quasi-steady way. Instead, it moved into the subsonic region and this upstream movement was accelerated, viewed in an absolute system. Finally, the shock became a compression wave and disappeared around the leading edge. The whole process was quite nonlinear, and the pressure waves, especially in the subsonic region, were highly distorted.

The result for 90 deg IBPA, using the fourth-order Shape Correction, is shown in Fig. 14, in which a similar feature was observed. To compare the methods used for the phase-shifted periodic condition, a calculation with the same IBPA (90 deg) using the Direct Store was also performed, as shown in Fig. 15. The general agreement between the results using the two methods for the phase-shifted periodicity is quite good, though there are some detailed differences. The upstream and downstream flow fields were well described by the fourth-order Shape Correction. If more detailed far-field flow structure is pursued, some higher-order Fourier components should be included.

Summary

A finite volume scheme for the time-marching Euler solution has been adopted to calculate unsteady flows induced by oscillating blades. The extra fluxes, due to dynamic finite volumes, are included directly in the integral form of the governing equations in the physical coordinate system. A zonal moving-grid technique is used to enhance computing efficiency.

For the phase-shifted periodicity condition, two methods to reduce the large computer storage required by the conventional method have been proposed and have shown their usefulness in the present calculations. The author feels that the applications of these methods to more general situations, such as calculations of unsteady flows, due to rotor-stator interactions, could be just as effective as in the present cases.

The present approach has been checked by comparing the calculated results with those by two linear methods for an oscillating flat plate cascade flow and some experimental data for a turbine cascade. The ability to handle unsteady transonic flows has been preliminarily demonstrated by calculations for an oscillating biconvex cascade with a shock wave moving in passage, which showed some strong nonlinear effects.

Acknowledgment

The author is indebted to Dr. J. D. Denton for his helpful and constructive supervision on the present work, and to Dr. H. P. Hodson for his supply of the development program. The research reported herein has been financially sponsored by Rolls-Royce plc. The author wishes to thank Dr. P. Stow, A. Cargill, and A. Suddhoo (Theoretical Science Group, Rolls-Royce, Derby) for their continuous interest, advice, and support to the present work.

References

Bölcs, A., and Fransson, T. H., 1986, "Aeroelasticity in Turbomachines—Comparison of Theoretical and Experimental Cascade Results," *Communication du Laboratoire de Thermique Appliquée et de Turbomachines*, No. 13, Lausanne, EPEL.

Bölcs, A., Fransson, T. H., and Platzer, M. F., 1987, "Numerical Investigation of Unsteady Compressible Flow Through Nozzles and Cascades," in: *Proceedings of the 4th Symposium on Unsteady Aerodynamics and Aeroelasticity of Turbomachines and Propellers*, Aachen, Federal Republic of Germany.

Carta, F. O., 1967, "Coupled Blade-Disk-Shroud Flutter Instabilities in Turbojet Engine Rotors," ASME *Journal of Engineering for Power*, Vol. 89, No. 3.

Denton, J. D., 1975, "A Time-Marching Method for Two- and Three-Dimensional Blade to Blade Flows," A.R.C. R&M No. 3775.

Denton, J. D., 1983, "An Improved Time-Marching Method for Turbomachinery Flow Calculations," ASME *Journal of Engineering for Power*, Vol. 105, pp. 514-524.

Erdos, J. I., and Alzner, E., 1978, "Computation of Unsteady Transonic Flows Through Rotating and Stationary Cascade," NASA Cr-2900.

Gerolymos, G. A., 1988, "Numerical Integration of the 3D-Unsteady Euler Equations for Flutter Analysis of Axial Flow Compressors," ASME Paper No. 88-GT-255.

Giles, M., 1987, "Calculation of Unsteady Wake Rotor Interaction," AIAA Paper No. 87-0006.

Giles, M., 1988, "Non-reflecting Boundary Conditions for the Euler Equations," MIT Report, CFDL-TR-88-1.

He, L., and Zhou, S., 1987, "An Euler Solver for Oscillating Cascade Flow With Inlet Perturbations," in: *Proceedings of the 4th Symposium on Unsteady Aerodynamics and Aeroelasticity of Turbomachines and Propellers*, Aachen, Federal Republic of Germany.

He, L., 1988, "Euler and Integral Boundary Layer Solutions for Unsteady Flows Around Oscillating Cascade," First Year Report, Cambridge University Engineering Department, United Kingdom.

Hodson, H. P., 1984, "An Inviscid Blade-to-Blade Prediction of a Wake-Generated Unsteady Flow," ASME Paper No. 84-GT-43.

Jameson, A., Schmidt, W., and Turkel, E., 1981, "Numerical Solutions of the Euler Equation by Finite Volume Method Using Runge-Kutta Time-Stepping Scheme," AIAA Paper No. 81-1259.

Joubert, H.,1984, "Supersonic Flutter in Axial Flow Compressor," in: *Proceedings of the 3rd Symposium on Unsteady Aerodynamics and Aeroelasticity of Turbomachines and Propellers*, Cambridge, United Kingdom.

MacCormack, R. W., 1969,"The Effect of Viscosity in Hypervelocity Impact Cratering," AIAA Paper No. 69-354.

Ni, R. H., 1981, "A Multiple Grid Scheme for Solving the Euler Equation," AIAA Paper No. 81-1025.

Smith, S. N., 1971, "Discrete Frequency Sound Generation in Axial Flow Turbomachines," PhD Dissertation, Cambridge University Engineering Department, United Kingdom.

Verdon, J. M., and Caspar, J. R., 1982, "Development of a Linear Unsteady Aerodynamics for Finite-Deflection Cascades," *AIAA Journal*, Vol. 20, No. 9.

Whitehead, D. S., 1982, "The Calculations of Steady and Unsteady Transonic Flow in Cascades," Cambridge University Engineering Department, Report CUED/A-Turbo/TR118, United Kingdom.

Self-Excited Oscillation of Transonic Flow Around an Airfoil in Two-Dimensional Channels

K. Yamamoto
Researcher,
Aeroengine Division,
National Aerospace Laboratory,
Chofu, Tokyo, Japan

Y. Tanida
Professor,
Research Center for Advanced Science and Technology,
University of Tokyo,
Tokyo, Japan

A self-excited oscillation of transonic flow in a simplified cascade model was investigated experimentally, theoretically and numerically. The measurements of the shock wave and wake motions, and the unsteady static pressure field predict a closed-loop mechanism, in which the pressure disturbance that is generated by the oscillation of boundary layer separation propagates upstream in the main flow and forces the shock wave to oscillate, and then the shock oscillation disturbs the boundary layer separation again. A one-dimensional analysis confirms that the self-excited oscillation occurs in the proposed mechanism. Finally, a numerical simulation of the Navier–Stokes equations reveals the unsteady flow structure of the reversed flow region around the trailing edge, which induces the large flow separation to bring about the antiphase oscillation.

Introduction

It is known that transonic flow often exhibits self-excited flow oscillation when the boundary layer separates at the shock foot. The self-excited oscillation, which is caused by the interaction between large-scale flow separation and shock wave, was studied by several researchers on isolated airfoil (Finke, 1975; McDevitt et al., 1976; Seegmiller et al., 1976; Gallus et al., 1986) and diffusers (Bogar, 1986; Maier et al., 1987). Large pressure fluctuation, which is induced by the shock oscillation, acts as the periodic force exciting the airfoil vibration or limits the operating range of diffusers. However, the mechanism of the phenomenon has not been understood enough yet, because the structures of the unsteady large separation and the unsteady shock-boundary-layer interaction look very complicated.

A similar phenomenon also can be expected to occur even in a cascade, because the blade passage flow rapidly changes its velocity, pressure, etc., so the boundary layer separates easily. In fact, Araki et al. (1983) reported a self-excited flow oscillation in a turbine cascade. The characteristics of the self-excited flow oscillation in cascades are not easily deduced from the results of airfoils or diffusers due to its complex flow boundaries.

In this study, we attempt to explain the fundamental mechanism of the self-excited flow oscillation in a cascade. To avoid the complexity, a simplified cascade model is employed. This model is a single biconvex circular-arc airfoil installed between two parallel endwalls. As is similar to the isolated airfoil case, the self-excited oscillation is observed. Figure 1 shows the instantaneous flowfield taken by a spark light source about every 90 deg in one cycle of oscillation. The shock waves and the separated boundary layer oscillate 180 deg out-of-phase between the upper and lower side of the airfoil. In a related experiment by the present authors (Yamamoto and Tanida, 1987), detailed measurements of the static pressure in the flowfield and the separated boundary layer behavior were carried out, and a preliminary consideration about the mechanism of the self-excited oscillation was made.

The present study consists of the experimental, theoretical, and numerical investigation. In the experiment, the measurements of the shock wave frequency and amplitude are made to clarify the characteristics of this oscillation, and the essential results of the pressure and boundary layer measurements are extracted from the previous experiment (Yamamoto and Tanida, 1987). Next, a simple theoretical analysis is made and compared with the experimental results. Finally, a numerical simulation by the two-dimensional Navier–Stokes equations is made for qualitative understanding of the unstable flow structure of the separation region, which is not easily measured in experiments.

Experiment

Experimental Apparatus and Procedure. The experiments were carried out in a blow-down-type wind tunnel. Figure 2 shows the test section of the wind tunnel. It has a 540 mm length and a 75 mm × 75 mm square section. A biconvex circular-arc airfoil of 75 mm chord and 75 mm span was installed at the center of the channel. Two kinds of airfoil, 10 percent and 12 percent thickness, were used to compare the effect of the airfoil surface curvature, although experiments were mostly made on the 10 percent one.

The Reynolds number cannot be controlled in this wind tunnel and is about 1.0×10^6. The boundary layer on the smooth airfoil surface is naturally kept laminar up to the shock wave position, and the interaction with the shock wave pro-

Contributed by the International Gas Turbine Institute and presented at the 34th International Gas Turbine and Aeroengine Congress and Exhibition, Toronto, Ontario, Canada, June 4–8, 1989. Manuscript received at ASME Headquarters January 4, 1989. Paper No. 89-GT-58.

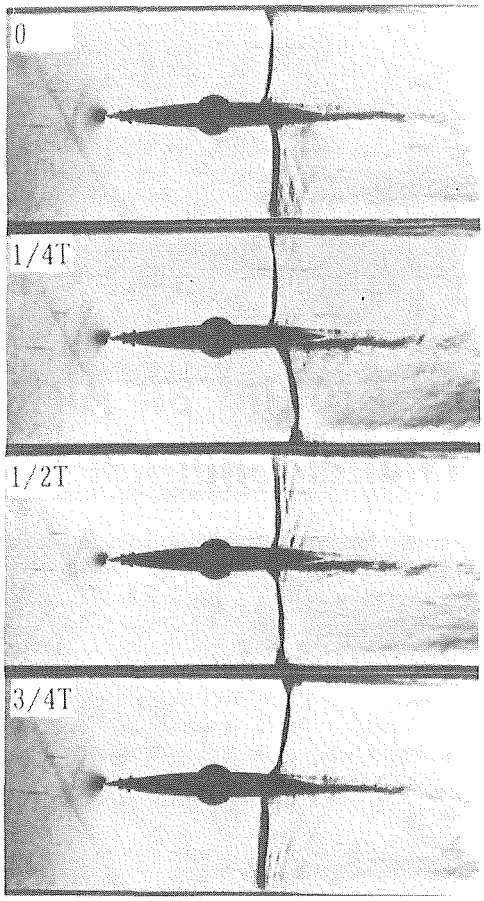

Fig. 1 Schlieren photographs of the instantaneous flowfield exhibiting self-excited oscillation of shock wave; P_b/P_0 = 0.665, 10 percent thickness, turbulent boundary layer

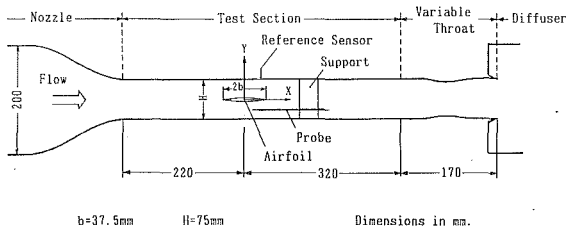

Fig. 2 Test section

duces a complex flowfield, such as shown by Gallus et al. (1987). In order to compare the boundary layer effects on the flow oscillation, the boundary layer was made turbulent by a 2 mm wide thin strip put on the surface at 7.0 mm distance from the leading edge.

Downstream of the airfoil, a static pressure probe is installed for the measurement of unsteady static pressure field. This probe is carried around the airfoil by an automatic traverse unit, which is placed on the test section. Rubber sponge is stuffed in the gap between probe support and walls to prevent the leakage of air. Inside this probe a semiconductor pressure sensor (Kulite XCS-062) is inserted and placed just behind the static holes to obtain good frequency response. A variable throat is set up at the exit of the test section to prevent the upstream propagation of the disturbance occurring in the diffuser section.

The shock wave motion and the boundary layer behavior are measured from the Schlieren flow visualization. The Schlieren image is taken by a video camera and saved in a digital memory unit after A/D conversion. The flow oscillation is too high (typically 600 Hz) to be scanned by a conventional video camera, so that the RETICON MC9128 modular camera was utilized for this purpose. This camera operates not only as a normal area camera, but also as a line camera with high scanning rate (9200 frame/s max.). The instantaneous shock wave position is determined as the darkest point in the image when

Nomenclature

For Experiment and Numerical Simulation

b = half chord of airfoil
H = channel height
P = static pressure
P_b = back pressure
P_0 = stagnation pressure upstream of test section
t = time (normalized by the ratio of chord length and speed of sound at stagnation)
X, Y = coordinates (origin at airfoil center)
X_s = shock wave position
θ = phase of reference signal

For Linearized Analysis

Note: All flow variables are normalized by using the time-mean density and sonic speed downstream of the shock wave, and the half chord of airfoil is used as the reference length. Capital and italic letters of the flow variable indicate the time-mean and the unsteady components, respectively.

A_s = cross-sectional area at the mean position of shock wave
A = unsteady component of cross-sectional area
c = speed of sound
i = $\sqrt{-1}$
M = Mach number
M_{sep} = convection Mach number of separated flow disturbance
p, P, p = static pressure
u, U, u = velocity in x-direction
u_{sw} = velocity of shock wave oscillation
v = velocity in y-direction (used at trailing edge)
x, y = coordinates
α = parameter of flow separation scale
γ = specific heat ratio
Δx_S = displacement of shock wave position
ω = eigenvalue

Subscripts

r = real part
i = imaginary part
S = shock wave position
SEP = property related to the flow separation
TE = trailing edge position
1 = property just upstream of shock wave
2 = property just downstream of shock wave
+, − = signifies the waves propagating downstream and upstream

Superscripts

$\bar{(\ )}$ = amplitude of unsteady component
$\sim$ = relative to the shock wave motion

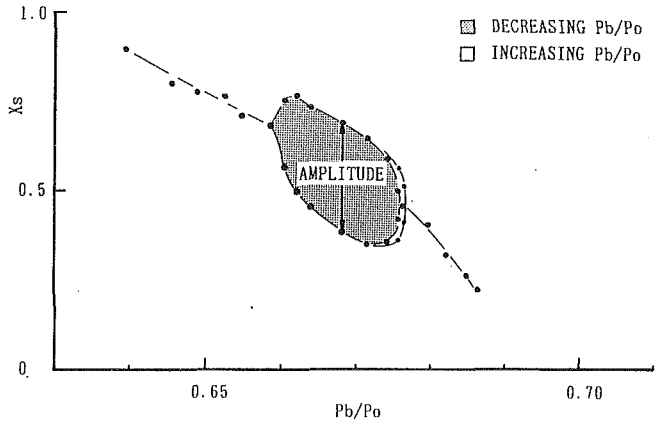

(a) 10% thickness, turbulent boundary layer.

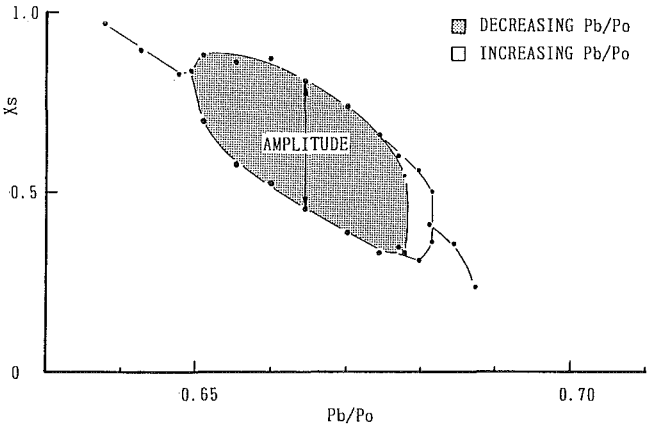

(b) 10% thickness, laminar boundary layer.

Fig. 3 Shock wave position and amplitude against back pressure

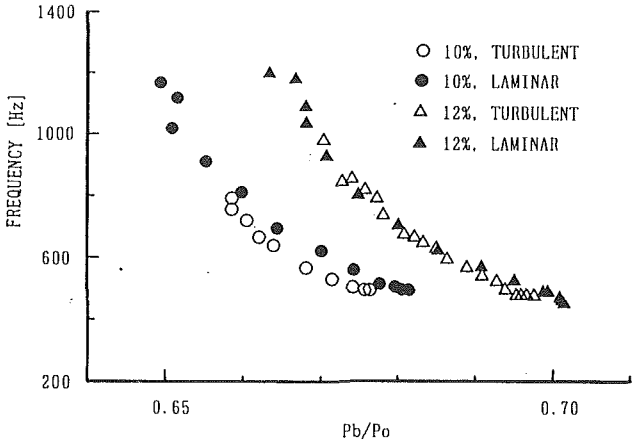

Fig. 4 Relation between shock wave frequency and back pressure

the knife edge is set normal to the flow. The boundary layer edge is determined as the brightness-changing point in the image with the knife edge placed parallel to the flow, which indicates the point where density rapidly varies in the Y-direction (see Yamamoto and Tanida, 1987).

The data measured at every point in the flowfield are ensemble-averaged referring to a phasing signal. As this reference signal, the static pressure at $X/b = 0.8$ on the upper wall was used, because it is easy to measure and has good correlation with the flow oscillation. The phase of signal θ is defined by the Hilbert transformation (see Wlezien and Way, 1979; Born and Wolf, 1965; or Yamamoto, 1988). The data from pressure probe or camera and the phasing signal are sampled simultaneously for many periods of oscillation (from 60 cycles to 100 cycles). They are stored in each digital memory unit after A/D-conversion, and then transferred, respectively, to a 16 bit microcomputer for several data processings.

Experimental Results and Discussion. Figure 1 shows the flowfield around the 10 percent thickness airfoil with the trip strip. The flow is choked on the airfoil with the upstream Mach number of 0.69, and the shock waves span fully between the upper and lower walls. The back pressure ratio P_b/P_0 is used to specify the flow condition, where P_b is the wall static pressure at $X/b = 4.53$ and P_0 is the stagnation pressure upstream of the test section.

Shock Wave Behavior. Figure 3 shows the relation between the shock wave oscillation amplitude and the back pressure. The shock wave motions were measured at $Y/b = 0.5$ (i.e., the middle height in the channel between airfoil and upper wall). $X_S = 0$ and 1 indicate the center and trailing edge of the airfoil, respectively. In the turbulent case of the 10 percent thickness airfoil, Fig. 3(*a*), the shock wave oscillates around $X/b = 0.5$ with the amplitude over $0.2b$ in the unstable range of the back pressure. In the laminar boundary layer case, Fig. 3(*b*), the oscillation amplitude becomes larger and the unstable back pressure range becomes wider. In both cases, the oscillation suddenly happens with large amplitude as the back pressure decreases. The oscillation also disappears abruptly at the lower P_b/P_0 limit, but some random oscillation of very small amplitude remains. A hysteresis phenomenon is observed at the higher P_b/P_0 limit, which is similar to the results on an 18 percent thick circular arc airfoil of McDevitt et al. (1976). Similar results are obtained on the 12 percent airfoil but with much larger amplitude (Yamamoto, 1988).

Figure 4 shows the relation between the frequency of shock wave and the back pressure. The shock wave frequency is determined as the peak frequency in the power spectrum of shock wave motion. It is noted that there is no marked difference in the frequency of shock oscillation between the turbulent and laminar cases of either airfoil. The fact that the frequency is independent of the Reynolds number was also found by Gallus et al. (1987) on an isolated airfoil. Further, the shock wave frequency increases as back pressure decreases, or as the mean shock position is transferred downstream. This suggests that the characteristic length of the flow oscillation is the distance between the shock wave mean position and the trailing edge or a certain point near there.

Therefore, it is inferred that the pressure wave propagation dominates in the self-excited oscillation mechanism, whereas the structure of the boundary layer affects the stability of the flowfield.

Unsteady Static Pressure and Wake Motion. The pressure and boundary layer measurements are made on the 10 percent thickness airfoil with trip strip at $P_b/P_0 = 0.668$, when the oscillation was fairly periodical with the frequency of 600 Hz. Figure 1 shows the flowfield oscillates 180 deg out-of-phase between the upper and lower side of the airfoil. This antiphase manner originates from the asymmetrical structure of the separated flow around trailing edge, which will be described in the numerical simulation. Therefore, the static pressure measurements were only made in the upper-side flowfield. The number of measuring points is 207 (23 × 9).

Figure 5 displays the static pressure contours and the boundary layer edge every 120 deg in one cycle of the oscillation. Below the airfoil in the figure, the 180 deg out-of-phase data are drawn. The growth of the flow separation, which reduces the pressure gradient in the flow direction, raises the pressure behind the shock wave, and then the shock moves upstream. On the other hand, the disappearance of the flow separation brings about the pressure decrease behind the shock wave, and

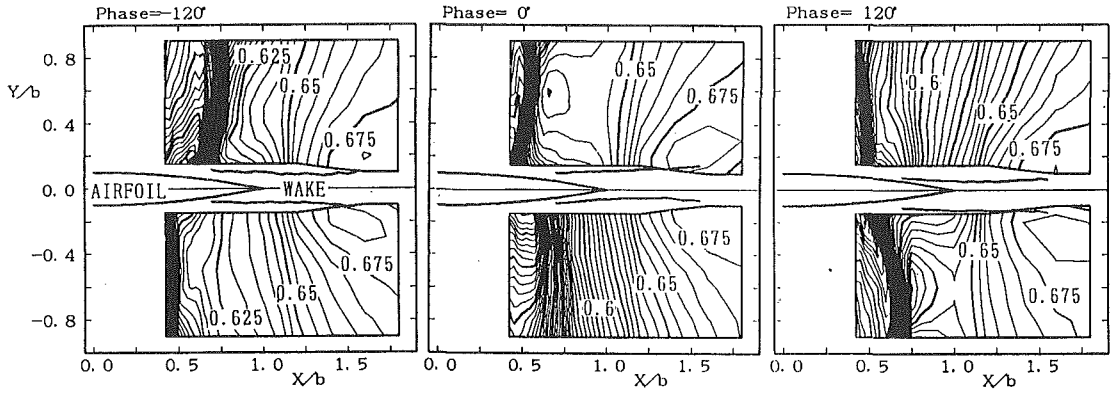

Fig. 5 Contours of static pressure P/P_0 in the flowfield

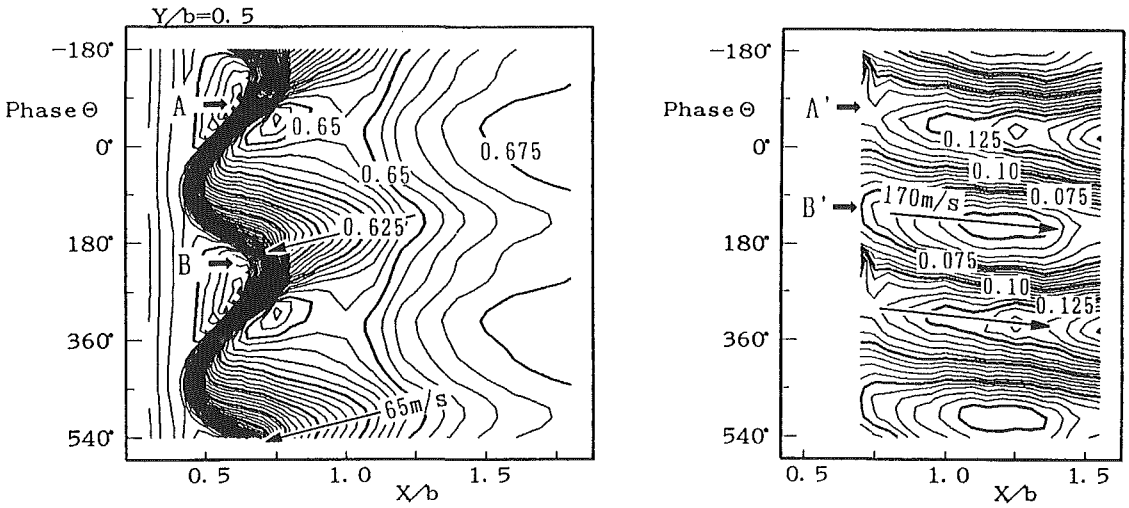

(a) Static pressure. (b) Boundary layer edge.

Fig. 6 Comparison between pressure P/P_0 and boundary layer edge height Y_w/b

then the shock moves back downstream. In the flow upstream of the trailing edge, the pressure distribution is mostly one-dimensional except for the region where the shock wave interacts with the boundary layer on the airfoil and the wall.

Figure 6(a) shows the variation of the pressure distribution for two cycles at $Y/b = 0.5$ in the flowfield (phase θ proceeds downward). The large pressure wave is observed in the region upstream of $X/b = 1.25$, where the amplitude of the pressure is so large that the propagation of the pressure wave is nonlinear as can be seen in the rapid increase and slow decrease of the pressure. The distorted shock wave motion is produced by this pressure variation. From $\theta = -120$ deg to 0 deg, the boundary layer separation causes the pressure rise downstream of the shock wave, but the propagation of the pressure wave is not clear. However, from $\theta = 60$ deg to 180 deg, the disappearance of the boundary layer separation causes the pressure decrease downstream of the shock wave, when the pressure wave is observed clearly to propagate upstream. The mean propagating speed of the pressure wave is about 65 m/s in average (indicated by arrows in the figure), which corresponds to the speed of sound propagating upstream in the flow of Mach number 0.8.

Figure 6(b) shows the variation of boundary layer edge (edge position measured from $Y = 0$) for two cycles. The boundary-layer thickness varies sinusoidally, in spite of the distorted shock wave motion and pressure variation. The disturbed boundary layer separation is convected downstream in contrast to the pressure. Behind the shock wave, the convection speed is small, and it increases gradually as convected downstream. The mean convection speed is about 170 m/s or about three-quarters of the outer flow velocity, that is caused by the convection of the vorticity in the separated flow.

The maximum pressure jump at the shock occurs almost in phase with the maximum height of the boundary layer edge at the shock (about $\theta = -90$ deg; "A" and "A′" in the figures), but the minimum pressure jump at the shock position ("B") appears about 90 deg behind the minimum boundary layer edge height (which indicates the disappearance of the separation; "B′" in the figure). This phase difference is considered to be caused by the delay time with which the fluctuation in the boundary layer is convected downstream, and the pressure disturbance is generated at the trailing edge and propagates back to the shock wave position.

The passage between airfoil and wall can be regarded as a diffuser. It is known that the shock wave standing in a diffuser is stable acoustically, because the pressure wave propagating upstream is absorbed by the shock wave motion, and then the reflected pressure wave becomes small (Culick and Rogers, 1983). However, the present results predict that the flowfield may become unstable when the disturbance due to the boundary layer separation at the shock foot is convected downstream to create the pressure wave near the trailing edge.

In the next section, a simple analysis is made to confirm this consideration.

Linearized One-Dimensional Analysis

Analysis. Figure 7 shows the flowfield model considered here. The passage flow between airfoil and wall is assumed to

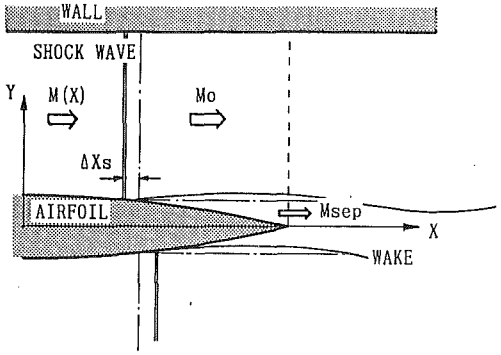

Fig. 7 Theoretical model of the flowfield

be one-dimensional and inviscid. The flow upstream of the shock wave is steady and given by a function of x only, while the flow downstream of the shock fluctuates about the mean flow. The mean flow downstream of the shock is assumed to be constant in the x-direction due to the displacement effect of the large flow separation. Referring to the experimental result, Fig. 6(*b*), the separated flow oscillation is simulated as a wavy wall traveling downstream with the Mach number M_{SEP} and gradually increasing its amplitude from the shock foot. Therefore, the boundary layer separation acts as the cross-sectional area change.

The unsteady components are assumed to be small as compared with the time-mean values, and oscillating harmonically,

$$\mathrm{p}=P+p, \quad p=\bar{p}\cdot e^{-i\omega t}$$

where ω is the eigenvalue of the flow oscillation. The real part ω_r expresses the frequency of the oscillation, while the imaginary part ω_i determines the stability. The flowfield becomes unstable when the imaginary part is positive. The flow variables are normalized by using the time-mean density and sonic speed downstream of the shock wave. (Pressure is normalized by the product of the density and the square of sonic speed.) The half chord of the airfoil is taken as the reference length.

Following the assumptions, the equation of pressure wave is obtained as

$$\left(\frac{D^2}{Dt^2}-\frac{\partial^2}{\partial x^2}\right)p=-\frac{D^2}{Dt^2}\frac{A}{A_S}$$

where

$$\frac{D}{Dt}=\frac{\partial}{\partial t}+\mathrm{M}_2\frac{\partial}{\partial \mathrm{x}}$$

The solution of equation (1) is given in the form

$$p=[\mathrm{P}_+e^{ik_+x}+\mathrm{P}_-e^{ik_-x}+\mathrm{P}_{\mathrm{SEP}}e^{ik_{\mathrm{SEP}}(x-x_S)}]\cdot e^{i\omega t} \tag{2}$$

where

$$k_+=\frac{\omega}{1+\mathrm{M}_2},\ k_-=\frac{-\omega}{1-\mathrm{M}_2},\ k_{\mathrm{SEP}}=\frac{\omega}{\mathrm{M}_{\mathrm{SEP}}}$$

The first and second terms in the right-hand side of equation (2) indicate the downstream and upstream propagating pressure wave, respectively, while the third term indicates the pressure wave caused by the separated flow traveling downstream.

It is assumed that the disturbance of the flow separation is generated initially in the same phase with the pressure jump at the shock wave, and then convected downstream with linearly increasing amplitude; that is

$$A=-(x-x_S)\cdot a\cdot\Delta \mathrm{x}_S\cdot \mathrm{e}^{ik_{\mathrm{SEP}}(x-x_S)} \tag{3}$$

where

$$a=\alpha\cdot e^{i\theta_{\mathrm{SEP}}},\ \theta_{\mathrm{SEP}}=\arg(p_2-p_1)$$

Δx_S is the displacement of the shock wave oscillation, α indicates the slope of the separation at the shock wave foot, which gives a scale of the separation, and $\arg(p_2-p_1)$ is the phase of the pressure jump at the shock wave.

Substituting equation (3) into equation (1) gives

$$\mathrm{P}_{\mathrm{SEP}}=[\mathrm{P}_{\mathrm{SEP}\ 1}\cdot(x-x_S)+\mathrm{P}_{\mathrm{SEP}\ 0}]\cdot\overline{\Delta x_s} \tag{4}$$

where

$$\mathrm{P}_{\mathrm{SEP}\ 1}=\frac{(\mathrm{M}_2-\mathrm{M}_{\mathrm{SEP}})^2}{(\mathrm{M}_2-\mathrm{M}_{\mathrm{SEP}})^2-1}\cdot\alpha$$

$$\mathrm{P}_{\mathrm{SEP}\ 0}=\frac{2\cdot\mathrm{M}_{\mathrm{SEP}}^2(\mathrm{M}_2-\mathrm{M}_{\mathrm{SEP}})}{[(\mathrm{M}_2-\mathrm{M}_{\mathrm{SEP}})^2-1]^2}\cdot\frac{i\alpha}{\omega}$$

The boundary condition at the mean shock wave position x_S can be derived from the Rankine–Hugoniot relation

$$\left(\frac{\mathrm{p}_2}{\mathrm{p}_1}\right)_S=\frac{2\gamma}{\gamma+1}\cdot(\tilde{\mathrm{M}}_1^2)_S-\frac{\gamma-1}{\gamma+1} \tag{5a}$$

$$\left(\frac{\tilde{\mathrm{u}}_2}{\tilde{\mathrm{u}}_1}\right)_S=\frac{2}{\gamma+1}\cdot\frac{1}{(\tilde{\mathrm{M}}_1^2)_S}+\frac{\gamma-1}{\gamma+1} \tag{5b}$$

where $\tilde{u}$ and $\tilde{M}$ are the velocity and Mach number relative to the shock motion, respectively.

Just downstream of the shock, the disturbance is caused by the pressure wave, that is given as

$$(\mathrm{p}_2)_S=P_2+(p)_S$$

$$(\tilde{\mathrm{u}}_2)_S=U_2+(u)_S-u_{sw}$$

where u_{sw} is the shock wave speed $(-i\omega\Delta x_S)$, while just upstream of the shock, the disturbance is caused by the shock motion as

$$(\mathrm{p}_1)_S=(P_1)_S+\left(\frac{dP_1}{dx}\right)_S\cdot\Delta x_S$$

$$(\tilde{\mathrm{u}}_1)_S=(U_1)_S+\left(\frac{dU_1}{dx}\right)_S\cdot\Delta x_S-u_{Sw}$$

$$(\tilde{\mathrm{M}}_1)_S=(\mathrm{M}_1)_S+\left(\frac{d\mathrm{M}_1}{dx}\right)_S\cdot\Delta x_S-\frac{u_{Sw}}{(c_1)_S}$$

Using these expressions, equations (5*a*, *b*) are linearized as

$$(p)_S=(\mathrm{P}_{SR}+i\omega\cdot\mathrm{P}_{S1})\cdot\Delta x_S \tag{6a}$$

$$(u)_S=(\mathrm{U}_{SR}+i\omega\cdot\mathrm{U}_{S1})\cdot\Delta x_S \tag{6b}$$

where

$$\mathrm{P}_{SR}=\frac{4\gamma}{\gamma+1}\left(P_1\mathrm{M}_1\frac{d\mathrm{M}_1}{dx}\right)_S+\left(\frac{P_2}{P_1}\frac{dP_1}{dx}\right)_S$$

$$\mathrm{P}_{S1}=\frac{4\gamma}{\gamma+1}\left(\frac{P_1\mathrm{M}_1^2}{U_1}\right)_S$$

$$\mathrm{U}_{SR}=-\frac{4\gamma}{\gamma+1}\left(\frac{U_1}{\mathrm{M}_1^3}\frac{d\mathrm{M}_1}{dx}\right)_S+\left(\frac{U_2}{U_1}\frac{dU_1}{dx}\right)_S$$

$$\mathrm{U}_{S1}=-\frac{4}{\gamma+1}\left(\frac{1}{\mathrm{M}_1^2}\right)_S+\left(\frac{U_2}{U_1}\right)_S-1$$

The second terms in the right-hand side of equations (6*a*, *b*) express the unsteady response of the shock wave to the pressure and velocity fluctuations just downstream of the shock wave.

The boundary condition at the trailing edge is a difficult problem itself when the boundary layer separation occurs. For the present, it is derived from the momentum equation in the y-direction.

$$\left(\frac{Dv}{Dt}+\frac{\partial p}{\partial y}\right)_{x=x_{TE}}=0 \tag{7}$$

In order to include the interaction of the upper and lower

flowfields about the airfoil, the pressure wave is assumed to have a form

$$(p)_{TE} = (\bar{p})_{TE} \cdot \sin(\pi y/2) \cdot e^{-i\omega t} \tag{8}$$

at the trailing edge. The Y-direction component of velocity at the trailing edge is assumed to be given by the particle velocity on the boundary layer edge.

$$(v)_{TE} = -\frac{DA}{Dt} \tag{9}$$

Then $(\bar{p})_{TE}$ in equation (8) is determined by equation (7). Finally, the characteristic equation derived from equations (2), (6*a*, *b*), and (7) is solved by the Newton–Raphson method for the specified x_S.

Theoretical Results and Discussion. Figure 8 shows the comparison between the theoretical and experimental results of the reduced frequency in the case of the flow around 10 percent thickness airfoil. The figure also shows the effects of the flow separation size α. M_{SEP} must be smaller than M_2 and is taken as 0.6 in the present calculation.

The calculated frequency agrees well with the experimental ones up to $x_S = 0.6$, but it tends to be much higher when x_S transfers to the trailing edge, because the one-dimensional analysis gives the infinite frequency when the shock wave is located at the trailing edge.

The unstable solution exists when the shock wave is located near the center of the airfoil, but it tends to be stable as the shock wave approaches the trailing edge. This is because, as x_S increases, the pressure disturbance, which is necessary to oscillate the shock wave, increases and finally exceeds the disturbance caused by the flow separation.

The parameter α affects the stability, although it does not affect the frequency so much. As α increases, the unstable region extends to the trailing edge, since the pressure disturbance caused by the flow separation becomes larger.

The limit of the self-excited oscillation is explained from Fig. 8 as follows. The limit at the low back pressure can be recognized as the point where the boundary layer separation cannot cause a pressure disturbance sufficient to oscillate the shock wave. On the other hand, the limit at the high back pressure does not appear in Fig. 8. This means that the flowfield is always unstable when the shock standing near the airfoil center induces moderate flow separation. Hence, it is considered that the hysteresis phenomenon at high back pressure in Fig. 3 is caused by the existence of the hysteresis between the initiation and disappearance of unsteady boundary layer separation.

Figure 9(*a*, *b*) shows the calculated results of the variation of the pressure distribution and the boundary layer thickness for two cycles of oscillation. As seen in the figures, the upstream propagation of the pressure wave and the downstream convection of the disturbed flow separation generate similar pressure variation to the experimental results, Fig. 6(*a*).

As a consequence, the proposed mechanism can explain the qualitative characteristics of the self-excited oscillation.

Numerical Simulation

The purpose of the present numerical simulation is to understand the qualitative structure of the separated flow region around the airfoil trailing edge, and the interaction between the upper and lower flowfields about the airfoil. The implicit finite difference procedure by Beam and Warming (1978) and Steger (1978) is used.

Boundary Conditions. A C-type grid is used in this calculation, which covers the region of 2.5 chords in the inlet and 4 chords to the exit from the center of airfoil. The back pressure (static pressure at exit) is specified to determine the flow condition. At the inlet, the static pressure is extrapolated from downstream and other variables are calculated from this pressure by the isentropic flow relation. At the exit, the variables, except for the pressure, are extrapolated from upstream. On the airfoil, nonslip condition is imposed, while the static pressure and temperature gradient in the direction normal to the surface are fixed to be zero. On the upper and lower walls, slip flow conditions are imposed. This condition is different from the actual flow but is not essential in the self-excited phenomenon. On the wake line, variables are found by averaging the linearly extrapolated ones from above and below.

In order to get a symmetrical stable solution for the initial condition, a "splitter plate" boundary condition is imposed on the wake line in some chord length behind the trailing edge, where the slip flow condition is used.

Calculation Procedure. In order to simulate the shock wave clearly, an adaptive grid procedure developed by Nakahashi and Deiwert (1986) is employed. The scheme is based on the tension and torsion spring analogy. Figures 10(*a–c*) show the initial grid (321 × 49), the grid adapted to the density gradient of the flow, and an example of the unsteady solution calculated by this adapted grid.

For the initial condition, a steady flow is calculated by preventing the wake oscillation with the splitter plate boundary condition. In this calculation, a spatially variable time step was used to accelerate the convergence. Next, the unsteady

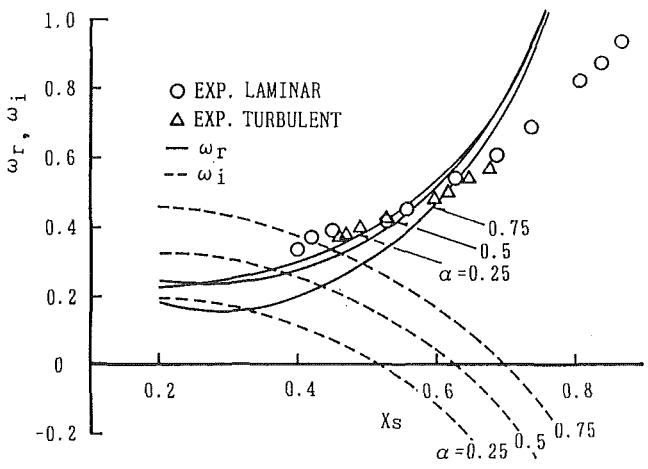

Fig. 8 Comparison of theory with experiment for reduced frequency; 10 percent thickness, $M_{SEP}/M_0 = 0.6$

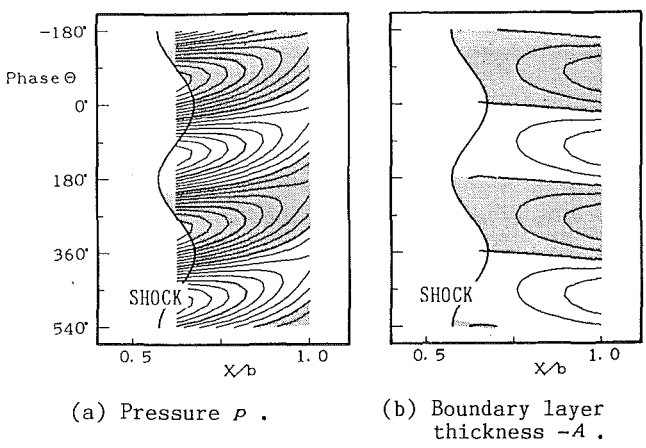

Fig. 9 Pressure wave and boundary layer separation thickness by theory; 10 percent thickness, $\alpha = 0.5$, $M_{SEP}/M_0 = 0.6$, $\Delta x_S = 0.05$, the shaded area indicates negative

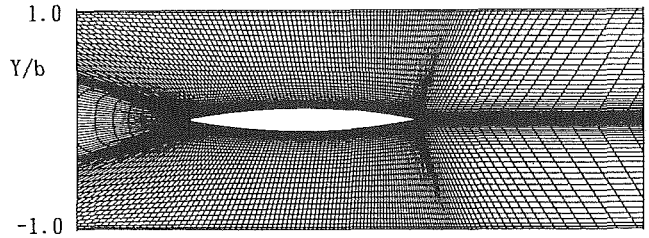

(a) Initial grid.

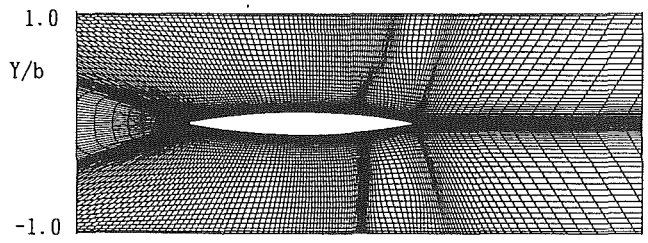

(b) Adapted grid.

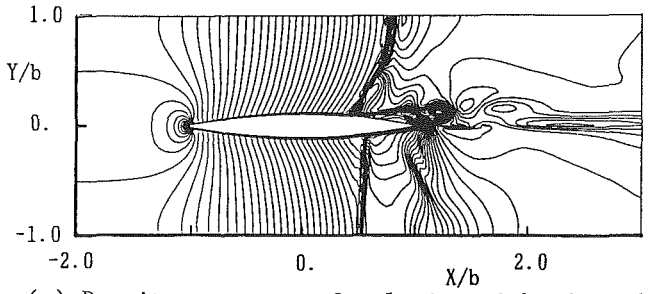

(c) Density contours of solution with adapted grid.

Fig. 10 Grid and density contours

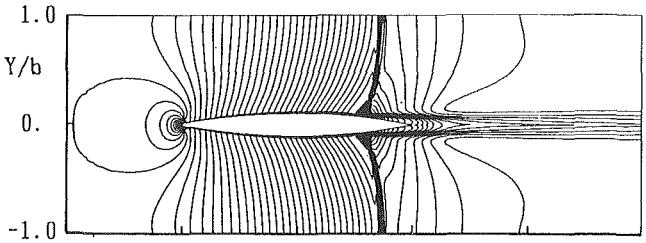

(a) Density contours.

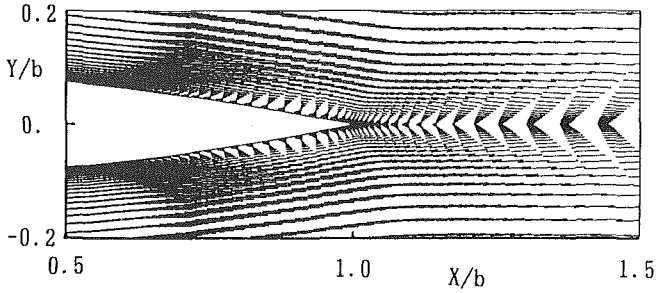

(b) Velocity vectors around trailing edge.

Fig. 11 Initial condition for unsteady computation

calculation was carried out by removing the splitter plate boundary condition from this steady solution to get the periodical flow.

In the unsteady flow calculation, the time step was taken as 0.001, where time is scaled with respect to the ratio of the airfoil chord and the sonic speed at the stagnation. The unsteady calculation was continued up to 16,000 time steps, and the adaptive grids were regenerated every 100 time steps.

For the turbulence model, an algebraic model developed by Baldwin and Lomax (1978) is used.

Results and Discussion. The numerical simulation was made on the case of the 10 percent thickness airfoil. The flow condition is set so that the shock stands at an appropriate location. In the present computation, the back pressure is $P_b/P_0 = 0.705$, and the Reynolds number $\mathrm{Re} = 0.5 \times 10^6$. The turbulence model is introduced from the 8 percent chord point downstream of the leading edge.

Figure 11 shows the density contours and velocity vectors of the initial solution. The boundary layer separates at the shock foot and the separated region extends over the trailing edge.

Figure 12 shows the whole flowfield around the airfoil expressed by density contours. It is seen that the symmetric flow begins to break from the boundary layer separation at $t = 4.5$, and then the large flow oscillation grows up to generate a large shock wave motion and flow separation. During $t = 7.0$ to 12.0, the mean shock position at $Y = 0.5b$ is $X_s = 0.71b$, and the shock oscillation amplitude is $0.54b$. The frequency calculated from the period of the oscillation is 780 Hz, which is almost the same with the experimental data for the mean shock position $X_S = 0.68b$. The simulated flow oscillation is similar to that of the experiment, although it has larger amplitude. This difference is considered to be caused from the results of the idealized two-dimensional calculation and the simple turbulence model. In the experiments, the boundary layer on the walls is actually developed as seen in Fig. 1, and three-dimensional structure must exist in the flow separation, particularly near the sidewall of the test section. Such boundary layer flow may stabilize the flow oscillation.

Figure 13 gives the velocity vectors around the trailing edge. It is noted that there is much difference in the size of the separated flow between the steady flow and the unsteady one. The recirculating flow on the lower side induces the flow turning round the trailing edge from the upper side into the lower side to form a counter-rotating vortex against the recirculating flow ($t = 9.0$–10.5). These two vortices interact with each other and make the flow separation much larger than the initial symmetric one on the lower side of airfoil, while the flow separation disappears on the upper side. In such a way, the recirculating flow in the boundary layer separation on each side of the airfoil interacts with the other around the trailing edge to grow up alternately and to produce large pressure disturbance. Therefore, the asymmetric self-excited flow oscillation is induced by the mechanism described in the previous section.

Conclusion

The experiments, theoretical analysis and numerical simulation of the transonic flow in a simplified cascade model were carried out to clarify the fundamental mechanism of the self-excited oscillation.

To sum up the results, the self-excited flow oscillation is caused by a closed process, as illustrated in Fig. 14, which consists of the upstream propagation of the pressure disturbance in the main flow, the downstream convection of the separated boundary layer disturbance, and the behavior of the unsteady flow that turns round the trailing edge to amplify the separation and to cause a large pressure disturbance in the outer flow. Consequently, the asymmetric self-excited oscillation of shock wave is induced. The frequency of the oscillation is then considered to be determined by the upstream propagating sound speed and the downstream convection ve-

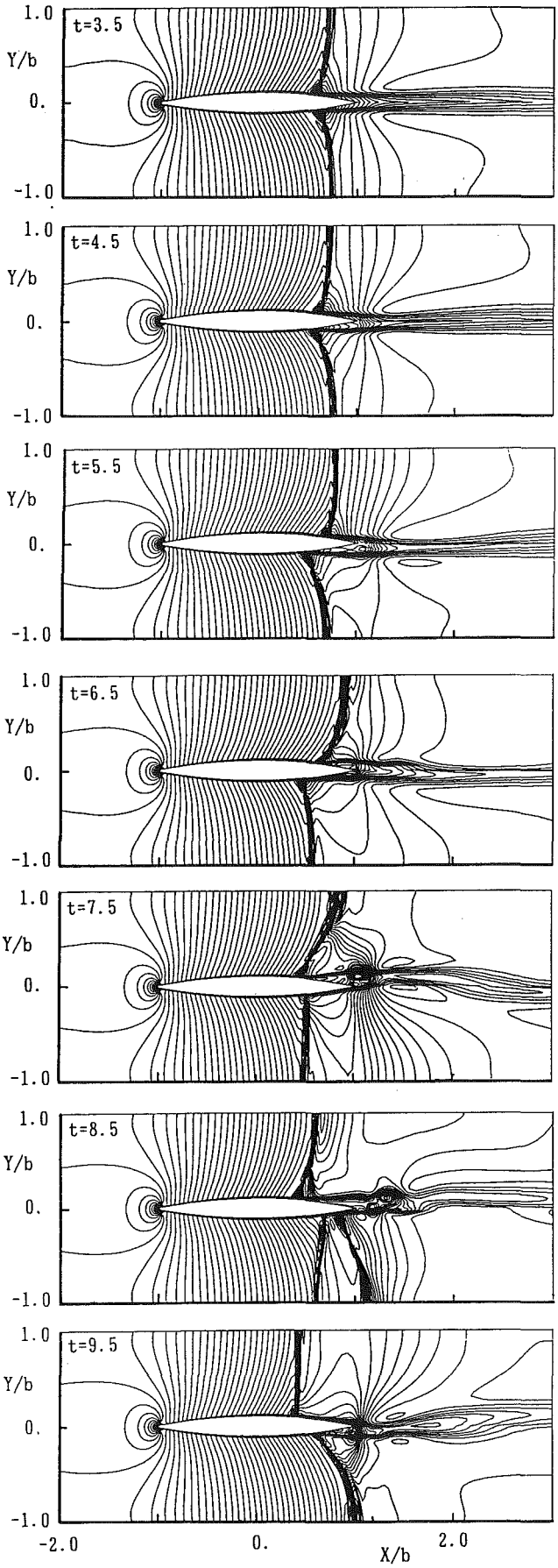

Fig. 12 Density contours of flowfield (t = 3.5–9.5)

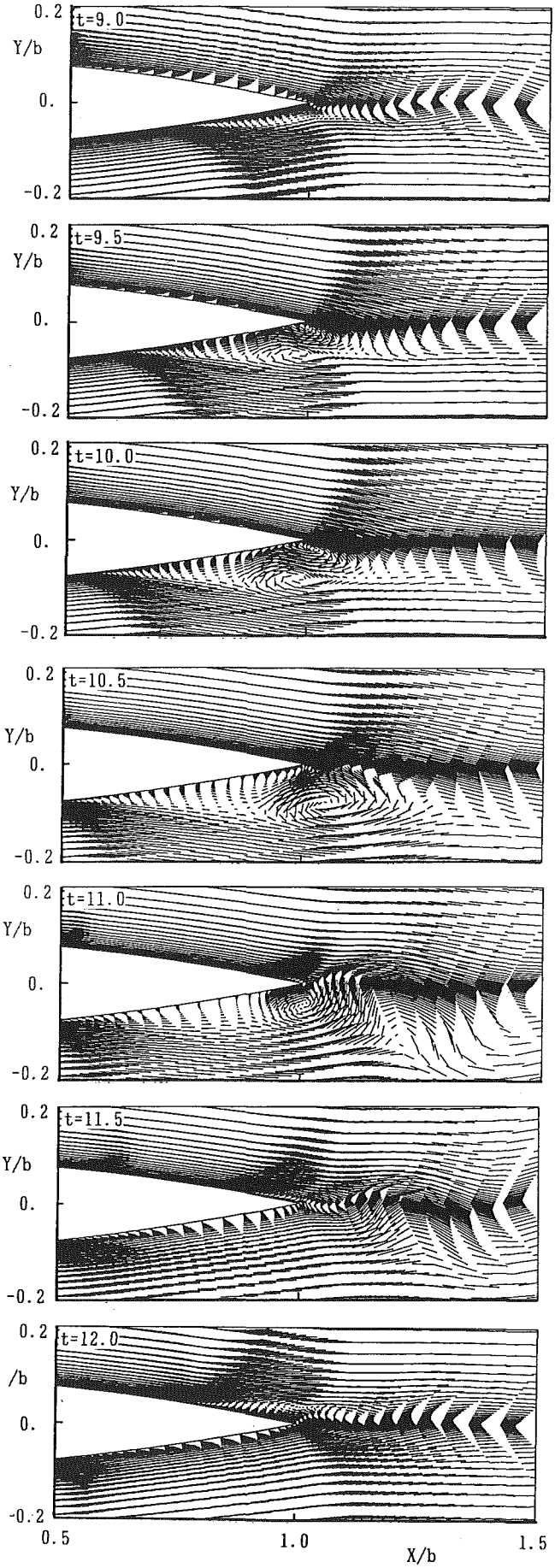

Fig. 13 Velocity vectors around trailing edge (t = 9.0–12.0)

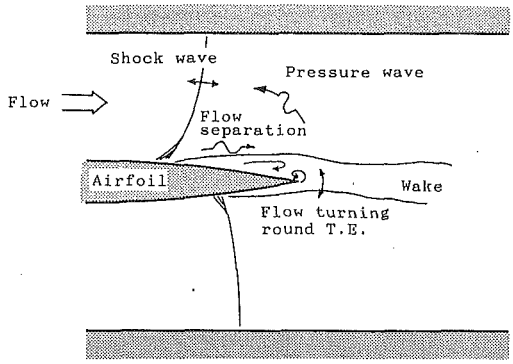

Fig. 14 Mechanism of the self-excited oscillation

locity of the disturbed separated flow, and the pressure wave generation mechanism near the trailing edge. With regard to the stability limit, when the shock wave stands near the center of the airfoil, the self-excited oscillation occurs by the moderate large flow separation. On the other hand, when the shock wave stands near the trailing edge, the flowfield becomes stable acoustically because the generation of much larger pressure disturbance is necessary to oscillate the shock wave.

Acknowledgment

The authors would like to express their gratitude to Associate Professor T. Nagashima of the University of Tokyo and to Associate Professor T. Shiratori of the Tokyo Metropolitan Institute of Technology for their helpful discussion and advice. The authors are indebted to Associate Professor K. Nakahashi of the Osaka Prefecture University in the numerical simulation. They further wish to thank Mr. S. Namekawa and Mr. T. Ohno for their helpful assistance during the experimental investigation. This work was partly supported by a Grant-in-Aid for Scientific Research from the Ministry of Education in Japan.

References

Araki, T., Okamoto, Y., and Ohtomo, F., 1983, "Self-Excited Flow Oscillation in the Low Pressure Steam Turbine Cascade," *Proceedings of the Symposium on Aeroelasticity in Turbomachinery*, Cambridge, pp. 171–186.

Baldwin, B. S., and Lomax, H., 1978, "Thin Layer Approximation and Algebraic Model for Separated Turbulent Flows," AIAA Paper No. 78-257.

Beam, R. M. and Warming, R. F. 1978, "An Implicit Factored Scheme for the Compressible Navier–Stokes Equations," *AIAA Journal*, Vol. 16, pp. 393–402.

Born, M., and Wolf, E., 1965, "Interference and Diffraction With Partially Coherent Light," *Principles of Optics*, Pergamon Press, Oxford, pp. 494–499.

Borgar, T. J., 1986, "Structure of Self-Excited Oscillation in Transonic Diffuser Flow," *AIAA Journal*, Vol. 24, pp. 54–61.

Culick, F. E. C., and Rogers, T., 1983, "The Response of Normal Shocks in Diffusers," *AIAA Journal*, Vol. 21, pp. 1382–1390.

Finke, K., 1975, "Shock Oscillations in Transonic Flows and Their Prevention," (*IUTAM*) *Symposium Transonicum II*, Oswatitsch, K., and Rues, D., eds., Springer-Verlag, pp. 57–65.

Gallus, H. E., Broichausen, K.D., and Henne, J. M., 1986, "Experimental Unsteady Shock-Boundary Layer Interaction at Single Blades and in Linear Cascades," ASME Paper No. 86-GT-218.

Maier, R., and Wachter, J., 1987, "Shock-Induced Flow Oscillations in Steam Turbine Diffusers," ASME Paper No. 87-GT-124.

McDevitt, J. B., Levy, Jr., L. L., and Deiwert, G. S., 1976, "Transonic Flow About a Thick Circular-Arc Airfoil," *AIAA Journal*, Vol. 14, No. 5, pp. 606–613.

Nakahashi, K., and Deiwert, G. S., 1986, "Three-Dimensional Adaptive Grid Method," *AIAA Journal*, Vol. 24, pp. 948–954.

Seegmiller, H. L., Marvin, J. G., and Levy, Jr., L. L., 1976, "Steady and Unsteady Transonic Flow," *AIAA Journal*, Vol. 16, pp. 1262–1270.

Steger, J. L., 1978, "Implicit Finite-Difference Simulation of Flow About Arbitrary Two-Dimensional Geometries," *AIAA Journal*, Vol. 6, pp. 679–686.

Wlezien, R. W., and Way, J. L., 1979, "Techniques for the Experimental Investigation of the Near Wake of a Circular Cylinder," *AIAA Journal*, Vol. 17, pp. 563–570.

Yamamoto, K., and Tanida, T., 1987, "Self-Excited Oscillation of Shock Waves on an Airfoil in Two-Dimensional Transonic Channel Flow," *Proceedings of the Fourth Symposium on Unsteady Aerodynamics and Aeroelasticity of Turbomachines and Propellers*, Aachen, pp. 769–783.

Yamamoto, K., 1988, "Self-Excited Oscillation of Transonic Flow Around an Airfoil in Two-Dimensional Channel," PhD Thesis, The University of Tokyo, Tokyo.

Unsteady Aerodynamic Damping Measurement of Annular Turbine Cascade With High Deflection in Transonic Flow

H. Kobayashi
Section Head,
Thermo-fluid Dynamics Division,
National Aerospace Laboratory,
Chofu, Tokyo, Japan

Unsteady aerodynamic forces acting on oscillating blades of a transonic annular turbine cascade were investigated in both aerodynamic stable and unstable domains, using a Freon gas annular cascade test facility. In the facility, whole blades composing the cascade were oscillated in the torsional mode by a high-speed mechanical drive system. In the experiment, the reduced frequency K *was changed from 0.056 to 0.915 with a range of outlet Mach number* $\bar{M}_2$ *from 0.68 to 1.39, and at a constant interblade phase angle. Unsteady aerodynamic moments obtained by two measuring methods agreed well. Through the moment data the phenomenon of unstalled transonic cascade flutter was clarified as well as the significance of* K *and* $\bar{M}_2$ *for the flutter. The variation of flutter occurrence with outlet flow velocity in the experiments showed a very good agreement with theoretical analysis.*

1 Introduction

For solution of aeroelastic problems in turbomachinery, namely flutter and forced vibration, clarification of unsteady aerodynamic forces acting on cascade blades is necessary as well as structural dynamic analysis of the cascade [1]. Many theoretical and experimental studies have been carried out by researchers [2–12] to predict the unsteady aerodynamic forces. Recently, with the development of numerical techniques, effects of blade thickness and aerodynamic load on the unsteady aerodynamic forces as well as three-dimensional effects began to be considered in predicting the forces moments acting on oscillating blade row. However, as regards to experiments, there seems to be very limited experimental data, especially in transonic flow, which is an important operating flow region in aero-engines, because of extreme difficulties in both experimental modeling and collection of resulting time-variant data [8–12].

Therefore, a controllable-oscillating annular cascade test facility [5] was developed that can yield unsteady aerodynamic force data both in transonic flow and at high reduced frequency corresponding to levels encountered in actual machines. To achieve the high reduced frequency in transonic flow, the author has chosen Freon gas as a working fluid and has developed a novel high-speed mechanical drive system. For measurement of the unsteady aerodynamic forces acting on oscillating blades in both aerodynamically stable and unstable domains, whole blades composing an annular cascade were forced to vibrate in torsional mode by the drive system, without using the vibratory resonance of the blade system.

With the facility, studies have been carried out in order to more deeply understand unsteady cascade phenomena better and to acquire unsteady aerodynamic data for the assessment of the validity of the present theoretical analyses and for the development of new theories, especially in transonic flow [5–7, 14, 15].

In the present paper, unsteady aerodynamic damping properties of a transonic turbine cascade with high deflection were clarified with the facility over a wide range of outlet flow Mach numbers and reduced frequencies. This paper describes the following: (1) two different measuring methods for unsteady aerodynamic moments, (2) correlation between unsteady aerodynamic moment and unsteady aerodynamic pressures on the blade surface, (3) effects of reduced frequency and outlet flow Mach number on unstalled transonic turbine cascade flutter, and (4) comparison between the author's experimental results and theoretical results. Effects on the flutter of movement of the shock wave and throat region due to blade oscillation are also presented in this paper.

2 Test Facility and Airfoil

An annular cascade test facility was conceived and constructed as a research tool in order to evaluate steady and unsteady characteristics of turbine and compressor cascades and to investigate flow mechanisms causing flutter through comparisons between experimental data and theoretical analysis data [5–7, 14, 15].

In the test section, shown in Fig. 1, an annular cascade with a fairly high hub/tip ratio has been chosen in order to exclude endwall effects in a linear cascade and to obtain approximately two-dimensional flow for comparing with theoretical works. The blade height is 25 mm and the hub/tip ratio is 0.844.

Contributed by the International Gas Turbine Division for publication in the JOURNAL OF TURBOMACHINERY. Manuscript received by the International Gas Turbine Institute September 5, 1984.

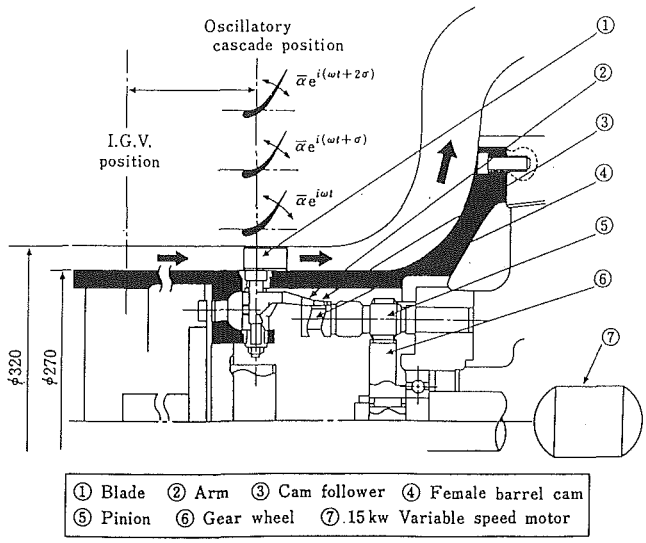

Fig. 1 Test section of annular cascade test facility and high-speed mechanical drive system

Freon gas (Freon 11) possessing a low sound velocity was chosen as a working fluid in the facility for yielding data of unsteady aerodynamic forces acting on blades, both in transonic flow and at a high reduced frequency corresponding to levels encountered in actual machines.

For measurement of the forces in both aerodynamically stable and unstable domains, it was necessary to maintain oscillating amplitudes and interblade phase angles of the blades at each oscillating frequency up to 500 Hz in both domains. To achieve the oscillation at the high reduced frequency, a high-speed mechanical drive system was developed. It was capable of controlled oscillation of the entire 16 blades composing the test annular cascade in torsional mode, without using vibratory resonance of the blade system, at frequencies up to 500 Hz and at arbitrary interblade phase angles.

The drive system consists of cam follower assemblies, female barrel cams, pinions, a gear, and a 15 kW motor, as shown in Fig. 1. Each airfoil is cantilevered radially from a rigid hub by a trunnion, which is attached to one of the cam follower assemblies. Each cantilevered airfoil trunnion is inserted through the hub casing wall and is supported on two bearings. The cam follower assembly consists of a connecting arm and a button follower. It couples with the female barrel cam and the pinion. The close-coupled connecting arm and button follower transmit three cycles of oscillating harmonic motion to the blade for each revolution of the cam. Sixteen assemblies of the female barrel cam and the pinion are aligned on the inside circle of the hub and are rotated by the 15-kW variable speed motor through the common gear.

Amplitude control is achieved by the cam groove design. The torsional amplitude of a blade is 1.0 deg. Any desired interblade phase angle of $2n\pi/16$ can be set by adjusting a spline combining the cam and the pinion. Blade oscillatory frequency is changed by altering the rotational speed of the motor.

The sound velocity of the working gas in the facility must be known for the calculation of reduced frequency. Thus, an apparatus for measuring the gas sound velocity was designed, constructed, and used in each experiment, which makes use of the principle of the resonance tube. The details of the annular cascade test facility, the drive system, and the apparatus are described in [5].

A transonic turbine cascade was designed and fabricated in order experimentally to evaluate effects of high deflection and transonic flow on the unsteady aerodynamic characteristics. The cascade geometry and definition of the signs are shown in Fig. 2. The torsional axis is at the 19.5 percent chord length distance from the leading edge. The chord length and stagger angle of the cascade are constant in the radial direction.

3 Measurement and Data Reduction

As the first step in a series of experiments, steady flow properties of the turbine cascade and the flow in the test section were studied. Steady flow upstream and downstream of the cascade was measured with 96 pressure taps fitted on the inner/outer wall of test section and the airfoil. The taps are connected to a scanivalve system containing two 48 channel units scanning in parallel. These steady-state data were recorded through a data acquisition/control unit on a dedicated minicomputer.

Periodicity of flows upstream and downstream of the cascade was determined with static pressure rows along the circumferential direction of the casing wall. Two traversing five-hole probes were located upstream and downstream of the cascade for measuring both radial and circumferential distributions of the inlet and outlet flow Mach number and flow angle.

The time-dependent data measured included airfoil oscillatory displacement, unsteady aerodynamic moment, and unsteady aerodynamic pressure distribution on the oscillating airfoil surface. All the time-dependent data were recorded on a data recorder and analyzed with a Fast Fourier Transform (FFT) analyzer.

Nomenclature

A = amplitude of unsteady pressure or signal [equation (8)], 1/rad
b = blade span length, mm
c = chord length, mm
C_p = pressure coefficient $= (P_{s1}(x) - \overline{P_{s2}})/(\overline{P_{t2}} - \overline{P_{s2}})$
C_m = unsteady aerodynamic moment coefficient, positive for blade nose-up [equations (3) and (4)], 1/rad
ΔE = unsteady aerodynamic local energy per cycle of blade oscillation [equation (7)], 1/rad
f = airfoil oscillating frequency, Hz
i = incidence angle, deg
K = reduced frequency = cw/U_2
M = Mach number
Mt = unsteady aerodynamic moment, N mm/rad
P = pressure, Pa
ΔPai = time-dependent pressure, Pa
Re = Reynolds number = cU_2/ν
t = time, s
U_2 = outlet flow velocity, m/s
x = coordinate in chordwise direction of blade
α = airfoil oscillating amplitude, rad
β = flow angle, deg
γ = stagger angle, deg
ν = kinetic viscosity, m^2/s
σ = interblade phase angle, deg
τ = blade pitch, mm
ϕ = phase lead of unsteady pressure or signals toward airfoil motion, deg
ω = airfoil oscillating angular frequency, Hz

Subscripts and Superscripts

1 = inlet of cascade
2 = outlet of cascade
s = static pressure
t = total pressure
$+$ = suction side
$-$ = pressure side

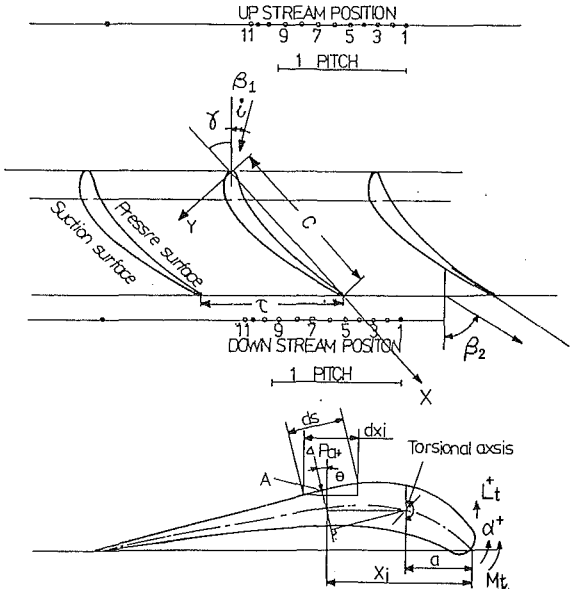

Tip, Mid span, Hub

Chord length = 72mm Pitch-chord ratio 0.873, 0.804, 0.763
Aspect ratio = 0.357 Max thickness ratio = 0.123
Camber angle = 60.8° Torsional axsis position
Stagger angle = 45.6° = (Xa = 0.195 , Ya = 0.11)

Fig. 2 Test turbine cascade geometry and definition of symbols

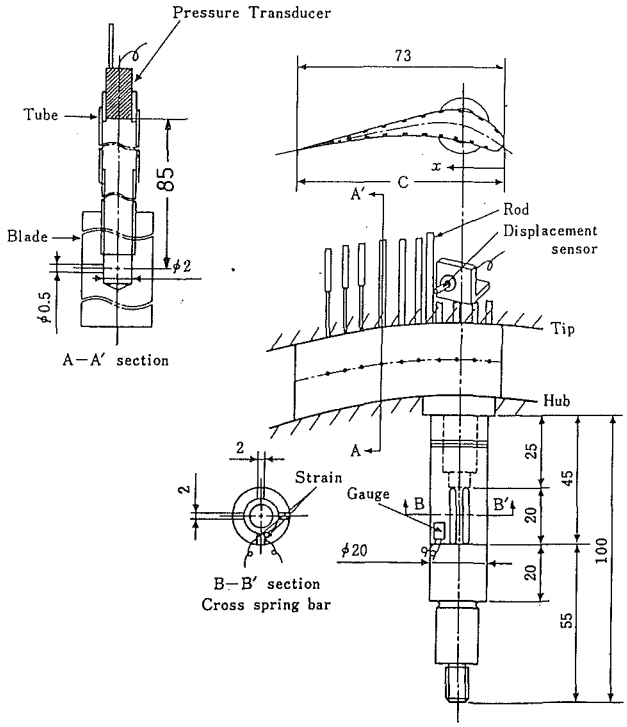

Fig. 3 Instrumented turbine airfoil

Motion of an instrumented airfoil was measured with an eddy-current type displacement sensor directed toward a small rod fixed on the airfoil tip section, shown in Fig. 3.

The unsteady aerodynamic moments were determined by two methods: direct measurement of unsteady moment (1) and a calculation from the measurement of unsteady aerodynamic pressures (2).

(1) One moment was measured with a network of dual strain gages on cross spring bars machined on the trunnion of an instrumented airfoil. It gives information on unsteady aerodynamic moment caused by aerodynamic forces acting on the entire blade surface. This method has the advantage of measuring the resultant unsteady phenomena of the oscillating airfoil, but it cannot offer information relative to local unsteady phenomena on the oscillating blade surface.

The moment (*Mtc* term in equation (3)) measured by the cross spring bar consists of two moments: a moment (*Mta*) due to unsteady aerodynamic force and a moment (*Mti*) due to an inertia force and a mechanical damping of the airfoil system. Therefore, the unsteady aerodynamic moment was calculated from the difference between the moment obtained by cascade oscillation in the flow and a reference value obtained by cascade oscillation in a vacuum state.

(2) The other unsteady aerodynamic moment was calculated from the measurement of unsteady pressure distribution on an oscillating blade surface. This method has the advantage of measuring the unsteady aerodynamic phenomena at local points of the blade surface. Twenty-two probe tube systems were prepared for measuring chordwise distributions of unsteady pressure on both the suction and the pressure surfaces of a blade, as shown in Fig. 3. The measurement by the probe tube system was an indirect pressure measurement; a probe tube was embedded in an airfoil for measuring static and unsteady pressures on the airfoil, and it was connected to a miniature pressure transducer through a vinyl tube of short length.

Therefore, the measured pressure amplitude A_o and phase lag ϕ_o have to be corrected with frequency response

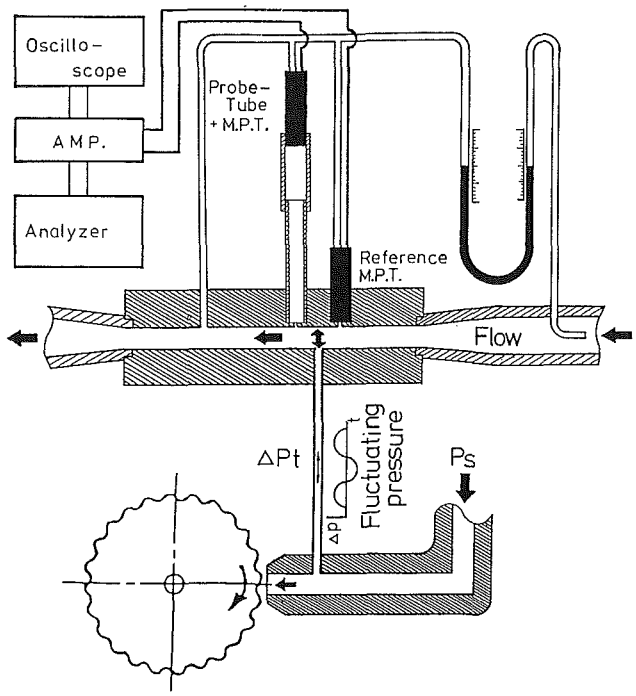

Fig. 4 Apparatus for measuring pressure frequency response characteristics of probe tube system

characteristic data of the probe tube system (A_s, ϕ_s), and of an electronic data acquisition system including d-c amplifiers (A_d, ϕ_d) and a data recorder (Ar, ϕ_r). Finally, corrected unsteady aerodynamic amplitude A_p and phase lag ϕ_p were obtained by

$$A_p = A_o/(A_s * A_D * A_r) \tag{1}$$

$$\phi_p = \phi_o + \phi_s + \phi_D + \phi_r \tag{2}$$

The frequency response characteristic (A_s, ϕ_s) of the probe

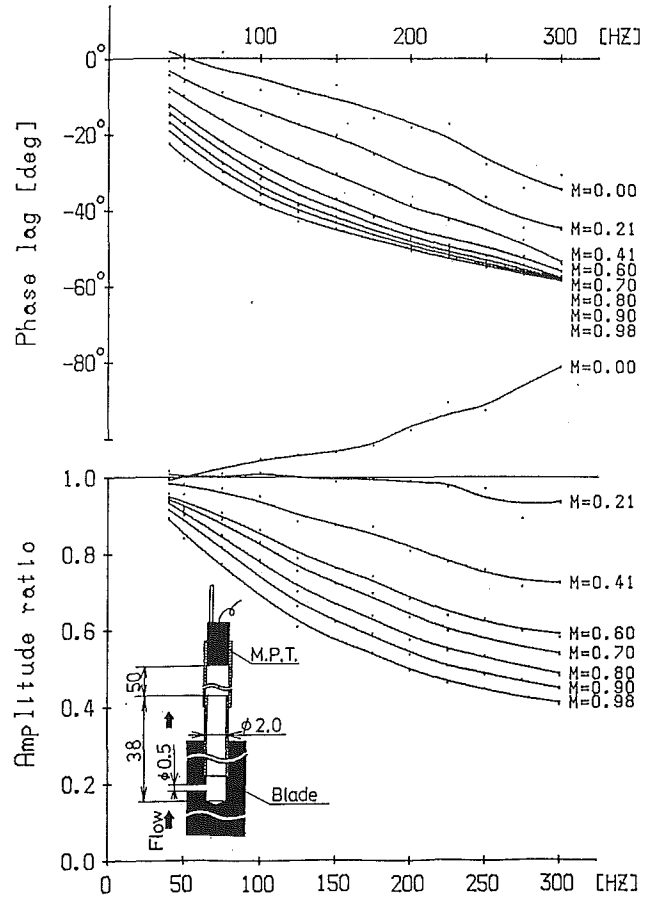

Fig. 5 Effect of grazing flow and pressure frequency on frequency response characteristics of probe tube system

tube system was determined with an apparatus designed for this purpose, shown in Fig. 4.

The mechanism for generating a harmonic time-variant pressure ΔP_t is as follows: It consists of a nozzle and a rotary disk possessing 24 teeth of sinusoidal shape on its outer circle. When the disk rotates, a gap between the nozzle and the disk edge changes harmonically. Therefore, when a jet from the nozzle is injected toward the rotating disk, a harmonic fluctuating pressure is produced in the nozzle tube. The frequency of fluctuating pressure is controlled by the rotational speed of the disk. This fluctuating pressure is exerted on flow in a test section, where a reference pressure transducer and the probe tube–pressure transducer system are aligned on a line perpendicular to the flow path. The frequency response of the probe tube system was determined by comparing signals from both the transducers, mainly as a function of pressure frequency and velocity of "grazing" flow at the point on the blade surface where the probe tube opens.

An example of experimental results obtained with this apparatus is illustrated in Fig. 5. The results testify that the frequency response of the probe tube system is strongly influenced by grazing flow velocity as well as frequency of fluctuating pressure. Frequency response data for the probe tube system were also collected by a different method of comparing signals from two pressure transducers. One was the probe tube pressure transducer system fixed on an oscillating airfoil in flow. The other was a miniature pressure transducer embedded in the same oscillating airfoil. The sets of response data from the same probe tube system, acquired by two different methods, resulted in a very good agreement.

The frequency response characteristics of the electronic data acquisition system, namely the d-c amplifier (A_d, ϕ_d) and the data recorder (A_r, ϕ_r), were also determined using a function signal generator and an FFT analyzer.

The time-dependent pressure signals and the strain gage signals were analyzed into 32 time-averaged function data referenced to the blade oscillatory displacement signals. Then, the following quantities were calculated through equations (3) to (8): unsteady aerodynamic torsional moments, chordwise distributions of unsteady pressure amplitude and phase lag referenced to the blade oscillation, and local aerodynamic energies produced by unsteady aerodynamic pressures.

In this paper, it was considered that cascade torsional flutter occurred when the imaginary part of the unsteady aerodynamic torsional moment had a positive value. The positive value of local aerodynamic energy indicates that the unsteady aerodynamic force acting on a small portion of blade surface stimulates the blade oscillation.

Calculation of Aerodynamic Quantities From Measurements

(A) Unsteady aerodynamic moment coefficient by cross spring bar C_{m1}

$$C_{m1}=\frac{M_{ta}}{1/2\rho U_2^2 c^2 b\alpha_1}=\frac{1}{1/2\rho U_2^2 c^2 b}\left(\frac{M_{tc}}{\alpha_{1c}}-\frac{M_{ti}}{\alpha_{ii}}\right) \quad (3)$$

(B) Unsteady aerodynamic moment coefficient (1), unsteady aerodynamic lift coefficient (2), and local aerodynamic energy (3) calculated from unsteady aerodynamic pressure data

(1) Unsteady aerodynamic moment coefficient, C_{m2}

$$C_{m2}=\frac{1}{1/2\rho U_2^2 c^2\alpha_1}\int_0^1 [\Delta P_{ai}*(a-x_i)-\Delta P_{ai}^{+}*(a-x_i^{+})]dx \quad (4)$$

(2) Unsteady aerodynamic lift coefficient, C_{Lt}

$$C_{Lt}=\frac{1}{1/2\rho U_2^2 c\alpha_1}\left[-\int_0^1 \Delta P_{ai}^{+}\,dx_i^{+}+\int_0^1 \Delta P_{ai}\,d\bar{x}_i\right] \quad (5)$$

(3) Aerodynamic energy and local aerodynamic energy acting on an oscillating blade

The aerodynamic energy per one cycle of an oscillating blade is

$$E=\oint M_t d\alpha_1=\oint \sum^{i}\Delta p_{ai*}\sin(\omega t+\phi_i)*L_i*\Delta X_i*d\alpha_1$$

$$=\pi\alpha_1\sum^{i}\Delta P_{ai}*\sin\phi_i*L_i*\Delta X_i \quad (6)$$

The local aerodynamic energy acting on a unit area of the blade surface is

$$\Delta E=\Delta P_{ai}*L_i*\sin\phi_i/(1/2\rho U_2^2 c\alpha_1) \quad (7)$$

The unsteady pressure amplitude is

$$A\equiv\Delta P_{ai}/1/2\rho U_2^2\alpha_1 \quad (8)$$

4 Experimental Results

Experiments were carried out for four cases of cascade outlet flow from high subsonic to supersonic: $\bar{M}_2=0.682$ (this flow state corresponds to the state of 20 percent mass flow control valve open area ratio), $\bar{M}_2=0.958$ (30 percent), $\bar{M}_2=1.242$ (40 percent), $\bar{M}_2=1.390$ (60 percent). In the experiment, inlet flow velocity of the cascade was subsonic from $\bar{M}_1=0.303$ to $\bar{M}_1=0.334$. The Reynolds number based on the chord length was in the range from $1.91*10^6$ to $4.0*10^6$. In each steady flow state, the oscillatory frequency of turbine cascade blades was changed from 25 Hz to 200 Hz, maintaining an interblade phase angle of 67.5 deg.

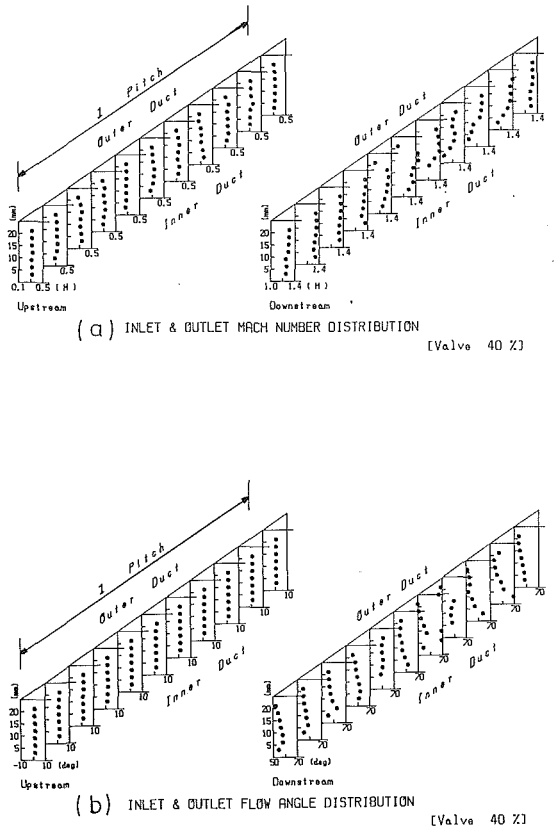

Fig. 6 Inlet and outlet flow angle and Mach number distributions (valve 40 percent)

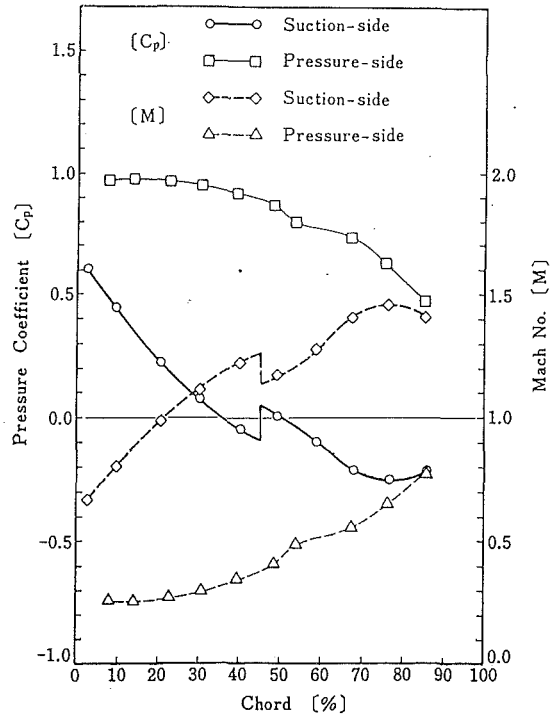

Fig. 7 Pressure and Mach number distribution on blade surface ($\bar{M}_2 = 1.242$)

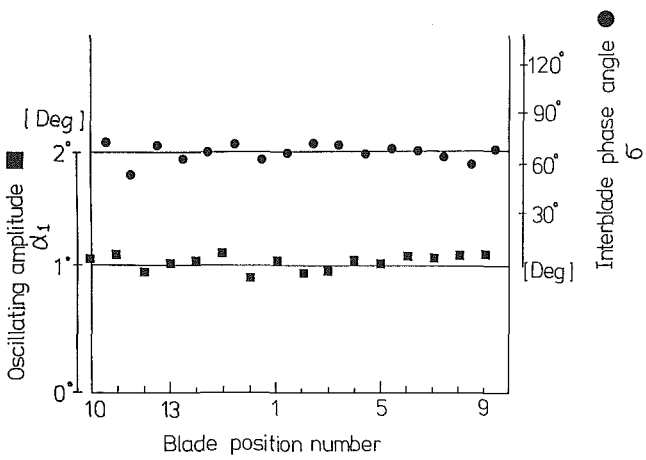

Fig. 8 Amplitudes and interblade phase angles of 16 oscillating blades (at 175 Hz)

4.1 Steady Flow Characteristics of Test Turbine Cascade. Examples of experimental results for the steady flow operation of the turbine cascade are shown in Figs. 6 and 7. The measuring positions indicated in Fig. 6 correspond to those shown in Fig. 2. Flow angle and velocity distributions over one pitch distance upstream and downstream of the cascade may be described as follows: Both inlet flow angle and velocity are uniform in the radial direction as well as in the circumferential direction, but the outlet flow angle and velocity are not as uniform due to blade wake and shock wave. Flows upstream and downstream of the cascade showed a good periodicity in the circumferential direction. The downstream flow has a little less periodicity than the upstream one due to blade wake and shock wave [5, 6].

Figure 7 indicates chordwise distributions of local pressure coefficient C_p and local velocity on both the suction and pressure surfaces of the blade for outlet Mach number 1.242. In this case, supersonic flow appeared on the suction surface. The throat region of the cascade was near 25 percent chord length position and the location of the shock wave was about 45 percent chord length, where a pronounced change of static pressure is observed in Fig. 7.

4.2 Annular Cascade Airfoil Oscillation. An oscillation test of the cascade airfoils was carried out with the mechanical drive system at a frequency up to 500 Hz [5]. The spectra of blade oscillation showed that the drive system could produce a torsional oscillating amplitude of 1.0 deg containing second and third harmonic components 20 dB below the fundamental evens at the maximum frequency of 500 Hz. The variation of airfoil amplitude for oscillatory frequency indicated that the drive system could oscillate blades at a constant amplitude up to a frequency of 500 Hz.

As an example of the blade oscillation data, Fig. 8 illustrates oscillatory amplitudes and interblade phase angles of the 16 blades at a frequency of 175 Hz. This figure shows that all of the 16 blades were forced to vibrate at almost the same amplitude of 1 deg and at almost the same interblade phase angle of 67.5 deg by the drive system. The averages and standard deviations of torsional amplitude and interblade phase angle in this case were 1.056 deg, 0.09 deg and 67.7 deg, 6.20 deg, respectively. These values were held almost constant up to a frequency of 200 Hz in this experiment. The oscillation test results indicated that the drive system could make the distributions of amplitude and interblade phase angle of the cascade blades consistent enough for flutter experiments.

4.3 Unsteady Aerodynamic Damping Characteristics of the Turbine Cascade. The unsteady aerodynamic damping characteristics of a transonic turbine cascade with a deflection angle of 61 deg were studied in the range of reduced frequency from $K = 0.056$ to $K = 0.915$, maintaining an interblade phase angle of 67.5 deg.

4.3.1 Region of Unstalled Cascade Flutter. Figure 9 il-

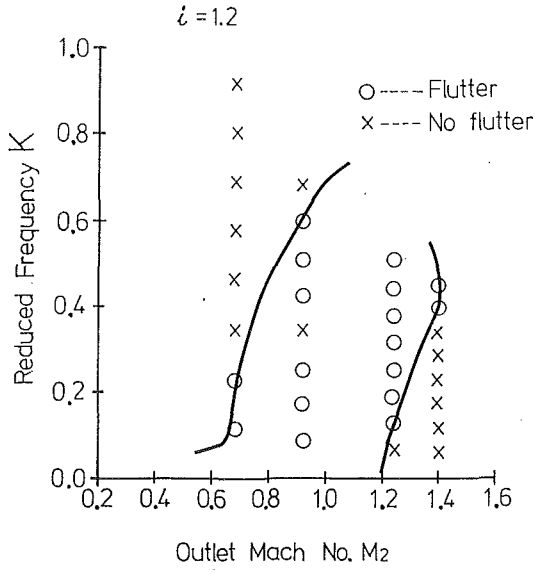

Fig. 9 Region of unstalled cascade flutter

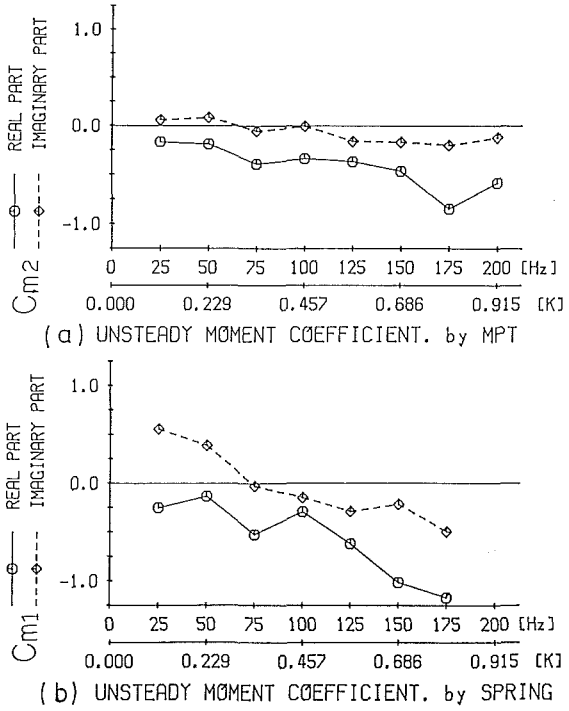

Fig. 10 Unsteady aerodynamic moment ($\bar{M}_2 = 0.682$)

lustrates the region of unstalled turbine cascade flutter clarified in this experiment. In the figure, the circle sign ○ indicates flutter occurrence points, while the cross sign × indicates a positive aerodynamic damping point. In this experiment, it was considered that unstalled cascade torsional flutter occurred when the imaginary part of the unsteady aerodynamic torsional moment had a positive value, namely in generating a negative aerodynamic damping. The figure shows that unstalled cascade flutter can occur over a wide range of outlet flow velocities from high subsonic to supersonic, and that transonic flow produces a remarkable increase in the reduced frequency range of flutter occurrence.

In the case of $\bar{M}_2 = 0.682$, where flows on both the pressure and suction surfaces of the blade are subsonic and the maximum local Mach number is 0.9, flutter occurs at reduced frequencies lower than $K = 0.25$. In the case of $\bar{M}_2 = 0.958$, where

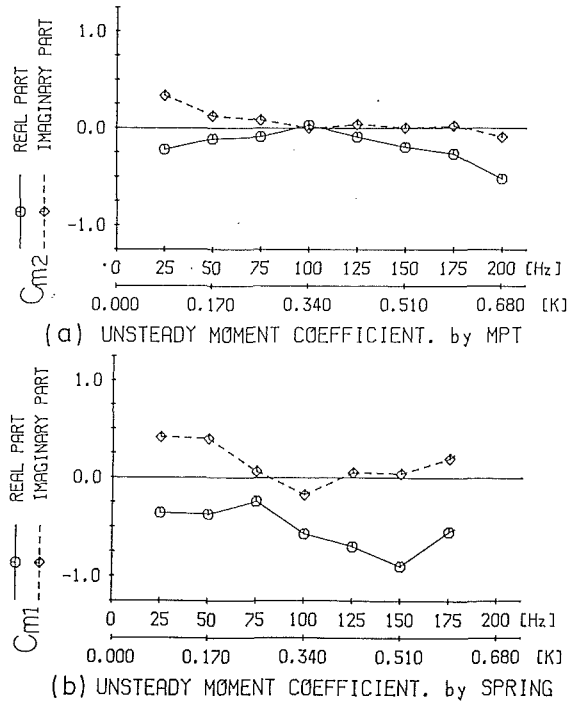

Fig. 11 Unsteady aerodynamic moment ($\bar{M}_2 = 0.958$)

the flow downstream of 20 percent chord position on the suction surface is supersonic and the maximum local Mach number is 1.2, the reduced frequency range of flutter occurrence spreads to $K = 0.65$. For an outlet Mach number of $\bar{M}_2 = 1.24$, flutter occurs at reduced frequencies higher than $K = 0.063$. In the case of outlet Mach number $\bar{M}_2 = 1.39$ and maximum local Mach number 1.70, flutter occurs at reduced frequencies higher than $K = 0.335$.

4.3.2 Effects of Outlet Flow Velocity and Reduced Frequency on Unsteady Aerodynamic Moment. Unsteady aerodynamic moments were acquired by two methods: calculation from the measurement data of chordwise unsteady pressure distributions (Method I) and measurement of torsional moment by the cross spring bar (Method II). Figures 10(*a*) to 12(*a*) show the unsteady aerodynamic moment Cm_2 obtained by Method I, while Figs. 10(*b*) to 12(*b*) indicate the unsteady aerodynamic moment Cm_1 obtained by Method II.

The effects of outlet flow velocity and reduced frequency on the unsteady aerodynamic moment can be examined through Figs. 10(*a*)-12(*b*). At subsonic flow (Fig. 10), the imaginary part of Cm_2 decreases in accordance with the increase in reduced frequency K and changes from a positive value to a negative one. At sonic outlet flow (Fig. 11), the imaginary part of Cm_2 gradually decreases between $K = 0.340$ and 0.595, but its value is almost positive. The real part of Cm_2 is almost negative. At supersonic outlet flow (Fig. 12), the imaginary part of C_{m_2} changes from a negative to a positive value around a reduced frequency of 0.120 and above this reduced frequency it is kept at an approximately constant positive value.

The variation of Cm_1 for reduced frequency significantly corresponded with the one of Cm_2 in the case of the same cascade outlet flow velocity. However, both the real and imaginary parts of Cm_1 were about twice as large as the corresponding values of Cm_2. As regards the cause of the differences, the following effects on unsteady aerodynamic moment were considered: (*i*) the effect of cascade solidity variation in the radial direction, and (*ii*) the effect of three-dimensional steady flow in the cascade, and (*iii*) the effect of

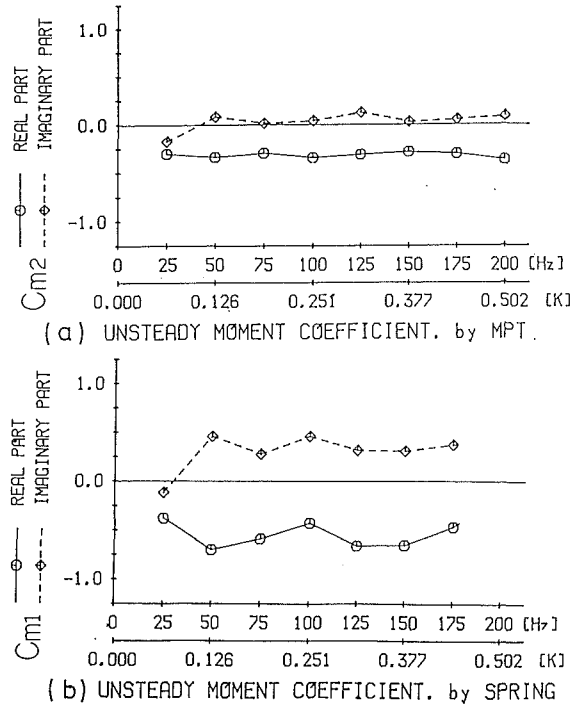

Fig. 12 Unsteady aerodynamic moment ($\bar{M}_2 = 1.242$)

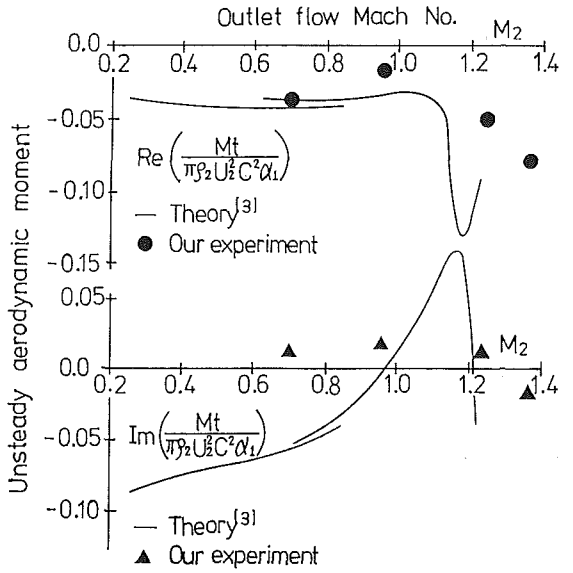

Fig. 13 Comparison between experimental result and theoretical analysis

secondary flow near inner and outer casing walls due to the small aspect ratio cascade. The variation of the observed unsteady aerodynamic properties due to these three effects are problems that need to be solved.

From the unsteady aerodynamic moment data and the steady flow data, it was suggested that the unsteady flow phenomena in the present high hub/tip ratio annular cascade were comparatively two dimensional, and so the measuring data at midspan could be used as the representative quantity of unsteady aerodynamic damping characteristics of the annular turbine cascade.

The work done by unsteady aerodynamic forces acting on the oscillating blade was also investigated. In the case of $\bar{M}_2 = 1.242$, the work changed from a negative value to a positive one in accordance with increase in reduced frequency K. As an example, at $K = 0.32$, the quantity of work was about

Table 1 Cascade conditions of experiment and theory

	Experiment	Theory
Space chord ratio	0.804	0.851
Stagger angle	45.5	45
Interblade phase angle	67.5	45
Torsional axis position	0.195%	0.334%

0.5 percent of aerodynamic energy $1/2\rho U_2^2 C$ per unit span length.

4.3.3 Comparison Between Experimental Results and Theoretical Analysis. Figure 13 shows a comparison between the author's experimental results and the theoretical results calculated by D. S. Whitehead's finite element method [3]. In the theoretical analysis, flow on the blade suction surface is subsonic at the leading edge side and supersonic at the trailing edge side, while flow on the pressure surface is subsonic. This flow state is the same as the one in the present experimental case. The cascade conditions of this experiment and Whitehead's theoretical analysis are described in Table 1. The two cascade conditions are similar to each other. The variation of flutter occurrence for outlet flow velocity in the present experiment showed a very good agreement with the one in the theoretical analysis, which predicted flutter disappearance at outlet Mach number 1.30. The cascade flutter occurs at the outlet flow Mach number of $\bar{M}_2 = 0.7$ and disappears at outlet Mach number of $\bar{M}_2 = 1.3$.

4.3.4 Effect of Unsteady Pressure Distribution on Flutter Occurrence. Figures 14 and 15 indicate unsteady pressure chordwise distributions (amplitude and phase lag) and local aerodynamic energy distributions on both suction and pressure blade surfaces. These are experimental results for three reduced frequencies in subsonic and supersonic outlet flows.

In the case of $\bar{M}_2 = 0.682$ (Fig. 14), on the pressure side, reduced frequency only weakly influences distributions of unsteady pressure amplitude and phase lag and local aerodynamic energy. The unsteady pressure phase lag referenced to blade oscillation changes only a little in the chordwise direction except in the leading edge region. Over most of the blade its value is about 20 deg phase lead. The unsteady pressure amplitude increases toward the rear of the blade. The local aerodynamic energy is negative over the blade pressure surface except for the region around leading edge. Its numerical magnitude increases toward the blade rear. The negative value of local aerodynamic energy indicates that the unsteady aerodynamic force acting on the small portion of blade surface damps the blade oscillation.

In contrast, on the suction side, the chordwise distributions of amplitude and phase lag are strongly dependent on reduced frequency. At the reduced frequency of $K = 0.915$, the unsteady pressure phase changes from 0 deg to 190 deg over the blade surface. This results in the variations of sign of local aerodynamic energy on the surface, and also the local aerodynamic energy of positive quantity is small.

The chordwise phase distribution at a reduced frequency of $K = 0.114$ is similar to the one at $K = 0.457$. These values of phase lead are about 90 deg over the surface except the leading edge side, and therefore in the region downstream of the torsional axis the local energy is positive. Its positive quantity increases toward the trailing edge side, especially at a lower reduced frequency. The positive value of local energy means that the aerodynamic force acting on that portion of the blade stimulates blade oscillation. The increase in positive local energy led the cascade to flutter at a reduced frequency lower than $K = 0.343$. The throat region movement produced by the oscillation of cascade blades produces large unsteady pressure

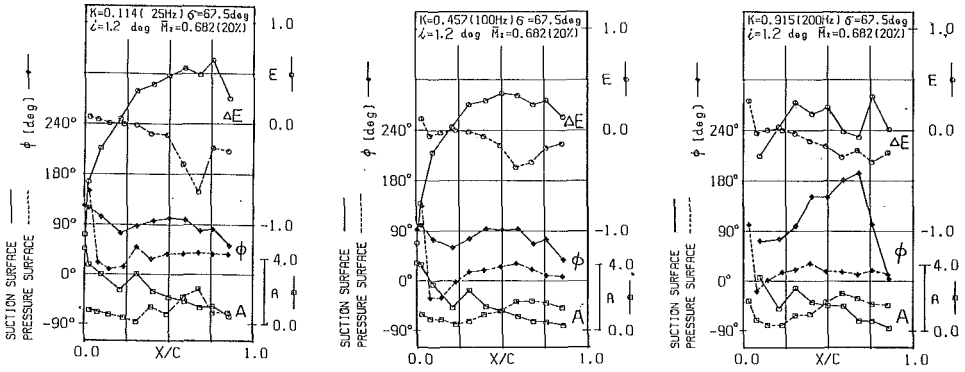

Fig. 14 Distribution of unsteady aerodynamic pressure and local aerodynamic energy on blade surface ($\bar{M}_2 = 0.682$)

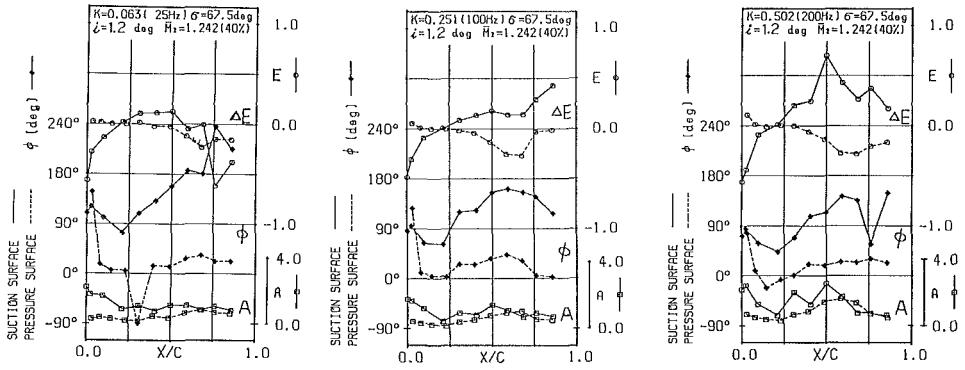

Fig. 15 Distribution of unsteady aerodynamic pressure and local aerodynamic energy on blade surface ($\bar{M}_2 = 1.242$)

amplitude near the throat flow point of 25 percent chord length on the suction surface for both high subsonic and transonic flows.

In the case of $\bar{M}_2 = 1.242$ (Fig. 15), the unsteady pressure and local energy distributions on the pressure surface are very similar to ones in the case of $\bar{M}_2 = 0.682$, while the distributions on the suction surface are remarkably different from those in the subsonic outlet flow case. The notable points in the supersonic flow case are a decrease in unsteady pressure amplitude over the suction surface, and the generation of large unsteady pressure amplitude in the shock wave region of the suction surface.

In the case of $\bar{M}_2 = 1.242$, on the blade suction surface, reduced frequency influenced the pressure phase chordwise distribution so significantly that flutter could occur in accordance with an increase in reduced frequency.

At $K = 0.063$ where no cascade flutter occurred, the phase lead on the suction side largely changes from 90 deg to 240 deg. Therefore, the region of positive local energy is narrow and local energies of large negative quantity appear in regions upstream of the torsional axis and around the trailing edge. In the cases of $K = 0.251$ and $K = 0.502$ where cascade flutter occurred, the phase lead changed from 90 deg to 160 deg over the suction surface and therefore the local aerodynamic energy of large positive quantity is generated in the region downstream of the torsional axis. The generation of large positive local energy caused the occurrence of flutter. At $K = 0.502$, the movement of the shock wave due to blade oscillation contributes significantly to the occurrence of cascade flutter [14].

5 Concluding Remarks

The unsteady aerodynmic damping characteristics of a transonic annular turbine cascade with high deflection were investigated using a Freon gas annular cascade test facility.

For measurement of the unsteady aerodynamic forces acting on oscillating blades in both aerodynamic stable and unstable domains, whole blades composing the turbine cascade were oscillated with a prescribed amplitude and frequency torsional mode by a high-speed mechanical drive system, without using vibratory resonance of blade system.

The measurement of unsteady aerodynamic forces was carried out by two different measuring methods, over a wide range of outlet flow Mach number M_2 from 0.68 to 1.39, for reduced frequencies K from 0.056 to 0.915, and at an interblade phase angle of 67.5 deg.

The main experimental results are as follows:

(*i*) Unstalled turbine cascade flutter in the torsional mode occurred within a wide range of reduced frequency and outlet flow velocity of the experiments. Especially in transonic flow, the reduced frequency of flutter occurrence was remarkably higher than that observed in subsonic flow. As regards the flutter occurrence and disappearance in accordance with increase in outlet flow velocity, the author's experimental results showed a good agreement with the theoretical results of Whitehead [3].

(*ii*) In high subsonic flow, unsteady aerodynamic forces acting on the blade suction surface downstream of the torsional axis played an important role in the occurrence of unstalled cascade flutter. With a decrease in reduced frequency, the effect of the forces changed from a blade oscillation damper into an oscillation stimulator and caused the occurrence of flutter.

In transonic flow, with increase in reduced frequency, local unsteady aerodynamic energy of large positive quantity was generated on the suction surface downstream of the torsional axis. The large positive aerodynamic energy led the cascade to flutter. In the flutter phenomenon, the role of shock wave movement due to blade oscillation was very important.

(*iii*) In the experiment, the occurrence of cascade torsional flutter was judged from the generation of a positive imaginary part of the unsteady aerodynamic moment acting on the oscillating blades. The unsteady aerodynamic moments were determined by two methods: the direct measurement of unsteady moment by a network of dual strain gages on the cross spring bar of blade, and a calculation from the measurement of unsteady aerodynamic pressures on both suction and pressure surfaces of a blade with 22 probe tube–transducer systems.

The variations of these two unsteady aerodynamic moments for reduced frequency were in a very good agreement qualitatively and quantitatively for four cases of cascade outlet flow velocity. Through these aerodynamic data, the phenomena of unstalled turbine cascade flutter were clarified.

Acknowledgments

The author is grateful to many colleagues at NAL for advice and assistance on this experiment. The author also wishes to thank the Moonlight Project of the Industrial and Technology Agency in the Ministry of International Trade and Industry for financial support of this research project.

References

1 Fleeter, S., "Aeroelasticity Research for Turbomachine Applications," *Journal of Aircraft*, Vol. 16, No. 5, 1979, pp. 320–326.

2 Namba, M., and Isikawa, A., "Three-Dimensional Aerodynamic Characteristics of Oscillating Supersonic and Transonic Annular Cascades," ASME *Journal of Engineering for Power*, Vol. 105, 1983, pp. 138–146.

3 Whitehead, D. S., "The Calculation of Steady and Unsteady Transonic Flow in Cascade," CUED/A-Turbo/TR 118, 1982.

4 Casper, J. R., Hobbs, D. E., and Davis, R. L., "Calculation of Two Dimensional Potential Cascade Flow Using Finite Area Methods," *AIAA Journal*, Vol. 18, No. 1, Jan. 1980, pp. 103–109.

5 Kobayashi, H., "Unsteady Aerodynamic Characteristics of Annular Cascade Oscillating in Transonic Flow, 1st Report, Measurement of Aerodynamic Damping With Freon Gas Controlled-Oscillating Annular Cascade Test Facility," *Bulletin of JSME*, Vol. 29, No. 256, Oct. 1986, pp. 3303–3312.

6 Kobayashi, H., "Measurement of Unsteady Pressure Distribution on Oscillating Airfoil in a Turbine Annular Cascade," ASME Paper No. 83-Tokyo-IGTC-69, 1983.

7 Kobayashi, H., "Unsteady Aerodynamic Characteristics of Compressor Annular Cascade Blades Oscillating in Transonic Flow," *Journal of Gas Turbine Society of Japan*, Vol. 13, No. 49, June 1985, pp. 65–73.

8 Riffel, R. E., and Fleeter, S., "The Experimental Modeling of Unstalled Supersonic Turbofan Flutter," AIAA Paper No. 80-0454, 1980.

9 Hanamura, Y., Fujimoto, K., and Yamaguchi, K., "High Speed Cascade Experiment in a Linear Cascade Using Freon Gas," *Proceedings of 22 Aeroengine Symposium*, Tokyo, Feb. 1982, pp. 6–9.

10 Kirschener, A. M., and Fosco, B., "Control of Vibration in Aeroelastic Cascade Experiments," *Proceedings of IUTAM Symposium on Aeroelasticity in Turbomachines*, Lausanne, Switzerland, Sept. 1980.

11 Boldman, D. R., Buggele, A. E., and Michalson, G. M., "Stall Flutter Experiment in a Transonic Oscillating Linear Cascade," NASA-TM 82655, 1981.

12 Whitehead, D. S., and Grant, R. J., "Force and Moment Coefficients for High-Deflection Cascades," *Proceedings of IUTAM Symposium on Aeroelasticity in Turbomachines*, Lausanne, Switzerland, Sept. 1980.

13 Tijdeman, H., "Investigations of the Transonic Flow Around Oscillating Airfoils," NLR-TR 77090 U, 1977, National Lucht-EN Ruimtevaart Laboratorium, The Netherlands.

14 Kobayashi, H., "Effects of Shock Waves on Aerodynamic Instability of Annular Cascade Oscillation in a Transonic Flow," ASME JOURNAL OF TURBOMACHINERY, Vol. 111, No. 3, July 1989, pp. 222–230.

15 Kobayashi, H., "Annular Cascade Study of Low Back-Pressure Supersonic Fan Blade Flutter," ASME Paper No. 89-GT-297, 1989; JOURNAL OF TURBOMACHINERY, Vol. 112, 1990, pp. 768–777.

Parametric Trends in the Flutter of Advanced Turboprops

E. F. Crawley

E. H. Ducharme

Gas Turbine Laboratory,
Massachusetts Institute of Technology,
Cambridge, MA 02139

The parametric trends in the aeroelastic behavior of an advanced turboprop were experimentally investigated using a subvelocity-scaled testing procedure. A 2-ft-dia subvelocity-scaled model was constructed and its flutter behavior was favorably correlated to that of a full-velocity-scaled UnDucted Fan™ model for which a flutter point had been documented. With the validity of the subvelocity-scaled procedure established, the inherent versatility was exploited through the construction and flutter testing of models which allowed for the parametric variation of sweep, mass distribution, and solidity. The correlation between an analytic model developed and the experiment is favorable for variation in mass distribution and sweep. As is typical of moderate mass ratio wings and blades, the flutter was found to be of a coalescence type, the onset of which is determined by a critical relative velocity with a slight dependence on loading and cascade effects.

Introduction

Propfan and UnDucted Fan™ blades possess aeroelastic parameters unlike those of previous lifting or propulsive airfoils. These advanced turboprop blades are designed to have low thickness, high sweep, high loading, large deformation, moderate solidity, moderate mass ratio, and significant anisotropic stiffness coupling. This nature has complicated the analysis of both the flutter and forced response.

Advanced turboprop blading is a hybrid between conventional turbofan blading and traditional propellers. The central question to be addressed is which features of turbofan versus propeller aeroelasticity will dominate the flutter behavior of the advanced turboprop? More specifically, to what extent will the moderate mass ratio cause the in-air resonances to deviate from the in-vacuo Campbell diagram? Is the solidity at the aeroelastically active outer part of the blade sufficiently high to cause the highly coupled system mode flutter typical of turbofans? And will changes in sweep and mass balance exhibit the classical isolated lifting surface influences on flutter?

To address these questions, it is important to conduct a thorough and fundamental set of experiments. The objective of this work is to contribute to the existing body of experimentation, and to the understanding of the underlying mechanisms of flutter in advanced turboprops. The approach used was to develop and verify an innovative subvelocity-scaled experimental technique, and then to conduct a well-controlled parametric experimental investigation.

Other investigations have used full-velocity-scaled model testing, in which models are run at high rotational speed, such that the velocity triangles and Mach numbers are matched to the full-scale turboprop. This full-velocity-scaled approach was employed by NASA and Hamilton Standard in the SR-n series of tests (Bansal et al., 1985; Mehmed and Kaza, 1986) and by NASA and General Electric in the MPS (Model Propulsion Simulator) tests of the UnDucted Fan™.

The alternative scale model approach used at MIT also involves sublength scale geometrically similar models, but operating at lower velocity. In such a subvelocity sublength-scaled approach, similar to that used in the development of fixed wing aircraft (Bisplinghoff et al., 1955), the thrust and torque coefficients and velocity triangles are similar to those of the full-scale fan, but the flow Mach numbers are not replicated. This option for scale model testing has been shown to match all of the important geometric, aerodynamic, static aeroelastic, and dynamic aeroelastic similarity parameters, with the exception of the Mach and Reynolds numbers (Hunt, 1973; Crawley and Ducharme, 1987). The advantages are that the low speeds result in low model stresses and low power requirements. Therefore, versatile models can be built which include such features as variable blade sweep, mass distribution and solidity. The experiments on these models yield valuable insight into the fundamental aeroelastic mechanisms of propfans in the subsonic regime. But these mechanisms also underlie the behavior in the transonic regime. In fact, the ability to completely predict the aeroelastic behavior in the subsonic regime can be thought of as a prerequisite to that ability in the transonic.

The initial goal of testing the baseline fan model was to simulate the flutter point of the full-velocity-scaled GE MPS F1 model, upon which the nominal configuration of the present subvelocity-scaled models was based. After a review of the scaling laws and design of the blades, this favorable correlation is presented. Next, the results of a series of experiments and analyses for the parametrically varied fan geometry are presented. The aeroelastic parameters that were varied are the sweep angle, solidity and mass distribution. The inferred trends in advanced turboprop flutter are then summarized.

Contributed by the International Gas Turbine Institute and presented at the 34th International Gas Turbine and Aeroengine Congress and Exhibition, Toronto, Ontario, Canada, June 4–8, 1989. Manuscript received at ASME Headquarters February 1, 1989. Paper No. 89-GT-280.

Blade Construction. The simple approach to the construction of reduced modulus anisotropic blades would be to select a fiber and matrix each with 6.3 percent of the elastic modulus of the graphite/glass fiber and epoxy matrix of the full-scale article, and replicate the blade laminate sequence. However, such low modulus laminate materials have proven to be difficult or impossible to obtain. Therefore, the approach developed was to use the lowest modulus fibers available (*E*-glass); the lowest modulus matrix material consistent with the material damping requirement (Shell Epon 828/871); the fiber volume fraction and ply stacking sequence which best match the anisotropic plate stiffness; and tungsten powder to adjust the average material density. The result was a blade model that closely simulated the frequencies and mode shapes of the full-scale fan.

A total of six model builds were constructed using this blade construction scheme. Each build was designated MnF1, where n is the build number. All blades were constructed using a wet layup in the split mold which had been cast from the original GE supplied F1 blade. Fans M1F1 through M3F1 were developmental builds of varied construction. The remainder of the blade sets were built with a 6 percent fiber volume of a $[13 \text{ deg} \pm 20 \text{ deg}]_{SYM}$ laminate, compared with a 60 percent fiber volume of the same laminate in the GE MPS F1 blades. The nominal geometry fan builds, designated M4F1 and M5F1, consisted of the glass/epoxy blade cast around an aluminum shank for disk attachment. The M4F1 was used for the nominal fan testing and modified for the variable mass distribution testing. The modification consisted of adding a single layer of 0.50 in. wide, 0.006 in. thick lead tape running 1.00 in. inward from the tip of both the suction and pressure sides. The tape could be positioned at the leading edge, midchord or trailing edge position, achieving a 13 percent section CG shift, based on the 80 percent typical section properties. The M5F1 blades were used for the variable solidity tests.

The M6F1 variable sweep blades consisted of two separate parts, a special shank with a sweep pivot hinge and a glass/epoxy blade cast around a metal insert which formed the other half of the sweep hinge. Since the dynamically active outer 70 percent of the span of the variable sweep blade was identical to that of the nominal blade, the presence of metal insert did not significantly affect the blade dynamics. The blades were designed to sweep ± 15 deg from the nominal F1 tip sweep of 37.5 deg. The sweep angle is defined as the tangent to the locus of midchord points. The sweep angle was set before testing with an indexing pin, and the hinge region of the blade was aerodynamically faired with aluminum foil tape.

Design of the Experimental Aparatus

Scaling Laws. Two options are available for scale model testing of advanced turboprops: the full-velocity sublength scale approach; and the subvelocity sublength approach. The scaling laws for both options were rigorously derived from an examination of the flutter equations (Ducharme and Crawley, 1987). The scaling laws establish the theoretical validity and limitations of each approach and the requirements for model design. In deriving the scaling laws, one must identify the geometric, aerodynamic, static aeroelastic, and dynamic aeroelastic parameters which should remain invariant to scaling. For the case of an advanced turboprop, the geometric parameters include blade shape, cascade stagger and solidity. The aerodynamic parameters are the velocity inflow triangles, and the Mach and Reynolds numbers. The static aeroelastic parameters are those which govern deformation due to dynamic pressure, as well as centrifugally induced blade stiffening, untwist, uncamber and unsweep. The dynamic aeroelastic parameters are reduced frequency and mass ratio.

If all of the similarity parameters are perfectly matched, then the aeroelastic behavior of the model will be identical to that of the full-scale device in a normalized sense. However, it is rarely possible to match exactly all of the aeroelastic and aerodynamic parameters simultaneously, and some compromises must be made in designing the model. Following the procedure for model scaling outlined in Bisplinghoff et al. (1955), a mass scale $[M_M/M_F]$, length scale $[L_M/L_F]$ and velocity scale $[U_M/U_F]$ were chosen as primitive variables and the scaling laws were derived. The model is assumed to be tested in a gas of the same density, speed of sound, and viscosity of the full-scale article, and that the geometry of the full-scale article is exactly replicated by the model design. But the model mass, length and velocity scales were maintained as free parameters.

Two scaling options emerge: the traditional full-velocity scaled option, in which the Mach number, but not the Reynolds number, is matched; and the subvelocity scaled option, in which neither the Mach nor Reynolds number is matched. If in the latter, the rotational speed is scaled by U_M/U_F then the velocity triangles (i.e., advance ratio) of the model will be similar to the full-scale fan. If the modulus of the blade is scaled by $[U_M/U_F]^2$, then all the static aeroelastic and centrifugal effects, including nonlinear deformations, will scale properly. If the blade density is matched, then the mass ratio and the reduced velocity are matched. The conclusion of this scaling analysis was that, while the Mach and Reynolds numbers will not be matched in a subvelocity-scaled test, all other similarity parameters can be exactly replicated. The blade for such a test must have all its dimensions scaled as $[L_M/L_F]$, all the anisotropic stiffnesses scaled as $[U_M/U_F]^2$, while the density and (implicitly) damping must be scaled as unity.

Blade Design. Six sets of such aeroelastically scaled anisotropic model fan blades were constructed and tested in the MIT Wright Brothers Wind Tunnel. The length scale factor L_M/L_F was chosen to be 0.175, due to the availability of a model blade of that scale. The General Electric Company (Aircraft Engine Business Group) supplied an MPS F1 (Model Propulsion Simulator, Forward stage, Mark 1 design) model blade, for which a flutter data point was known from a full-velocity-scaled test conducted by GE early in the UDF™ development program. The subvelocity scaled models were made in a mold which was cast from the MPS F1 blade, ensuring exact geometric similitude. The choice of length scale factor resulted in a 0.63 m (2.1 ft) dia model fan, an appropriate scale for the 7×10 ft wind tunnel.

The velocity scale factor U_M/U_F was chosen to be 0.25 in order to operate within the speed/power envelope of the wind tunnel and the 15 hp propeller test stand. The requirement that the modulus of the blade scale by $[U_M/U_F]^2$ indicated that a very flexible anisotropic construction would be required for the model. The material must be only 6.3 percent as stiff as the graphite/glass/epoxy lamina of the full-scale blades, but have the same density and material damping.

This combination of velocity and length scale factors yields a model Mach scale $[U_M/U_F]$ of 0.25, and a Reynolds scale $[U_M L_M/U_F L_F]$ of 0.044. At the 80 percent span typical section and design takeoff conditions, this gave an axial Mach number of 0.05, a relative Mach number of 0.29 and a Reynolds number of 500,000. The model operated at 0.05 percent of the full-scale power, which scales by $[U_M^3 L_M^2/U_F^3 L_F^2]$, 0.2 percent of the full-scale torque, which scales by $[U_M^2 L_M^2/U_F^2 L_F^2]$, and 6.3 percent of the full-scale stress, which scales by $[U_M/U_F]^2$.

Blade Structural Dynamics. As a precursor to the aeroelastic experiments, the natural frequencies and mode shapes of the blades were measured on the bench and under rotating in-vacuo conditions. The bench testing provided the nonrotating frequencies and mode shapes of the blades. Rotating tests provided information on the centrifugal stiffening of the blade natural frequencies in-vacuo. These experimentally

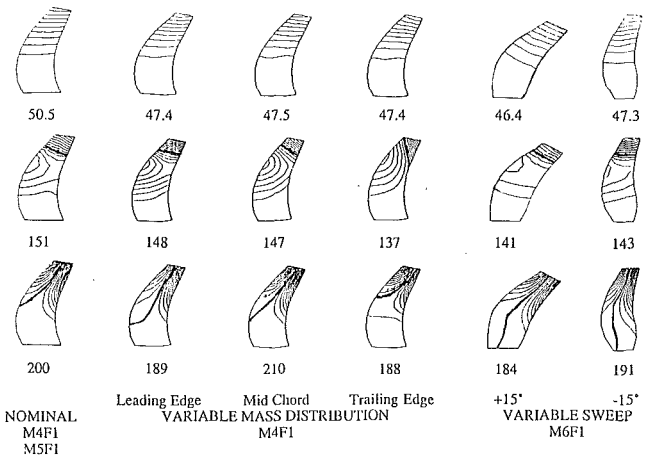

Fig. 1 Experimentally measured mode shapes of the blades (frequency shown below blade in Hz)

measured mode shapes and stiffening trends were used in the analytical flutter model.

The accuracy of scaling can be inferred by comparing the natural frequencies, mode shapes and damping of the nominal configuration-scaled blades (M4F1) with those of the GE MPS F1 full-velocity-scaled blades. The mode order is consistent between the M4F1 and MPS F1 models and the mode shapes were also in good agreement. The average modal damping ratio of 0.012 was just slightly higher than that of the MPS F1 blades. For a target velocity-scale factor of 0.25, the M4F1 model blade frequencies should be 0.25 times those of the MPS F1. The actual first three nonrotating frequencies (1B, 2B, 1T) are scaled from the MPS F1 blades by a factor of 0.23, 0.33, and 0.32, respectively. At the rotation speed which will be seen to correspond to flutter (50 rps), the in-vacuo frequencies are scaled by 0.34,0.33 and 0.33, respectively. Considering the developmental nature of the anisotropic model construction, this was considered excellent correlation, and indicates that the achieved velocity scale factor is about 0.33.

The first mode of the nominal blade is at 50.5 Hz and appears as a pure flatwise bending mode with almost no bending-torsion coupling (Fig. 1). The maximum blade-to-blade variation in frequency present in this mode was 2.5 Hz. The second mode of the blade, with a frequency of 151.4 Hz, is primarily a second bending mode with a significant torsion component present. The amount of torsion present in the second mode will be seen to be a sensitive parameter for aeroelastic stability of the fan. The third mode of the blade at 200.4 Hz is primarily a first torsion mode. The modes shapes of the M4F1 blade are qualitatively similar to those of the MPS F1. Also shown in Fig. 1 are the modes of the M4F1 blade with the lead tape in the three positions. The most striking effects of the change in tape position are evident in the second mode. The leading edge tape position 2B mode has almost no bend-twist coupling near the tip, while the 2b mode of the trailing edge tape position has a large torsion component.

The variable sweep M6F1 fan was bench-tested in its three sweep positions, two of which are shown in Fig. 1. In the nominal sweep position, the fan had frequencies of 46.3, 141, and 186 Hz, all about 8 percent lower than the corresponding M4F1 frequencies. However, the modes shapes are very similar to those of the nominal M4F1 fan. Thus it would be expected that the flutter behavior of the variable sweep fan in the nominal position would be very similar to that of the nominal fan.

The rotating in-vacuo natural frequencies of the nominal (M4F1) blades at takeoff pitch were determined in a spin stand. The data were used to estimate Southwell coefficients for the various blade modes. The spin stand tests were only conducted for the nominal fan. In the flutter analysis, the rotating frequencies of all the fans were predicted by applying the stiffing trends of the nominal fan to the nonrotating bench frequency of the particular fan in question.

Table 1 Flutter parameters of the nominal fan

	Experimental		Analysis
r/r_{tip}	1.0	0.8	0.8
r [m]	0.313	0.274	0.274
Ω_{FL} [RPS]	48.8	48.8	50.4
U_{ax} [m/s]	25.2	25.2	25.9
$U_{rel\ 0.8}$ [m/s]	99.2	90.7	93.4
ω_{FL} [Hz]	134.0	134.0	163.0
$k_{FL\ 0.8}$	--	0.272	0.321
$U_{FL\ 0.8}$	--	3.68	3.11

Wind Tunnel Apparatus and Instrumentation. The fans were assembled onto disks and mounted on the propeller test stand in the wind tunnel. Two split disks were used. The first was designed with eight blade slots, and was used for the M4F1 and M6F1 tests. The second, variable solidity disk, retained each blade in an individual collet and allowed for incremental blade counts from 2 to 12 blades. The fan models were mounted on, and powered by, an instrumented single rotation tractor configuration test stand containing a 15 hp d-c electric drive motor, instrumentation slip rings, and a set of fan thrust, torque and yaw force flexures (Crawley and Ducharme, 1987).

The test procedures and instrumentation were typical of fan aeroelastic testing. The eight blades were each instrumented with bending sensitive semiconductor strain gages. Two blades also were instrumented with a torsion sensitive gage. All strain gages were monitored on synchronized oscilloscopes, and two selected blade strain signals could be patched into a spectrum analyzer. The combination of time domain and frequency monitoring of the blade response allowed for reliable detection of the flutter onset point.

Aeroelastic Behavior of the Nominal Fan

Flutter Behavior. The objectives of the tests on the nominal fan were to identify the flutter mechanisms of the model, to validate the subvelocity scaling technique by correlation with the known full-velocity flutter occurrence in the GE MPS F1 fan, and to calibrate the simplified analytical model. Since the MPS F1 had fluttered in the unstalled takeoff configuration, all nominal testing was done in this configuration. At the takeoff design advance ratio $J_{DES} = 0.82$ ($J = U/\Omega D$), the model fluttered at a rotational speed of $\Omega_{FL} = 48.8$ rps (2930 rpm), a tunnel axial speed of 25.2 m/sec, and an axial speed of 34.1 m/sec at the plane of the propeller (corrected for induced velocity based on thrust measurements and actuator disk theory). The average flutter frequency ω_{FL} was 134 Hz, which corresponds to a reduced frequency $k_{FL} = \omega_{FL}\, b/U_{rel}$ at the 80 percent typical section of 0.27 (Table 1). The flutter frequency occurs between the in-vacuo Campbell diagram measurements of the first mode (95 Hz) and the second mode (180 Hz), as shown in Fig. 2. Measurements of the wind-on natural frequencies of the blades, made in the wind tunnel, also are plotted in Fig. 2. Comparison of the in-vacuo and wind-on natural frequencies clearly shows the influence of the unsteady

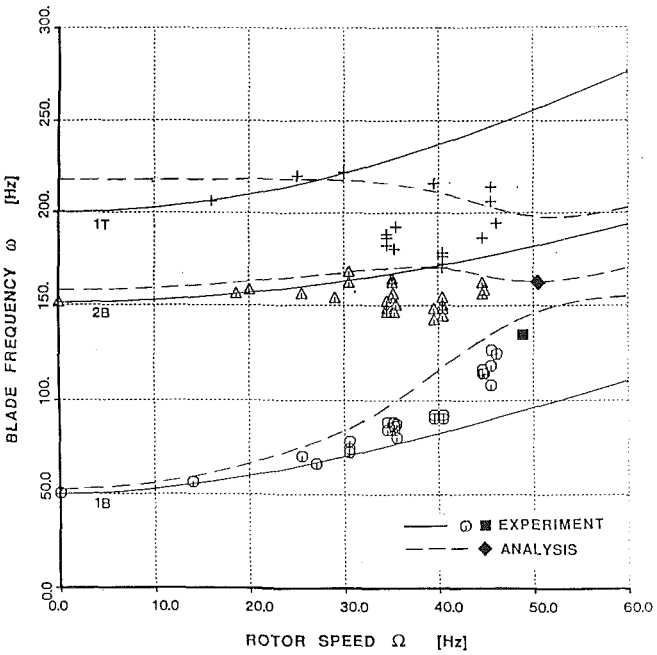

Fig. 2 Campbell diagram for the nominal (M4F1) fan, showing the curve fit to the experimentally determined in-vacuo Southwell coefficients (solid lines), the in-air natural frequencies measured in the wind tunnel (open symbols), the predicted in-air natural frequencies (broken lines), and the measured and predicted flutter points (solid symbols)

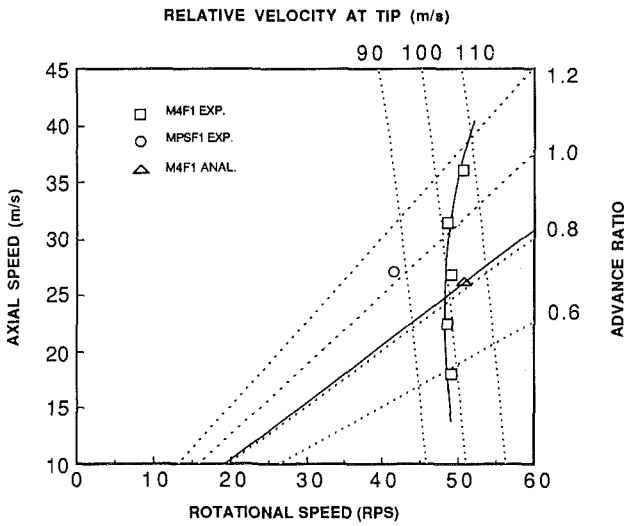

Fig. 3 Experimentally determined flutter boundary of the nominal (M4F1) fan and the normalized flutter point of the MPSF1 fan; the solid lines show the design advance ratio and predicted flutter relative velocity

aerodynamics below the flutter speed, and the coalescence of the first and second modes at flutter. Such coalescence behavior also was observed in the SR3C-X2, the GE MPS F1 and the CR-A7. This coalescence of modes is typical of low mass ratio wing flutter (Bisplinghoff et al., 1955); however, it is quite unlike the behavior usually observed in the flutter of higher mass ratio turbofans (Bendiksen and Friedmann, 1980). Since the mass ratio of the typical section of the advanced turboprop (22) is much closer to the range for an isolated wing (5–20) than a solid titanium turbofan blade (100–200), this coalescence behavior should not be unexpected.

For the fan operating at advance ratios other than J_{DES}, the rotational speed for flutter displayed only a small dependence on tunnel axial velocity. The flutter boundary is shown in Fig. 3, along with lines of constant tip geometric advance ratio and

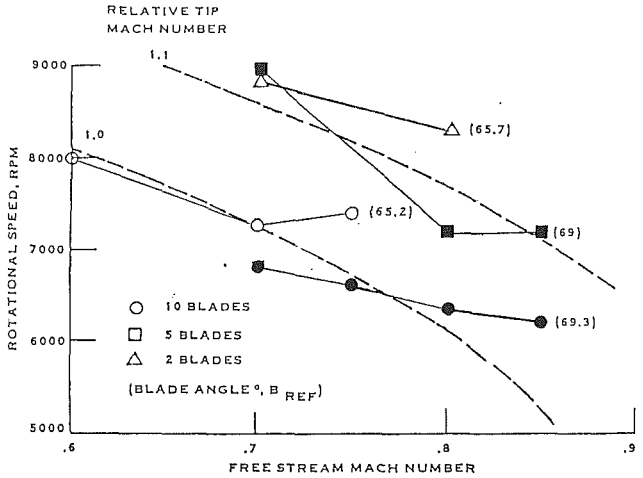

Fig. 4 Measured flutter boundaries for fixed blade angle of the SR-5 fan (from Mehmed et al., 1982), showing the stabilizing influence of higher advance ratio

lines of constant tip relative velocity (neither corrected for induced velocity affects). Interpretation of Fig. 3 gives further insight into the flutter mechanism. The onset of flutter can be seen to occur at some threshold value of relative velocity (or dynamic pressure, which follows the same isopleths). A destabilizing effect of increased blade loading at lower advance ratios also is evident, as predicted by theory (Whitehead, 1962). The same trend can be seen in the data from the SR-5 in Fig. 4, from Mehmed et al. (1982). Note the reversal of the axes in Fig. 4 from Fig. 3.

At low axial speeds the onset of flutter would typically be observed when one or more blades, not necessarily neighbors, would begin to vibrate at the flutter frequency. If the operating point of the fan was driven about 5 percent further into the unstable region, a system mode would result. At higher axial speeds, the inception of flutter would sometimes occur with the sudden dramatic onset of a system mode. Typically, system modes were one or two nodal diameter backward traveling modes.

Correlation With Full-Velocity Scale Model. One of the objectives of the nominal fan-testing was to validate the subvelocity scaled approach by simulating the flutter of the full-velocity scale MPS F1 model. The MPS F1 was observed to flutter in the takeoff configuration at $M = 0.20$ and 78 percent rotational speed ($\Omega_{FL} = 104$ rps or 6210 rpm). This corresponds to an advance ratio of $J = 1.04$ and a relative Mach number of 0.56 at the 80 percent span typical section, a fully subsonic operating point. The flutter frequency of 336 Hz was between the in-vacuo centrifugally stiffened first and second mode frequencies of 283 Hz and 538 Hz. The flutter occurred as a coalescence of the first two blade modes, and in a three nodal diameter backward traveling system mode. By normalizing the rotor speed at flutter by $(\omega_{FL})_{M4F1} / (\omega_{FL})_{MPS}$, a normalized flutter point for the MPS F1 can be plotted on Fig. 3. The MPS F1 normalized flutter point is 15 percent lower in rotational speed than the M4F1 model flutter boundary. With no axial inflow corrections applied, the reduced frequency at the typical section of the MPS at flutter is 0.32, 14 percent higher than the uncorrected reduced frequency for the M4F1 of 0.28. If the M4F1 were a perfect subvelocity-scaled model of the MPS F1, the scaling laws imply that these normalized flutter parameters would coincide. The lack of perfect correlation is probably attributable to realistic constraints in the structural scaling and the stabilizing influences of compressibility on the MPS.

The observed flutter phenomena are, however, very similar,

Both the MPS F1 and the M4F1 fans fluttered in a coalescence at a frequency which is between the first and second rotating natural frequencies as indicated on an in-vacuo Campbell diagram. Both fluttered in a backward system mode, three nodal diameter for the MPS F1, and one and two for the M4F1. The analysis discussed next indicates only a weak variation in the flutter relative velocity for the various nodal diameter modes.

The M4F1 replicated reasonably well the normalized flutter speed and reduced frequency of the MPS F1, reproduced the coalescence nature of the flutter in a backward traveling system mode of the MPS F1, and exhibited the flutter phenomena similar to several other full-velocity experimental fans. It can be concluded that, while the subvelocity testing will not necessarily exactly reproduce the flutter parameters of a full-scale fan, the understanding of the aeroelastic phenomena and trends gained from such testing should be directly applicable to full-scale devices.

Correlation With the Analytical Model. Since the objectives of this model were not the prediction of the flutter boundaries, but rather the correlation of the trends observed in the experimental data, a simplified analytical model was developed, similar to that of Turnberg (1983). The flutter equations of motion were derived for a rotor consisting of tuned blades fixed to a rigid hub. The equations were based on a truncated modal model which contained the first three experimentally measured mode shapes. Addition of higher mode shapes was not found to significantly change the predicted behavior. The assumptions were made that the natural frequencies of the blades increase with rotation speed, as was observed in the in-vacuo spin test of the nominal fan, but that the mode shapes remain unchanged with rotation speed. This latter assumption introduces a weakness into the analysis, in view of the known changes with speed in mode shapes of the higher modes of propfan blades (Srinivasan et al., 1986).

The unsteady subsonic aerodynamic theory of Smith (1973), in the form of the LINSUB computer code (Whitehead, 1987), was used in a strip theory calculation. The blades were divided into five spanwise computation stations at which the forces were calculated using the local flow parameters. In accordance with the sweep correction of Bisplinghoff et al. (1955), the loads were multiplied by the cosine of the sweep angle of the strip at its midchord. Despite the absence of a duct, no-spanwise rolloff of the load was applied. The modal effect of each strip was summed along the span, resulting in a quasi-three-dimensional model. Once the unsteady aerodynamic coefficients were calculated for the N permissible interblade phase angles and the advance ratio of interest, the flutter equations of motion were solved using the p-k flutter solution technique (Hassig, 1971).

The analytical modal flutter model was correlated with the experimental results for the nominal fan. For operation at the design advance ratio, the second mode branch is predicted to go unstable at a rotational speed Ω_{FL} of 50.4 rps as shown in Fig. 3. The predicted flutter rotational speed is 3 percent higher than the experimentally observed speed of 48.8 rps at the takeoff design advance ratio. The flutter frequency is predicted at 163.2 Hz, which when compared to the experimental flutter frequency of 134 Hz is an overprediction of 22 percent. The predicted blade natural frequencies as a function of rotor speed are overplotted in Fig. 2. The strong modifying effect that the aerodynamics have on the natural frequencies is evident, even below the flutter speed. The analysis indicates flutter is actually due to an interaction of the first three modes, each contributing roughly equally to the mode shape.

Parametric-Dependence on Sweep

Flutter Behavior. Having established the validity of the approach, the subvelocity scaled models were used to perform a series of experiments involving the variation of blade sweep, solidity and mass distribution on the planform. The remainder of this paper will describe the dependence of the aeroelastic stability on these parameters as observed in experimental testing and compare the experimental results with the predictions of the analytical model.

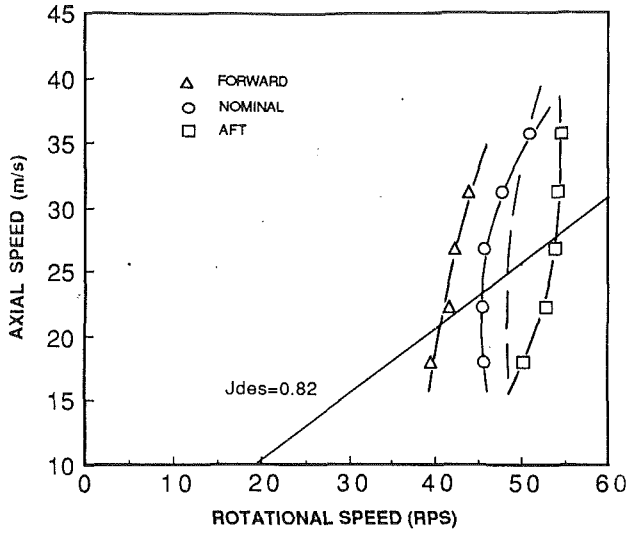

Fig. 5 Measured flutter boundaries of the variable sweep (M6F1) fan; the measured boundary of the nominal (M4F1) fan is shown as the broken line

The first parametric variation to be discussed is the dependence on sweep. The variable sweep mechanism in the M6F1 fan design allowed for a ±15 deg variation in sweep angle from the nominal midchord sweep of the F1 fan of 37.5 deg at the tip or 32.5 deg at the 80 percent span typical section. The change in blade stagger and incidence distribution of the fan is small for this small range of sweep. Since the model incorporates a constant length of the variable sweep portion of the blade, a nonconstant fan radius results as the blade sweep angle is changed. This approach to variable sweep testing has been termed by Barmby et al. (1951) as the rotated model technique; as opposed to the constant blade radius/variable blade length, or sheared model technique. The advantage of the rotated model approach is that the constant blade length results in relatively constant blade dynamics, the mode shapes being simply rotated with respect to the streamwise direction. The advantage of the sheared model approach is that the fan radius, and therefore the projected area, remains constant, resulting in a relatively constant fan thrust level. However, the structural dynamics of a sheared model also change with changing blade length. This approach makes it difficult to separate the relative effects of the changing structural dynamics from the changing aerodynamics, when interpreting the results. The sheared model approach would also clearly require a different fan build for each desired sweep angle.

The variable sweep fan fluttered in a manner similar to that of the nominal (M4F1) fan. The flutter boundary for the variable sweep fan is shown in Fig. 5. The stabilizing effect of increasing sweepback is apparent in this rotated model approach. The flutter boundary for the M4F1 fan also is plotted on the figure, showing that the M6F1 fan in the nominal sweep position was only slightly less stable than the nominal M4F1 fan. This is due to the effects of a slightly more flexible blade root due to the sweep hinge mechanism.

A flutter velocity parameter for the various sweep positions of the M6F1 fan is found by considering the intersection of the flutter boundaries with the line of constant design takeoff advance ratio. This condition allows for the comparison of the flutter behavior of the various sweep configurations of the fan of similar flow fields (Table 2). The flutter velocity pa-

Table 2 Variation of flutter parameters with sweep position

	Forward		Nominal		Aft	
$\Lambda_{0.8}$ [°]	17.5		32.5		47.5	
$r_{0.8}$ [m]	0.284		0.274		0.255	
$b_{0.8}$ [m]	0.0283		0.0293		0.0303	
	Exp.	Anal.	Exp.	Anal.	Exp.	Anal.
Ω_{FL} [RPS]	40.9	39.5	45.4	47.4	54.0	68.5
U_{ax} [m/s]	21.6	20.9	23.1	24.1	25.4	32.2
$U_{rel\,0.8}$ [m/s]	79.9	77.2	84.2	87.8	92.1	116.1
ω_{FL} [Hz]	147.0	144.0	132.0	182.0	122.0	175.0
$k_{FL\,0.8}$	0.327	0.332	0.289	0.380	0.252	0.286
$U_{FL\,0.8}$	3.06	3.01	3.47	2.63	3.97	3.49

rameter is taken as the relative velocity (corrected for induced velocity) at the 80 percent span typical section station at the flutter boundary intersection point with the line of takeoff advance ratio. The variation of U_{FL} with sweep position is shown in Fig. 6. Also plotted on the curve is a fit to the data of a function of the form: $U_{FL} = U_{FL0} / (\cos \Lambda)^{1/2}$, where Λ is the typical section sweep angle. This good correlation is in agreement with the isotropic fixed wing results of Barmby et al. (1951) in which the flutter speed ratio data are bounded by $1/(\cos \Lambda)$ and $1/ (\cos \Lambda)^{1/2}$.

The nominal sweep configuration of the M6F1 fan at J_{DES} fluttered at a rotational speed of 45.4 rps or a typical section relative velocity U_{FL} of 84.2 m/s (Table 2). For the aft sweep configuration, the fan flutter boundary intersection with the J_{DES} line occurred at speeds Ω_{FL} = 54.0 rps and U_{FL} = 92.1 m/s, which were 19 percent and 9 percent higher than their respective nominal sweep position values. For the forward sweep configuration, the intersection occurred at Ω_{FL} = 40.9 rps and U_{FL} = 79.9 m/s, which were 10 percent and 5 percent lower than the corresponding values observed in the nominal sweep configuration testing.

Correlation With the Analytical Model. The analytical model was used to predict the stability of the variable sweep fan (Fig. 6). The analytical results are shown for three different aerodynamic correction schemes: the cosine Λ sweep correction in the aerodynamic loads, with no-tip rolloff (the scheme used to correlate the nominal fan in Fig. 3); no-sweep correction with no-spanwise rolloff; and no-sweep correction, but including an elliptical spanwise rolloff of the aerodynamic loads in the outer 50 percent of the span. The general trend of increasing stability with increasing sweep angle that was observed experimentally is predicted by all three correction schemes. Surprisingly, the best correlation is with the scheme which does not explicitly make a correction for sweep in the aerodynamics. The cosine Λ sweep corrections with a flat spanwise loading distribution overpredicts the effect of sweep on the stability boundary. The rolled-off loads predict the correct trend, but consistently overpredict the stability. It is important to note that many important physical effects are not included in this analytical model, such as changes in incidence, loading and three-dimensional (radial flow) effects. In particular, the three-dimensional effects would be expected to be more apparent for the apt sweep experimental results because of the lower aerodynamic aspect ratio of the blades (based on radial height) in that configuration. Another possible source of error introduced in the structural model was the use of the same Southwell stiffening trends for all three sweep positions.

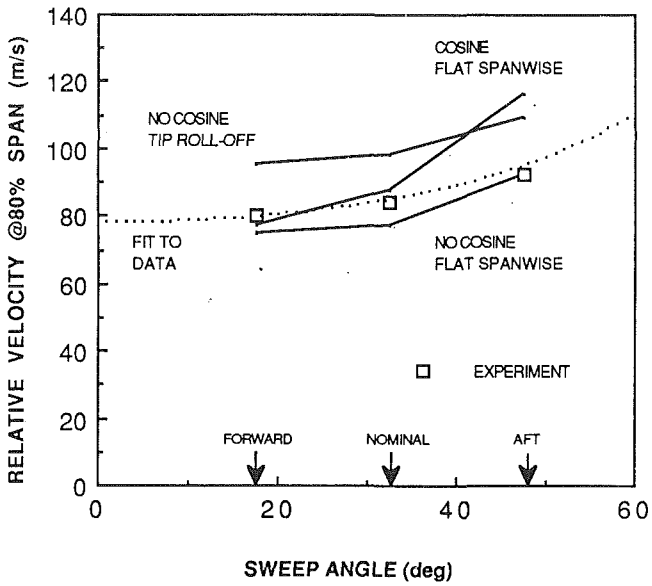

Fig. 6 Dependence of flutter relative velocity at flutter on sweep (both measured at 80 percent span); the broken line is the fit to the data of $1/(\cos \Lambda)^{1/2}$ and the solid lines are three analytical predictions

The analysis indicates that the nature of the flutter mode varies with sweep. As the blade is rotated forward, the first torsion mode shape becomes the largest component of the flutter mode while, as the blade is rotated aft, the second bending component dominates.

The results of the rotated blade sweep testing indicated the stabilizing effects of sweeping a constant length blade. This is an indication that the classical reduction in aerodynamic loads with sweep takes place in moderate solidity props. In the application of this result to the design of a swept fan, one must consider the fact that for rotated blade sweep testing, sweeping back the blade reduces the fan radius, as well as the thrust and power levels. In the alternate sheared blade, or constant fan radius approach, larger sweep angles have relatively longer and more flexible blades. These blades tend to be less stable than blades with smaller sweep (Kielb and Kaza, 1985). These trends have been reported by Bansal et al. (1985) in the SR-n series of tests.

Parametric-Dependence on Solidity

Flutter Behavior. With the solidity of 0.28 at the 80 percent span, lower than that of turbofans but higher than that of conventional propellers, there is some question as to what significance cascade effects will have on the stability. Due to the design of the variable solidity disk, a system was available for flutter testing of the model fan with fine gradations in solidity. The disk allowed for operation with single blade increments of from 2 to 12, but only the 4, 6, 8, 10 and 12-bladed configurations were tested. The M5F1 blade set used in the variable solidity experiments were identical to the nominal M4F1 blades.

The flutter points for the various configurations of the variable solidity fan are shown in Fig. 7. The flutter boundary is similar to that seen in the flutter testing of other fan builds, in that the onset of flutter was strongly dependent on the rotational speed with a much weaker dependence on the axial velocity. It is difficult to discern any trends in the solidity-dependence of the flutter boundary from the plot of Fig. 7.

The flutter relative velocity at the typical section U_{FL} was found to be roughly constant to slightly increasing with solidity over the range tested (0.14 to 0.42 at the 80 percent section). This result would seem to be contradictory to the results of

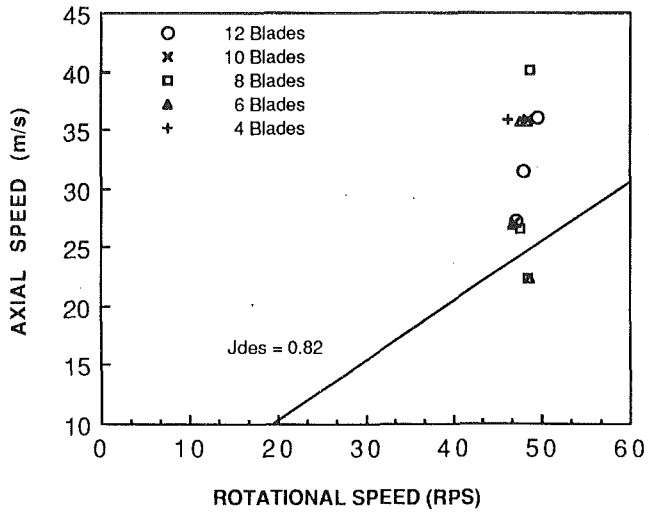

Fig. 7 Measured flutter boundary of the variable solidity (M5F1) fan

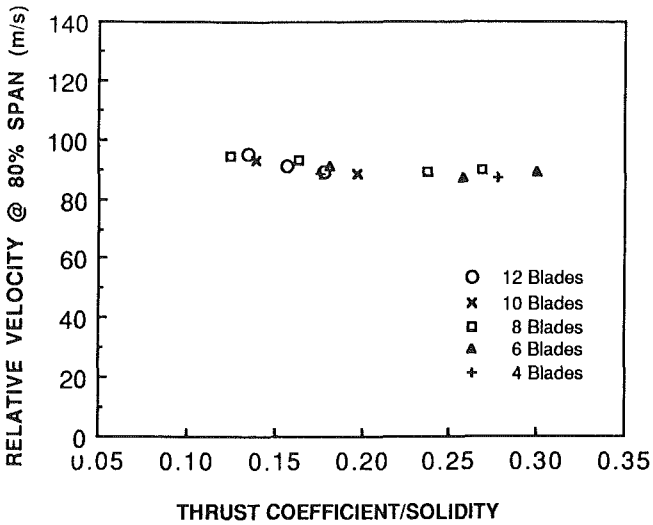

Fig. 8 Dependence of flutter relative velocity at flutter on normalized thrust coefficient

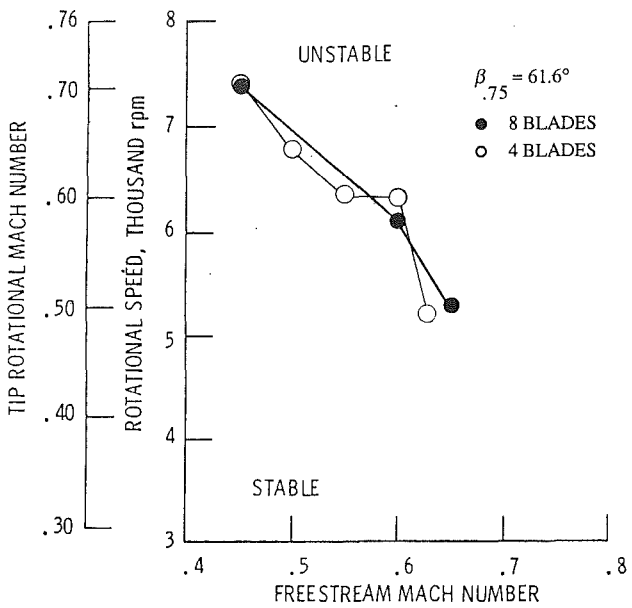

Fig. 9 Flutter boundary of the SR3C-X2 with 4 and 8 blades, showing the relative insensitivity of flutter to solidity (from Mehmed and Kaza, 1986)

cascade flutter analyses, and contrary to the conclusions drawn by Mehmed and Kaza (1986) for the SR3C-X2. Obviously, some other effects are modifying the typically destabilizing effects of increased solidity to result in this net constant, or slightly increasing dependence of flutter velocity on solidity.

One possible explanation for the flutter-speed dependence on solidity seen in the experimental results is an influence due to loading. It was seen in the flutter behavior of the nominal fan of Fig. 3 and the SR-5 in Fig. 4 that flutter speed decreased with an increase in loading; i.e., a decrease in advance ratio. A common measure of blade loading used in helicopter blade flutter (Ham, 1973) is the thrust coefficient normalized by the solidity of the typical section, C_T / σ. The thrust coefficient definition is

$$C_T = \frac{T}{A\rho(\Omega R_{Tip})^2}$$

where T is the fan thrust and A is the annular area of the fan. The flutter relative velocities are plotted as a function of C_T / σ in Fig. 8. Note that presenting the flutter data in this form causes it to show a slight decreasing trend with increasing load or C_T / σ; however, the sensitivity to loading is not very strong. It also is evident that the flutter points for the higher solidity fan configurations tended to occur at lower values of C_T / σ, but at slightly higher values of U_{FL}. Conversely, the lower solidity fan configurations tended to flutter under conditions of higher loading, C_T / σ, and lower values of U_{FL}.

In moderate solidity fans there is a balance between the destabilizing effects of loading with decreasing solidity (Whitehead, 1962) and the destabilizing effects of cascade influences at higher solidity (Crawley and Hall, 1985). For this fan, in this range of solidity and operating points, the modification of the critical flutter speed was more dependent on the destabilizing effects of loading than on the destabilizing cascade effects. These trends were observed at the takeoff blade stagger setting, which tends to be the operating point of highest fan disk loading. A stronger dependence on the cascade effects may be observed in high speed and advance ratios, where loading is lower, and the blade stagger angle setting is lower, increasing the propensity for cascade interaction.

No serious attempt to correlate the flutter trend with solidity with that predicted by the analytical model was made. This is because the Smith aerodynamic code always tends to predict lower stability with increased solidity. Neither the two-dimensional Smith code, nor the three-dimensional aerodynamic models currently being used for flutter prediction of advanced turboprops (Williams and Hwang, 1986), model turning of the flow or loading of the blades. Therefore, they do not capture one of the two competing influences of solidity on flutter. The observed dependence on loading implies that the analytical aerodynamic models used in flutter prediction should include these loading effects.

The results of the M5F1 solidity variation tests indicate that the onset of flutter of the fan is dominated by the isolated blade effects driving the coupled modes of the blade toward a classical coalescence flutter. Despite the assertion of Mehmed and Kaza (1986) to the contrary, cascade influences have been found to be weak in the flutter of other fans which exhibited bending torsion coalescence, such as the SR3C-X2, the flutter boundaries of which are overplotted for two values of solidity at a fixed stagger angle in Fig. 9. The cascade aerodynamic effects do not seem to play the dominant role in incipience flutter. However, the presence of system modes upon a deep penetration of the flutter boundary indicates that once the onset of flutter occurs in any particular blade, the cascade effects will tend to lock in a more organized response of the system. The one notable exception to this trend was the cascade

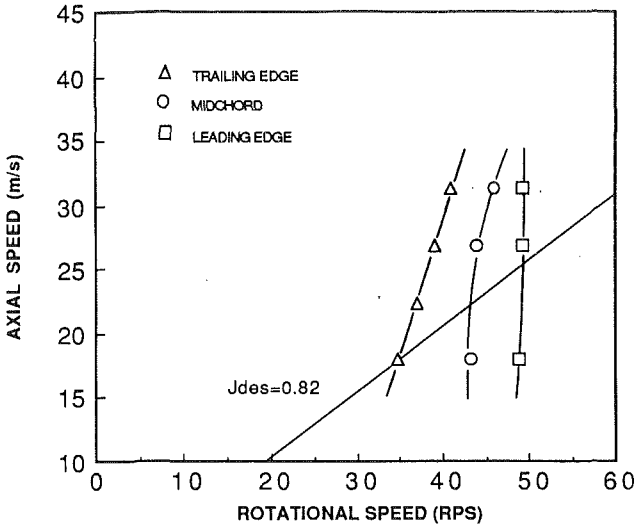

Fig. 10 Measured flutter boundary of the variable mass distribution (M4F1) fan

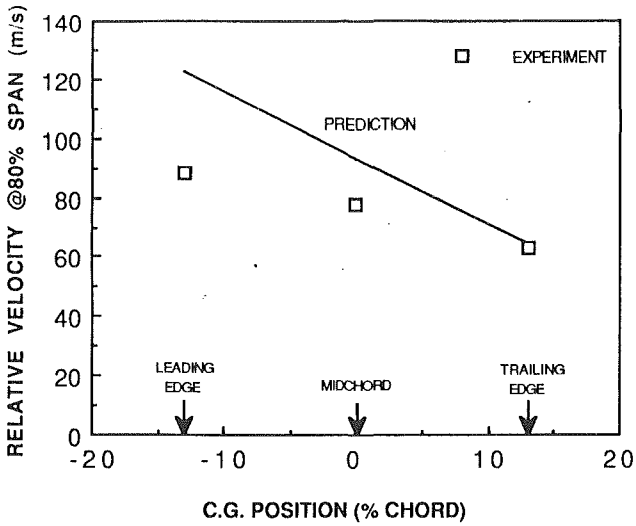

Fig. 11 Dependence of the flutter relative velocity at flutter on the C.G. position at the typical section

flutter of the highly swept SR-5, in which a strong system flutter mode was observed, and a decrease in solidity noticeably altered the stability boundary (Fig. 4).

Parametric-Dependence on Mass Distribution

Flutter Behavior. The distribution of mass of the blade has important implications for the stability of the fan. This has long been recognized for wings, and more recently has been analytically investigated for turbofans (Kielb, 1986; Bendiksen and Friedmann, 1980) and propfans (Ramsey and Kaza, 1986). A general rule which applies to the bending/torsion coalescence flutter is that a forward shift in the chordwise location of the sectional C.G. is stabilizing. The influence of mass distribution has practical implications for the design of internal metal spars, the use of metal leading edge erosion strips and the placement of development test instrumentation.

The mass distribution experiment was performed on the nominal configuration fan (M4F1) through the placement of lead foil tape at three chordwise positions near the tip. The placements of the tape had a significant effect on the mode shapes and the natural frequency of the blades. To isolate the effects on flutter due to lowering the natural frequencies of the blades from those due to the mode shape changes, a reference mass balance configuration was defined. The reference configuration, with the tape at the midchord, retained the C.G. location of the nominal blade, but included the frequency lowering effect. The effect of adding the tape was to lower the fan average first bending frequency from 50.5 Hz to 47.5 Hz, while leaving the mode shapes largely unchanged. An additional result of adding the tape was to locally increase the airfoil thickness by 24 percent of the typical section maximum thickness. Symmetric application of the tape to the suction and pressure sides caused no chamber change, and in incompressible flow such a change in thickness to a thin section should not change its lifting characteristics.

The addition of the mass balance tape at midchord had the effect of decreasing the stability of the nominal fan. The flutter boundary of the midchord mass balanced fan intersects the line of design advance ratio at a rotational speed of 42.8 rps, or an 80 percent span typical section relative velocity of 77.6 m/s (Fig. 10). This was 12 percent lower in rotational speed, and 14 percent lower in relative velocity, compared to the corresponding nominal fan flutter boundary intersection with the design advance ratio line, which occurred at a rotational speed of 48.8 rps and a typical section relative velocity of 90.7 m/s (all relative velocities corrected for induced axial velocity).

Table 3 Variation of flutter parameters with mass position

	Leading Edge		Mid Chord		Trailing Edge	
	Exp.	Anal.	Exp.	Anal.	Exp.	Anal.
Ω_{FL} [RPS]	48.8	67.64	42.8	51.25	34.8	35.40
U_{ax} [m/s]	24.78	34.35	21.74	26.03	17.67	17.96
$U_{rel\,0.8}$ [m/s]	88.43	122.45	77.58	92.87	63.10	64.13
ω_{FL} [Hz]	113.0	179.3	115.0	147.2	94.0	112.3
k_{FL} 0.8	0.235	0.270	0.273	0.292	0.274	0.322
U_{FL} 0.8	4.25	3.71	3.66	3.43	3.65	3.10

The location of the tape was then shifted to the blade leading and trailing edges. The tape shifted the C.G. location of the blade by ±13 percent of the chord. The resulting dependence of the fan flutter boundary on the mass balance position is shown in Fig. 11 and in Table 3. Along the line of the design takeoff advance ratio, the stabilizing effect of the leading edge mass balance can be seen. The flutter rotational speed was 48.8 rps and the corresponding typical section relative velocity U_{FL} was 88.4 m/s, an increase of 14 percent in both parameters over the midchord mass balance reference configuration. Following the same line of constant takeoff advance ratio, the destabilizing effect of the trailing edge mass balance also can be seen. The flutter rotational speed for that configuration was 34.8 rps and the typical section flutter relative velocity was 63.1 m/s, or 19 percent less than their respective midchord reference configuration values.

The sensitivity of flutter relative velocity to mass balance is primarily due to the effects of the mode shape changes, especially in the second mode. The analysis of the nominal configuration fan has shown that the second mode branch is predicted to be the least stable. Examining the mode shapes in Fig. 1, one sees that a streamwise section of the second mode at the typical section for the aft mass-balanced blade shows a large degree of bend-twist coupling. This is in contrast to that smaller degree of coupling observed in the second mode of the leading edge mass-balanced blade.

It is interesting to note that, although the first bending natural frequencies of the mass-balanced blades were decreased by 9 percent (from 50.5 Hz to 47.5 Hz), the flutter boundary

for the leading edge mass-balanced fan is almost identical to that of the baseline rotor (see Figs. 3 and 10). A practical design implication which can be inferred from this result is that it is possible to add mass perturbations to the blade, such as leading edge erosion strips, without a penalty in aeroelastic stability. It may even be possible to enhance the flutter stability through the perturbation of the inertial properties.

Correlation With Analytical Model. The analytical model incorporating the appropriate bench mode shapes was used to determine flutter stability for each of the three mass distribution configurations. The unsteady aerodynamic calculations were performed using the cos Λ sweep correction and no-spanwise rolloff of the modal loads. The results of the analysis are summarized in Table 3. The analytical model overpredicted the shift in fan stability with mass distribution, as compared to experiment as shown for U_{FL} at the design advance ratio in Fig. 11. The shift in mass balance from the midchord resulted in a predicted 32 percent increase in U_{FL}, as compared to the 14 percent increase that was observed experimentally. The shift from the midchord to the trailing edge resulted in a predicted 31 percent decrease in U_{FL}, whereas the experimentally observed decrease was only 19 percent. This would indicate that the analytical model is significantly more sensitive to changes in mode shape than was experimentally observed. The flutter frequency also changed with the tape position, but less than was predicted by the analytical model.

The calculated flutter eigenvector for the midchord position shows that the flutter mode consists primarily of the third mode (first torsion) with significant participation of both the first and second bending modes. The flutter mode for the leading edge case indicates that the flutter eigenvector is primarily a torsion mode, with much smaller participation of the other two modes. The flutter eigenvector for the trailing edge case indicates that the flutter mode consists primarily of the second bending mode.

The experimental and analytical trends indicated that the flutter behavior is significantly affected by changes in its inertia properties. The classical stabilizing effects of forward shifts, and the destabilizing effects of aft shifts, were observed. This result was consistent with the flutter behavior of other lifting surfaces whose stability is dominated by the modal coalescence. The analytical model predicted these trends, but was more sensitive to these changes than was observed experimentally.

Conclusions

A subvelocity-scaled experimental technique for the investigation of advanced turboprop aeroelastic behavior has been developed. By comparison with the previously documented flutter characteristics of the specific full-velocity-scaled fan after which it was modeled, the GE MPS F1, the subvelocity-scaled model was shown to reproduce both the quantitative parameters and the qualitative behavior of the unstalled flutter at takeoff conditions. In view of this agreement, as well as correlation with the trends of several other full-velocity fan tests, it can be concluded that the phenomena and trends observed in the aeroelastic testing of the sub-velocity-scaled fans yield insight into the aeroelastic behavior of propfans. Caution must be exercised, however, in directly extrapolating the normalized flutter behavior to the full-scale fan, particularly when the unsteady aerodynamics are fundamentally dependent on a specific Reynolds number on Mach number regime, as would be the case in separated flow or transonic buzz flutter.

Based on measurements and analysis of the subvelocity-scaled fans, and corroboration with other full-velocity-scaled testing, the following trends in the aeroelastic behavior can be inferred.

1 Due to the low mass ratio, the unsteady aerodynamic forces significantly modify the natural frequencies at speeds even well below the flutter boundary. These forces must be included in any calculation of the "in-air Campbell diagram," and will have significant influence on the design of the blading to avoid resonance crossings in the operating speed range. Since the influence of the unsteady aerodynamic forces scales with the mass ratio, this influence will be weaker at altitude than at sea level. Thus the location of the resonance crossings on the in-air Campbell diagram will be a function of altitude.

2 For the range of sweep, solidity and mass ratio under consideration, the flutter mechanism which dominates is the modal coalescence in a single blade, not the highly coupled single mode cascade flutter of turbofans. Therefore, the blading should be susceptible to the aero elastic tailoring options known to strongly influence coalescence flutter, such as mass distribution and anisotropic stiffness tailoring.

3 As evidenced by the variable solidity experiment, the cascade influence in advanced turboprops of moderate sweep and mass ratio is considerably weaker than in a typical turbofan. The monotonic increase in stability, with decrease in solidity, predicted by unloaded cascade aerodynamics was not found. The flutter was clearly triggered by a coalescence, and after flutter had initiated, it became organized into a system mode. Except for the higher mass ratio and highly swept SR-5, the flutter boundaries for other propfans that have been reported also reveal a weak-dependence on solidity. The flutter system modes of propfans are often dominated by one or several blades, also indicating a weak cascade influence. The implication is that small changes in the blade count in a fan will probably not have a fundamental impact on flutter behavior.

4 A dependence of the flutter boundary on the fan loading was observed. This manifested itself in the increase in flutter relative velocity of a given fan as it operated at higher advance ratio and therefore lower loading, and by a correlation of the flutter relative velocity with the normalized thrust coefficient for the variable solidity fan. This destabilizing influence of higher loading at low solidity tends to offset the stabilizing influence of weaker cascade interaction at low solidity, the net result being uncertain. The destabilizing effect of loading should be included in aerodynamic models for the accurate prediction of flutter boundaries.

5 The parametric-dependence of sweep, as measured in a *rotated* model experiment, was completely classical. The relative velocity at flutter increased roughly as the square root of the sweep, as has been found in isolated wing coalescence flutter. The implication is that for a fixed length blade, the influence of sweep is mildly stabilizing. However, one must be careful in extrapolating this result to the design of fixed radius fans, for which the blade length increases with sweep back, classically causing a decrease in stability.

6 The flutter speed-dependence on mass distribution was also classical, but weaker than predicted. A forward shift in typical section CG stabilized the fan, and the aft shift destabilized the fan. In the case of this experiment, the destabilizing influence of adding the extra mass to perform the mass position parametric experiment was almost exactly equal to the stabilizing influence of moving the mass from the midchord to the leading edge. The design implication is that it may be possible to add leading edge erosion strips to a blade without significantly reducing its stability.

Acknowledgments

This research was sponsored by the Aircraft Engine Business Group of the General Electric Company, Evendale, Ohio, with Dr. Tom Tseng and Mr. James Smith serving as contract monitors. The support of GE is gratefully acknowledged. The additional observations, comments and data supplied by Dr. Robert Kielb of NASA were invaluable in the preparation of this paper.

References

Bansal, P. N., Arseneaux, P. J., Smith, A. F., Turnberg, J. E., and Brooks, B. M., 1985, "Analysis and Test Evaluation of the Dynamic Response and Stability of Three Advanced Turboprop Models," NASA CR-174814.

Barmby, J. G., et al., 1951, "Study of Effects of Sweep on the Flutter of Cantilever Wings," NACA TR 1014, formerly NACA TN 2121.

Bendiksen, O., and Friedmann, P., 1980, "Coupled Bending-Torsion Flutter in Cascades," *AIAA Journal*, Vol. 18, No. 2, pp. 194–201.

Bisplinghoff, R. L., Ashley, H., and Halfman, R., 1955, *Aeroelasticity*, Addison-Wesley, Reading, MA.

Crawley, E. F., and Ducharme, E. H., 1987, "Velocity-Scaled Aeroelastic Testing of Advanced Turboprops," ASME Paper No. 87-GT-209.

Crawley, E. F., and Hall, K. C., 1985, "Optimization and Mechanisms of Mistuning in Cascades," ASME *Journal of Engineering for Gas Turbines and Power*, Vol. 107, No. 2, pp. 418–426.

Ducharme, E. H., and Crawley, E. F., 1987 "Velocity-Scaled Aeroelastic Testing of an UnDucted Fan," MIT Gas Turbine Laboratory Report No. 191.

Ham, N. D., 1973, "Helicopter Blade Flutter," AGARD Report 607.

Hassig, H. J., 1971, "An Approximate True Damping Solution of the Flutter Equation by Determinant Iteration," *Journal of Aircraft*, Vol. 8, No. 11, pp. 885–889.

Hunt, G. K., 1973, "Similarity Requirements for Aeroelastic Models of Helicopter Rotors," Aeronautical Research Council C.P. No. 1245.

Kielb, R. E., Kaza, K. R. V., 1985, "Flutter of Swept Fan Blades," ASME *Journal of Engineering for Gas Turbines and Power*, Vol. 107, pp. 394–398.

Kielb, R. E., 1986, "Mass Balancing of Hollow Fan Blades," ASME *Journal of Engineering for Gas Turbines and Power*, Vol. 108, No. 4, pp. 577–582.

Mehmed, O., Kaza, K. R. V., Lubomski, J. F., Kielb, R. E., 1982, "Bending-Torsion Flutter of a Highly Swept Advanced Turboprop," NASA TM 82975.

Mehmed, O., and Kaza, K. R. V., 1986, "Experimental Classical Flutter Results of a Composite Advanced Turboprop Model," NASA TM 88792.

Ramsey, J. K., and Kaza, K. R. V., 1986, "Concentrated Mass Effects on the Flutter of a Composite Advanced Turboprop Model," NASA TM 88854.

Smith, S. N., 1973, "Discrete Frequency Sound Generation in Axial Flow Turbomachines," Aeronautical Research Council Reports and Memoranda, No. 3709.

Srinivasan, A. V., Kielb, R. E., Lawrence, C., 1986, "Dynamic Characteristics of an Assembly of Prop-Fan Blades," ASME *Journal of Engineering for Gas Turbines and Power*, Vol. 108, pp. 306–312.

Turnberg, J. E., 1983, "Classical Flutter Stability of Swept Propellers," 83-0847-CP AIAA/ASME/ASCE/AHS 24th Structures, Structural Dynamics and Materials Conference, May.

Whitehead, D. S., 1987, "Classical Two-Dimensional Methods," *AGARD Manual on Aeroelasticity in Axial Flow Turbomachines*, Vol. 1, AG-298, M. Platzer and F. Carta, eds.

Whitehead, D. S., 1962, "Bending Flutter of Unstalled Cascade Blades at Finite Deflection," Aeronautical Research Council Reports and Memoranda, No. 3386.

Williams, M. H., and Hwang, C. C., 1986, "Three-Dimensional Unsteady Aerodynamics and Aeroelastic Response of Advanced Turboprops," 86-0846-CP AIAA/ASME/ASCE/AHS 27th Structures, Structural Dynamics, and Materials Conference, San Antonio, TX, May.

Optical Measurement of Unducted Fan Blade Deflections

A. P. Kurkov
National Aeronautics and Space Administration, Lewis Research Center, Cleveland, OH 44135

A nonintrusive optical method for measuring unducted fan (or propeller) blade deflections is described and evaluated. The measurement does not depend on blade surface reflectivity. Deflection of a point at the leading edge and a point at the trailing edge in a plane nearly perpendicular to the pitch axis is obtained with a single light beam generated by a low-power, helium–neon laser. Quantitative analyses are performed from taped signals on a digital computer. Averaging techniques are employed to reduce random errors. Measured static deflections from a series of high-speed wind tunnel tests of a counterrotating unducted fan model are compared with available predicted deflections, which also are used to evaluate systematic errors.

Introduction

In this method a concentrated light beam, such as generated by a laser, is directed to the blade pressure surface in a plane approximately perpendicular to the pitch axis. The incident light beam forms a small angle relative to the chord, usually about 10 deg. The overall schematic of the experiment is given in Fig. 1, and the relationship of the beam and the undeflected and deflected blades in Figs. 2 and 3. (Note that in these figures the coordinate systems are fixed with respect to the blade.) As the blades rotate, the leading and trailing edges intersect the light beam. Therefore, by placing a photodetector in the light beam path on the opposite test section wall, one can obtain a series of negative pulses, each associated with the period of time when the light was shadowed from the detector by a blade. If, in addition, a once-per-revolution reference pulse is generated, these pulses can provide an indication of the instantaneous blade positions for each revolution in a rotating reference frame. This method complements the already established optical blade deflection method (Nieberding and Pollack, 1977; Kurkov, 1984; Lawrence and Meyn, 1985), which relies on blade tip reflection of the incident light beam and thus requires that the casing be close to the blade tips.

Other available methods for measuring blade deflections that, like the present method, do not require the close proximity of the rotor casing are either intrusive or rely on photographic records or visual observation (Taylor, 1935; Stargardter, 1977; Srinivasan and Fulton, 1984). All quantitative analyses in the present method are performed from the taped signals on a minicomputer. Random errors are reduced by averaging in the time and space domains. Note also that, unlike in the reflected-light method, here one light beam essentially measures the deflection of two points, one at the leading and one at the trailing edge, and the measurement does not depend on surface reflectivity.

Contributed by the International Gas Turbine Institute and presented at the 34th International Gas Turbine and Aeroengine Congress and Exhibition, Toronto, Ontario, Canada, June 4–8, 1989. Manuscript received at ASME Headquarters February 14, 1989. Paper No. 89-GT-298.

Experimental data from the high-speed test of a series of 0.61-m-dia model rotors incorporated in a counterrotating, unducted fan arrangement built by the General Electric Company illustrate the use of the method. The test was performed in the NASA Lewis Research Center's 8 by 6 ft (2.44 by 1.83 m) wind tunnel (Fig. 4). In this figure, the laser beam is shown intercepted by a blade tip. All the blades tested had a composite shell. Their plan view is given in Fig. 5. Additional information on the F7 blade and its performance is available (Sullivan, 1987).

This report also includes predicted deflections that were obtained from the aerostructural, finite-element code outputs supplied by the manufacturer. To compare experimental and predicted deflections, one can always calculate the particular deflection component that is being measured. However, because in the present case the measured component is not a generally accepted or easily defined quantity, and because it

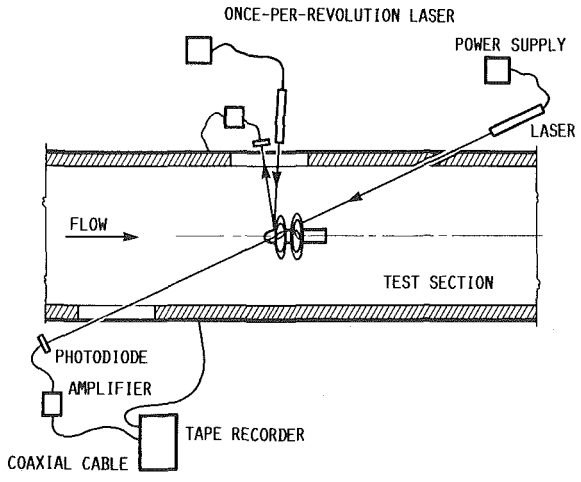

Fig. 1 Test schematic

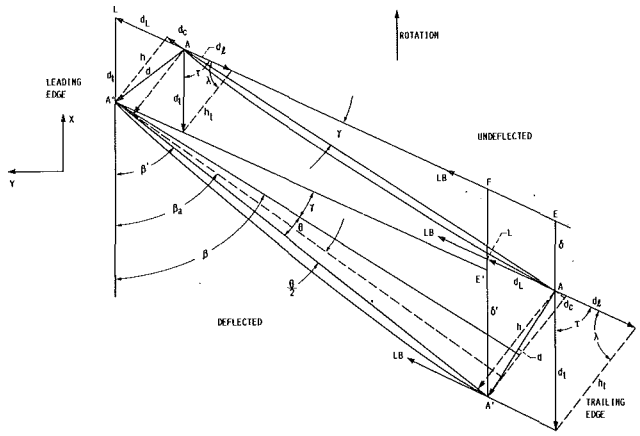

Fig. 2 Geometry of laser beam and blade section

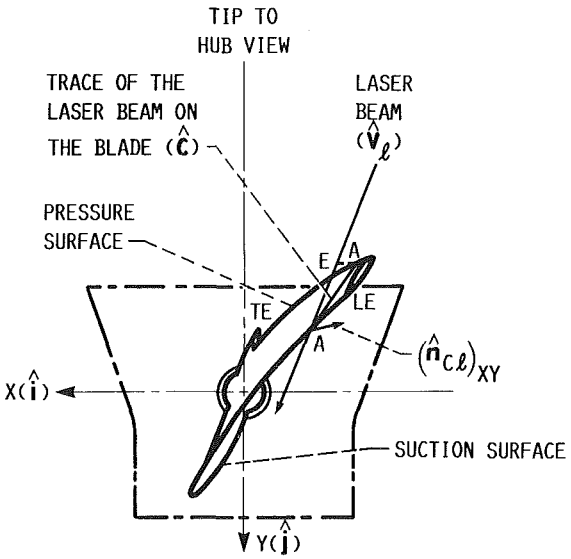

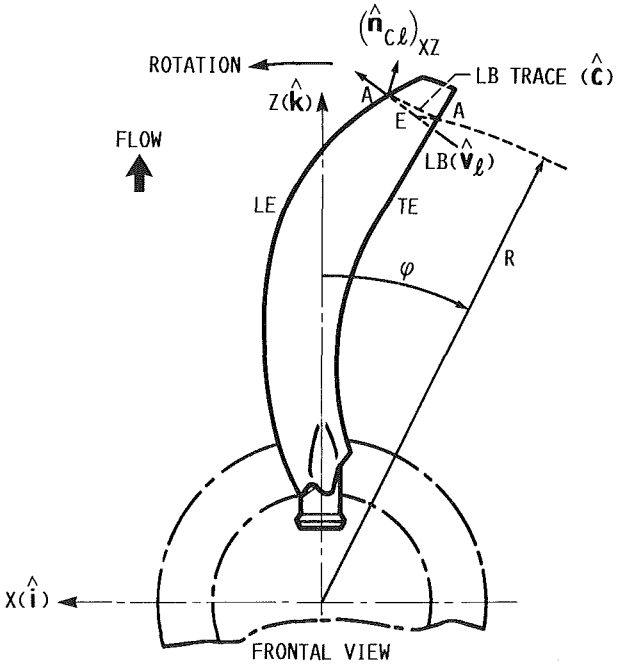

Fig. 3 Blade coordinate systems

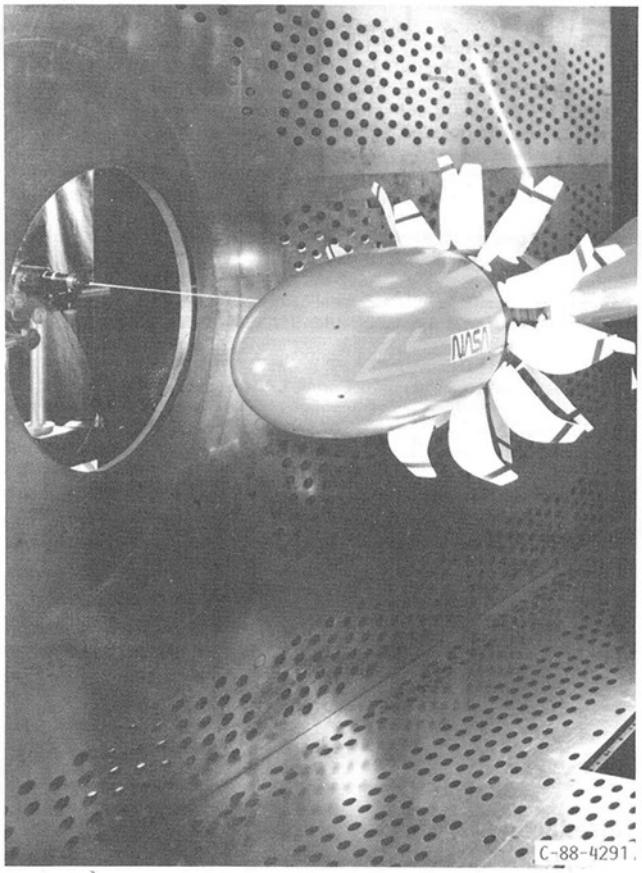

Fig. 4 Counterrotating unducted fan and two lasers installed in the 8 by 6-ft wind tunnel

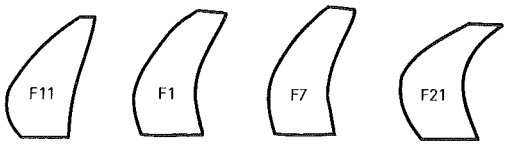

Fig. 5 Blade schematics, plan view

could easily be misinterpreted, the more commonly accepted deflection parameters, such as bending and twist deflections, were derived from experimental measurements and compared with predictions. Both these deflections can be obtained from measurements because they depend on the displacement perpendicular to the chord and the light beam makes only a small angle relative to the chord. The errors associated with these estimates are largely caused by the finite incidence angle of the laser beam relative to the blade and the fact that the sensor (i.e., the combination of laser beam and detector) is fixed in space, and not with respect to the blade as is a strain gage, for example. The net effect is that a blade edge is free to slip relative to the laser beam during blade deformation. Because these errors are inherent in the experimental procedure, they can be classified as systematic, or bias, errors.

The measured twist and bending deflections can only be relied upon if one shows that these errors are small. Systematic errors are estimated by cutting the finite-element, deflected-blade contour with a line coincident with the laser beam in the same way that the real deflected blade is cut by a laser beam during the test. Since in this case, the true displacements of the original contact points between the undeflected blade and the laser beam also are known, the incidence and the slip effects can be evaluated.

Note that when exact knowledge of the deflected-blade shape

is assumed in this paper, it is to illustrate where the measured deflections fall short of the true deflections and to estimate systematic errors. Only the undeflected-blade, finite-element contour is used for defining the initial geometric conditions for measured deflections.

Because only incomplete information was available for the F21 blade, the systematic-error analysis for this blade could not be fully completed. For this reason, the F21 results are presented separately in the last part of the section "Results."

Experimental Measurements

Experimental Equipment. Low-power, helium–neon lasers were selected for this experiment because of their low cost and rugged, compact construction and because they provide a monochromatic light source. Large-area silicon photodiodes manufactured by United Detector Technology (UDT) were selected for the detectors. The detector output was coupled to UDT model 201A amplifier. The data were recorded on the frequency-modulated wideband II tape recorder at 120 in./sec (304.8 cm/s).

This basic system, consisting of a laser and a photodiode, was enhanced by using a commercial beam expander to focus the laser beam onto a blade, and by using an optical line filter to shield the extraneous light from the detector. The overall experiment schematic is given in Fig. 1.

In addition to the blade signals, it also was necessary to generate a once-per-revolution signal of the same quality. This was achieved by attaching a small mirror to the fan hub and reflecting the nearly perpendicular incident laser beam onto a photodiode detector placed (at the time of reflection) opposite the mirror. For assurance that optical alignment was not changed during a run, alignment checks were made before and after each test run.

Laser Beam Alignment. Figure 2 describes the geometry of the laser beam and the deflected and undeflected blades, neglecting the deviations away from the XY-plane. The coordinate system is fixed with respect to the blade. The Y axis is coincident with the rotational axis, and the Z axis is coincident with the blade pitch axis and points upward. Lines that are either in the direction of the average chord line or are perpendicular to it are shown as dashed lines for ease of recognition.

The laser beam entered the tunnel through one of the boundary layer bleed holes (Fig. 4). The hole was selected so that the following requirements were met as closely as possible: (1) The trace of the beam on the blade pressure surface was coincident with a marked line perpendicular to the pitch axis; (2) the incidence on the blade was less than 12 deg but sufficiently high so that the beam was either cut or uncovered only by the blade edges and required only a small rotation to complete the intersection; and (3) the beam tilt relative to the axis was sufficient to pass the beam past one of the blade rows and, at the same time, have it incident on the upstream window area.

In this report, only the data for the forward rotor are presented. For it, the tilt direction required to bypass the rear rotor was toward the axis, the same direction required by the tunnel window.

The laser beam intercepts at the leading and trailing edges on the alignment blade could be easily located by rotating this blade slightly and observing the beam trace on the blade. The tangential length of the trace (distance AA in Fig. 2) and the incidence angle γ between it and the beam also were measured directly. This, together with the known finite-element description of the undeflected blade, was sufficient to define measured twist and bending parameters.

Experimental Data Reduction. Prerecorded signals from the magnetic tape were processed on a system consisting of a minicomputer, an eight-channel digitizer, and high-volume disk storage peripherals. It was determined that about 12,000 points per revolution provided sufficient resolution for the recorded signals. An example of each pulse after it was digitized is given in Figs. 6 and 7.

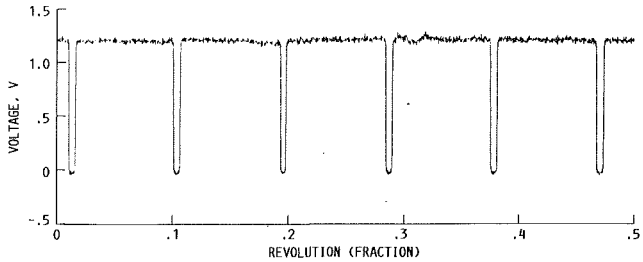

Fig. 6 Blade-tip pulses, F11 blade

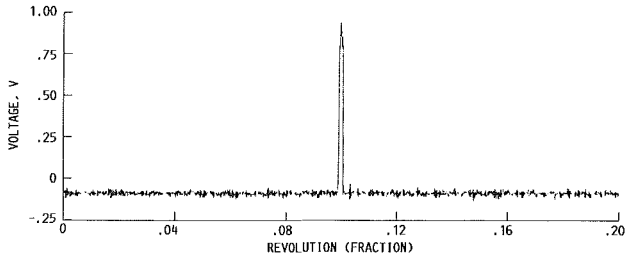

Fig. 7 Once-per-revolution pulse, F11 hub

The once-per-revolution pulse subdivides the continuous blade-pulse train into consecutive revolutions. From this, one can obtain the shaft rotational speed and then express each blade pulse position in terms of a relative angular coordinate in the rotational plane. These blade positions were typically averaged over about 50 revolutions.

The data were taken at some low reference speed, where blade deflections were very small and consequently could be neglected, and at higher speeds, including the design speed, where deflections were significant. Subtracting the two corresponding angular positions in the rotational plane for a particular blade gives angular deflection in the tangential direction (i.e., the polar angle subtended by vector $\mathbf{d}_t$ in Fig. 2). The tangential deflections were then spatially averaged over all blades. Depending on the model, the number of blades varied from eight to eleven. Note that for static deflections spatial averaging removes some of the random blade-to-blade variations. These signals cannot be eliminated by time-averaging, which only removes the self-excited dynamic signals such as flutter.

Analysis

In Fig. 2, the deflected and undeflected chords are purposely shown to be different in length. To a large extent this is caused by the fact that the blade is free to slip relative to the laser beam as dictated by the geometry of the deflected blade and the beam. Because of the unequal sweeps at blade leading and trailing edges, any slip along the radial direction will be reflected in Fig. 2 as a change in the apparent deflected-blade chord length. Since experimental twist angle is essentially computed from the change in the projected chord length in the tangential direction, the apparent chord-length change caused by the slip effect will introduce an error in the measured twist. So that this error can be evaluated, experimental conditions are simulated by cutting the calculated deflected-blade contour with a line coincident with the laser beam rotating in the relative reference frame. Since the entire calculated deflected-blade section is known, one can evaluate the twist angle with and without assuming constant chord length. Note, however, that

even when the chord-length change in predicted results has been accounted for, there remains some slip effect because points A and A' for undeflected and predicted deflected sections are not necessarily associated with the same blade particles. Hence, one also should obtain the predicted twist angle strictly by following the blade particles at the leading and trailing edges, where the beam is tangent to the undeflected blade. Although both errors are largely caused by the fact that the blade is free to slip relative to the beam, to differentiate between these errors, the first will be referred to as the error due to the constant-chord assumption, and the second will simply be referred to as the slip effect error.

Linear interpolation is used to evaluate the coordinates of point A' from the predicted deflected-blade contour for the case of true deflection (i.e., following the blade particle associated with point A). Coordinates of points A at the leading and trailing edges are known from initial conditions, and the coordinates of the endpoints of finite-element edge segments for undeflected and deflected-blade contours are available from the finite-element code outputs. (The appropriate edge segments are selected so that in the undeflected configuration they contain points A.) To evaluate coordinates of points A' for simulated experimental conditions, one must obtain equations of lines containing appropriate edge segments as well as the equation of the line coincident with the laser beam, as depicted in Fig. 2. Rotating this line until it intersects either edge-segment line results in a quadratic equation whose solution gives coordinates of associated points A' (Kurkov, 1988).

There are three displacement vector diagrams in Fig. 2. In the first, the total displacement $\mathbf{d}$ is resolved in the tangential direction and along the laser beam. Thus

$$\mathbf{d} = \mathbf{d}_t + \mathbf{d}_L \tag{1}$$

The second vector diagram, given by

$$\mathbf{d} = \mathbf{d}_c + \mathbf{h} \tag{2}$$

resolves vector $\mathbf{d}$ along the average chord direction and perpendicular to it. These two vector diagrams assume knowledge of deflected-blade coordinates A' and, therefore, they can only be obtained for predicted results. In the experiment bending h and twist θ must be deduced from the measured tangential displacement d_t and the knowledge of angles β and γ (Fig. 2). Estimates for h and θ are obtained by resolving $\mathbf{d}_t$ into components perpendicular to the average chord, $\mathbf{h}_t$, and along the laser beam, $\mathbf{d}_l$. Thus

$$\mathbf{d}_t = \mathbf{d}_l + \mathbf{h}_t \tag{3}$$

which is the third vector diagram in Fig. 2. Note that quantities $\mathbf{h}$ and $\mathbf{d}$ cannot be obtained from the experiment because $\mathbf{d}_L$ and $\mathbf{d}_c$ cannot be measured with one laser beam. Thus equations (1) and (2) are used only for predicted results. For experimental results equation (3) gives $\mathbf{h}_t$, which serves as an approximation to $\mathbf{h}$. (In the experiment, the measured quantity is the polar angle subtended by vector $\mathbf{d}_t$. Thus $\mathbf{d}_t$ can be considered known.)

First, the exact equations will be given, that is, the equations assuming knowledge of the coordinates of points A and A'. For true deflections, A and A' correspond to the same blade particles and, for simulated experimental results, they are determined from the geometry of the laser beam and the blade. Subsequently, it will be shown how these equations are modified to obtain experimental deflections. The vector $\mathbf{h}$ is given by

$$\mathbf{h} = \mathbf{d} - \hat{\mathbf{C}}_a(\mathbf{d} \cdot \hat{\mathbf{C}}_a) \tag{4}$$

and its plane by

$$\hat{\mathbf{n}}_{ch} = \hat{\mathbf{C}}_a \times \hat{\mathbf{h}} \tag{5}$$

The average unit chord vector $\hat{\mathbf{C}}_a$ is the normalized average of the undeflected $\mathbf{C}$ and the deflected $\mathbf{C}'$ chords, which are defined as the difference between the leading and trailing-edge point vectors $\mathbf{r}_A$ or $\mathbf{r}_{A'}$ (Fig. 2). (Note that the primes are associated with the deflected-blade section.)

The polar angular coordinate φ is chosen to be positive opposite to the rotational direction (Fig. 3). The average R direction is then defined by

$$\varphi_a = [(\varphi_A + \varphi_{A'})_{LE} + (\varphi_A + \varphi_{A'})_{TE}]/4 \tag{6}$$

and the average bending plane by

$$\hat{\mathbf{n}}_h = \frac{\hat{\boldsymbol{\delta}}_{ta} \times \hat{\mathbf{C}}_a}{|\hat{\boldsymbol{\delta}}_{ta} \times \hat{\mathbf{C}}_a|} \tag{7}$$

where

$$\hat{\boldsymbol{\delta}}_{ta} = (\cos \varphi_a,\ 0,\ \sin \varphi_a) \tag{8}$$

Projection of h onto this plane is given by

$$\mathbf{h}_p = \mathbf{h} - \hat{\mathbf{n}}_h(\mathbf{h} \cdot \hat{\mathbf{n}}_h) \tag{9}$$

For simulated experimental conditions, h_t is computed from

$$\hat{\mathbf{n}}_{tl} = \frac{\hat{\mathbf{d}}_t \times \hat{\mathbf{V}}_l}{|\hat{\mathbf{d}}_t \times \hat{\mathbf{V}}_l|} \tag{10}$$

$$\hat{\mathbf{h}}_t = \frac{\hat{\mathbf{C}}_a \times \hat{\mathbf{n}}_{tl}}{|\hat{\mathbf{C}}_a \times \hat{\mathbf{n}}_{tl}|} \tag{11}$$

$$h_t = \frac{d_t}{\hat{\mathbf{d}}_t \cdot \hat{\mathbf{h}}_t + |\hat{\mathbf{d}}_t \cdot \hat{\mathbf{V}}_l|\ |\hat{\mathbf{h}} \times \hat{\mathbf{d}}_t| / |\hat{\mathbf{d}}_t \times \hat{\mathbf{V}}_l|} \tag{12}$$

where $\hat{\mathbf{V}}_l$ is the unit vector in the laser beam direction pointing, as shown in Fig. 2 and vector $\mathbf{d}_t$ can be computed given that its endpoints must lie on the constant R. Note that to obtain $\hat{\mathbf{V}}_l$ at the trailing edge, one must rotate the original $\hat{\mathbf{V}}_l$ at the leading edge about the Y axis by the angle subtended by δ (Fig. 2). The plane of $\mathbf{h}_t$ is defined by the unit normal vector $\hat{\mathbf{n}}_t$ given by

$$\hat{\mathbf{n}}_t = \frac{\hat{\mathbf{h}}_t \times \hat{\mathbf{d}}_t}{|\hat{\mathbf{h}}_t \times \hat{\mathbf{d}}_t|} \tag{13}$$

Projection of $\mathbf{h}_t$ onto the plane defined by $\hat{\mathbf{n}}_h$ is denoted by $\mathbf{h}_{tp}$, and it is computed similarly to $\mathbf{h}_p$, equation (9).

The absolute twist angle is given by

$$\left|\theta_{n_c}\right| = \tan^{-1}\left(\frac{|\mathbf{C}' \times \mathbf{C}|}{|\mathbf{C}' \cdot \mathbf{C}|}\right) \tag{14}$$

$$\hat{\mathbf{n}}_c = \frac{\mathbf{C}' \times \mathbf{C}}{|\mathbf{C}' \times \mathbf{C}|} \tag{15}$$

Twist angle also was computed by projecting $\mathbf{C}$ and $\mathbf{C}'$ onto three other planes. Given that

$$\mathbf{C}_n = \mathbf{C} - \hat{\mathbf{n}}(\mathbf{C} \cdot \hat{\mathbf{n}}) \tag{16}$$

(and, similarly, for $\mathbf{C}'_n$), θ_n is computed from

$$\theta_n = \tan^{-1}\left[\frac{(\mathbf{C}'_n \times \mathbf{C}_n) \cdot \hat{\mathbf{n}}}{\mathbf{C}'_n \times \mathbf{C}_n}\right] \tag{17}$$

where n_{cl}, n_h, or k should be substituted for n. The unit vector $\hat{\mathbf{n}}_{cl}$ is defined by

$$\hat{\mathbf{n}}_{cl} = \frac{\mathbf{C} \times \hat{\mathbf{V}}_l}{|\mathbf{C} \times \hat{\mathbf{V}}_l|} \tag{18}$$

and $\hat{\mathbf{k}}$ denotes the unit vector for the Z axis (Fig. 3).

Experimental Deflections. It is desirable to use the same set of equations for computing the predicted and experimental twist angles. However, in the experiment the coordinates of points A' and the deflected chord vector are unknown and must be obtained from some preliminary estimates of deflections in order to start the iteration. As an initial estimate of the twist angle the equation

$$C \sin\left(\frac{\theta}{2}\right) = (R_A)_{\mathrm{TE}} \sin\left[\frac{(\Delta\varphi_t)_{\mathrm{TE}} - (\Delta\varphi_t)_{\mathrm{LE}}}{2}\right] \frac{\sin(\beta + \gamma)}{\cos(\gamma + \theta/2)} \tag{19}$$

was used. (This equation also involves iteration.) It was derived

from Fig. 2 upon assuming planar geometry and neglecting the difference between C and C' (Kurkov, 1988). The angles $\Delta\varphi_t$ are measured averaged quantities.

One can now estimate the direction of $\hat{\mathbf{C}}_a$ by rotating $\mathbf{C}$ in the plane perpendicular to $\hat{\mathbf{n}}_{cl}$ by the angle $\theta/2$. The magnitude of $\mathbf{d}_t$ is again computed by using the fact that its endpoints subtend the measured $\Delta\varphi_t$'s and lie on a constant R. This allows one to compute $\mathbf{h}_t$ as described previously and to estimate coordinates of points A' as follows

$$\mathbf{r}_{A'} \cong \mathbf{r}_A + \mathbf{h}_t$$

Once these coordinates are obtained, vector $\mathbf{C}_a$ can be recalculated and the new iteration can be started. The resulting $\mathbf{C}'$ at the end of iteration is used to obtain the absolute twist angles as described previously.

Results

Experimental Variables. The complete results are given for three blades designated as F11, F1, and F7, which are all forward rotors of the twin-rotor counterrotating unducted fan model. The rotor speed was varied from a low reference speed to the design value. However, for the F11 blade, the rotor speed achieved in the test was only 0.952 of the design. Table 1 lists the initial conditions for this test. The Z coordinate was normalized by using its maximum value at the leading edge.

Detailed results for the displacements of the leading and trailing edges normal to the average chord direction, and the absolute twist angles, are presented first in tabular form for the design (or maximum) speeds. Deflections are then presented graphically to illustrate their variation with speed as well as the agreement between experimental and predicted values.

Table 1 Test variables

Blade	Design rotational speed, rpm	Test speed fraction	Nominal blade angle, β_{nom}	Mach number	Z/Z_{max} fraction	
					Leading edge	Trailing edge
F11	8089	0.952	60.3	0.80	0.973	0.960
F1	8185	.996	57.1	.72	.975	.973
F7	8314	.993	58.5	.72	.963	.961

In addition to experimental deflections the tables include calculated deflections incorporating the laser beam slip effect and the rigorous deflections obtained by strictly following leading and trailing-edge blade particles. By comparing these two deflections, the error associated with laser beam slip can be evaluated. The tables for twist angles also include predicted results calculated by using the constant-chord-length assumption; hence, the effect of this assumption can also be evaluated. (This assumption is used when calculating twist from experimental data.)

The deflections in the tables are signed quantities where the positive sign is as defined in Fig. 2. (Equations (12) and (17) yield correct signs.) Note, however, that when constructing vectorial deflections, one should take the absolute value of the tabulated quantities as the true magnitude associated with the appropriate unit vector.

Leading and Trailing-Edge Displacements. Leading and trailing-edge displacements perpendicular to the chord (i.e., bending displacements) are given in Table 2. The table includes signed deflections and the associated normal unit vectors that define the appropriate planes. Superscripted h and $\hat{\mathbf{n}}$ symbols in the column headings allow the differentiation between three types of tabulated results. A bar above a symbol indicates the no-slip condition, a tilde indicates experimental results, and unmodified h and $\hat{\mathbf{n}}$ indicate predicted results with the slip effect.

Deflections h_t in Table 2 were not calculated for the no-slip condition because the definition of h_t requires some slip along the blade relative to the original undeflected reference point. On the other hand, for the experimental results $\tilde{h}$ was not available because the measurement is performed with only one laser beam, and $\tilde{h}_t$ must serve as an approximation to $\tilde{h}$.

Examining first the two groups of columns in Table 2, one finds that h and the associated unit vector $\hat{\mathbf{n}}_{ch}$ are good approximations to $\bar{h}$ and $\bar{\hat{\mathbf{n}}}_{ch}$. A slight improvement is achieved by projecting h onto a plane perpendicular to $\hat{\mathbf{n}}_h$ (i.e., h_p). However, predicted results with slip show that up to about 7.5 percent error (for the F1 blade) can result by approximating h_p with h_{tp} (or h with h_t). As already mentioned, this error arises because the displacement along the laser beam cannot be measured. Figure 8 illustrates variation of $\tilde{h}_{tp}$ with speed and includes predicted $\bar{h}_p$ at the design condition as well as

Table 2 Bending deflections

Blade	Symbol	Plane	True predicted				Predicted with slip				Experimental (relative to reference point)			
			$\bar{h}$, cm	$\bar{\hat{\mathbf{n}}}$			h, cm	$\hat{\mathbf{n}}$			$\tilde{h}$, cm	$\tilde{\hat{\mathbf{n}}}$		
				$\hat{i}$	$\hat{j}$	$\hat{k}$		$\hat{i}$	$\hat{j}$	$\hat{k}$		$\hat{i}$	$\hat{j}$	$\hat{k}$
F11	h	$\hat{\mathbf{n}}_{ch}$	0.6375	-0.0601	-0.0801	0.9950	0.6347	-0.0970	-0.0550	0.9938	------	-------	-------	------
			.8334	-.1051	-.0423	.9936	.8245	-.1704	.0073	.9853	------	-------	-------	------
	h_p	$\hat{\mathbf{n}}_h$	.6345	-.1342	-.0176	.9908	.6340	-.1338	-.0239	.9907	------	-------	-------	------
			.8329	-.1342	-.0176	.9908	.8235	-.1338	-.0239	.9907	------	-------	-------	------
	h_t	$\hat{\mathbf{n}}_{t\ell}$	------	-------	-------	------	.6543	-.0844	-.0345	.9958	0.7419	-0.0837	-0.0349	0.9959
			------	-------	-------	------	.8486	-.1762	-.0019	.9843	.8903	-.1748	-.0026	.9846
	h_{tp}	$\hat{\mathbf{n}}_h$	------	-------	-------	------	.6535	-.1338	-.0239	.9907	.7412	-.1339	-.0244	.9907
			------	-------	-------	------	.8479	-.1338	-.0239	.9907	.8893	-.1339	-.0244	.9907
F1	h	$\hat{\mathbf{n}}_{ch}$	0.5311	-0.0448	0.0133	0.9989	0.5314	-0.0545	0.0183	0.9983	------	-------	-------	------
			.7506	-.0920	.0621	.9938	.7470	-.1291	.0953	.9870	------	-------	-------	------
	h_p	$\hat{\mathbf{n}}_h$	.5298	-.0927	.0627	.9937	.5306	-.0926	.0575	.9940	------	-------	-------	------
			.7506	-.0927	.0627	.9937	.7460	-.0926	.0575	.9940	------	-------	-------	------
	h_t	$\hat{\mathbf{n}}_{t\ell}$	------	-------	-------	------	.5710	-.0376	.0457	.9982	0.7196	-0.0359	0.0448	0.9983
			------	-------	-------	------	.7851	-.1405	.0796	.9869	1.0414	-.1393	.0789	.9871
	h_{tp}	$\hat{\mathbf{n}}_h$	------	-------	-------	------	.5702	-.0926	.0575	.9940	.7186	-.0936	.0560	.9940
			------	-------	-------	------	.7841	-.0926	.0575	.9940	1.0404	-.0936	.0560	.9940
F7	h	$\hat{\mathbf{n}}_{ch}$	0.8816	-0.0255	-0.0058	0.9997	0.8806	-0.0522	0.0100	0.9986	------	-------	-------	------
			.9698	-.0629	.0268	.9977	.9642	-.1238	.0723	.9897	------	-------	-------	------
	h_p	$\hat{\mathbf{n}}_h$	.8786	-.0879	.0485	.9950	.8796	-.0877	.0408	.9953	------	-------	-------	------
			.9693	-.0879	.0485	.9950	.9629	-.0877	.0408	.9953	------	-------	-------	------
	h_t	$\hat{\mathbf{n}}_{t\ell}$	------	-------	-------	------	.9144	-.0382	.0329	.9987	1.1984	-0.0372	0.0324	0.9988
			------	-------	-------	------	1.0124	-.1286	.0635	.9896	1.4879	-.1279	.0631	.9898
	h_{tp}	$\hat{\mathbf{n}}_h$	------	-------	-------	------	.9134	-.0877	.0408	.9953	1.1971	-.0906	.0386	.9951
			------	-------	-------	------	1.0114	-.0877	.0408	.9953	1.4864	-.0906	.0386	.9951

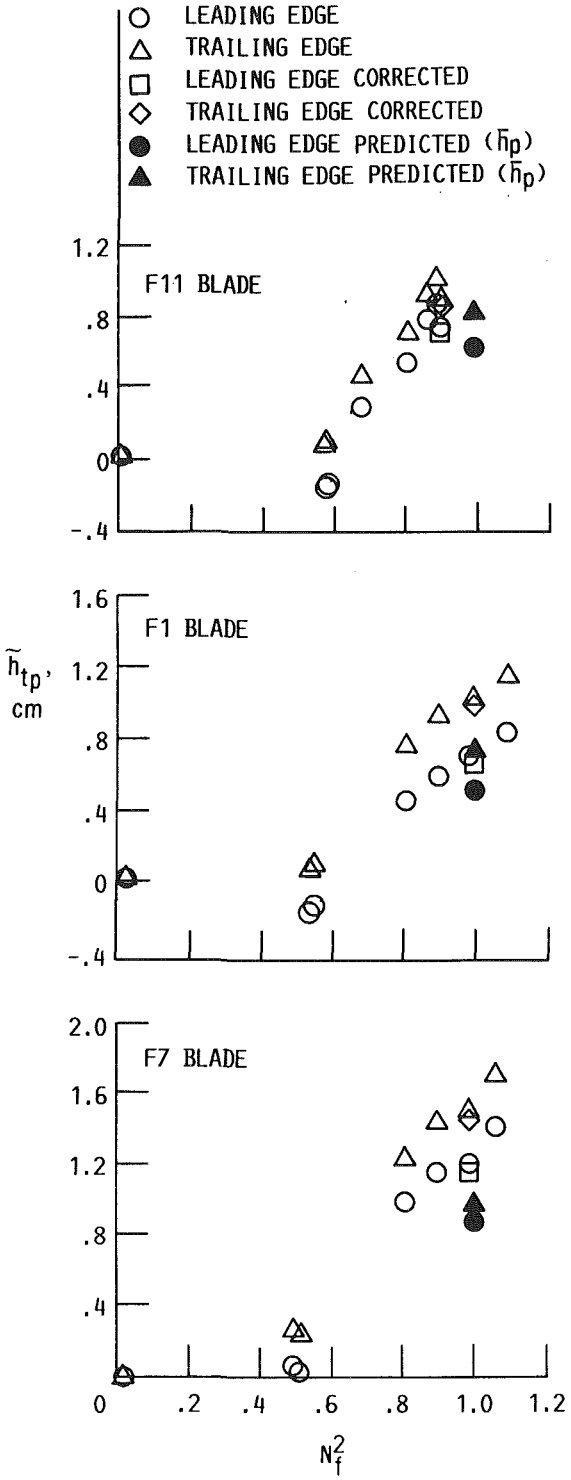

Fig. 8 Bending deflections

corrected experimental $\tilde{h}_{tp}$. The abscissa in Fig. 8 (N_f^2) is the square of the ratio of rotational speed to the design rotational speed. The correction is derived from simulated experimental results. The measured displacements in the third group of columns in Table 2 were not corrected. The measured bending deflections in Fig. 8 are all higher than predicted but, in general, the agreement is reasonable.

Twist Angles. Table 3 presents results for absolute twist angles. Note that positive twist corresponds to a β angle decrease relative to the reference value. In addition to the apparent total twist angle (plane $\hat{\mathbf{n}}_c$), twist angles in the initial plane $\hat{\mathbf{n}}_{ci}$, in the average bending plane $\hat{\mathbf{n}}_h$, and perpendicular to the pitch axis $\hat{\mathbf{k}}$ also are given in the table. The first three groups of columns from the left are associated with the same results as for bending (i.e., with the true predicted twist angle, the predicted twist angle that includes the laser beam slip effect, and the measured absolute twist). The fourth group of columns was added in these tables to evaluate the effect of the constant-chord-length assumption made in calculating twist angles from measurements. The θ_n'' and $\hat{\mathbf{n}}''$ are derived identically as in the experiment except that the measured angles in the tangential direction $\Delta\varphi_t$ are obtained from predicted blade contours. Thus subtracting θ_n from θ_n'' gives the correction factor associated with the constant-chord-length assumption. Comparing the appropriate unit vectors from column groups two and four indicates how this assumption affects the orientation of the associated planes.

Comparing group one and two results ($\bar{\theta}$ and θ) in Table 3 shows the error associated with the slip effect to be appreciable. Thus vectorial subtraction of the associated twist angles gives absolute errors of 0.53, 0.41, and 0.65 deg for the F11, F1, and F7 blades, respectively. However, the maximum errors for these blades for the planes defined by $\hat{\mathbf{n}}_{ci}$, $\hat{\mathbf{n}}_h$, and $\hat{\mathbf{k}}$ unit vectors are, respectively, 0.10, 0.12, and 0.16 deg. On the other hand, comparing θ and θ'' indicates that the error associated with the constant-chord-length assumption is fairly independent of $\hat{\mathbf{n}}$. The error is the largest for the F7 blade, amounting to about 0.2 deg. Considering now both the slip and the constant-chord-length errors, the maximum error is less than about 1/8 deg for any of the planes defined by $\hat{\mathbf{n}}_{ci}$, $\hat{\mathbf{n}}_h$, or $\hat{\mathbf{k}}$ unit vectors. It is simplest therefore to choose the XY-plane defined by the $\hat{\mathbf{k}}$ unit vector for reporting the twist angles. The experimental measurement error associated with this test is estimated to be less than 1/4 deg. The errors associated with the recorder and electronics were very small (Kurkov, 1988).

If desired, the measured twist angles can be corrected for these two systematic errors. The correction is more accurate the closer the predicted and experimental twist angles are. However, even a rough estimate can considerably reduce these errors. For example, for a 50 percent error in estimating this correction, in the present case the total systematic measurement error would be reduced to 1/16 deg. In the plots presented in Fig. 9, the measured twist angles include corrected points (square symbols) at the design speed so that the effect of correction can be evaluated. Also included in Fig. 9 are the true predicted absolute twist angles $\bar{\theta}_k$ at the design speed. In general, the agreement between predicted and experimental twist angles, taking into account all blades in Fig. 9, is not very good.

Note that, in Figs. 8 and 9, the first two points beyond the reference point (which is close to the origin of the axes) correspond to windmill conditions. Hence, deflections for these points are attributed to centrifugal forces.

The results for the 21 blade, presented in Fig. 10, are significant because the deflections for this blade are the largest and the agreement between predicted and measured deflections is the best. For this blade, the complete finite-element outputs were unavailable, but rather only the blade sections (deflected and undeflected) associated with the plane defined by the unit vector $\hat{\mathbf{n}}_{ci}$. Thus the true deflections ($\bar{\theta}$ and $\bar{h}$) and the slip-effect corrections could not be evaluated. (Which is why the results for this blade were not included in the tables.) Predicted results in Fig. 10 are therefore θ_k and h_p, and corrected twist includes only the chord correction effect. However, on the basis of previous results the good agreement between predicted and measured deflections demonstrated in Fig. 10 would likely prevail for true predicted deflections. The test conditions for the F21 blade were close to the nominal design conditions: N = 8085 rpm, Mach 0.8, and β = 61.8 deg. The leading and

Table 3 Absolute twist angles

Blade	Twist angle	True predicted				Predicted with slip				Experimental (relative to reference point)				Predicted with slip and constant chord			
		$\bar{\theta}$, deg	$\hat{n}$			θ, deg	$\hat{n}$			$\tilde{\theta}$, deg	$\hat{n}$			θ'', deg	$\hat{n}''$		
			$\hat{i}$	$\hat{j}$	$\hat{k}$		$\hat{i}$	$\hat{j}$	$\hat{k}$		$\hat{i}$	$\hat{j}$	$\hat{k}$		$\hat{i}$	$\hat{j}$	$\hat{k}$
F11	θ_{n_c}	2.6149	-0.2457	0.0788	0.9661	2.6305	-0.3904	0.2027	0.8980	2.1629	-0.4619	0.2661	0.8461	2.6869	-0.3786	0.1923	0.9054
	$\theta_{n_{c\ell}}$	2.5955	-.1533	.0023	.9882	2.4332	-.1533	.0023	.9882	1.9623	-.1533	.0023	.9882	2.5612	-.1533	.0023	.9882
	θ_{n_h}	2.5857	-.1342	-.0176	.9908	2.4652	-.1338	-.0239	.9907	1.9327	-.1339	-.0244	.9907	2.5331	-.1330	-.0243	.9908
	θ_k	2.5519	0	0	1.0000	2.3884	0	0	1.0000	1.8502	0	0	1.0000	2.4594	0	0	1.0000
F1	θ_{n_c}	2.8421	-0.2026	0.1766	0.9632	2.8783	-0.2986	0.2718	0.9148	4.2322	-0.2655	0.2390	0.9340	2.8447	-0.2904	0.2637	0.9198
	$\theta_{n_{c\ell}}$	2.8186	-.1129	.0883	.9897	2.7723	-.1129	.0883	.9897	4.1286	-.1129	.0883	.9897	2.7493	-.1129	.0883	.9897
	θ_{n_h}	2.8052	-.0927	.0627	.9937	2.7421	-.0926	.0575	.9940	4.0930	-.0936	.0560	.9940	2.7197	-.0915	.0569	.9942
	θ_k	2.7390	0	0	1.0000	2.6351	0	0	1.0000	3.9565	0	0	1.0000	2.6185	0	0	1.0000
F7	θ_{n_c}	1.3597	-0.3882	0.3127	0.8669	1.6552	-0.6060	0.5028	0.6164	4.3063	-0.3623	0.2903	0.8857	1.7790	-0.5558	0.4585	0.6935
	$\theta_{n_{c\ell}}$	1.2522	-.1019	.0669	.9925	1.1706	-.1019	.0669	.9925	4.0292	-.1019	.0669	.9925	1.3799	-.1019	.0669	.9925
	θ_{n_h}	1.2398	-.0879	.0485	.9949	1.1374	-.0877	.0408	.9953	3.9855	-.0906	.0386	.9951	1.3461	-.0862	.0402	.9955
	θ_k	1.1792	0	0	1.0000	1.0210	0	0	1.0000	3.8186	0	0	1.0000	1.2346	0	0	1.0000

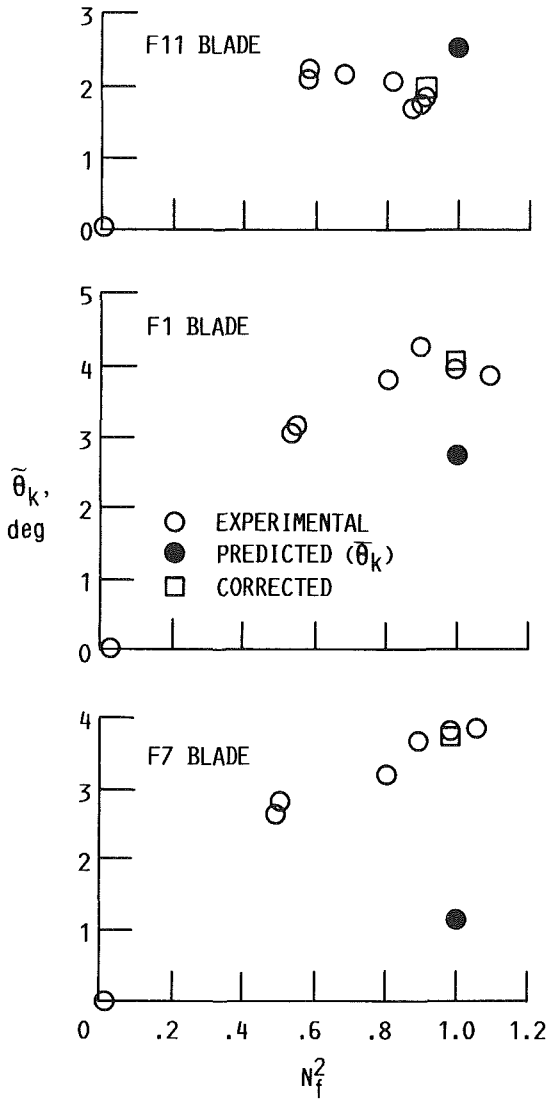

Fig. 9 Absolute twist angle

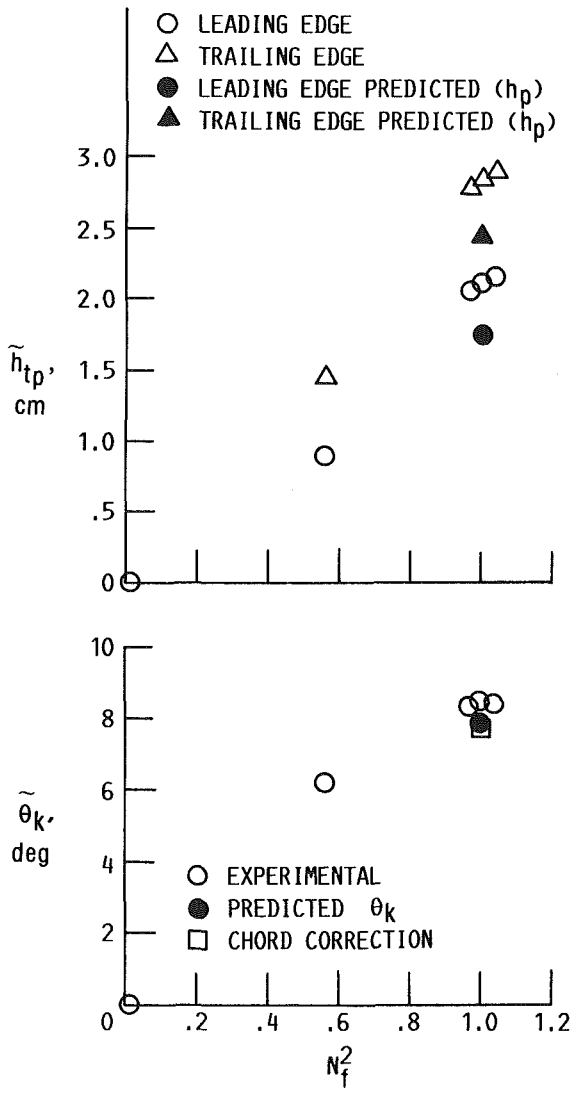

Fig. 10 Bending and twist deflections, F21 blade

trailing-edge Z coordinates corresponding to laser beam tangency points were 29.50 and 29.68 cm.

Concluding Remarks

The unducted fan blade deflections caused by centrifugal and aerodynamic loads were measured with a nonintrusive optical method that uses low-power, helium–neon lasers. The method was applied to four recently designed blade prototypes. Measurements were made in a plane nearly perpendicular to the pitch axis. Twist angles and leading and trailing-edge bending deflections were obtained for the near tip span with the total systematic (and therefore correctable) error of less than 1/8 deg. The experimental measurement error was estimated to be about 1/4 deg.

The agreement between predicted and experimental bending

deflections was generally fair. However, the agreement between the corresponding twist angles was poor, except for one blade prototype, for which it was very good.

References

Kurkov, A. P., 1984, "Measurement of Self-Excited Rotor-Blade Vibrations Using Optical Displacements," ASME *Journal of Engineering for Gas Turbines and Power*, Vol. 106, No. 1, pp. 44–49.

Kurkov, A. P., 1988, "Optical Measurement of Propeller Blade Deflections," NASA TP-2841, 1988.

Lawrence, C., and Meyn, E. H., 1985, "The Use of an Optical Data Acquisition System for Bladed Disk Vibration Analysis," *Vibrations of Blades and Bladed Disk Assemblies*, R. E. Kielb and N. F. Rieger, eds., ASME, New York, pp. 65–73.

Nieberding, W. C., and Pollack, J. L., 1977, "Optical Detection of Blade Flutter in YF-100 Turbofan Engine," ASME Paper No. 77-GT-66 (NASA TM X-73573).

Srinivasan, A. V., and Fulton, G. B., 1984, "Advanced Turboprop Vibratory Characteristics," R84-956627-1, United Technologies Research Center, East Hartford, CT, NASA CR-174708.

Stargardter, H., 1977, "Optical Determination of Rotating Fan Blade Deflections," ASME *Journal of Engineering for Power*, Vol. 99, No. 2, pp. 204–209.

Sullivan, J. T., 1987, "Aerodynamic Performance of a Scale-Model, Counter-Rotating Unducted Fan," *Advanced Technology for Aero Gas Turbine Components*, AGARD CP-421, AGARD, Paris, pp. 22–1 to 22–16.

Taylor, L. M., 1935, "Sighting Devices for Propeller Blade Observations," Air Corps Technical Report 4160, Dec. 7.

The Aerodynamics of an Oscillating Cascade in a Compressible Flow Field

D. H. Buffum
National Aeronautics and Space Administration,
Lewis Research Center,
Cleveland, OH 44135

S. Fleeter
Thermal Sciences and Propulsion Center,
School of Mechanical Engineering,
Purdue University,
West Lafayette, IN 47907

Fundamental experiments are performed in the NASA Lewis Research Center Transonic Oscillating Cascade Facility to investigate and quantify the aerodynamics of a cascade of bioconvex airfoils executing torsion mode oscillations at realistic reduced frequency values. Both steady and unsteady airfoil surface pressures are measured at two inlet Mach numbers, 0.65 and 0.80. and two incidence angles, 0 and 7 deg, with the harmonic torsional airfoil cascade oscillations at realistic high reduced frequency and unsteady data obtained at several interblade phase angle values. The time-variant pressures are analyzed by means of discrete Fourier transform techniques, with these unique data compared with predictions from a linearized unsteady cascade model. The experimental results indicate that the interblade phase angle has a major effect on the chordwise distributions of the airfoil surface unsteady pressure, with the effects of reduced frequency, incidence angle, and Mach number somewhat less significant.

Introduction

In the rotating blade rows of turbomachines and turboprops, the severe flow conditions associated with off-design positive incidence operation make the possibility of flutter a continual concern. Unfortunately, flutter prediction and, in particular, the modeling of nonzero incidence angle unsteady cascade aerodynamics, has not kept pace with the overall advances and new requirements of turbomachine and turboprop designs. As a result, current semi-empirical flutter design systems are often unreliable.

The development of analyses to predict oscillating cascade aerodynamics is an item of fundamental research interest at both zero and nonzero incidence angles. Classical unsteady aerodynamic models are based on linearized theory, with the unsteady flow assumed to be a small perturbation to a uniform steady flow. The problem is thus reduced to analyzing the unsteady aerodynamics of a cascade of flat plates operating at zero mean incidence (Smith, 1971; Fleeter, 1973). As a result, the unsteady aerodynamic effects due to the interactions between the steady and unsteady flow fields, i.e., the effects of blade geometry and nonzero incidence angle (steady loading), are not considered. To overcome these limitations, models are being developed in which the unsteady flow is coupled to a nonuniform steady flow field; for example, Atassi and Akai (1979); Verdon and Caspar (1980, 1984); Whitehead and Grant (1981); Chiang and Fleeter (1986); Usab and Verdon (1986).

To direct the development of advanced unsteady aerodynamic models and to evaluate these as well as existing analyses, data obtained from oscillating cascade experiments are needed, particularly in the high subsonic and transonic flow regimes. However, these flow regimes are relatively unexplored. Unsteady pressure data have been obtained in a transonic linear cascade in which only the instrumented airfoil was forced to harmonically oscillate (Szechenyi and Girault, 1980). In the subsonic compressible through supersonic flow regimes, an annular cascade has been utilized to obtain unsteady moment data from strain gages (Davies and Whitehead, 1984). Of particular interest herein, unsteady pressure measurements have been made at NASA Lewis on a bioconvex airfoil in a transonic oscillating cascade (Shaw et al., 1985). Unfortunately, there are some discrepancies in the acquisition and analysis of these unsteady data as well as the steady airfoil surface static pressure data. These are associated with not maintaining the profile of the airfoil instrumented with static pressure taps, an unreliable airfoil motion signal, and the misinterpretation of the schlieren flow visualization.

In this paper, the aerodynamics of a cascade of bioconvex airfoils executing torsion mode oscillations at realistic reduced frequency values in the NASA Lewis Transonic Oscillating Cascade Facility are investigated and quantified. The previously noted steady and unsteady data analysis discrepancies are eliminated and additional new unsteady aerodynamic data are analyzed and presented. In particular, flush-mounted high response miniature pressure transducers are used to measure the unsteady airfoil surface pressures for several interblade phase angles at inlet Mach numbers of 0.65 and 0.80 and incidence angles of 0 and 7 deg. The time-variant pressures on the surfaces of the oscillating cascade airfoils are then analyzed with discrete Fourier transform techniques.

Contributed by the International Gas Turbine Institute and presented at the 34th International Gas Turbine and Aeroengine Congress and Exhibition, Toronto, Ontario, Canada, June 4–8, 1989. Manuscript received at ASME Headquarters February 21, 1989. Paper No. 89-GT-271.

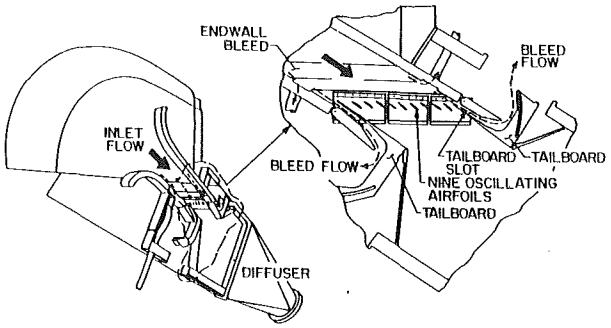

Fig. 1 NASA Lewis transonic oscillating cascade facility

Oscillating Cascade Facility

The NASA Lewis Transonic Oscillating Cascade Facility, shown in Fig. 1, is a linear wind tunnel capable of test section Mach numbers approaching unity. Air drawn from the atmosphere passes through a smoothly contracting inlet section, into a constant area 9.78 cm by 19.21 cm test section, and then through a diffuser and exhaust header with a nominal pressure of 3.0 N/cm^2. The flow rate is controlled by two valves located in the header. Upstream of the test section, a partitioned bleed system applies suction to the endwall boundary layers, thus reducing endwall viscous effects. Suction also is applied through tailboard slots to reduce effects due to the upper and lower cascade endwalls.

A major feature of this facility is the high-speed mechanical drive system, which imparts controlled torsional oscillations to the nine cascade airfoils. Nine barrel cams, each with a six-cycle sinusoidal groove machined into its periphery, are mounted on a common shaft driven by a 74.6 kW electric motor. Connecting arms, joined to one end of each airfoil by trunnions, have buttons on the opposite end to follow the cam grooves. The amplitude of the airfoil motion is 1.2 deg, dictated by the cam and follower geometry. Different interblade phase angle oscillations are achieved by changing the relative positions of the cams. In this investigation, the maximum oscillatory frequency is 500 Hz, corresponding to a reduced frequency of 0.462 with a cascade inlet Mach number of 0.80.

Airfoils and Instrumentation

The cascade is comprised of nine uncambered biconvex airfoils with a chord of 7.62 cm, a thickness-to-chord ratio of 0.076, a solidity of 1.3, and a 53-deg stagger angle, Fig. 2. The radius of curvature of the airfoil surfaces is 27.4 cm, with the leading and trailing edges rounded with a 0.025 cm radius of curvature. The airfoils are supported by two midchord trunnions, resulting in a midchord elastic axis location.

The steady flow airfoil surface pressure distributions are measured with conventional static pressure tap instrumented airfoils. There are 16 chordwise measurement locations, with four additional taps to assure the spanwise uniformity of the pressure distribution. Rows of sidewall static pressure taps, located upstream and downstream of the cascaded airfoils (Fig. 1), are used to determine the mean inlet and exit pressures.

The primary dynamic data quantify the complex unsteady surface pressures on the oscillating cascade airfoils. These data are obtained by flush mounting six Kulite transducers symmetrically along the chord of one airfoil surface (Table 1). Thus, to obtain the unsteady pressure data on both airfoil surfaces, the experiments are performed in two phases with data acquired on one surface at a time. The transducers, each

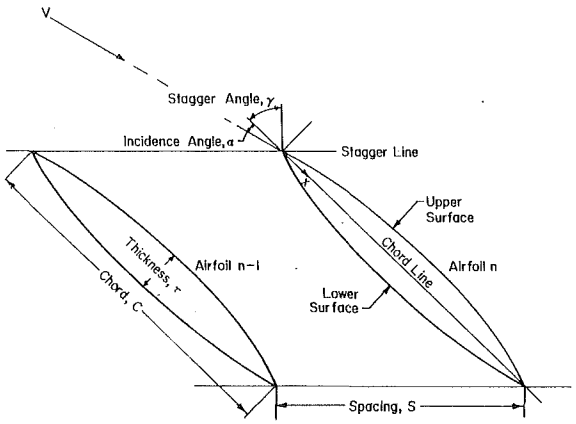

Fig. 2 Cascade geometry

Table 1 Cascade geometry and experimental conditions

AIRFOIL	
Type	biconvex, no camber
Surface radius of curvature	27.4 cm
Leading and trailing edge radii of curvature	0.025 cm
Maximum airfoil thickness, τ	0.58 cm
Chord, C	7.62 cm
Elastic axis	midchord
Dynamic pressure transducer locations, (% chord)	60,75,88
CASCADE	
Number of airfoils	9
Solidity, C/S	1.3
Spacing, S	5.86 cm
Stagger angle, γ	53 degrees
Amplitude of motion	1.2 degrees

EXPERIMENT CONDITIONS

Mach Number	Mean-Incidence Angle (degrees)	Interblade Phase Angle (degrees)	Reduced Frequency		
0.65	0	0, + 90, - 90	0.223,	0.390,	0.557
0.65	7	0, + 90, - 90	0.223,	0.390,	0.557
0.80	7	0, + 90, - 90	0.185,		0.462

Nomenclature

C = airfoil chord
C_M = unsteady momentum coefficient about midchord $= \int_0^1 \left(\frac{1}{2}-\frac{x}{C}\right) \Delta C_p d\left(\frac{x}{C}\right)$
$\bar{C}_p$ = steady surface static pressure coefficient $= (p_{in}-p_0)/(\frac{1}{2}\rho V^2)$
C_p = unsteady pressure coefficient $= p_1/(\frac{1}{2}\rho V^4 \alpha_1)$
C_{pl} = lower surface unsteady pressure coefficient
C_{pu} = upper surface unsteady pressure coefficient
k = reduced frequency $= \omega C/2V$
M = free-stream Mach number
$\bar{p}$ = steady static pressure
p = time variant static pressure
p_{in} = inlet static pressure
p_1 = unsteady static pressure first harmonic
S = airfoil spacing
V = free-stream velocity
α_0 = mean flow incidence angle
$\bar{\alpha}$ = torsional oscillation amplitude
γ = stagger angle
ΔC_p = $C_{pl}-C_{pu}$
σ = interblade phase angle (positive when airfoil n leads airfoil $n-1$)
τ = maximum airfoil thickness
ϕ = phase lead relative to airfoil motion
ω = oscillatory frequency

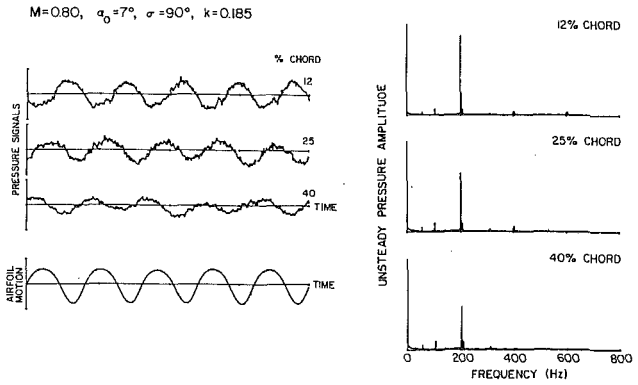

Fig. 3 Time-variant signals and averaged pressure spectra

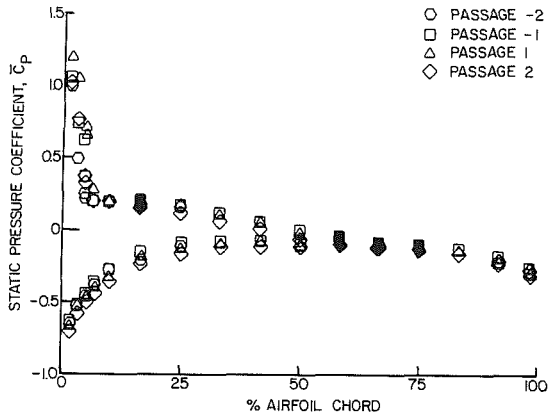

Fig. 4 Periodicity of steady flow airfoil surface pressure distribution, M = 0.80, α_o = 7 deg

with an active sensor diameter of 0.097 cm, 1.3 percent of the airfoil chord, are placed in milled slots and potted in RTV to isolate them from airfoil strain.

The time-variant position of the oscillating instrumented airfoil is determined by two independent measurements. The results of Shaw et al. (1986) were derived using an electro-optical displacement meter to track the motion of the instrumented center airfoil. The second measure of the airfoil motion is provided by a capacitance-type proximity sensor, which produces a voltage proportional to the air gap between it and an adjacent object. This sensor is positioned to face a six-cycle sinusoidally shaped cam mounted on the same shaft as the airfoil drive cams and to be in phase with the instrumented airfoil motion. The proximity probe signal is virtually noise-free, in contrast to the optical probe signal. Unfortunately, at times, the optical signal noise is of such intensity that there is no discernible sinusoid.

The two signals are generally in good agreement, with a difference of 5 deg or less in the phase measurement of the airfoil motion. Either signal can then be used as a reference for the unsteady pressure measurements. However, in some cases there are large phase differences between the two measurements, most likely due to the excessive noise in the optical signal or the dropout of that signal altogether. Because of the high reliability of the proximity probe signal, it is used to measure the airfoil motion in the results presented herein.

Data Acquisition and Analysis

Conventional instrumentation is used to quantify the steady flow field. An average of the upstream sidewall static pressures along with the atmospheric pressure are used to calculate the inlet Mach number. Steady flow airfoil surface static pressures are calculated from an average of at least 40 samples.

All of the unsteady signals are a-c coupled and recorded on magnetic tape for post-experiment processing. During tape playback, the signals are simultaneously digitized at rates suf-

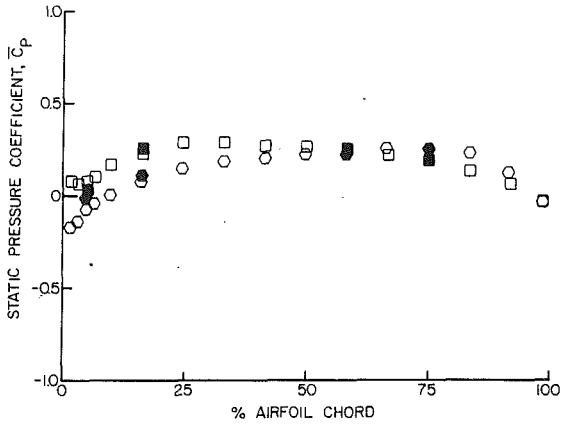

Fig. 5 Steady flow airfoil surface pressure distribution, M = 0.65, $\bar{\alpha}$ = 0 deg

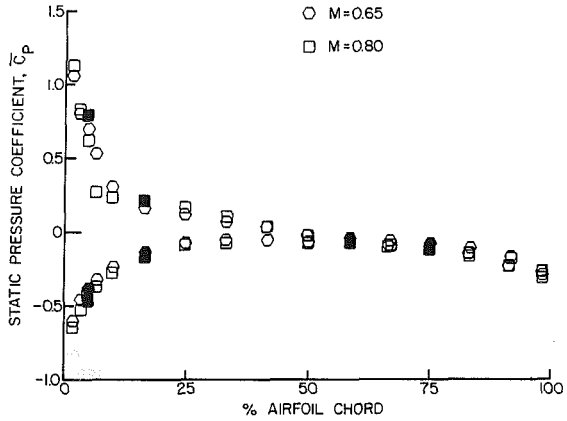

Fig. 6 Steady flow airfoil surface pressure distribution, $\bar{\alpha}$ = 7 deg

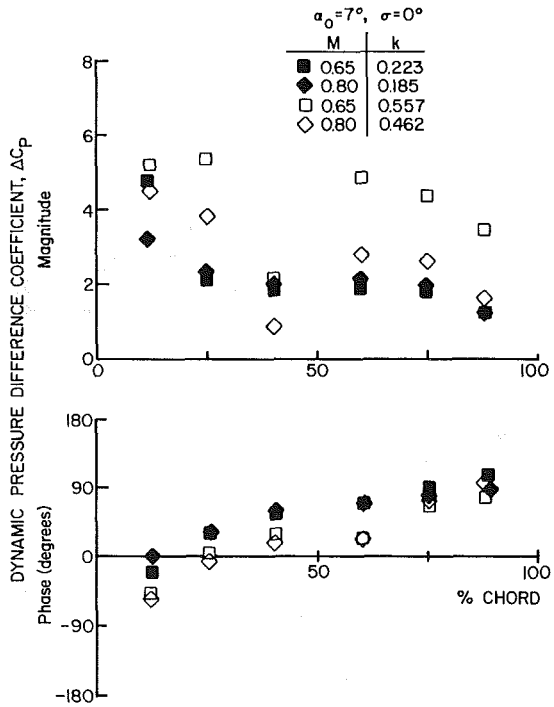

Fig. 7 Effect of Mach number on dynamic pressure difference coefficient

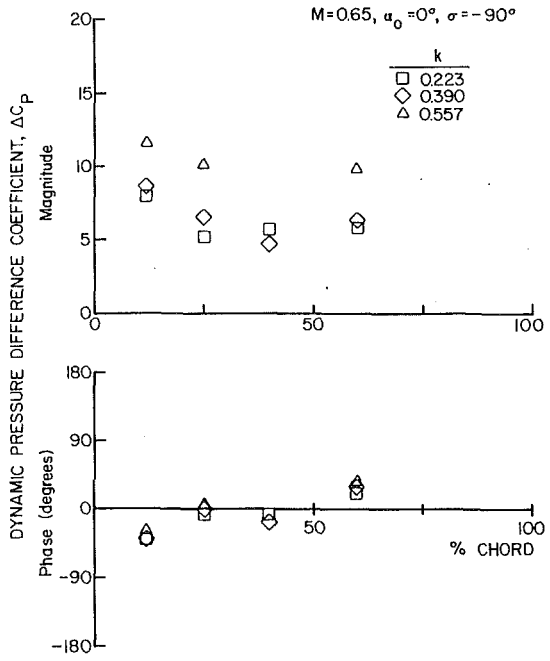

Fig. 8 Reduced frequency effect on dynamic pressure difference coefficient, $\sigma = -90$ deg

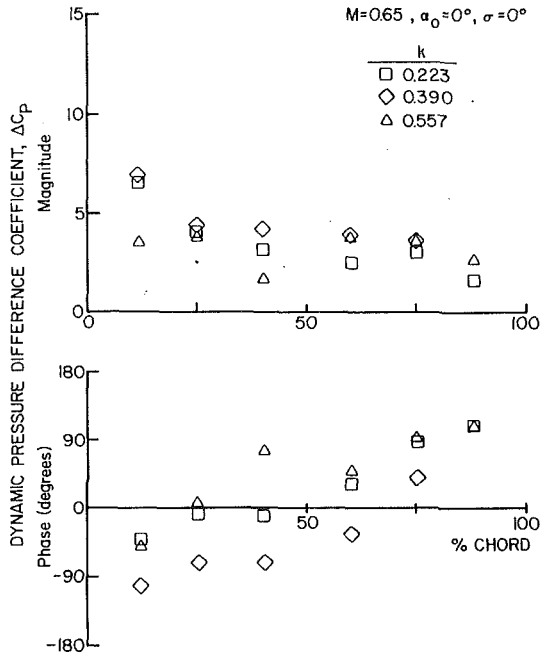

Fig. 10 Reduced frequency effect on dynamic pressure difference coefficient, $\sigma = 0$ deg

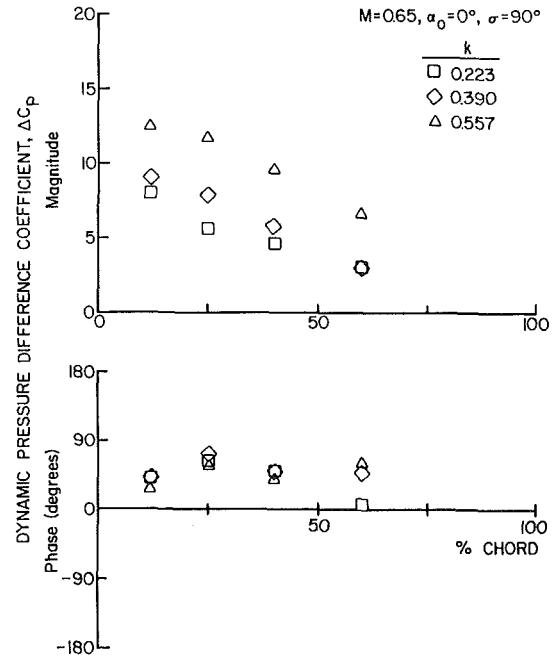

Fig. 9 Effect of reduced frequency on dynamic pressure difference coefficient, $\sigma = +90$ deg

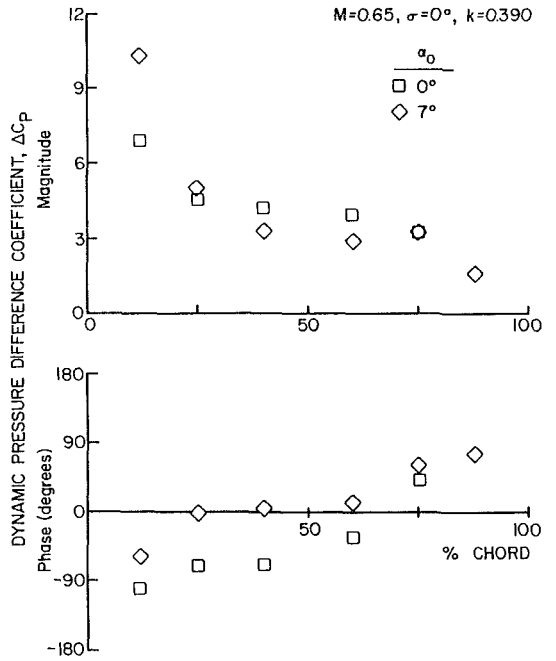

Fig. 11 Mean flow incidence effect on dynamic pressure difference coefficient, $\sigma = 0$ deg, $k = 0.390$

ficient to capture at least three harmonics of the oscillation frequency, with 32,768 samples taken per channel. Each data channel is divided into blocks, typically with 2048 samples, and then Fourier decomposed and referenced to the airfoil motion by subtracting the phase of the motion signal from the pressure signal. With all of the transducer signal blocks decomposed, the results are averaged and data points with wideband noise spectra discarded. To minimize errors due to spectral leakage, a correction scheme is applied to the decomposed results in conjunction with a Hanning window (Burgess, 1975).

This data analysis technique is demonstrated in Fig. 3, which presents the pressure transducer signals and the resulting averaged pressure spectra. The dominant response appears in the spectra at 200 Hz, which corresponds to the airfoil cascade oscillation frequency. The small spikes at the lower frequencies are due to wind tunnel tones. The lack of any broadband components indicates that the noise evident in the pressure signals has been successfully removed.

The final unsteady pressure data are in the form of a complex dynamic pressure difference coefficient, ΔC_p, which defines the nondimensional pressure difference across the chordline of an airfoil. These data are presented in the format of a magnitude and a phase referenced to the airfoil motion, with a positive phase corresponding to the unsteady pressure leading the airfoil motion.

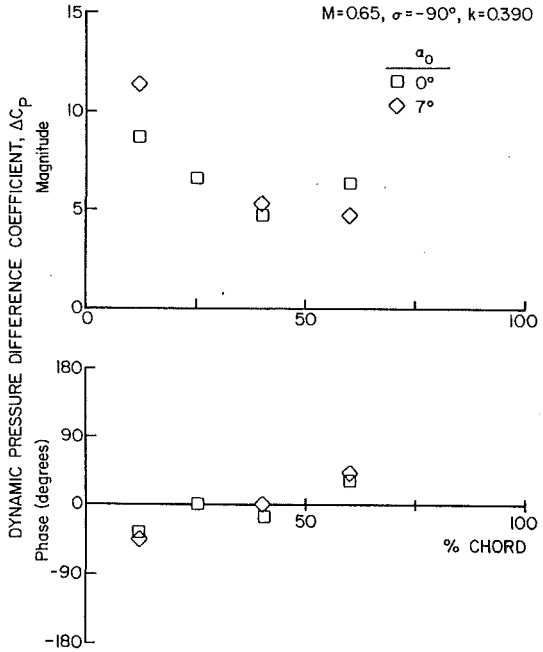

Fig. 12 Effect of mean flow incidence on dynamic pressure difference coefficient, $\sigma = -90$ deg, $k = 0.390$

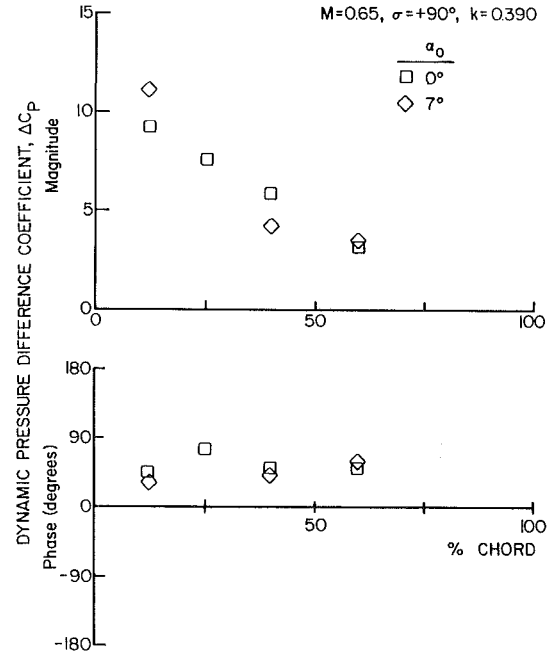

Fig. 13 Mean flow incidence effect on dynamic pressure difference coefficients, $\sigma = +90$ deg, $k = 0.390$

Results

A series of experiments are performed to investigate and quantify the effects of inlet Mach number, reduced frequency, interblade phase angle, and mean flow incidence angle on the unsteady aerodynamics of the oscillating cascade. A summary of the experimental conditions is presented in Table 1. The airfoil motion is defined in equation (1):

$$\alpha(t) = \alpha_0 + \bar{\alpha}\cos\omega t \tag{1}$$

where the oscillatory amplitude, $\bar{\alpha}$, is 1.2 deg and α_0 is the mean flow incidence angle.

Steady-State Aerodynamics. Airfoil surface pressure distributions are presented for the three steady flow conditions. To demonstrate periodicity at the steady-state conditions, airfoil surface pressure distributions are obtained for multiple passages in the cascade. For example, Fig. 4 presents data for the four cascade passages surrounding the center airfoil at $M = 0.8$, $\bar{\alpha} = 0.7$ deg. Passage 1 data are the pressure distributions for the airfoil 0 (the center airfoil in the cascade) upper surface and the airfoil $+1$ lower surface; passage -1 data are for the airfoil 0 lower surface and the airfoil -1 upper surface, etc. The good periodicity attained in the cascade is readily apparent.

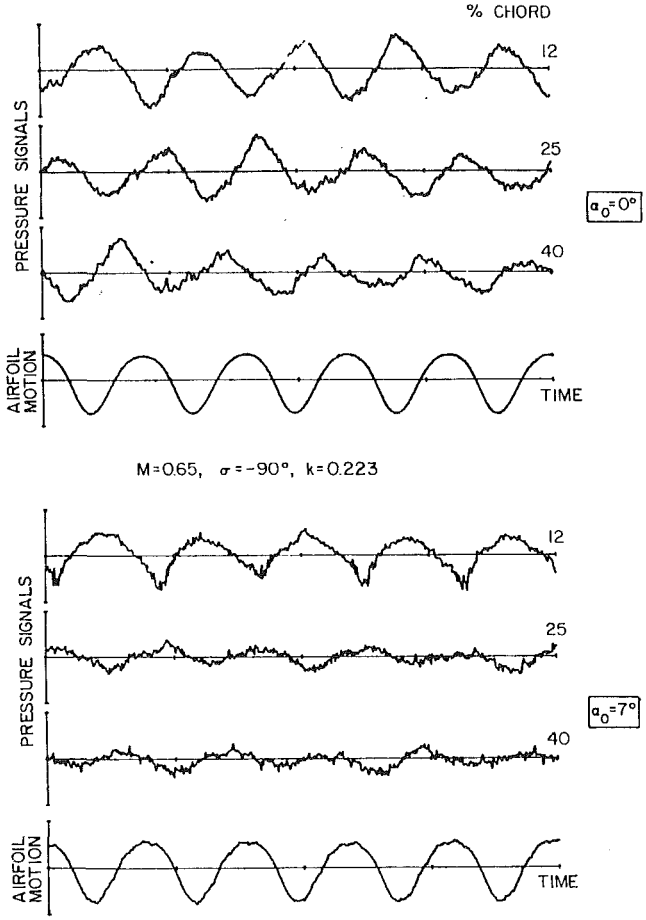

Fig. 14 Airfoil upper surface unsteady signals

Figures 5 and 6 present the steady flow airfoil surface pressure coefficient distributions for the center airfoil. At $M = 0.65$ and $\bar{\alpha} = 0$ deg, Fig. 5, the airfoil has some loading due to cascading effects. The additional spanwise pressure taps, indicated by the darkened symbols, show good spanwise uniformity except very near the leading edge. At $\bar{\alpha} = 7$ deg, Fig. 6, the pressure coefficient distributions are nearly identical for the two inlet Mach numbers. The aft half of the airfoil is not loaded. At Mach 0.8, schlieren images indicate the presence of a weak leading edge shock on the upper surface.

Mach Number. At a Mach number of 0.65, the flow field is compressible and shock-free. At the higher Mach number of 0.80, a shock is present in the flow field, confirmed by schlieren images of the oscillating upper airfoil surface leading edge shock (Shaw et al., 1986). Figure 7 presents the dynamic pressure difference coefficient data at 7 deg of incidence with a 0-deg interblade phase angle at oscillatory frequencies of 200 and 500 Hz. The phase data show minimal variations with Mach number. At the lower reduced frequency, the Mach number has little effect on the magnitude data. At the higher reduced frequency, however, the Mach number has a large

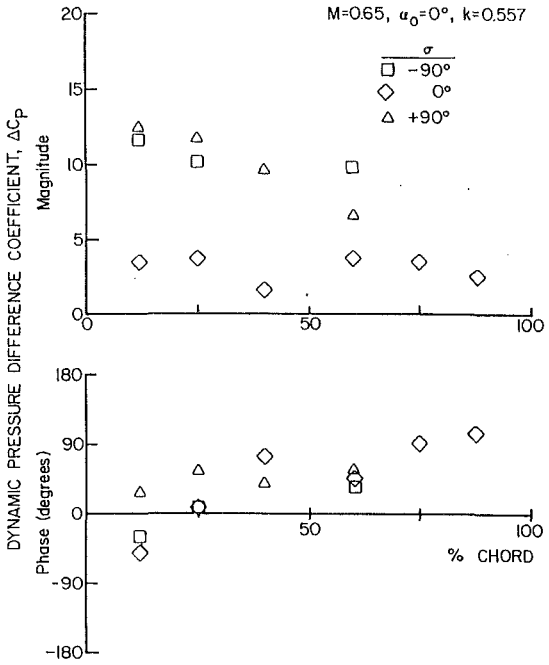

Fig. 15 Effect of interblade phase angle on dynamic pressure difference coefficient, M = 0.65

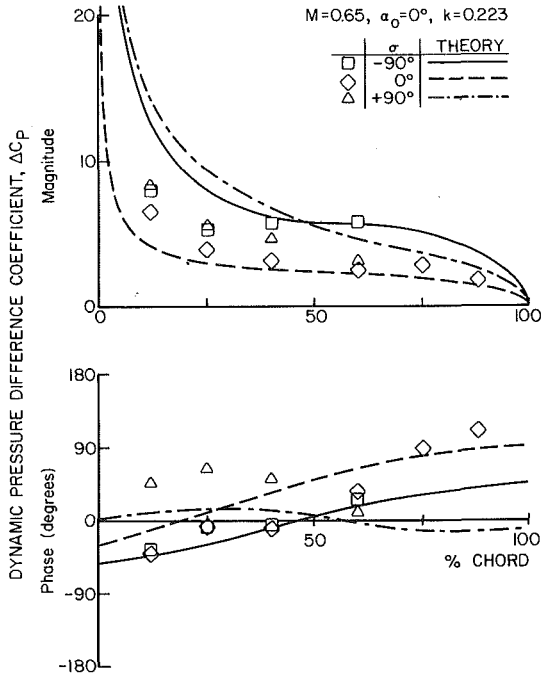

Fig. 17 Data-linearized theory correlation, M = 0.65, α_o = 0 deg, k = 0.223

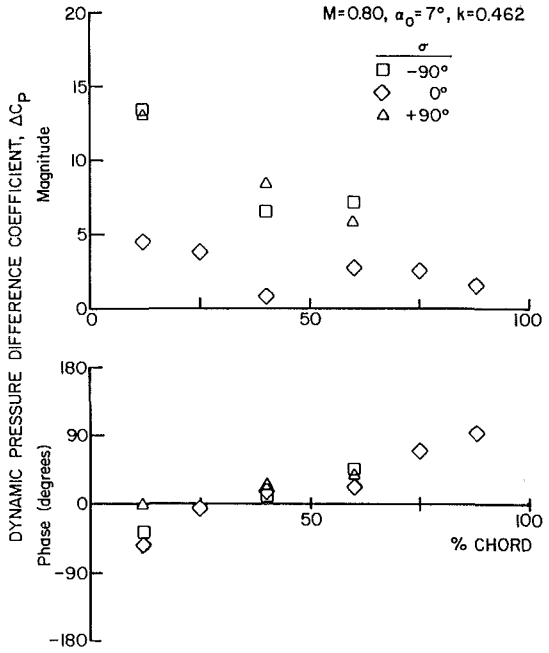

Fig. 16 Interblade phase angle effect on dynamic pressure difference coefficient, M = 0.80

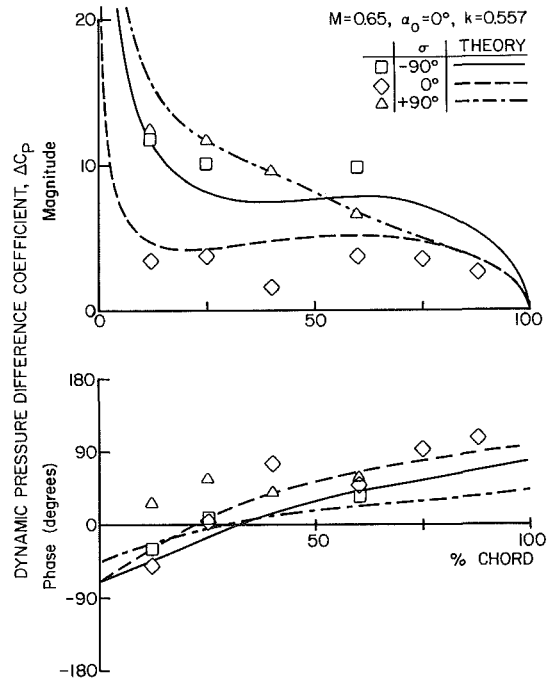

Fig. 18 Data-linearized theory correlation, M = 0.65, α_o = 0 deg, k = 0.557

effect, with the largest pressure levels associated with the lowest Mach number data.

Reduced Frequency. Reduced frequency significantly affects the phase of the dynamic pressure coefficient data only at a 0-deg interblade phase angle value. This is demonstrated for −90, +90, and 0-deg interblade phase angle values in Figs. 8–10, respectively. The magnitude data generally increase as the reduced frequency increases for interblade phase angles of −90 and +90 deg, with the lowest reduced frequency data having the smallest values. Note that unsteady data with wideband noise pressure spectra have been discarded.

Mean Incidence Angle. At the lower Mach number of 0.65, data were obtained and analyzed at both 0 and 7 deg of incidence. The dynamic pressure difference coefficient phase data are dependent on the mean flow incidence only at an interblade phase angle of 0 deg, for example, Figs. 11–13. This result is analogous to that previously noted in the reduced frequency discussion. As the incidence angle increases, the dynamic pressure difference coefficient magnitude data are generally increased in value near the leading edge, decreasing to lower values with increasing chord.

Time histories of the unsteady pressure signals were investigated for evidence of flow separation. Carta and Lorber (1987) found that separation on an oscillating airfoil is characterized by an abrupt change in the pressure level with time

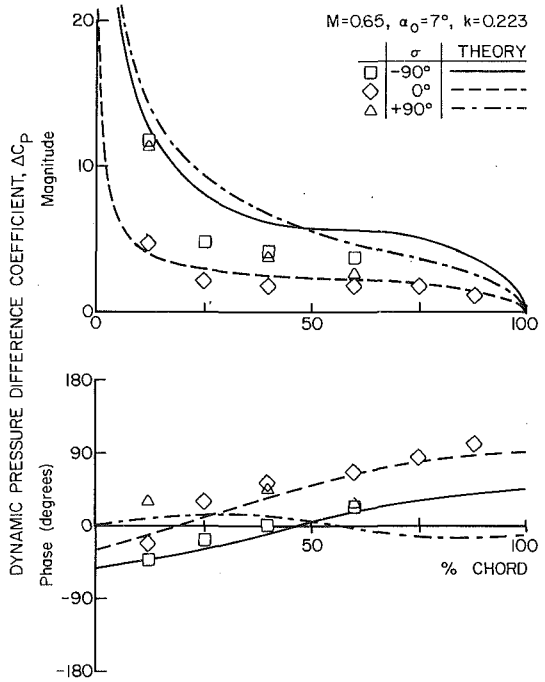

Fig. 19 Data-linearized theory correlation, M = 0.65, α_o = 7 deg, k = 0.223

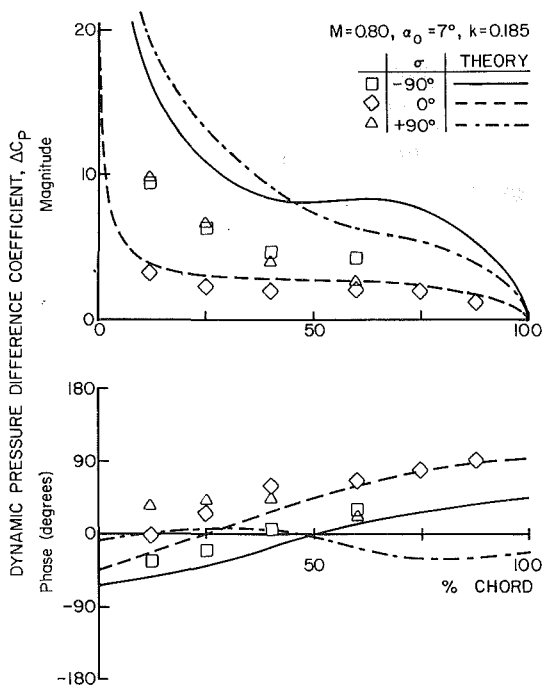

Fig. 21 Data-linearized theory correlation, M = 0.80, α_o = 7 deg, k = 0.85

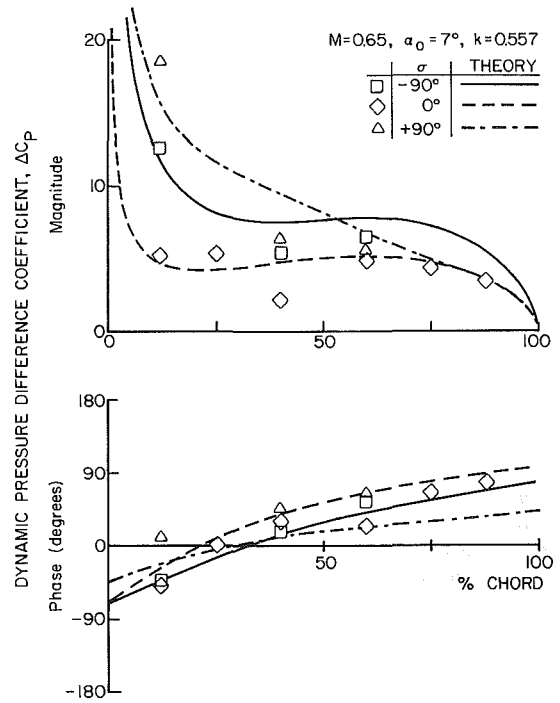

Fig. 20 Data-linearized theory correlation, M = 0.65, α_o = 7 deg, k = 0.557

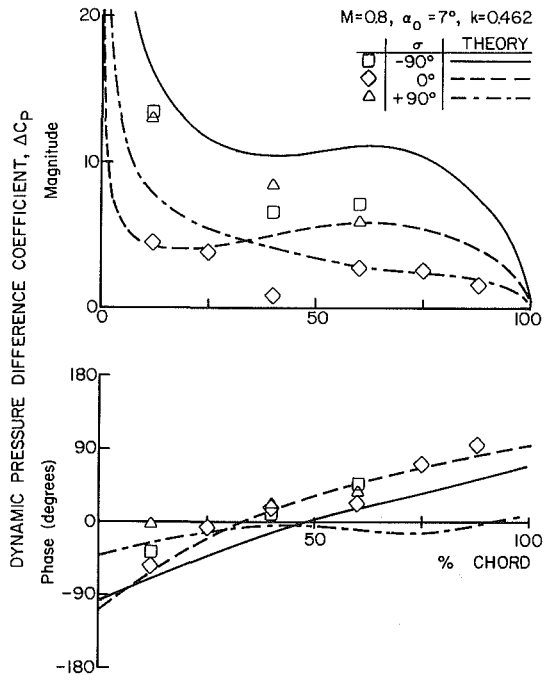

Fig. 22 Data-linearized theory correlation, M = 0.8, α_o = 7 deg, k = 0.462

accompanied by an increase in the level of high-frequency pressure fluctuations. The pressure histories of the 12, 25, and 40 percent chord transducer signals are shown in Fig. 14 for an inlet Mach number of 0.65. At 0 deg of incidence, the pressure signals are sinusoidal with disturbances superimposed. Since separation is unlikely at 0 deg of incidence, the disturbances are representative of nonseparated flow fluctuations. At 7 deg of incidence, the 12 percent chord pressure signal shows increased magnitude high-frequency fluctuations in the vicinity of the pressure minima. However, there is no indication of massive flow separation.

Figure 3 presented the pressure signals at a Mach number of 0.80 and a mean flow incidence angle of 7 deg. Although there are large random fluctuations, the precipitous changes in pressure indicative of flow separation or shock motion are not present. For these flow conditions, Shaw et al. (1986) concluded that massive separation from the airfoil leading edge occurred as the airfoil pitched upward toward maximum incidence angle. This conclusion was based on schlieren movies, which clearly show a region cyclically forming on the upper surface of the airfoils. Because the unsteady pressure data show no evidence of massive flow separation, including the correlation of these data with an attached flow prediction to be presented later in this paper, there is reason to believe that the

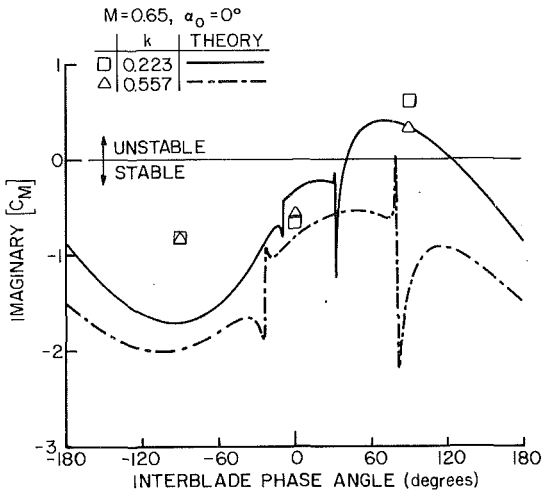

Fig. 23 Imaginary moment coefficient variation with Mach number M = 0.65, α_o = 0 deg

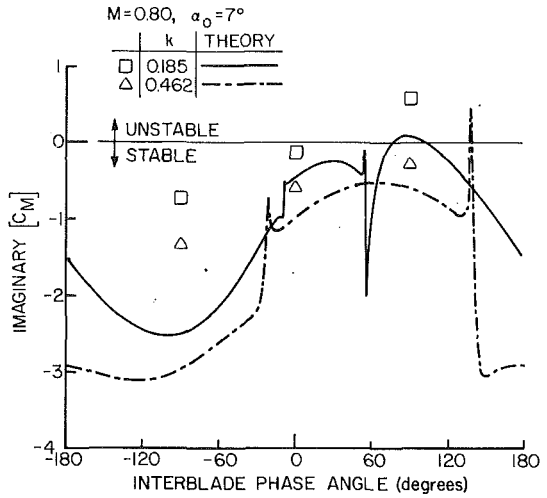

Fig. 24 Imaginary moment coefficient variation with interblade phase angle, M = 0.65, α_o = 7 deg

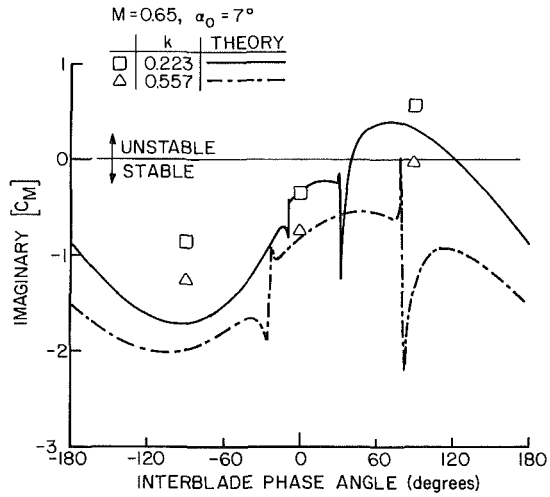

Fig. 25 Imaginary moment coefficient variation with interblade phase angle, M = 0.80, α_o = 7 deg

flow visualization was misinterpreted, with the gradient in the schlieren movies most likely due to endwall viscous effects.

Interblade Phase Angle. Figures 15 and 16 show the effect of interblade phase angle on the dynamic pressure difference coefficient for inlet Mach numbers of 0.65 and 0.80, respectively. For both +90 and −90 deg interblade phase angle values, the magnitude data have approximately equal amplitudes near the leading edge, decreasing with increasing chordwise position. However, for a 0-deg interblade phase angle, the magnitude data are decreased relative to the nonzero interblade phase angle data, with no leading edge maxima evident. Also, the phase data increase in a linear manner with increasing chordwise position.

Data-Linearized Theory Correlation. The dynamic pressure coefficient data obtained in these experiments are correlated with predictions from the unsteady, small perturbation, subsonic, flat plate cascade analyses of Smith (1971) and Fleeter (1973). Figures 17 and 18 present the results for reduced frequency values of 0.223 and 0.557, respectively, for an inlet Mach number of 0.65 and a mean incidence angle of 0 deg. The phase lead data and predictions exhibit general trendwise agreement, with the quality of the magnitude correlation generally good. Increasing the mean incidence angle to 7 deg while maintaining the reduced frequency and Mach number values has a favorable effect on the correlation of the phase angle, with the magnitude correlation still good, Figs. 19 and 20. With the incidence angle kept at 7 deg, the inlet Mach number is increased to 0.80, resulting in reduced frequency values of 0.185 and 0.462. As shown in Figs. 21 and 22, this results in generally good correlation of the phase angle data at both reduced frequency values, but reduced correlation of the magnitude data at a reduced frequency of 0.185, but not as good as a 0.462 reduced frequency.

To indicate in general how these unsteady cascade pressure difference data relate to stability, the torsion mode unsteady aerodynamic moment coefficients, C_M, are calculated from the unsteady pressure difference coefficient data. This is accomplished by: (1) assuming there is a zero pressure difference at the leading and trailing edges of the airfoil; (2) fitting a smooth curve through the chordwise distribution of the data; and (3) numerically integrating the resulting chordwise distribution of the pressure difference.

The imaginary part of these experimentally determined moment coefficients, together with the corresponding predictions, are presented as a function of the interblade phase angle value in Figs. 23–25. The data and predictions exhibit the same trends as the interblade phase angle increases from −90 toward +90 deg. However, at an interblade phase angle of +90 deg, a flutter instability is indicated by some of the data. However, the corresponding predictions are consistently lower in value, indicating a more stable condition, i.e., the predictions are not conservative.

Summary and Conclusions

Fundamental experiments were performed in the NASA Lewis Transonic Oscillating Cascade Facility to investigate and quantify the aerodynamics of a cascade of biconvex airfoils executing torsion mode oscillations at realistic reduced frequency values in a compressible flow field. Flush-mounted high response pressure transducers were used to measure the unsteady airfoil surface pressures for several interblade phase angles at inlet Mach number of 0.65 and 0.80 and incidence angles of 0 and 7 deg.

The analysis of these unique data shows that the interblade phase angle has a major effect on the chordwise distributions of the airfoil surface unsteady pressure, with the effects of reduced frequency, incidence angle, and Mach number somewhat less significant. Also, both the unsteady pressure difference and imaginary moment coefficient data generally exhibit

good correlation with predictions from a linearized cascade model. However, at an interblade phase angle of +90 deg where the data indicates a flutter instability, the corresponding predictions are consistently lower in value, indicating a more stable condition, i.e., the predictions are not conservative.

Acknowledgments

The NASA Lewis Research Center and, in particular, Larry Bober, Dan Hoyniak, Don Boldman, and Cal Ball, are most gratefully acknowledged for their encouragement, discussions, and support.

References

Atassi, H., and Akai, T. J., 1979, "Aerodynamic and Aeroelastic Characteristics of Oscillating Loaded Cascades at Low Mach Number," ASME Paper No. 79-GT-111.

Burgess, J. C., 1975, "On Digital Spectrum Analysis of Periodic Signals," *Journal of the Acoustical Society of America*, Vol. 58, No. 3, Sept.

Carta, F. O., and Lorber, P. F., 1987, "Experimental Study of the Aerodynamics of Incipient Torsional Stall Flutter," *AIAA Journal of Propulsion*, Vol. 3, No. 2, March-April.

Chiang, H. D., and Fleeter, S., 1986, "Locally Analytical Numerical Method for Inviscid Oscillating Airfoil Aerodynamics," SIAM 1986 National Meeting, July.

Davies, M. R. D., and Whitehead, D. S., 1984, "Unsteady Aerodynamic Moment Measurements in a Transonic Annular Cascade," *Unsteady Aerodynamics of Turbomachines and Propellers*, Cambridge University, Cambridge, England.

Fleeter, S., 1973, "Fluctuating Lift and Moment Coefficients for Cascade Airfoils in a Nonuniform Compressible Flow," *AIAA Journal of Aircraft*, Vol. 10, No. 2, Feb.

Shaw, L. M., Boldman, D. R., Buggele, A. E., and Buffum, D. H., 1986, "Unsteady Pressure Measurements on a Bioconvex Airfoil in a Transonic Oscillating Cascade," ASME *Journal of Engineering for Gas Turbines and Power*, Vol. 108, No. 1.

Smith, S. M., 1971, "Discrete Frequency Sound Generation in Axial Flow Turbomachines," *Cambridge University Report CUED/A-Turbo/TR29*.

Szechenyi, E., and Girault, J. P., 1980, "A Study of Compressor Blade Flutter in a Straight Cascade Wind Tunnel," *Aeroelasticity in Turbomachines*, Juris-Verlag, Zurich, Switzerland.

Verdon, J. M., and Caspar, J. R., 1980, "Subsonic Flow Past an Oscillating Cascade With Finite Mean Flow Deflection," *AIAA Journal*, Vol. 18.

Verdon, J. M., and Caspar, J. R., "A Linearized Unsteady Aerodynamic Analysis for Transonic Cascades," *Journal of Fluid Mechanics*, Vol. 149, Dec.

Usab, W. J., and Verdon, J. M., 1986, "On the Application of a Linearized Unsteady Potential Flow Analysis to Fan-Tip Cascades," ASME Paper No. 86-GT-87.

Whitehead, D. S., and Grant, R. J., 1981, "Force and Moment Coefficients for High Deflection Cascades," *Proceedings 2nd International Symposium on Aeroelasticity in Turbomachines*, P. Suter, ed.

Annular Cascade Study of Low Back-Pressure Supersonic Fan Blade Flutter

H. Kobayashi
National Aerospace Laboratory,
Chofu, Tokyo, Japan

Low back-pressure supersonic fan blade flutter in the torsional mode was examined using a controlled-oscillating annular cascade test facility. Precise data of unsteady aerodynamic forces generated by shock wave movement, due to blade oscillation, and the previously measured data of chordwise distributions of unsteady aerodynamic forces acting on an oscillating blade, were joined and, then, the nature of cascade flutter was evaluated. These unsteady aerodynamic forces were measured by direct and indirect pressure measuring methods. Our experiments covered a range of reduced frequencies based on a semichord from 0.0375 to 0.547, six interblade phase angles, and inlet flow velocities from subsonic to supersonic flow. The occurrence of unstalled cascade flutter in relation to reduced frequency, interblade phase angle, and inlet flow velocity was clarified, including the role of unsteady aerodynamic blade surface forces on flutter. Reduced frequency of the flutter boundary increased greatly when the blade suction surface flow became transonic flow. Interblade phase angles that caused flutter were in the range from 40 to 160 deg for flow fields ranging from high subsonic to supersonic. Shock wave movement due to blade oscillation generated markedly large unsteady aerodynamic forces which stimulated blade oscillation.

Introduction

Recently, many experimental and numerical studies in relation to transonic flow problems in turbomachinery have been performed for development of turbofan engines, gas turbines and steam turbines. These studies are mostly for steady flow problems and only a few studies on flutter related unsteady flow problems have been carried out (Fleeter, 1979). Unsteady flows in fan, compressor and turbine blade rows cause oscillatory fatigue of blades and therefore analysis of the unsteady aerodynamic forces acting on blades are necessary for solution of the blade fatigue problems (Fransson, 1984; El-Aini, 1986).

Several researchers have measured the aerodynamic forces or moments acting on an oscillating blade, using linear or annular cascade test facilities (Whitehead, 1976; Davies, 1984; Riffel, 1980a, 1980b; Szechenyi, 1984; Kirschner, 1980; Shaw, 1985). An example is the aerodynamic moment measurement made by Whitehead (1976) and Davies (1984), using an annular blade row oscillating in the torsional mode. For this study, a resonance-type blade vibration was used for blade oscillation. Therefore, aerodynamic moment data for unstable cascade conditions seem to be difficult to measure and, in addition, they were limited to low values of reduced frequency. Riffel and Rothrock (1980) measured the chordwise distribution of unsteady aerodynamic forces on blade surfaces, using a linear cascade oscillating in the torsional mode. However, the number of pressure measuring points in the chordwise direction of blade surface was not sufficient to evaluate the aerodynamic instability of the DCA cascade, and also unsteady aerodynamic forces generated by shock waves, due to blade oscillation, could not be observed. The one blade oscillation method used by Szechenyi (1984) for measuring unsteady aerodynamic moments acting on an oscillating blade row is considered to be insufficient for flows containing shock waves.

For controlled oscillation of all blades composing an annular blade row, a Freon gas annular cascade test facility was contrived (Kobayashi, 1986a). A high-speed mechanical drive system in the facility imparts controlled oscillations to all blades composing the annular blade row at a constant blade oscillatory amplitude and arbitrary interblade phase angles. Utilizing this facility, unsteady aerodynamic forces were measured at blade oscillatory frequencies up to 350 Hz, which correspond to actual reduced frequencies in turbomachinery (Kobayashi, 1984, 1986b).

In our previous flutter experiment for evaluation of unsteady aerodynamic torsional moments acting on an oscillating blade of fan DCA cambered blade row, the unsteady aerodynamic pressure chordwise distribution was measured at 18 pressure measuring points on blade suction and pressure surfaces, and then the possibility of unstalled flutter of the fan blade row was examined. From this study, valuable information relative to flutter phenomena was obtained (Kobayashi, 1986b). However, it is believed that more precise data relative to unsteady aerodynamic forces generated by shock wave movement due

Contributed by the International Gas Turbine Institute and presented at the 34th International Gas Turbine and Aeroengine Congress and Exhibition, Toronto, Ontario, Canada, June 4–8, 1989. Manuscript received at ASME Headquarters February 14, 1989. Paper no. 89-GT-297.

to blade oscillation is necessary to more accurately understand the cascade flutter phenomena and to evaluate the flutter boundary.

Therefore, 13 pressure measuring points were aligned at intervals of 2 mm in the chordwise direction on the blade surface region influenced by shock waves, so that unsteady aerodynamic forces generated by shock waves could be precisely measured. Significant unsteady aerodynamic forces were generated by shock wave motion, due to blade oscillation, which greatly affected the occurrence of fan blade flutter as well as that of turbine cascades (Kobayashi, 1984; 1986b). The nature of shock wave effects for both turbine and fan blade rows were reported by the author (Kobayashi, 1988). These additional data were combined with the previously measured data of chordwise distribution of unsteady aerodynamic pressures on blade surfaces, and then the nature of low back-pressure unstalled torsional fan blade flutter was examined.

Our experiments covered a range of reduced frequency based on the semichord from 0.0375 to 0.547, five inlet flow Mach numbers from 0.732 to 1.130, and six interblade phase angles. The occurrence of low back-pressure unstalled torsional fan blade flutter was clarified in relation to such parameters as interblade phase angle, reduced frequency and inlet flow velocity. The role of unsteady aerodynamic blade surface forces on flutter occurrence and the range of interblade phase angles for which flutter occurred also were clarified.

Test Facility and Airfoil

Figures 1 and 2 show a section of the annular cascade test facility where an inlet guide vane (IGV), a test fan blade row, and a high-speed mechanical drive system are installed. Annular blade rows with a fairly high hub/tip ratio were chosen in order to exclude endwall effects, which occur in linear cascades, and to obtain an approximately two-dimensional flow for compatibility with theoretical investigations. The blade height is 25 mm and the hub/tip ratio is 0.844. Freon gas (Freon 11) was used as a working fluid in this facility to obtain highly reduced frequencies in a transonic flow.

The high-speed mechanical drive system was developed for established controllable oscillation of the 16 blades composing the test annular cascade and for making meaningful measurements of unsteady aerodynamic forces acting on oscillating

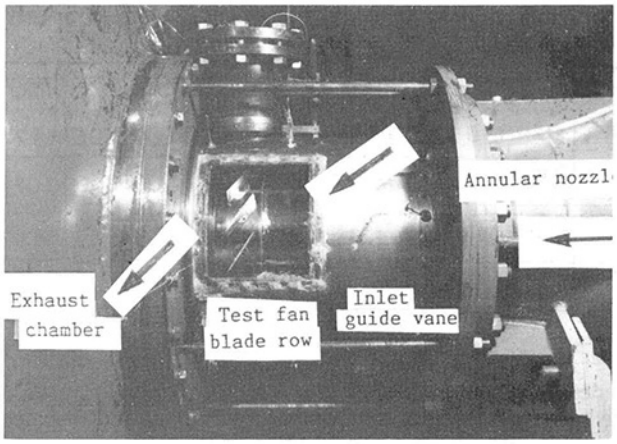

Fig. 1 View of test section of annular cascade test facility

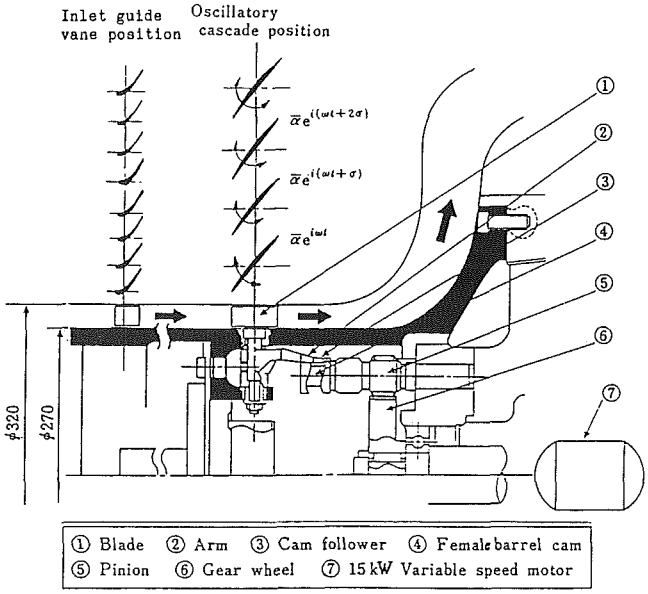

Fig. 2 Test section of annular cascade test facility and high-speed mechanical drive system

Nomenclature

a = coordinate of blade torsional axis, which exists at 50 percent of chord
A = amplitude of unsteady aerodynamic force; 1/rad, defined by equation (5)
b = blade span length, mm
C = chord length, mm
C_{mt} = unsteady aerodynamic moment coefficient, positive sign in blade nose-up; 1/rad, defined by equation (3)
ΔE = local unsteady aerodynamic energy per cycle of blade oscillation; 1/rad, defined by equation (4)
f = airfoil oscillating frequency, Hz
i = incidence angle, deg
K = reduced frequency, $k = C\omega/2U_1$
M_1 = inlet flow Mach number
ΔP_{ai} = unsteady aerodynamic pressure acting on blade surface
ΔP_t = unsteady aerodynamic pressure due to shock wave movement
ΔP_s = static pressure rise on blade surface due to shock wave
Re = Reynolds number $= CU_1/\nu$
t = time, s
U_1 = inlet flow velocity, m/s
X/C = coordinate along chord of airfoil, measured from leading edge
α_1 = airfoil oscillating amplitude, rad
ν = kinetic viscosity, m^2
ρ = density of Freon gas, kg/m^3
σ = interblade phase angle, deg
ϕ = phase lead of unsteady pressure or signals toward airfoil motion
ω = airfoil oscillating angular frequency Hz

Subscripts

1 = inlet of cascade
2 = outlet of cascade
+ = suction side of blade
− = pressure side of blade

Table 1 Oscillatory amplitude and interblade phase angle of all 16 oscillating blades

Amp. & Phase \ Frequency Hz		25	50	75	100	125	150	175	200
Amplitude [°]	Mean	0.97	0.99	1.02	1.04	1.03	1.07	1.06	1.12
	Standard Deviation	0.04	0.05	0.06	0.08	0.08	0.08	0.10	0.07
Interblade phase angle [°]	Mean	67.5	64.3	66.8	67.1	68.0	67.6	67.7	68.0
	Standard Deviation	5.52	5.36	5.89	6.84	6.41	6.36	6.20	6.23

blades under both stable and unstable cascade conditions. The drive system consists of cam follower assemblies, female barrel cams, pinions, a gear and a 15 kW motor.

Each airfoil is cantilevered radially from a rigid hub by a trunnion, which is attached to one of the cam follower assemblies. Each trunnion is inserted through the hub casing wall and is supported on two bearings. The cam follower assembly consists of a connecting arm and a button follower. It couples with a female barrel cam and a pinion. The closed-coupled connecting arm and button follower transmit 3 cycles of oscillating harmonic motion to the airfoil for each revolution of the cam. Sixteen of the female barrel cam and pinion assemblies are aligned on the inside circle of the hub and are rotated by the 15 kW variable speed motor through the common gear.

Amplitude control is achieved by the cam groove design. The torsional amplitude of the blade motion is 1.0 deg and is maintained constant up to a frequency of 500 Hz. Any desired interblade phase angle of $2n\Pi/16$ can be set by adjusting a spline combining the cam with the pinion. The blade oscillatory frequency is changed by altering the rotational speed of the motor. In order to directly visualize the air flow around the cascade, the compact drive system was designed to fit inside the massive hub. The test section was provided with a window to allow observation of the air flow by various optical measuring devices.

At a higher frequency than 450 Hz, the vertex of the airfoil displacement signal was not smooth, due to the impact of the ditch of the female barrel cam with the button follower. However, this signal distortion did not affect the harmonic oscillation of a blade. Spectral analysis of the blade oscillatory displacement signals showed that the mechanical drive system produced a torsional oscillating amplitude of 1.0 deg containing the second and third harmonic components 20 dB lower even at the maximum frequency of 500 Hz.

As an example of blade oscillation, Table 1 shows mean values and standard deviations of oscillatory amplitude and interblade phase angle for blade oscillatory frequencies from 25 Hz to 200 Hz, at a nominal interblade phase angle of 67.5 deg. This table indicates that a small variation of these values with blade oscillatory frequency does exist. These values were almost constant at frequencies from 200 to 350 Hz. The blade oscillation results proved that the drive system could provide approximately uniform distributions of amplitude and interblade phase angle of the test blade row and, therefore, the system was considered to be suitable for carrying out flutter experiments.

A detailed explanation of the annular cascade test facility and the high-speed mechanical drive system is given by Kobayashi (1986a).

Axial flow was steadily accelerated over inlet guide vanes installed at a distance of 5 vane chords upstream of the test cascade. They acted as supersonic nozzles accelerating and turning the flow onto the fan blades. The IGV wakes passed between these blades. The airfoil of the fan cascade was a cambered double circular arc airfoil with its torsional axis at 50 percent of the chord. Chord length and stagger angle of the cascade were constant in the radial direction. Details of the steady and unsteady experimental conditions are listed in Table 2.

Table 2 Steady and unsteady cascade data

Working Fluid	Freon 11 CCl_3F	
Overall Dimensions		
Tip Diameter	320 mm	Hub Diameter 270 mm
Hub/Tip ratio	0.844	Annular height 25 mm
Inlet Guide Vanes (IGV)		
Number of blades	32	
Spacing at mean diameter	29 mm	
True chord	45 mm	
Stagger angle	45°40″	
Air outlet angle	60°50″	
Test Compressor cascade		
Number of blades	16	
Spacing at mean diameter	58 mm	
Chord length	72 mm	
Space/chord ratio	0.873(Tip), 0.804(Mid), 0.736(Hub)	
Stagger angle	58°	
Thickness	4 %	
Blade inlet angle	61°	
Blade outlet angle	55°	
Type	Doble-circular arc (Camber angle 6°)	
Reynolds number	$2.05*10^6$ - $3.3*10^6$	
Unstable Data		
Frequency (in experiment)	0 - 350 Hz	
Reduced frequency based on half chord	0.0375 - 0.547	
Torsional axis	mid chord	
Interblade phase angle	+135.0°, +90.0°, +67.5°, 0.0°, -67.5°, -157.5°	

Measurement and Data Reduction

As the first step for flutter experiments, the steady flow characteristics of the fan cascade were examined. The steady flow upstream and downstream of the test cascade and on the blade surfaces was quantified using a large number of static pressure taps positioned on the inner and outer walls of the test section and on the blade surfaces. The taps were connected to a scanivalve system containing two 48-channel units scanning in parallel and recorded through a data acquisition/control unit on a dedicated minicomputer.

Periodicity of the flow upstream and downstream of the test cascade was evaluated by the circumferential distribution of static pressure on the wall. Two traversing five-hole cobra probes were installed upstream and downstream of the cascade for measuring radial distributions of inlet and outlet flows.

Measurement of time-dependent data includes the airfoil oscillatory displacement and time-variant pressures on the oscillating airfoil surface. Motion of an instrumented airfoil was measured with an eddy-current-type displacement sensor directed toward a small rod fixed on the airfoil tip section. Time-variant pressures were measured by two methods, as shown in Fig. 3. One was an indirect pressure measurement, in which a miniature pressure transducer was mounted by means of a short vinyl tube on the end of a probe tube embedded in the airfoil, for measuring both static and time-variant pressures on the airfoil surface. The other was a direct pressure measurement with a pressure transducer embedded in an airfoil.

Unsteady aerodynamic torsional moments acting on an oscillating airfoil were calculated, using chordwise distributions of the unsteady airfoil surface pressure acting on both suction and pressure surfaces of the oscillating blade, which included precise data of unsteady aerodynamic pressures generated by shock wave movement due to blade oscillation. For this purpose, two special instrumented airfoils were prepared. One was

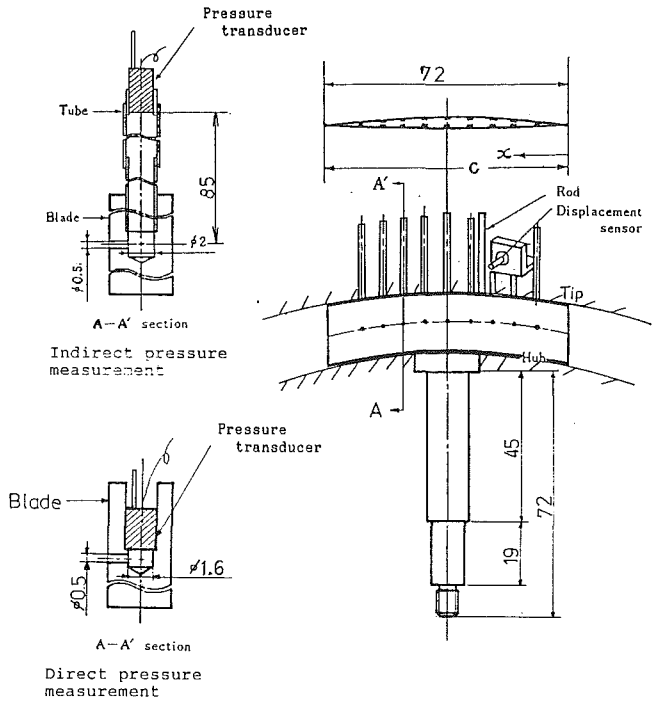

Fig. 3 Instrumented fan airfoil

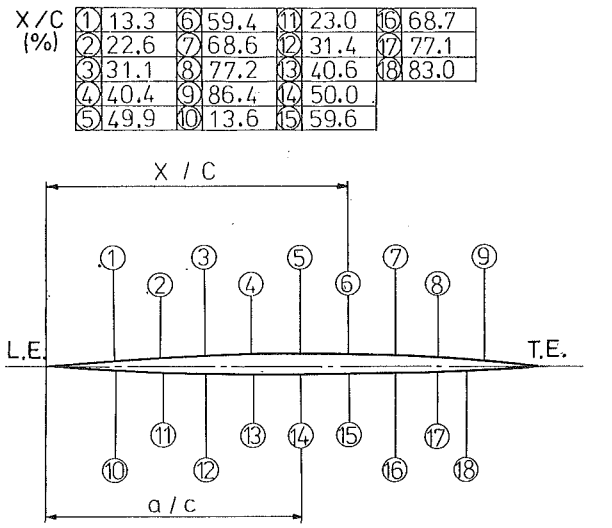

(*a*) Instrumented airfoil for measuring chordwise pressure distribution

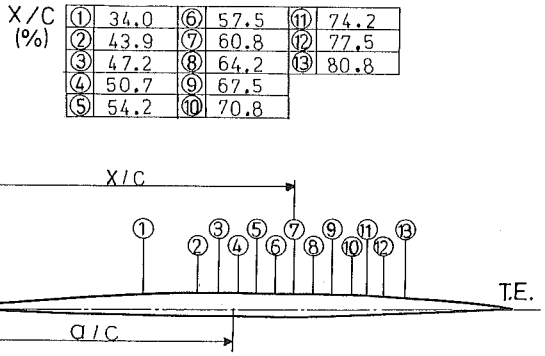

(*b*) Instrumented airfoil for measuring effects of shock wave movement

Fig. 4 Time-variant pressure measuring points on blade surface

an instrumented airfoil on whose suction and pressure surfaces 18 pressure measuring points were set, as shown in Fig. 4(*a*). The other was a special instrumented airfoil on whose surface region influenced by shock wave movement 13 pressure measuring points were aligned at intervals of 3 percent chord length (2-mm intervals) in the chordwise direction, as shown in Fig. 4 (*b*). For the airfoil in Fig. 4(*a*), probe tubes of three different inner diameters from 0.7 to 2.0 mm were used. For the airfoil in Fig. 4(*b*), probe tubes of inner diameter 1.0 mm were used. For the measurement, both the indirect and direct measurement techniques were used.

For the indirect pressure measurement, frequency response characteristics of the probe tube-pressure transducer system have to be known, in advance, for correction of the measured time-variant pressure (amplitude and phase lead). The factors having an influence on frequency response of the system are the frequency of unsteady pressure, the size of coupling of the probe tube and vinyl tube, the state of the Freon gas (temperature and static pressure), and the grazing velocity of the blade surface flow at the opening of the probe tube.

The response function (A_s, ϕ_s) of the probe tube system was determined, using two different methods. One method used a flush-mounted pressure transducer and the probe tube system faced to the flow including the controlled fluctuating pressure, with a specially designed apparatus described by Kobayashi (1986a). The second method used an oscillatory airfoil in the flow to collect frequency response data of the same probe tube system. In this second method, signals from two pressure transducers were compared. The first transducer was a probe tube pressure transducer system fixed on an oscillating airfoil in the flow, the second transducers was a miniature pressure transducer embedded in the same location of the oscillating airfoil section. The two sets of response data for the same probe tube system acquired by the two different methods resulted in a very good agreement.

An example of the frequency response of the probe tube system with a probe tube inner diameter of 1.0 mm is illustrated in Fig. 5. The figure indicates that the frequency response of the probe tube system is strongly influenced by the grazing flow velocity, as well as the frequency of the fluctuating pressure. As shown in the figure, increasing the grazing flow velocity or frequency of the fluctuating pressure results in a decreased amplitude response and increased phase lag. The measured time-dependent pressure, namely, the amplitude A_o and phase lead ϕ_0 have to be corrected using the frequency responses of the probe tube system (A_s, ϕ_s), the electronic data acquisition system including a d-c amplifier (A_d, ϕ_d) and a data recorder (A_r, ϕ_r). Finally, the unsteady aerodynamic pressure amplitude A_p and phase lead ϕ_p can be obtained using equations (1) and (2).

$$A_p = A_0/(A_s * A_r * A_d) \tag{1}$$

$$\phi_p = \phi_0 + \phi_s + \phi_r + \phi_d \tag{2}$$

Quantities calculated from the airfoil surface pressure data are:

(*i*) Unsteady aerodynamic torsional moment coefficient, C_{mt}

$$C_{mt} = \frac{1}{\frac{1}{2}\rho\, U_1^2\, C^2 \alpha_1} \int_0^1 \{\Delta P_{ai}^- * (a - x_i^-) - \Delta P_{ai}^+ * (a - x_i^+)\}\, dx \tag{3}$$

(*ii*) Local unsteady aerodynamic energy ΔE acting on a small portion of the oscillating blade surface

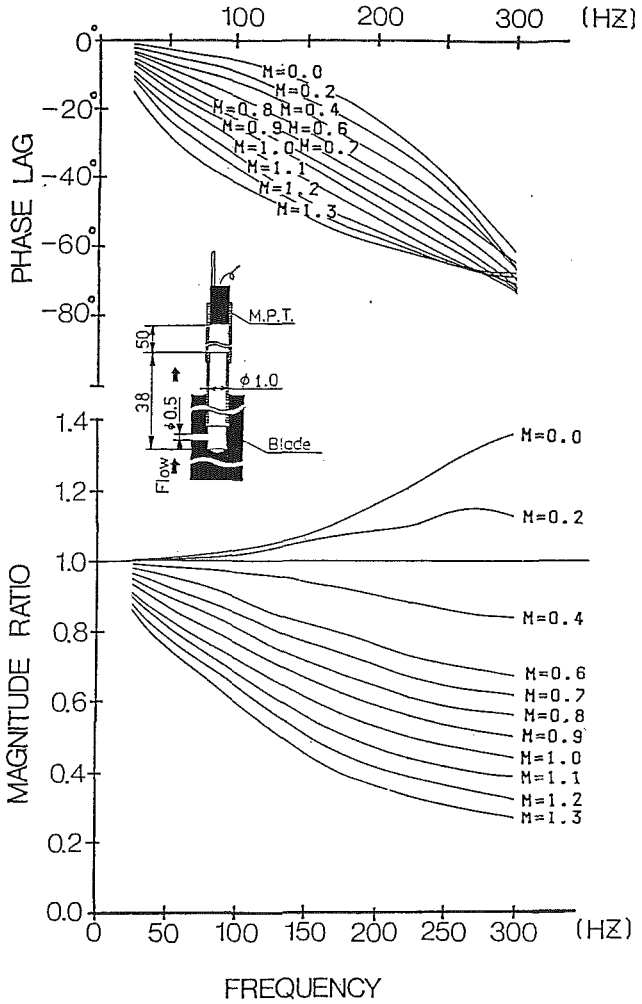

Fig. 5 Frequency response property of probe tube pressure measuring system

$$\Delta E = \Delta P_{ai} * (a - x_i) \bullet \sin\phi_i / \left(\frac{1}{2}\rho\, U_1^2\, C\, \alpha_1\right) \tag{4}$$

(*iii*) Unsteady aerodynamic force amplitude per unit surface area

$$A \equiv \Delta P_{ai} / \left(\frac{1}{2}\rho\, U_1^2\, \alpha_1\right) \tag{5}$$

In this report, it is considered that cascade torsional flutter occurs when the phase lead of the unsteady aerodynamic torsional moment ranges between 0 and 180 deg, which corresponds to a positive value of the imaginary part of the unsteady aerodynamic torsional moment. A positive value of local aerodynamic energy means that the unsteady aerodynamic force, acting on a small portion of the blade surface, stimulates blade oscillation.

Experimental Results

Experimental Region. Tests were carried out for the five inlet Mach numbers 0.732, 0.831, 0.945, 1.073 and 1.130. Each inlet flow condition corresponds to static pressure ratios P_{s_2}/P_{s_1} of 1.045, 1.069, 1.142, 1.112 and 1.052, respectively. The static pressure P_{s_2} is a one-pitch mean value of static pressures downstream of the cascade, while static pressure P_{s_1} is that upstream of the cascade. For each inlet flow, combinations of reduced frequency (blade oscillatory frequency) and interblade phase angle were selected and then the unsteady aerodynamic

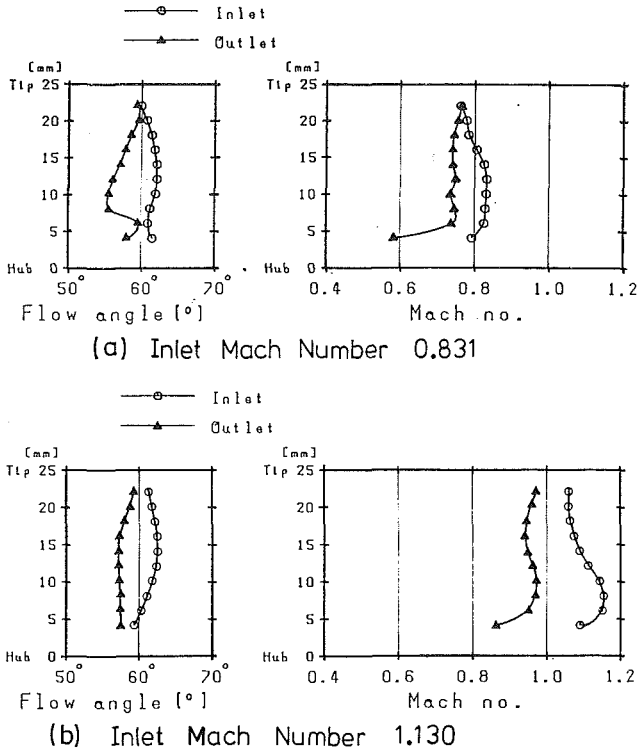

Fig. 6 Radial distribution of inlet and outlet flows

forces, acting on an oscillating airfoil, were measured. The reduced frequency based on the semichord, ranged from 0.0375 to 0.547 and the tested interblade phase angles were +67.5 deg, + 90 deg, + 135 deg, 0.0 deg, −67.5 deg, and −157.5 deg. The experimental Reynolds number based on chord length was in the range from $2.05 * 10^6$ to $3.3 * 10^6$.

Steady Flow Characteristics of Fan DCA Cascade. Figure 6 shows, as an example, radial distributions of flow angle and Mach number for two inlet Mach numbers. The deviations in inlet flow Mach number and flow angle are relatively small around a midspan region where unsteady aerodynamic pressures were measured. Wall static pressures upstream of the cascade showed a good periodicity in the circumferential direction. Chordwise distributions of local velocity on the blade suction and pressure surfaces are shown for five inlet flow Mach numbers in Fig. 7. For the cases of inlet flow Mach number of 0.945, 1.073, and 1.130, a supersonic flow region appears on the suction surface of blades. A prominent change of flow velocity attributable to a normal shock is observed near 65 percent of the chord.

Unsteady Aerodynamic Characteristics of Fan DCA Cascade. 240 tests for investigating the unstalled torsional flutter characteristics of the fan DCA cascade were carried out in combination with flow velocity, interblade phase angle, and reduced frequency. For each test, chordwise distributions of unsteady aerodynamic pressures acting on an oscillating blade were measured including unsteady aerodynamic pressures generated by shock wave movement. Then, unsteady aerodynamic torsional moments were calculated with these data.

Effect of Interblade Phase Angle on Aerodynamic Instability of Cascade. Variations of the imaginary part of the unsteady aerodynamic torsional moment with interblade phase angle are shown in Fig. 8 for three reduced frequencies at an inlet Mach number of 1.130. Unstalled cascade flutter can occur when the imaginary part of the unsteady aerodynamic torsional moment is positive and the blade has no mechanical damping. As shown, the interblade phase angle strongly influences imaginary part

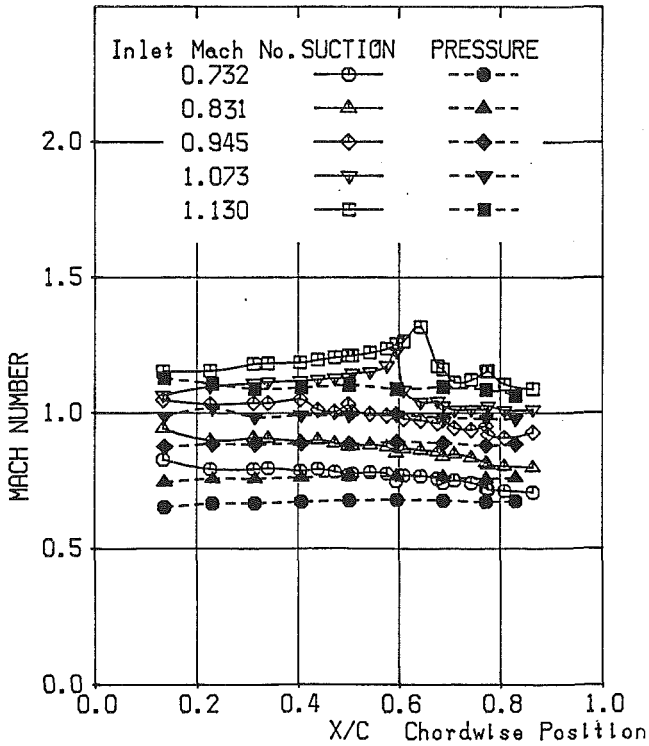

Fig. 7 Chordwise velocity distribution on blade surface at midspan position

values, particularly flutter occurrence. Its value is positive between 40 and 160 deg, while around 280 deg its value is highly negative. Therefore, unstalled torsional cascade flutter can occur within the interblade phase angle range of 40 to 160 deg. An interblade phase angle of 90 deg produces the most unstable condition of the cascade, while 280 deg generates the most stable condition. For flows from subsonic to supersonic in our experiment, the variation of unsteady aerodynamic torsional moments with interblade phase angle was similar to that of Fig. 8.

Effect of Reduced Frequency on Aerodynamic Instability of Cascade. When the reduced frequency was increased while maintaining the inlet Mach number and interblade phase angle constant, the imaginary part of the unsteady aerodynamic torsional moment changed from positive values to negative values in most experimental cases, as shown in Fig. 9. It indicates that an increase in reduced frequency damps blade oscillation. This tendency was the same in cases of other inlet flow Mach numbers and interblade phase angles.

As an example, variation of the imaginary part of aerodynamic moment with reduced frequency at an interblade phase angle 90 deg is shown in Fig. 9 for two inlet Mach numbers. The moments change from a positive value to a negative one according to the increase in reduced frequency. In the figure, the moments of Case ① were obtained from calculation containing both the precise pressure data due to shock wave movement and the unsteady aerodynamic pressure chordwise distribution, while the moments of Case ② were obtained from the unsteady aerodynamic pressure data measured only by the instrumented airfoil shown in Fig. 4(*a*). The figure indicates that reduced frequency of the flutter boundary in Case ① is lower than that of Case ② for the same inlet flow Mach number and interblade phase angle.

Occurrence of Unstalled Cascade Torsional Flutter. The occurrence of unstalled cascade torsional flutter is plotted on a map of reduced frequency versus inlet Mach number for the

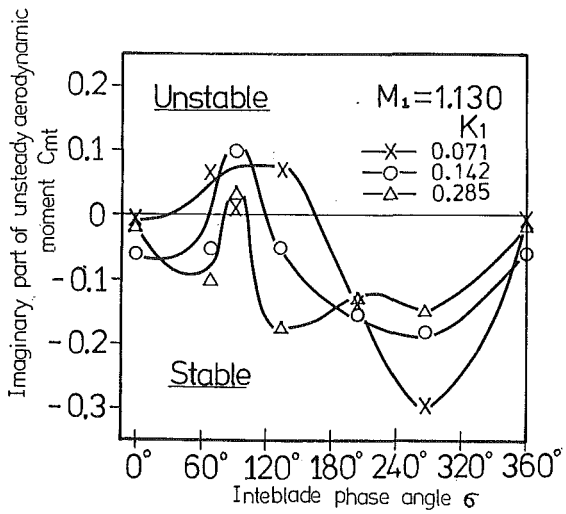

Fig. 8 Variation of unsteady aerodynamic moment with interblade phase angle

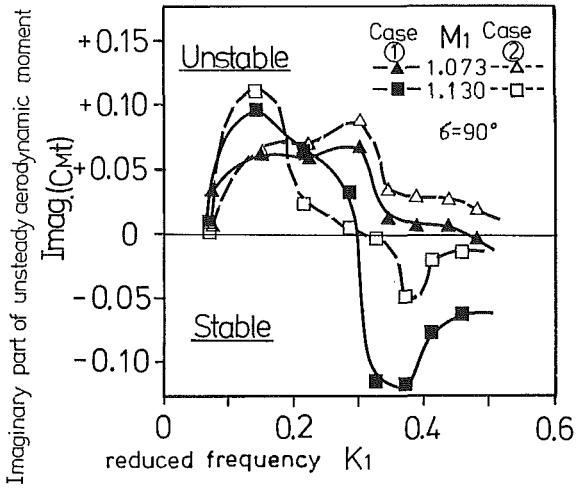

Fig. 9 Variation of unsteady aerodynamic moment with reduced frequency

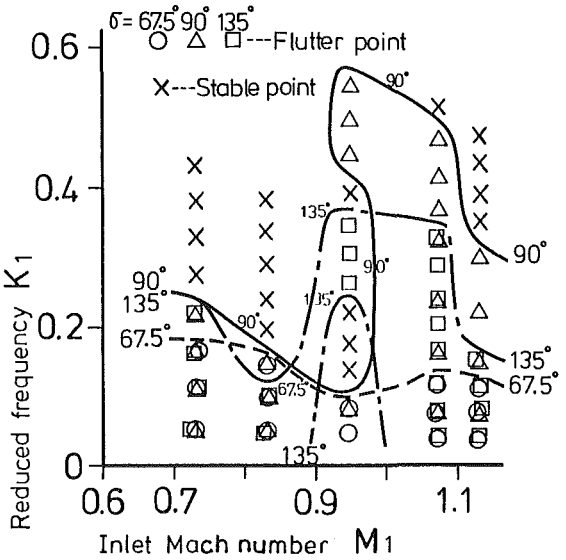

Fig. 10 Occurrence of unstalled torsional cascade flutter

interblade phase angle, as shown in Fig. 10. In our experiment flutter occurred at interblade phase angles of 67.5, 90, and 135 deg. Flutter occurrence points correspond to a positive

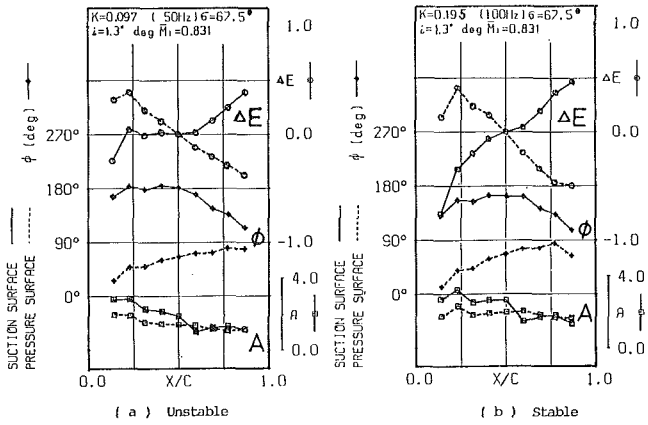

Fig. 11 Chordwise distribution of unsteady aerodynamic pressure for subsonic inlet flow

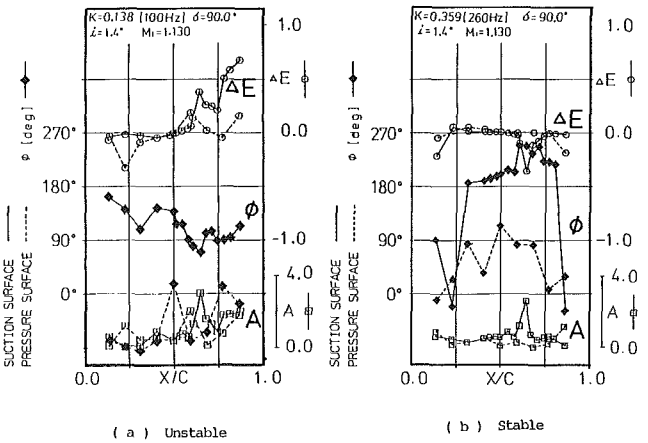

Fig. 12 Chordwise distribution of unsteady aerodynamic pressure for supersonic inlet flow

imaginary part of the unsteady aerodynamic torsional moment. It is clear that unstalled cascade flutter occurred over a wide range of inlet flow Mach numbers ranging from high subsonic to supersonic, and that the reduced frequency of the flutter boundary increased greatly at an inlet Mach number higher than 0.945.

For subsonic inlet Mach numbers of 0.732 and 0.831, the reduced frequency of flutter boundary decreased according to the increase in inlet Mach number. This decrease is considered to be due to effects of flow compressibility on flutter. For higher inlet flow Mach numbers 0.945 and 1.073, where flows on the suction surface of the blade were transonic or supersonic, the flutter reduced frequency strongly increased to about three times that for subsonic flow cases. The maximum value of flutter reduced frequency in our experiments reached a value of 0.547 at an interblade phase angle of 90 deg.

Conversely, with an increase in inlet flow Mach number from 1.073 to 1.130, the reduced frequency of the flutter boundary significantly decreased, in the cases where the flow on both the suction and pressure surfaces of blade were supersonic.

Behavior of Chordwise Unsteady Aerodynamic Forces for Flutter. From examination of data of the unsteady aerodynamic pressure chordwise distribution, the following common phenomena can be emphasized. For flows from subsonic to supersonic, in general, unsteady aerodynamic forces acting on the suction surface upstream of the torsional axis cause positive aerodynamic damping, but forces downstream of the axis cause negative aerodynamic damping. On the pressure surface, unsteady aerodynamic forces upstream of the torsional axis cause negative aerodyamic damping, but forces downstream of the axis cause positive aerodynamic damping. These phenomena were influenced by reduced frequency, interblade phase angle and inlet flow velocity by a small amount only.

Variation of Unsteady Aerodynamic Force Effects With Reduced Frequency. Chordwise distributions of unsteady aerodynamic forces, namely, amplitude and phase lag, and the local unsteady aerodynamic energy on the suction and pressure surfaces are shown, as an example of experimental results, in Figs. 11 (*a*, *b*) for a subsonic inlet flow and in Figs. 12 (*a*, *b*) for a supersonic inlet flow. Figures (*a*) are for aerodynamically unstable cases, while figures (*b*) are for stable cases. A positive value of the local unsteady aerodynamic energy means that the unsteady aerodynamic force acting on a small portion of the blade surface can stimulate blade oscillation.

For subsonic inlet flow, when the reduced frequency decreases while maintaining the other parameters constant, the effects of unsteady aerodynamic forces, acting on the suction surface, upstream of the torsional axis, changed from a positive aerodynamic damping (negative ΔE) into a negative aerodynamic damping, or a small positive aerodynamic damping. At the same time, unsteady aerodynamic forces acting on the pressure and suction surfaces downstream of the torsional axis changed little with the decrease in reduced frequency. Therefore, the value of the imaginary part of unsteady aerodyamic torsional moment changed from negative to positive, with decreasing reduced frequency. When the interblade phase angle or inlet velocity was changed while maintaining other parameters constant, unsteady aerodynamic forces acting on the suction surface upstream of torsional axis played the same important role on flutter occurrence.

For supersonic inlet flow, amplitudes of the unsteady aerodynamic forces acting on the suction surface of the blade were smaller than those for subsonic inlet flow, except for unsteady aerodynamic forces generated by shock waves. Therefore, values of the local unsteady aerodynamic energy also were smaller. Amplitudes of unsteady aerodynamic forces acting on the pressure surface were as large as those for subsonic inlet flow, though the amplitudes were dependent on the interblade phase angle. It is believed that cascade flutter was caused by the following three major phenomena, which accompany a decrease in the reduced frequency: a decrease in positive aerodynamic damping forces on the suction surface upstream of the torsional axis, a large increase in negative aerodynamic damping forces on the suction surface downstream of the axis, and an increase in negative aerodynamic damping forces on the pressure surface upstream of the axis.

Variation of Unsteady Aerodynamic Forces With Increasing Inlet Flow Velocity. Variation of the unsteady aerodynamic forces on the blade suction surface with an increase in the inlet flow velocity are illustrated in Figs. 13 and 14 for two interblade phase angles. Each figure shows three chordwise distribution curves of the aerodynamic energy for inlet flows from subsonic to supersonic.

Increasing the inlet flow velocity from high subsonic to supersonic flow while maintaining reduced frequency almost constant destabilized the cascade. The following two phenomena were considered as causes for this: One was a very large decrease in positive aerodynamic damping forces acting on the suction surface upstream of the torsional axis. The other was an increase in negative aerodynamic damping forces acting on the suction surface downstream of the axis. The tendency of aerodynamic destabilization of the cascade with increasing inlet flow velocity did not change when other reduced frequencies or interblade phase angles were selected.

Variation of Unsteady Aerodynamic Forces With Interblade

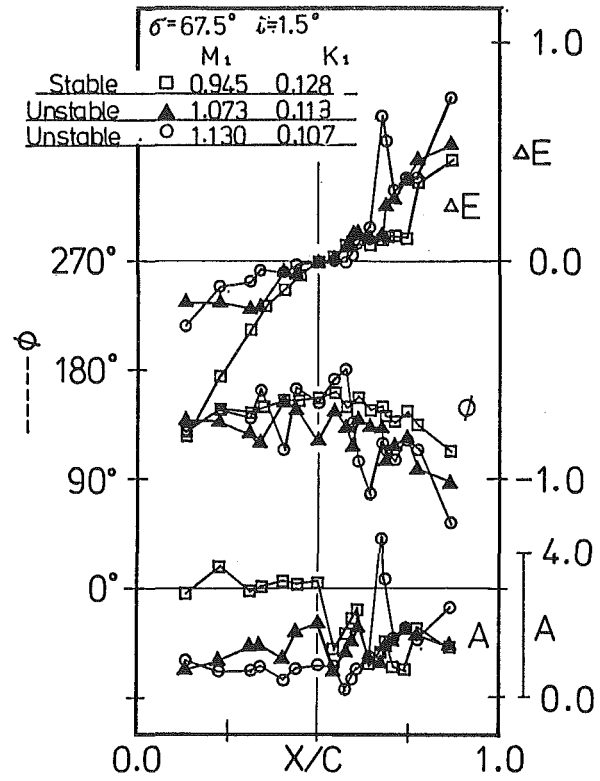

Fig. 13 Variation of unsteady aerodynamic forces with inlet flow velocity at interblade phase angle of 67.5 deg

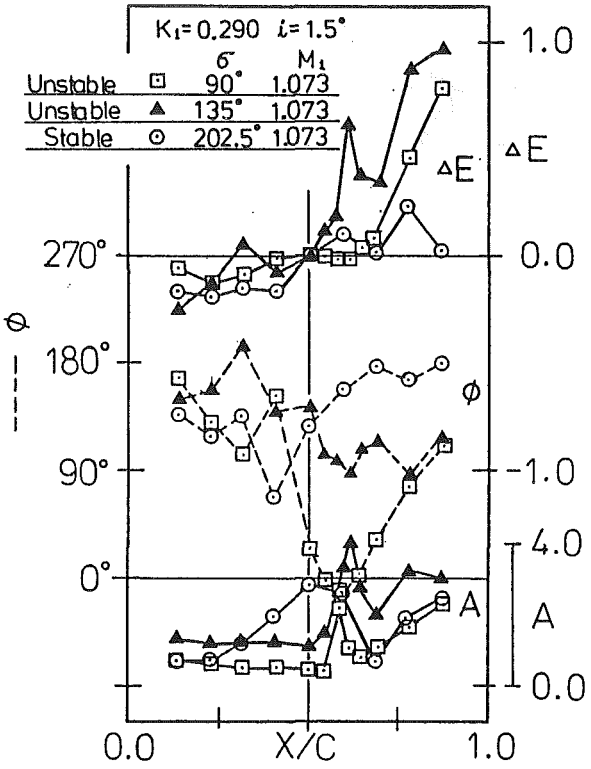

(a) On suction surface

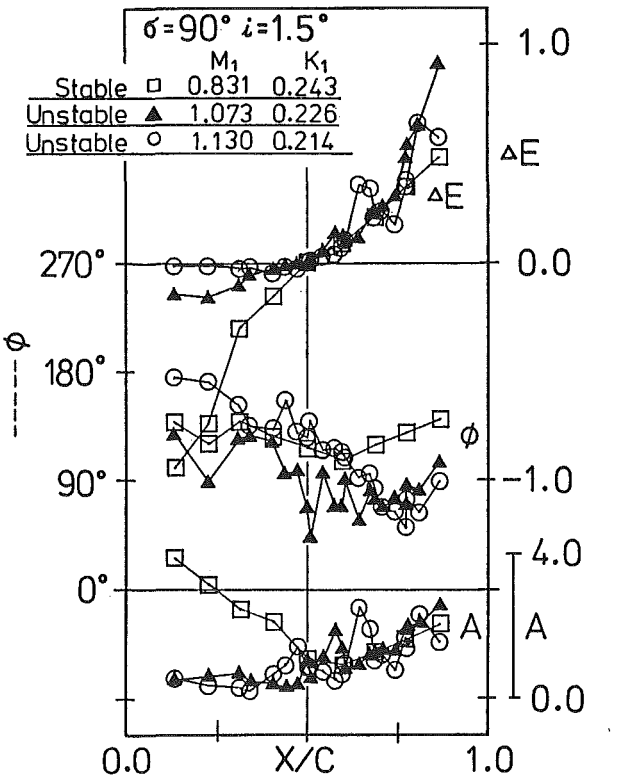

Fig. 14 Variation of unsteady aerodynamic force distribution with inlet flow velocity at interblade phase angle of 90 deg

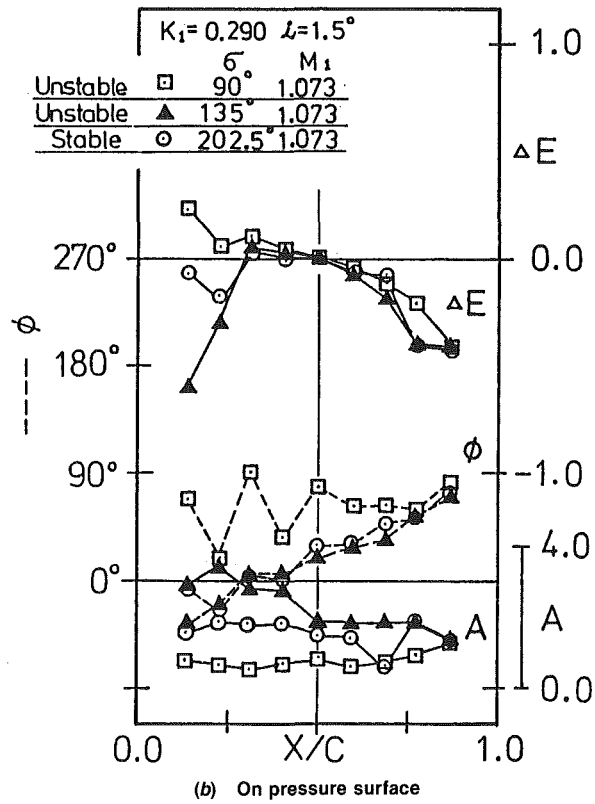

(b) On pressure surface

Fig. 15 Variation of unsteady aerodynamic forces with interblade phase angle

Phase Angle. For subsonic inlet flow, when the interblade phase angle changed, aerodynamic instability of the cascade was caused by a decrease in positive aerodynamic damping on the suction surface and an increase in negative aerodynamic damping on the pressure surface upstream of the torsional axis.

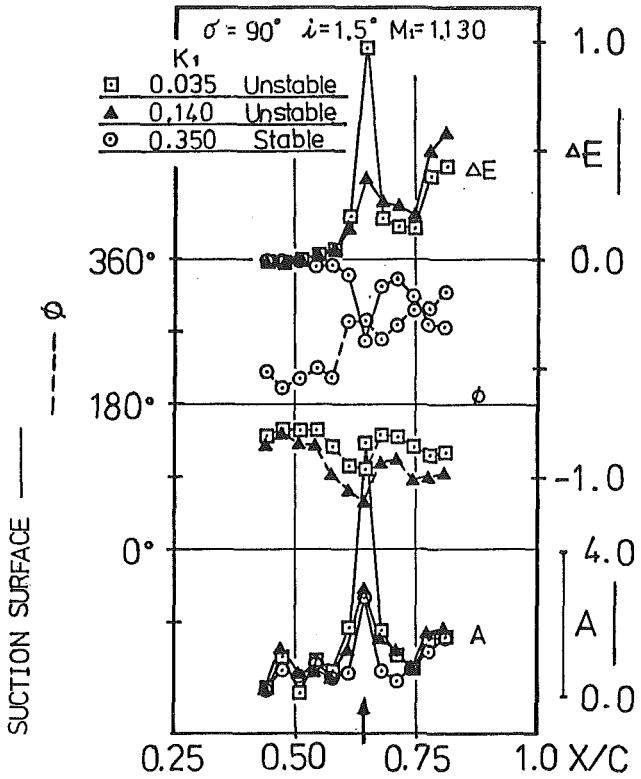

Fig. 16 Unsteady aerodynamic force generated by shock wave movement at interblade phase angle of 90 deg

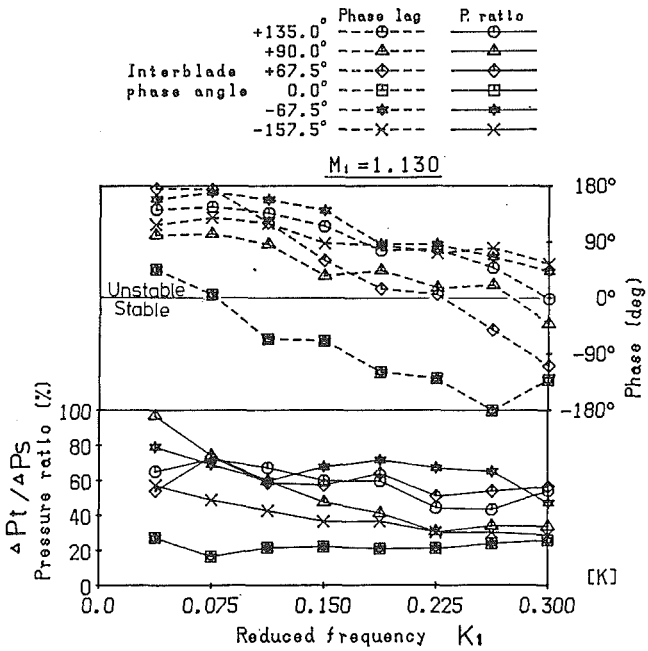

Fig. 17 Variation of shock wave effects with reduced frequency

As an example, for supersonic inlet flow, variations of the unsteady aerodynamic forces on both the suction and pressure blade surfaces for three interblade phase angles are shown in Figs. 15 (*a*, *b*). For interblade phase angles of 135 and 90 deg, the cascade was aerodynamically unstable, while for an interblade phase angle of 202.5 deg, the cascade was aerodynamically stable.

For supersonic inlet flow, when the interblade phase angle changed, cascade flutter occurred. For interblade phase angles of 90 and 135 deg, the positive aerodynamic damping forces on the suction surface, upstream of the torsional axis, were smaller than ones for an interblade phase angle of 202.5 deg. In addition, for $\sigma = 90$ and 135 deg, the negative aerodynamic damping forces on the suction surface downstream of the torsional axis were markedly bigger than those for $\sigma = 202.5$ deg. Therefore, as a whole, the unsteady aerodynamic forces acting on the suction surface acted as a blade motion exciter. The aerodynamic damping forces on the pressure surface upstream of the axis changed from positive values to negative values when interblade phase angle changed from 202.5 to 90 deg. Therefore, the effects of unsteady aerodynamic forces on the whole pressure surface approached being a small blade motion exciter. As a result of these phenomena, cascade flutter occurred at interblade phase angles of 90 and 135 deg.

Effects of Shock Wave Movement Due to Blade Oscillation on Aerodynamic Instability. For higher subsonic and supersonic inlet flow velocities, a normal shock wave occurred at a position between 55 and 65 percent of the chord on the suction surface of the blade. The shock wave moved on the blade surface due to blade oscillation, so that very large unsteady aerodynamic forces were generated on the suction surface, as indicated by the arrow in Fig. 16. With an increase in the reduced frequency, the amplitude of the force decreased and its effect changed. For two reduced frequencies of 0.035 and 0.140, where the cascade was aerodynamically unstable, the forces produced negative aerodynamic damping and promoted instability of blade oscillation. In contrast, for a reduced frequency of 0.350, the forces produced positive aerodynamic damping. The chordwise region of the blade suction surface influenced by the shock wave movement was estimated to be about 6 percent of the chord length.

Variation of the unsteady aerodynamic forces generated by the shock waves with reduced frequency are shown in Fig. 17 for six interblade phase angles. The pressure ratio $\Delta P_t/\Delta P_s$ is the ratio of the unsteady aerodynamic force ΔP_t generated by the shock wave to the static pressure rise ΔP_s across the same shock wave on the blade suction surface. Amplitudes of the ratio $\Delta P_t/\Delta P_s$ were in a range from 60 to 95 percent at comparatively low reduced frequency ($K_1 = 0.04$), depending on the interblade phase angle. The pressure ratio amplitude at an interblade phase angle of 0 deg is about 20 percent and is much smaller than those for the other interblade phase angles. With an increase in reduced frequency, the amplitude of pressure ratio decreases and also the phase lead of the pressure ratio changes from a large positive value to a small positive or a negative value. This means that the effects of unsteady aerodynamic forces generated by the shock waves, due to blade oscillation, changed from a blade motion stimulator to a blade motion damper and their magnitude decreased with an increase in reduced frequency.

These experimental results obtained in our experiment were similar to ones obtained in a single airfoil oscillation test made by Tijdeman (1977, 1980) and Shiratori (1983). It is suggested that, with an increase in blade oscillatory frequency, the displacement amplitude of the shock wave became smaller and also the phase lag between the shock wave displacement and the blade oscillatory displacement increased, so that the unsteady aerodynamic forces generated by the shock wave weakened and their effects changed from negative aerodynamic damping to positive damping.

Conclusions

In a series of studies on the unsteady aerodynamic characteristics of DCA fan cascade, low back-pressure supersonic unstalled fan blade flutter in the torsional mode has been examined. For this study, a Freon gas annular cascade test facility was utilized, which has a high-speed mechanical drive system providing controlled oscillation of all the blade com-

posing a blade row in the torsional mode. For measuring the unsteady aerodynamic pressures, acting on an oscillating blade, both direct and indirect pressure measuring techniques were developed. With this facility and measuring techniques, unsteady aerodynamic forces generated by shock wave movement, due to blade oscillation and chordwise distributions of unsteady aerodynamic pressures, acting on an oscillating blade, were precisely measured. Combining these data, the nature of the cascade flutter was investigated.

Tests were carried out over a range of inlet Mach number M_1 from 0.732 to 1.130 and reduced frequency K_1 based on the semichord from 0.0375 to 0.547 for 6 interblade phase angles. The extent of flutter occurrence relative to reduced frequency, inlet flow velocity and interblade phase angle was clarified as well as the significance of the parameters affecting flutter. The role of unsteady aerodynamic forces acting on portions of blade surface on flutter occurrence was clarified including the effects of the forces generated by shock waves on the aerodynamic instability of the cascade.

The following conclusions can be made:

1 Low back-pressure unstalled torsional flutter occurred over a wide range of inlet flow velocities, reduced frequencies and interblade phase angles. For entirely subsonic flow fields, the reduced frequency of the flutter boundary decreased with increased inlet flow velocity. This decrease was considered to be due to effects of flow compressibility on flutter.

When flow on the suction surface became supersonic, the reduced frequency of the flutter boundary markedly increased to three times that for subsonic inlet flow, and the maximum reduced frequency reached 0.545 at an interblade phase angle of 90 deg. Conversely, the reduced frequency of the flutter boundary decreased markedly when the inlet flow Mach number increased from 1.073 to 1.130 where flows on the suction and pressure surfaces were supersonic.

2 The interblade phase angle of flutter occurrence ranged from 40 to 160 deg. The most aerodynamically unstable condition was observed at an interblade phase angle of 90 deg, while the most aerodynamically stable condition appeared at an interblade phase angle of 280 deg. These phenomena were not influenced by reduced frequencies or inlet velocities.

3 With an increase in reduced frequency, while maintaining the other parameters constant, the imaginary part of the unsteady aerodynamic torsional moment generally changed from a positive value to a negative value. Reduced frequencies of the flutter boundary obtained from calculation of the unsteady aerodynamic moment, using precise unsteady pressures due to shock wave movement, were lower than ones evaluated without them. For evaluation of the flutter boundary, the unsteady aerodynamic forces generated by shock wave motion were significant.

4 For subsonic flow, when the reduced frequency was decreased, while maintaining the other parameters constant, cascade flutter was caused by the following two major phenomena: change of the unsteady aerodynamic forces acting on the suction surface upstream of the torsional axis from positive aerodynamic damping into negative aerodynamic damping or a small positive aerodynamic damping, and no change of force effects on other portions of the blade surface.

5 For supersonic inlet flow, when the reduced frequency was decreased, while maintaining the other parameters constant, cascade flutter was caused by the following three major phenomena: a decrease in positive aerodynamic damping on the suction surface upstream of the torsional axis, an increase in negative aerodynamic damping on the suction surface downstream of the axis, and an increase in negative aerodynamic damping on the pressure surface upstream of the axis. When the interblade phase angle was changed, cascade flutter was caused by the same three phenomena. When the inlet flow velocity was increased, cascade flutter was caused by the decrease in positive damping upstream and the increase in negative damping downstream of the axis on the suction surface.

6 Very large unsteady aerodynamic forces were generated on the suction surface by the shock wave movement due to blade oscillation. The chordwise region of the blade suction surface influenced by the shock wave movement was estimated to be about 6 percent of the chord length. The amplitude of the force was in a range between 95 to 40 percent of the static pressure rise across the shock wave; this amplitude depended markedly on the interblade phase angle. With an increase in the reduced frequency, the amplitude of the force decreased and the effect changed from a blade motion stimulator to a blade motion damper.

Acknowledgments

The author is grateful to his many colleagues both in and outside NAL for giving valuable advice, and to Mr. Hideshi Oinuma and the many students for offering assistance during this experiment. The present study has been undertaken as a part of an advanced gas turbine project of the Industrial and Technology Agency, Ministry of International Trade and Industry, Japan.

References

Davies, M. R. D., and Bryanston-Cross, P. J., 1984, "Holographic Measurements and Theoretical Predictions of the Unsteady Flow in a Transonic Annular Cascade," ASME Paper No. 84-GT-174.

El-Aini, Y. M., Bankhead, H. R., and Meece, C. E., 1986, "Subsonic/Transonic Stall Flutter Investigation of an Advanced Low Pressure Compressor," ASME Paper No. 86-GT-90.

Fleeter, S., 1979, "Aeroelasticity Research for Turbomachine Applications," *Journal of Aircraft*, Vol. 16, No. 5, pp. 320–336.

Fransson, T., 1984, "Two-Dimensional and Quasi-Three-Dimensional Experimental Standard Configurations for Aeroelastic Investigations in Turbomachine Cascades," *Symposium Proceedings of Unsteady Aerodynamics of Turbomachines and Propellers*, Cambridge, United Kingdom, pp. 361–395.

Kirschner, A. M., and Fosco, B., 1980, "Control of Vibration in Aeroelastic Cascade Experiments," *Proceedings of IUTAM Symposium on Aeroelasticity in Turbomachines*, Lausanne, Switzerland.

Kobayashi, H., 1984, "Unsteady Aerodynamic Force Acting on Controlled-Oscillating Transonic Annular Cascade," *Symposium Proceedings of Unsteady Aerodynamics of Turbomachines and Propellers*, Cambridge, United Kingdom, pp. 343–360.

Kobayashi, H., 1986a, "Unsteady Aerodynamic Characteristics of Annular Cascade Oscillating in Transonic Flow, (1st Report) Measurement of Aerodynamic Damping With Freon Gas Controlled-Oscillated Annular Cascade Test Facility," *Bulletin of the Japanese Society Mechanical Engineers*, Vol. 29, No. 256, pp. 3303–3312.

Kobayashi, H., 1986b, "Unsteady Aerodynamic Characteristics of Annular Cascade Oscillating in Transonic Flow, (3rd Report) Low Back-Pressure Supersonic Compressor Blade Flutter," *Transaction of the Japanese Society Mechanical Engineers*, Vol. 52, No. 480, pp. 2920–2929.

Kobayashi, H., 1988, "Effect of Shock Wave Movement on Aerodynamic Instability of Annular Cascade Oscillating in Transonic Flow," ASME Paper No. 88-GT-187.

Riffel, R. E., and Fleeter, S., 1980, "The Experimental Modeling of Unstalled Supersonic Turbofan Flutter," AIAA Paper No. 80-045.

Riffel, R. E., and Rothrock, M. D., 1980, "Experimental Determination of Unsteady Blade Element Aerodynamics in Cascades," NASA CR-159831.

Shaw, L. M., et al., 1985, "Unsteady Pressure Measurements on a Biconvex Airfoil in a Transonic Oscillating Cascade," ASME Paper No. 85-GT-212.

Shiratori, T., and Tanida, Y., 1983, "Aerodynamic Characteristics of an Airfoil Oscillating in Transonic Flow Between Parallel Walls," presented at the Tokyo International Gas Turbine Congress, 83-GT-IGTC-85.

Szechenyi, E., et al., 1984, "A Straight Cascade Wind-Tunnel Study of Fan Blade Flutter in Started Supersonic Flow," *Symposium Proceedings of Unsteady Aerodynamics of Turbomachines and Propellers*, Cambridge, United Kingdom, pp. 447–458.

Tijdeman, H., 1977, "Investigations of the Transonic Flow Around Oscillating Airfoils," NLR-TR 77090 U.

Tijdeman, H., and Seebass, R., 1980, "Transonic Flow Past Oscillating Airfoils," *Ann. Rev. Fluid Mech.*, pp. 181–222.

Whitehead, D. S., et al., 1976, "An Experiment to Measure Moment Coefficients for Aerofoils Oscillating in Cascade," *Symposium of Aeroelasticity in Turbomachines*, Paris, France, pp. 123–134.

Blade Vibration With Nonlinear Tip Constraint: Model Development

L. F. Wagner
Westinghouse Electric Corporation,
Science and Technology Center,
Pittsburgh, PA 15235

J. H. Griffin
Professor,
Department of Mechanical Engineering,
Carnegie-Mellon University,
Pittsburgh, PA 15213-3890

Turbine blades having integrally machined tip shrouds, with associated gaps between adjacent shrouds, often exhibit unusual vibratory responses with significant differences between the amplitudes and frequencies of individual blades on the same stage. These differences result from unavoidable variations in the shroud gaps causing, for large enough excitation, nonlinear constraint at the blade tips which varies from blade to blade. This study shows that the blade stresses cannot be adequately represented by the type of single-degree-of-freedom models that are often used for dynamic impact studies, but require the participation of higher frequency beam-type modes. The extension of the resulting beam model to multi-degree-of-freedom systems will allow the study of the "gap mistuning" phenomenon for practical bladed disks.

1 Introduction

The manufacturers of both steam and gas turbines design blading having integrally machined shrouds at the blade tips. An illustration of a row of integrally shrouded airfoils is shown in Fig. 1. These shrouds serve to enclose the flow and increase the efficiency of the stage. Furthermore, integral shrouds mitigate or eliminate problems related to the blade-shroud connection, such as rivet creep or accelerated corrosion at the interface. Unlike continuous shroud designs, integral shrouds may not be coupled to the shrouds of adjacent blades, and during operation, centrifugal and thermal loading will tend to create gaps between adjacent shrouds. If the blades are twisted, the centrifugal loading will reduce the gap dimension due to blade untwist, and may even create friction interfaces if the gaps close (Bazan et al., 1986). However, many blades are not twisted and operate with significant gaps.

Recent experiences with aircraft turbomachinery using the integral shroud design have involved blade cracking during service. This problem has been attributed to excessive blade vibration. Test data indicates that some of the shrouds come into contact under rotating conditions and that this irregular tip constraint may induce a type of blade mistuning which significantly alters the dynamic response of the stage. It is conjectured that a severe mistuning due to different shroud gaps and the resulting shroud contact may be the reason for blade failures on some stages, while nominally identical stages do not fail.

Initial studies of the nonlinear vibration of shrouded blades with gaps would logically commence with the assumption that all shroud gaps are equal. The complicated bladed-disk system could then be reduced to a single effective blade for which response to harmonic excitation could easily be calculated. All other blades would respond with the same amplitude, but with differences in phase. The extension of these single-blade techniques to multiple-blade systems with nonuniform gaps comprises the broader scope toward which this effort is ultimately directed. The prime objective of this paper is to show the development of a representative model for a single integrally shrouded blade which can be used effectively to study steady-state stresses and displacements resulting from harmonic excitation. Later work will address the use of this model in the analysis of actual bladed disks.

The body of literature available on the subject of "gap dynamics" is comprised mostly of works related to the dynamics of simple single-degree-of-freedom (SDOF) systems. The direct relationship of these results to blade dynamics is tenuous, being of obvious use only if the shroud is massive relative to the airfoil. It is more likely that actual blade response involves participation of higher beam-type modes with maximum stresses occurring along the length of the airfoil.

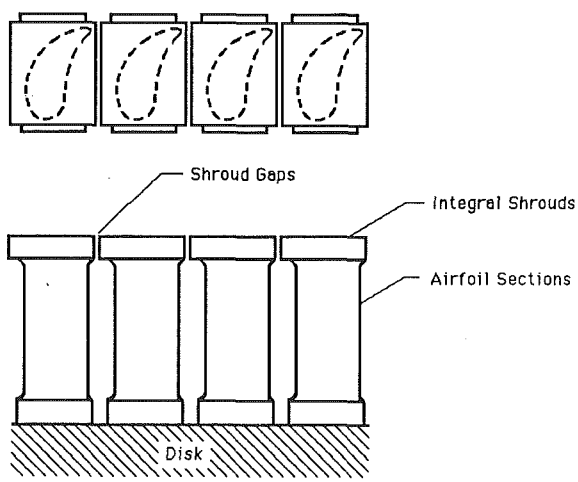

Fig. 1 Partial row of integrally shrouded turbine blades

Contributed by the International Gas Turbine Institute and presented at the 34th International Gas Turbine and Aeroengine Congress and Exhibition, Toronto, Ontario, Canada, June 4-8, 1989. Manuscript received at ASME Headquarters February 14, 1989. Paper No. 89-GT-293.

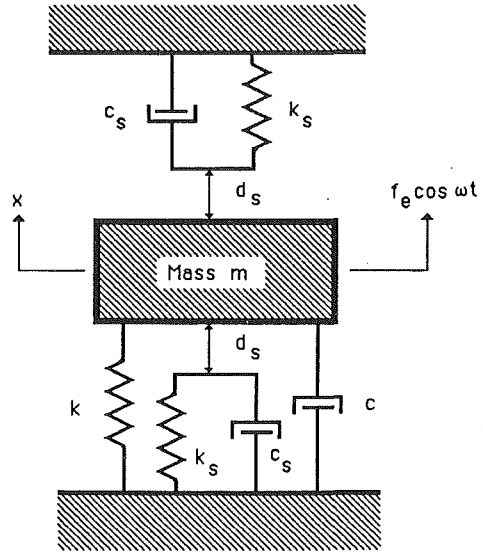

Fig. 2 Single-degree-of-freedom system including a gap

Exact and approximate solutions for harmonic excitation of an SDOF system including a gap (see, e.g., Fig. 2) are contained in a variety of sources (Den Hartog, 1936; Masri, 1978; Watanabe, 1984; Nayfeh, 1979; Nguyen, 1986). One of the earliest studies by Den Hartog and Heiles (1936), found periodic solutions for a similar bilinear system, but with a relatively mild nonlinearity. Masri (1978) shows for his particular beam structure and constraint, which is similar to a tip-shrouded turbine blade with a soft shroud spring, that an analytical SDOF model can provide excellent agreement with experiment. Watanabe (1984) indicates that an approximate SDOF solution, based on the technique of harmonic balance (Nayfeh and Mook, 1979), gives almost identical vibratory amplitudes as the exact solution, even for large nonlinearities Nguyen et al. (1986) examined a nonlinear, harmonically excited SDOF oscillator, using a time-history approach, with emphasis on wear rate and noise. This study noted two major types of response, periodic and erratic, with the former being much more common in systems, particularly those having a low frequency of contacts. A specific result common to all these references is the manifestation of multivalued branches on the frequency response curve. These branches are referred to as "drop-jump phenomena" (Timoshenko et al., 1974) which become evident when the nonlinearity becomes, in some sense, large.

The nonlinear harmonic response of a continuous cantilevered beam system including a gap at the beam tip and with support displacement excitation has been studied by Watanabe (1978). Watanabe compared the results of the continuous system to those of an SDOF system having the same frequency and generalized mass as the lowest mode of the continuous system. He found that the simple model was a reasonable match for the continuous model for nonlinearities that were not too extreme. His numerical examples, however, did not include participation of beam modes higher than the first.

Analysis of the integrally shrouded blade problem begins with the development of a multi-degree-of-freedom model for the entire stage. Reduction of this system to an SDOF model allows economical investigation of the dynamic behavior for a "tuned" system, which means that each blade is assumed to be identical in all respects. Next, the tuned model is extended to include the participation of higher frequency beam-type modes, which were unavailable in the SDOF model. The comparison of these approximate single-blade models for development of a practical multi-blade stage model including mistuning, and the ramifications for dynamic stress evaluation constitute the basis for this study. Additional comparisons to more accurate time-history results also have been undertaken.

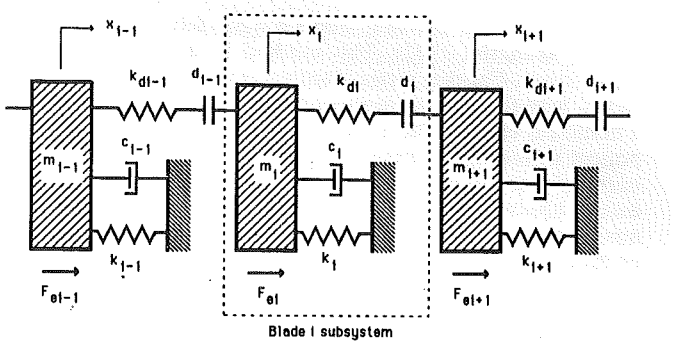

Fig. 3 Multiple blade system represented by SDOF oscillators coupled by nonlinear gap elements

2 Description of General Model and Method of Solution

A model for a typical integrally shrouded blade stage is shown in Fig. 3. The representation of each of the blades as an SDOF system is effected for expediency and allows a more lucid description of later reduction to a tuned-system model. The suitability of the SDOF single-blade model will be examined later. The modal mass and stiffness for the ith blade are represented by m_i and k_i. Coupling between each of the blades is developed through a spring k_{di} and a gap of length d_i. Sources of damping, such as those caused by aerodynamic and material effects, are approximated as viscous in nature and represented by c_i. The external excitation force, F_{ei}, is assumed to be an individual Fourier component relative to a particular harmonic (engine-order) of operating speed. As such, this force is sinusoidal in time and differs only in phase from blade to blade, i.e.,

$$F_{ei} = f_e \cos(\omega t - \psi_i) \tag{1}$$

where ω is the forcing frequency, ψ_i the phase associated with blade i, and the amplitude f_e is assumed identical for each blade. The blade motion is constrained to the plane of the disk, thus effectively eliminating disk coupling effects.

The governing equation of motion for the ith mass may be written as

$$m\ddot{x}_i + c\dot{x}_i + kx_i = F_{ei} + F_{di-1} - F_{di} \tag{2}$$

where $i = 1,2,3, \ldots, N$, and N is the number of blades. The circular symmetry of an actual bladed disk enforces the coupling of blades 1 and N. Implicit in the foregoing equation is the assumption that all blades are identical except for the possibility of variations in the gap between adjacent shrouds. Thus the i subscript has been dropped from the parameter values. The system nonlinearity is contained in the F_{di} terms, which are the forces applied to mass i due to gap closure. The nonlinearity is represented by the bilinear spring with a deadband for the gap. This formulation admits the possibility of a displaced dynamic equilibrium position due to gap asymmetry.

Solution of the complete N-blade system of nonlinear equations for the steady-state harmonic response can be accomplished by computing the time history for the system until all degrees of freedom have reached stationary amplitude values. For a large system, having 50–100 blades, this can be a computationally expensive undertaking, and one certainly not amenable to parametric studies.

An alternative steady-state solution method is the *harmonic balance technique* (also called the describing function method

in control system theory); (see e.g., Nayfeh, 1979; Nguyen, 1986; Takahashi, 1972). This method is approximate and is based on a Fourier series decomposition of the nonlinear terms, with the assumption that the only significant output of a nonlinear element for a sinusoidal input is a sinusoidal component at the input frequency. If restricted to only the first harmonic, as will be done in this work, the method is effective, easy to apply, computationally efficient, and can handle large nonlinearities. However, using only the first harmonic ignores certain nonlinear interactions (such as subharmonics, superharmonics, combination resonances, chaos, etc.) that occur in real systems. This shortcoming is not considered severe for blade systems, since these interactions tend to occur over rather small parameter ranges, are sometimes inhibited by damping, and harmonic, steady-state motion seems to be the norm. This statement has been confirmed by large numbers of time simulation analyses.

In implementing the harmonic balance (HB) technique, it is assumed that the steady-state response is essentially harmonic with a possible offset from the static equilibrium position. The solution to (2) in terms of relative blade motion can be written as

$$x_{ri} = x_i - x_{i+1} = D_i \cos\theta_i + E_i \tag{3}$$

where D_i and E_i are unknown, and $\theta_i = \omega t - \beta_i$ with β_i being the phase angle for relative displacements. The terms D_i, E_i, and β_i can easily be related to the absolute displacement amplitudes.

The nonlinear gap contact force can be written in terms of θ_i in the following manner

$$F_{di} = \begin{cases} 0, & \theta_i > \theta_i^* \\ k_d(D_i\cos\theta_i + E_i - d_i), & \theta_i < \theta_i^* \end{cases} \tag{4}$$

The value of θ_i, which defines the zero value for the nonlinear gap force, is given by θ_i^*, which can be found from

$$\theta_i^* = \cos^{-1}\left[\frac{d_i - E_i}{D_i}\right] \tag{5}$$

Noting that the gap force will have the same phase as the relative displacement, the discontinuous expression in (4) can be replaced by

$$F_{di}(\theta_i) = R_i\cos\theta_i + S_i \tag{6}$$

where R_i and S_i are obtained by Fourier decomposition, which, after integration, results in

$$R_i = \frac{k_d}{\pi}\left[D_i\theta_i^* + \sin\theta_i^*(E_i - d_i)\right] \tag{7}$$

and

$$S_i = \frac{k_d}{\pi}\left[D_i\sin\theta_i^* + (E_i - d_i)\theta_i^*\right] \tag{8}$$

Expanding the relative contact force in (2) gives

$$F_{di-1} - F_{di} = [R_{i-1}\cos\beta_{i-1} - R_i\cos\beta_i]\cos\omega t + [R_{i-1}\sin\beta_{i-1} - R_i\sin\beta_i]\sin\omega t + S_{i-1} - S_i \tag{9}$$

Substituting (1), (3) and (9) into the governing system of differential equations (2), and applying the method of harmonic balance, which requires the linearly independent sine and cosine terms to be equated, results in a system of $3N$ nonlinear algebraic equations. This system can be solved using a multidimensional Newton–Raphson technique (Conte and de Boor, 1984), but this is only effective if the nonlinearities are small, i.e., if none of the blades contains jump phenomena in their response spectra. Solution of the more general multidimensional nonlinear problem will be a topic of future efforts.

3 Equivalent Single-Degree-of-Freedom System for Tuned Response

A tuned blade system is made up of individual blades that have identical dynamic properties, including shroud gaps. The only factor constraining the blades to different responses is the excitation phase. Thus all blade amplitudes will be identical, but the motion of adjacent blades will differ by a constant phase $\Delta\psi = 2\pi e/N$, where e is the excitation order. Noting this, it is possible to reduce the entire blade system to an equivalent SDOF system such as that shown in Fig. 2.

The dynamic characteristics, m, k, and c of the equivalent SDOF system depend only upon the particular blade mode involved, but the "equivalent contact stiffness," k_s, depends upon interblade relationships and can be deduced from the preceding equations for the general blade system as

$$k_s = 2k_d\sin^2(\Delta\psi/2) \tag{10}$$

In addition, an "equivalent shroud gap," d_s, must also be determined as

$$d_s = \frac{d}{2\sin(\Delta\psi/2)} \tag{11}$$

Contact damping effects are assumed to be small and are ignored in this study (i.e., $c_s = 0$). Note that for lower excitation orders and a large number of blades, the equivalent contact stiffness can be lower than the actual contact stiffness by as much as two orders of magnitude.

Equations (10) and (11) can be seen to be reasonable by considering two limiting cases. If all blades of the system are excited in-phase, the response of each blade will be in-phase with the response of all other blades. In this case, the equivalent shroud gap will be infinite, and the equivalent contact stiffness will be zero. Consequently, motion of a specific blade will not be influenced by its neighbors. This effect is readily seen in (10) and (11) when $\Delta\psi = 0$ deg. Conversely, if each blade moves with phase opposite to that of the adjacent blades ($\Delta\psi = 180$ deg), the effective shroud gap will be one-half that of the assembled shroud gap, and contact stiffness will be maximum.

The equation of motion for the equivalent tuned system is written

$$m\ddot{x} + c\dot{x} + kx = f_e\cos\omega t - F_d(x) \tag{12}$$

where the nonlinear shroud force is given by

$$F_d(x) = \begin{cases} k_s(x - d_s) & x > d_s \\ 0 & -d_s \le x \le d_s \\ k_s(x + d_s) & x < -d_s \end{cases} \tag{13}$$

Solution of the nonlinear ordinary differential equation can be obtained approximately by the method of harmonic balance previously described. Assume the solution to (12) has the excitation frequency but differs from the force by the phase ϕ, thus $x = A\cos\theta$ where $\theta = \omega t - \phi$. The following expressions for the amplitude A and the phase angle ϕ are ultimately obtained

$$A^2\{[1 - \bar{\omega}^2 + K_s(A)/k]^2 + (2\zeta\bar{\omega})^2\} = (f_e/k)^2 \tag{14}$$

$$\tan\phi = \frac{2\zeta\bar{\omega}}{1 - \bar{\omega}^2 + K_s(A)/k} \tag{15}$$

where $\bar{\omega} = \omega/\omega_n$, $\omega_n^2 = k/m$ is the first undamped natural frequency of the unconstrained blade, $\zeta = c/c_c$ is the critical damping factor, and the nonlinear term $K_s(A)$ is given by

$$K_s(A) = \frac{2}{\pi}k_s\left(\theta^+ - \frac{1}{2}\sin 2\theta^+\right) \tag{16}$$

with $\cos\theta^+ = d_s/A$.

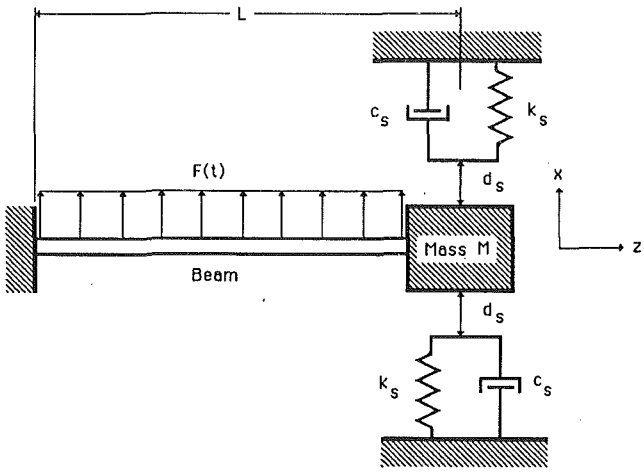

Fig. 4 Beam model for tuned response of a turbine blade with shroud gaps

The frequency at which response is a maximum for the equivalent SDOF blade can be found from (14) by differentiating A with respect to $\bar{\omega}$, setting this equal to zero, and solving for $\bar{\omega}$. The resulting expression is

$$\bar{\omega}_{\max A} = \sqrt{1 + 2\zeta^2 K_s(A)/k} \tag{17}$$

This result will be used in later comparisons.

4 Beam Model for Tuned Response

An SDOF model for an individual blade may be useful for systems that are not greatly constrained at the tip. However, if the excitation is large and the shroud is stiff, blade tip motion will tend to be geometrically constrained (i.e., tip movement cannot be much larger than the gap dimension) and be very insensitive to parameter variations. A more representative model for this situation would include higher mode participation, such as that included in a beam model for a shrouded blade. Inclusion of the higher beam modes would provide a more realistic picture of the stress distribution; one that is unavailable with the SDOF model. In addition, the excitation can be distributed over the beam length, rather than lumped at the tip. A model of this type for tuned response is shown in Fig. 4. The gap parameters are the same as those defined for the SDOF model.

Incorporation of the nonlinear tip constraint into a beam model for the integrally shrouded blade is accomplished, using modal superposition and a Lagrange multiplier technique similar to that used by Dowell (1982). In order to minimize the computational effort in this analysis, the formulation will be directed so that the only unknowns remaining will be those associated with the nonlinearity at the shroud. Thus, after the solution is complete, possibly involving many iterations, displacements or moments along the length of the beam can be found in terms of the shroud displacements. This method can be of even greater advantage when applied to a multiple blade system.

To begin the analysis, the beam deflection, $x(z,t)$, is expressed as a superposition of n beam modes, namely,

$$x(z,t) = \sum_{i=1}^{n} a_i(t)\phi_i(z) \tag{18}$$

where a_i are unknown coordinates, and ϕ_i are the undamped modes for a Bernoulli–Euler cantilever beam. These modes are given by

$$\phi_i(z) = \frac{1}{\Delta_\phi}[(\sin\beta_i L - \sinh(\beta_i L)(\sin\beta_i z - \sinh\beta_i z) + (\cos\beta_i L + \cosh\beta_i L)(\cos\beta_i z - \cosh\beta_i z)] \tag{19}$$

where $\Delta_\phi = -2\sin\beta_i L \sinh\beta_i L$, $\beta_i^4 = \omega_i^2 \rho A/EI$ corresponds to the natural frequency ω_i, and normalization has been imposed so that $\phi_i(L) = 1$. Assuming the motion of the beam to be steady-state and harmonic, the kinetic energy is given by

$$T = \frac{1}{2}\sum_{i=1}^{n} m_i \dot{a}_i^2 + \frac{1}{2} M_s \dot{x}_s^2 \tag{20}$$

with m_i the beam modal masses, M_s the shroud mass, and x_s the displacement of the shroud ($z = L$). The potential energy is

$$V = \frac{1}{2}\sum_{i=1}^{n} m_i \omega_i^2 a_i^2 \tag{21}$$

and the dissipation energy for proportional damping may be written as

$$D = \frac{1}{2}\sum_{i=1}^{n} 2\zeta_i \omega_i m_i \dot{a}_i^2 \tag{22}$$

with ζ_i being the damping factor for the ith mode.

Noting that the shroud mass and the beam are connected at the tip of the blade leads to the constraint equation

$$f = \sum_{i=1}^{n} a_i(t)\phi_i(L) - x_s = 0 \tag{23}$$

The generalized forces are given by

$$Q_i = F(t)\int_0^L \phi_i(z)dz + F_d\phi_i(L) \tag{24}$$

where $F(t)$ is an excitation which is uniformly distributed spatially, and F_d is the nonlinear contacting force given by (13).

The equations of motion for the nonlinear system can be developed from Lagrange's equation resulting in the following system (refer to Dowell (1982) for details)

$$m_i(\ddot{a}_i + 2\zeta_i\omega_i\dot{a}_i + \omega_i^2 a_i) = F(t)\int_0^L \phi_i dz + \beta\phi_i(L) \tag{25}$$

$$M_s\ddot{x}_s + \beta = F_d$$

Here β denotes the Lagrange multiplier. Application of harmonic excitation $F(t) = F_c\cos\omega t$, and use of harmonic balance with retention of only a single harmonic in the response implies that the generalized coordinates and the Lagrange multiplier can be written in the following forms:

$$a_i = a_i^c\cos\omega t + a_i^s\sin\omega t$$

$$x_s = x_s^c\cos\omega t + x_s^s\sin\omega t \tag{26}$$

$$\beta = \beta^c\cos\omega t + \beta^s\sin\omega t$$

Now, rewrite the shroud displacement in terms of an amplitude A and phase ψ as

$$x_s = A\cos\theta \tag{27}$$

where $\theta = \omega t - \psi$. Using harmonic balance, the resulting shroud force becomes

$$F_d(\theta) = -K_s(A)A\cos\theta \tag{28}$$

where $K_s(A)$ is given by (16). Substitution of (26)–(28) into the equations of motion in (25), and the separation of linearly independent terms, results in the following nonlinear system for the unknown shroud displacements:

$$\begin{aligned}[1 + (K_s - \omega^2 M_s)\Sigma_\omega]x_s^c - [(K_s - \omega^2 M_s)\Sigma_\zeta]x_s^s &= \Sigma_{\omega F} \\ [(K_s - \omega^2 M_s)\Sigma_\zeta]x_s^c - [1 + (K_s - \omega^2 M_s)\Sigma_\omega]x_s^s &= \Sigma_{\zeta F}\end{aligned} \tag{29}$$

where

$$\Sigma_\omega = \sum_{i=1}^{n} \frac{(\omega_i^2 - \omega^2)\phi_i^2(L)}{m_i \Delta_i}$$

$$\Sigma_\zeta = \sum_{i=1}^{n} \frac{2\zeta_i \omega_i \omega \phi_i^2(L)}{m_i \Delta_i}$$

$$\Sigma_{\omega F} = \sum_{i=1}^{n} \frac{(\omega_i^2 - \omega^2)\bar{F}_i \phi_i(L)}{m_i \Delta_i}$$

$$\Sigma_{\zeta F} = \sum_{i=1}^{n} \frac{2\zeta_i \omega_i \omega \bar{F}_i \phi_i(L)}{m_i \Delta_i}$$

and

$$\Delta_i = (\omega_i^2 - \omega^2)^2 + (2\zeta_i \omega_i \omega)^2$$

$$\bar{F}_i = F_c \int_0^L \phi_i(z)\, dz$$

Thus a nonlinear expression for the amplitude of the shroud vibration can be found to be

$$A = \sqrt{(\Sigma_{\omega F}^2 + \Sigma_{\zeta F}^2)/\Gamma} \tag{30}$$

where

$$\Gamma = [1 + (K_s - \omega^2 M_s)\Sigma_\omega]^2 + (K_s - \omega^2 M_s)^2 \Sigma_\zeta^2$$

Equation (30) can be easily solved using the Newton-Raphson method, but a more effective approach that guarantees extraction of all possible solutions uses the bisection method at a given excitation frequency with the amplitude A being the independent variable. Thus the response of a tuned, shrouded blade system, often containing amplitude jump responses, can be completely defined.

The frequency for maximum response of the blade using the beam model can be found by maximizing A relative to ω in (30). Thus $\omega_{\max A}$ can be found implicitly from the following relation

$$A^2 \left[(1 + K_s^* \Sigma_\omega)\left(K_s^* \frac{d\Sigma_\omega}{d\omega} - 2\omega M_s \Sigma_\omega\right) + K_s^* \left(K_s^* \frac{d\Sigma_\zeta}{d\omega} - 2\omega M_s \Sigma_\zeta \right) \right] = \Sigma_{\omega F} \frac{d\Sigma_{\omega F}}{d\omega} + \Sigma_{\zeta F} \frac{d\Sigma_{\zeta F}}{d\omega} \tag{31}$$

with

$$K_s^* = K_s - \omega^2 M_s$$

Once a solution to (30) has been obtained for a given excitation frequency, the vibratory amplitudes can be found at any point along the length of the beam. Returning to the constraint equation (23) and the equations of motion (25) with known values for x_s^c and x_s^s, and separating these equations into cosine and sine components allows solution for the Lagrange multiplier components β^c and β^s, and ultimately the amplitude components for the beam transverse motion, a_i^c and a_i^s. Once these amplitude components are known it is a straightforward extension to obtain stress amplitudes along the beam length.

5 Comparison of Different Blade Models

The SDOF model for an integrally shrouded blade offers distinct computational advantages for analysis of multiple blade systems. Programming is simple and computer execution time is minimized. Previous investigators have found its use to be adequate for mildly nonlinear systems. The beam model, although more complex, includes consideration of the distribution of displacement and stress, and is thus more accurate, particularly for greater nonlinearities. Note that the number of degrees of freedom used in the nonlinear system of equations is the same for both the SDOF and beam models. The intent of this section is to compare these two models and to determine the limits of usage for the SDOF model. In addition, results from each model will be compared to steady-state time history results. These comparisons will validate the HB approach as well as usage of a particular model. In order to reduce the number of parameters involved, the shroud mass M (see Fig. 4) will be zero.

The study of the nonlinear vibratory systems considered in this work requires the use of a number of different reference frequencies. They are related primarily to the type of model and the amount of tip constraint. The SDOF model has two reference frequencies of significance here, namely:

(*a*) The natural frequency, ω_n, of the mass fixed to the linear spring of the blade

$$\omega_n^2 = k/m \tag{32}$$

(*b*) The natural frequency, ω_{nc}, of the mass fixed to the blade spring and the tip constraint spring

$$\omega_{nc}^2 = (k + k_s)/m \tag{33}$$

The important reference frequencies for the beam system are the first cantilever mode with unconstrained tip, ω_1, the natural frequency of the cantilever with the tip simply supported, ω_p, and the natural frequency of the cantilever with a spring at the tip, ω_s. The first two cantilever reference frequencies are given by the equation

$$\omega = \frac{(\beta L)^2}{L^2} \sqrt{\frac{EI}{\rho A}} \tag{34}$$

with $\beta L = 1.8751$ for ω_1, and $\beta L = 3.9266$ for ω_p. The natural frequency ω_s, must be found from a more complicated expression or by numerical means. The beam first-mode frequency, ω_1, will be used as a basis for comparison in much of this work.

A valid comparison between the alternate models is possible only with the proper choice of parameters for the SDOF model such that matching, in some sense, is obtained. In this case, the resonant response of the tip of the beam in its first mode is to be matched to the resonant response of the SDOF mass. One way to do this is to set the mass of the SDOF system, m, equal to the first-mode generalized mass of the beam, m_{g1}, the stiffness, k, equal to $\omega_1^2 m_{g1}$, and the force amplitude, f_e, equal to the first mode generalized force amplitude, f_{g1}, of the beam. The beam generalized mass and force are expressed in terms of the first mode shape integrated over the beam length, viz,

$$m_{g1} = \rho A \int_0^L \phi_1^2 dz \tag{35}$$

and

$$f_{g1} = F_c \int_0^L \phi_1 dz \tag{36}$$

Formal nondimensionalization of (14) results in five independent variables, namely,

(1) The frequency variable, $\bar{\omega} = \omega/\omega_1$,
(2) The gap stiffness variable, $\bar{K}_s = k_s/k$,
(3) The excitation variable, $\bar{F} = f_e/kd_s$,
(4) The response amplitude variable, $\bar{A} = A/d_s$, and
(5) The critical damping factor, ζ.

This nondimensionalization provides the basis for the presentation of the results. Throughout this study, the effect of damping variations will be considered small, and the critical damping factor will be constrained to one percent.

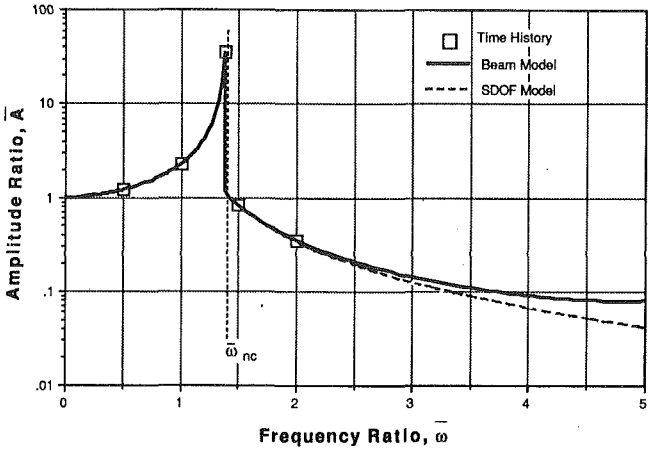

Fig. 5 Comparison of SDOF and beam model frequency response ($\bar{F}=1$, $\bar{K}_S=1$)

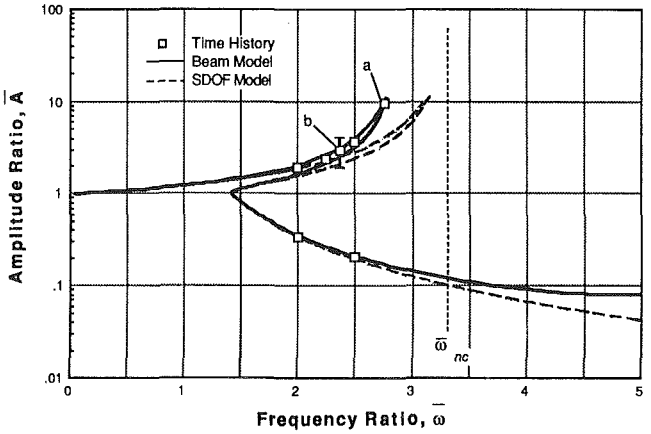

Fig. 6 Comparison of SDOF and beam model frequency response ($\bar{F}=1$, $\bar{K}_S=10$)

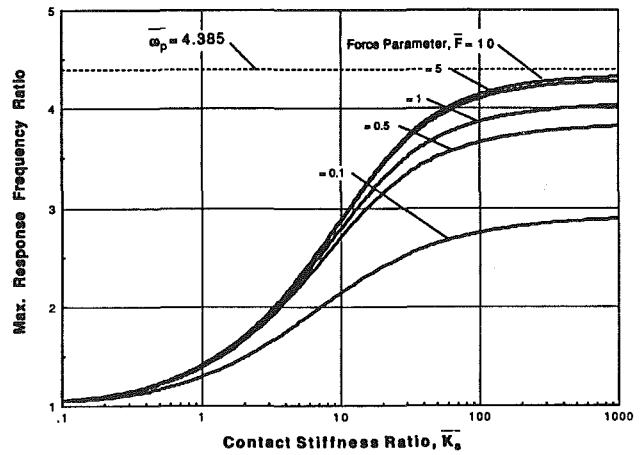

Fig. 7 Frequency ratio for maximum tip response

Comparisons of the SDOF and beam response amplitude spectra are shown in Figs. 5 and 6 for a force level considered to be in the range representative for turbomachinery ($\bar{F}=1$). The set of curves in Fig. 5 corresponds to a small contact stiffness ratio ($\bar{K}_s=1$), and the comparison is very good for frequency ratios below about three. For this set of results, the nonlinearity of the system is small enough that the jump phenomenon is not apparent. Steady-state amplitude results, obtained from time-history calculation for a beam model, also are shown. The set of curves shown in Fig. 6 is for a contact

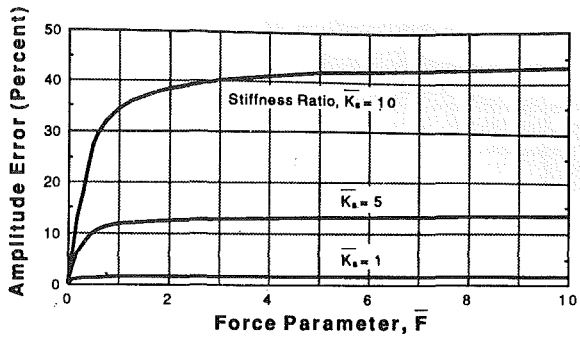

(a) Amplitude error

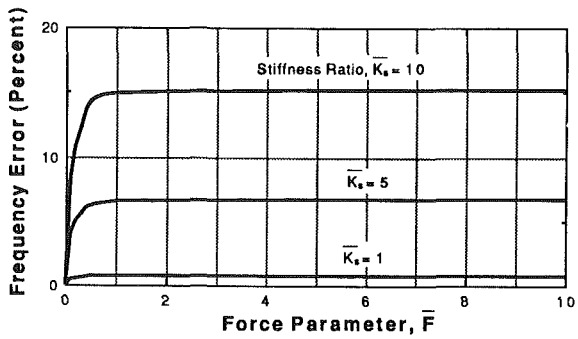

(b) Frequency error

Fig. 8 Tip displacement amplitude and frequency errors for SDOF model

stiffness ratio that is an order of magnitude larger ($\bar{K}_s=10$). The divergence between the beam and SDOF results is easily distinguished. Note, however, that the beam model is more accurate as evidenced by comparison with the time-history results. For larger contact stiffness ratios, the SDOF and beam results have even greater separation, with the SDOF maximum response frequency ratio increasing without bound. The beam results cannot peak at frequencies greater than the pinned tip frequency, ω_p.

Retention of only a single term in the HB method leads to the question of how well this simple sinusoid approximates the more complex steady-state response of the single-blade system. Over a single excitation cycle, the time-history steady-state amplitude results for the beam model, corresponding to point "a" in Fig. 6, cannot be visually distinguished from a pure sine wave. The presence of higher odd harmonics (even harmonics do not occur in this symmetric system), which tend to "clip" a sine wave, has not significantly influenced the response at lower frequencies. In fact, an FFT analysis of the time history shows that the third harmonic accounts for only about two percent of the total, and higher harmonics are negligible. Thus the comparison of the more comprehensive time-history results with the HB method results is quite good.

As the contact stiffness is increased, the maximum tip response frequency for the beam model asymptotes to the pinned-tip frequency, ω_p. This behavior is illustrated in Fig. 7. The maximum response frequency for the SDOF model continues to increase in proportion to the square root of the contact stiffness ratio. Thus stiffer contacts create larger errors in the SDOF model. The amplitude and frequency errors associated with tip displacement of the SDOF model are shown in Fig. 8. These results were obtained for the maximum response points (e.g., point "a" of Fig. 6) and reflect the difference between the beam and SDOF results given by equa-

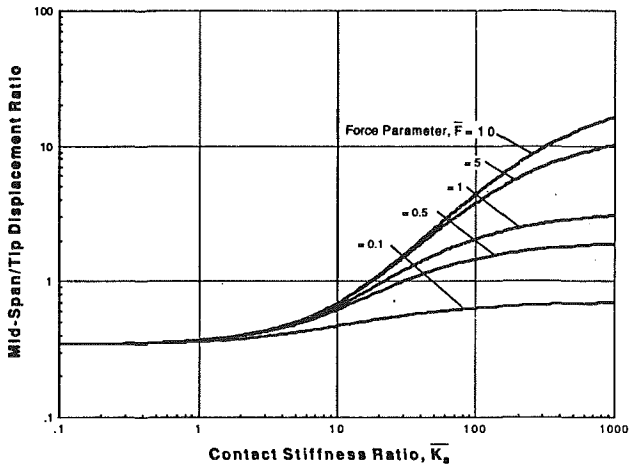

Fig. 9 Ratio of beam midspan to tip displacement

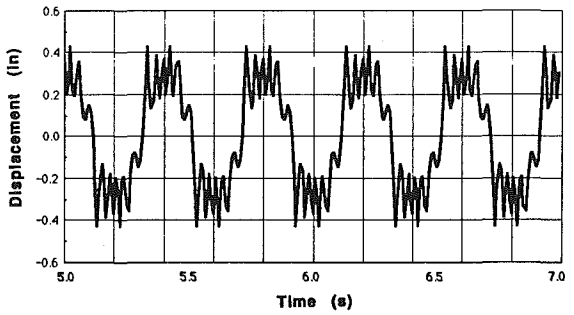

(a) SDOF model

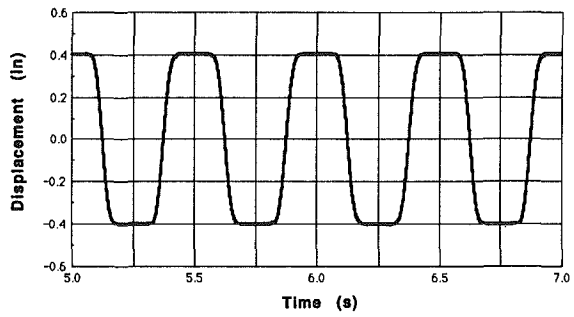

(b) Beam model

Fig. 10 Comparison of chatter response for equivalent SDOF and beam models

tions (31) and (17). The errors increase with both increased force and increased contact stiffness. At greater force levels, both models approach their linear representations for which the gap dimension has become negligible and the error between model results has become constant. Note that the resonant peak for the SDOF model approaches ω_{nc}, and that for the beam model becomes ω_s. Thus, for example, to use the SDOF model with varying force parameter and less than five percent error in peak frequency, the contact stiffness ratio, $\bar{K}_s$, must be limited to values no greater than about three.

Failure of a turbine blade is usually related to stress rather than tip displacement. The only way to obtain these stresses with an SDOF model is by scaling the associated modal information. Using a beam representation for a turbine blade allows an accurate description of results which vary along the blade length, such as moments and stresses. The results shown in Fig. 9 illustrate the need for the beam model. This figure shows the midspan to tip displacement ratio, R_δ, as a function of contact stiffness ratio. If the displacement ratio exceeds 1.0, the midspan has a larger vibration amplitude than the tip. This occurs for increasing $\bar{K}_s$, and the point of maximum stress would tend to move away from the root of the blade.

6 Discussion

The Lagrange multiplier method, used in this work for the beam analysis, is not limited to the Bernoulli–Euler beam model. A more complex Timoshenko model, or numerical modal results also could be implemented. The power of this approach, however, is its ability to reduce a complex nonlinear system to a set of nonlinear equations that involve only the degrees of freedom associated with the nonlinearity, thus minimizing computational intensity. In this sense, the method is akin to the receptance modeling technique that has been widely used in the dynamic analysis of blades and bladed-disk assemblies (Bazan et al., 1986).

The work of Nguyen et al. (1986) indicates the possibility and gives an example of an SDOF system periodic response with multiple impacts which was termed "chatter" response. The system had stiff contacts ($\bar{K}_s = 100$) and was forced well below its natural frequency ($\bar{\omega} = 0.1987$, $\bar{F} = 1.875$). This response has been duplicated and is shown in Fig. 10(a). An equivalent beam model responded at the tip, as shown in Fig. 10(b), showing no chatter. Thus, due to its distribution of mass and stiffness, a beam may not exhibit chatter as readily as a SDOF system.

Nguyen also reported "erratic," chaoticlike, response for one set of conditions in his study ($\bar{\omega} = 1.026$, $\bar{K}_s = 167$, $\bar{F} = 3.75$). Time-history analysis for an equivalent beam showed similar behavior under the same conditions. However, this was the only situation in which such behavior was observed.

An interesting response obtained by the time-history solution for a particular parameter set (point "b" in Fig. 6) showed a steady-state condition (after 800 cycles of excitation) that contained a significant beating. FFT analysis of the time trace showed two response peaks, one at the excitation frequency, and the other at a frequency approximately five percent greater than the excitation frequency with an amplitude 15 percent greater than the synchronous amplitude. The beating would not sustain for frequency perturbations around the original frequency. The point to be noted here, however, is that the average response amplitude was equivalent to the amplitude predicted by the HB method, and that the maximum amplitude was 30 percent greater than the average. This range of response is indicated on the figure. Thus, in this instance, the HB method gave an adequate approximation to the overall response, despite its inability to predict the combination resonance phenomena. While these nonharmonic phenomena (chatter, chaos, etc.) are of some interest, the vast majority of results from time-history analysis converged to stable, steady-state periodic motion.

7 Conclusions

A study has been conducted to devise an accurate and effective approach for modeling blade vibration with nonlinear constraint at the blade tip, primarily directed toward integrally-shrouded blades. Simple single-degree-of-freedom models, while capable of capturing the phenomena, become progressively more inaccurate as the strength of the nonlinearity increases. In particular, accurate stress evaluation is impossible with the SDOF model. Thus a beam model has been proposed to address these shortcomings. Combination of this model with the harmonic balance method for steady-state harmonic response results in an efficient method that addresses only the nonlinear degrees of freedom as unknowns. The accuracy of the technique has been verified by com-

parison to more accurate, but computationally more expensive, time-history results.

The manufacture and assembly of integrally shrouded blades result in unavoidable variations in the shroud gaps. If the excitation forces are large enough to cause shroud contacting, it is clear from the current work that the different gap sizes would result in a kind of mistuned response with large differences in individual blade amplitudes. The response frequency spectra for a given rotational speed, including all blades on the disk, would tend toward a wide spread, with higher peaks occurring at seemingly random frequencies. The spectra for a nominally identical bladed-disk with the same excitation could have a spread with a completely different character. Results of this nature have been observed on tests of aircraft turbine stages. Future studies on integrally shrouded blades are planned, which will use this type of model to study this gap mistuning phenomenon for practical multidegree-of-freedom bladed disks.

References

Bazan, E., Bielak, J., and Griffin, J. H., 1986, "An Efficient Method for Predicting the Vibratory Response of Linear Structures With Friction Interfaces," ASME *Journal of Engineering for Gas Turbines and Power*, Vol. 108, pp. 633–640.

Conte, S. D., and de Boor, C., 1980, *Elementary Numerical Analysis, An Algorithmic Approach*, 3rd ed., McGraw-Hill, New York.

Den Hartog, J. P., and Heiles, R. M., 1936, "Forced Vibrations With Various Combinations of Linear Springs," ASME *Journal of Applied Mechanics*, Vol. 3, pp. 127–130.

Dowell, E. H., 1982, "Component Mode Analysis of a Simple Non-linear, Non-conservative System," *Journal of Sound and Vibration*, Vol. 80, pp. 233–246.

Masri, S. F., 1978, "Analytical and Experimental Studies of a Dynamic System With a Gap," ASME *Journal of Mechanical Design*, Vol. 100.

Nayfeh, A. H., and Mook, D. T., 1979, *Nonlinear Oscillations*, Wiley, New York.

Nguyen, D. T., Noah, S. T., and Kettleborough, C. F., 1986, "Impact Behavior of an Oscillator With Limiting Stops, Part I: A Parametric Study," *Journal of Sound and Vibration*, Vol. 109, No. 2, pp. 293–307.

Takahashi, Y., Rabins, M. J., and Auslander, D. M., 1972, *Control and Dynamic Systems*, Addison-Wesley, Reading, MA.

Timoshenko, S., Young, D. H., and Weaver, W., Jr., 1974, *Vibration Problems in Engineering*, 4th ed., Wiley, New York.

Watanabe, T., 1978, "Forced Vibration of Continuous System With Nonlinear Boundary Conditions," ASME *Journal of Mechanical Design*, Vol. 100, pp. 487–491.

Watanabe, T., 1984, "Forced Vibration of Nonlinear System With Symmetrical Piecewise-Linear Characteristics," *Bull. JSME*, Vol. 27, No. 229, pp. 1493–1498.

Effect of Weak Swirling Flow on Film Cooling Performance

C. Gau

W. B. Hwang

Institute of Aeronautics and Astronautics,
National Cheng Kung University,
Tainan, Taiwan

Experiments have been performed in a large circular pipe to study and obtain the film cooling effectivenesses with the presence of weak swirling flow in the mainstream. The swirling flow is generated by a flat vane swirler situated upstream. Cooling film is injected from an annular slot formed by the pipe wall and the circular cover plate. The radial temperature distribution measurements at several axial locations were used to infer the rate of mixing of film jet with swirling flow. The swirl number, which increases with turbulence intensity and swirl velocity in the mainstream, can significantly increase the mixing rate of film jet with swirl flow and decrease the film cooling effectiveness. During the course of the experiments, the blowing ratio ranged from 0.5 to 1.75 and the swirl number ranged from 0 to 0.6. Correlation equations for the film cooling effectiveness, which account for the effect of swirling flow, are obtained.

1 Introduction

Film cooling performance has been studied extensively in the past due to the wide applications in cooling such high-temperature systems as combustors, turbine blades, afterburners, and nozzles. Cooling air is usually injected from or along the hot surface and forms an insulation layer to protect the surface from being overheated. A film jet can also mix with the hot gas near the wall and effectively reduce the heat transfer from hot gas to the wall. An extensive review article on both analytical and experimental studies of film cooling is available (Goldstein, 1971). However, in the past the studies have been primarily focused on the ideal situations where both the mainstream and the film jet are uniform flows and have relatively low turbulence intensity that does not considerably affect the film cooling effectiveness (Kacker et al., 1967; Seban et al., 1968). The parameters that have been found to affect the film cooling performance are the blowing ratio, the density ratio, the slot height, and the slot lip thickness (Sivasegaram and Whitelaw, 1969; Burns and Stollery, 1969; Lefebvre, 1983). Film cooling effectiveness has been well correlated in terms of these parameters.

However, in a real situation the mainstream may not be uniform and may have relatively high turbulence intensity, and the wall surface may become rough due to deposition and corrosion by the contaminants and carbon particles in the hot gas. Marek and Tacina (1975) have found that the film cooling effectiveness decreases as much as 50 percent as the free-stream turbulence intensity is increased from 7 to 35 percent. For discrete hole injection Goldstein et al. (1985) have found that at a low blowing ratio the roughness of the wall can decrease the spanwise-averaged effectiveness for injection geometries of both a single row and double rows of holes. However, at a high blowing ratio, the roughness of the wall causes a significant increase in the effectiveness for one-row injection and only a small increase for two-row injection.

In a combustor, the inlet air is usually issued through a swirler to increase the mixing rate of fuel jet with air and, therefore, the combustion efficiency (Beer and Chigier, 1972; Lilly, 1977; Gouldin, 1985); the wall is cooled and protected with film air. It is expected that the swirling flow, which has relatively high turbulence intensity and swirl velocity in the combustor, may have a significant effect on the film cooling performance. Therefore, the objective of this paper is to provide and understand the results of film cooling measurement with the presence of a weak swirling flow (i.e., $S<0.6$) over a film jet. The method of film heating is used to obtain the film cooling effectiveness. The radial temperature distributions at several locations have been measured and used to infer the mixing process of film jet with the swirl flow. Correlations for the film cooling effectiveness that account for the weak swirling flow effect are also obtained.

2 Apparatus

Experiments were performed in a circular plexiglass pipe, as shown in Fig. 1. The pipe was 100 cm long, with a 13.9-cm in-

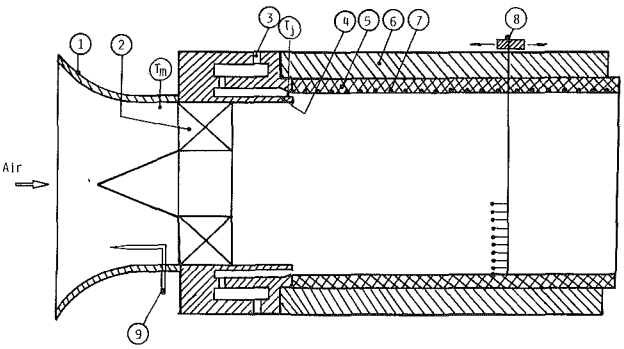

Fig. 1 Schematic diagram of test section: (1) contraction, (2) flat-vaned swirler, (3) film flow inlet, (4) circular cover plate, (5) plexiglass wall, (6) insulation, (7) thermocouple, (8) thermocouple rack, (9) pitot tube

Contributed by the International Gas Turbine Institute for publication in the JOURNAL OF TURBOMACHINERY. Manuscript received by the International Gas Turbine Institute April 1987.

side diameter and a 1-cm wall thickness. Uniform air flow entering the pipe was supplied from and discharged into the outside environment by an open cycle wind tunnel. The velocity of the uniform air flow was maintained at 20 m/s and the maximum turbulence intensity was kept less than 0.7 percent. A single, flat-vaned swirler, having both vane aspect ratio and space-chord ratio of approximately unity, was located at the entrance of the pipe to generate swirling flow. Film heating air was injected axially from a 6-mm-wide annular slot that was formed between the pipe wall and a circular plate, 60 mm long and 3.5 mm thick. To reduce the turbulence intensity of the film jet, a contraction was made near the slot exit by an exit gap width of 4 mm. The axial turbulent intensity in the middle of the slot height was found to be 6 percent. According to the results of Kacker and Whitelaw (1968), this small turbulence intensity has a negligible effect on the film cooling effectiveness. However, a contradictory report (Simon, 1986) indicates that 6 percent turbulence intensity at the slot can have a significant effect. The contradictory results from both reports could not be clarified at the present stage.

The swirler was made of steel and has 10 pieces of 1-mm-thick flat vanes. A total of seven different swirlers having inside diameters of 12.4 cm and hub diameters of 5 cm were made. The vane angles of these swirlers are 0, 7.7, 15, 22, 28, 34, and 39 deg, respectively. However, the swirling flow is usually characterized by the swirl number S, which is a nondimensional parameter representing axial flux of swirl momentum divided by axial flux of axial momentum times swirler radius. It has been shown (Beer and Chigier, 1972) that the swirl vane angle and the swirl number are related by

$$S=\frac{2}{3}\left[\frac{1-(D_h/D_s)^3}{1-(D_h/D_s)^2}\right]\tan\theta \tag{1}$$

Accordingly, the swirl numbers of the swirling flow made by these swirlers are 0, 0.1, 0.2, 0.3, 0.4, 0.5, and 0.6, respectively. To avoid flow recirculation and generation of turbulence caused by the swirl hub before the air enters the swirler, a guide cone was placed in front of the hub, as shown in Fig. 1. The swirler on the lip of the slot can be rotated at different angles and replaced for different sets of experiments. The distance from the outlet of swirler to the slot lip edge was maintained at 45 mm. Therefore, the ratio of this distance to the vane spacing is 1.19.

The secondary air was filtered and pumped by a small centrifugal fan of variable speed. Before entering the slot the secondary air was heated to approximately 20°C higher than the ambient and the temperature was measured and controlled within 0.1°C. After passing through the heater, a rotameter, and a flow straightener, the heated air was distributed into 25 small insulated tubes, which were made equal in length and were connected to a small plenum chamber of annular shape. The standard deviation of dynamic pressures at the tube exits was found to be 0.1 percent. The small plenum chamber was used to reduce the turbulence intensity and enabled air to enter the slot uniformly so that a film jet of uniform injection velocity could be obtained. To reduce the heat loss, both the plenum chamber and the lip of the slot were made of plexiglass, which has a relatively low thermal conductivity, and were well insulated outside to simulate an adiabatic wall. The heat loss rate to the environment was estimated to be less than 1.3 percent.

All the temperatures were measured with copper-constantan thermocouples. A total of 41 equally spaced thermocouples were used to measure the adiabatic temperature distribution in the axial direction of the pipe wall. Each of the thermocouples was inserted radially from outside into a small hole 1.2 mm in diameter until its junction reached the surface of the pipe wall. After installation, the holes were sealed and the inside wall was polished. The pitch between adjacent thermocouples was 8 mm. A total of 20 other thermocouples, having a wire diameter of 0.127 mm, were made into a rack, which could be inserted into the pipe wall through a small diameter hole at several axial locations, to measure the radial temperature distributions. A closer spacing was made of thermocouples near the wall where temperatures might have a large variation. The pitch between adjacent thermocouples near the wall was 1.75 mm. Near the central region the pitch was 3.5 mm. The holes not being used were plugged. The temperatures of the injection air at exit and the mainstream before entering the swirler were also measured and used to calculate the film cooling effectiveness.

Results and Discussion

A single traversing thermocouple was originally designed to measure the axial wall temperature distribution at different angles. All of the temperature distributions measured at different angles were found to be identical when the mainstream was uniform and the swirler was not in the pipe. A slight variation of temperature distribution at different angles was found when the mainstream was swirled. To save experimental labor and time, one row of embedded thermocouples was used to measure and obtain the temperature distributions, by rotating the swirler, every 90 deg. The film cooling effectiveness presented in the following is the averaged value every 90 deg. The maximum standard deviation of the cooling effectiveness is 3 percent.

When the swirler is absent and the mainstream is uniform, the film cooling effectiveness measured at various blowing ratios is compared with the results from the empirical equations for the case of film cooling over a flat plate. The agreement, as shown in Fig. 2, was found to be best with the equations of Ko and Liu (1980). Both results indicate that the film cooling effectiveness increases with blowing ratio up to $M=2$. The local maximum in film cooling effectiveness, which moves toward a higher blowing ratio and disappears gradually downstream, is also observed in the data of Ko and Liu, which are not shown here. For the case where the slot lip thickness approaches zero, the local maximum appears only at $M=1$ (Goldstein et al., 1971). It appears that the slot lip thickness, which creates a wake region behind, can have a peculiar effect on the film cooling effectiveness. However, the local maximum cannot be clearly identified in the data of Sivasegaram and Whitelaw (1969), possibly due to the large increment of blowing ratio ($\Delta M=0.5$) used in the experiment. A comparison was also made with the empirical equation of Ballal and Lefebvre (1973) in which the slot lip thickness effect was

Nomenclature

D_h = diameter of swirler hub
D_s = inside diameter of swirler
M = blowing ratio $= U_j/U_m$
S = swirl number
T = temperature
U = velocity
x = axial distance from slot exit
y = radial distance from pipe wall
y_c = slot height
η = film cooling effectiveness $=(T_{aw}-T_m)/(T_j-T_m)$
θ = vane angle

Subscripts

j = refers to film jet at slot exit
m = refers to mainstream
aw = refers to adiabatic wall

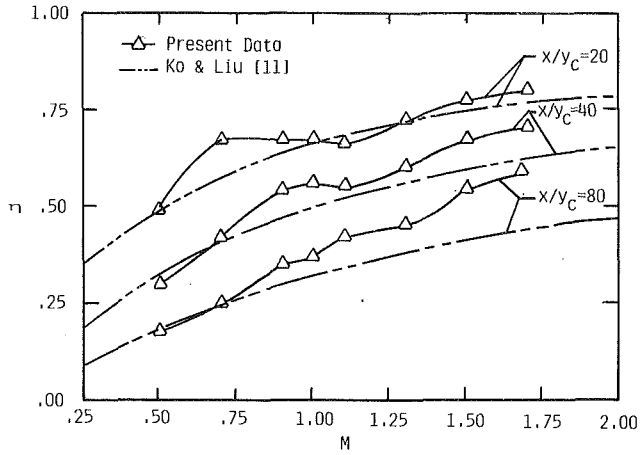

Fig. 2 Comparison of film cooling effectiveness with that of previous result

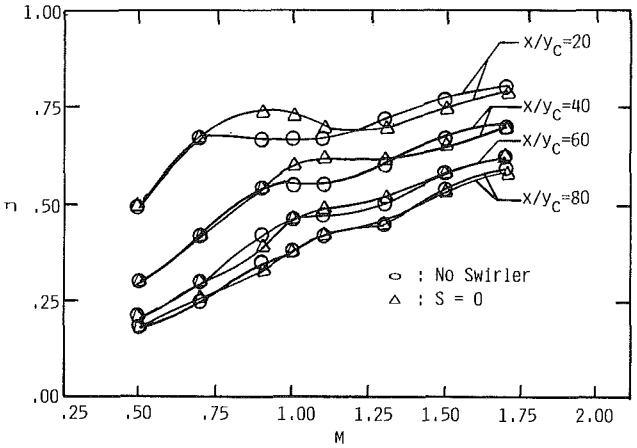

Fig. 3 Comparison of film cooling effectiveness between the case with a swirler having $S = 0$ and the case without a swirler in the mainstream

accounted for explicitly. For clarity the results from Ballal and Lefebvre are not shown in Fig. 2. The agreement is good only for $x/y_c < 40$, that is, within the regime where the correlation of Ballal and Lefebvre can be used accurately.

The higher film cooling effectiveness than that of Ko and Liu, especially for $M > 1$ and in the downstream region, can be attributed to the reduction of the rate of the mixing process between the mainstream and the annular film jet around the outside. As the axial momentum transfers radially from the annular film jet toward the center of mainstream, the mass available to absorb momentum is reduced more rapidly and becomes less than for the case of film cooling over a flat plate, and causes a higher velocity of flow in the mainstream. Therefore, the velocity difference between the film jet and the mainstream in its vicinity is reduced. A reduction of rate of mixing process for the case of annular film cooling can be expected.

When the swirler is placed upstream of the mainflow, the flow field can be significantly changed. Before entering the swirler the flow accelerates due to the presence of the front cone; this increases the mean velocity by 20 percent. After impinging on the swirl vane, the flow is swirled and turbulence is generated. However, both the swirl velocity and turbulence intensity in the mainstream are expected to increase with the vane angle or the swirl number. Due to the swirling effect and the surface of swirl vane, the axial velocity distribution can be significantly distorted. A wake region is also created behind the hub and the flow decelerates downstream.

A comparison of the film cooling effectiveness for the case

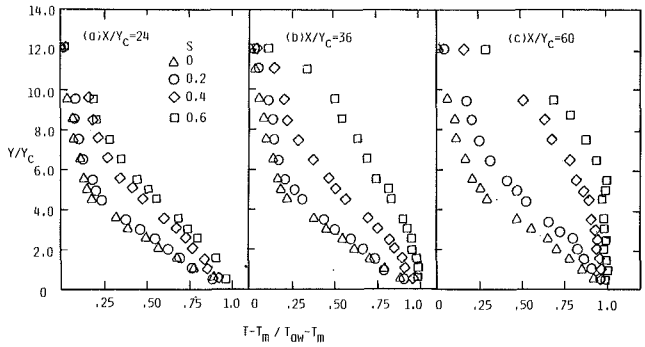

Fig. 4 Effect of swirl number on radial temperature distributions for $M = 1$ at (a) $x/y_c = 24$, (b) $x/y_c = 36$, and (c) $x/y_c = 60$

where the swirler has a zero degree vane angle and the case where the swirler is absent is shown in Fig. 3. The agreement between the two cases is excellent. With the presence of swirler only a slightly higher film cooling effectiveness is obtained upstream for a blowing ratio between 0.7 and 1.3. The local maximum in film cooling effectiveness has a high value and occurs at a slightly higher blowing ratio.

The results conclude that the initial velocity distortion caused by the swirl vane, the flow acceleration by the guide cone, and the deceleration by the wake after the hub region do not have a significant effect on the film cooling effectiveness. These findings agree somewhat with the results from Seban and Back (1962) that flow acceleration in a region downstream of the initial mixing zone has little effect on film cooling effectiveness, and with the results from Kacker and Whitelaw that the effect of upper lip boundary layer thickness (initial velocity distortion) on film cooling effectiveness is less than 5 percent (small). However, a slight increase of film cooling effectiveness in the near slot region can be observed.

3.1 Temperature Distribution Measurement. Due to the difficulty in visualizing the flow structure and the mixing process in both the mainstream and the film jet for this configuration, the radial temperature distributions at various axial locations were measured, as shown in Figs. 4(*a*), 4(*b*), and 4(*c*), and used to infer the flow structures and the rate of mixing of film jet with mainstream. When the swirler is absent or present with zero degree of vane angle, the radial dimensionless temperature distributions at different locations, as shown in Fig. 4, are very similar. The steep temperature gradient near the wall and the slight diffusion of the temperature profile (i.e., the thermal energy) toward the center of the mainstream in the downstream region suggest that within the range of blowing ratio under study, the change of flow structure and the mixing rate of film jet with mainstream are not significant. As the swirl number increases, more rapid diffusion of the dimensionless temperature profile toward the central region can be observed, as shown in Figs. 4(*a*), 4(*b*), and 4(*c*), and becomes significant in the downstream region. The increase in diffusion rate of the dimensionless temperature profile (i.e., the thermal energy) with the swirl number can be attributed to the rate of increase in momentum exchange in the swirling flow and between the film jet and the mainstream.

At a certain vane angle or swirl number a uniform temperature distribution near the wall region can be clearly observed, as shown in Figs. 4(*b*) and 4(*c*), which suggests that the energy exchange or the mixing between the film jet and the mainstream is so significant that the film jet structure is completely destroyed and mixed uniformly with the swirling flow. The completely mixed region becomes thicker downstream. A higher swirl number combined with a lower blowing ratio makes the completely mixed region thicker. Complete mixing of the film jet with the mainstream has not been found for film cooling over a flat plate. Even when the blowing ratio is

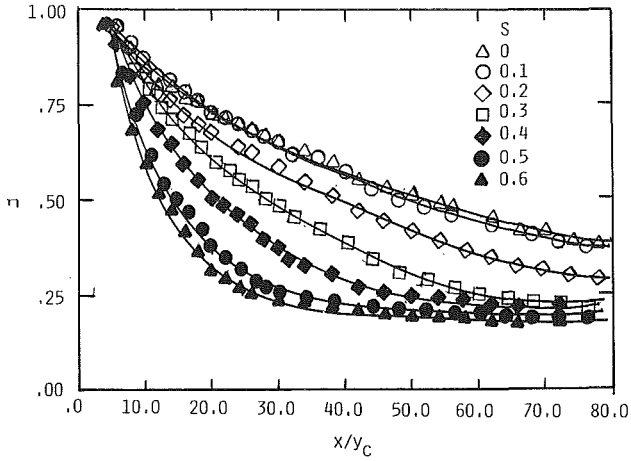

Fig. 5 Effect of swirl number on film cooling effectiveness

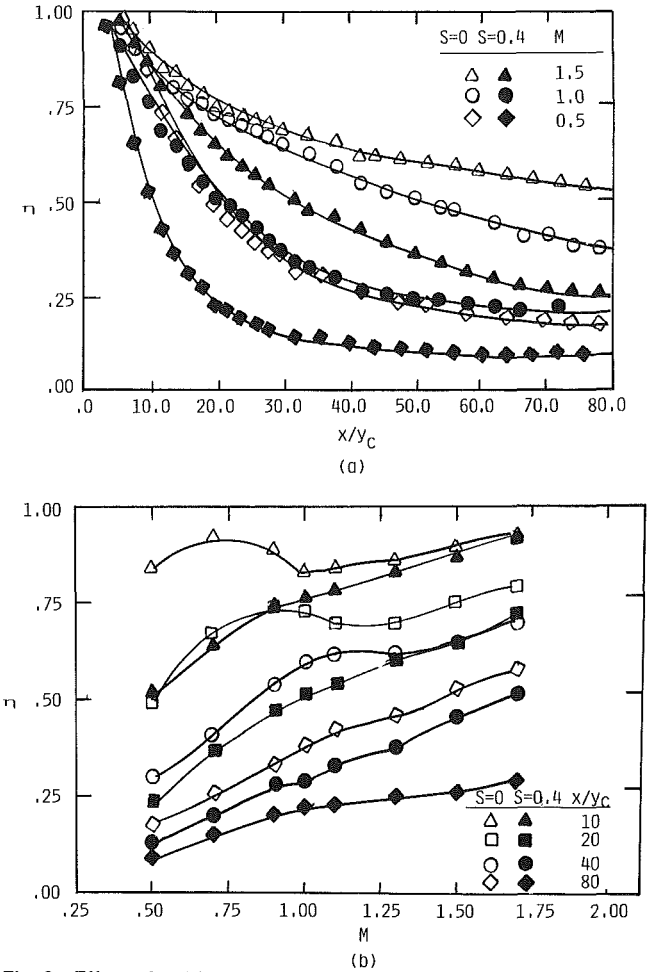

Fig. 6 Effect of swirl number on film cooling effectiveness: (*a*) at low and high blowing ratios and (*b*) at several locations

unity, which has the lowest mixing rate for film cooling over a flat plate, a high rate of mixing of the film jet with the mainstream due to the swirling of the mainflow can be inferred from the temperature measurements. Increase in film jet velocity can preserve film jet structure a little farther downstream (Hwang, 1986). A decrease in film jet velocity can cause earlier destruction of film jet structure.

The increase of the mixing rate with swirl number can be attributed to the increased level of both swirl flow and turbulence intensity. However, the increase in turbulence intensity in the mainstream causing a reduction in film cooling effectiveness was observed by Marek and Tacina (1975), who attributed this phenomenon to the increase of mixing rate of film jet with mainflow. More detailed velocity distribution measurements in both the radial and axial directions and turbulence intensity measurements at various locations might be performed in the future to delineate the dominant mechanism for the mixing process between the film jet and the mainflow.

3.2 Film Cooling Effectiveness. Figure 5 indicates that film cooling effectiveness decreases downstream and the rate of reduction significantly increases with increase of swirl number. It appears that the film cooling effectiveness decreases monotonically with the swirl number, except for the case of $S=0$, and the monotonic decrease occurs for the blowing ratio in the entire range from 0.5 to 1.75 (Hwang, 1986). These results suggest that the swirl number can be selected and used as a correlation parameter for the film cooling effectiveness.

In general, the rate of reduction of film cooling effectiveness is attributed to the rate of mixing of film jet with mainflow. Therefore, the swirl, which can increase the mixing rate of the film jet with the mainstream, can significantly reduce the film cooling effectiveness. However, the swirling flow has the opposing effects of both increasing the mixing rate of the film jet with the mainstream due to the swirl mixing and turbulence, and decreasing the mixing rate due to the stabilizing effect of the adverse radial pressure gradient caused by the centrifugal force of the swirl. It is not difficult to understand that the adverse radial pressure gradient caused by the swirl can reduce the mixing rate of the film jet with the mainstream in the radial direction. In the near slot region the swirl mixing and turbulence are significantly larger than the stabilizing effect of the swirl flow, which can destroy the film jet structure rapidly. However, both the turbulence and the swirl mixing decay rapidly. In the downstream region the film jet structure has already been destroyed substantially. The stabilizing effect of swirl becomes important and may suppress the mixing process between the film jet and the mainstream.

Figure 5 indicates that the film cooling effectiveness for $S=0.1$ is slightly lower at the near slot region, due to the effects of swirl mixing and turbulence, but higher downstream, due to the stabilizing effect of swirl, than for $S=0$. The peculiar phenomenon occurs only for blowing ratio $M \geq 1$. At high swirl number the film cooling effectiveness reaches a constant value downstream. It can be inferred that the mixing process of the film jet with the mainstream at this stage, therefore, is largely suppressed and the mixing rate is negligible. The constant value of the film cooling effectiveness has never been observed for the case of film cooling over a flat plate, and for the case with the swirler having zero degree vane angle.

A comparison of the temperature distribution and film cooling effectiveness measurements has been made and the results suggest that as the film cooling effectiveness reaches a constant value, the film jet has completely mixed with the swirling main flow. The higher the swirl number, the earlier the film cooling effectiveness reaches a constant value, and the thicker the mixing region downstream appears, which results is a lower film cooling effectiveness.

A comparison of film cooling effectiveness between the case of $S=0$ and the case of $S=0.4$ for several specific blowing ratios is presented in Fig. 6(*a*). In both the low and the high blowing ratio ranges, the swirl can significantly reduce the film cooling effectiveness. For the same swirl number a higher blowing ratio causes a higher film cooling effectiveness. This results from the fact that the film jet structure can be preserved and destroyed at a later stage. At a lower blowing ratio and $S=0.4$, the film cooling effectiveness decreases rapidly at the initial stage, due to the strong mixing rate of the film jet

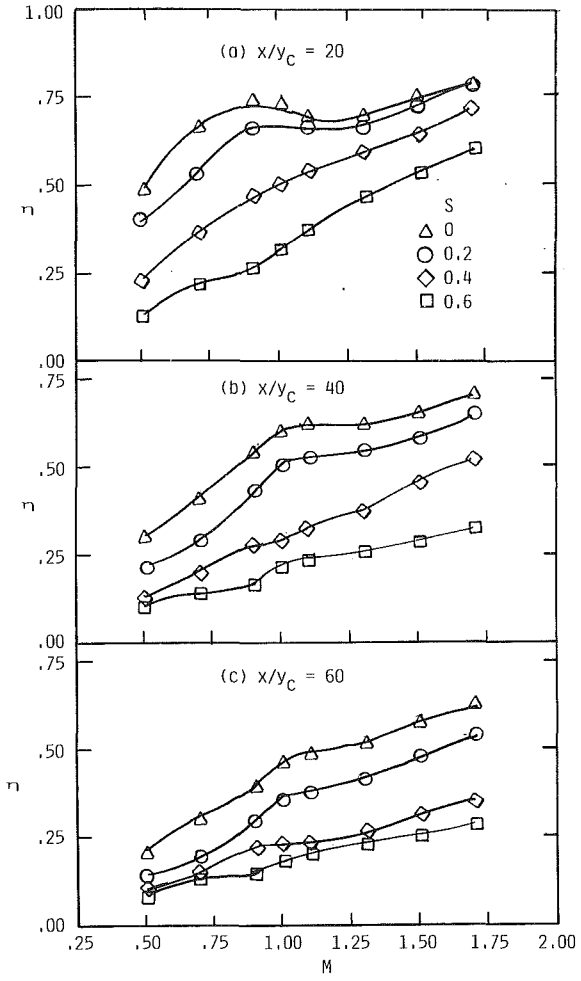

Fig. 7 Effect of swirl number on film cooling effectiveness at (*a*) $x/y_c = 20$, (*b*) $x/y_c = 40$, and (*c*) $x/y_c = 60$

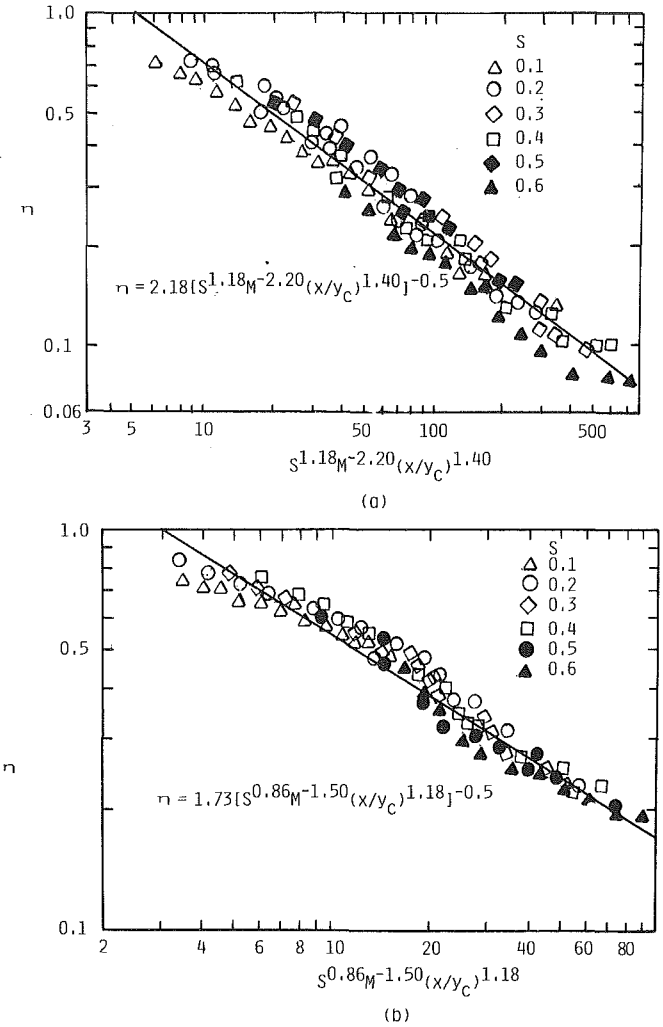

Fig. 8 Film cooling effectiveness correlation for (*a*) $0.5 \le M \le 10$, $0.1 \le S \le 0.6$, and $20 \le x/y_c \le 60$, and (*b*) $1.0 \le M \le 1.7$, $0.1 \le S \le 0.6$, and $20 \le x/y_c \le 80$

with the swirling flow, and reaches at an earlier stage a lower constant value because the available energy from the jet is less.

A stabilizing effect of the swirl can also be observed and inferred from the constant value of the film cooling effectiveness downstream in both the high and the low blowing ratio ranges. Comparison of film cooling effectiveness for the case of $S=0$, $M=0.5$ and the case of $S=0.4$, $M=1$ can be readily made in Fig. 6(*a*). A lower value of film cooling effectiveness in the near slot region for the case of $S=0.1$, $M=1$ than for the case of $S=0$, $M=0.5$ can be attributed to the swirl mixing and turbulence, which increases the mixing rate between the film jet and the mainstream. In the same time, however, a higher value downstream can be attributed to the stabilizing effect of swirl, which decreases the mixing rate.

A comparison of film cooling effectiveness for the cases of $S=0$ and $S=0.4$ at several specific locations is presented in Fig. 6(*b*). At high swirl number significant reduction of film cooling effectiveness can be observed, except in the region very near the slot. Especially at the higher blowing ratio rings, where the film jet still preserves its complete structure, the reduction of film cooling effectiveness is relatively small. The local maximum of film cooling effectiveness does not appear for the case of $S=0.4$, which can be attributed to the strong swirling flow that reduces the wake region behind the cover plate. In this case, the slot lip thickness does not appear to affect the cooling performance and cause a local maximum in the film cooling effectiveness. A monotonic increase of film cooling effectiveness with blowing ratio at high swirl number can be observed. The rates of increase of film cooling effectiveness with blowing ratio at various locations are almost identical except in the far downstream ($x/y_c = 80$) where the distinct film structure has largely been destroyed. In this region, the increase of film cooling effectiveness is mainly due to the increase of film jet flow rate. The increase of film cooling effectiveness with M at $x/y_c = 80$ for the case of $s=0.4$ is not as significant as for the case of $S=0$ except at a very high blowing ratio, where the film jet can preserve its structure farther downstream.

A significant reduction of film cooling effectiveness η with various swirl numbers is shown in Figs. 7(*a*), 7(*b*), and 7(*c*) at different locations. A local maximum still appears for $S<0.4$ where the swirling flow may not have been strong enough to reduce the wake region and overcome the effect of slot lip thickness. Film cooling effectiveness η increases monotonically with blowing ratio for $S>0.4$. However, at each different location and swirl number there is always one parallel curve to represent the variations of η with M. In addition, η decreases with S and increases with M. These results suggest again that, in addition to M, the swirl number can be used as a correlation parameter for η.

At the near slot region the rate of reduction of film cooling effectiveness with S is significant at a low blowing ratio, as shown in Fig. 7(*a*), and can be attributed to the strong mixing of film jet with swirling flow. However, at a high blowing ratio the rate of reduction of film cooling effectiveness with S becomes less due to the fact that the high speed of the film jet has a tendency to preserve its structure. When $S=0.6$ a 70 per-

cent reduction of film cooling effectiveness occurs at $M=0.5$ while a 25 percent reduction of film cooling effectiveness occurs at $M=1.7$. The large rate of reduction of film cooling effectiveness with S moves gradually toward a high blowing ratio downstream, as shown in Fig. 7(*b*) ($x/y_c \leq 40$). For the lower blowing ratio ranges, the small rate of reduction of film cooling effectiveness with S is due to the fact that the degree of mixing of the film jet with the mainstream has already been very substantial at this stage, and further increase of swirl number does not significantly increase the mixing rate. Farther downstream the rate of reduction of film cooling effectiveness with S becomes small and is almost the same among various blowing ratios because the film jet structure has already been substantially destroyed at this stage.

Various correlation equations of film cooling effectiveness for film cooling over a flat plate have been reported that do not account for the effect of swirling flow. The usual dimensionless parameters used in the correlation were the blowing ratio and the dimensionless distance x/y_c. With the account of the effect of swirling flow the additional dimensionless parameter, that is, the swirl number, is selected and included in the correlation. Two different correlation equations have been obtained for $M \leq 1$ and $M \geq 1$, and the comparisons with data are shown in Figs. 8(*a*) and 8(*b*).

For $0.5 \leq M \leq 1.0$, $0.1 \leq S \leq 0.6$, $20 < x/y_c \leq 60$, the least-square fit of data is

$$\eta = 2.18\,[S^{1.18} M^{-2.20} (x/y_c)^{1.40}]^{-0.5} \tag{2}$$

For $1.0 \leq M \leq 1.75$, $0.1 \leq S \leq 0.6$, $30 \leq x/y_c \leq 80$, the best fit of the data is

$$\eta = 1.73\,[S^{0.86} M^{-1.50} (x/y_c)^{1.18}]^{-0.5} \tag{3}$$

Both correlation equations indicate that by accounting for the swirl effect the film cooling effectiveness significantly increases with blowing ratio and decreases with swirl number.

4 Conclusion

Weak swirling flow has a significant effect on the film cooling performance. The swirl flow and turbulence intensity generated by the swirler can significantly increase the mixing rate of a film jet with the mainstream and reduce the cooling effectiveness, especially at the near slot region. At far downstream locations a complete mixing of film jet with swirl flow can be concluded from the temperature distribution and adiabatic wall temperature measurements. The swirl flow can stabilize the flow and reduce the mixing rate of the film jet with the mainstream so that film cooling effectiveness can maintain a constant value. The magnitude of film cooling effectiveness at this stage depends on the thermal energy available from the film jet (blowing ratio). The experimentally determined film cooling effectiveness can be correlated in terms of relevant dimensionless parameters.

Acknowledgments

This research was sponsored by the National Science Council of Taiwan under contract No. NSC75-0401-E006-19. The authors would like to thank Dr. W. Shy for his help in correcting the English of the manuscript during the earlier revision process. The authors are also indebted to Mr. T. L. Kung who has carefully redrawn all of the figures in this report.

References

Beer, J. M., and Chigier, N. A., 1972, *Combustion Aerodynamics*, Wiley, New York, pp. 100–146.

Burns, W.-K., and Stollery, J. L., 1969, "The Influence of Foreign Gas Injection and Slot Geometry on Film Cooling Effectiveness," *International Journal of Heat and Mass Transfer*, Vol. 12, pp. 935–951.

Goldstein, R. J., 1971, "Film Cooling," in: *Advances in Heat Transfer*, Vol. 7, J. P. Hartnett and T. F. Irvine, Jr., eds., Academic Press, New York, pp. 321–379.

Goldstein, R. J., Eckert, E. R. G., Chiang, H. D., and Elovic, E., 1985, "Effect of Surface Roughness on Film Cooling Performance," ASME *Journal of Engineering for Gas Turbines and Power*, Vol. 107, pp. 111–116.

Gouldin, F. C., Depsky, J. S., and Lee, S. L., 1985, "Velocity Field Characteristics of a Swirling Flow Combustor," *AIAA Journal*, Vol. 23, No. 1, pp. 95–102.

Hwang, W. B., 1986, "Film Cooling Performance With Presence of Weak Swirling Flow," M. S. Thesis, National Cheng Kung University, Taiwan.

Kacker, S. C. and Whitelaw, J. H., 1967, "The Dependence of Impervious Wall Effectiveness of a Two-Dimensional Wall Jet on the Thickness of the Upper Lip Boundary Layer," *International Journal of Heat and Mass Transfer*, Vol. 10, pp. 1623–1624.

Kacker, S. C., and Whitelaw, J. H., 1968, "The Effect of Slot Height and Slot Turbulence Intensity on the Effectiveness of the Uniform Density, Two-Dimensional Wall Jet," ASME *Journal of Heat Transfer*, Vol. 90, pp. 469–475.

Ko, S. Y., and Liu, D. Y., 1980, "Experimental Investigations on Effectiveness, Heat Transfer Coefficient, and Turbulence of Film Cooling," *AIAA Journal*, Vol. 18, No. 8, pp. 907–912.

Lefebvre, A. H., 1983, *Gas Turbine Combustion*, Hemisphere Publishing Corp., Washington, D.C.

Lilley, D. G., 1977, "Swirl Flows in Combustion: A Review," *AIAA Journal*, Vol. 15, No. 8, pp. 1063–1078.

Marek, C. J., and Tacina, R. R., 1975, "Effect of Free-Stream Turbulence on Film Cooling," NASA TN D-7958.

Nina, M. N. R., and Whitelaw, J. H., 1971, "The Effectiveness of Film Cooling With Three-Dimensional Slot Geometries," ASME *Journal of Engineering for Power*, Vol. 93, pp. 425–430.

Seban, R. A., and Back, L. H., 1962, "Effectiveness and Heat Transfer for a Turbulent Boundary Layer With Tangential Injection and Variable Free-Stream Velocity," ASME *Journal of Heat Transfer*, Vol. 84, pp. 235–244.

Simon, F. F., 1986, "Jet Model for Slot Film Cooling With Effect of Free-Stream and Coolant Turbulence," NASA Tech Paper 2655.

Sivasegaram, S., and Whitelaw, J. H., 1969, "Film Cooling Slots: The Importance of Lip Thickness and Injection Angle," *Journal of Mechanical Engineering Science*, Vol. 11, No. 1, pp. 22–27.

Journal of Turbomachinery

Technical Briefs

Predictions of Aerodynamic Performance of Wells Turbines From Aerofoil Data

S. Raghunathan,[1] T. Setoguchi,[2] and K. Kaneko[3]

Data from Wells turbine tests are correlated with two-dimensional aerofoil data. The correlations show that the performance of the Wells turbine can be predicted from wind-tunnel data of aerofoils.

Nomenclature

A_a = annular area $= (\pi D_t^2/4)\,(1-h^2)$
A_b = blade plane from area $l \times c$
AR = blade aspect ratio $= l/c$
c = chord length
C_d = blade drag coefficient $= D/\frac{1}{2}\rho V^2 A_b$
C_l = blade lift coefficient $= L/\frac{1}{2}\rho V^2 A_b$
C_T = blade chordwise force coefficient $= C_l \sin\alpha - C_d \cos\alpha$
C_x = blade normal force coefficient $= C_l \cos\alpha + C_d \sin\alpha$
C_{xo} = value of C_x corresponding to isolated aerofoil in two-dimensional flow
$\dot{C}_x$ = normal force curve slope $= dC_x/d\alpha$
$\dot{C}_{xo}$ = value of $\dot{C}_x$ corresponding to isolated aerofoil in two-dimensional flow
D = drag force
$D_{t,h}$ = turbine tip diameter, hub diameter
h = hub-to-tip ratio $= D_h/D_t$
l = blade height
L = lift force
n = number of blades
M = Mach number
Q = volume flow rate through the turbine
Δp = pressure drop across rotor
p^* = nondimensional pressure drop $= \Delta p/\rho\omega^2 D_t^2$
Re = blade-chord Reynolds number $= U_t\, c/\nu$
T_u = turbulence level
U, U_t = mean peripheral velocity, tip velocity
V = relative velocity $= \sqrt{U+V_x}$
V_x = axial airflow velocity
W = power output
W^* = nondimensional power output $= W/\rho\omega^2 D_t^5$
α = angle of incidence
ϕ = mean flow coefficient $= V_x/U$
η = efficiency $= W/(\Delta p \cdot Q)$
σ = turbine solidity $= 2nc/\pi\, D_t(1+h)$
ω = angular velocity
ρ = air density
ν = kinematic viscosity of air

Subscripts

0 = isolated aerofoil in two-dimensional flow
M = maximum value
s = stall value

1 Introduction

The Wells turbine is a self-rectifying air turbine. It has an application in wave-energy devices that use the principle of an oscillating water–air column. In such wave-energy devices a water column oscillating due to wave motion is used to drive an oscillating air column, which can be converted into mechanical energy by a Wells turbine, which has symmetric aerofoil blades with a stagger angle of 90 deg, as shown in Fig. 1. For this turbine the direction of tangential force coefficient C_T and therefore torque is independent of the direction of the oscillating air column. There are several reports describing the performance of the Wells turbine. For example see Raghunathan et al. (1981, 1985), Gato et al. (1984), and Inoue et al. (1986). The performance of the Wells turbine can be predicted from experimental data of an isolated aerofoil in two-dimensional flow by applying a correction factor for the mutual interference between blades. The correction factor is based on potential flow analysis of blades in two-dimensional cascade with 90 deg stagger angle (Grant et al., 1981; Gato et al., 1984; Raghunathan et al., 1985). The object of this note is to correlate the available experimental data from the Wells turbine tests with wind-tunnel data of isolated aerofoils in two-dimensional flow. The data for correlation are primarily based on tests on the Wells turbine without guide vanes.

[1]Reader, Aeronautical Engineering, Queen's University, Belfast, Northern Ireland, United Kingdom.
[2]Associate Professor, Department of Mechanical Engineering, Saga University, Saga, Japan.
[3]Professor, Department of Mechanical Engineering, Saga University, Saga, Japan.

Contributed by the Advanced Energy Systems Division for publication in the JOURNAL OF TURBOMACHINERY. Manuscript received by the Advanced Energy Systems Division September 21, 1988.

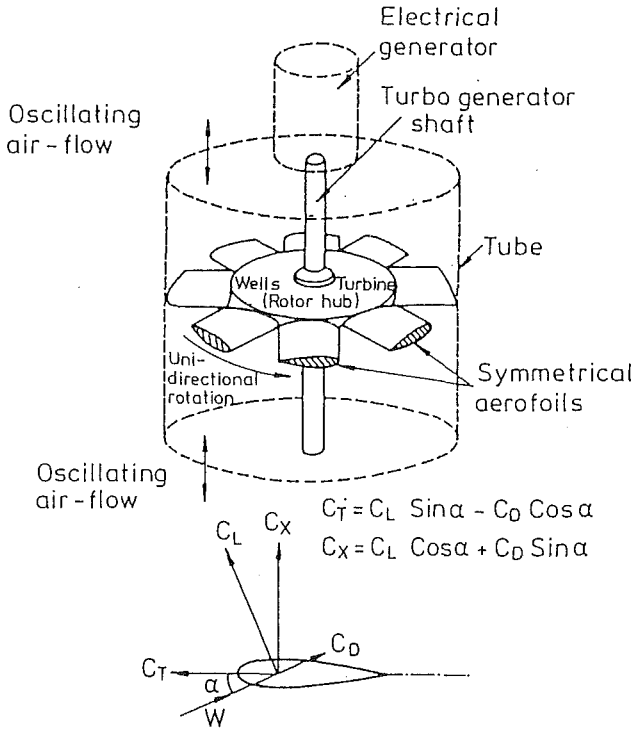

Fig. 1 Schematic diagram of Wells turbine

2 Performance Related to Aerodynamic Forces on the Blades

The axial force F_x and the power output W for the Wells turbine can be expressed in terms of mean aerodynamic force coefficients for the blades as

$$F_x = nC_x \tfrac{1}{2}\rho V^2 A_b \tag{1}$$

$$W = nC_T \tfrac{1}{2}\rho V^2 A_b U \tag{2}$$

and

$$F_x = \Delta p A_a \tag{3}$$

The nondimensional pressure drop p^* and nondimensional power output W^* can be expressed as

$$p^* = \Delta p/(\rho\omega^2 D_t^2) \tag{4}$$

and

$$W^* = W/(\rho\omega^3 D_t^5) \tag{5}$$

with assumptions that the absolute velocity of airflow at the inlet to the turbine is axial and invariant with the radius and the blades are of constant chord along the radius. Equations (1)–(5) can be reduced to

$$p^* = \frac{1}{32} C_x \sigma (1+h)^2 (1+\phi^2) \tag{6}$$

and

$$W^* = \frac{\pi}{512} C_T \sigma (1+h)^3 (1-h^2)(1+\phi^2) \tag{7}$$

where the mean tangential and axial aerodynamic force coefficients C_T and C_x, respectively, are functions of several parameters.

$$\left.\begin{matrix} C_R \\ C_x \end{matrix}\right\} = fn(M, \mathrm{Re}, \phi, \sigma, AR, T_u) \tag{8}$$

The aerodynamic efficiency can be expressed as

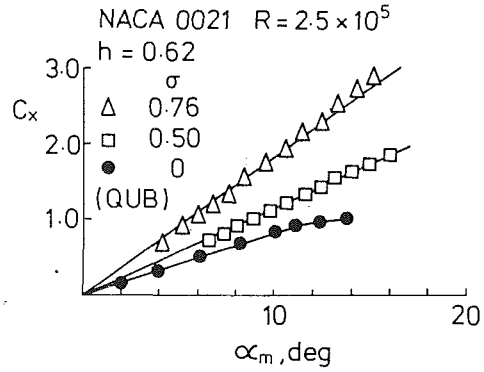

Fig. 2(a) Variation of C_x with α

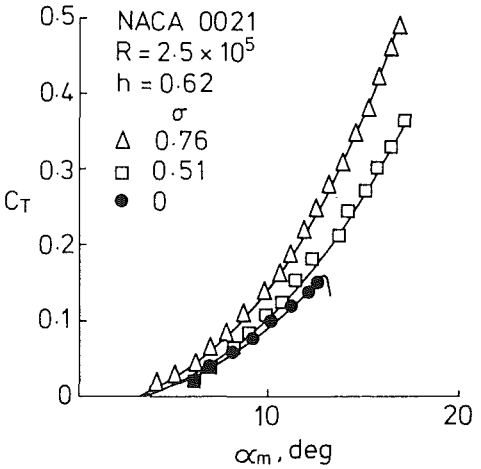

Fig. 2(b) Variation of C_T with α

$$\eta = \frac{C_T}{C_x}\left(\frac{1}{\phi}\right) \tag{9}$$

3 Correlations With Wind-Tunnel Data

Typical variation of C_x and C_t with mean airflow incidence to the blades $\alpha(\tan^{-1}\phi)$ based on the experiments of Raghunathan et al. (1983) are shown in Figs. 2(*a*) and 2(*b*). The experimental data are based on pressure differences measured across the rotor with pressure tappings on the turbine inlet and outlet duct. The results shown here are for a turbine with NACA0021 blade, $h = 0.62$, $\mathrm{Re} = 2.5 \times 10^5$, and $\sigma = 0.5$ and 0.76. Also shown in these figures are the results of two-dimensional wind-tunnel tests of isolated aerofoils based on the experiments of Raghunathan et al. (1988). Both the turbine and wind-tunnel results show a linear variation of C_x with α for incidences up to stall angle. The C_T versus α curves are nonlinear and for small angles of incidence the values of C_T are negative. The negative region corresponds to power absorption in a cycle, which, however, is only a small fraction of total power. It is observed from these figures that at any given airflow incidence, the aerodynamic forces increased with turbine solidity.

For a given value of σ the axial force curve slope for the turbine blades is given by $\dot{C}_X = (dC_x/d\phi)$ and this value is normalized with respect to the corresponding value for an isolated aerofoil in two-dimensional flow $\dot{C}_{xo}$. The calculated values of the ratio from the test results of Raghunathan et al. (1981, 1983, 1985), Inoue et al. (1986a, 1986b), Suzuki et al. (1985), Tagori et al. (1987), Gato et al. (1988), and Grant et al. (1981) are plotted against solidity σ in Fig. 3. The corresponding aerofoil data for these calculations are obtained from the work of Jacobs et al. (1937) and Raghunathan et al. (1988).

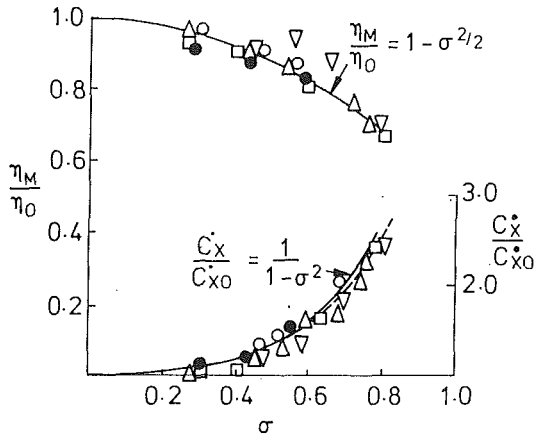

Prediction ---- Weinig
Experiments

	Profile	R	h	Ref
□	NACA 0021	2.5×10^5	0.5	Raghunathan et al
○	"	"	0.62	"
Δ	"	"	0.75	"
●	NACA 0012	5.6×10^5	0.5	Gato et al
▽	NACA 0015	2×10^5	0.7	Inoue et al

Fig. 3 Effect of solidity on axial force curve slope and efficiency

Also shown in the figure is the prediction based on the analysis of Weinig (1935). Considering that the data are taken from several experimental rigs, the correlation between $(\dot{C}_x/\dot{C}_{xo})$ and σ, within the range of test Reynolds number, is remarkable. This correlation can be expressed as

$$\dot{C}_x/\dot{C}_{xo} = 1/(1-\sigma^2) \tag{10}$$

This correlation of experimental data agrees well with the prediction based on the potential flow method of Weining (1935).

Also shown in Fig. 3 are the calculated values of maximum turbine efficiency from η_M equation (4) normalized with respect to the corresponding two-dimensional aerofoil efficiency η_o. Once again there is good correlation between (η_M/η_o) and σ, which can be expressed as

$$\eta_M/\eta_o = 1 - \sigma^2/2 \tag{11}$$

and within the Reynolds number of the tests both correlations are not very sensitive to turbine hub-to-tip ratio h or aerofoil profile. A Wells turbine performance can therefore be predicted, with reasonable accuracy, from two-dimensional aerofoil data using equations (1), (5), and (6).

Figure 4 shows the present prediction for the variation of aerodynamic efficiency with the flow coefficient ϕ_t for a turbine of $\sigma = 0.59$ and $\mathrm{Re} = 5.6\times10^5$ compared with the prediction and experimental results of Gato et al. (1988). It can be observed that the present correlation agrees favorably with the predictions and experimental results of Gato et al. (1988).

The scale effects on the turbine maximum efficiency η_M are shown in Fig. 5. The figure includes experimental data from several turbine tests, predictions for a Wells turbine with NACA0018 aerofoil blades (solid line) and predictions based on a scaling law for turbines in general (NASA SP290, 1972) given by

$$(1-\eta_1)/(1-\eta_2) = A + B(\mathrm{Re}_2/\mathrm{Re}_1)^{0.2} \tag{12}$$

(dotted line). Here the experimental data are adjusted for a constant solidity of $\sigma = 0.67$, which will have self-starting characteristics for a Wells turbine (Raghunathan et al., 1981).

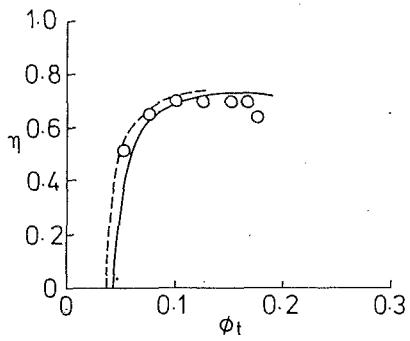

NACA 0012 Aerofoil profile
$R = 5.6\times10^5$ $\sigma = 0.59$
—— Present prediction
---- Prediction Gato et al
○ Expt "

Fig. 4 Comparison of present correlation for efficiency with other predictions

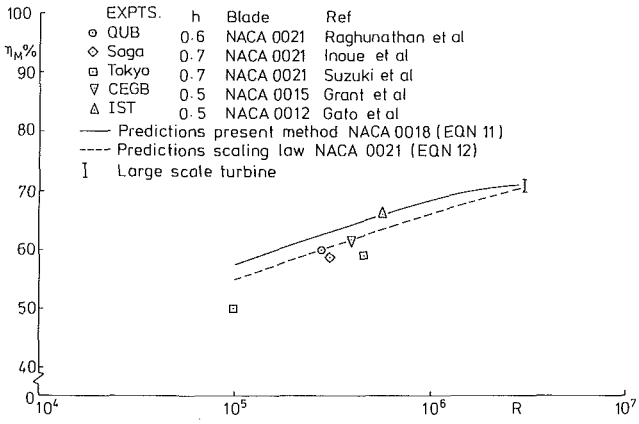

Fig. 5 Scale effects on maximum efficiency

It should be noted that the experimental results of Grant et al. (1981) are obtained from Wells turbine tests with guidevanes that affect the turbine's performance. The predictions by equation (6) are given for a turbine with NACA0018 blades only because the data for NACA0021 aerofoils over a wide range of Reynolds number are not available. In predicting using the scale law by equation (7), values of A and B are assumed as 0.4 and 0.6, respectively, and the bench work (η_1, Re_1) for scaling was the QUB results with NACA0021 aerofoil blades. It can be observed that there is a scatter in data at low Reynolds numbers. The discrepancy between the predictions and experimental data and the scatter of the experimental data at very low Reynolds numbers ($\mathrm{Re} \sim 10^5$) could be due to the following reasons. At low Reynolds number (small scale) tests the friction in the bearings and windage losses forms a significant part of the total power measured and the calculation of aerodynamic efficiency is subject to considerable errors. The prediction method based on equation (7) is based on the assumption that the boundary layer on the blades is essentially turbulent, which is unlikely at low Reynolds numbers. The predictions show that for a turbine of $\sigma = 0.67$, the maximum aerodynamic efficiency η_M for a large-scale Wells turbine ($\mathrm{Re} > 10^6$) can be 70 percent.

4 Conclusions

Some of the available experimental data from the Wells turbine tests, when correlated with two-dimensional aerofoil

tests, show that the performance of a Wells turbine can be predicted with reasonable accuracy from aerofoil data using simple correlations.

References

Gato, L. M. C., and Falcao, A. F. de O., 1984, "On the Theory of Wells Turbine," ASME JOURNAL OF ENGINEERING FOR GAS TURBINES AND POWER, Vol. 106, No. 3, pp. 628–633.

Gato, L. M. C., and Falcao, A. F. de O., 1988, "Aerodynamics of Wells Turbine," *Int. J. of Mechanical Sciences*, Vol. 30, No. 6, pp. 383–395.

Grant, R. J., Johnson, C. G., and Sturge, G. P., 1981, "Performance of a Wells Turbine for Use in a Wave Energy System," *IEE Conference*, No. 132, pp. 117–122.

Inoue, M., Kaneko, K., and Setoguchi, T., 1986a, "Studies on Wells Turbine for Wave Power Generator (Part 4)," *Bulletin of JSME*, Vol. 29, No. 250, pp. 117–1182.

Inoue, M., Kaneko, K., Setoguchi, T., and Raghunathan, S., 1986b, "Simulation of Starting Characteristics of the Wells Turbine," AIAA/ASME 4th Fluid Mechanics, Plasma Dynamics and Lasers Conference, Atlanta, GA, Paper No. 86-1122.

Jackobs, E. N., and Sherman, A., 1937, "Airfoil Section Characteristics Affected by Variation of Reynolds Number," NACA Report No. 586.

Raghunathan, S., Tan, C. P., Wells, N. A. J., and McIlhagger, D. S., 1981, "Efficiency, Starting Torque and Prevention of Runaway With Wells Self Rectifying Air Turbine," *Proc. Int. Conf. on Wave and Tidal Energy*, Cambridge, pp. 207–217.

Raghunathan, S., and Tan, C. P., 1983, "Aerodynamic Performance of Wells Turbine," *J. of Energy*, Vol. 7, No. 3, pp. 226–230.

Raghunathan, S., Tan, C. P., and Ombaka, O. O., 1985, "Performance of the Wells Self Rectifying Air Turbine," *The Aeronautical Journal*, Vol. 89, No. 890, pp. 369–379.

Raghunathan, S., Harrison, J. R., and Hawkins, B. D., 1988, "Thick Aerofoil at Low Reynolds Number and High Incidence," *J. of Aircraft*, Vol. 25, No. 7, pp. 669–671.

Suzuki, M., Arakawa, D., and Tagori, T., 1985, "Wells Turbine Flows on the Rotating Blades for Wave Power Generator," *Turbomachinery Society of Japan*, Vol. 5, No. 8, pp. 91–94.

Tagori, T., Arakawa, C., and Suzuki, M., 1987, "Estimation of Prototype Performance and Optimum Design of Wells Turbine," *Research on Natural Energy*, SPEY 20, Japan, pp. 127–132.

"Turbine Design and Applications," 1972, NASA SP290.

Weining, F., 1935, *Die Stromung um die Schaufeln von Turbomachinen*, Joh. Ambr. Barth, Liebzig, Federal Republic of Germany.

A Note on Efficiency Sensitivity to Tip Clearance Changes in Axial Flow Compressors

I. N. Moyle[1]

1 Introduction

The efficiency changes associated with tip clearance variations in axial compressors have frequently been described, or modeled, in terms of the flow losses in or around the tip gap. The models are calibrated from changes in experimental stage efficiency measured for the model evaluation or collected from other studies. These efficiency changes are frequently generated by cropping the blade or increasing the case radius in an otherwise constant stage configuration. The stage is typically operated on a constant-speed throttle line.

The ratio of observed efficiency change to normalized clearance gap change varies significantly for different compressors in the literature. Typical results, for mainly single stages, are shown in Fig. 1. The sensitivity (slope or $\Delta\eta/\Delta e/b$) magnitude varies from 0.75 to 2.25 around the one percent level in e/b for constant flow conditions in different compressors.

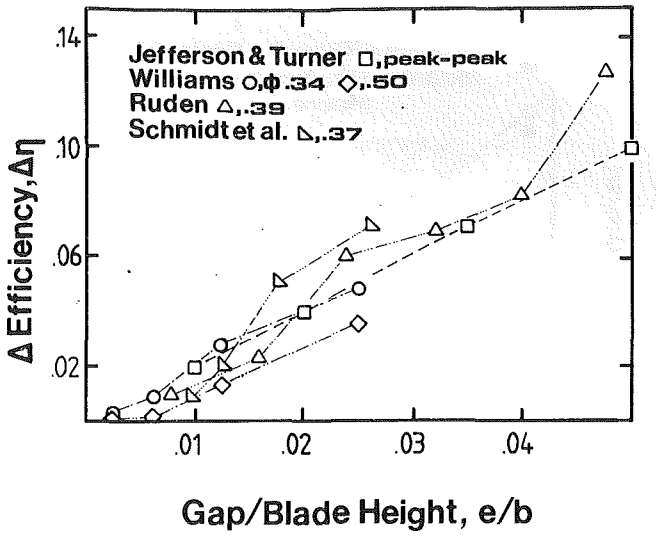

Fig. 1 Efficiency decrement at constant flow as a function of gap/blade height, derived from various studies; flow coefficient values are indicated in the legend

2 Analysis of Sensitivity Data

While attempting to correlate the sensitivity spread described, it was noted that the sensitivity also varied with flow rate or stage flow coefficient, Φ, in the same compressor. Consequently, a more general definition of the sensitivity was examined.

Definition Based on Losses. The primary effect of a clearance variation is a change in stage pressure rise at any flow rate. As this process can be thermodynamically characterized in terms of the shaft power converted into flow work per unit time and the power lost to inefficiencies, a general definition of the losses is given by

$$L = P - \Phi\Pi$$

where the lost work rate (L) plus the flow work rate ($\Phi\Pi$) equals the power input (P). The aggregate lost work rate can be related to the blade element loss coefficients by appropriate manipulation. For any change of compressor geometry from one configuration to another, for example from clearance 1 to clearance 2, the change in losses is given by

$$L_1 - L_2 = P_1 - P_2 - \Phi\Pi_1 + \Phi\Pi_2$$

and if the stage efficiency is introduced as $\eta = \Phi\Pi/P$, then the efficiency to loss relationship is

$$L_1 - L_2 = P_1 \cdot (1 - P_2/P_1 - \eta_1 + \eta_2 \cdot (P_2/P_1))$$

It is apparent from this formulation that the change in efficiency is not generally equivalent to the lost work rate change between two configurations. Alternatively, a change in efficiency only directly reflects a change in losses between two configurations when the efficiency change is determined at the same input power level, i.e., if $P_1 = P_2 = P$ then

$$(L_2 - L_1)/P = \eta_1 - \eta_2$$

3 Efficiency Sensitivity at Constant Power

The correlations of efficiency with gap/blade height shown in Fig. 1 result from determining efficiency differences, at

[1]Research Associate, Department of Aeronautics, Naval Postgraduate School, Monterey, CA 93943.

Contributed by the International Gas Turbine Institute and based on a paper presented at the 33rd International Gas Turbine and Aeroengine Congress and Exhibition, Amsterdam, The Netherlands, June 5–9, 1988. Manuscript received by the International Gas Turbine Institute December 22, 1987. Paper No. 88-GT-216.

tests, show that the performance of a Wells turbine can be predicted with reasonable accuracy from aerofoil data using simple correlations.

References

Gato, L. M. C., and Falcao, A. F. de O., 1984, "On the Theory of Wells Turbine," ASME JOURNAL OF ENGINEERING FOR GAS TURBINES AND POWER, Vol. 106, No. 3, pp. 628–633.

Gato, L. M. C., and Falcao, A. F. de O., 1988, "Aerodynamics of Wells Turbine," *Int. J. of Mechanical Sciences*, Vol. 30, No. 6, pp. 383–395.

Grant, R. J., Johnson, C. G., and Sturge, G. P., 1981, "Performance of a Wells Turbine for Use in a Wave Energy System," *IEE Conference*, No. 132, pp. 117–122.

Inoue, M., Kaneko, K., and Setoguchi, T., 1986a, "Studies on Wells Turbine for Wave Power Generator (Part 4)," *Bulletin of JSME*, Vol. 29, No. 250, pp. 117–1182.

Inoue, M., Kaneko, K., Setoguchi, T., and Raghunathan, S., 1986b, "Simulation of Starting Characteristics of the Wells Turbine," AIAA/ASME 4th Fluid Mechanics, Plasma Dynamics and Lasers Conference, Atlanta, GA, Paper No. 86-1122.

Jackobs, E. N., and Sherman, A., 1937, "Airfoil Section Characteristics Affected by Variation of Reynolds Number," NACA Report No. 586.

Raghunathan, S., Tan, C. P., Wells, N. A. J., and McIlhagger, D. S., 1981, "Efficiency, Starting Torque and Prevention of Runaway With Wells Self Rectifying Air Turbine," *Proc. Int. Conf. on Wave and Tidal Energy*, Cambridge, pp. 207–217.

Raghunathan, S., and Tan, C. P., 1983, "Aerodynamic Performance of Wells Turbine," *J. of Energy*, Vol. 7, No. 3, pp. 226–230.

Raghunathan, S., Tan, C. P., and Ombaka, O. O., 1985, "Performance of the Wells Self Rectifying Air Turbine," *The Aeronautical Journal*, Vol. 89, No. 890, pp. 369–379.

Raghunathan, S., Harrison, J. R., and Hawkins, B. D., 1988, "Thick Aerofoil at Low Reynolds Number and High Incidence," *J. of Aircraft*, Vol. 25, No. 7, pp. 669–671.

Suzuki, M., Arakawa, D., and Tagori, T., 1985, "Wells Turbine Flows on the Rotating Blades for Wave Power Generator," *Turbomachinery Society of Japan*, Vol. 5, No. 8, pp. 91–94.

Tagori, T., Arakawa, C., and Suzuki, M., 1987, "Estimation of Prototype Performance and Optimum Design of Wells Turbine," *Research on Natural Energy*, SPEY 20, Japan, pp. 127–132.

"Turbine Design and Applications," 1972, NASA SP290.

Weining, F., 1935, *Die Stromung um die Schaufeln von Turbomachinen*, Joh. Ambr. Barth, Liebzig, Federal Republic of Germany.

A Note on Efficiency Sensitivity to Tip Clearance Changes in Axial Flow Compressors

I. N. Moyle[1]

1 Introduction

The efficiency changes associated with tip clearance variations in axial compressors have frequently been described, or modeled, in terms of the flow losses in or around the tip gap. The models are calibrated from changes in experimental stage efficiency measured for the model evaluation or collected from other studies. These efficiency changes are frequently generated by cropping the blade or increasing the case radius in an otherwise constant stage configuration. The stage is typically operated on a constant-speed throttle line.

The ratio of observed efficiency change to normalized clearance gap change varies significantly for different compressors in the literature. Typical results, for mainly single stages, are shown in Fig. 1. The sensitivity (slope or $\Delta\eta/\Delta e/b$) magnitude varies from 0.75 to 2.25 around the one percent level in e/b for constant flow conditions in different compressors.

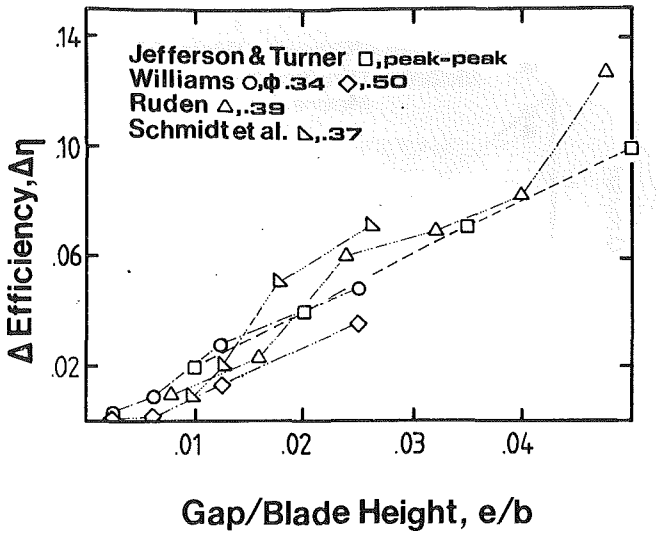

Fig. 1 Efficiency decrement at constant flow as a function of gap/blade height, derived from various studies; flow coefficient values are indicated in the legend

2 Analysis of Sensitivity Data

While attempting to correlate the sensitivity spread described, it was noted that the sensitivity also varied with flow rate or stage flow coefficient, Φ, in the same compressor. Consequently, a more general definition of the sensitivity was examined.

Definition Based on Losses. The primary effect of a clearance variation is a change in stage pressure rise at any flow rate. As this process can be thermodynamically characterized in terms of the shaft power converted into flow work per unit time and the power lost to inefficiencies, a general definition of the losses is given by

$$L = P - \Phi\Pi$$

where the lost work rate (L) plus the flow work rate ($\Phi\Pi$) equals the power input (P). The aggregate lost work rate can be related to the blade element loss coefficients by appropriate manipulation. For any change of compressor geometry from one configuration to another, for example from clearance 1 to clearance 2, the change in losses is given by

$$L_1 - L_2 = P_1 - P_2 - \Phi\Pi_1 + \Phi\Pi_2$$

and if the stage efficiency is introduced as $\eta = \Phi\Pi/P$, then the efficiency to loss relationship is

$$L_1 - L_2 = P_1 \cdot (1 - P_2/P_1 - \eta_1 + \eta_2 \cdot (P_2/P_1))$$

It is apparent from this formulation that the change in efficiency is not generally equivalent to the lost work rate change between two configurations. Alternatively, a change in efficiency only directly reflects a change in losses between two configurations when the efficiency change is determined at the same input power level, i.e., if $P_1 = P_2 = P$ then

$$(L_2 - L_1)/P = \eta_1 - \eta_2$$

3 Efficiency Sensitivity at Constant Power

The correlations of efficiency with gap/blade height shown in Fig. 1 result from determining efficiency differences, at

[1]Research Associate, Department of Aeronautics, Naval Postgraduate School, Monterey, CA 93943.

Contributed by the International Gas Turbine Institute and based on a paper presented at the 33rd International Gas Turbine and Aeroengine Congress and Exhibition, Amsterdam, The Netherlands, June 5–9, 1988. Manuscript received by the International Gas Turbine Institute December 22, 1987. Paper No. 88-GT-216.

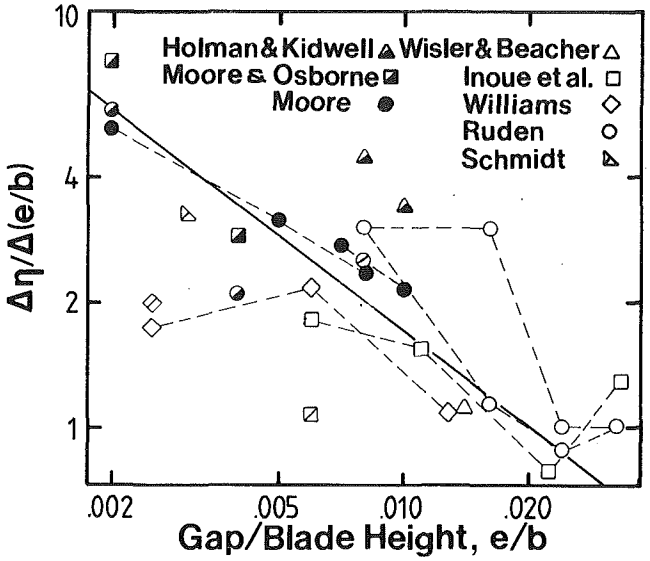

Fig. 2 Log-log correlation of constant power and peak-to-peak efficiency sensitivity to gap/blade height for high (solid symbols) and low-speed (open symbols) stages; peak-to-peak data are slashed diagonally

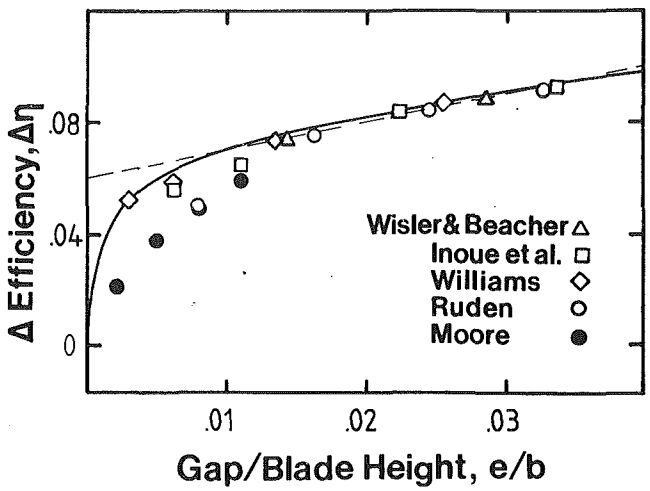

Fig. 3 Efficiency decrement correlation with gap/blade height developed by integration of the approximation to the data of Fig. 2 cross-plotted with test data

constant flow, over a range of clearance increments. In order to standardize the sensitivities, experimental data were plotted in a ΦΠ versus P graphic format and the efficiency decrements and clearance sensitivities determined at constant power. A detailed description of the procedure is given by Moyle (1988). Data from four low-speed compressor experimental programs are shown plotted on Fig. 2. The data are all for air compressors except Williams' stage, which was for water. High-speed data were also examined and are included in the figure.

Figure 2 is a log-log plot of sensitivity ($\Delta\eta/\Delta e/b$) versus gap/blade height (e/b). It is apparent from this figure that the high and low-speed data fall in a sloping band. The log sensitivity ($\Delta\eta/\Delta e/b$) can be roughly correlated with log (e/b) by a straight line of significant slope. The slope is obviously far from the horizontal line, which would be consistent with the linear $\Delta\eta$ versus e/b trend of Fig. 1. The slope uniformity implied that a relationship of the form

$$\Delta\eta/\Delta e/b = C(e/b)^{-a}$$

could be applied to the data, where C varies from compressor to compressor and a is generally constant for all the data. The C generates most of the scatter observed in the plot.

Correlation of the Sensitivity at Constant Power. The approximate straight line dependence of the log sensitivity data to log e/b shown on Fig. 2 can be integrated to yield the efficiency decrease with clearance at constant power. The curve (Fig. 3) shows an initially rapid increase in the efficiency decrement associated with the clearance very close to the wall and a gradual tapering-off of the decrement toward the limit of a 1 percent efficiency decrease for a 1 percent clearance increase, at clearances greater than one percent. This limiting curve is shown on the figure intersecting the $\Delta\eta$ axis at 0.06.

The constant power efficiency curve strictly represents the lost work rate change associated with a clearance change. The expression for the approximate curve shown in Fig. 3 is

$$\Delta\eta = 0.214(e/b)^{0.227} - 0.005$$

It should be stressed that this correlation is an approximation to the data sample addressed and it is expected it could be refined with more data over a wider range of machines and clearances.

4 Conclusion

It can be seen that the general form of the constant power sensitivity correlation with gap/blade height suggests that the losses increase very rapidly at small clearance levels and that different geometries or flow conditions of the compressors do not affect this loss trend significantly. The efficiency decrement, at constant power, increases less rapidly with increasing clearance gap. This observed trend is not predicted by many of the models that describe the efficiency change as a function of tip gap.

References

Holman, F. F., and Kidwell, J. R., 1975, "Effects of Casing Treatment on a Small, Transonic Axial Flow Compressor," ASME Paper No. 75-WA/GT-5.

Inoue, M., Kuroumaru, M., and Fukahara, M., 1986, "Behavior of Tip Leakage Flow Behind an Axial Compressor Rotor," ASME *Journal of Engineering for Gas Turbines and Power*, Vol. 108, pp. 7–14.

Moore, R. D., 1982, "Rotor Tip Clearance Effects on Overall Blade-Element Performance of Axial-Flow Transonic Fan Stage," NASA TP-2049.

Moore, R. D., and Osborne, W. M., 1977, "Effects of Tip Clearance on Overall Performance of Transonic Fan Stage With and Without Casing Treatment," NASA TM-X-3479.

Moyle, I. N., 1988, "Analysis of Efficiency Sensitivity Associated With Tip Clearance in Axial Flow Compressors," ASME Paper No. 88-GT-216.

Ruden, P., 1944, "Investigation of Single Stage Axial Fans," NACA TM 1062 (originally published in 1937 in German).

Schmidt, M. J. P., Agnew, B., and Elder, R. L., 1987, "Tip Clearance Flows—Part II, Study of Various Models and Comparison With Test Results," presented at the Eighth ISABE Conference, Cincinnati, OH, June.

Williams, A. D., 1960, "The Effect of Tip Clearance Flows on Performance of Axial Flow Compressors," A. E. Thesis, California Institute of Technology, Pasadena, CA.

Wisler, D. C., and Beacher, B. F., 1986, "Improved Compressor Performance Using Recessed Clearance (Trenches) Over the Rotor," AIAA Paper No. 86-1745.